

**Rotary Balance Data for a Typical
Single-Engine General Aviation
Design for an Angle-of-Attack
Range of 8° to 90°**

I - Influence of Airplane Components for Model D

John N. Ralston

CONTRACT NAS1-16205
MARCH 1983

NASA

**Rotary Balance Data for a Typical
Single-Engine General Aviation
Design for an Angle-of-Attack
Range of 8° to 90°**

I - Influence of Airplane Components for Model D

John N. Ralston
Bihrl Applied Research, Inc.
Jericho, New York

Prepared for
Langley Research Center
under Contract NAS1-16205



National Aeronautics
and Space Administration

**Scientific and Technical
Information Branch**

1983

SUMMARY

The influence of airplane components, as well as wing location and tail length, on the rotational flow aerodynamics is discussed for a 1/6-scale general aviation airplane model. The airplane was tested in a build-up fashion (i.e., body, body-wing, body-wing-vertical, etc.) in the presence of two wing locations and two body lengths. Data were measured, using a rotary balance, over an angle-of-attack range of 8° to 90° , and for clockwise and counter-clockwise rotations covering an $\Omega b/2V$ range of 0 to 0.9.

The vertical tail, in the absence of the low horizontal tail, provided yaw damping through 90° angle of attack. The addition of the horizontal tail, in the presence of a low wing, decreased the vertical tail's damping effectiveness above 30° angle of attack, such that the damping was entirely negated by 40° angle of attack and the vertical tail became propelling beyond an angle of attack of 40° . This adverse horizontal tail interference was reduced or eliminated between 30° and 60° angle of attack by vertically relocating the wing. Shortening the tail moment arm also significantly minimized the adverse horizontal tail interference at low rotation rates up to 90° angle of attack. The influence of these geometric changes on horizontal tail interference would not be predicted by existing tail design criterion and could only be discerned through rotary balance testing.

The wing and horizontal tail determined the airplane's pitch characteristics both statically and with rotation. Relocating the wing

or changing the aft body length produced a static pitch change, but had little effect on the rotational characteristics. This airplane's rolling moment properties were solely a function of the wing geometry.

INTRODUCTION

The NASA Langley Research Center is conducting a broad general aviation stall/spin research program, which includes spin-tunnel and free-flight radio-control model tests, as well as full-scale flight tests for a number of configurations typical of light, general aviation airplanes. As a part of this effort, rotary balance tests were conducted in the Langley Spin Tunnel to establish a rotational flow aerodynamic base for analysis of model and full-scale flight results.

Rotary balance data were obtained for a representative, single-engine, general aviation model, referred to as model D. The test results were divided into three areas, each of which is discussed in a separate report. The aerodynamic effectiveness of the controls and their influence on predicted spin modes are discussed in reference 1. Reference 2 discusses the effect of horizontal tail location in the presence of each of two wing locations and two body lengths. This report presents the influence of each airplane component, as well as body length and wing location, on the rotational aerodynamic characteristics. The Appendix in each of these reports contains all the data measured during the subject studies.

SYMBOLS

The units for physical quantities used herein are presented in the International System of Units (SI) and U.S. Customary Units. The measurements were made in the U.S. Customary Units, equivalent dimensions were determined by using the conversion factors given in reference 3.

b	wing span, m (ft)
c	mean aerodynamic chord, cm (in.)
C_L	lift-force coefficient, $\frac{\text{Lift force}}{qS}$
C_N	normal-force coefficient, $\frac{\text{Normal force}}{qS}$
C_A	axial-force coefficient, $\frac{\text{Axial force}}{qS}$
C_Y	side-force coefficient, $\frac{\text{Side force}}{qS}$
C_l	rolling-moment coefficient, $\frac{\text{Rolling moment}}{qSb}$
C_m	pitching-moment coefficient, $\frac{\text{Pitching moment}}{qSc}$
C_n	yawing-moment coefficient, $\frac{\text{Yawing moment}}{qSb}$
q	free-stream dynamic pressure, N/m ² (lb/ft ²)
S	wing area, m ² (ft ²)
V	free-stream velocity, m/sec (ft/sec)
α	angle of attack, deg
β	angle of sideslip, deg
Ω	angular velocity about spin axis, rad/sec
$\Omega b/2V$	spin coefficient, positive for clockwise spin

δ_a aileron deflection, positive when right
aileron is down, $(\delta_{a_{right}} - \delta_{a_{left}})/2$, deg

δ_H horizontal tail deflection, positive when
trailing edge is down, deg

δ_r rudder deflection, positive when trailing
edge is to left, deg

Abbreviations:

cg center of gravity

SR spin radius

TEST EQUIPMENT

A rotary balance measures the forces and moments acting on a model while it is subjected to rotational flow conditions. Historical background for this testing technique is discussed in reference 4. A photograph and sketch of the rotary balance apparatus installed in the Langley Spin Tunnel are shown in figures 1 and 2, respectively. The system's rotary arm, which rotates about a vertical axis at the tunnel center, is supported by a horizontal boom and is driven by a motor mounted external to the test section.

A NASA six-component strain gauge balance, affixed to the bottom of the rotary balance apparatus and mounted inside the model, is used to measure the normal, lateral, and longitudinal forces, and the yawing, rolling, and pitching moments acting about the model body axis. Controls located outside of the tunnel test section are used to activate motors on the rotary rig, which position the model to the desired attitude. The angle-of-attack range of the rig is 0° to 90° , and the sideslip angle

range is $\pm 15^\circ$. Spin radius and lateral displacement motors are used to position the moment center of the balance on, or at a specific distance from, the spin axis. (This is done for each combination of angle of attack and sideslip angle.) It is customary to mount the balance to the model such that its moment center is at the location about which the aerodynamic moments are desired. Electrical currents from the balance and to the motors on the rig are conducted through slip rings. Figure 2 describes various components of the rig and shows how the rig is positioned in angle of attack and sideslip.

The system is capable of rotating up to 90 rpm in either direction. A range of $\Omega b/2V$ values can be obtained by adjusting rotational speed and/or tunnel air flow velocity. (Static aerodynamic forces and moments are obtained when $\Omega=0$.)

The data acquisition, reduction, and presentation system is composed of a 12-channel scanner/voltmeter, a mini-computer with internal printer, a plotter, and a CRT display. This equipment permits data to be presented via on-line digital print-outs and/or graphical plots.

TEST PROCEDURES

Rotary aerodynamic data are obtained in two steps. First, the inertial forces and moments (tares) acting on the model at different attitudes and rotational speeds must be determined. Ideally, these inertial terms would be obtained by rotating the model in a vacuum, thus eliminating all aerodynamic forces and moments. As a practical approach,

this is approximated closely by enclosing the model in a sealed spherical structure, which rotates with the model without touching it, such that the air immediately surrounding the model is rotated with it. As the rig is rotated at the desired attitude and rate, the inertial forces and moments generated by the model are measured and stored on magnetic tape for later use.

The second step is to remove the enclosure and record force and moment data with the air on. The tares, measured in step one, are then subtracted from these data, leaving only the aerodynamic forces and moments, which are converted to coefficient form and stored on magnetic tape.

MODEL

A 1/6-scale model, representing a single-engine general aviation airplane, was constructed from foam/fiberglass and aluminum. A three-view drawing of the low-wing, short-body model is shown in figure 3. As shown, for these tests the horizontal tail was located in a low position, referred to as tail location 2 in reference 2. It was possible to mount the wing in either a low or high position, as shown in figures 3 and 4, respectively. The body length could be varied by using an alternate aft fuselage section. For the long-body configuration, the vertical tail was moved aft and the fuselage was faired smoothly to the rudder, whose span was increased to the bottom of the fuselage, as shown in figure 5. For both body configurations, the vertical-horizontal tail

relationship remained unchanged. Dimensional characteristics of the model are given in Table I. A photograph of the model installed on the rotary balance in the Langley Spin Tunnel is presented in figure 1.

TEST CONDITIONS

The tests were conducted in the spin tunnel at a tunnel velocity of 7.62 m/sec (25 ft/sec), which corresponds to a Reynolds number of 128,000 based on the model mean aerodynamic chord. All the configurations were tested through an angle-of-attack range of 8° to 90° , at a zero sideslip angle. For angles of attack above 30° , the spin axis passed through the cg location of 0.25c, and 91.4cm(36 in.) forward (full-scale) of the cg for angles of attack below 35° . Consequently, data were obtained for both a 0 and 91.4 cm spin radius at 30° and 35° angles of attack. At each spin attitude, measurements were obtained for nominal $\Omega b/2V$ values of 0.1, 0.2, 0.3, 0.4, 0.5, 0.6, 0.7, 0.8, and 0.9, in both clockwise and counter clockwise directions, as well as for $\Omega b/2V=0$ (static value).

DATA PRESENTATION

All data measured for this study are presented in the Appendix. Table II identifies the configurations tested and their corresponding appendix figure numbers. The body-axis aerodynamic coefficients, plotted as functions of $\Omega b/2V$, are presented for each configuration in six

sequentially numbered figures in the following order: C_n , C_l , C_m , C_N , C_Y , C_A . Each figure, in turn, consists of four pages, which present the subject aerodynamic coefficient vs $\Omega b/2V$ for the following angles of attack and spin radii:

- a) $\alpha = 8, 10, 12, 14, 16$ deg $SR = 91.4\text{cm (36 in.) full scale}$
- b) $\alpha = 18, 20, 25, 30, 35$ deg $SR = 91.4\text{cm (36 in.) full scale}$
- c) $\alpha = 30, 35, 40, 45, 50$ deg $SR = 0$
- d) $\alpha = 55, 60, 70, 80, 90$ deg $SR = 0$

All moment data are presented for a cg position of 0.25c.

In addition to the data presented in the appendix, figures 6 through 18 utilize some of the same data replotted for comparison of various configurations' moment characteristics. These plots are referenced in the following discussion to illustrate the influence of components, wing location, and body length.

DISCUSSION

The variation of the three aerodynamic moments with rotation determines the existence and nature of an airplane's spin modes. The source of these moment characteristics can be determined by examining the contribution of each airplane component.

For analysis purposes, the rolling and yawing moment coefficients will frequently be referred to as damped or propelling with rotation. Moment data lying in the second and fourth quadrants, when plotted as a function of $\Omega b/2V$, are damped for a left and right spin respectively.

Conversely, data lying in the first and third quadrants are undamped (autorotative).

Effect of Components

To demonstrate the contribution of each airplane component to the three aerodynamic moments, component buildup plots are presented in figures 6 through 8 for the low wing, long body, low horizontal tail (tail 2) configuration. This horizontal tail location was chosen for component testing because it was found to greatly influence the vertical tail's yawing moment contribution, as discussed in reference 2.

Pitch Characteristics:

The influence of each component on pitching moment is presented in figure 6 for selected angles of attack. The body's contribution to the static pitching moment coefficient is small, with little variation due to rotation, as seen in figure 6. The addition of the wing produces a negative C_m increment that becomes more negative with angle of attack and rotation. The addition of the horizontal tail produces a significant static nose-down increment, as expected, and the static pitching moment becomes increasingly more nose-down with increasing angle of attack. The horizontal tail's negative C_m contribution also increases non-linearly with rotation for angles of attack above 20° . This increase due to rotation is approximately the same as that of the wing. Additional analysis concerning the effects of the horizontal tail location on pitching moment is presented for this aircraft in reference 2.

Roll Characteristics:

Figure 7 presents the component buildup plots of the rolling moment coefficient versus rotation rate. The body alone is neutral in roll for all angles of attack. As seen in this figure, the addition of the wing defines the total airplane's rolling moment characteristics, the vertical and horizontal tails contributing very little C_l , as is normally the case.

At pre-stall angles of attack (e.g. figure 7a), the rolling moment is damped for all rotation rates. Following stall and persisting through 25° angle of attack, the rolling moment is propelling at the lower $\Omega b/2V$ values, as shown in figure 7b at 20° . Autorotative rolling moments in the immediate post-stall angle of attack region are frequently experienced and may result in a rolling departure from controlled flight. These autorotative moments are caused by asymmetric stalling of the rotating wing. At 30° angle of attack (figure 7c), the rolling moment is damped with rotation, but by 40° and beyond (figures 7d-7g), the rolling moment is propelling for low rotation rates.

Yaw Characteristics:

Figure 8 presents the component buildup plots of yawing moment coefficient versus rotation rate. The body studied herein generates virtually no yawing moment at any angle of attack or rotation rate. The wing, however, does influence the yawing moment characteristics with rotation. The influence of the wing on yawing moment results from the angle of attack variation along the rotating wing, the angle of attack

increasing inboard of the fuselage and decreasing outboard. The wing's axial force component varies as a function of the wing angle of attack, as shown in figure 9, where positive C_A indicates a force aft along the body axis. The difference in axial force between the two wing semi-spans produced by the angle of attack variation on a rotating wing, in turn, produces a yawing moment. If the inboard wing produces less axial force than the outboard wing, a damped yawing moment results, as seen at low $\Omega b/2V$ for angles of attack below stall (e.g. figure 8a). At higher rotation rates, a significant portion of the inboard wing is above stall in a region of increasing axial force (figure 9), and a loss of damping results. As shown in figure 9, in the immediate post-stall angle-of-attack range, the inboard wing, operating at a higher angle of attack produces more positive axial force than the outboard wing and, therefore, a propelling yawing moment, as seen in figure 8b at 20° . At higher angles of attack, damped yawing moments can again result if the inboard wing produces less axial force than the outboard wing.

The vertical tail provides damped yawing moment increments that generally increase with increasing angle of attack and increasing rotation rate in the absence of a horizontal tail, as shown in figure 10. However, the addition of the low horizontal tail adversely influences the vertical tail's yaw damping contribution above 30° angle of attack (figure 8c). By 40° (figure 8d), the presence of the horizontal tail completely negates the large damping contribution of the vertical tail. Beyond 40° (see figures 8e-8g), the presence of the horizontal tail results in a propelling vertical tail contribution. The total airplane

yawing moment consequently becomes neutrally damped or autorotative for rotation rates between $\Omega b/2V$ values of ± 0.4 above 40° angle of attack. This phenomenon is apparently the result of an adverse pressure field generated by the outboard panel of the horizontal tail (see reference 4) and can be alleviated through the relocation of the horizontal tail with respect to the vertical, as discussed in reference 2.

Effect of Wing Location

The effect of wing location on the aircraft moment data is illustrated for the long body airplane configuration in figures 11 through 14.

Pitch Characteristics:

The variation of static pitching moment with angle of attack for the two wing locations tested is presented in figure 11. The only significant difference in the static pitching moment due to wing location is that the pitching moment for the high wing airplane varies more linearly with angle of attack in the stall region, whereas the low-wing configuration exhibits a large nose-down pitching moment break at stall.

The effect of rotation on the pitching moment coefficients for these two configurations is presented in figure 12 for selected angles of attack. The wing position did not significantly influence the rotational pitching moment characteristics.

Roll Characteristics:

Figure 13 presents a comparison of the high and low wing configuration rolling moment characteristics plotted as a function of $\Omega b/2V$. In general, below 25° angle of attack the location of the wing has a negligible effect on the rolling moment variation with rotation and has only a slight influence at angles of attack above 25° .

Yaw Characteristics:

The effect of rotation on the yawing moment for the high and low wing configurations is presented in figure 14. At 8° angle of attack (figure 14a), there is no difference between the yawing moment characteristics of the two wing locations. In the angle of attack region following stall, illustrated by figure 14b at 25° , the high wing configuration exhibits slightly more yaw damping than the low wing one. This difference in damping due to wing location becomes more pronounced with increasing angle of attack such that at 40° and 50° (see figures 14c and 14d, respectively) the high wing is significantly more damped than the low wing. Further increases in angle of attack diminish the damping advantage of the high wing location. At 60° angle of attack (figure 14e), for example, the damping advantage of the high wing is reduced, and by 80° (figure 14f), the high and low wing data are essentially the same.

For this airplane, therefore, wing location influences the airplane's post stall yaw damping characteristics. The mechanism of this phenomenon is indicated in figure 15. As illustrated at 50° and 80°

angle of attack, in the absence of the horizontal tail, the vertical tail contributes a significant damping increment which is unaffected by the vertical location of the wing. However, in the presence of the horizontal tail, the vertical tail's contribution is shown to be propelling rather than damping in this angle of attack region, as illustrated at 50° and 80° , for the low wing configuration. For the high wing location, the detrimental horizontal tail interference at 50° angle of attack is completely eliminated for $\Omega b/2V$ values less than 0.4. As one would suspect, wing location does not influence horizontal tail interference by 80° angle of attack. Therefore, although the vertical location of the wing does not directly influence the damping effectiveness of the vertical tail, it does so indirectly by influencing the level of adverse interference resulting from the presence of the horizontal tail. Obviously, the degree to which vertical wing location influences yaw damping depends on the level of adverse vertical tail interference associated with a given horizontal tail location which, as mentioned previously, was appreciable for the tail studied herein. The existing tail design criterion used for predicting satisfactory spin and recovery characteristics does not address this effect. Other shortcomings of the criterion are discussed in reference 5.

Effect of Body Length

The influence of tail moment arm on the three aerodynamic moment coefficients was determined by varying the body length, as shown in figure 4. Decreasing the body length decreases the nose down static

pitching moment contributed by the horizontal tail, as seen in figure 16. The variation of pitching moment with rotation is, however, essentially unchanged with body length at all angles of attack (compare appendix figure A57 with A15). Body length also had no influence on rolling moment (compare appendix figure A56 with A14).

At the lower angles of attack (8° to 40°), tail length has only a minimal influence on the yawing moment characteristics, as shown in figure 17a for 8° . At 50° angle of attack and beyond, however, the short tail length configuration exhibits somewhat improved yaw damping compared to the long tail length configuration for $\Omega b/2V$ values between ± 0.4 (see figure 17b and 17c at 60° and 90° angle of attack respectively). For higher rotation rates, the longer tail length provides better damping, as one would normally assume. The long tail configuration exhibits improved yaw damping for all rotation rates in the absence of the horizontal tail (figure 18). Apparently, the greater damping afforded by the increased moment arm is more than nullified by the resulting increase in horizontal tail interference also noted with the longer body. The beneficial effect realized at low rotation rates by shortening the tail approximately 10 percent is significant because the short tail length configuration is damped at all rotation rates for angles of attack between 50° and 90° , whereas the long tail length configuration is propelling at low rotation rates over the same angle of attack range. Again, the existing tail design criterion would not have properly predicted the influence of tail moment arm on tail damping.

CONCLUDING REMARKS

The influence of components, including the effect of wing location and body length, on the rotational flow aerodynamics of general aviation model D, configured with a low horizontal tail, is summarized below.

- o For the baseline configuration (low wing, long body), the wing, and vertical tail (in the absence of a low horizontal tail) generally provided damping in yaw through 90° angle of attack. However, above 30° angle of attack, the addition of the horizontal tail decreased the vertical tail's damping effectiveness, such that the damping was completely negated at 40° angle of attack and propelling beyond an angle of attack of 40° . Consequently, the baseline airplane exhibited autorotative yawing moments above 40° angle of attack.
- o Although the vertical location of the wing did not directly influence the damping effectiveness of the vertical tail, it does so indirectly by influencing the level of adverse interference resulting from the presence of the horizontal tail in the 30° to 60° angle-of-attack region. This adverse horizontal tail interference was reduced or eliminated by locating the wing in the high position. Shortening the tail moment arm was also found to be beneficial relative to minimizing the adverse horizontal tail interference

and consequently improving the yaw damping in the 50° to 90° angle of attack range for $\Omega b/2V$ magnitudes less than 0.4. The improvements in yaw damping realized with these geometric changes would not have been predicted by existing tail design criterion and could only be discerned through rotary balance testing.

- o The airplane's pitch characteristics, both statically and with rotation, were determined by the wing and horizontal tail. Both contributed nose-down pitching moments that became more nose-down with increasing angle of attack and rotation rate. .
- o The static pitching moment was, obviously, influenced by wing position and tail moment arm. However, the incremental nose-down pitching moment due to rotation remained essentially unchanged for both the high and low wing locations, as well as for the long and short fuselage lengths.
- o The rolling moment characteristics were determined entirely by the wing geometry and were not influenced by vertical wing location or tail moment arm length.

REFERENCES

1. Ralston, John N. and Barnhart, Billy: Rotary Balance Data for a Typical Single-Engine General Aviation Design for an Angle-of-Attack Range of 8° to 90° . III - Influence of Control Deflection on Predicted Model D Spin Modes. NASA CR-3248, 1983.
2. Barnhart, Billy: Rotary Balance Data for a Typical Single-Engine General Aviation Design for an Angle-of-Attack Range of 8° to 90° . II - Influence of Horizontal Tail Location for Model D. NASA CR-3247, November 1982.
3. Standard for Metric Practice. E 380-79, American Society for Testing and Materials, c.1980.
4. Bihrlle, W., Jr. and Bowman, J.S., Jr.: Influence of Wing, Fuselage, and Tail Design on Rotational Flow Aerodynamics Beyond Maximum Lift, Journal of Aircraft, Volume 18, Number 11, November 1981.
5. Burk, Sanger, M., Jr., Bowman, James S., Jr., and White, William L.: Spin-Tunnel Investigation of the Spinning Characteristics of Typical Single-Engine General Aviation Airplane Designs. I - Low-Wing Model A: Effects of Tail Configurations. NASA TP-1009, Sept. 1977.

TABLE I.- DIMENSIONAL CHARACTERISTICS OF THE BASIC MODEL

Overall length, short fuselage, m (ft) . . .	1.3	(4.3)
Overall length, long fuselage, m (ft) . . .	1.425	(4.675)
Wing		
Span, m (ft)	1.8	(5.91)
Area, m ² (ft ²)	0.448	(4.825)
Root chord, cm (in.)	26.7	(10.5)
Tip chord, cm (in.)	17.9	(7.03)
Mean aerodynamic chord, cm (in.)	24.5	(9.64)
Leading edge of \bar{c} , distance rearward of leading edge of root chord, cm (in.) . .	5.44	(2.14)
Aspect ratio		7.24
Taper ratio		0.67
Dihedral, low wing, deg		7
Dihedral, high wing, deg		1.5
Incidence:		
Root, deg		2.0
Tip, deg		-1.0
Airfoil section:		
Root	NASA 65 ₂ 415	
Tip	NASA 65 ₂ 415 mod	
Horizontal tail		
Span, m (ft)	0.508	(1.67)
Area, m ² (ft ²)	0.065	(.696)
Aspect ratio		4.0
Airfoil section.	NACA 0012	
Vertical tail		
Area, m ² (ft ²)	0.03	(.328)
Sweep at leading edge		33.9
Aspect ratio		1.47
Airfoil section	NASA 63A012	

TABLE II.- CONFIGURATIONS TESTED AND FIGURE INDEX
 (All configurations tested through $\alpha=8^{\circ}$ to 90° at $\beta=0^{\circ}$)

CONFIGURATION	SHORT TAIL FIG. NO.	LONG TAIL FIG. NO.
LOW WING		
Body		A31-A36
Body, wing		A37-A42
Body, wing, vertical	A1-A6	A43-A48
Body, wing, horizontal	A7-A12	A49-A54
Complete configuration	A13-A18	A55-A60
HIGH WING		
Body, wing		A61-A66
Body, wing, vertical	A19-A24	A67-A72
Complete configuration	A25-A30	A73-A78

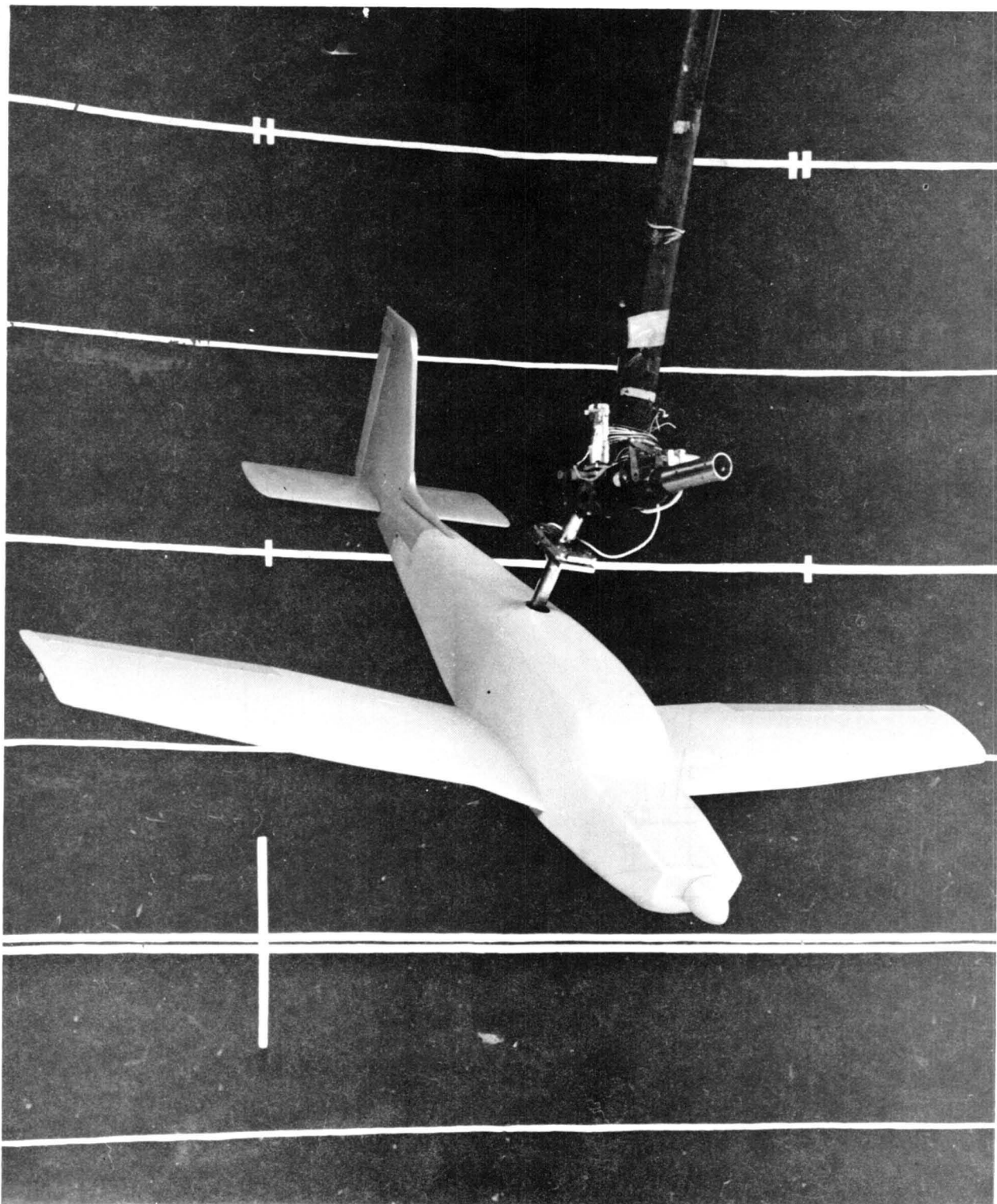
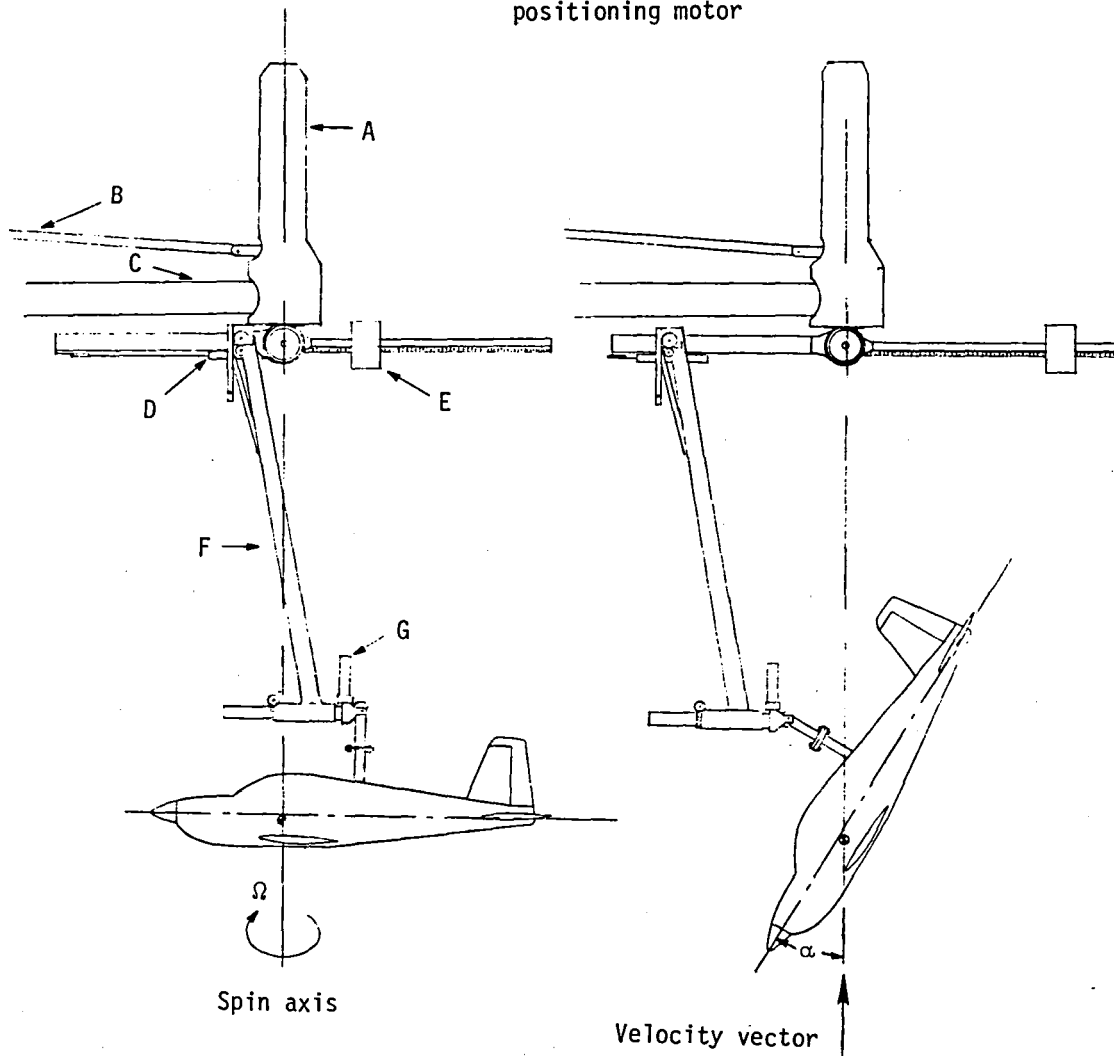


Figure 1.- Photograph of 1/6-scale model installed on rotary balance apparatus in the Langley 20-ft spin tunnel.

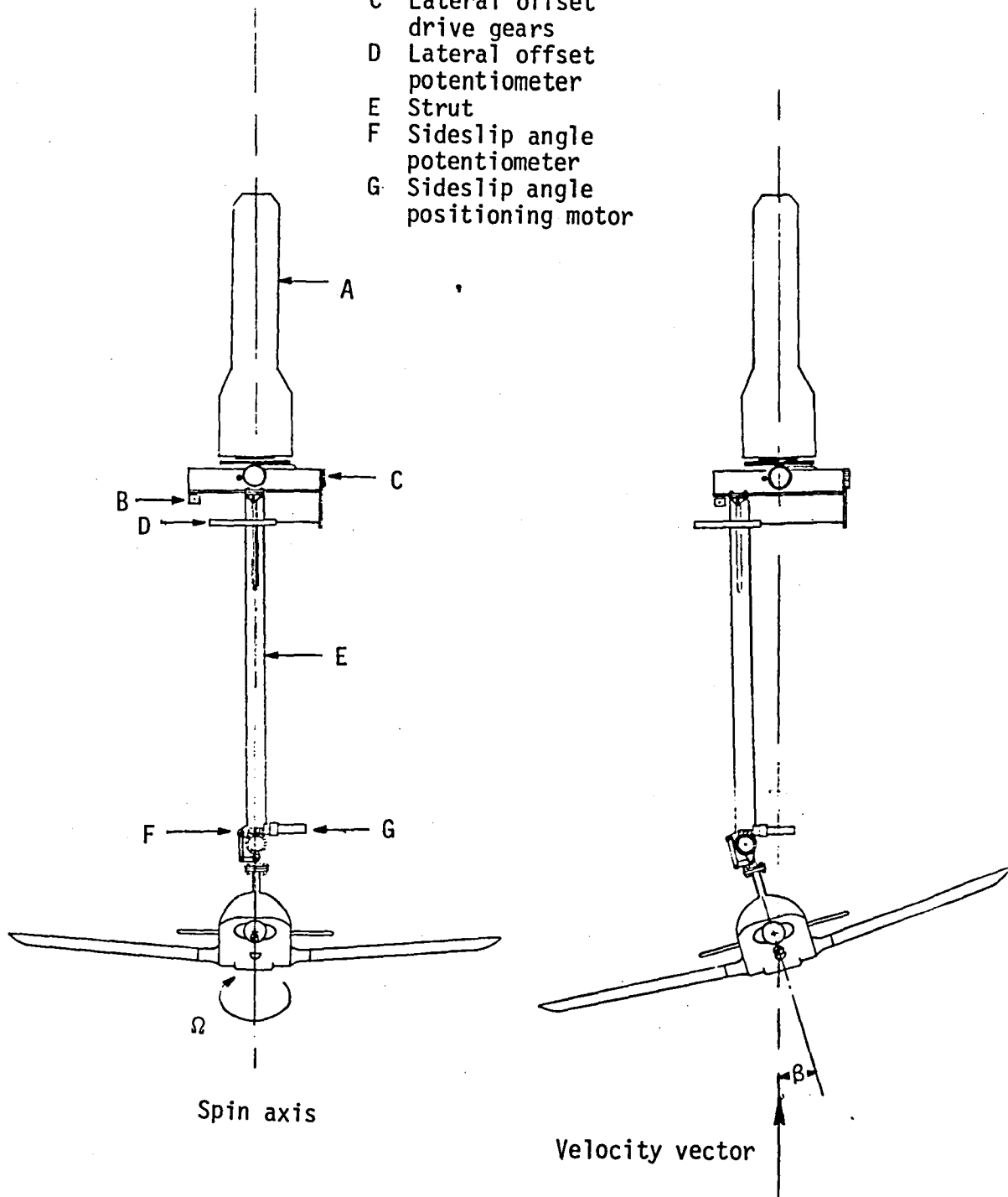
- A Slip ring housing
- B Drive shaft
- C Support boom
- D Spin radius offset potentiometer
- E Counterweight
- F Strut
- G Angle of attack positioning motor



(a) Side view of model.

Figure 2.- Sketch of rotary balance apparatus.

- A Slip ring housing
- B Spin radius offset potentiometer
- C Lateral offset drive gears
- D Lateral offset potentiometer
- E Strut
- F Sideslip angle potentiometer
- G Sideslip angle positioning motor



(b) Front view of model.

Figure 2.- Concluded.

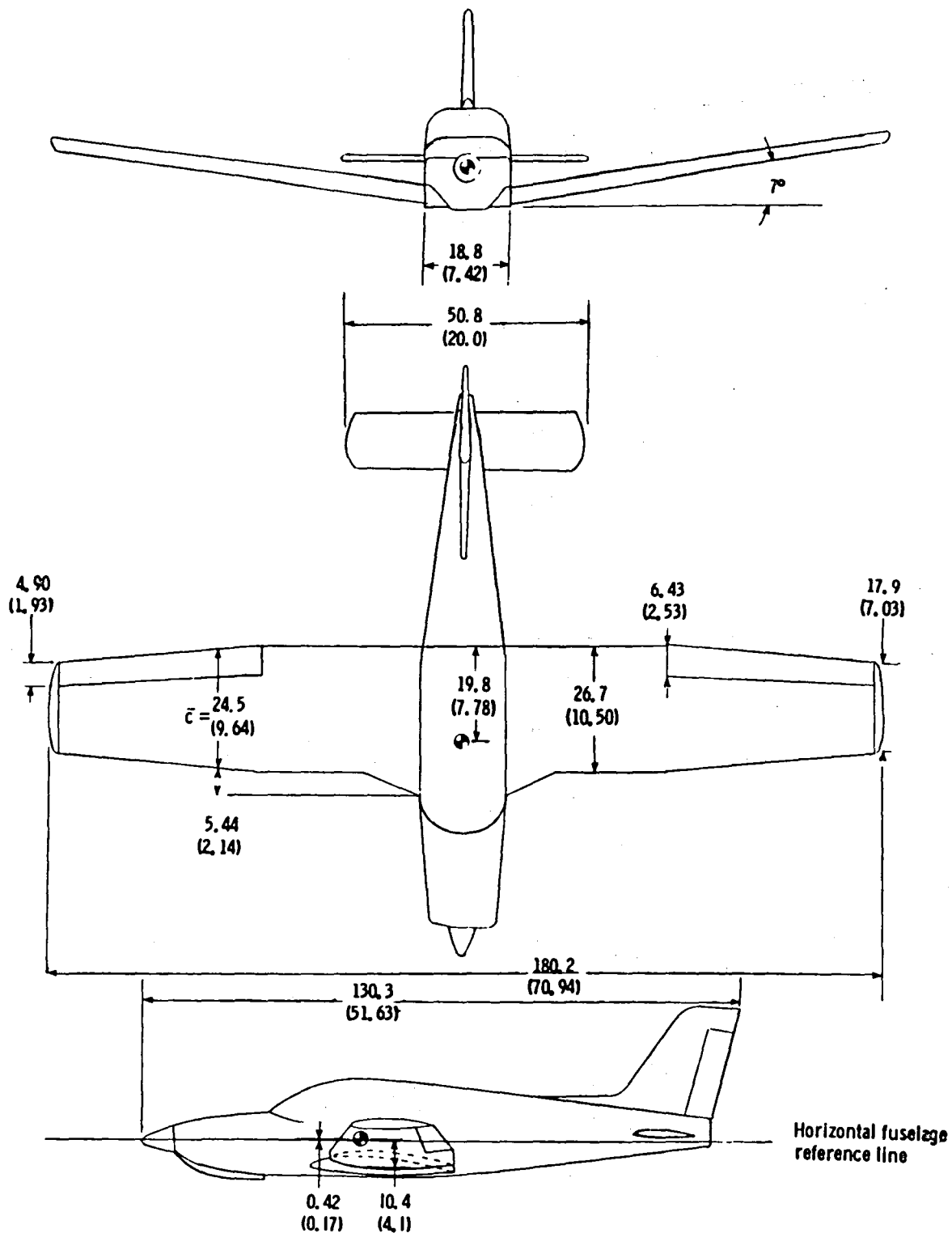


Figure 3.- Three-view drawing of 1/6-scale low wing, short body configuration. Center of gravity positioned at $0.25\bar{c}$. Dimensions are given in centimeters (inches), model scale.

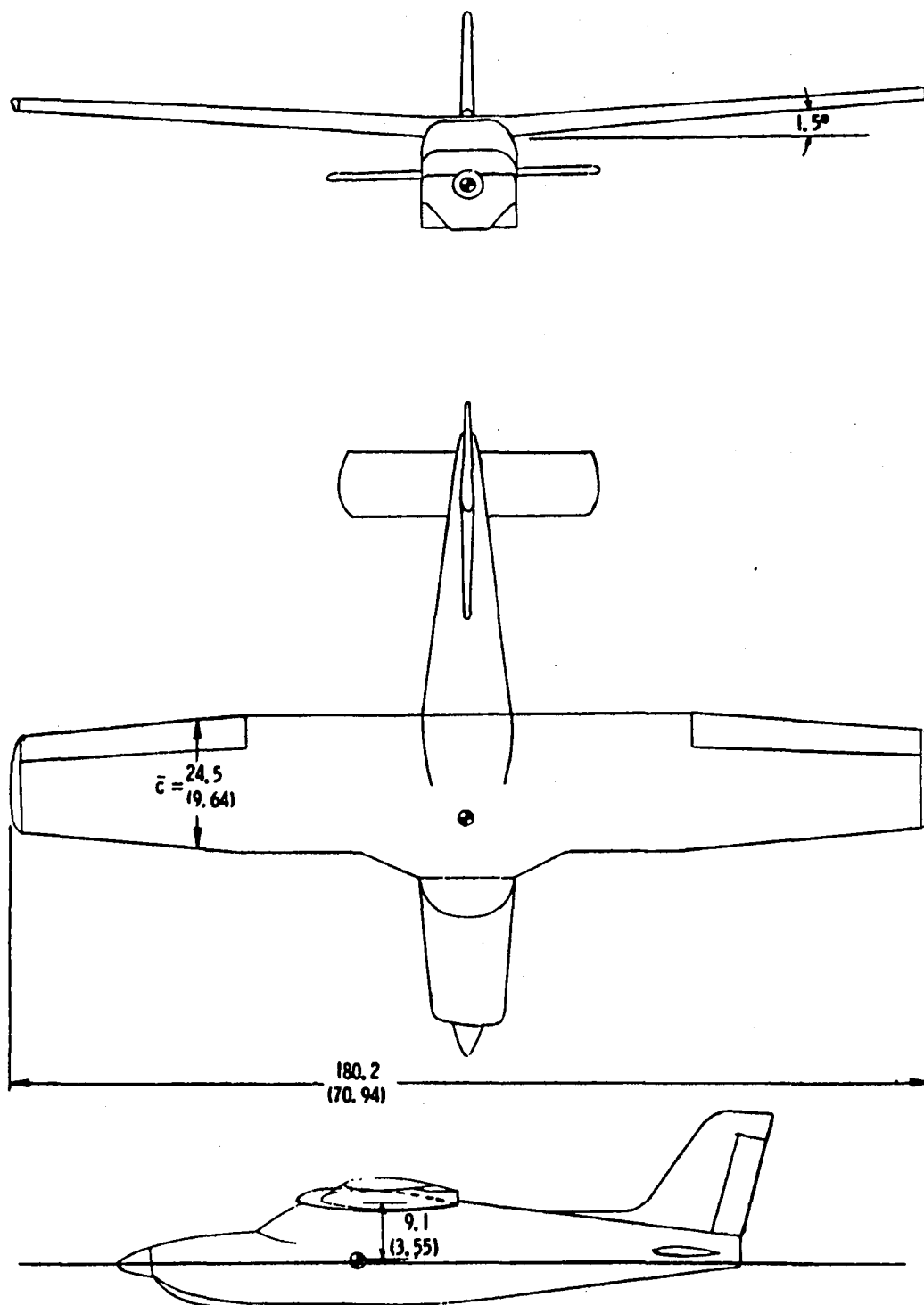


Figure 4.- Three-view drawing of 1/6-scale high wing, short body configuration. Center of gravity positioned at $0.25\bar{c}$. Dimensions are given in centimeters (inches), model scale.

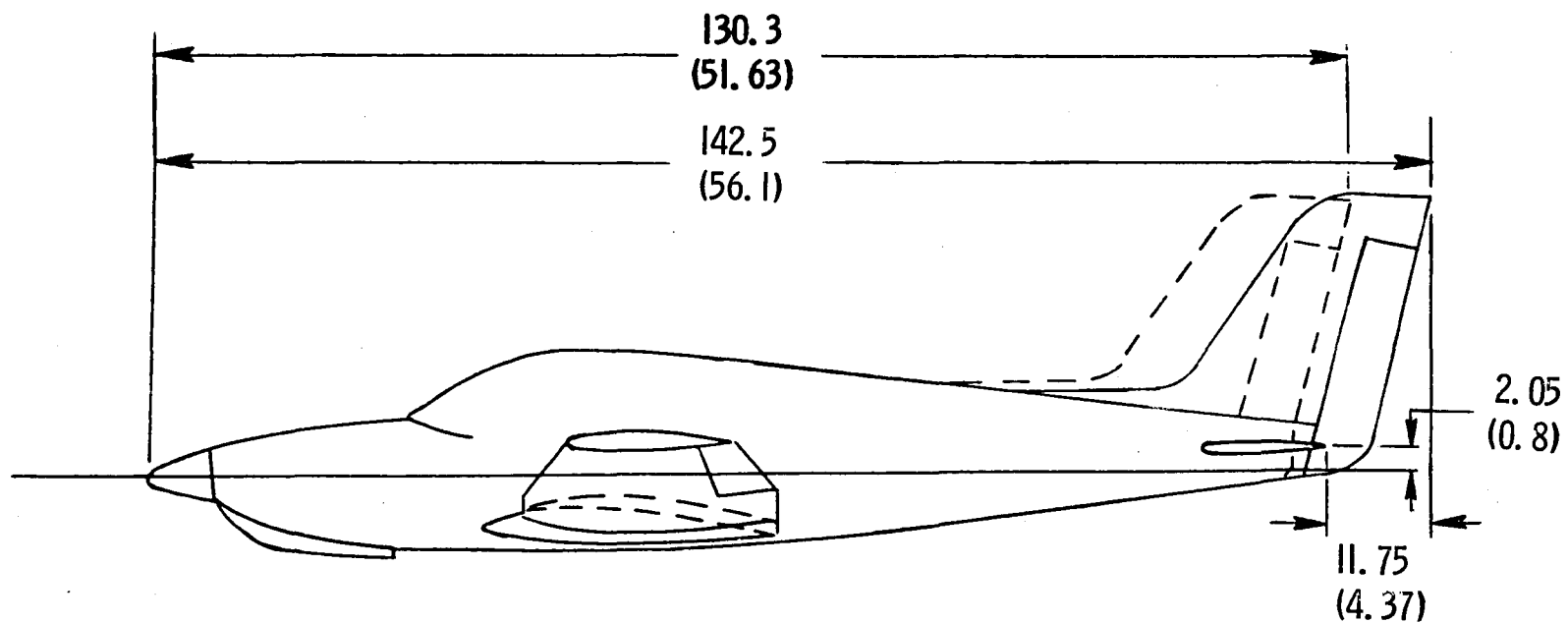
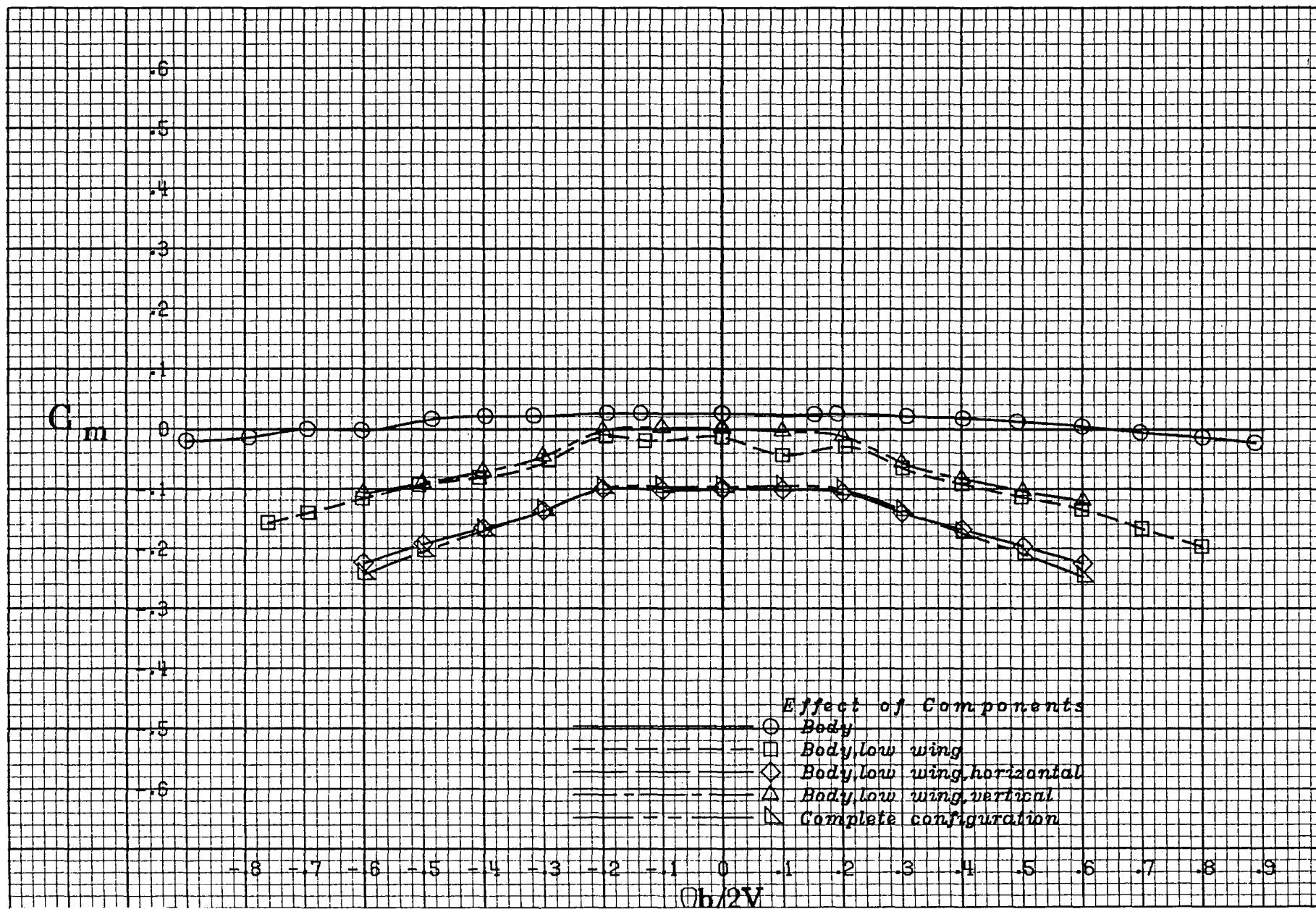
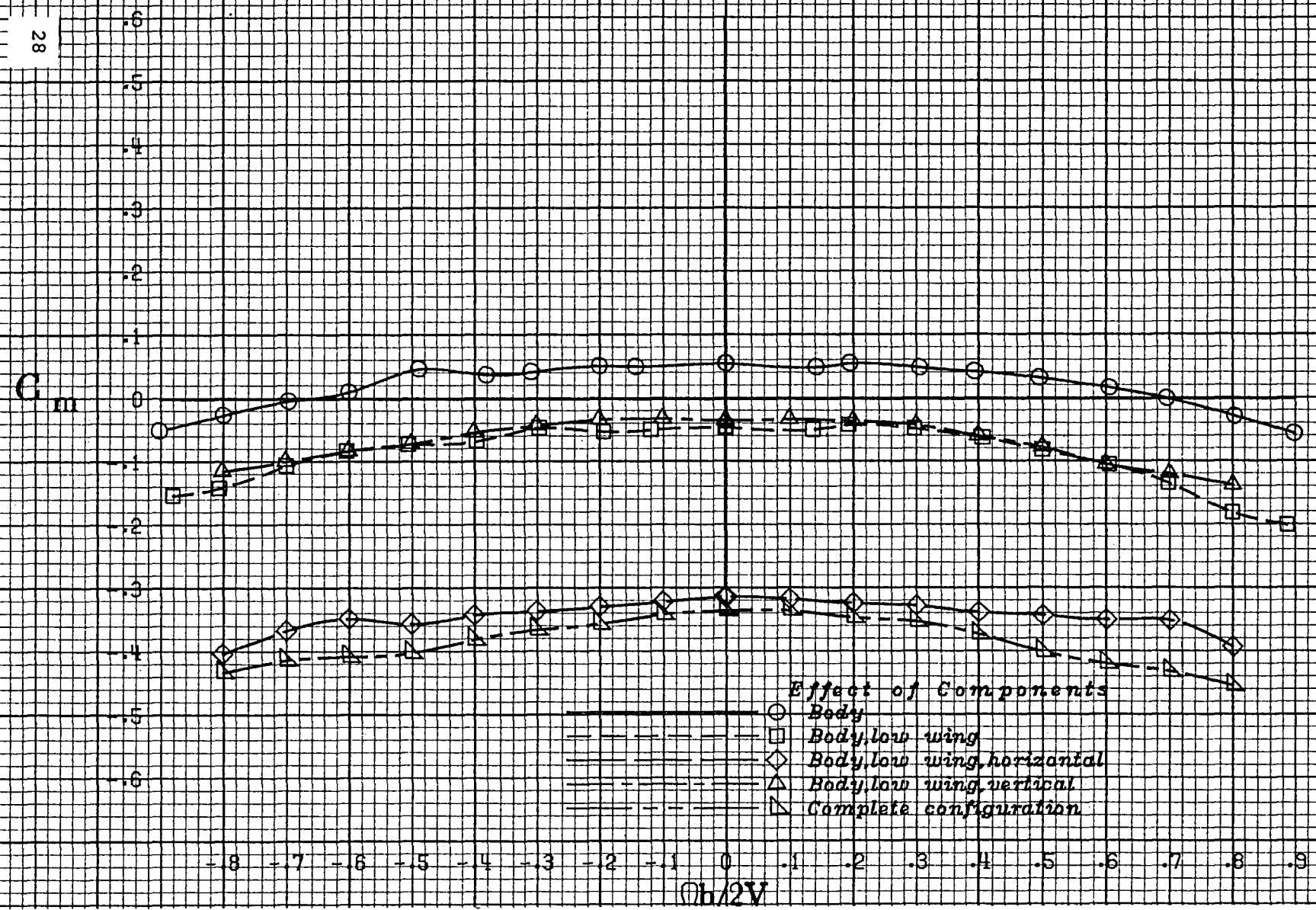


Figure 5.- Comparison of 1/6-scale long and short body configurations.
Dimensions are given in centimeters (inches), model scale.



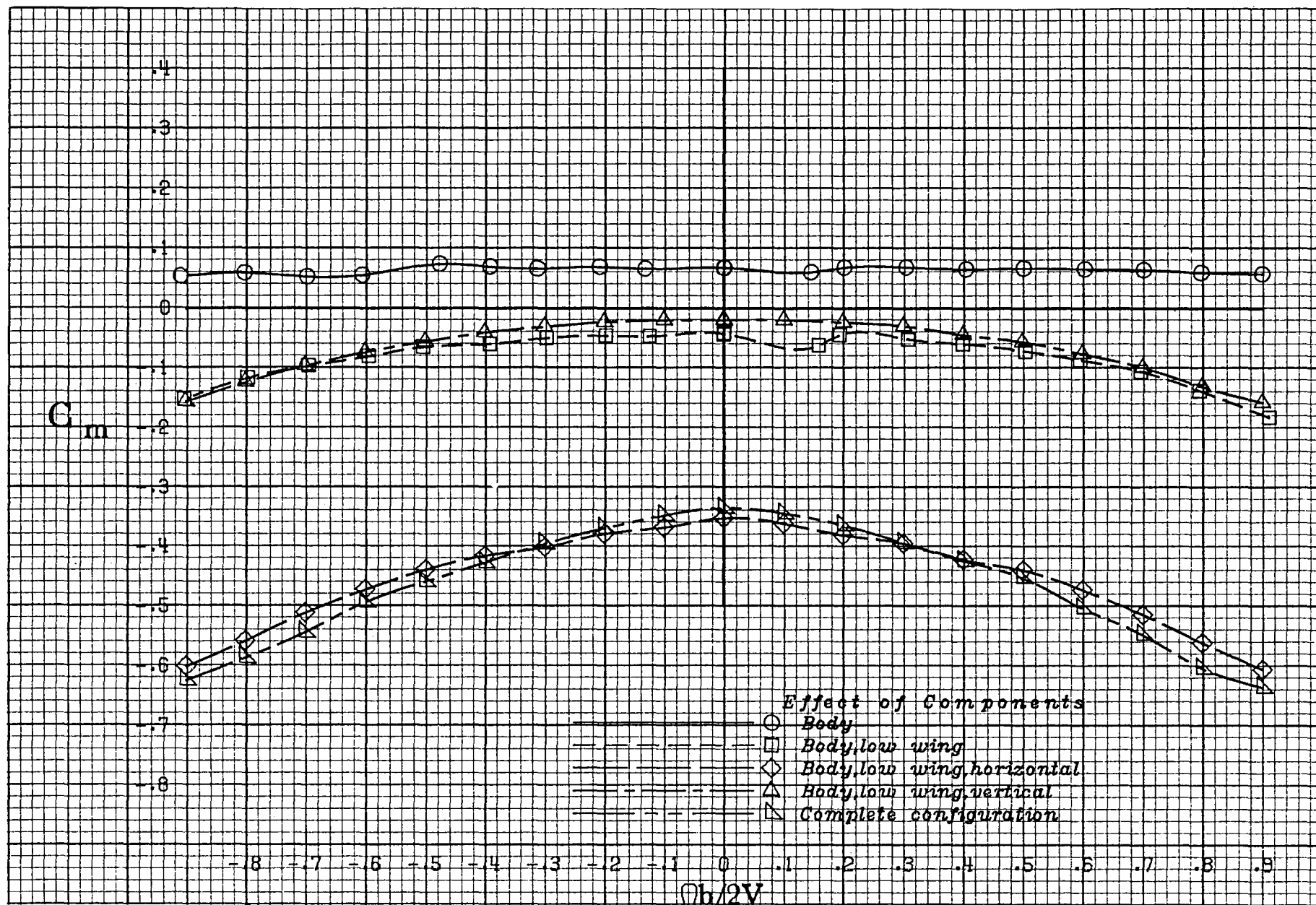
a) 8° angle of attack.

Figure 6.- Effect of components on pitching-moment coefficient.



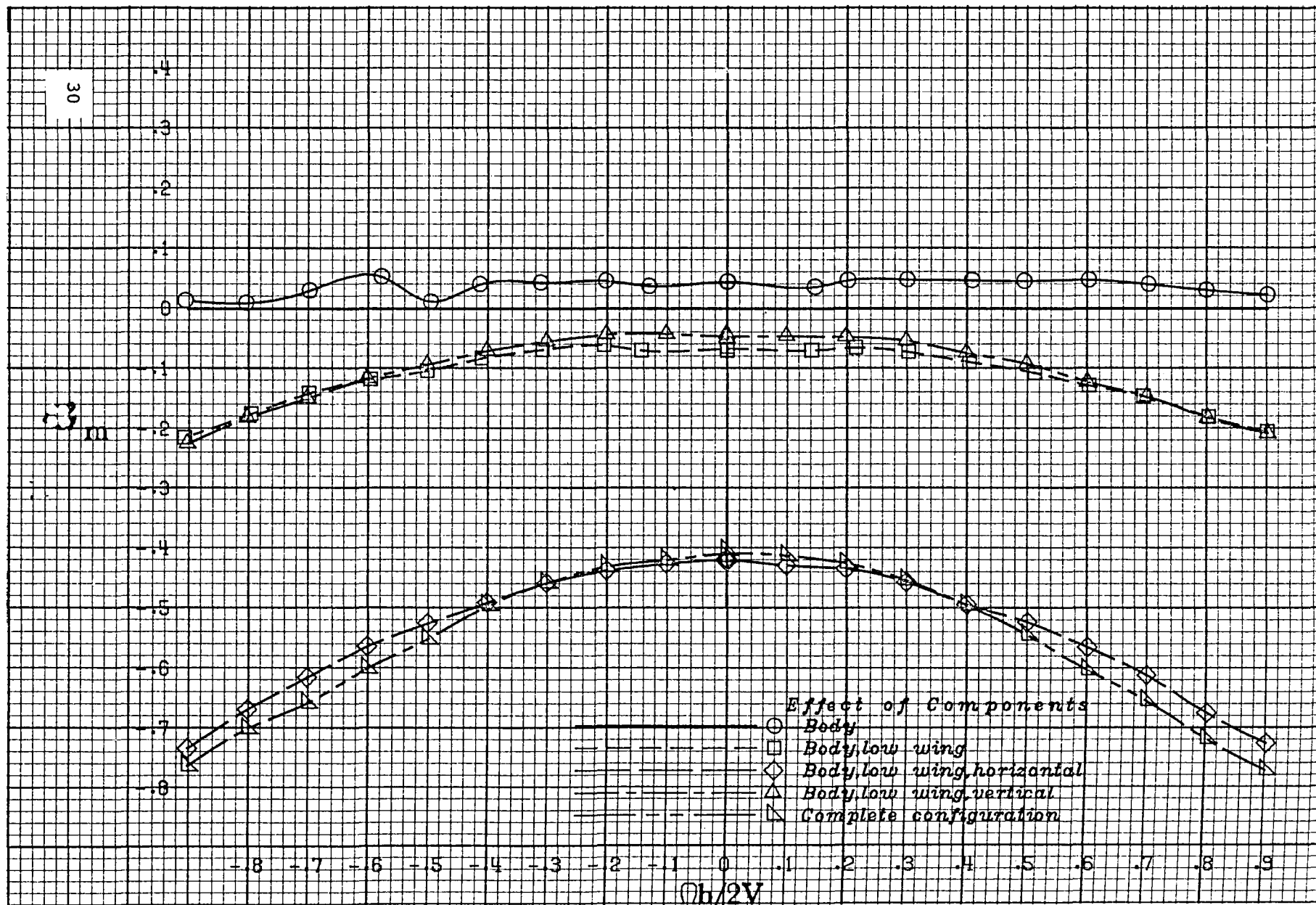
b) 20° angle of attack.

Figure 6.- Continued.



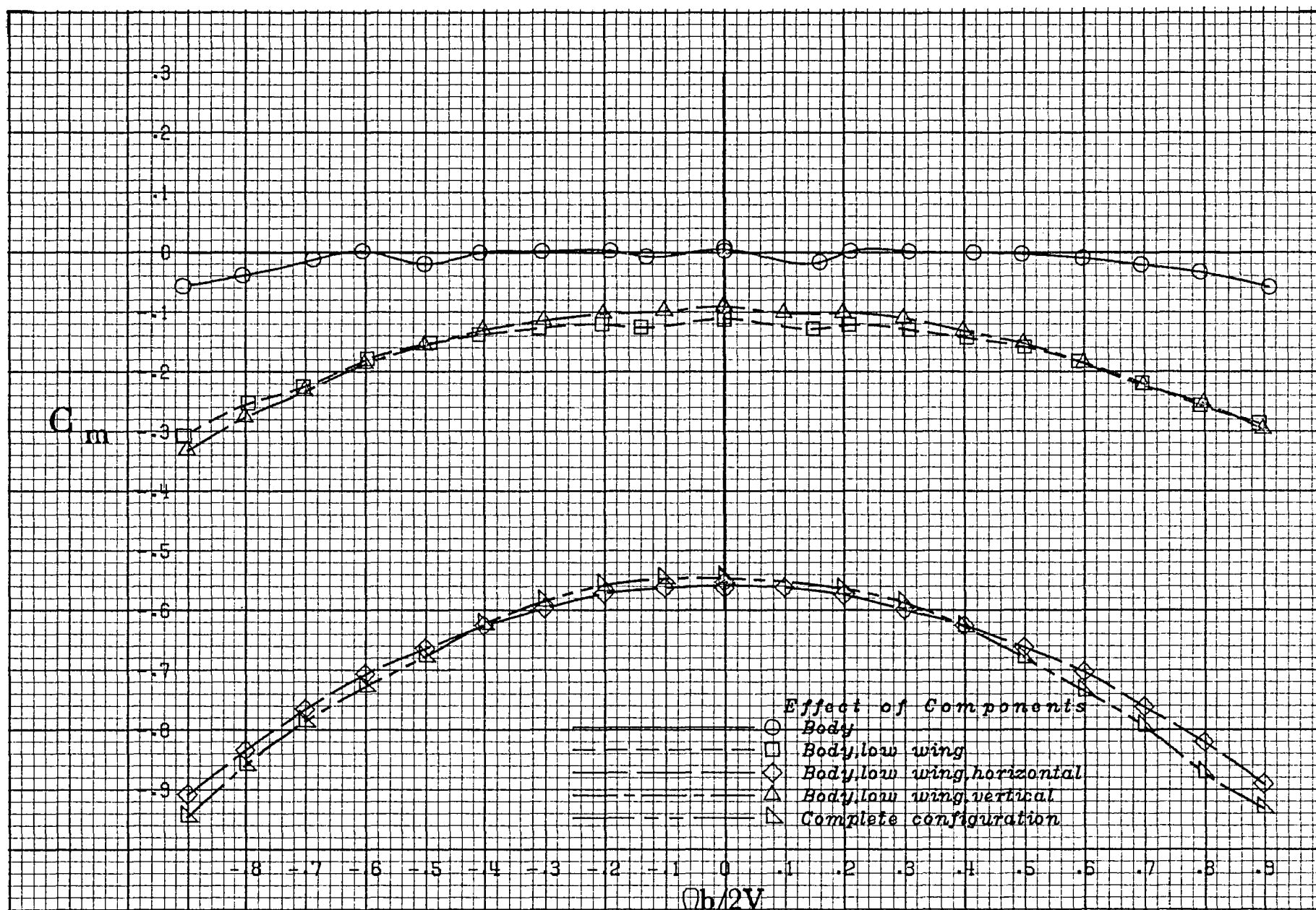
c) 30° angle of attack.

Figure 6.- Continued.



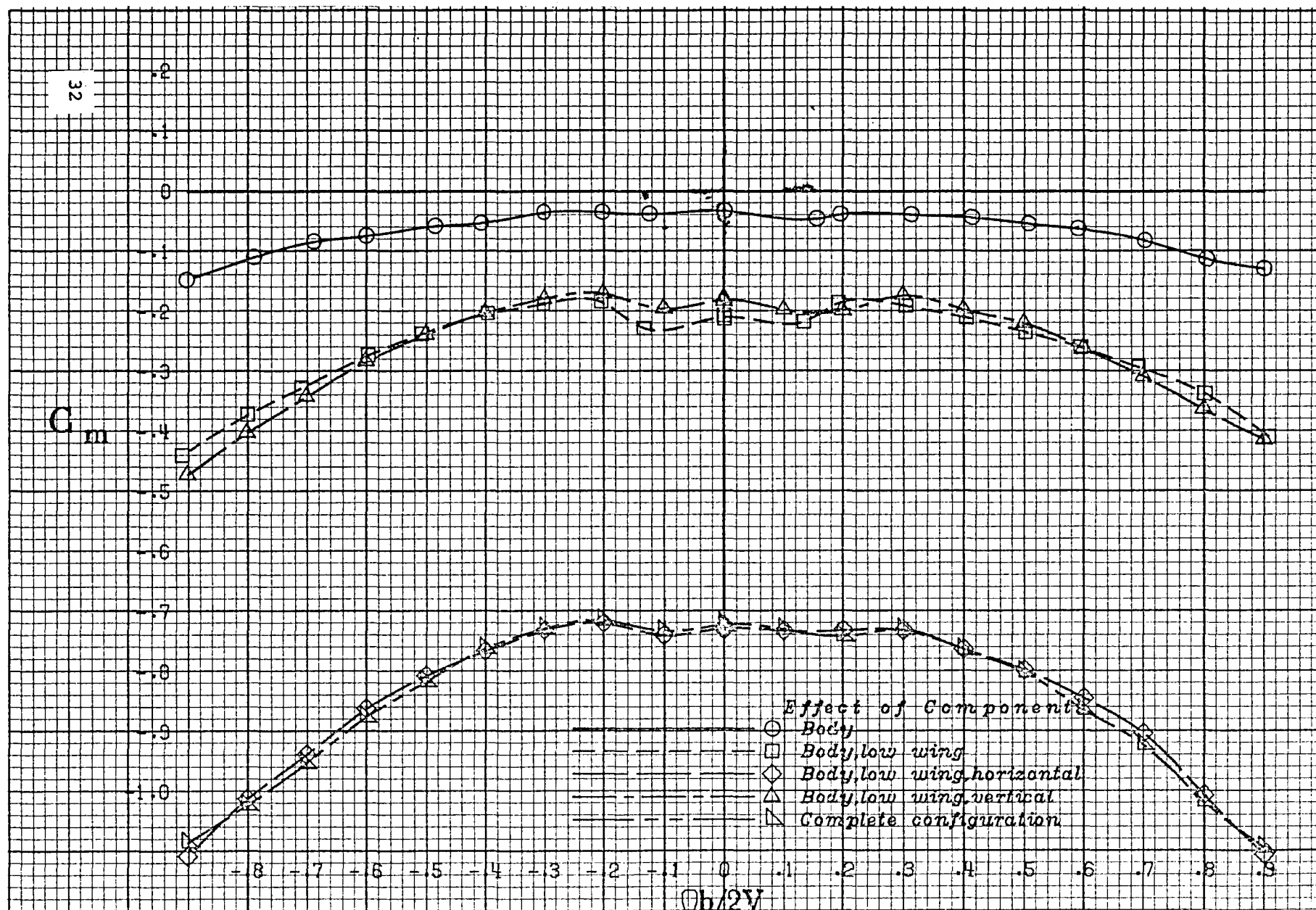
d) 40° angle of attack.

Figure 6.- Continued.



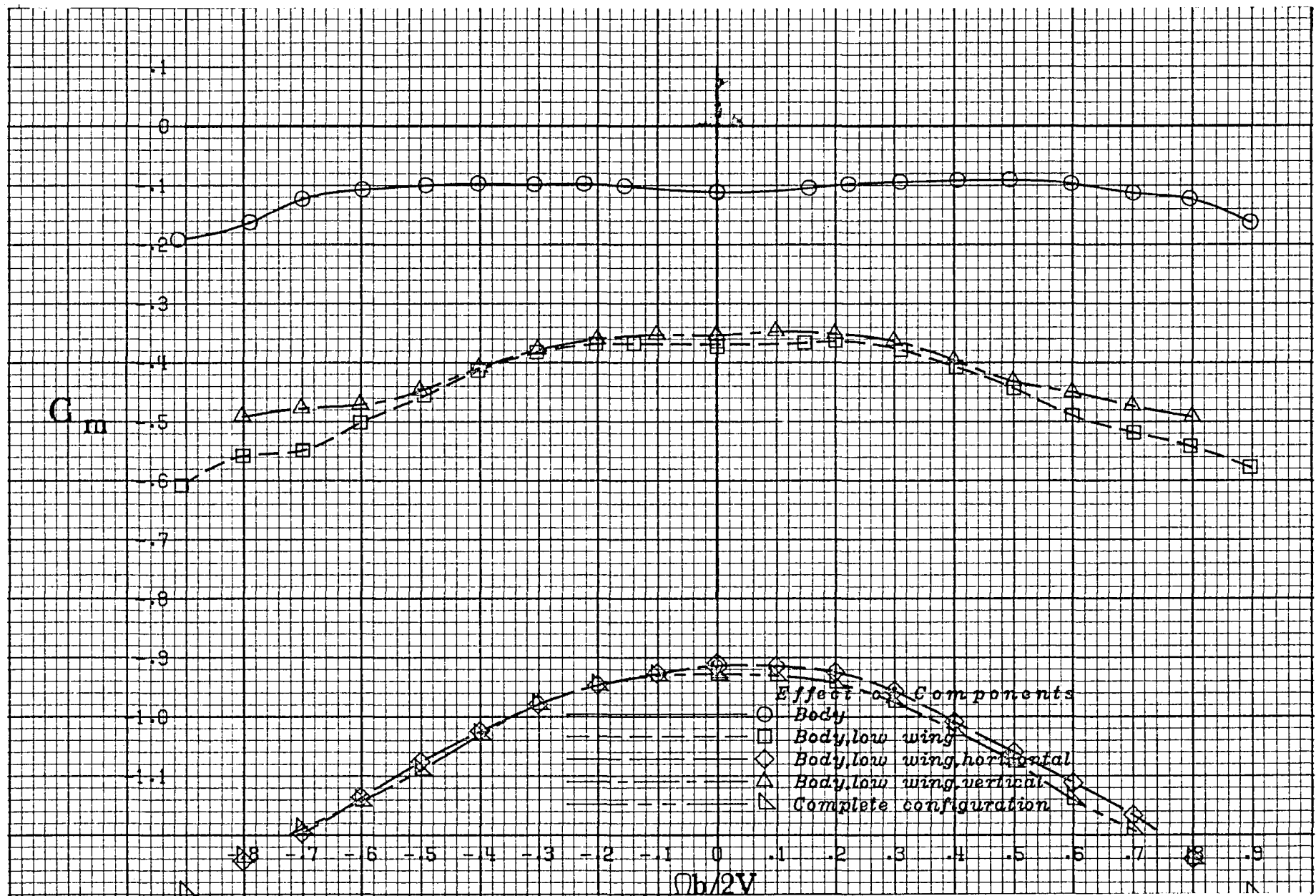
e) 50° angle of attack.

Figure 6.- Continued.

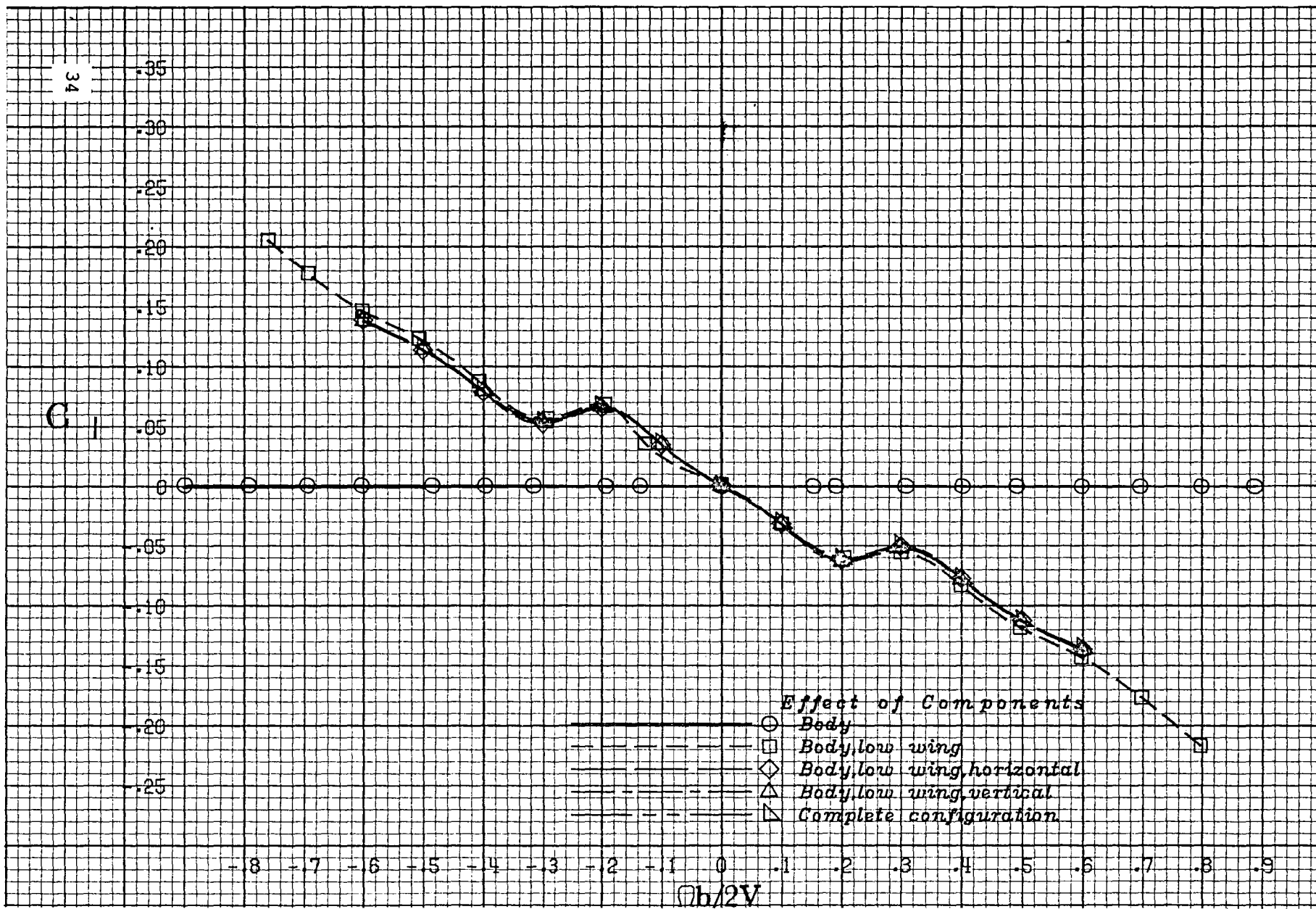


f) 60° angle of attack.

Figure 6.- Continued.

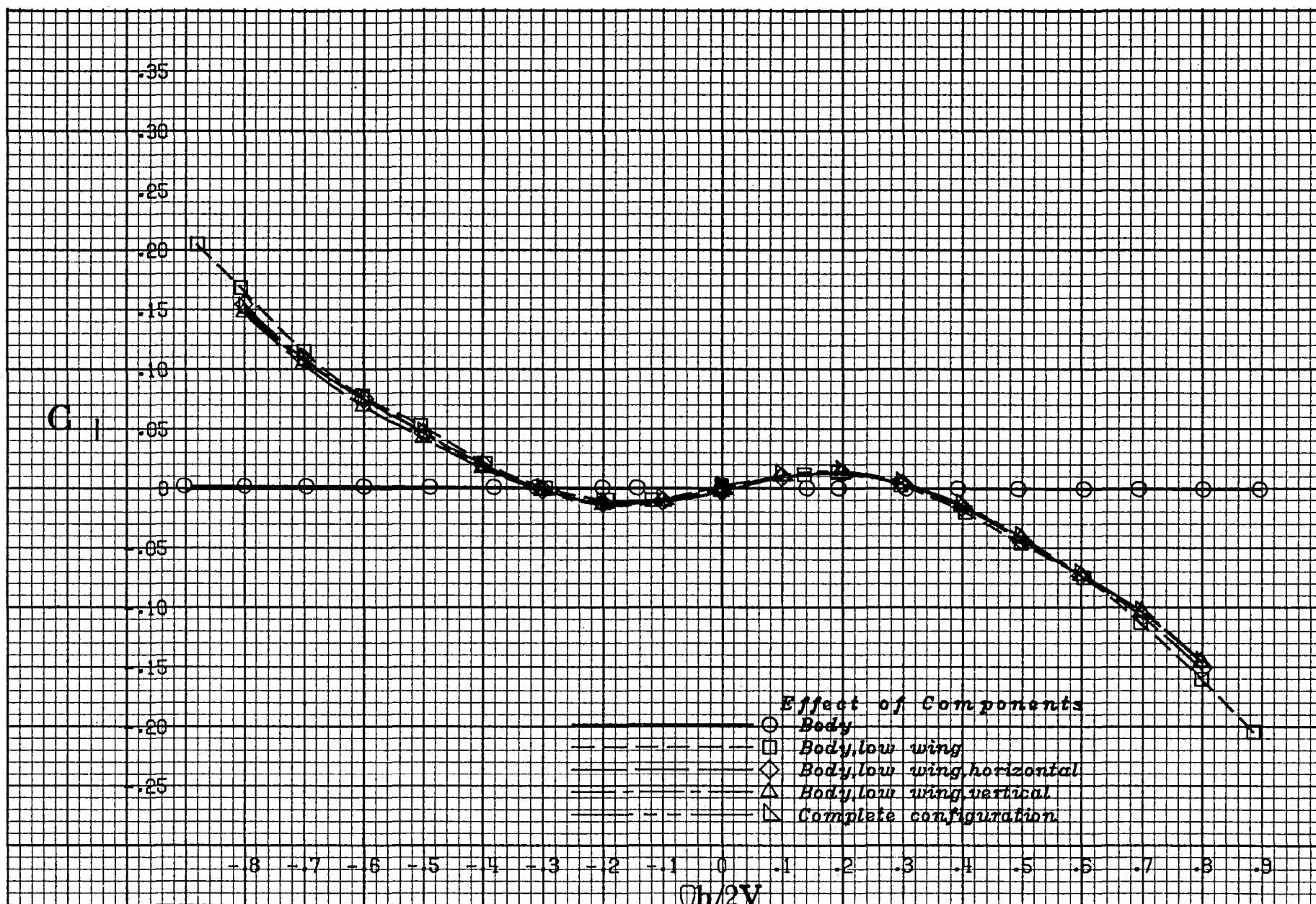


g) 80° angle of attack.
Figure 6.- Concluded.



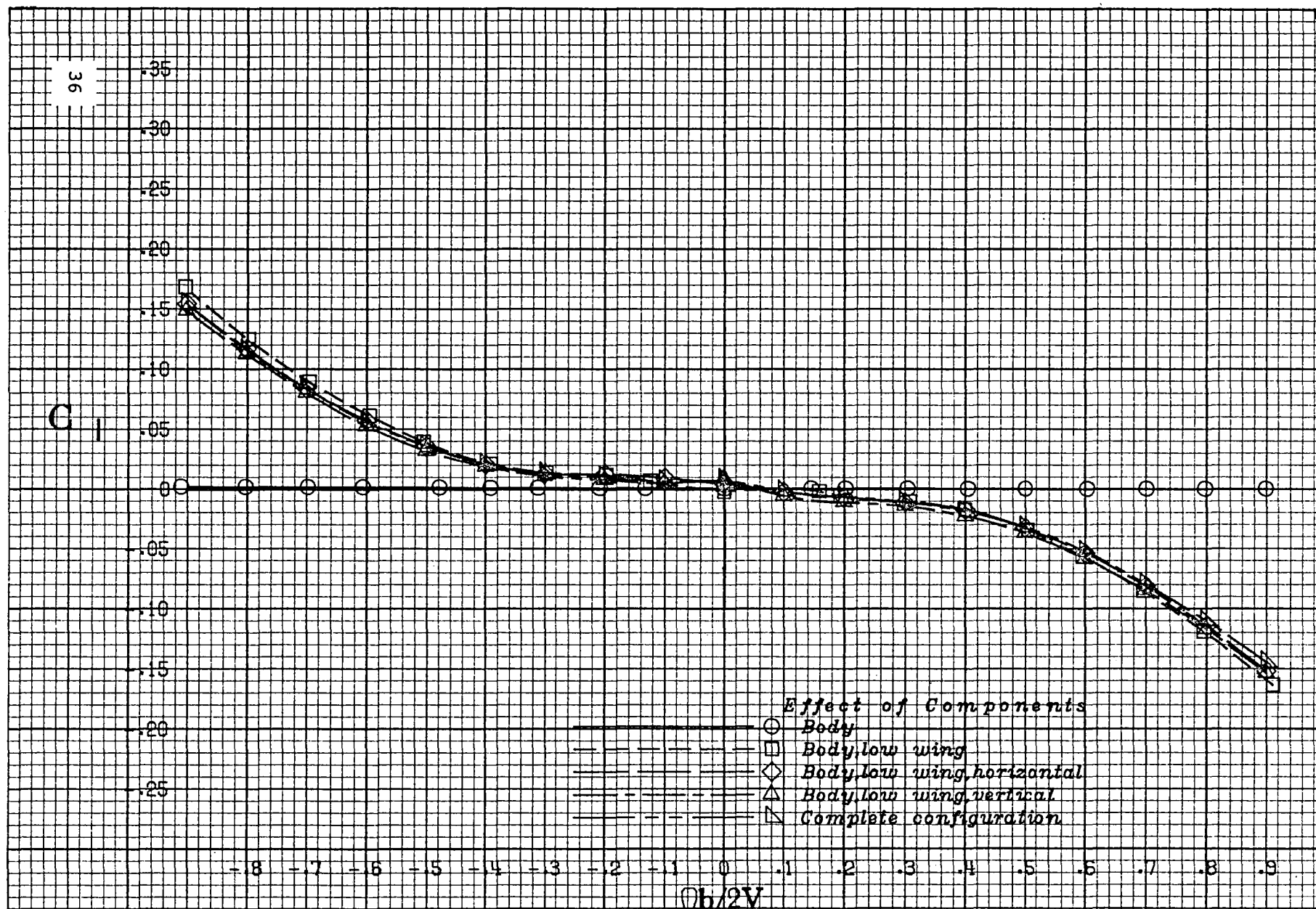
a) 8° angle of attack.

Figure 7.- Effect of components on rolling-moment coefficient.



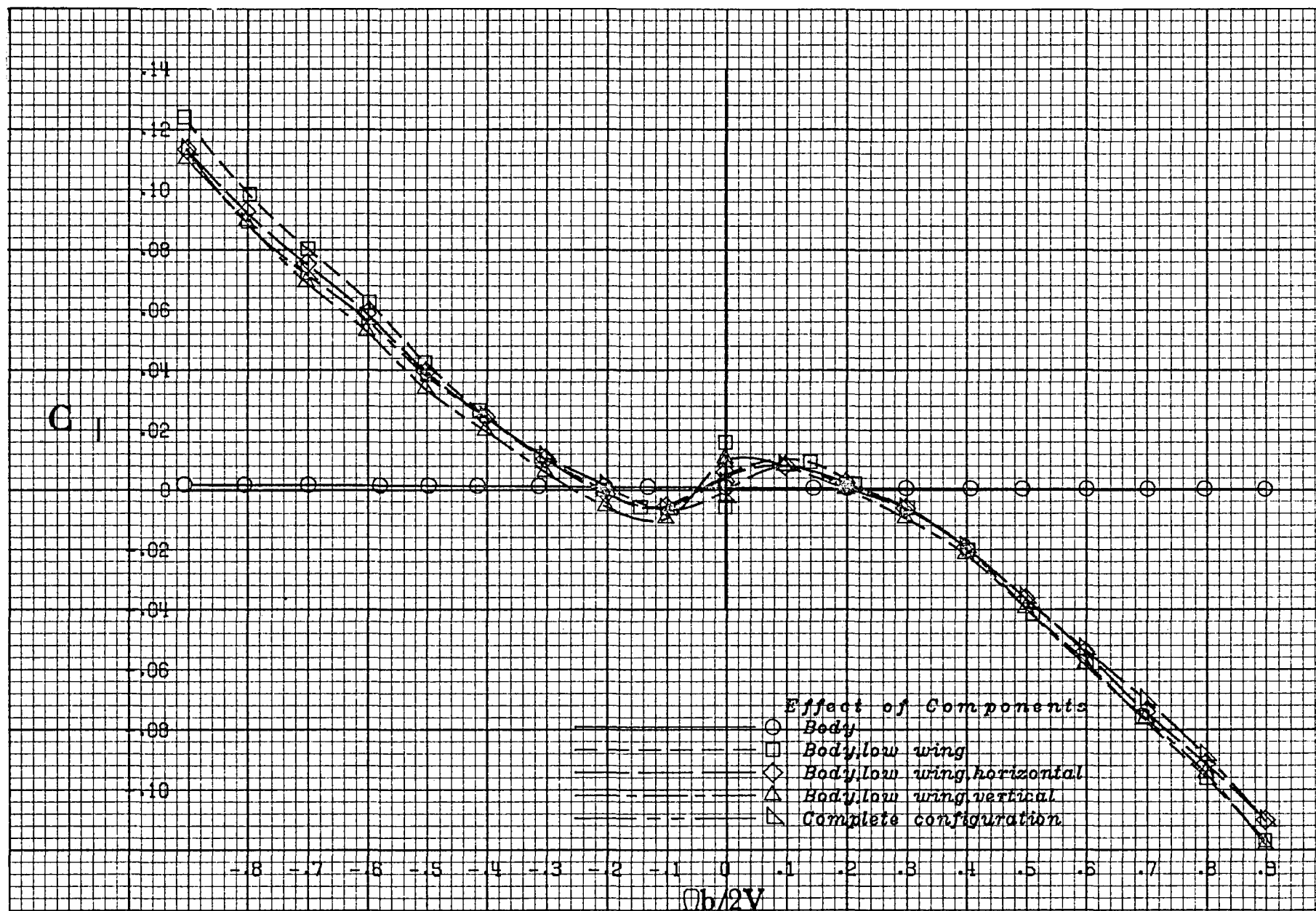
b) 20° angle of attack.

Figure 7.- Continued.

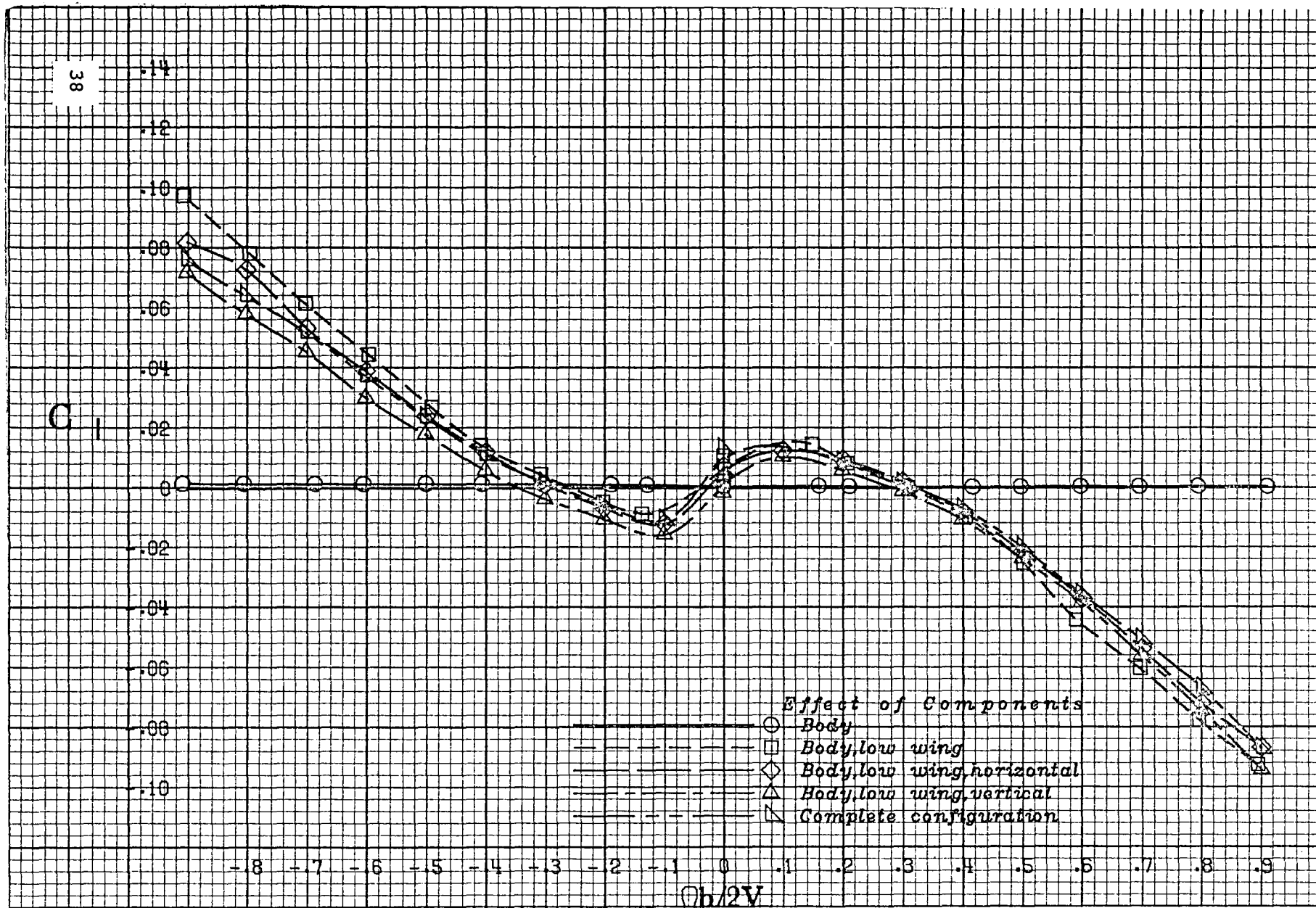


c) 30° angle of attack.

Figure 7.- Continued.

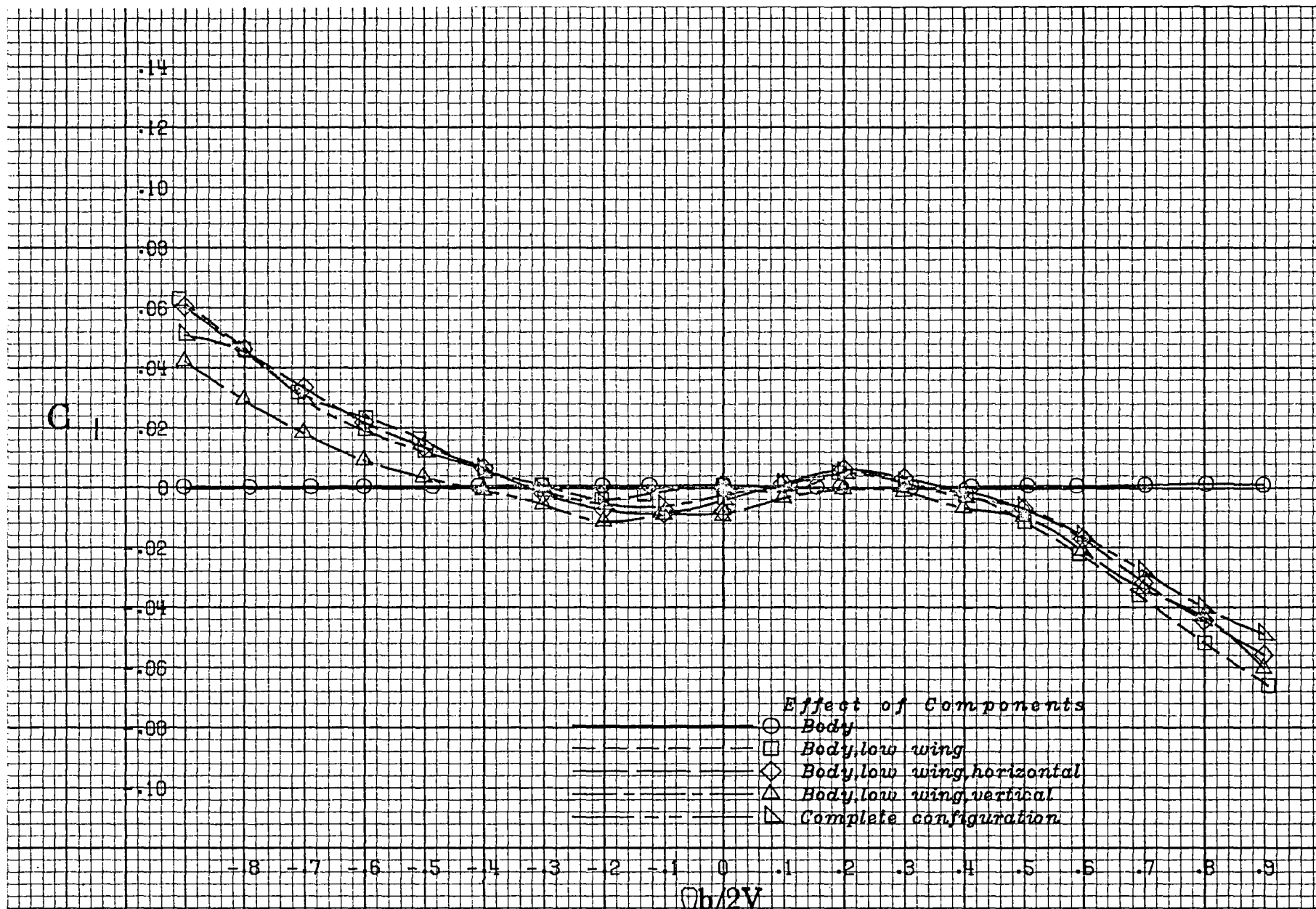


d) 40° angle of attack.
Figure 7.- Continued.



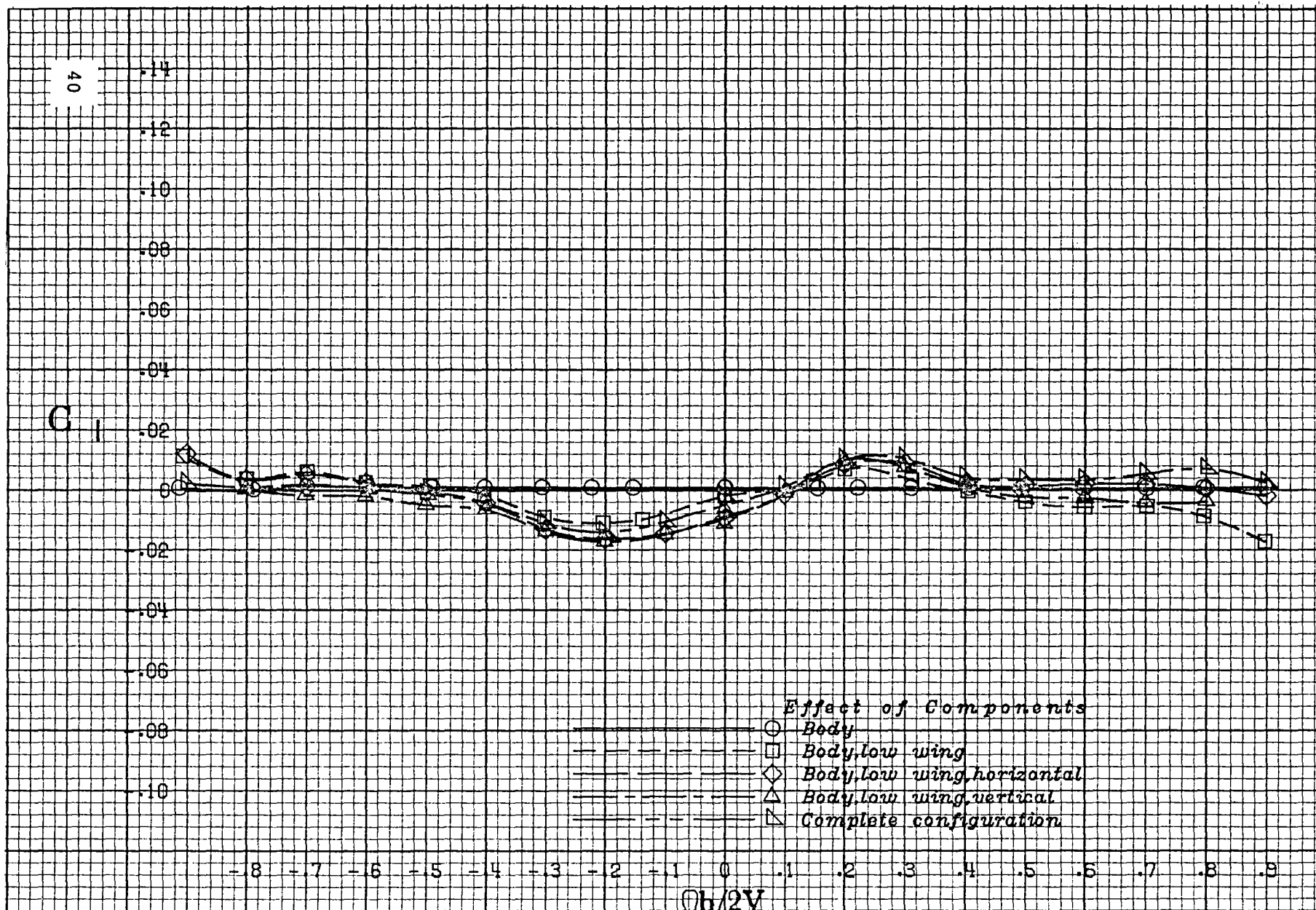
e) 50° angle of attack.

Figure 7.- Continued.



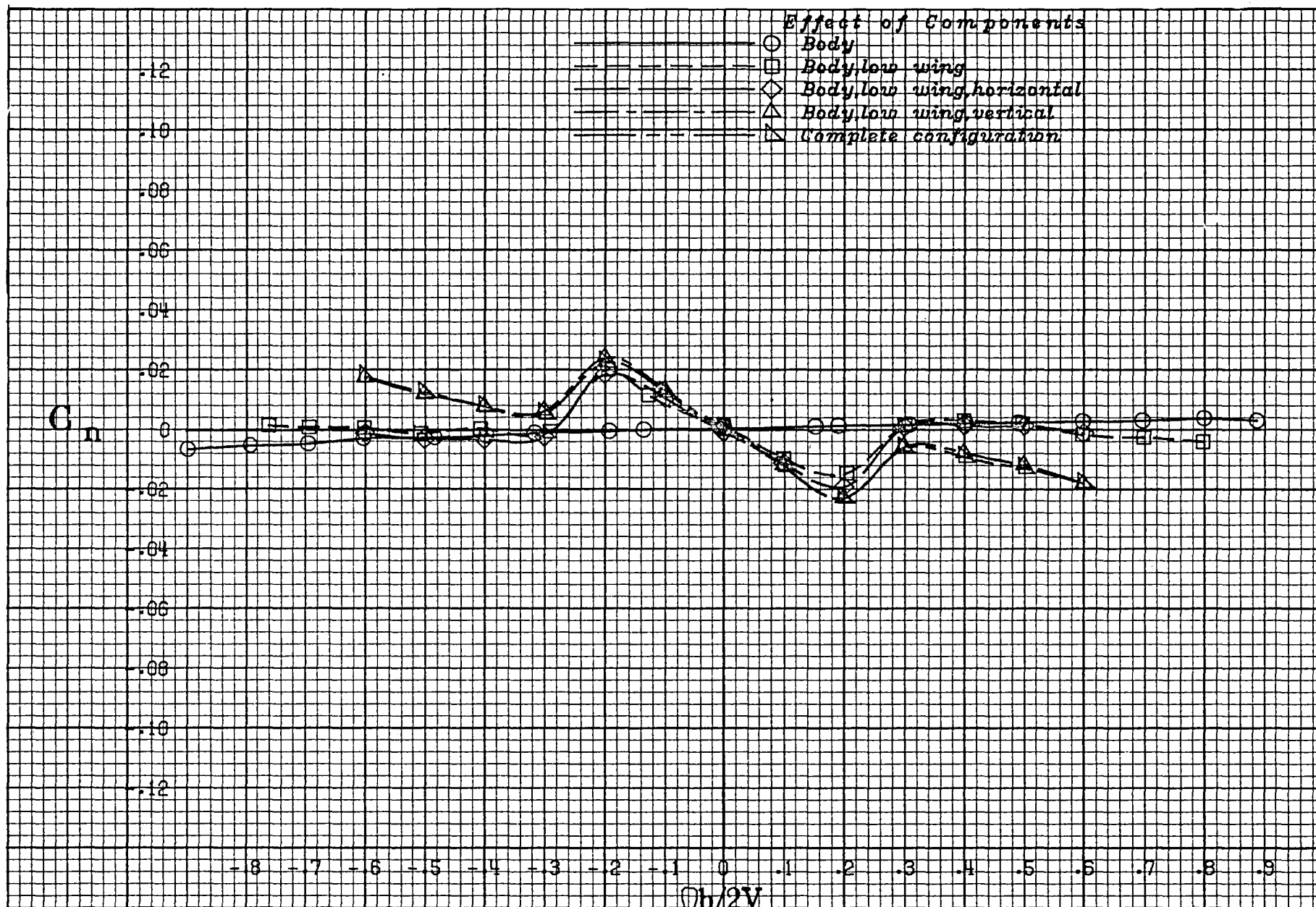
f) 60° angle of attack.

Figure 7.- Continued.



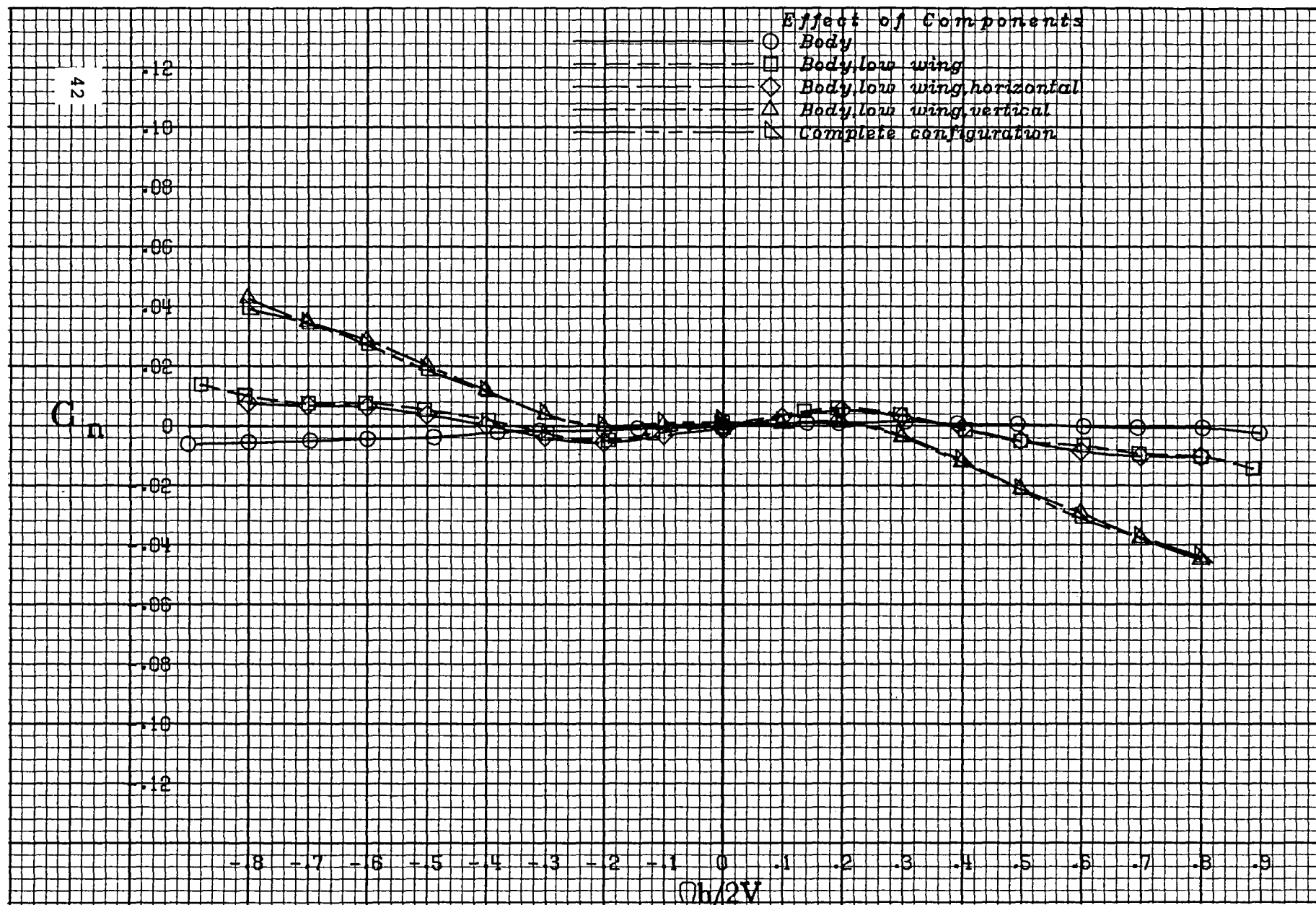
g) 80° angle of attack.

Figure 7.- Concluded.



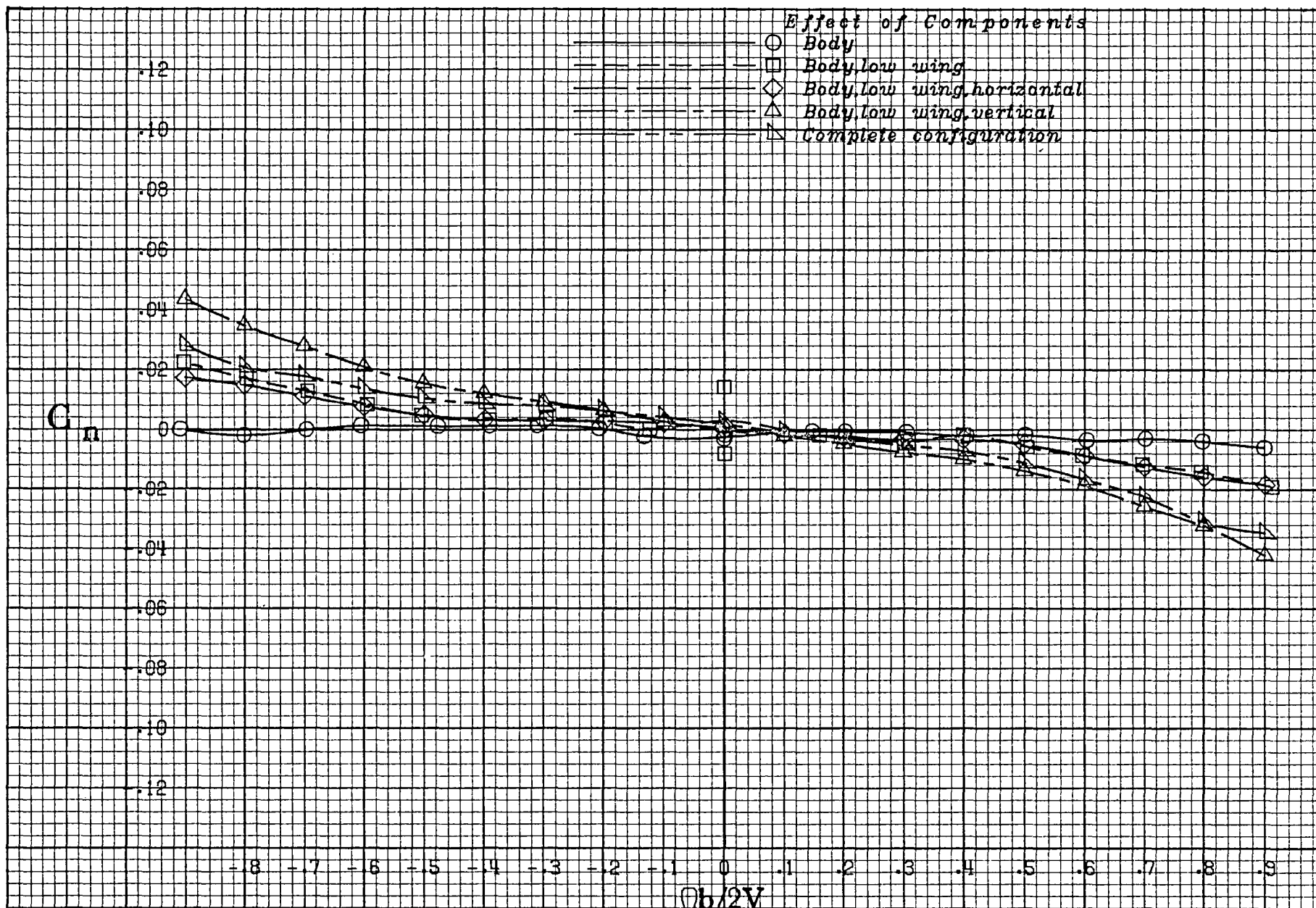
a) 8° angle of attack.

Figure 8.- Effect of components on yawing-moment coefficient.

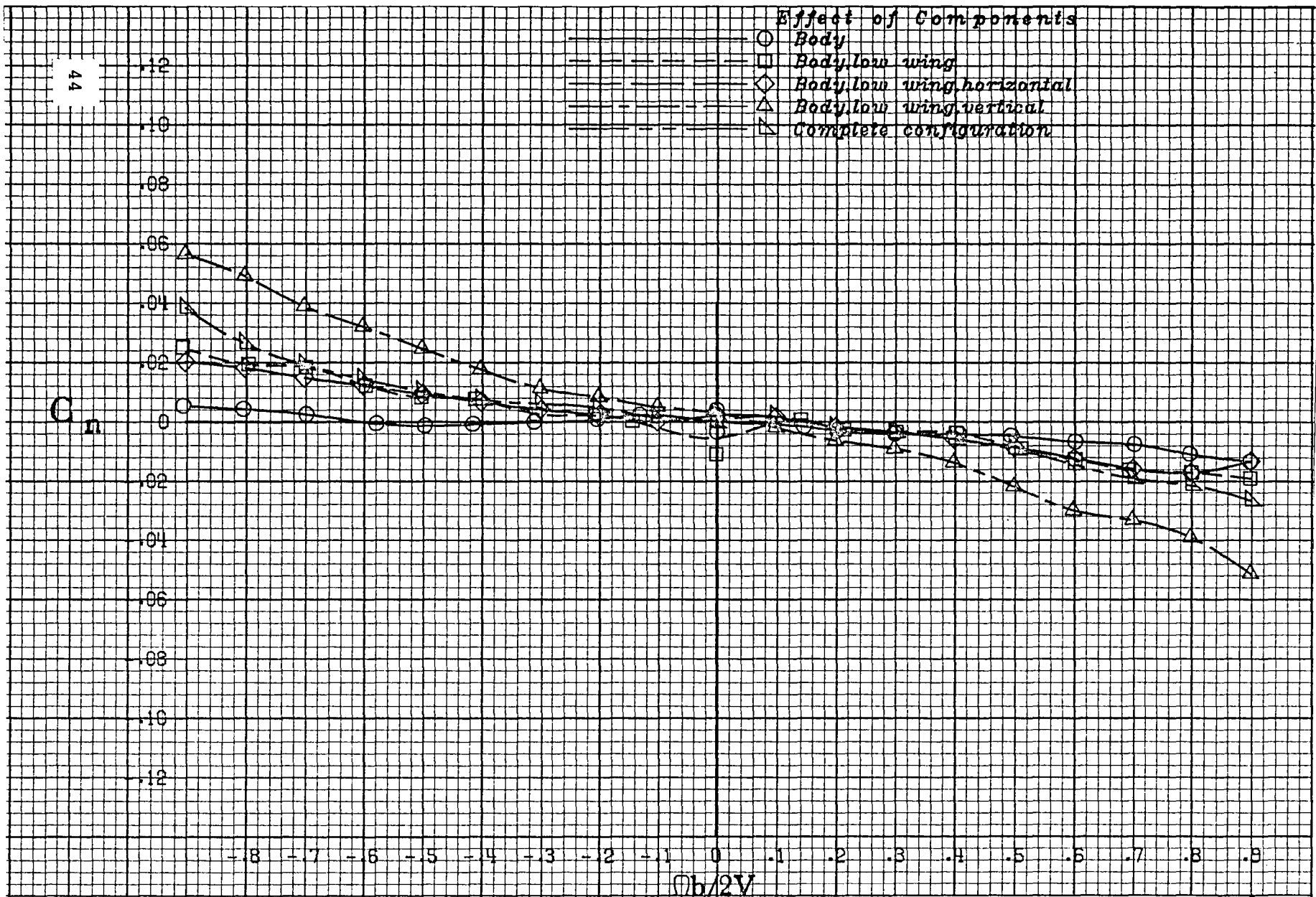


b) 20° angle of attack.

Figure 8.- Continued.

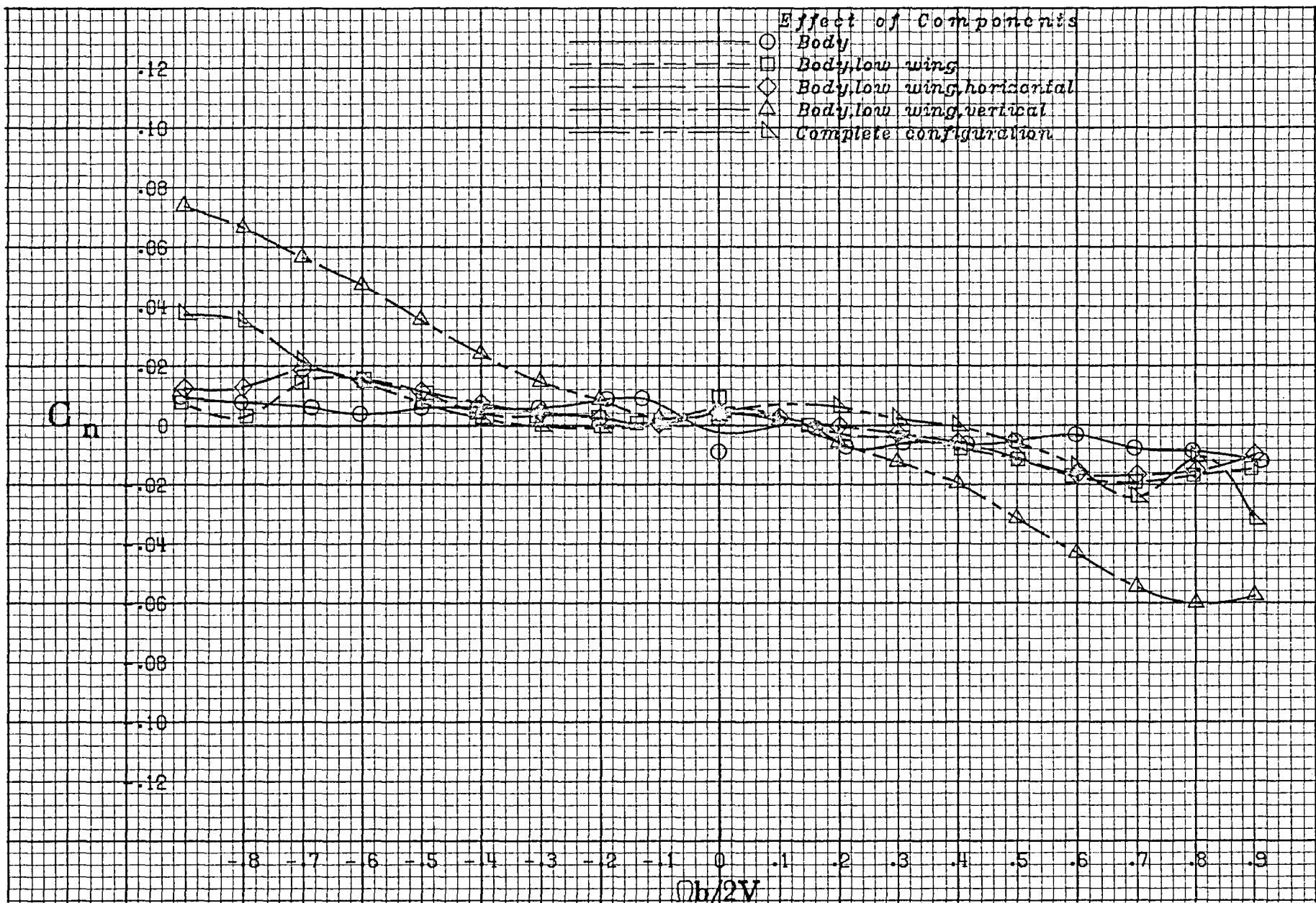


c) 30° angle of attack.
Figure 8.- Continued.



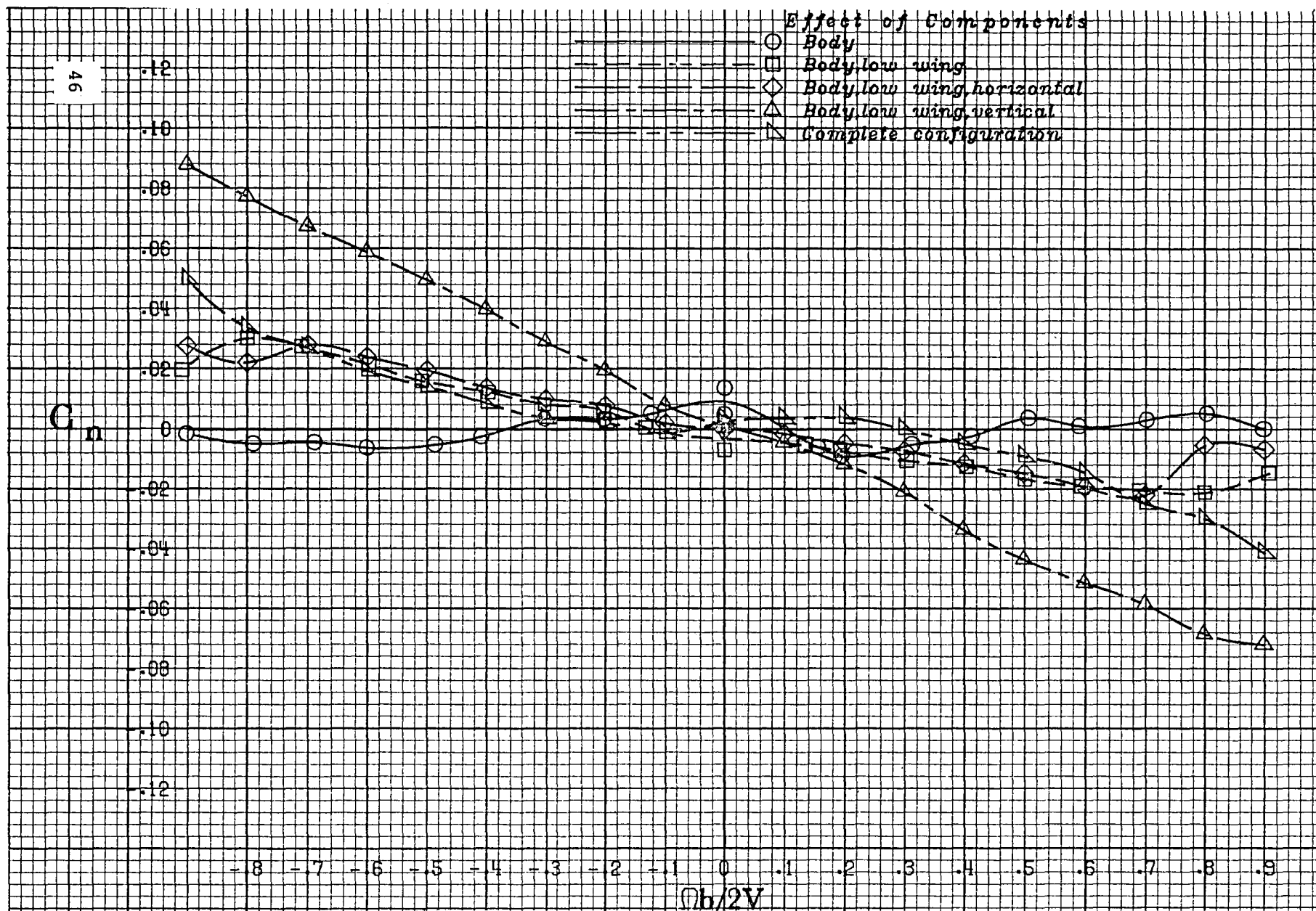
d) 40° angle of attack.

Figure 8.- Continued.



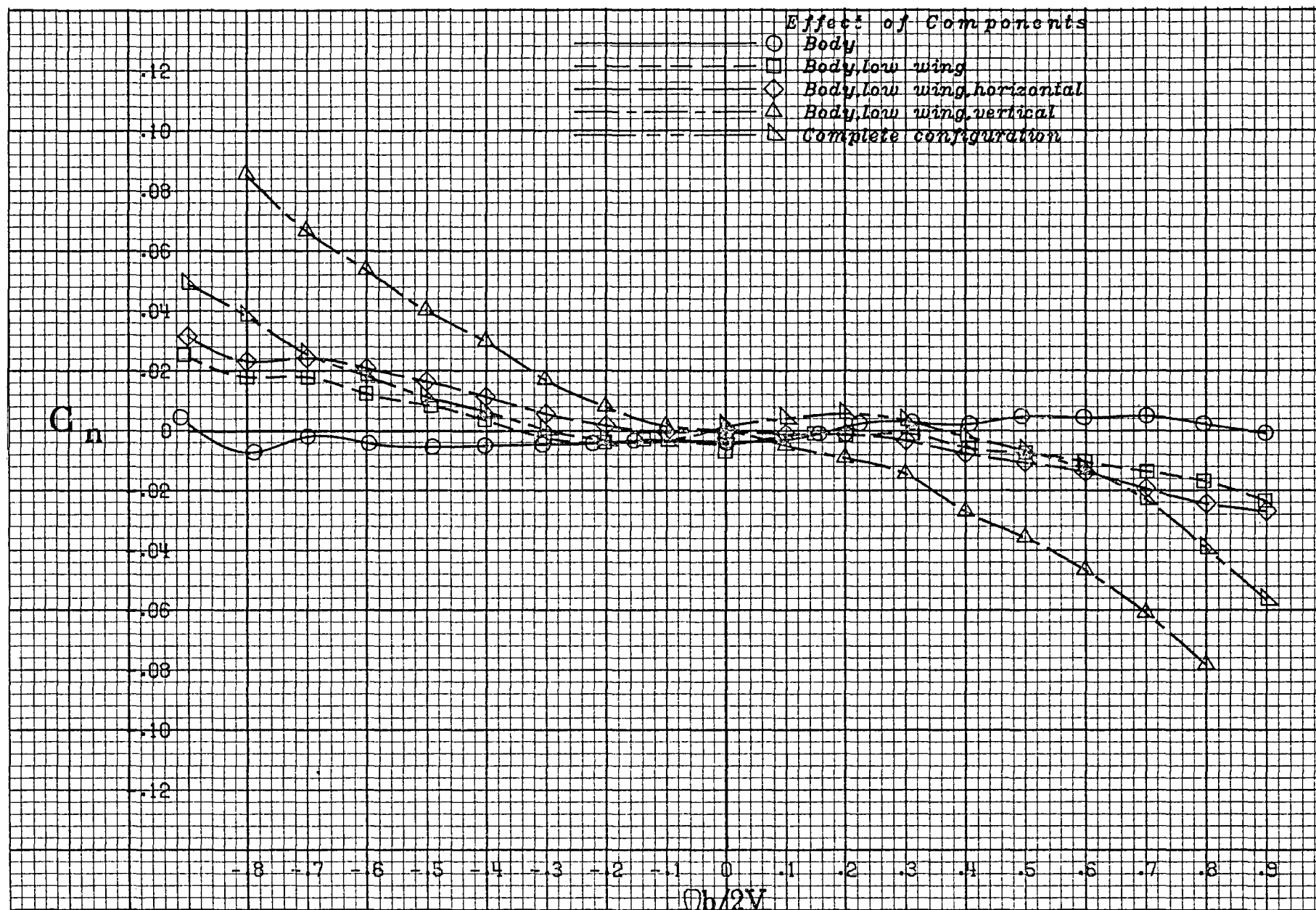
e) 50° angle of attack.

Figure 8.- Continued.



f) 60° angle of attack.

Figure 8.- Continued.



g) 80° angle of attack.

Figure 8.- Concluded.

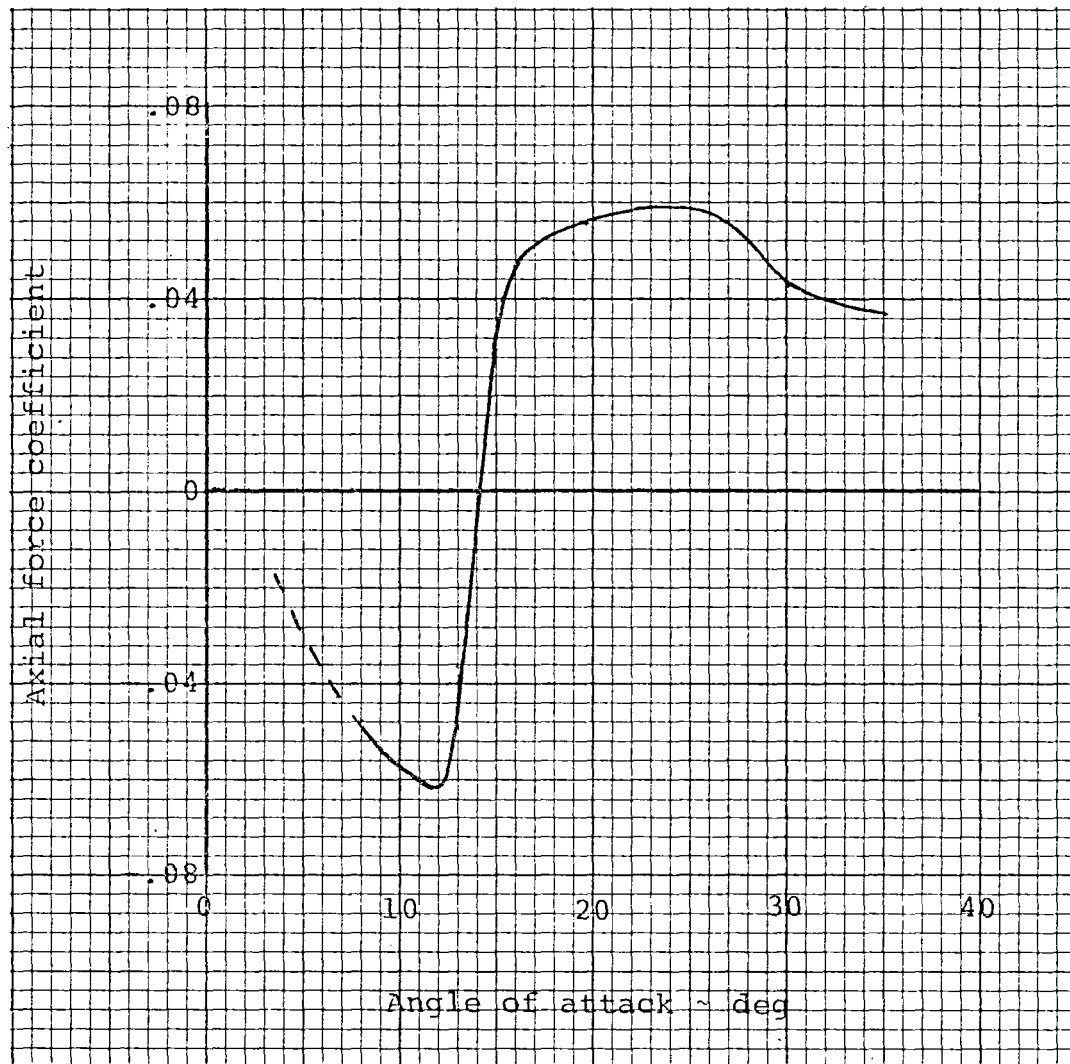


Figure 9.- Static wing axial-force coefficient as a function of angle of attack.

Incremental C_n due to vertical tail.

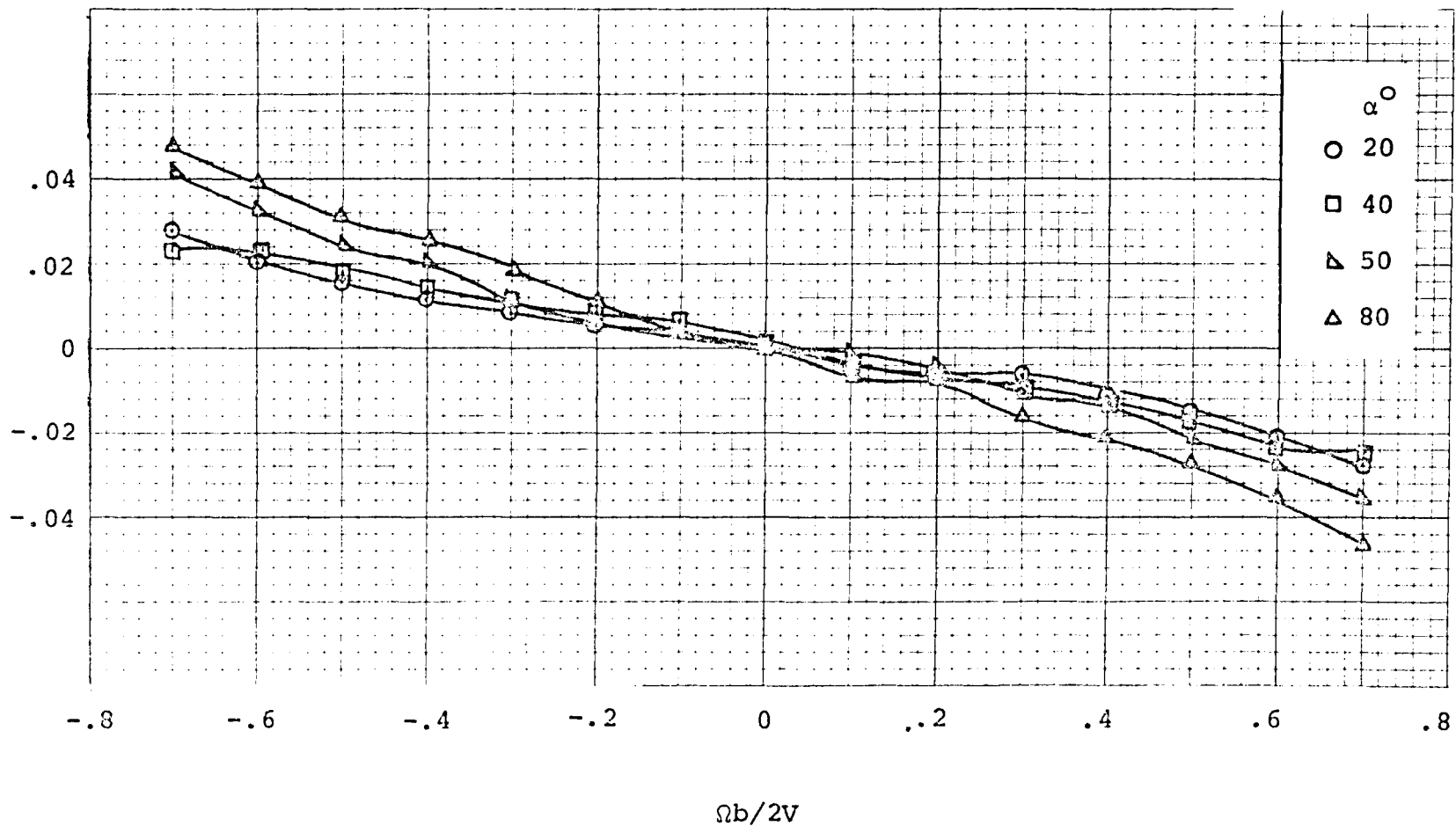


Figure 10.- Vertical tail effectiveness in the presence of the body-wing at various angles of attack. Incremental $C_n = C_n$ (body-wing-vertical) minus C_n (body-wing).

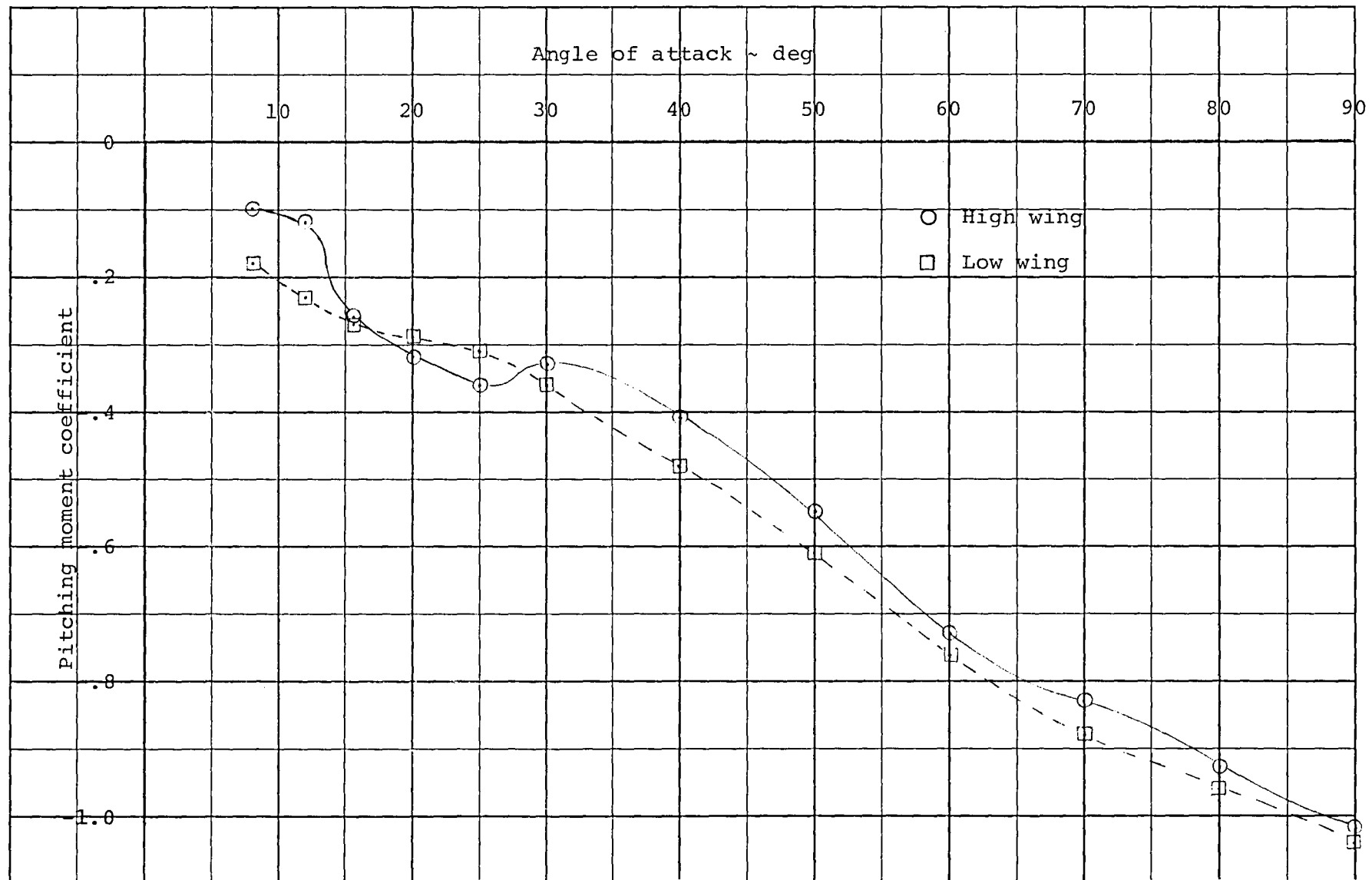
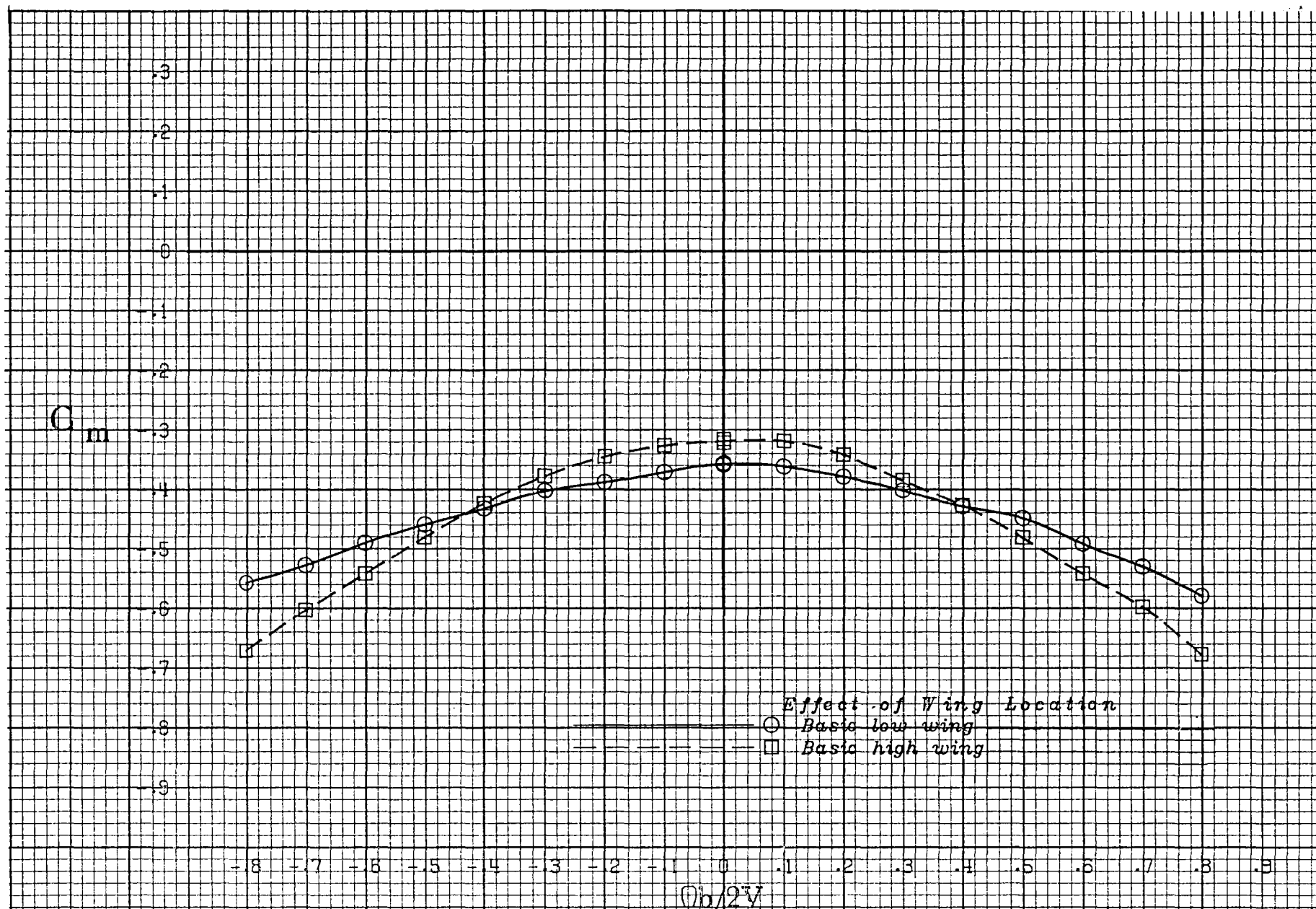
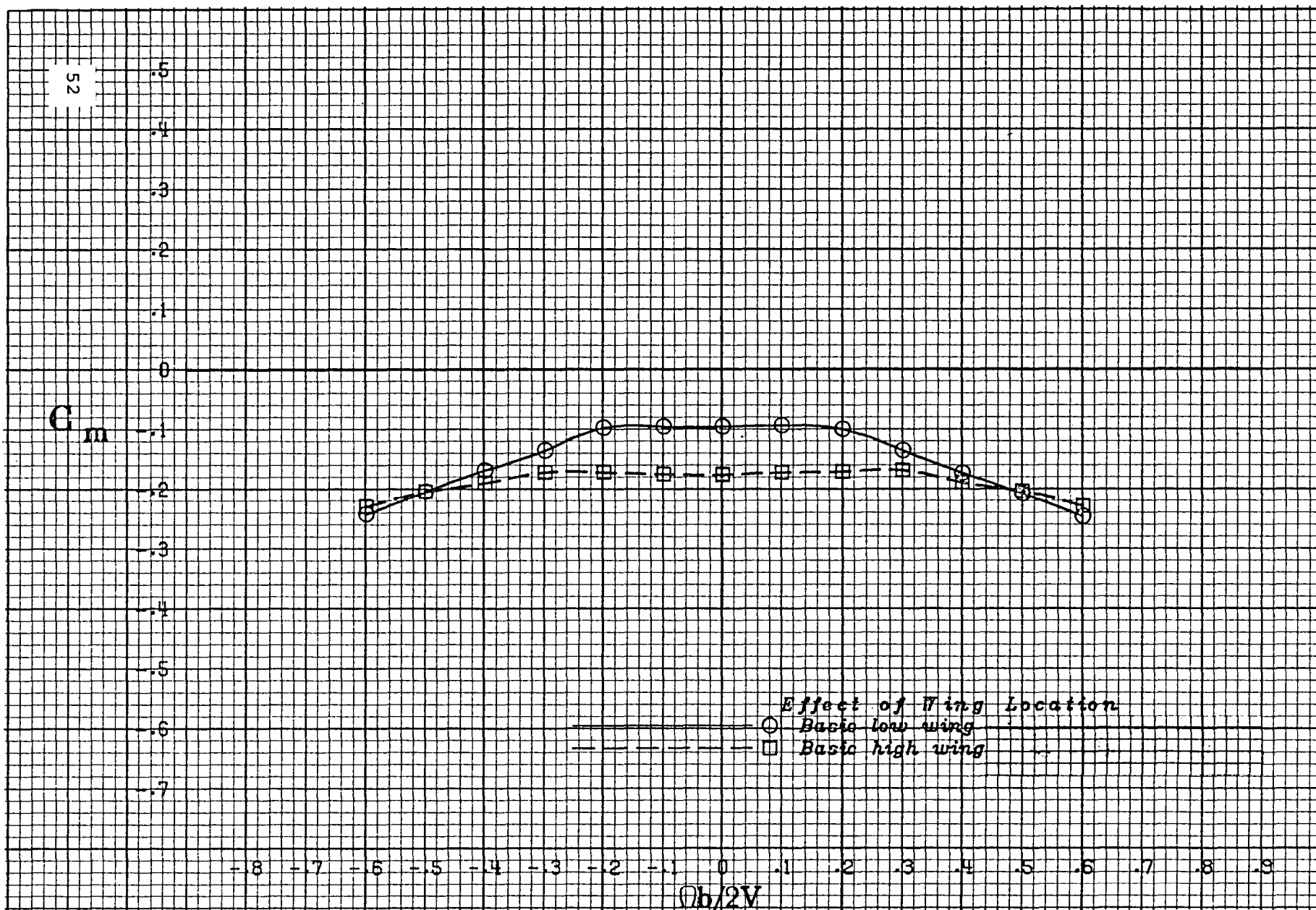


Figure 11.- Static pitching-moment coefficient as a function of angle of attack for the high and low wing configurations.



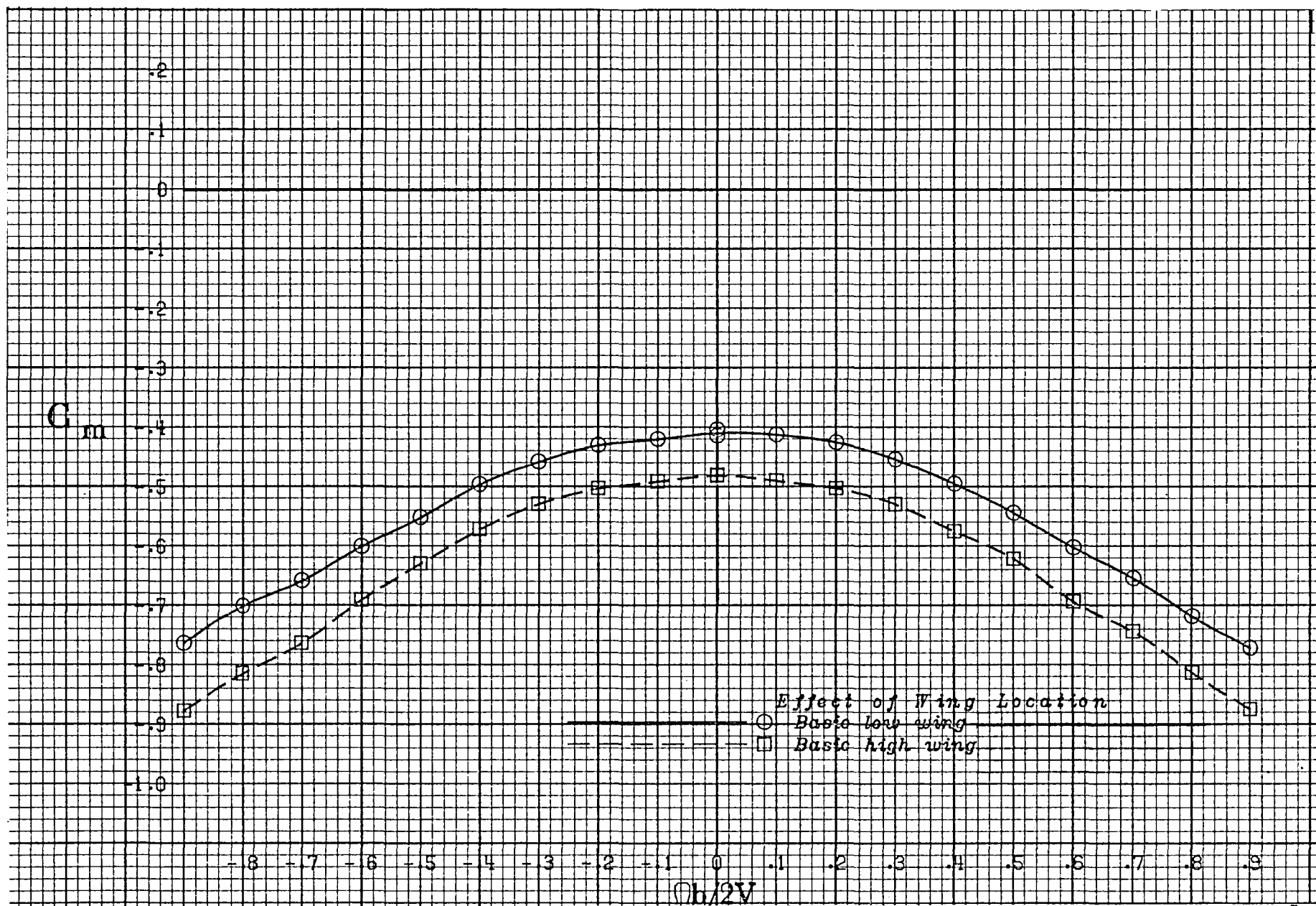
a) 8° angle of attack.

Figure 12.- Effect of wing location on pitching-moment coefficient.

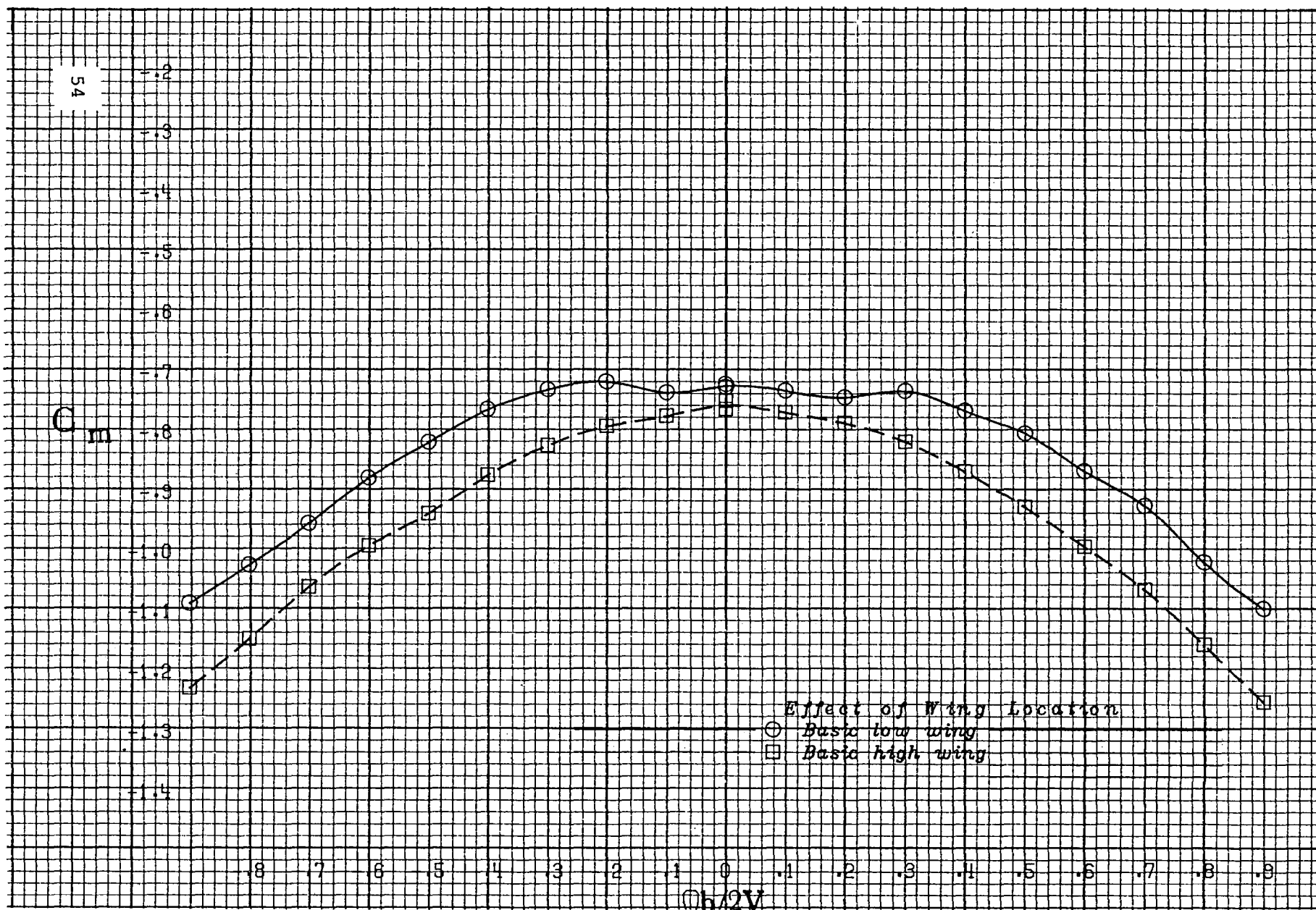


b) 25° angle of attack.

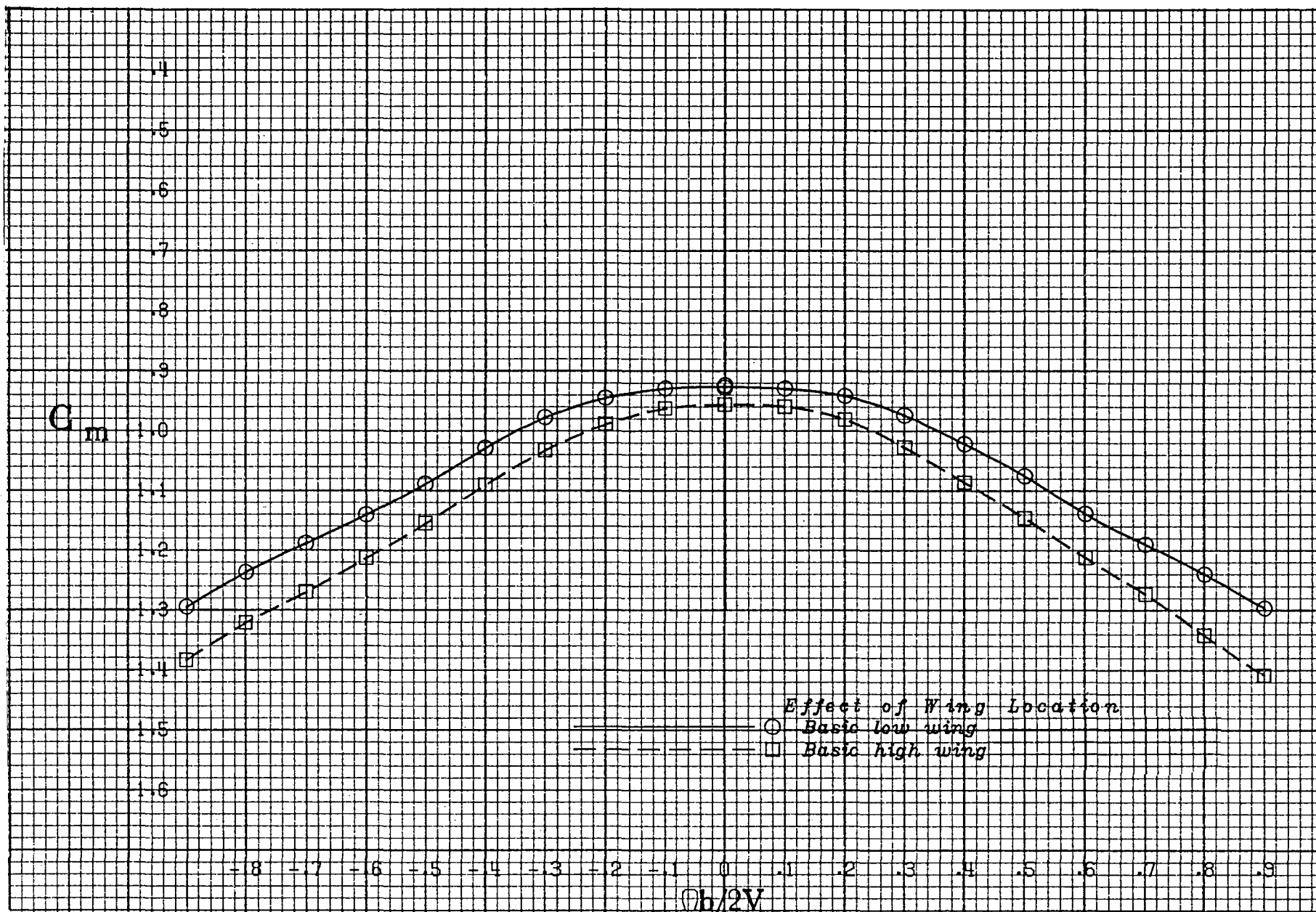
Figure 12.- Continued.



c) 40° angle of attack.
 Figure 12.- Continued.

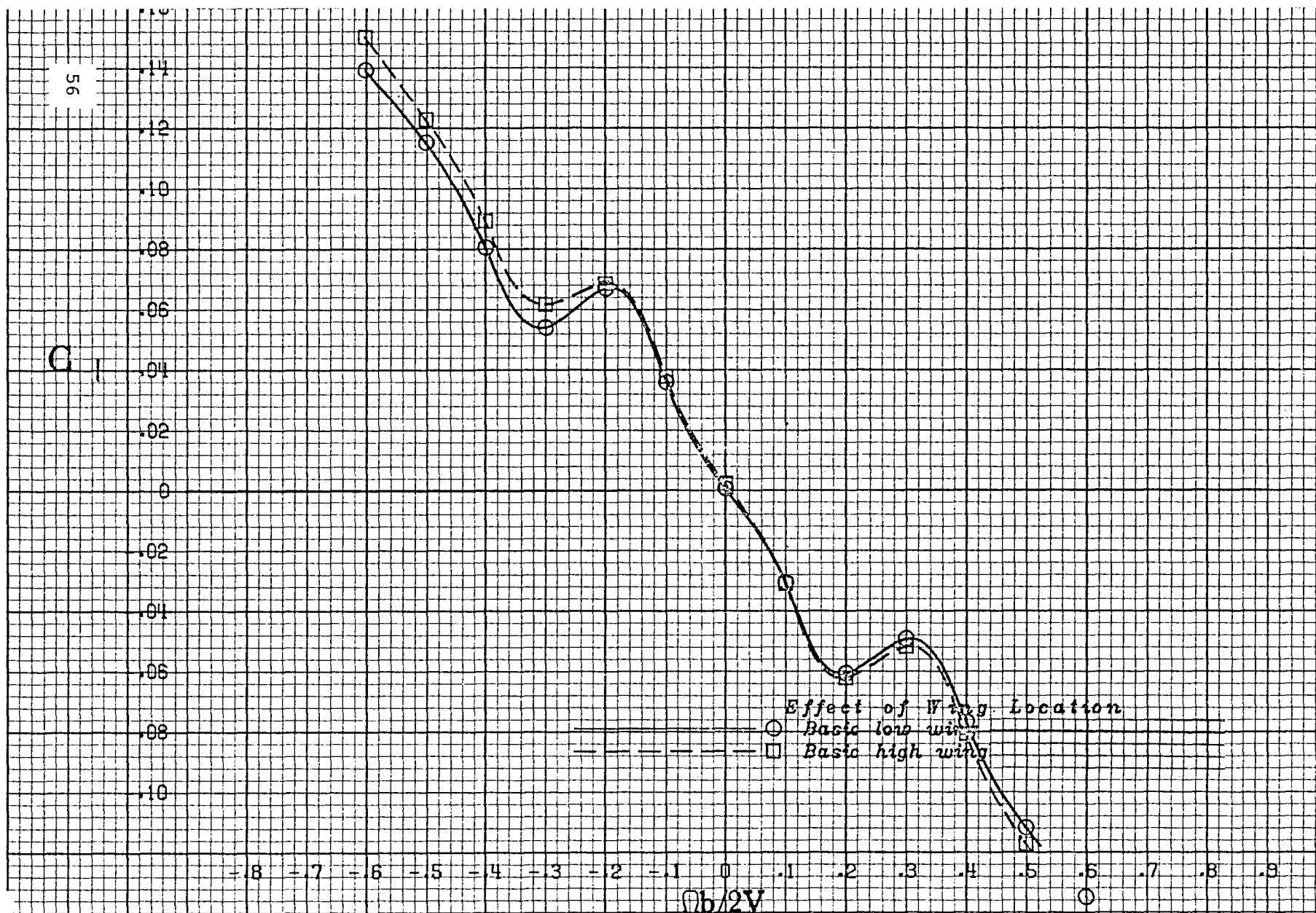


d) 60° angle of attack.
Figure 12.- Continued.



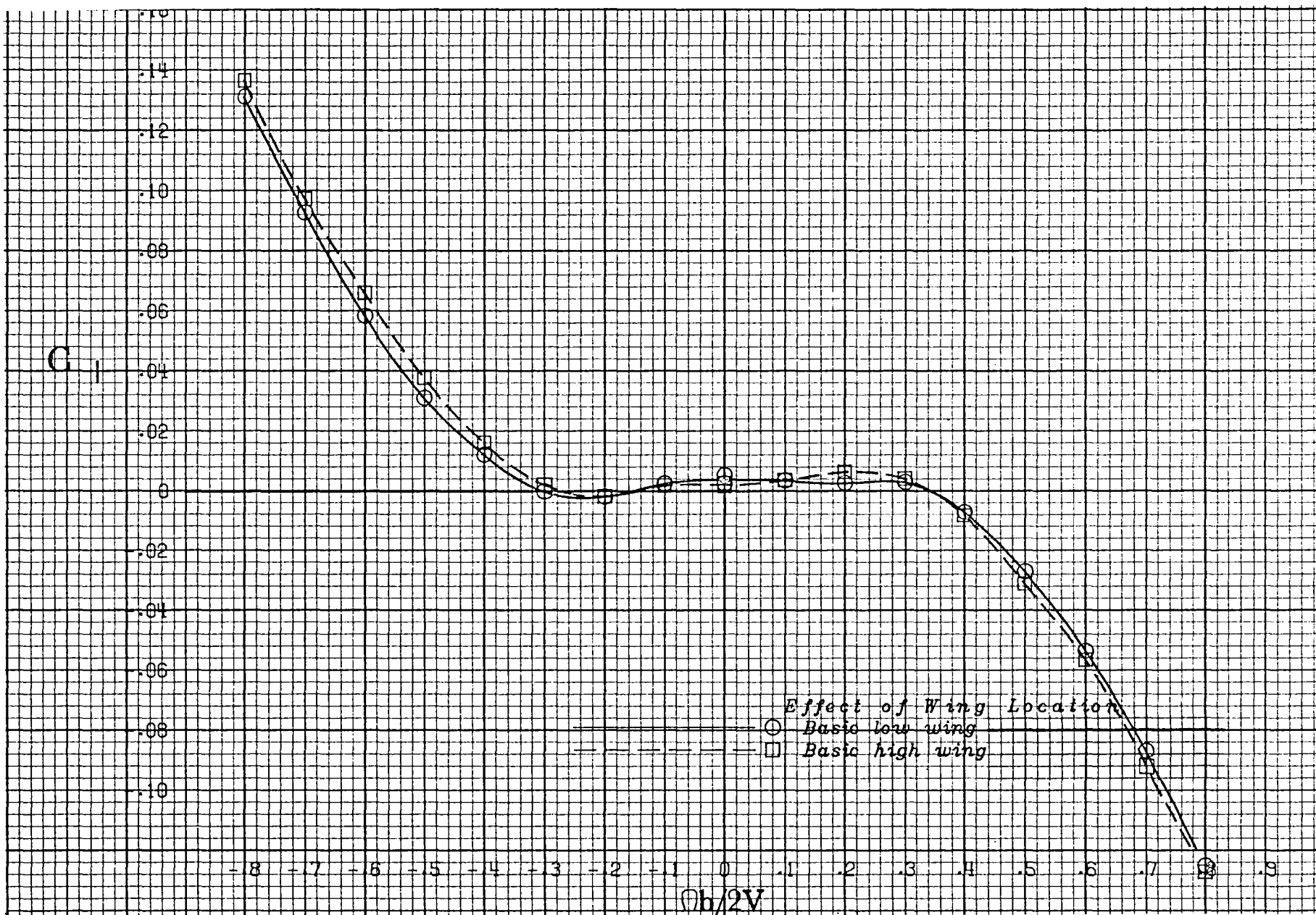
e) 80° angle of attack.

Figure 12.- Concluded.



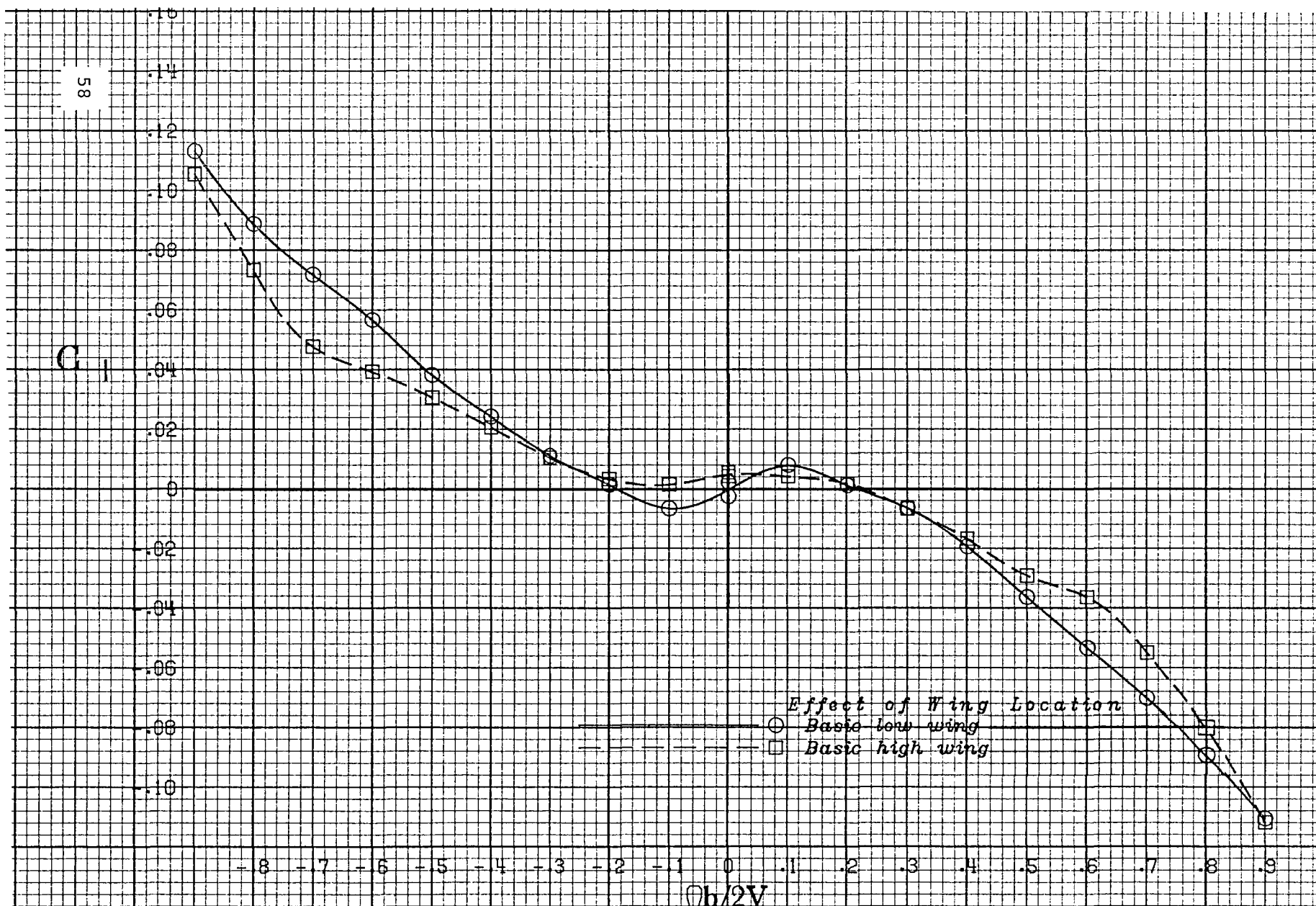
a) 8° angle of attack.

Figure 13.- Effect of wing location on rolling-moment coefficient.

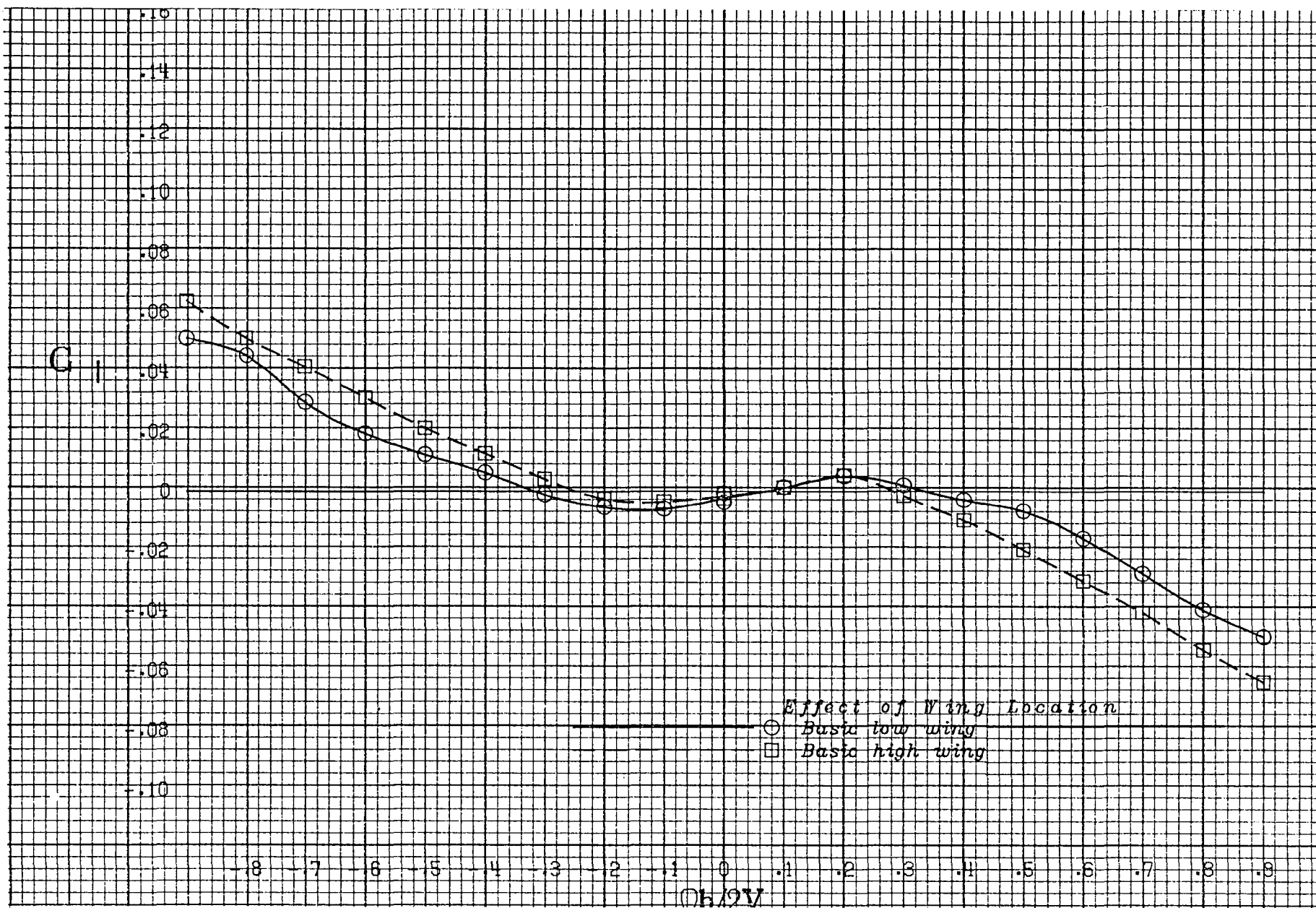


b) 25° angle of attack.

Figure 13.- Continued.

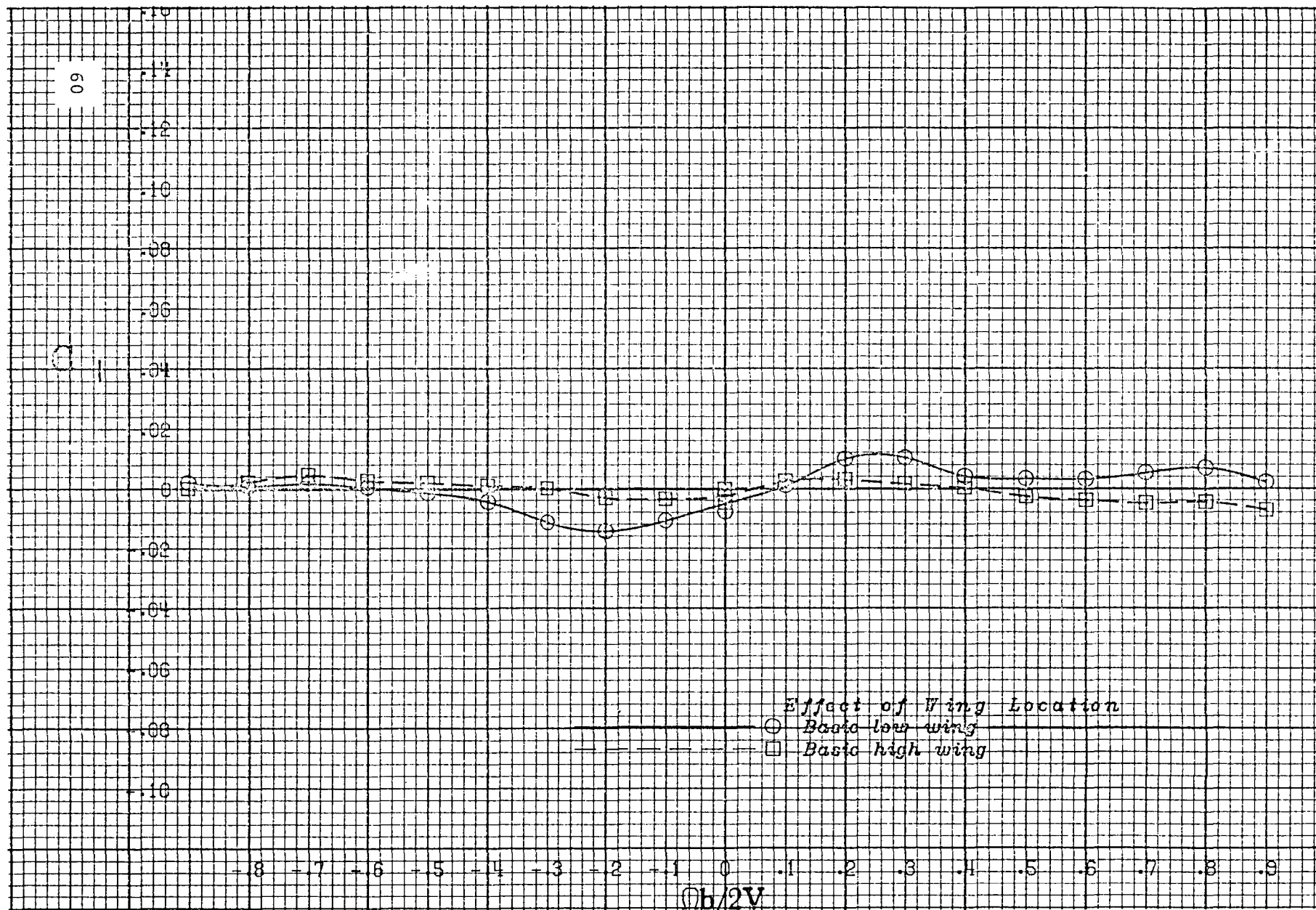


c) 40° angle of attack.
Figure 13.- Continued.



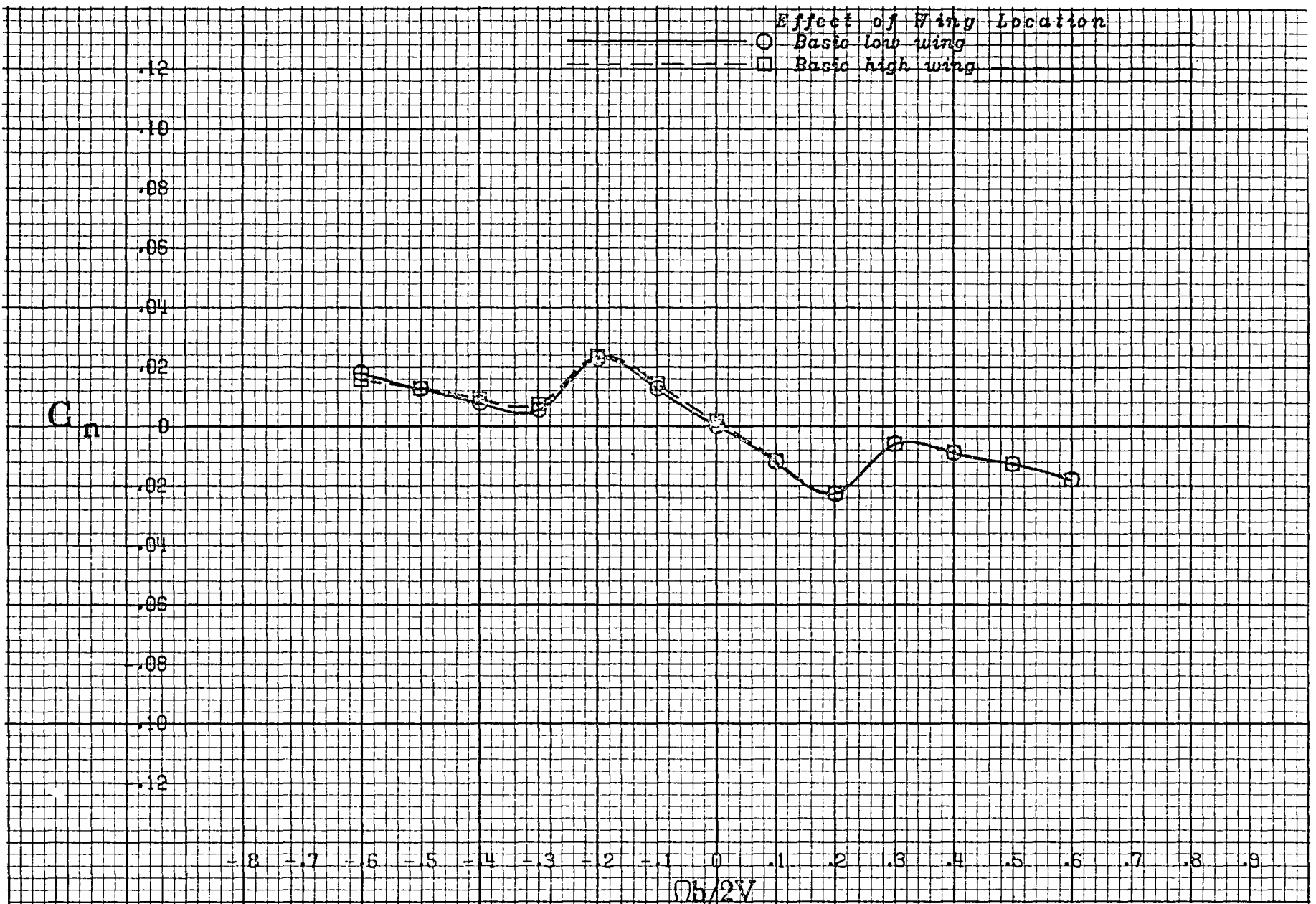
d) 60° angle of attack.

Figure 13.- Continued.



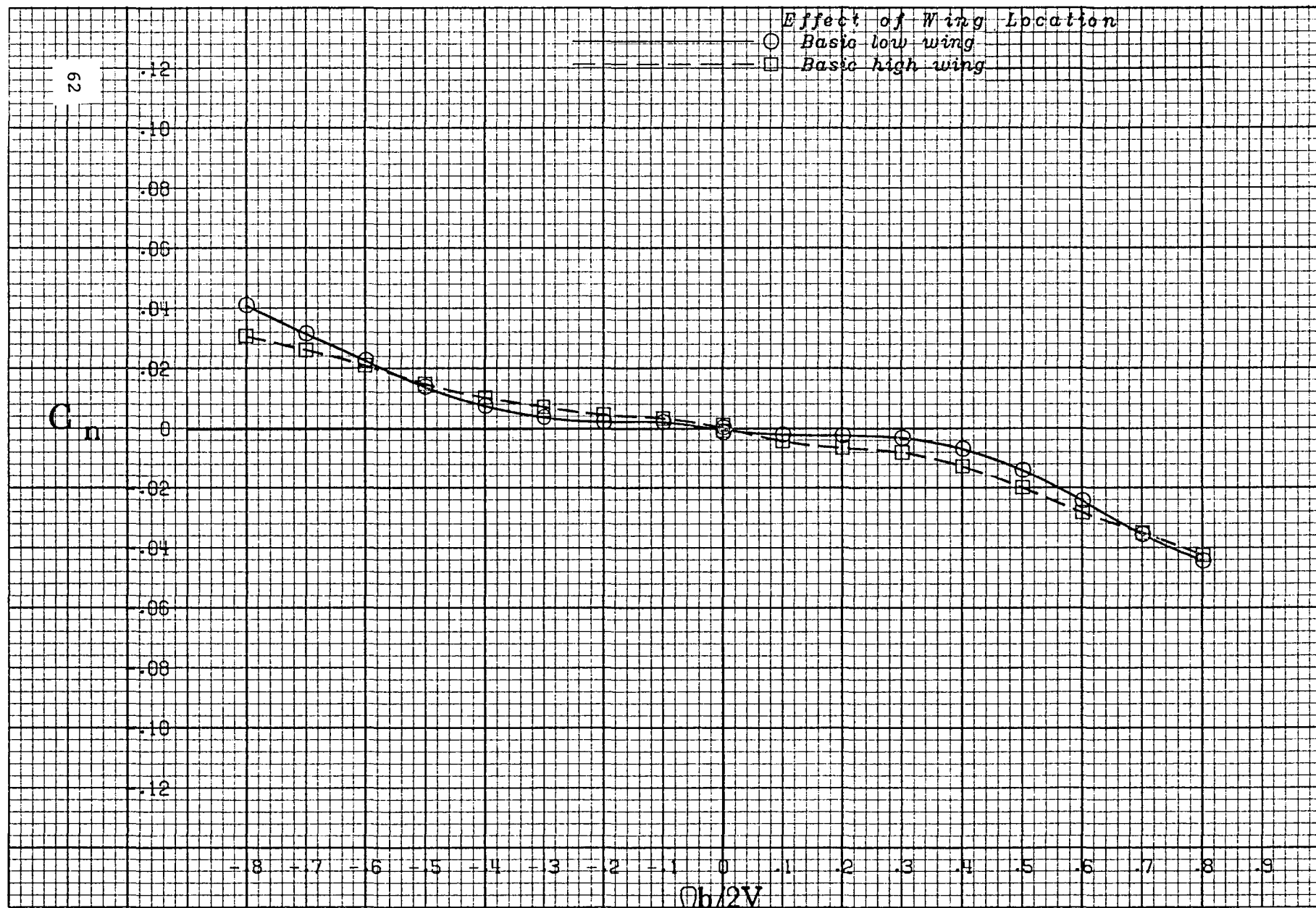
e) 80° angle of attack.

Figure 13.- Concluded.



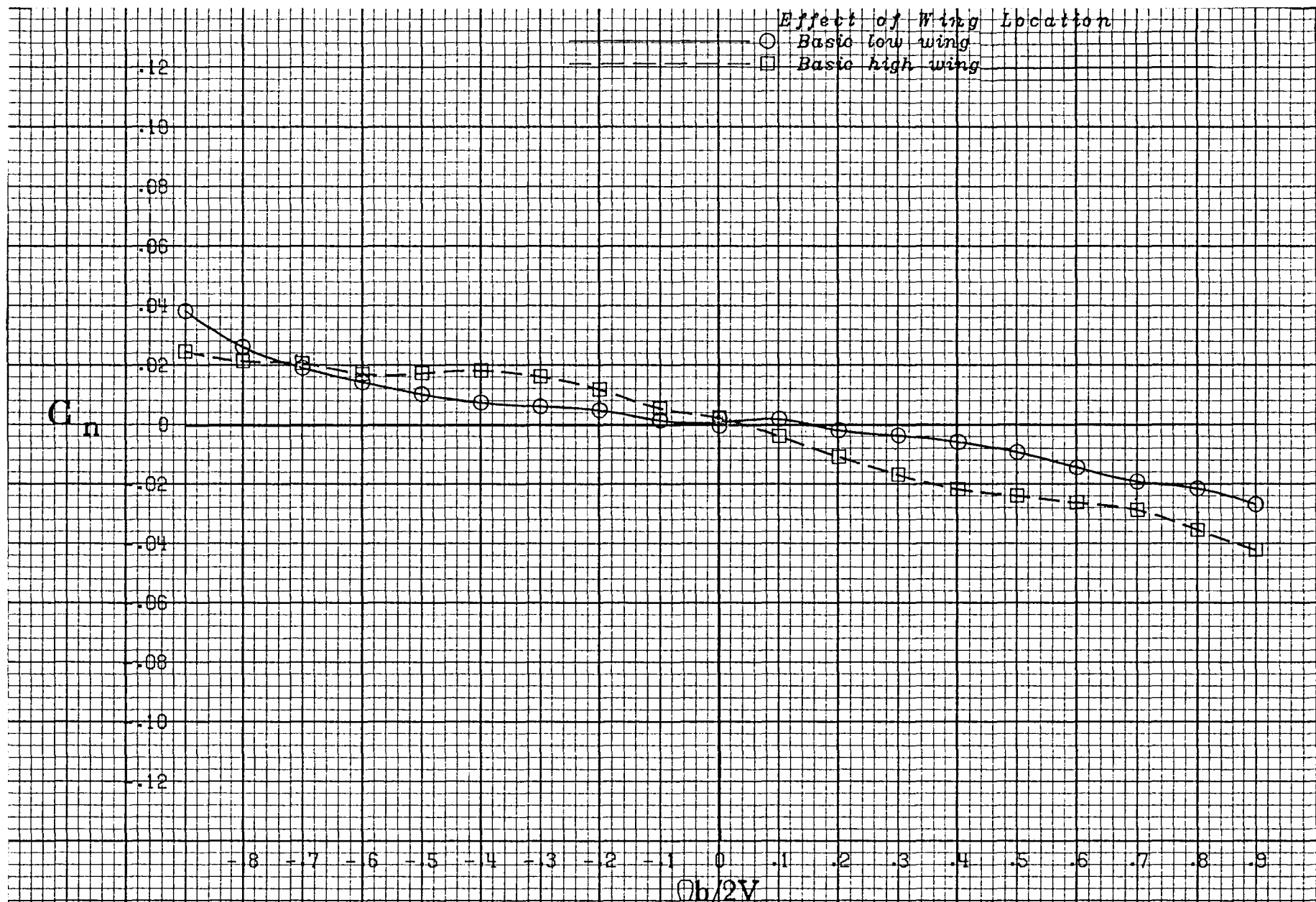
a) 8° angle of attack.

Figure 14.- Effect of wing location on yawing-moment coefficient.



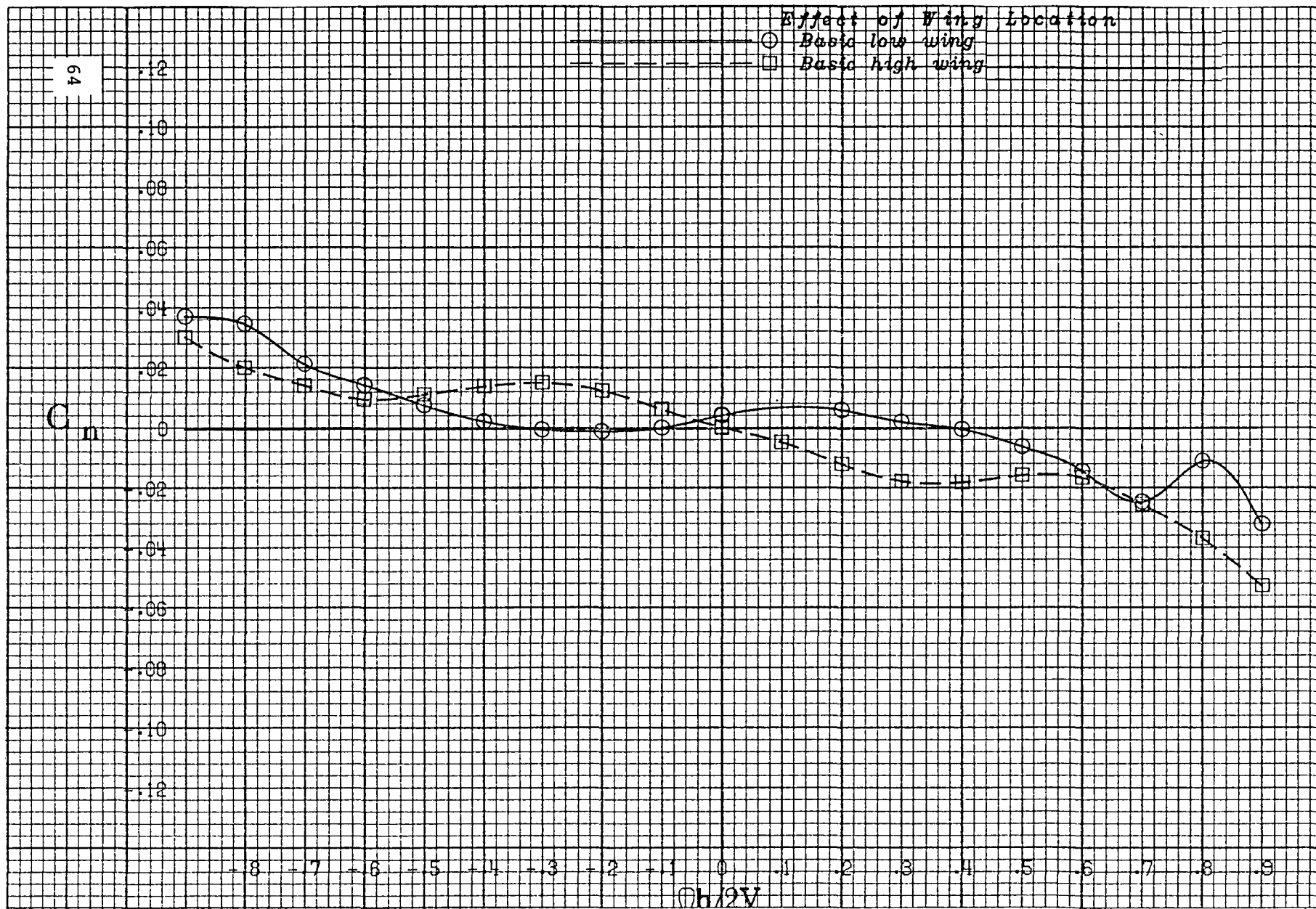
b) 25° angle of attack.

Figure 14.- Continued.



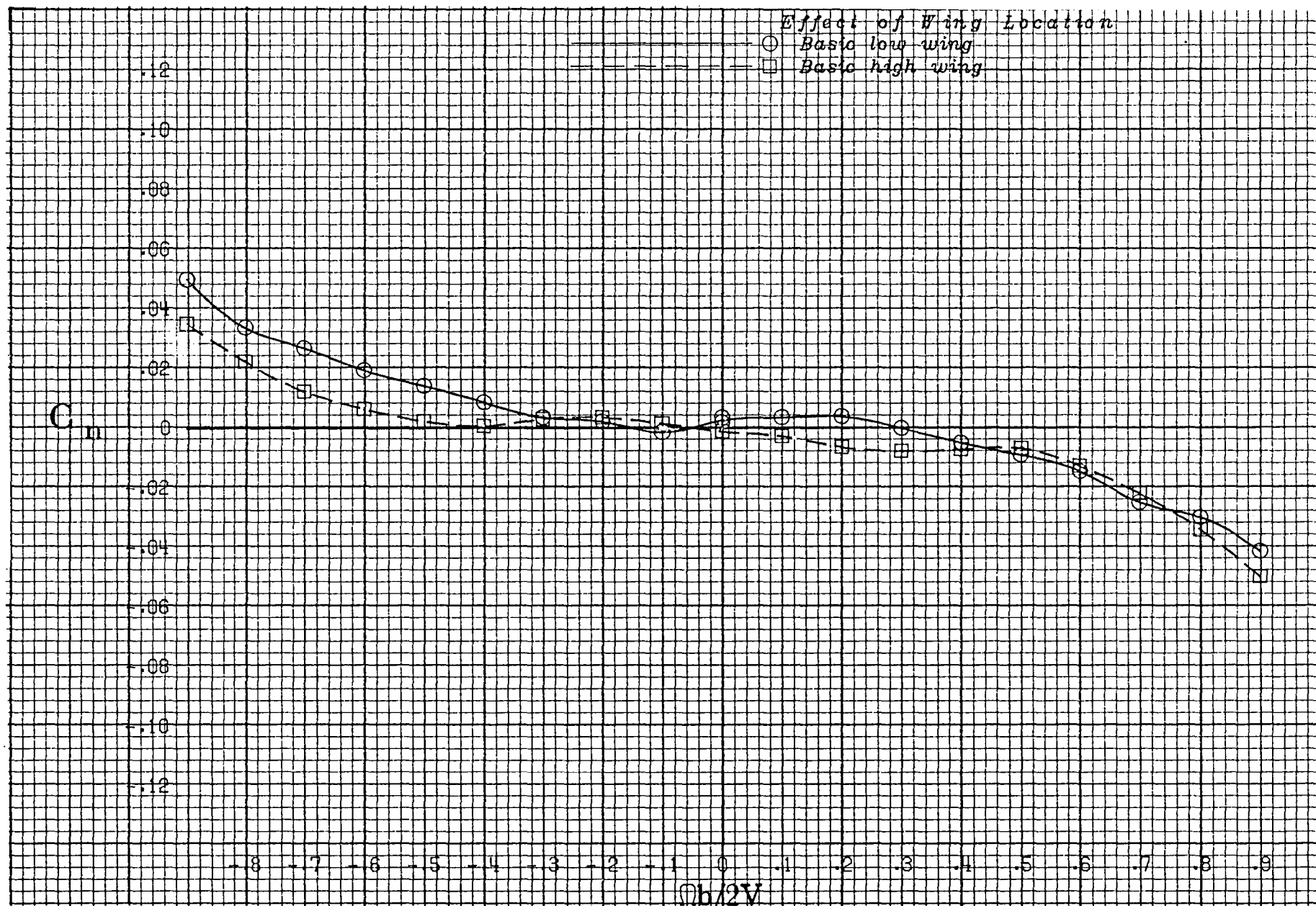
c) 40° angle of attack.

Figure 14.- Continued.

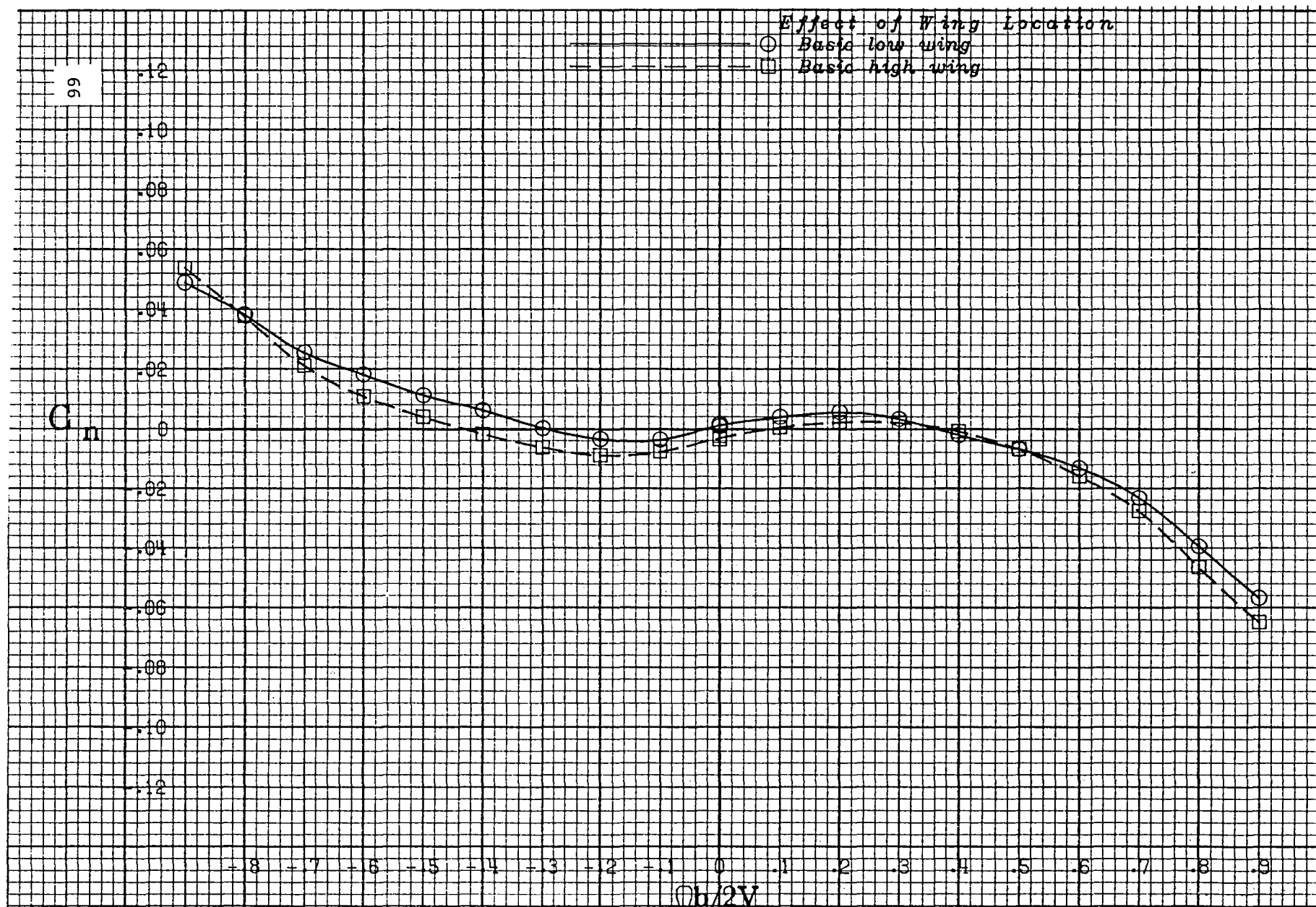


d) 50° angle of attack.

Figure 14.- Continued.



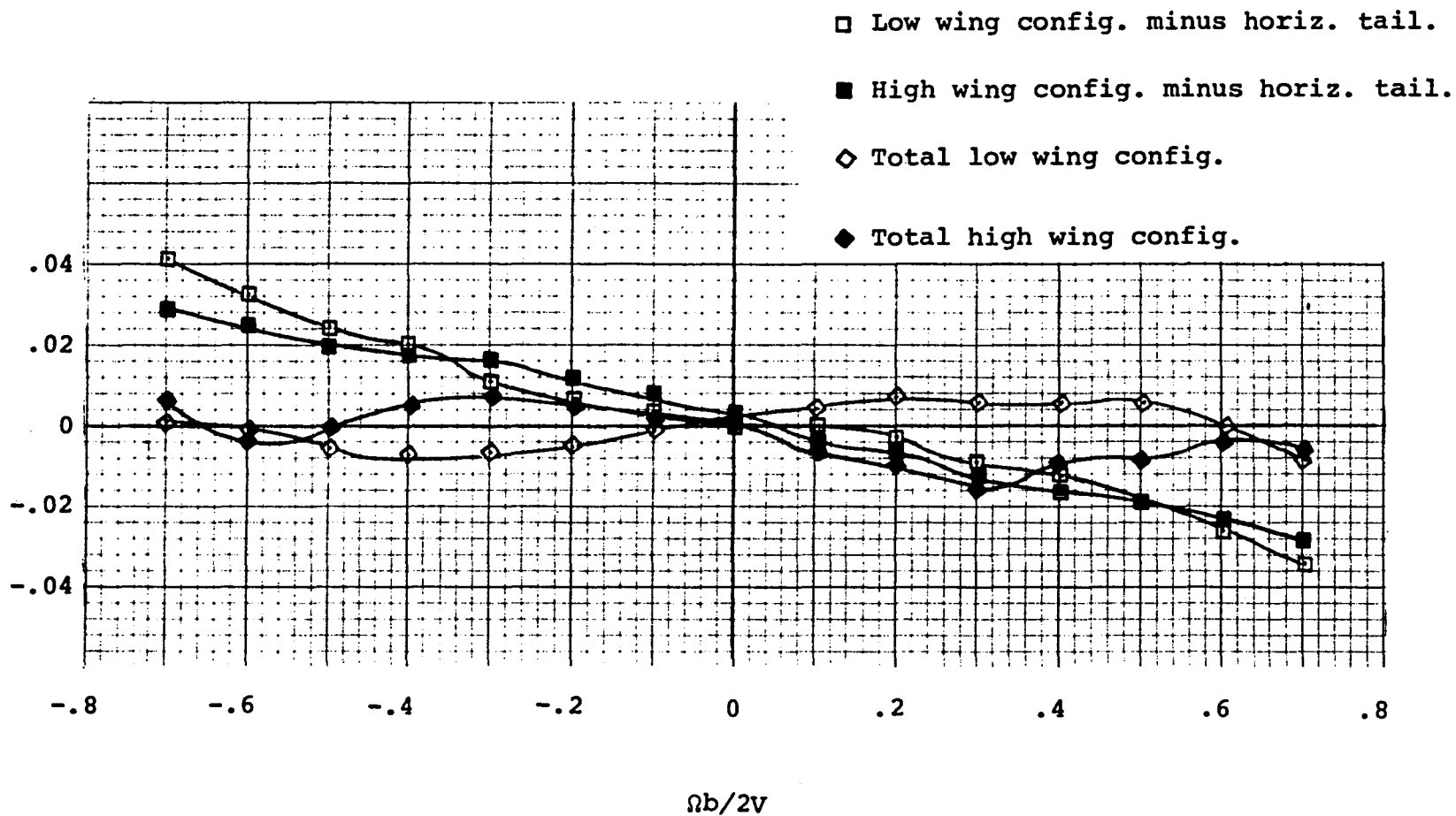
e) 60° angle of attack.
Figure 14.- Continued.



f) 80° angle of attack.

Figure 14.- Concluded.

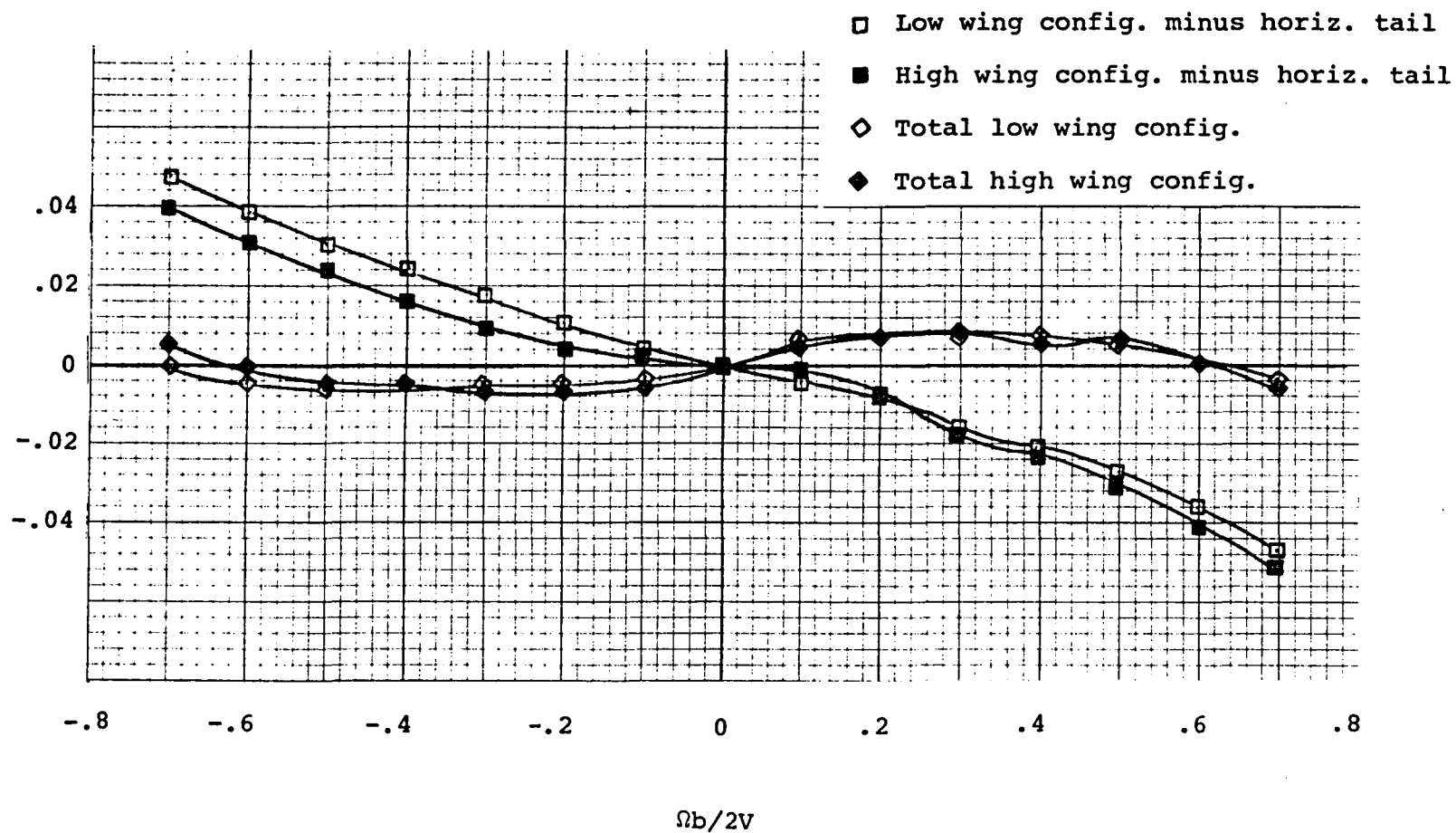
Incremental C_n due to vertical tail.



a) 50° angle of attack.

Figure 15.- Influence of horizontal tail on vertical tail effectiveness for the high and low wing positions.

Incremental C_n due to vertical tail.



b) 80° angle of attack.
Figure 15.- Concluded.

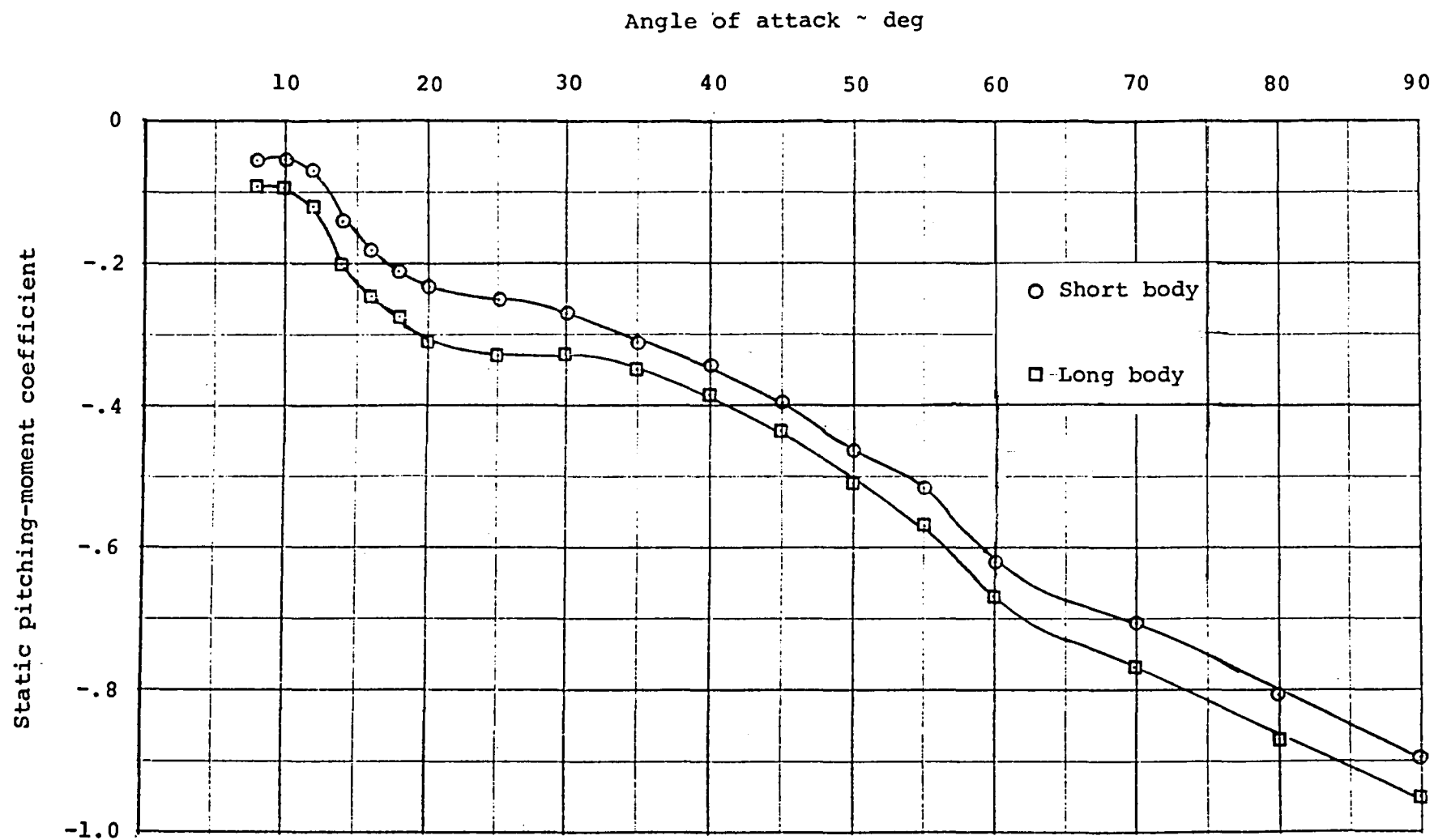
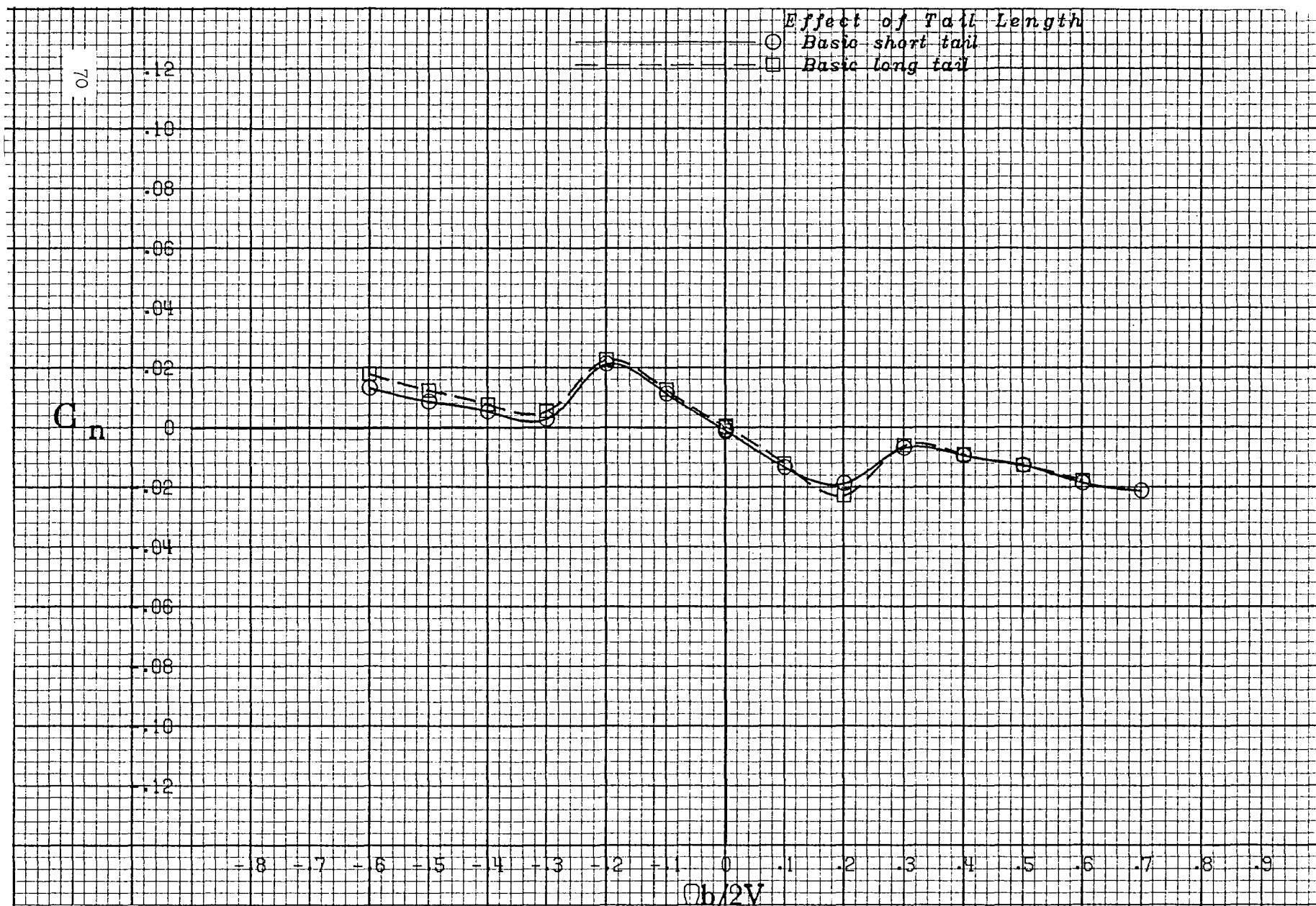
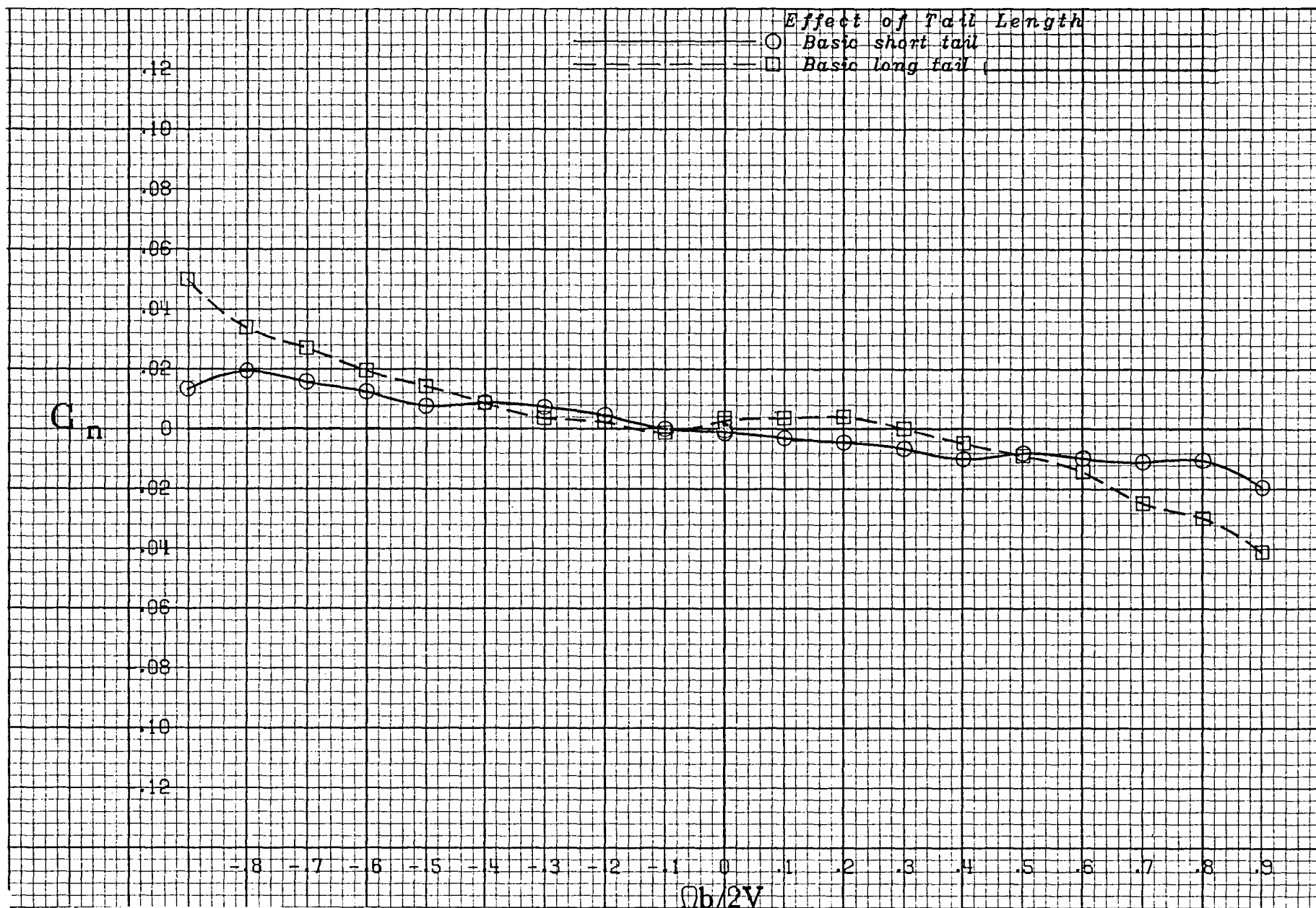


Figure 16.- Static pitching-moment coefficient as a function of angle of attack for the long and short body configurations.



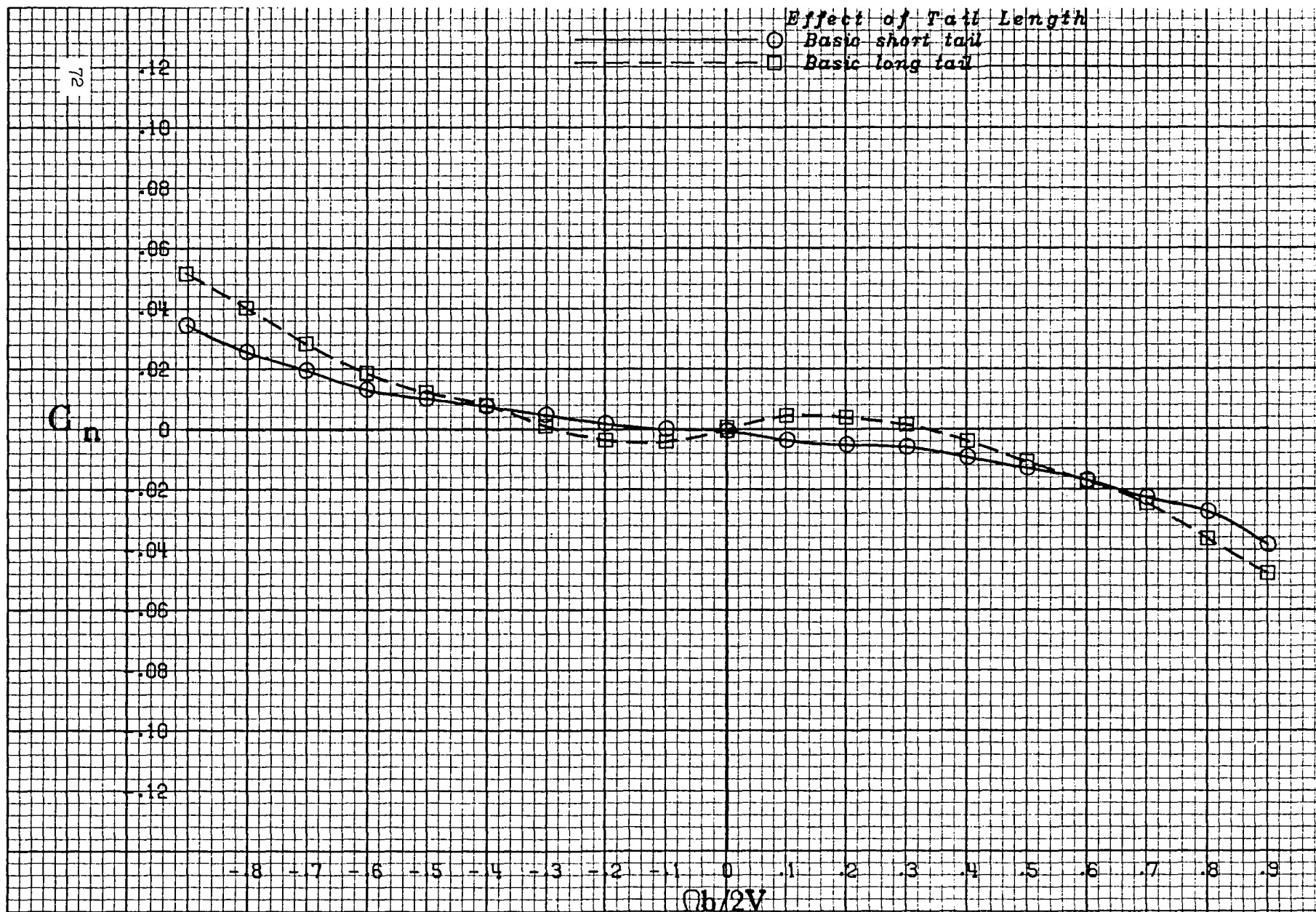
a) 8° angle of attack.

Figure 17.- Effect of tail length on yawing-moment coefficient.



b) 60° angle of attack.

Figure 17.- Continued.



c) 90° angle of attack.

Figure 17.- Concluded.

Incremental C_n due to body length.

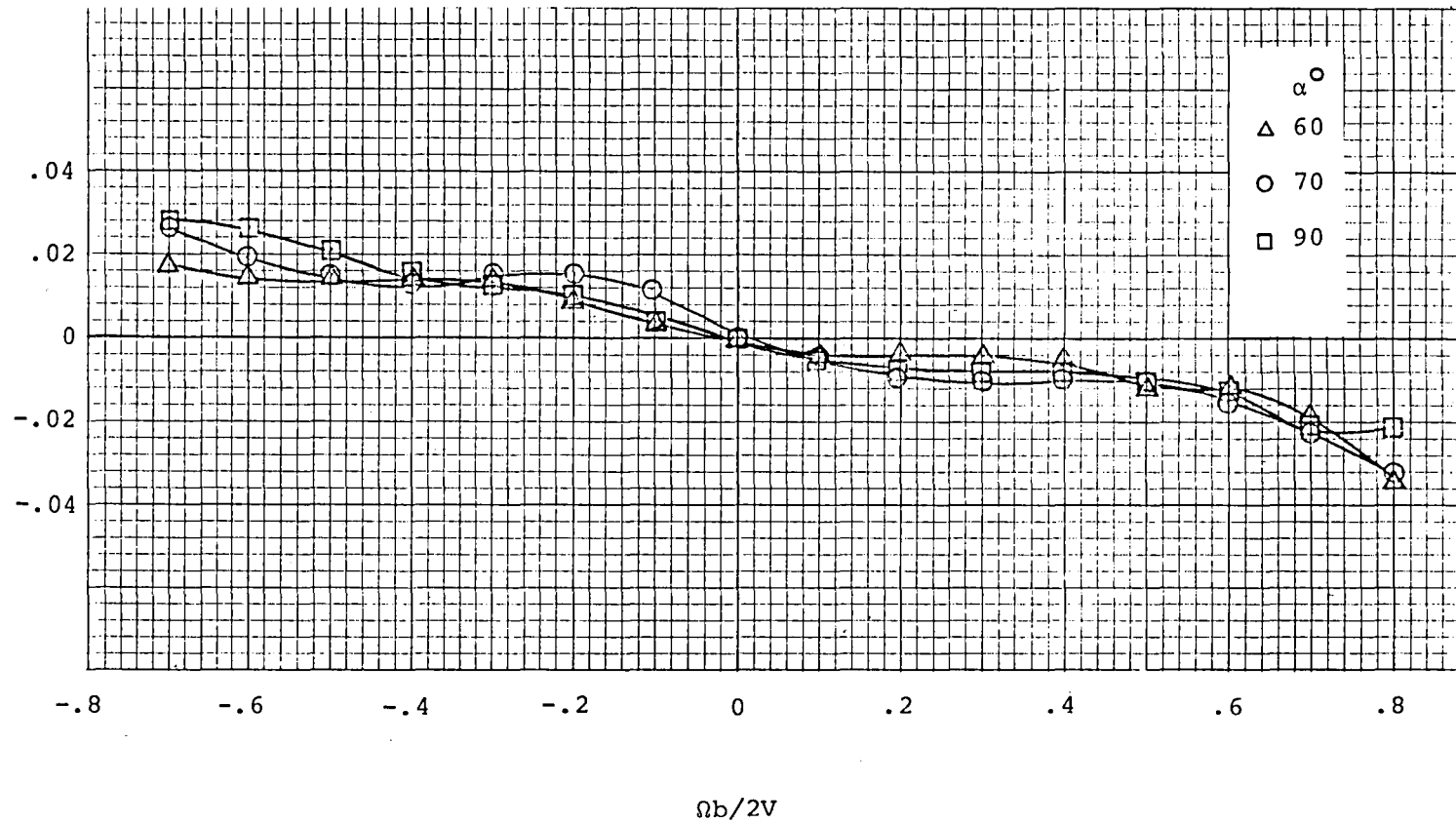
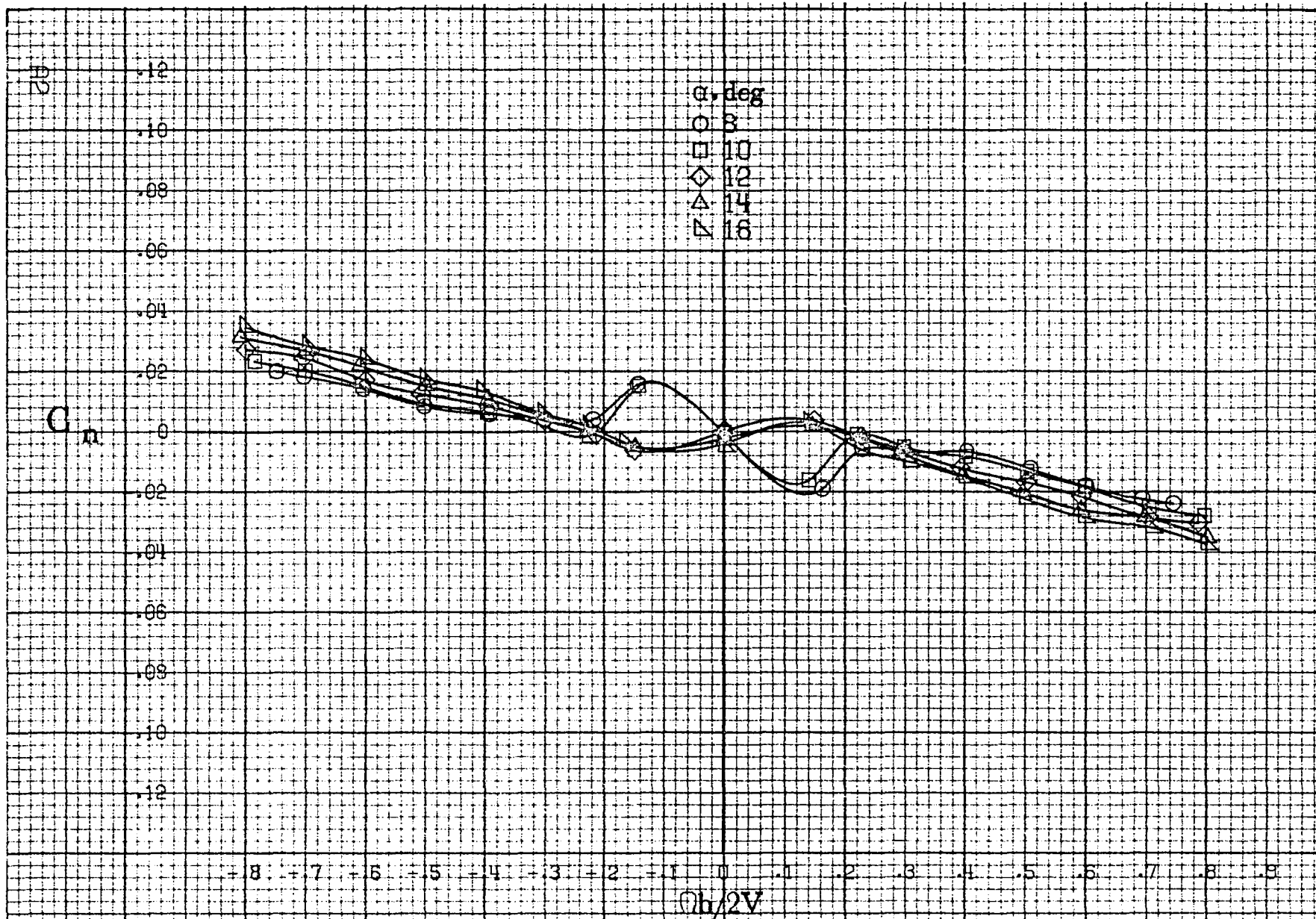


Figure 18.- Influence of body length on yawing moment in the absence of a horizontal tail for various angles of attack. Incremental $C_n = C_n$ (long body-wing-vertical) minus C_n (short body-wing-vertical).

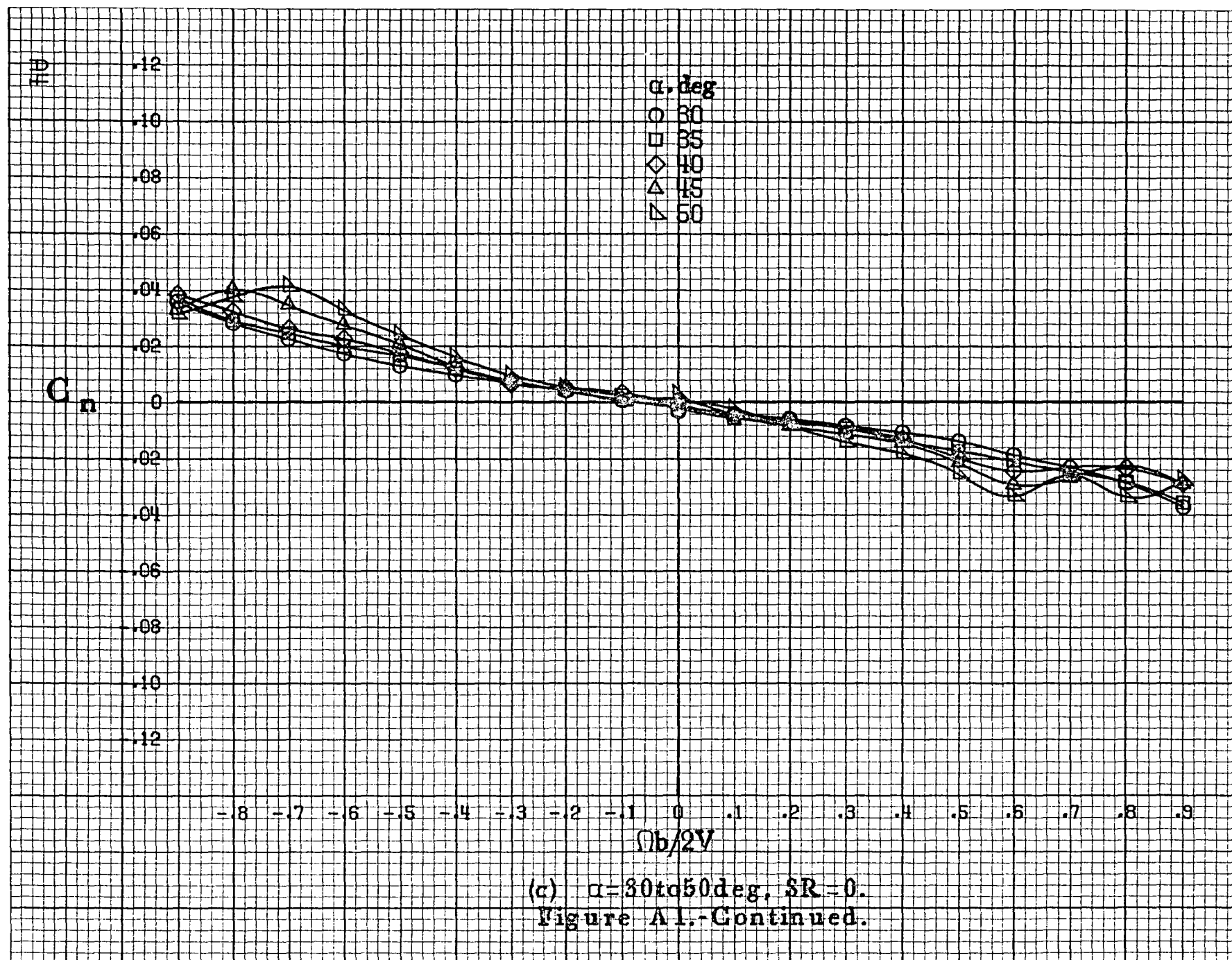
APPENDIX

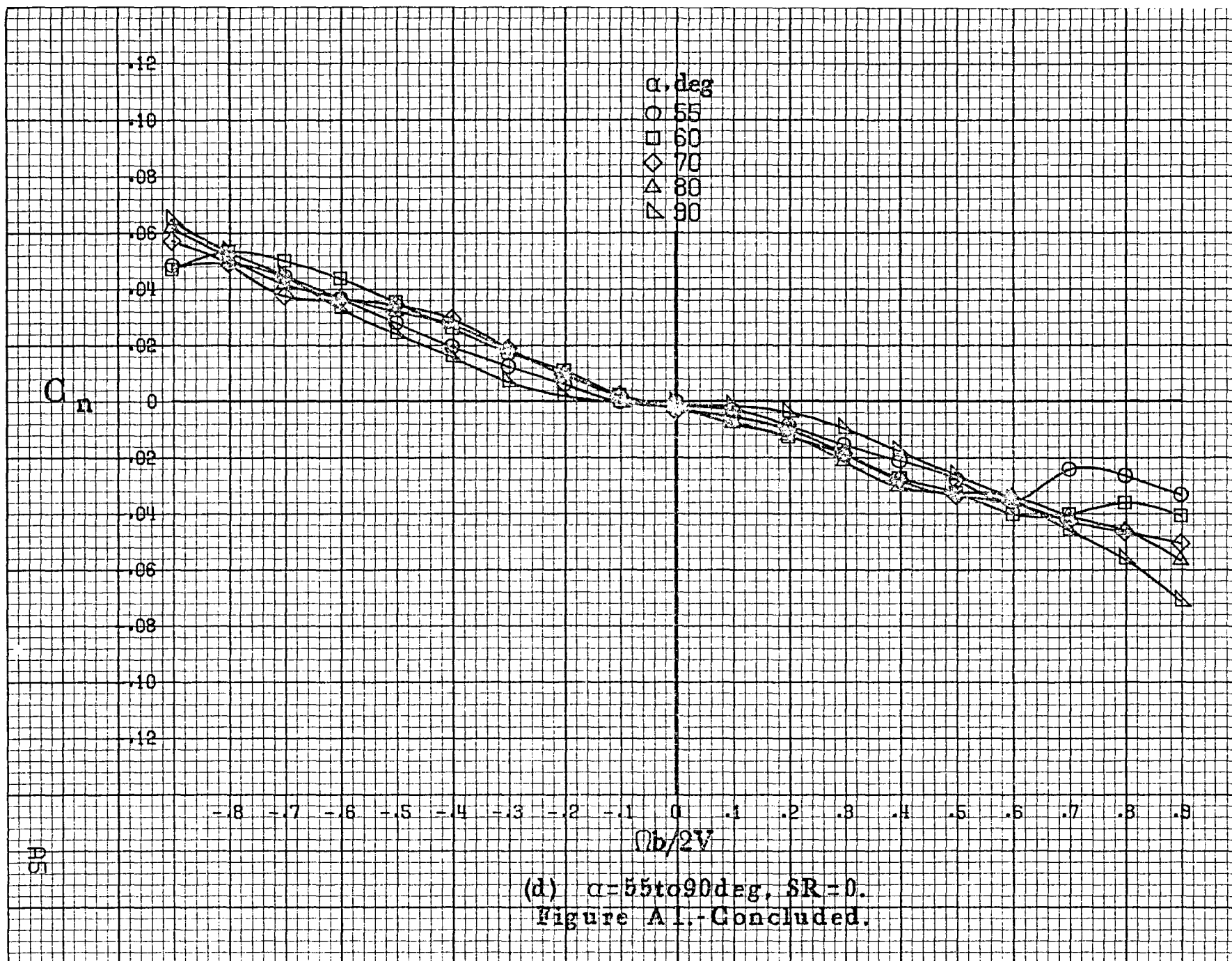


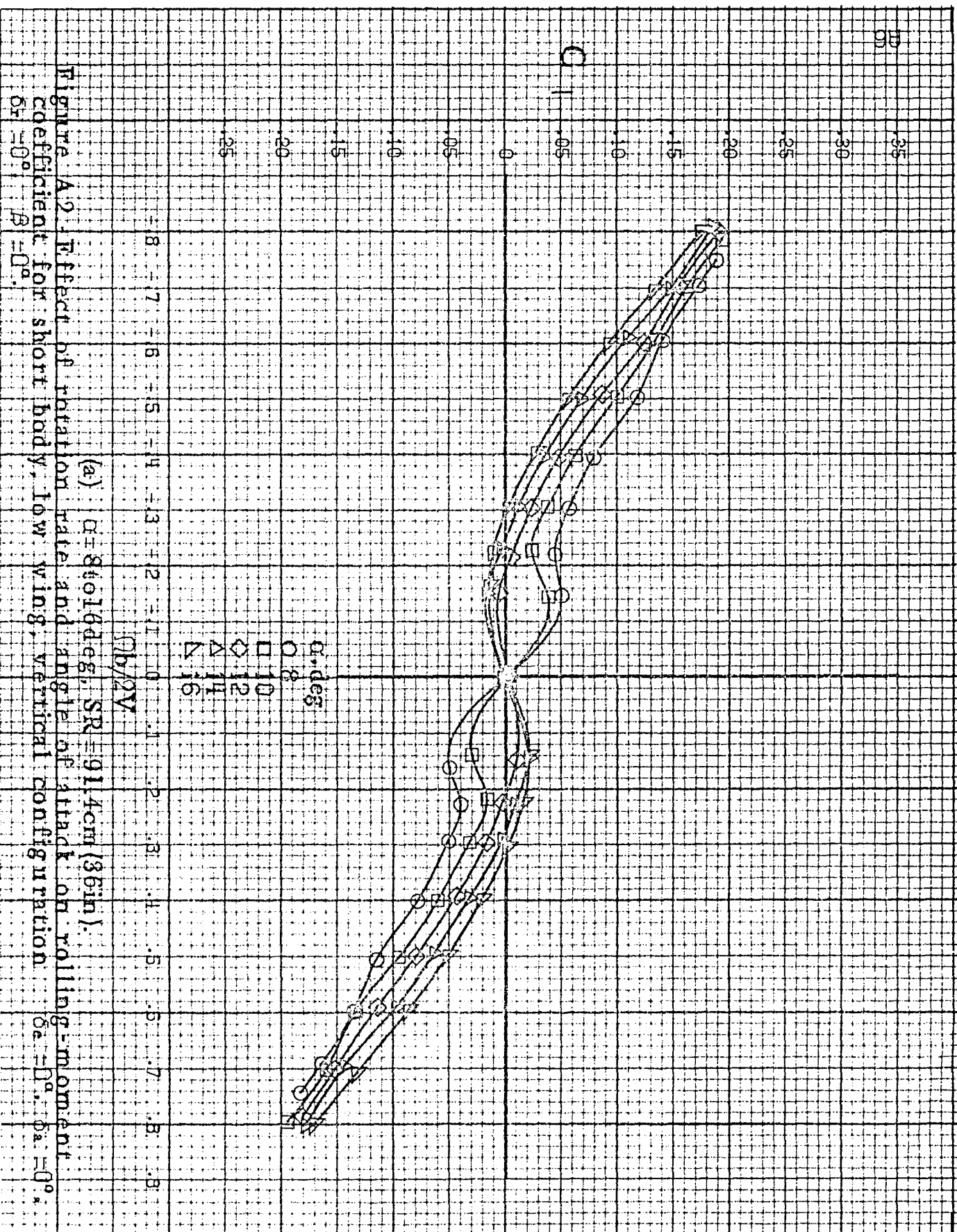
(a) $\alpha=8$ to 16° , $SR=91.4\text{cm}(36\text{in})$.

Figure A1 - Effect of rotation rate and angle of attack on yawing-moment coefficient for short body, low wing, vertical configuration $\delta_e=0^\circ$, $\delta_a=0^\circ$, $\delta_r=0^\circ$, $\beta=0^\circ$.











88

C₁

.18
.16
.14
.12
.10
.08
.06
.04
.02
0
-.02
-.04
-.06
-.08
-.10

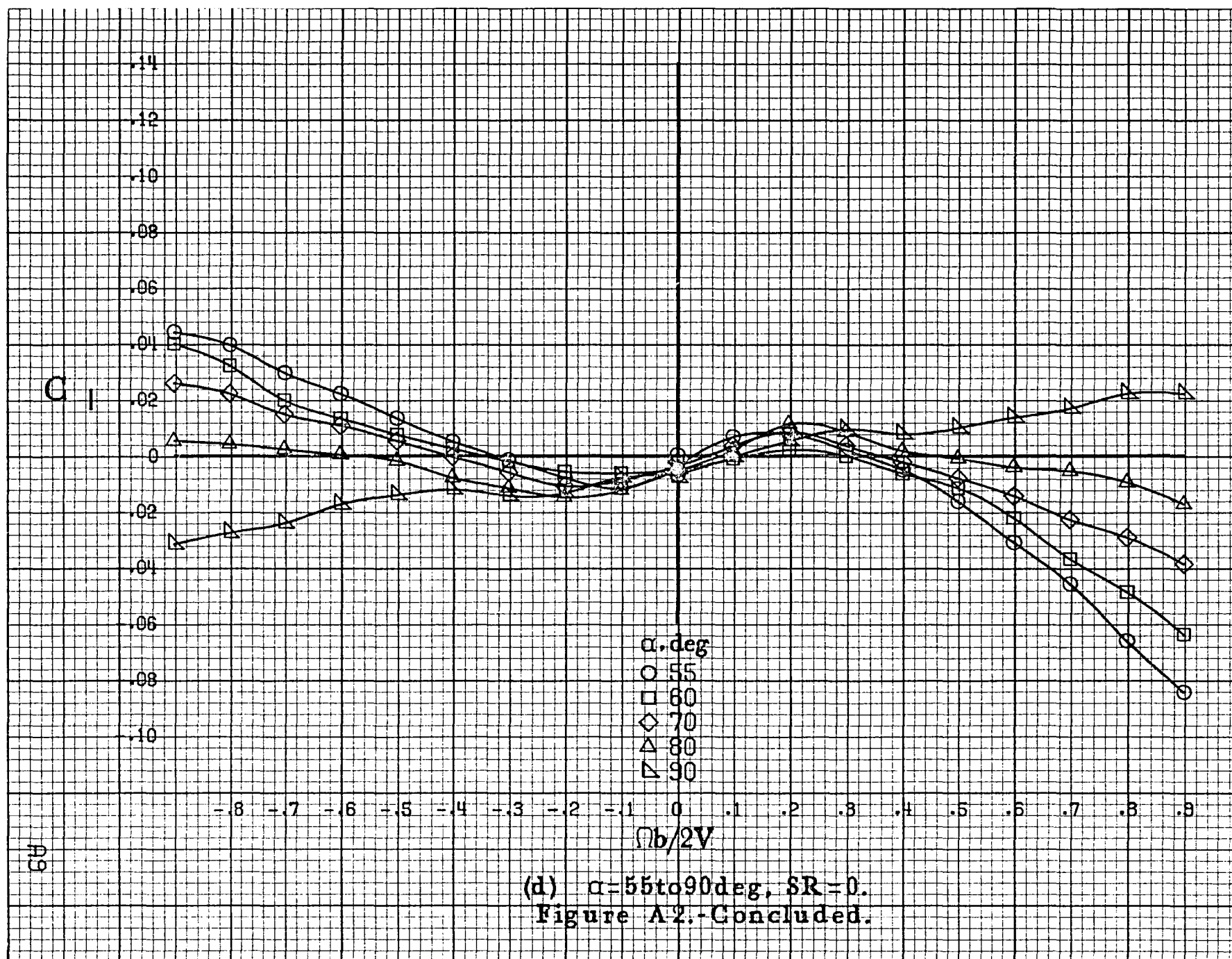
-.8 -.7 -.6 -.5 -.4 -.3 -.2 -.1 0 .1 .2 .3 .4 .5 .6 .7 .8 .9

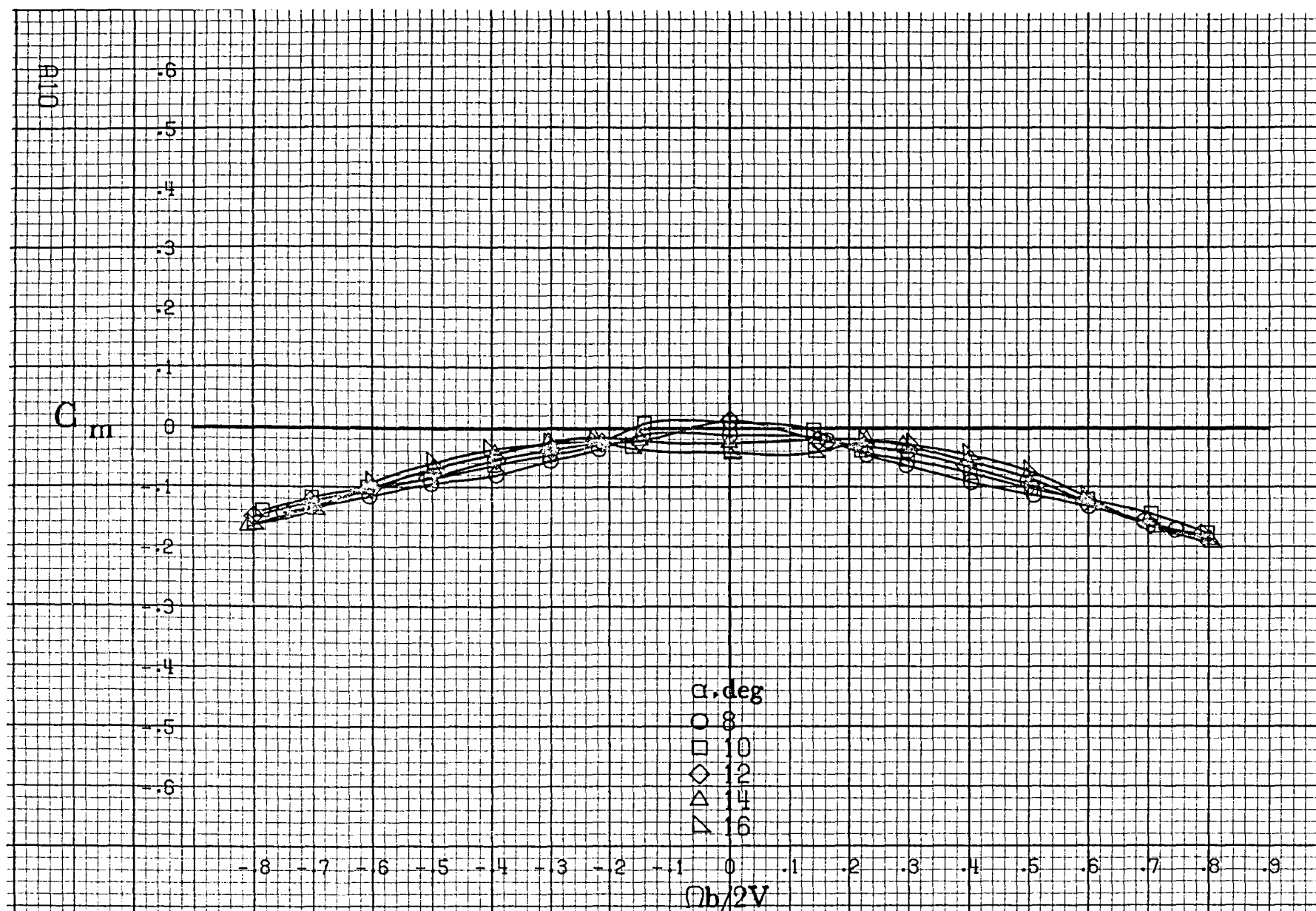
α, deg
○ 30
□ 35
◇ 40
△ 45
▽ 50

$\Omega b/2V$

(c) $\alpha=30$ to 50 deg, $SR=0$.
Figure A2.-Continued.

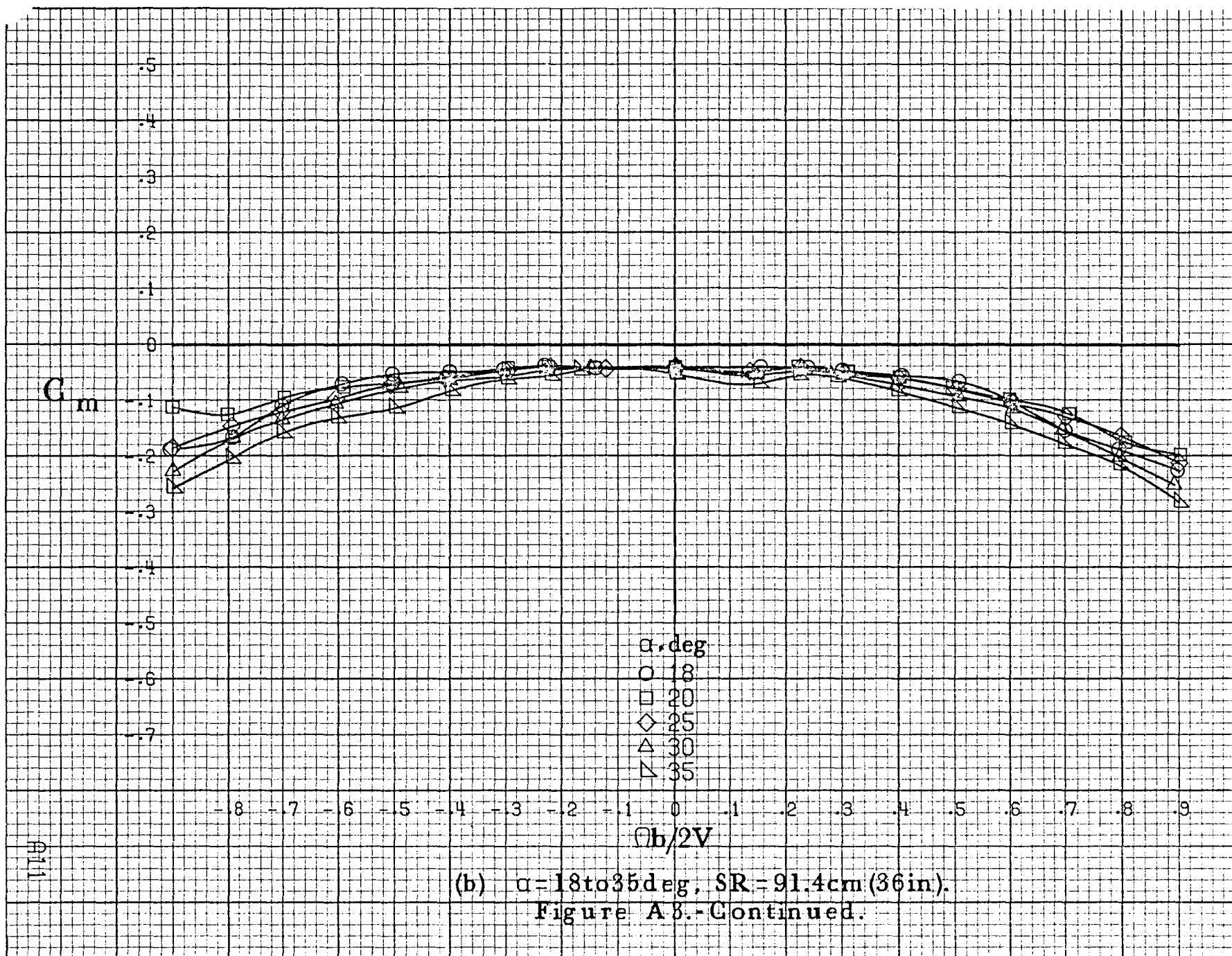
○

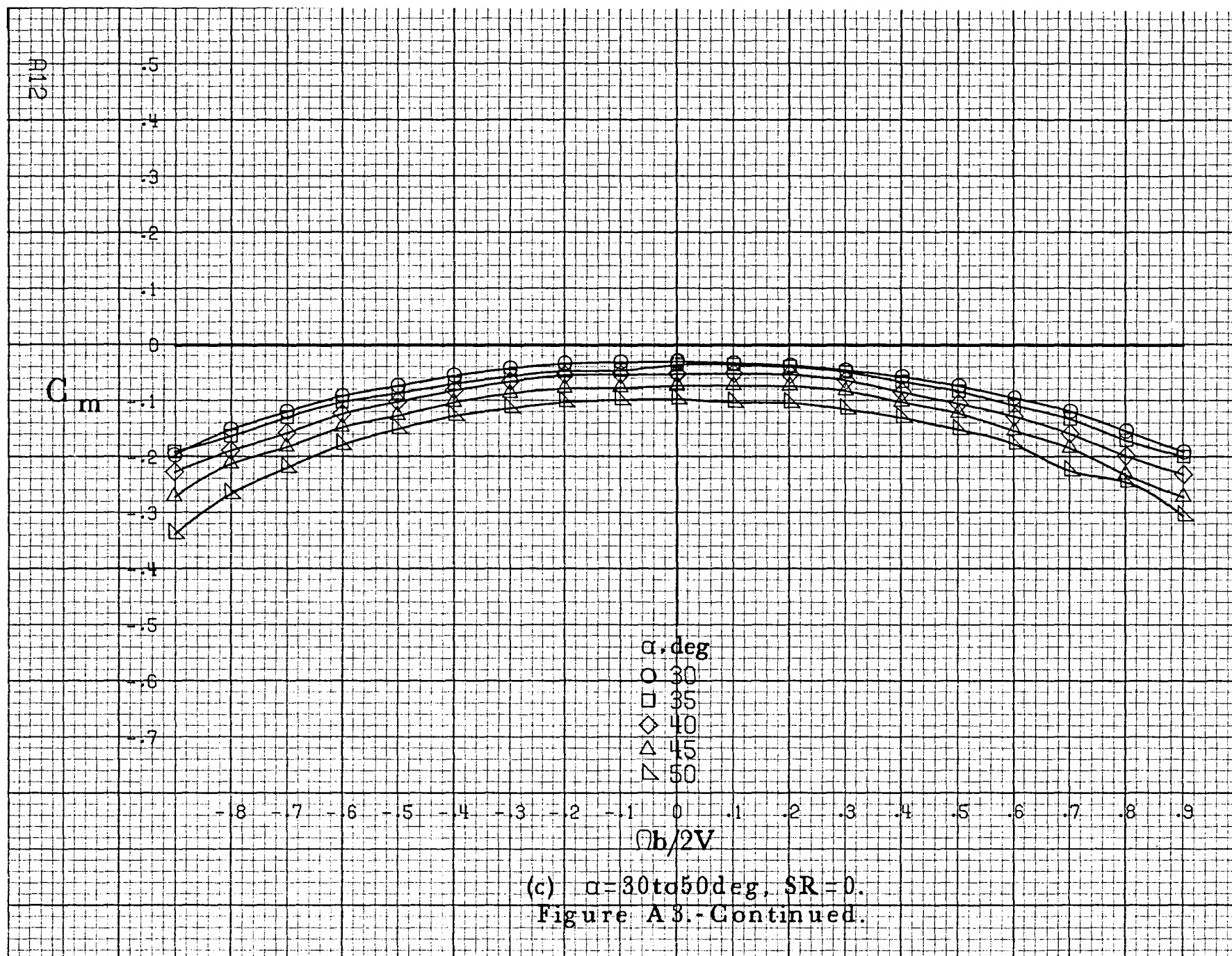


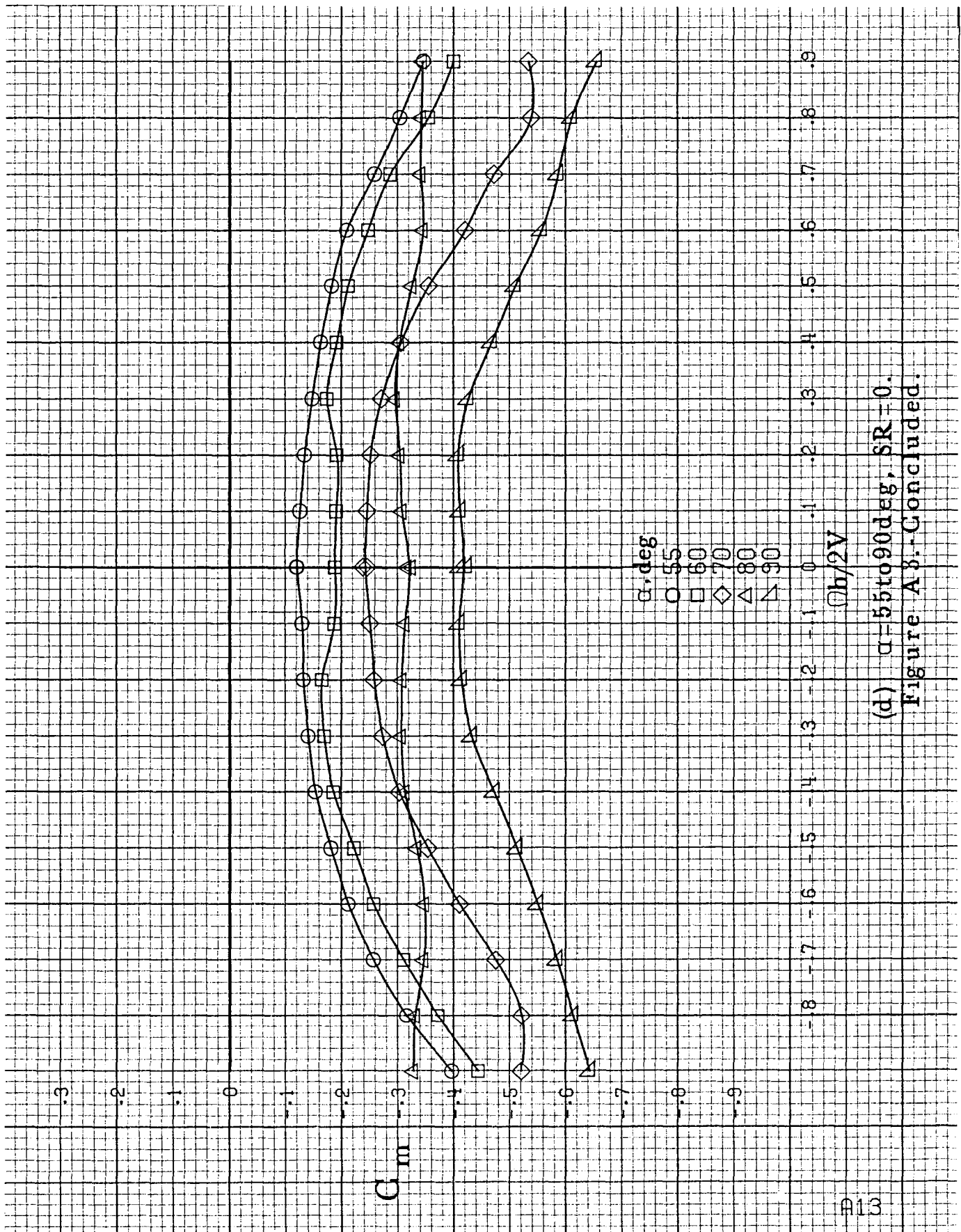


(a) $\alpha = 8$ to 16° , $SR = 91.4\text{cm (36in)}$.

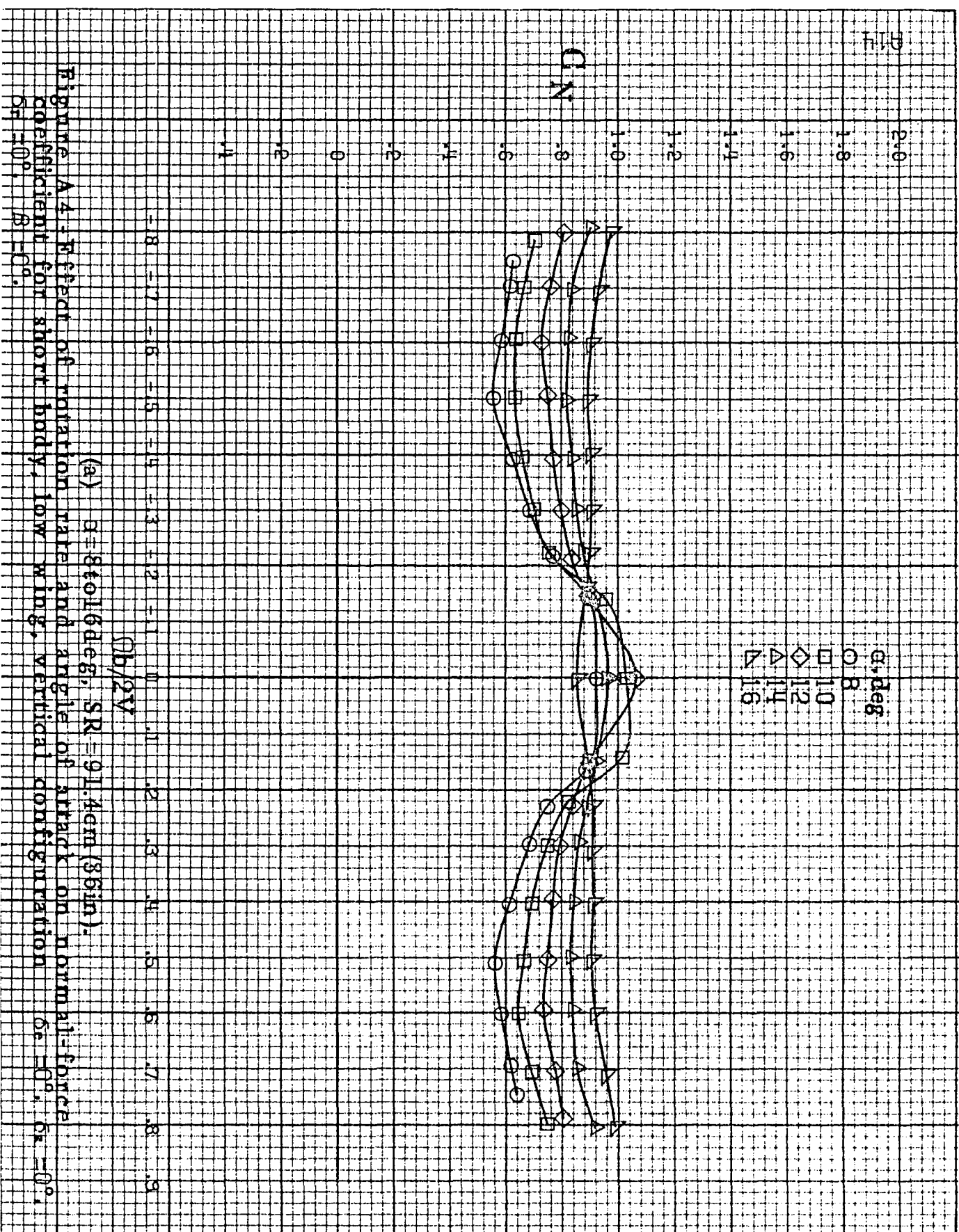
Figure A3.- Effect of rotation rate and angle of attack on pitching-moment coefficient for body, low wing, vertical configuration. $\delta_e = 0^\circ$, $\delta_a = 0^\circ$, $\delta_r = 0^\circ$, $\beta = 0^\circ$.

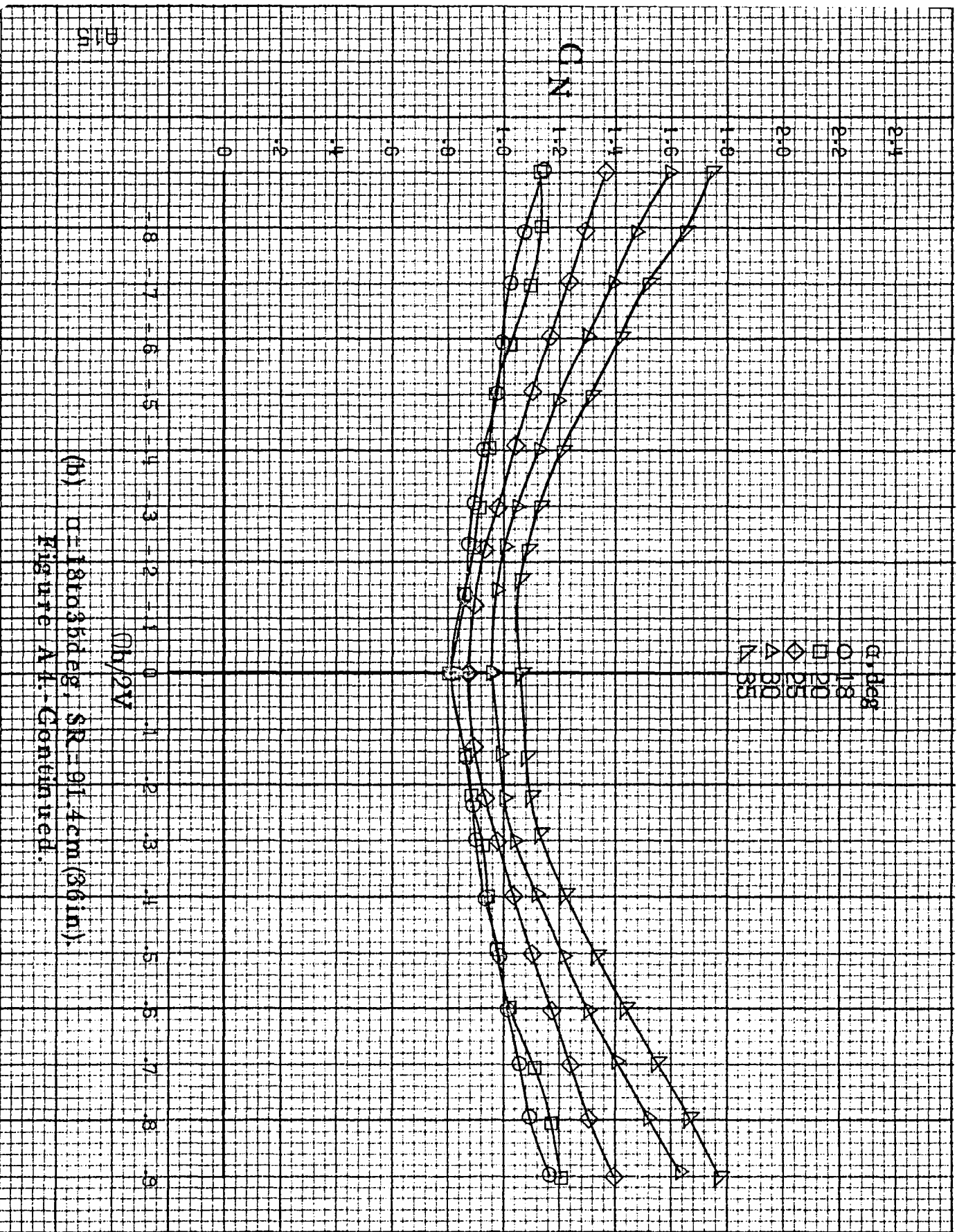




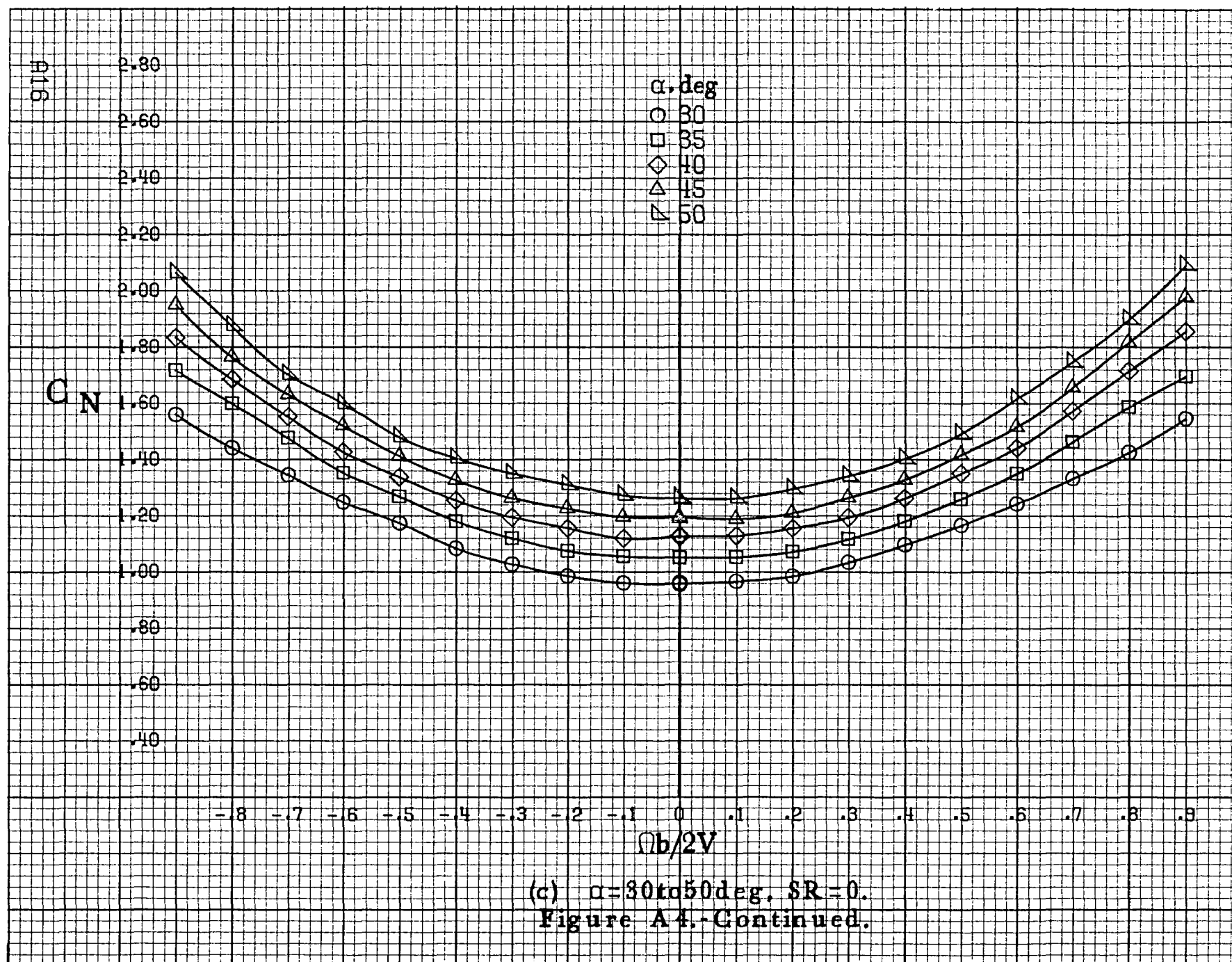


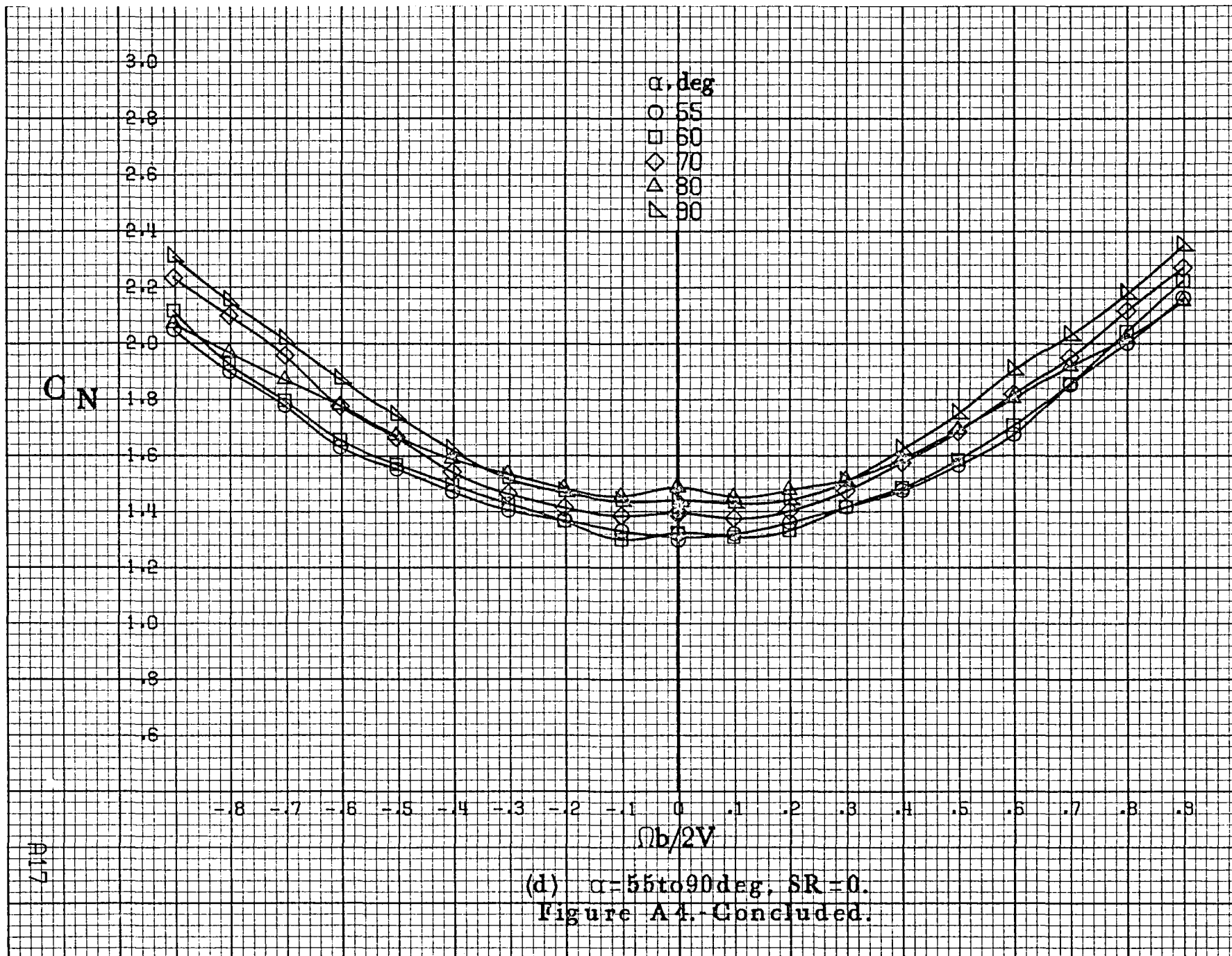
(d) $\alpha=55$ to 90° , $SR=0$.
Figure A3.-Concluded.

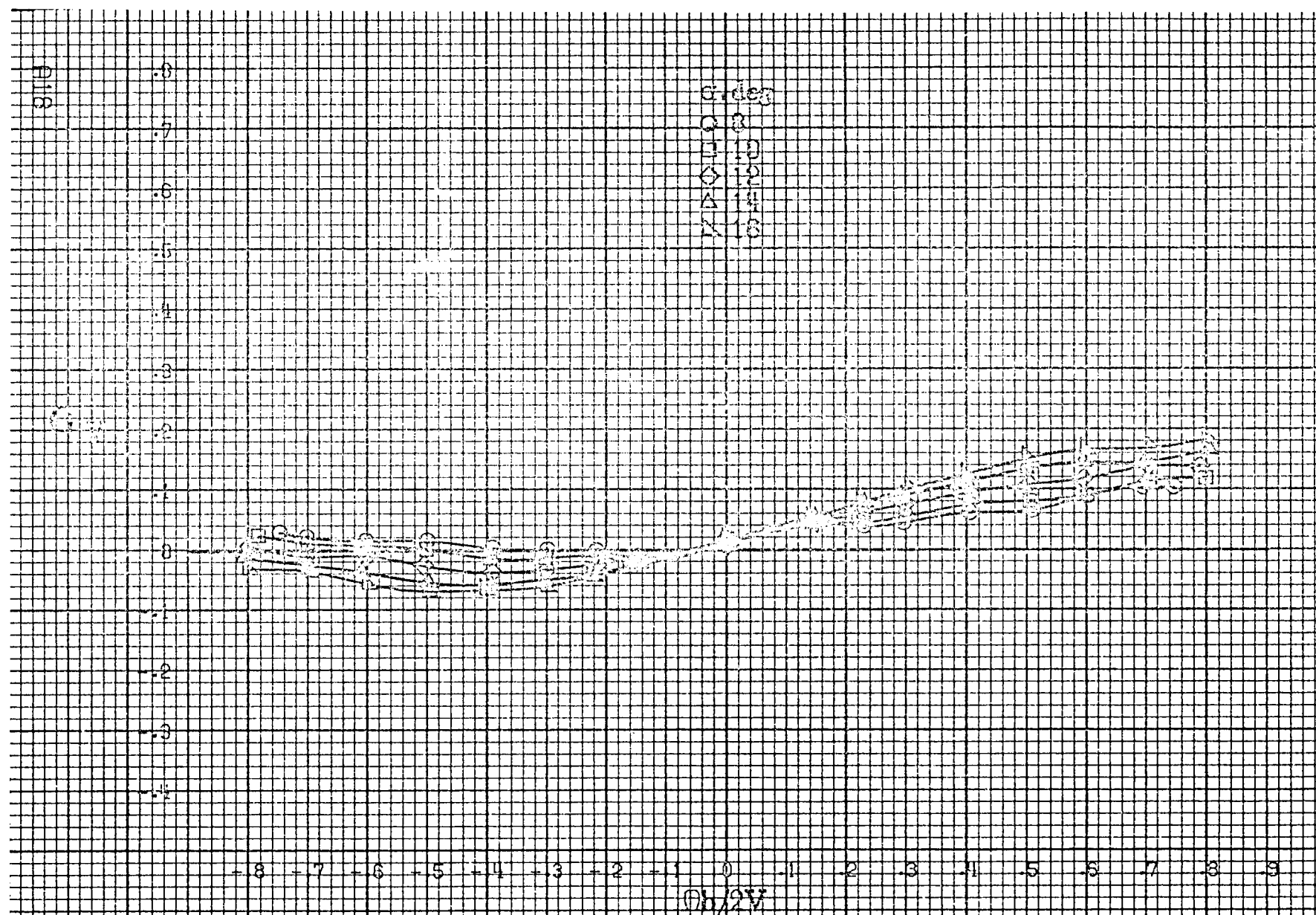




(b) $\alpha = 18$ to 33 deg, $SR = 91.4$ cm (36 in.).
Figure A4.-Continued.

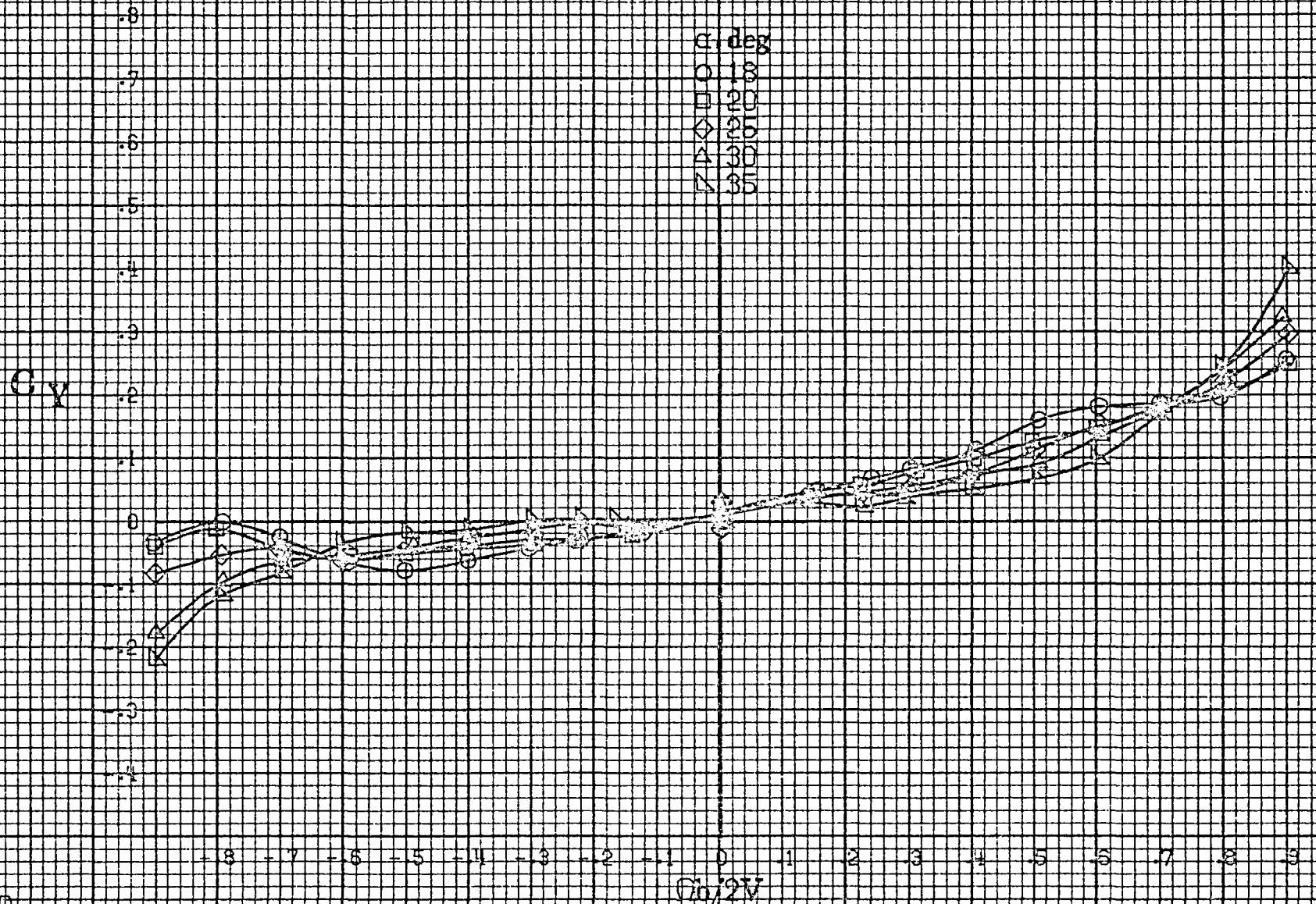




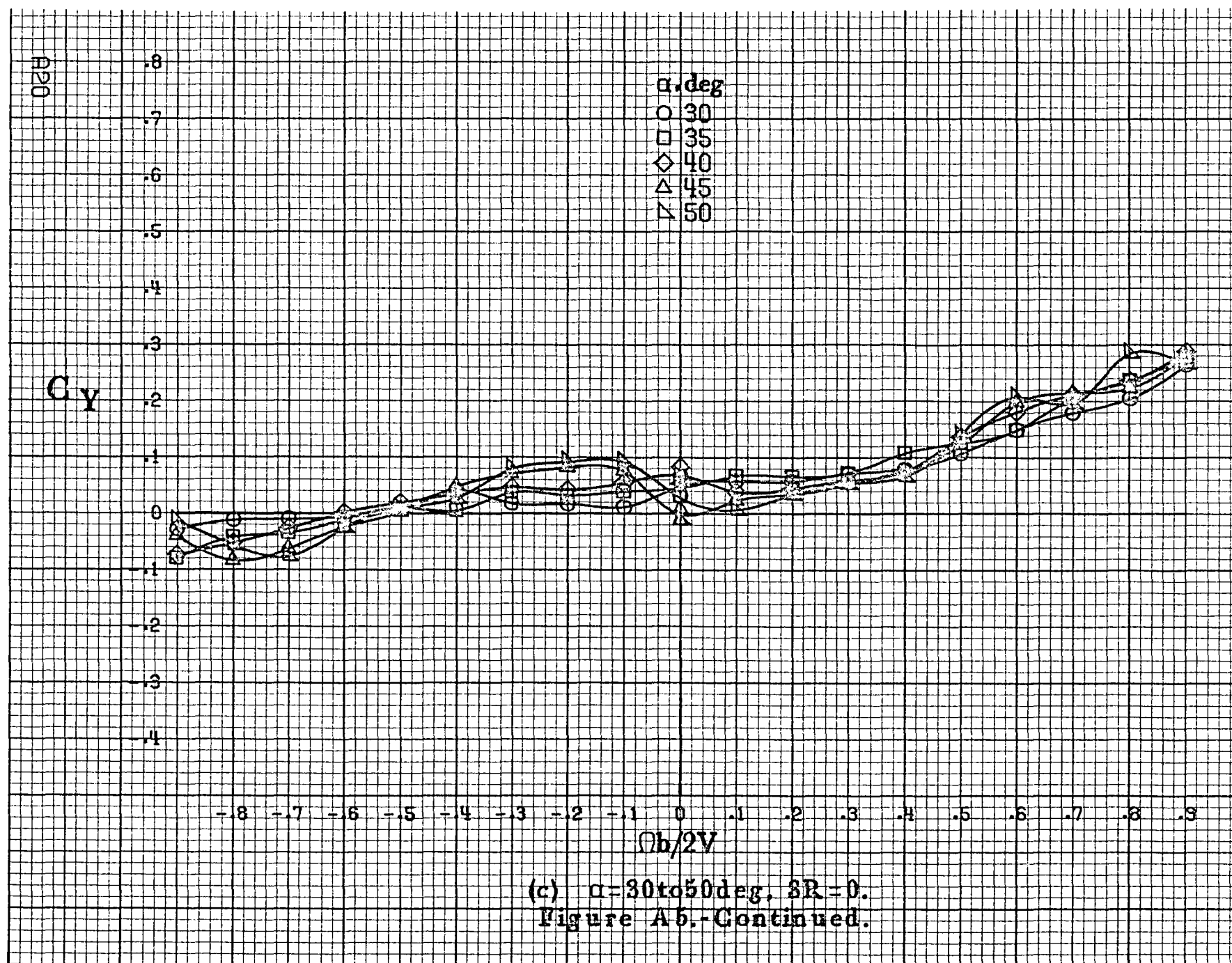


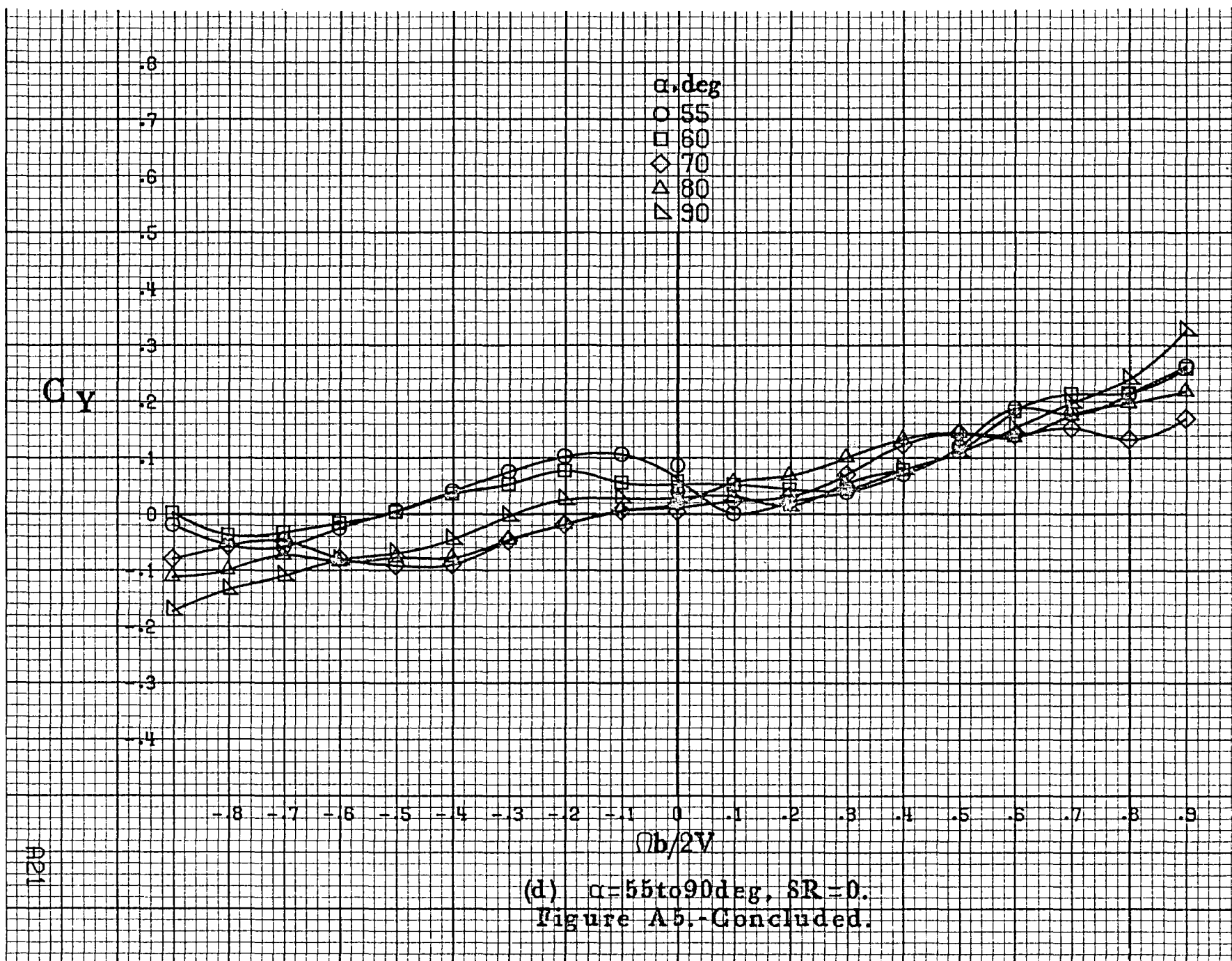
(a) $\alpha = 8$ to 16° , $SR = 91.4\text{cm (36in.)}$.

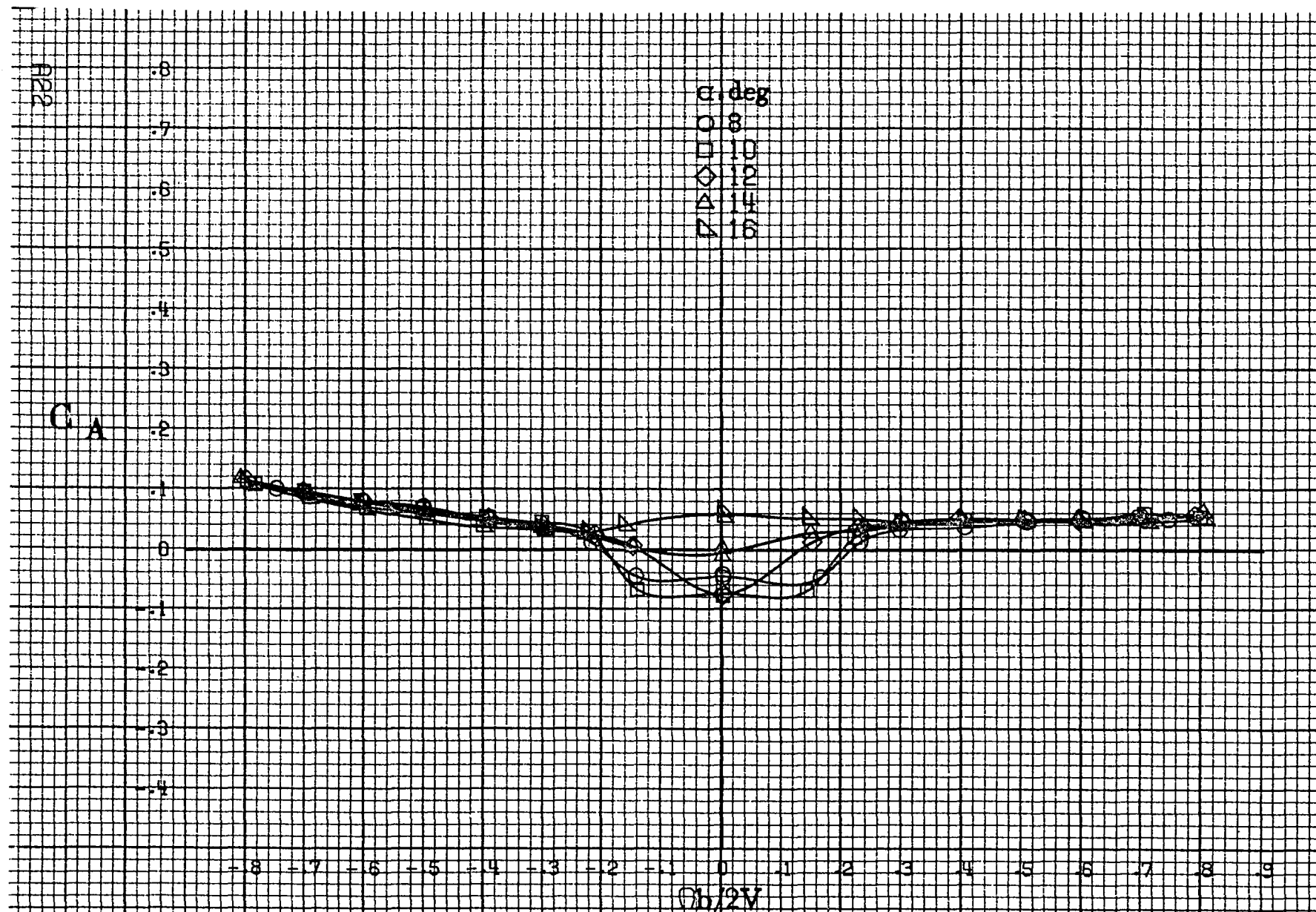
Figure A5 - Effect of rotation rate and angle of attack on side-force coefficient for short body, low wing, vertical configuration $\delta_a = 0^\circ$, $\delta_r = 0^\circ$, $\delta_n = 0^\circ$, $\beta = 0^\circ$.



(b) $\alpha = 18$ to 35 deg, $SR = 91.4$ cm (36 in).
Figure A5. Continued.

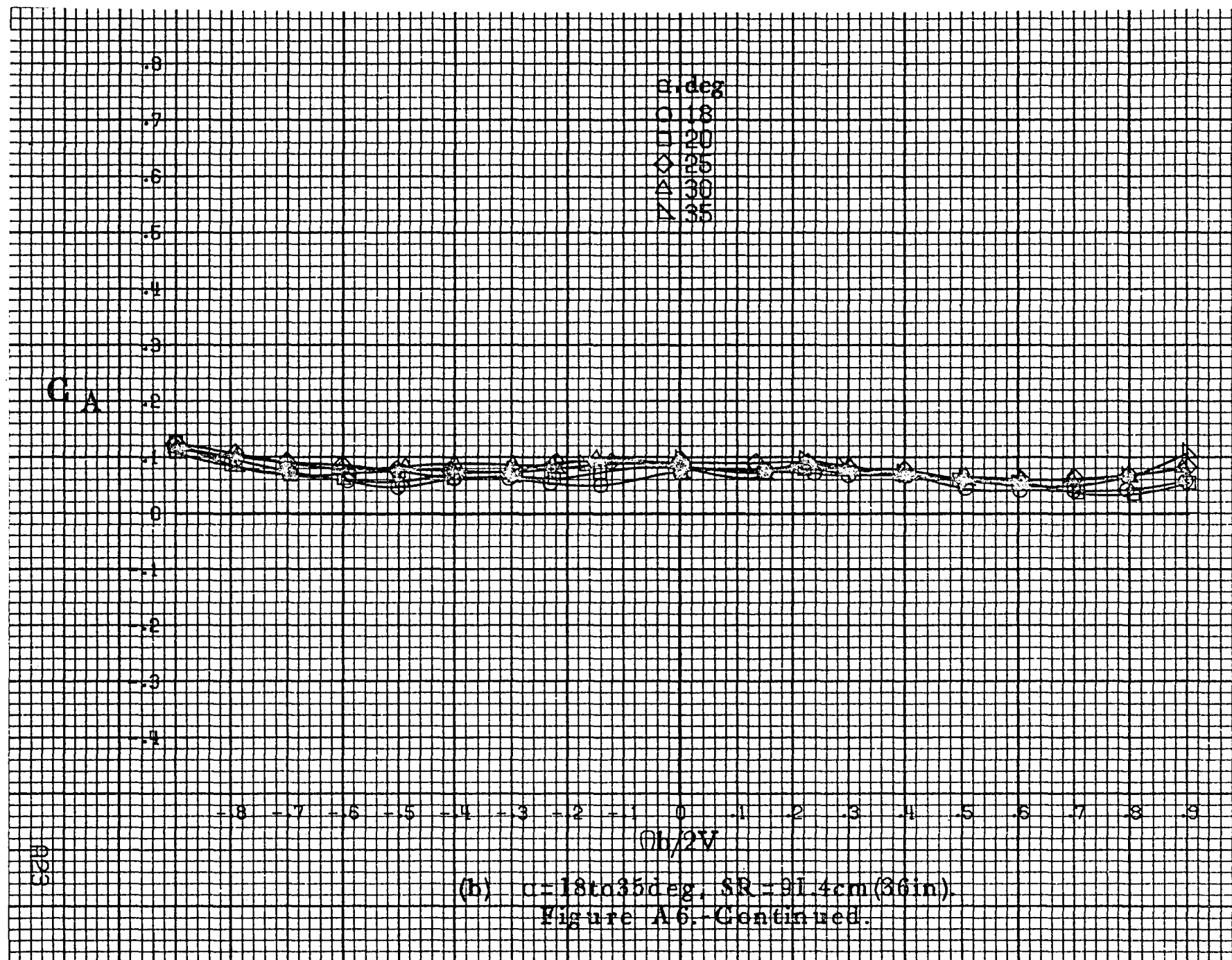


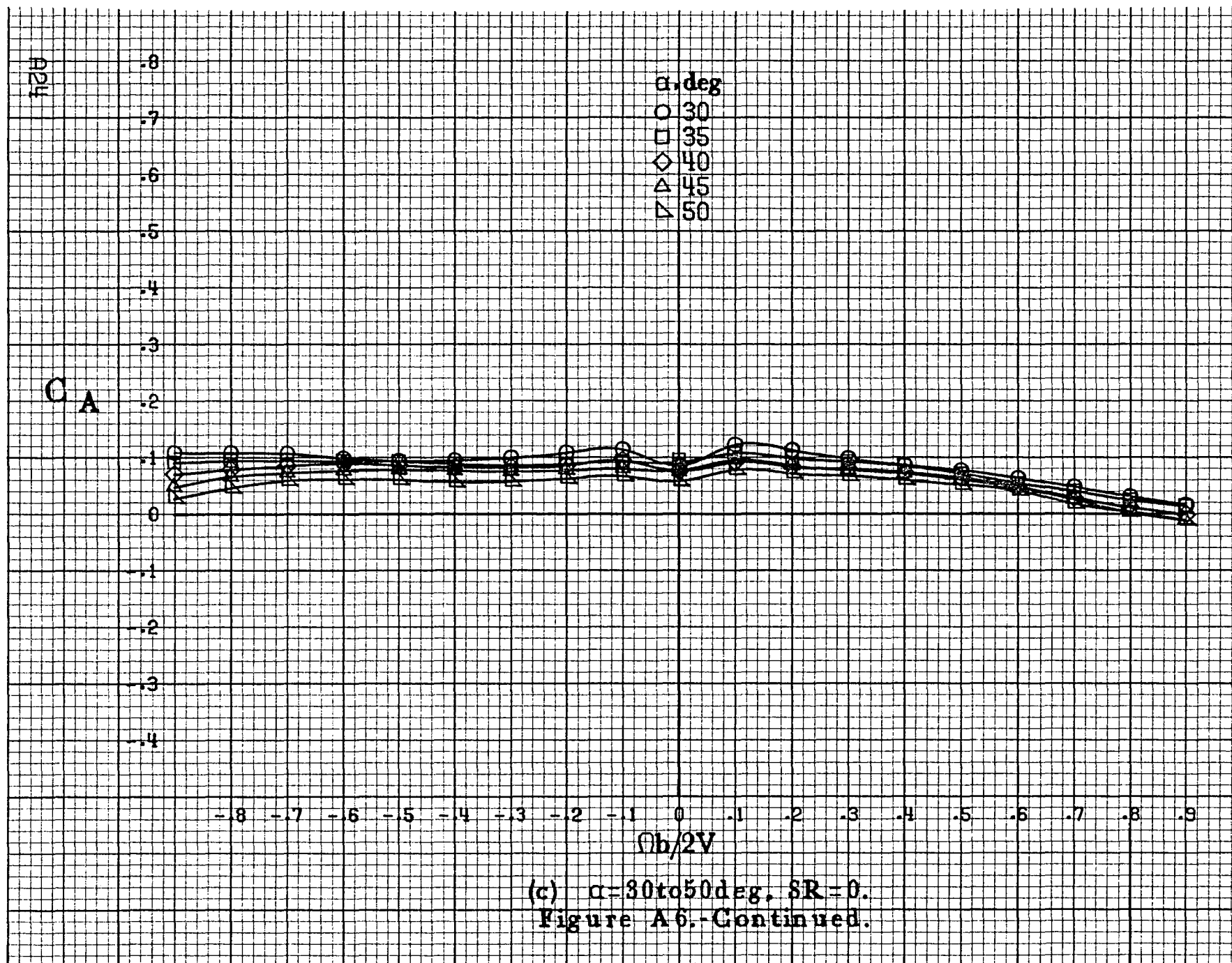


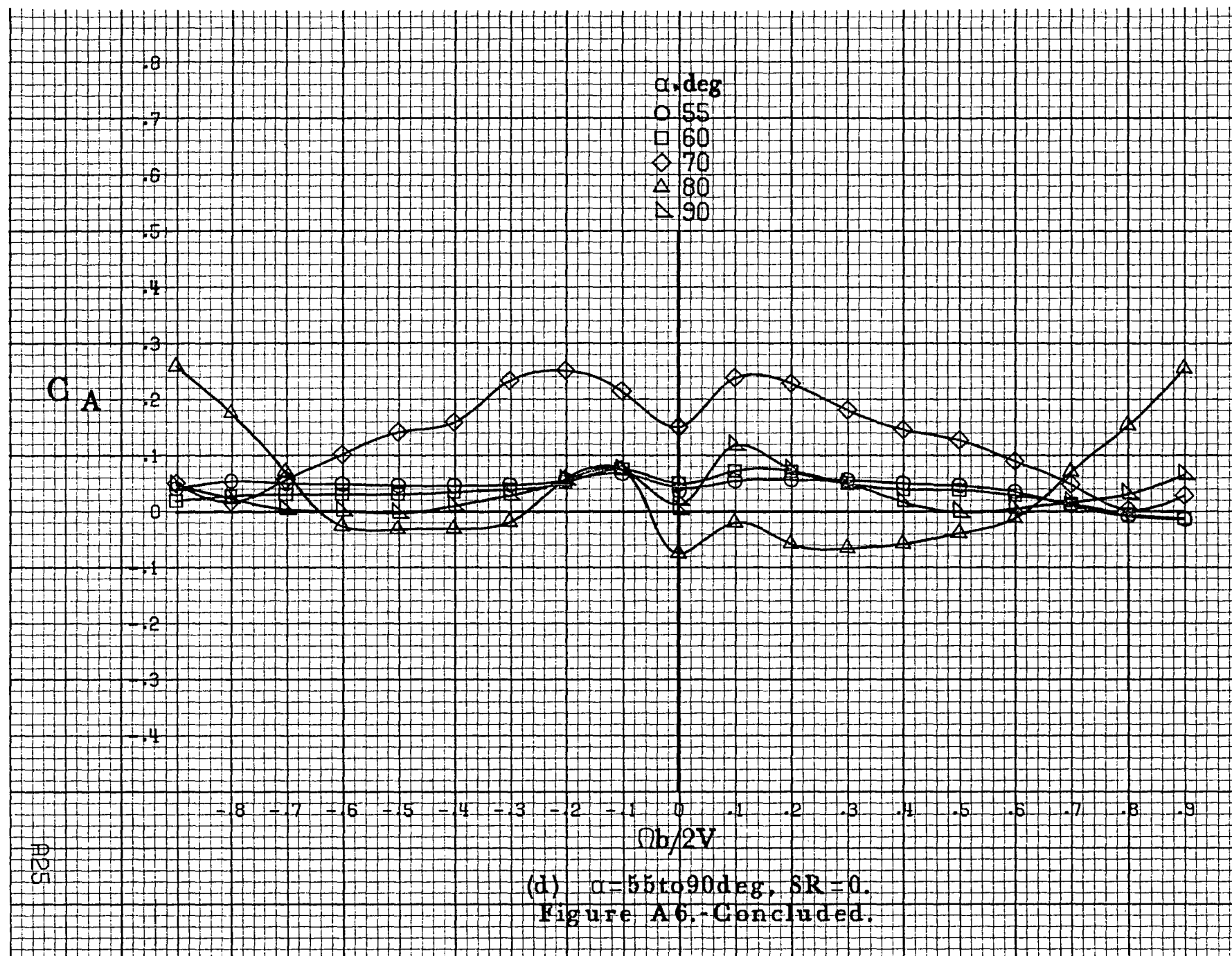


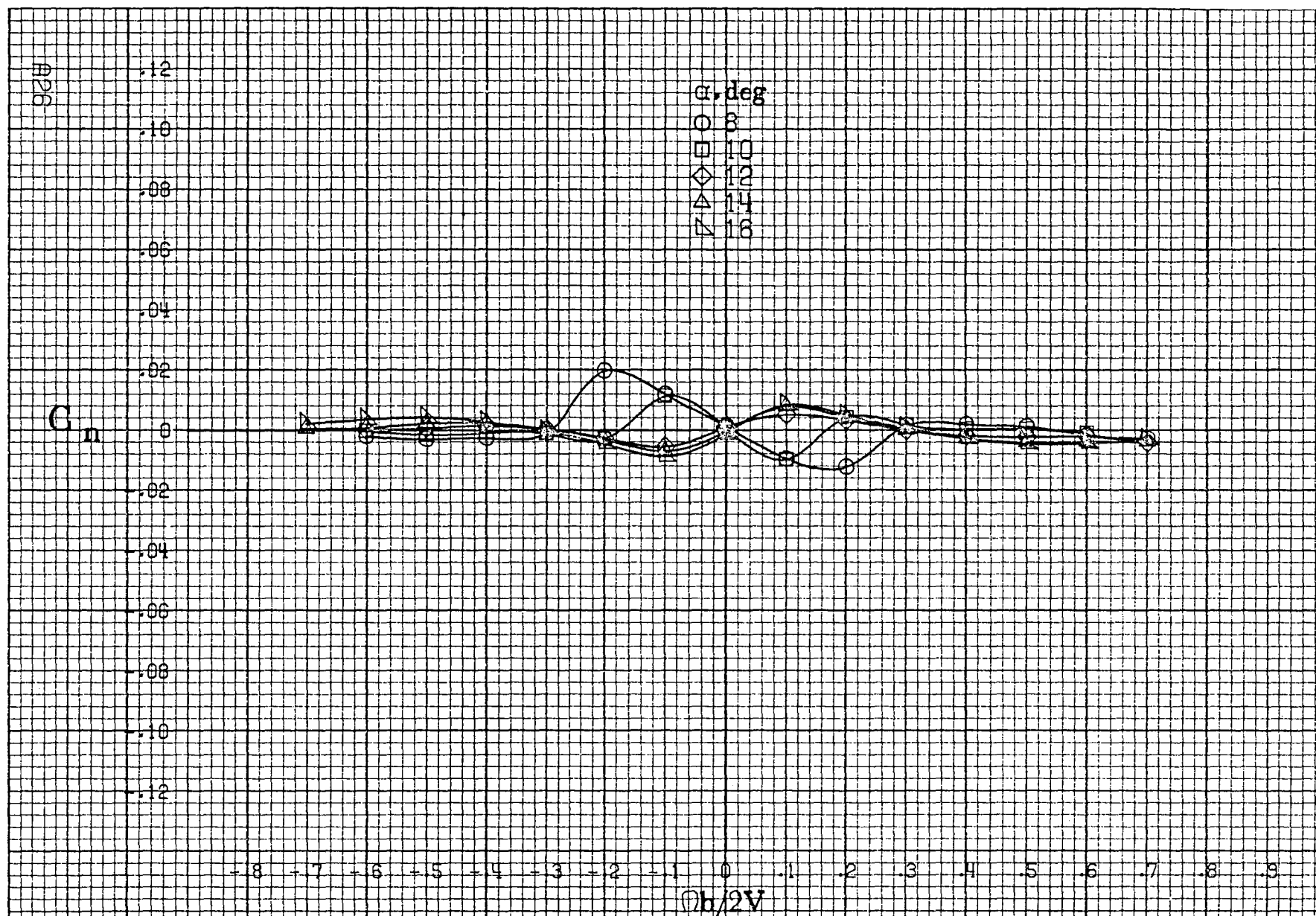
(a) $\alpha = 8$ to 16° , $SR = 91.4 \text{ cm (36 in)}$.

Figure A6.-Effect of rotation rate and angle of attack on axial-force coefficient for short body, low wing, vertical configuration $\delta_r = 0^\circ$, $\delta_n = 0^\circ$, $\delta_a = 0^\circ$, $\beta = 0^\circ$.



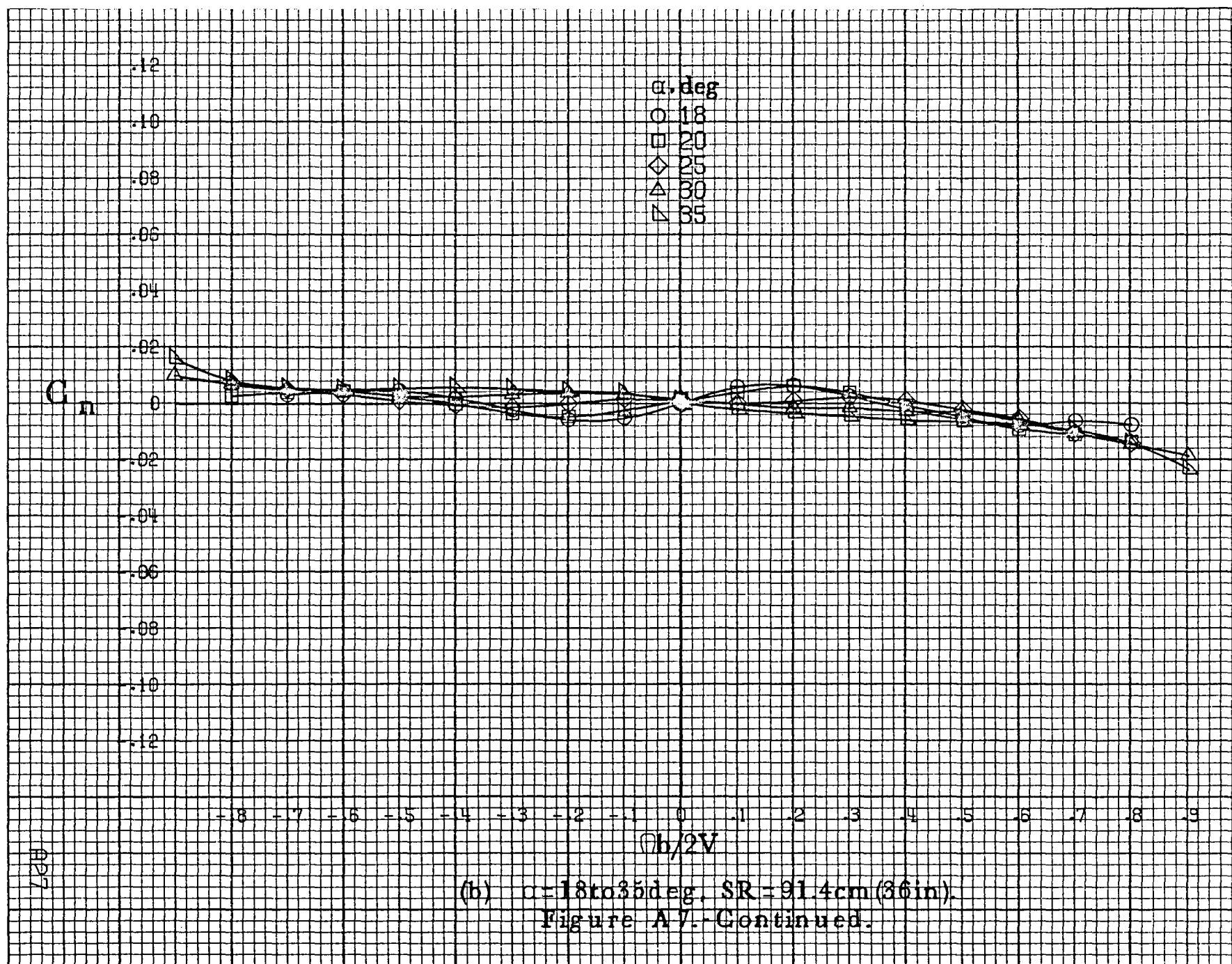




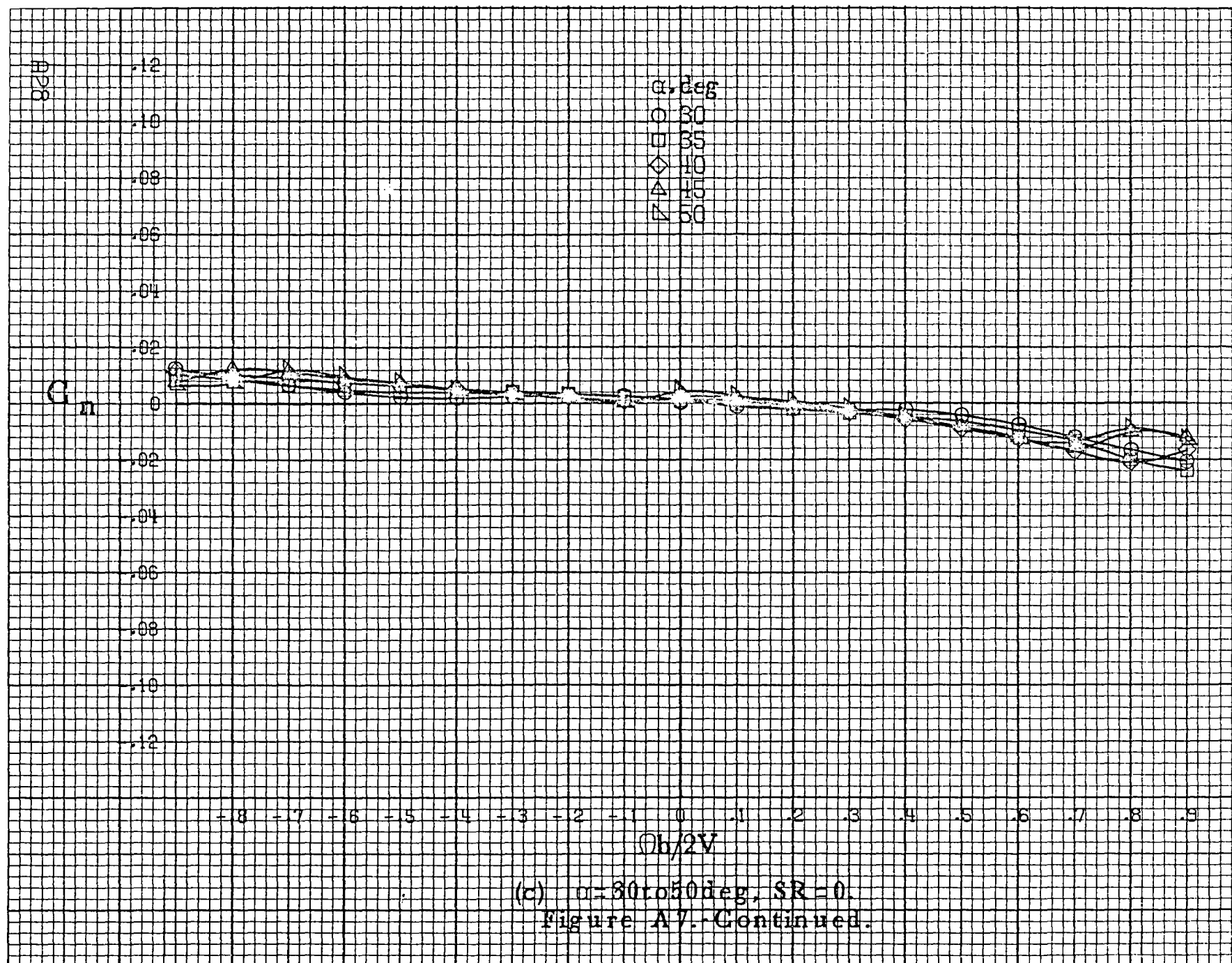


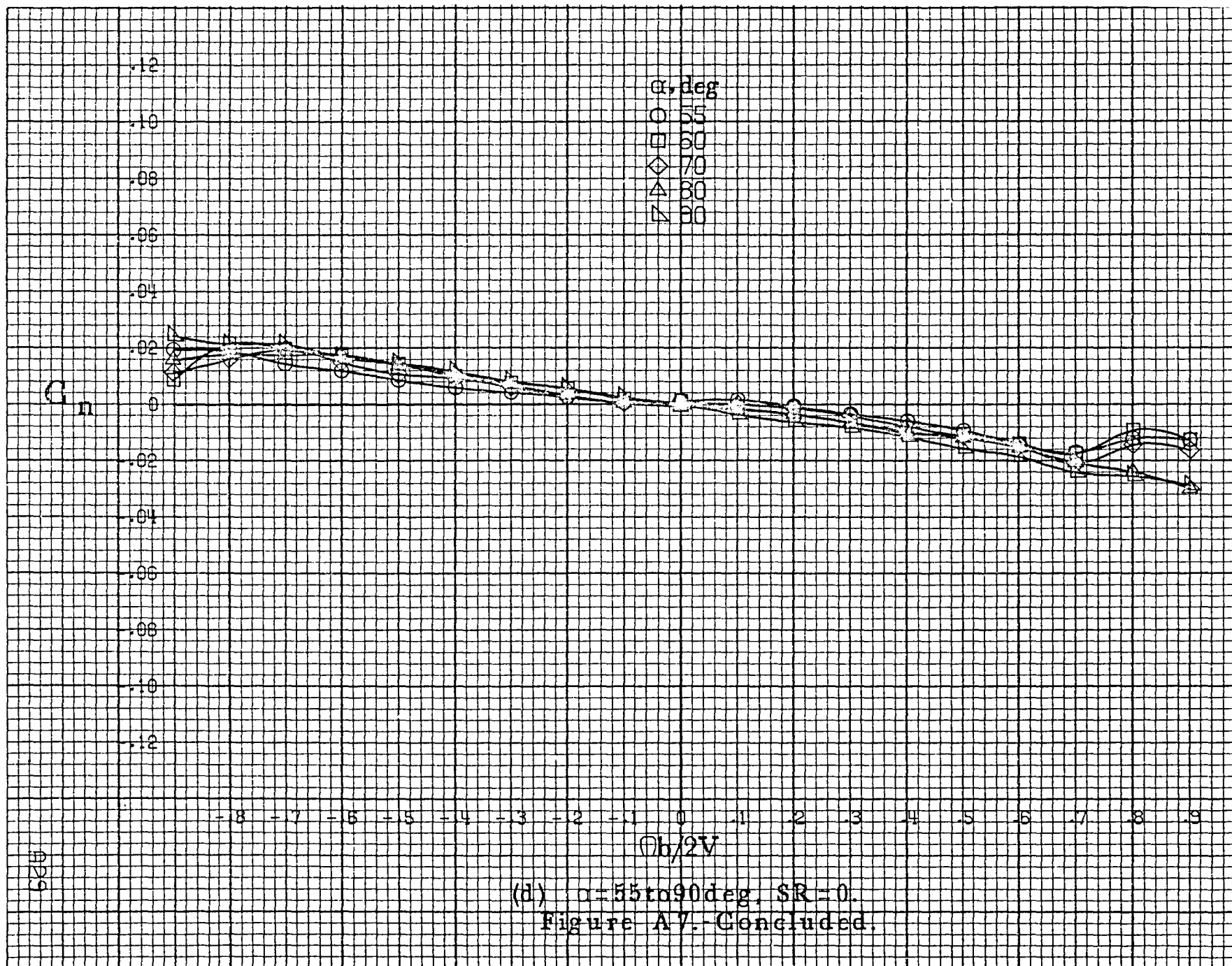
(a) $\alpha = 8 \text{ to } 16 \text{ deg}$, $SR = 91.4 \text{ cm (36 in)}$.

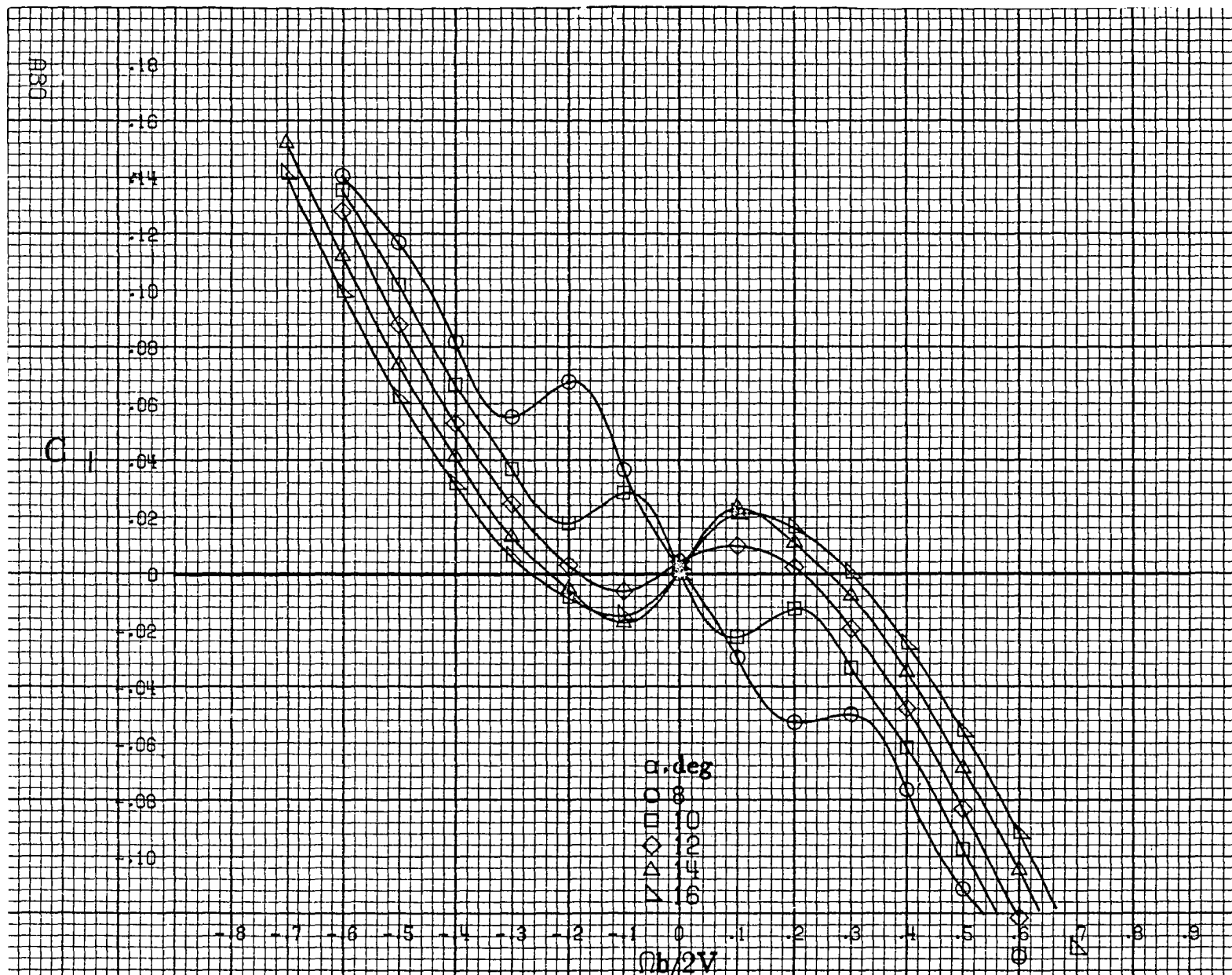
Figure A7: Effect of rotation rate and angle of attack on yawing-moment coefficient for short body, low wing, tail 2 configuration. $\delta_e = 0^\circ$, $\delta_a = 0^\circ$, $\delta_r = 0^\circ$, $\beta = 0^\circ$.



(b) $\alpha=18$ to 35 deg. SR=91.4cm (36 in).
Figure A7.-Continued.

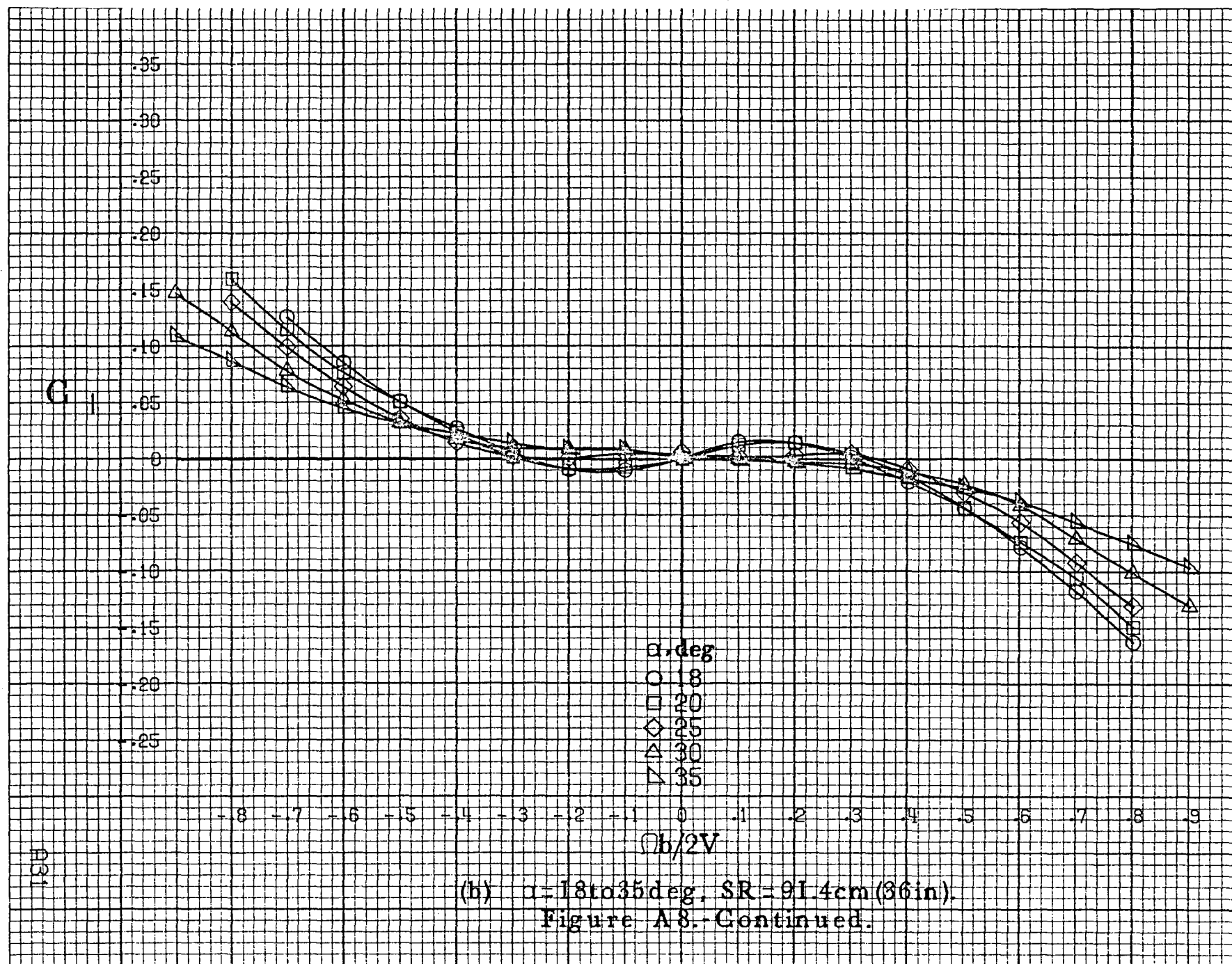


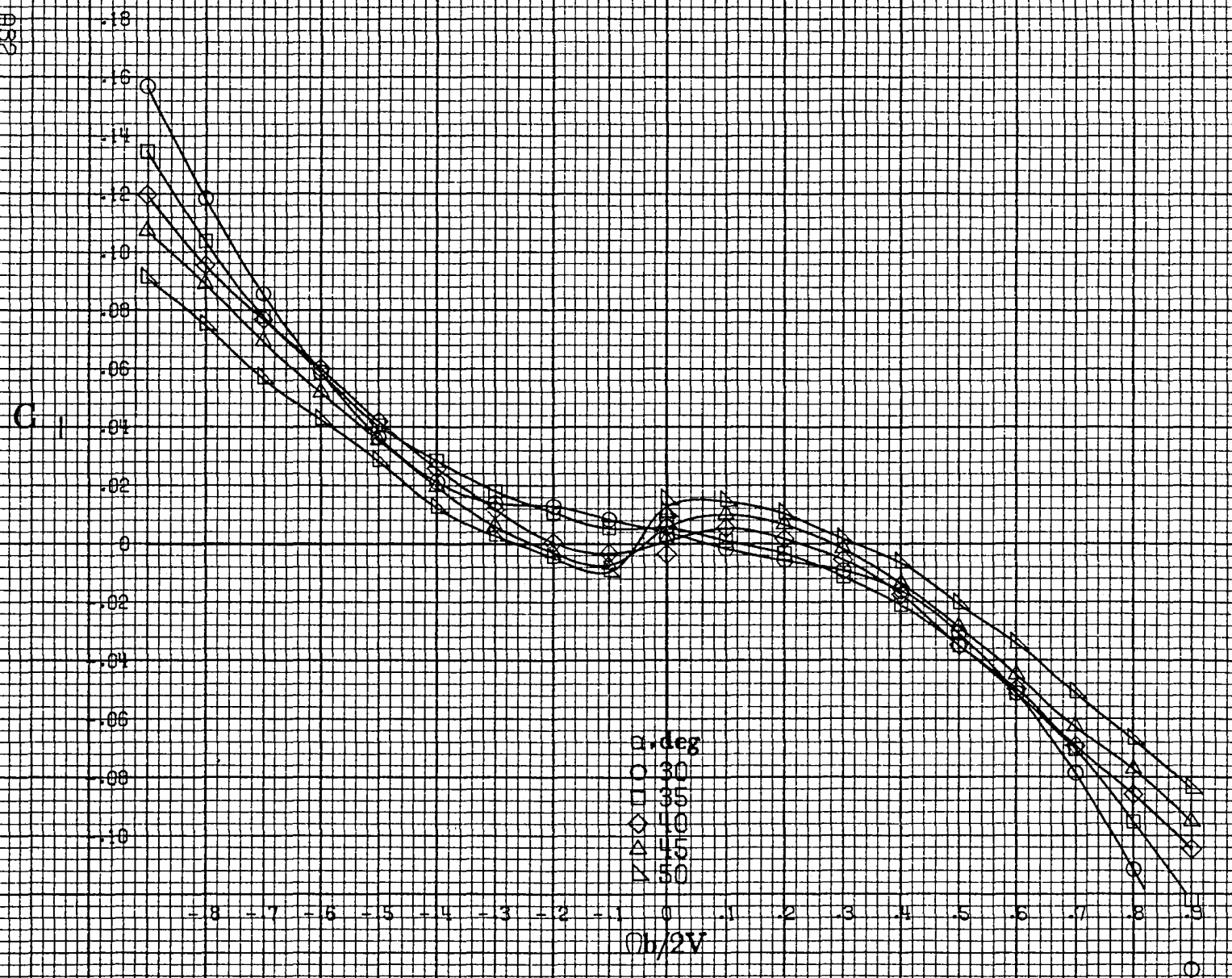




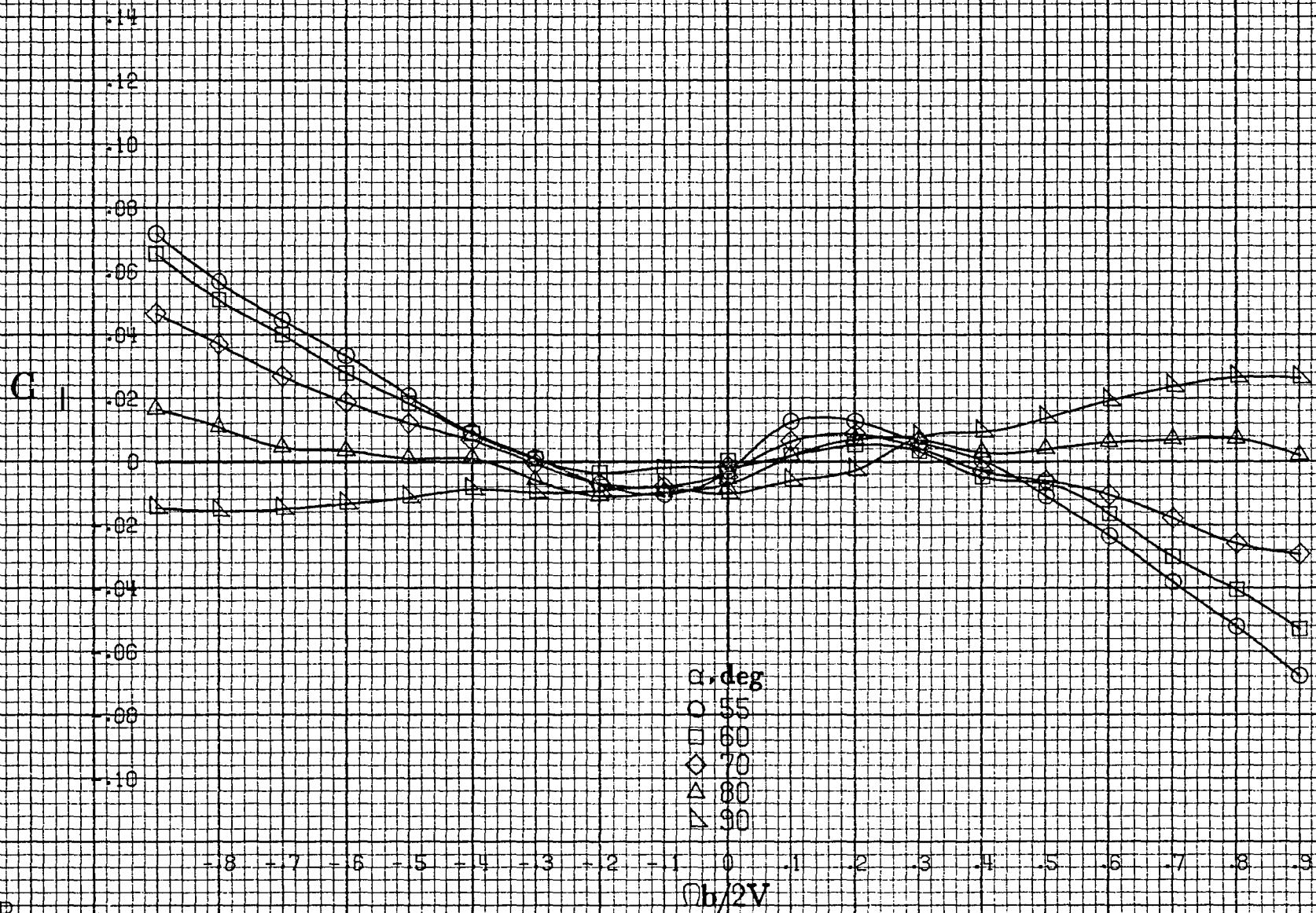
(a) $\alpha = 8$ to 16 deg, $SR = 91.4$ cm (36 in).

Figure A8 - Effect of rotation rate and angle of attack on rolling-moment coefficient for short body, low wing, tail 2 configuration. $\delta_e = 10^\circ$, $\delta_a = 10^\circ$, $\delta_r = 10^\circ$, $\delta_b = 0^\circ$.

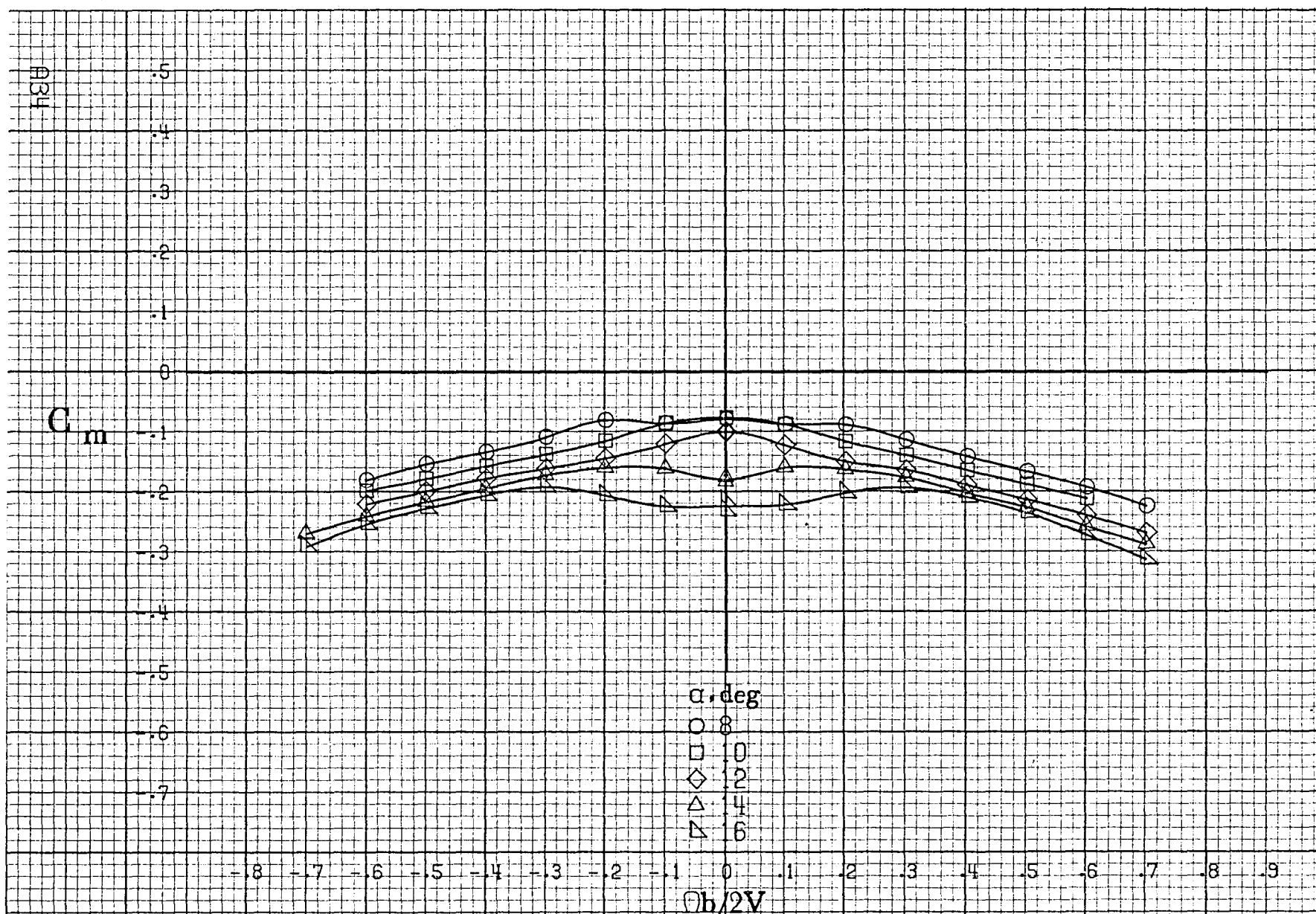




(c) $\alpha=30$ to 50 deg, $SR=0$
Figure A8.-Continued.

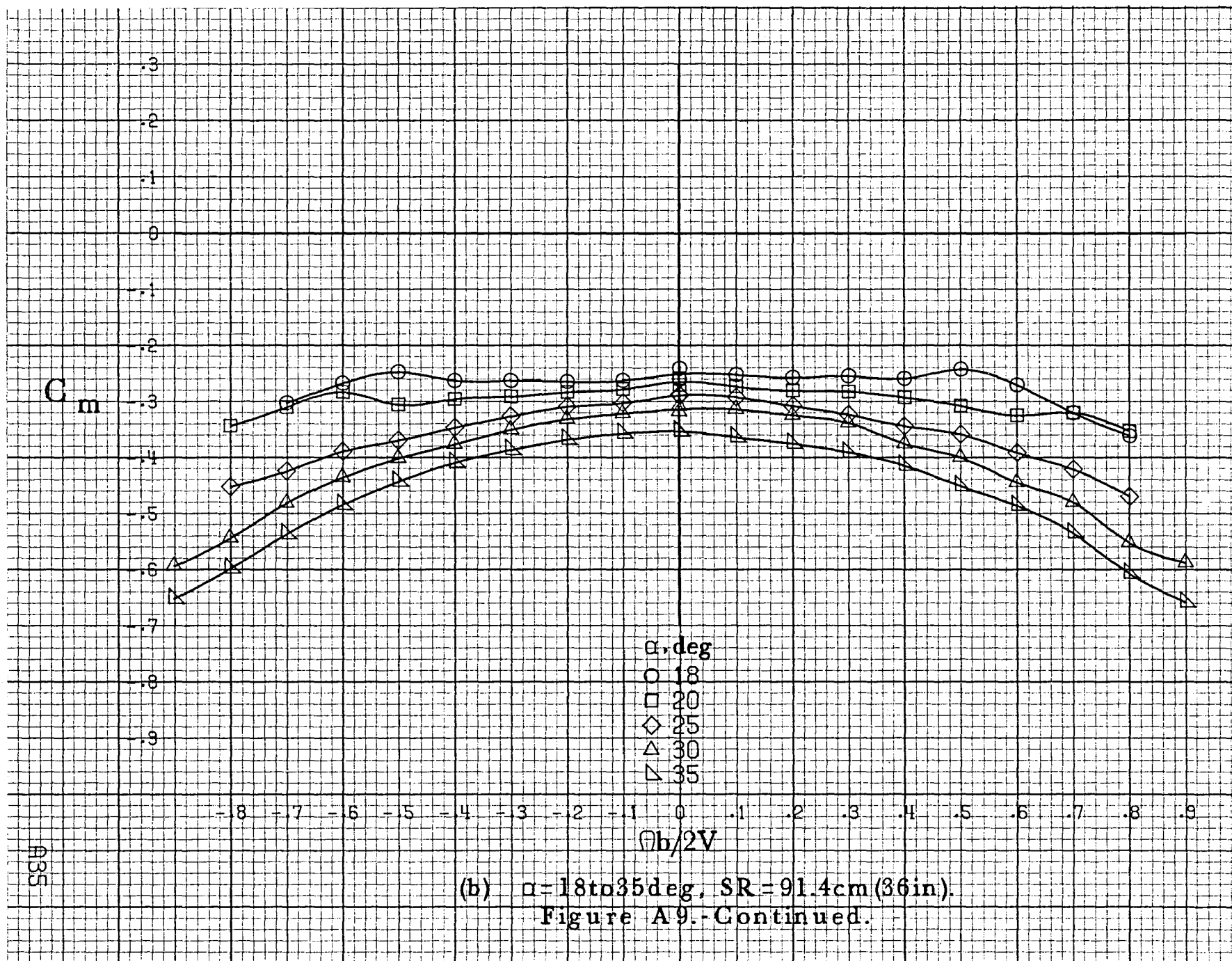


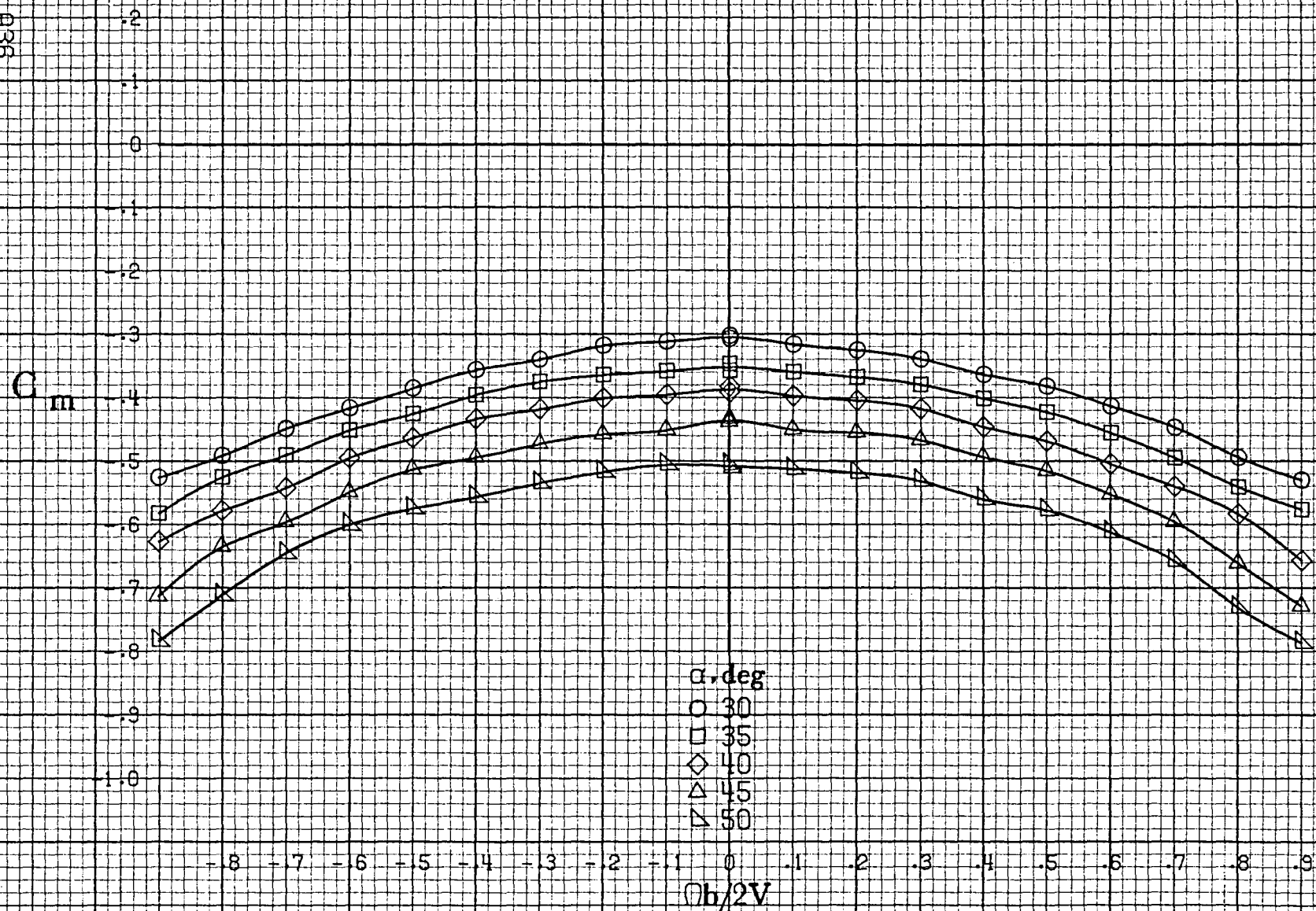
(d) $\alpha=55$ to 90 deg, $SR=0$.
Figure A 8.-Concluded.



(a) $\alpha = 8 \text{ to } 16 \text{ deg}$, $SR = 91.4 \text{ cm (36 in)}$.

Figure A.9 - Effect of rotation rate and angle of attack on pitching-moment coefficient for body, low wing, horizontal no. 2 configuration. $\delta_e = 0^\circ$, $\delta_a = 0^\circ$, $\delta_r = 0^\circ$, $\beta = 0^\circ$.





(c) $\alpha = 30$ to 50° , $SR = 0$.

Figure A9.-Continued.

C_m

-.2
-.3
-.4
-.5
-.6
-.7
-.8
-.9
-1.0
-1.1
-1.2
-1.3
-1.4

α, deg

○ 55

□ 60

◇ 70

△ 80

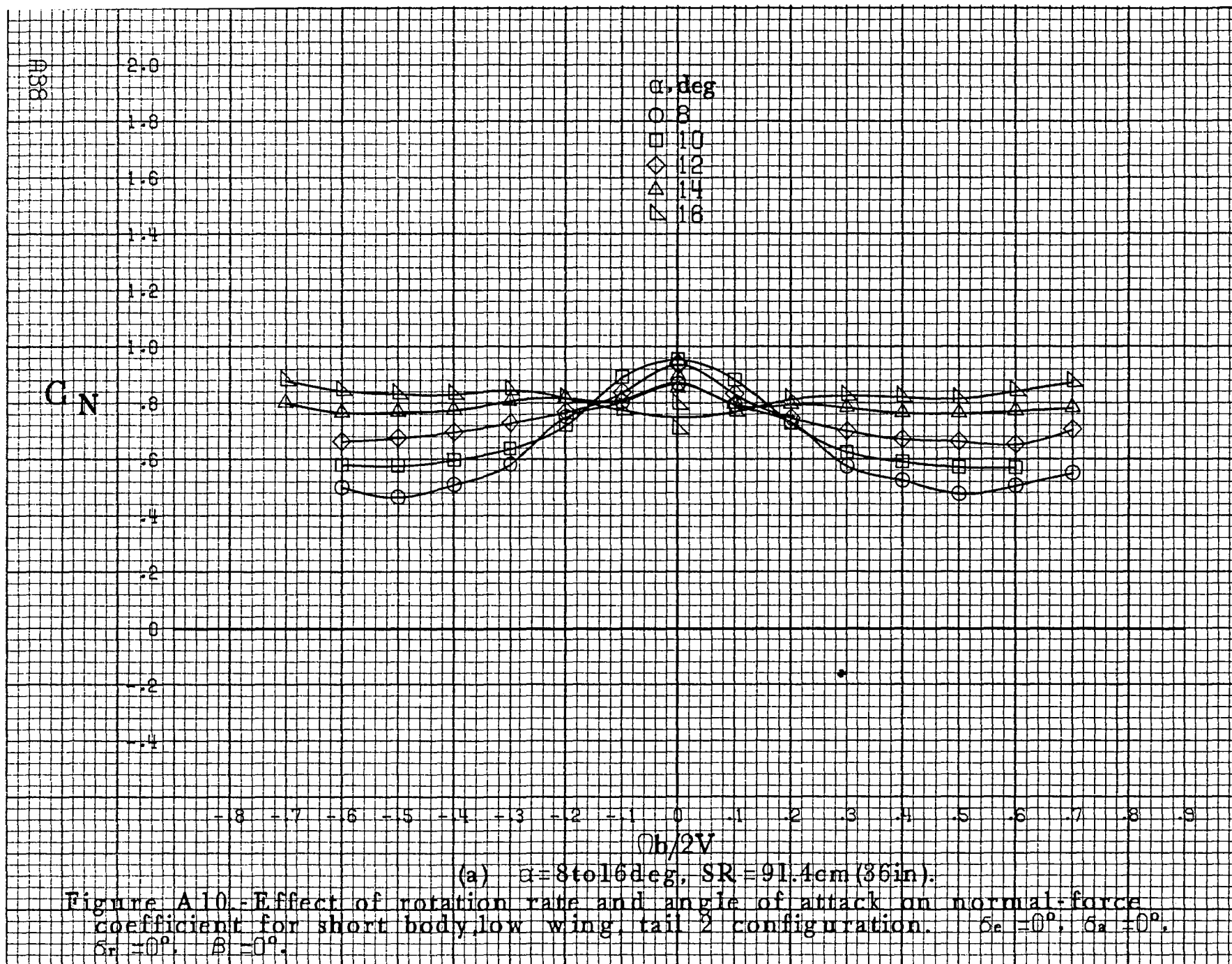
▽ 90

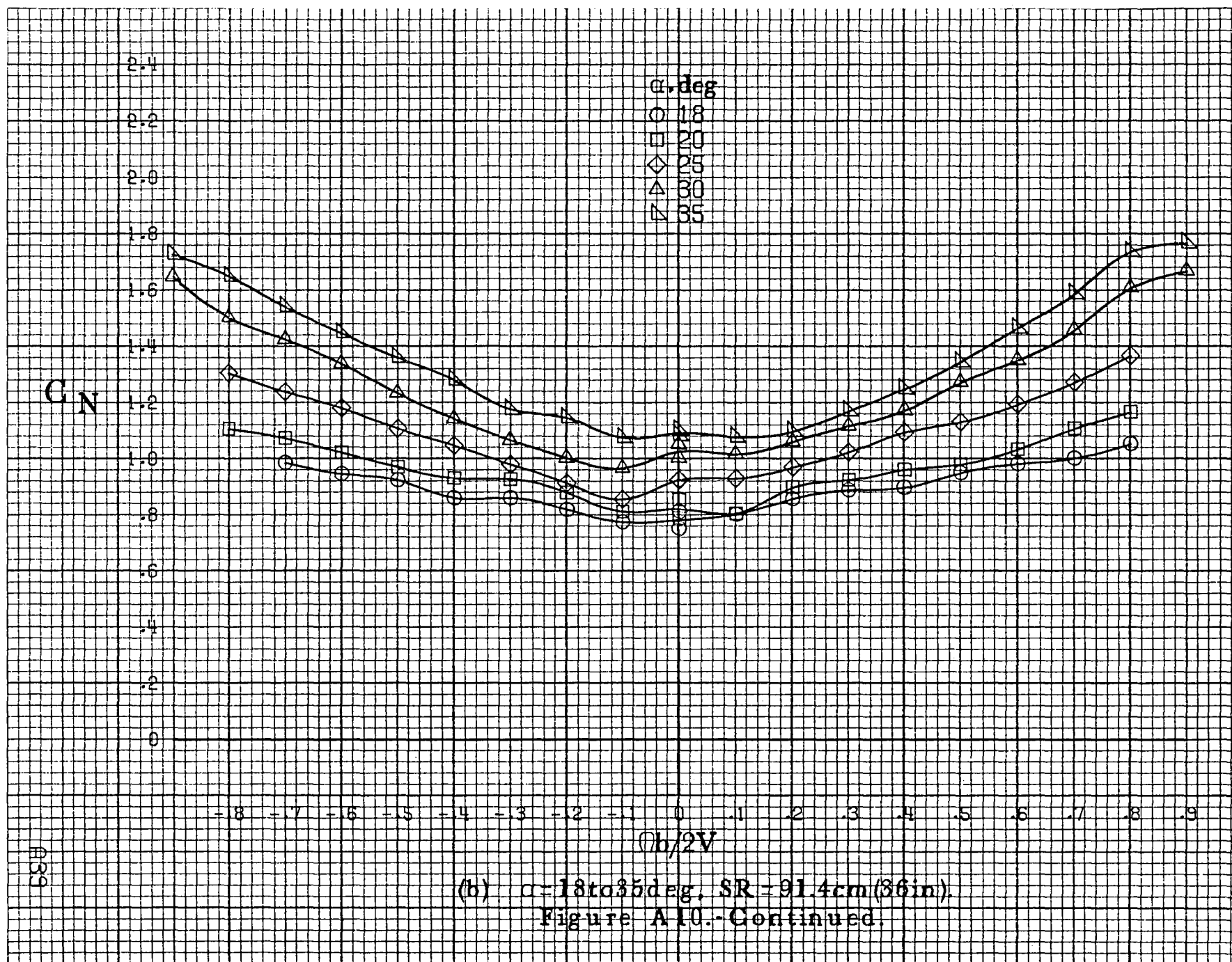
-.8 -.7 -.6 -.5 -.4 -.3 -.2 -.1 0 .1 .2 .3 .4 .5 .6 .7 .8 .9

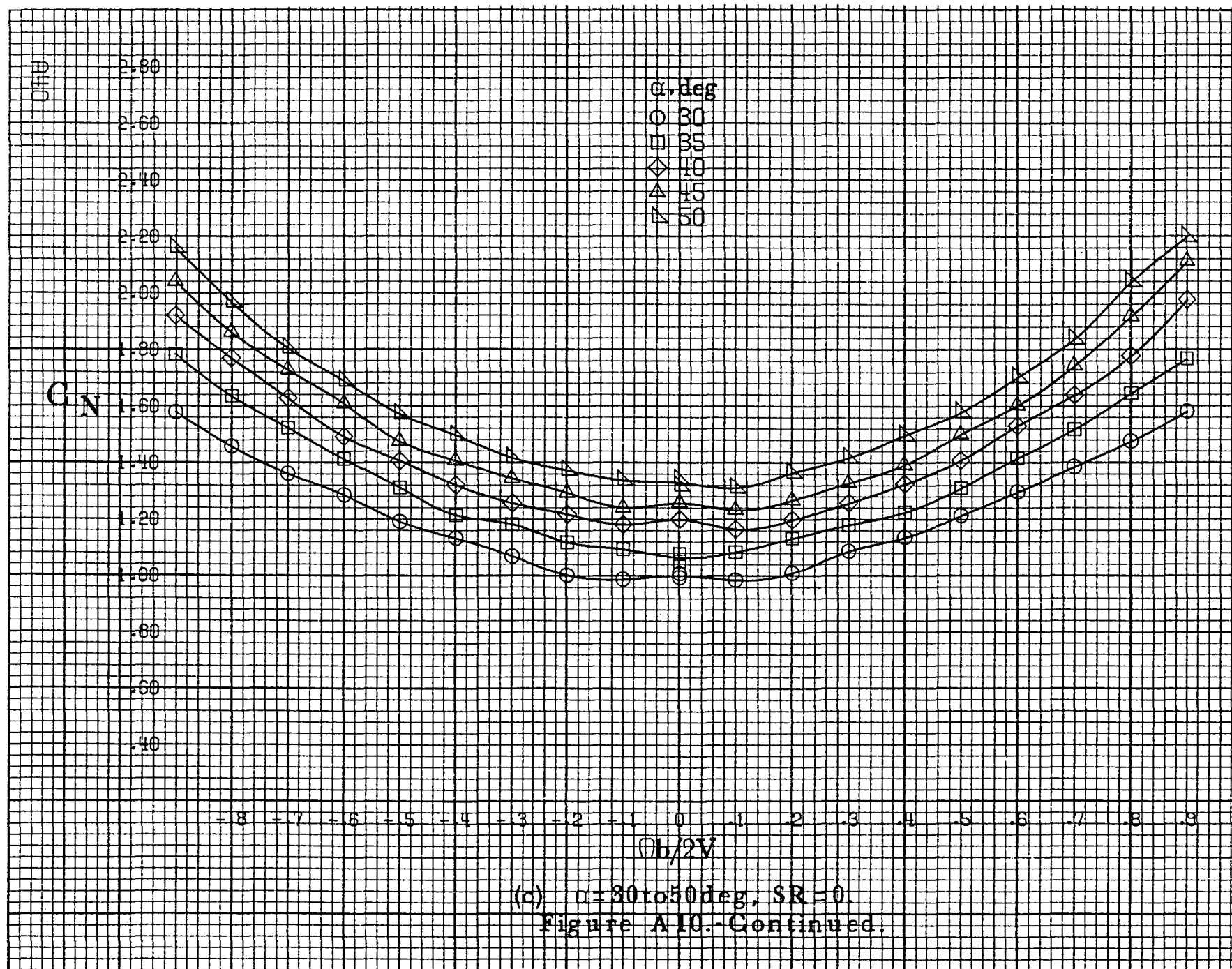
$Ob/2V$

(d) $\alpha=55\text{to}90\text{deg}$, $SR=0$.

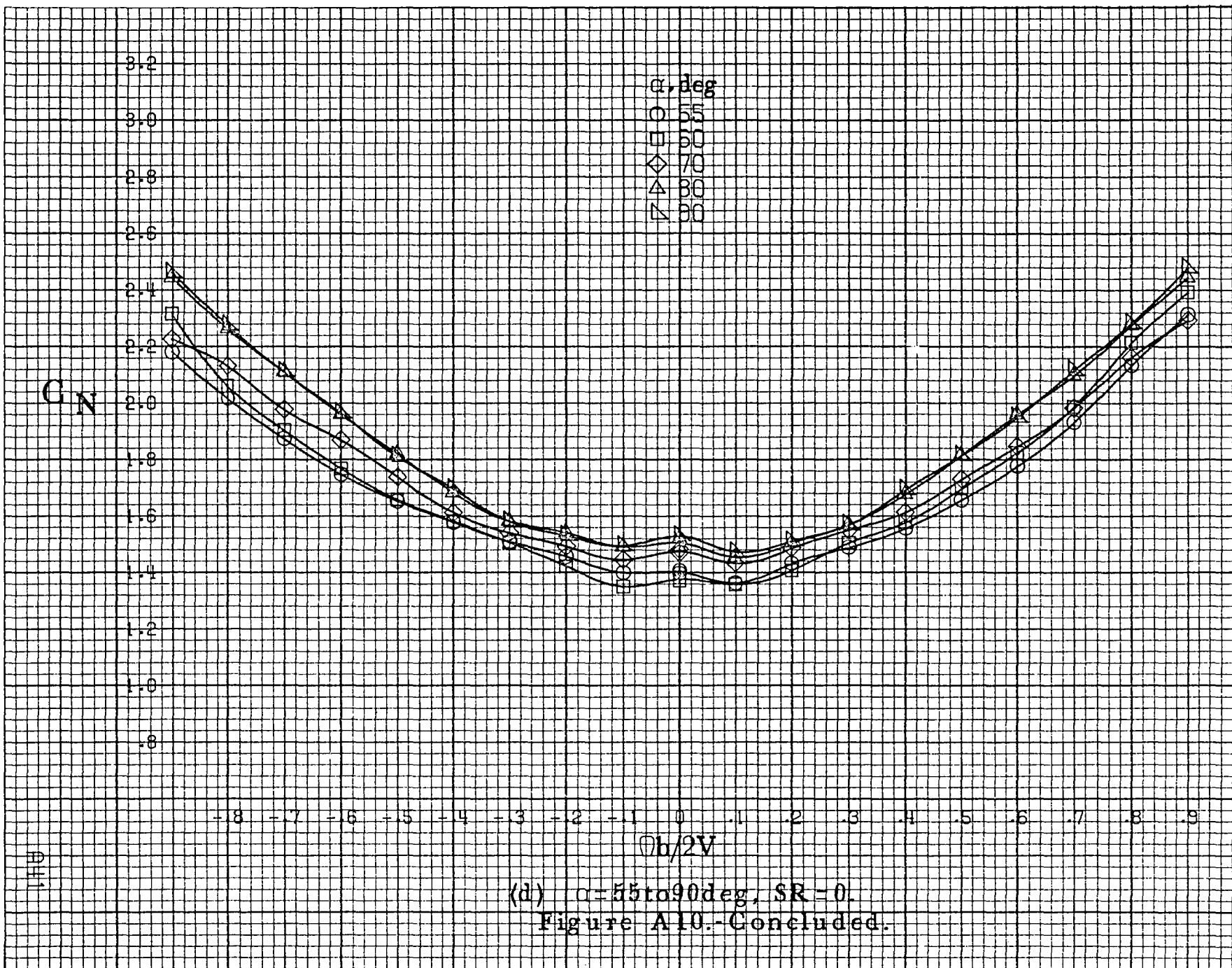
Figure A9.-Concluded.

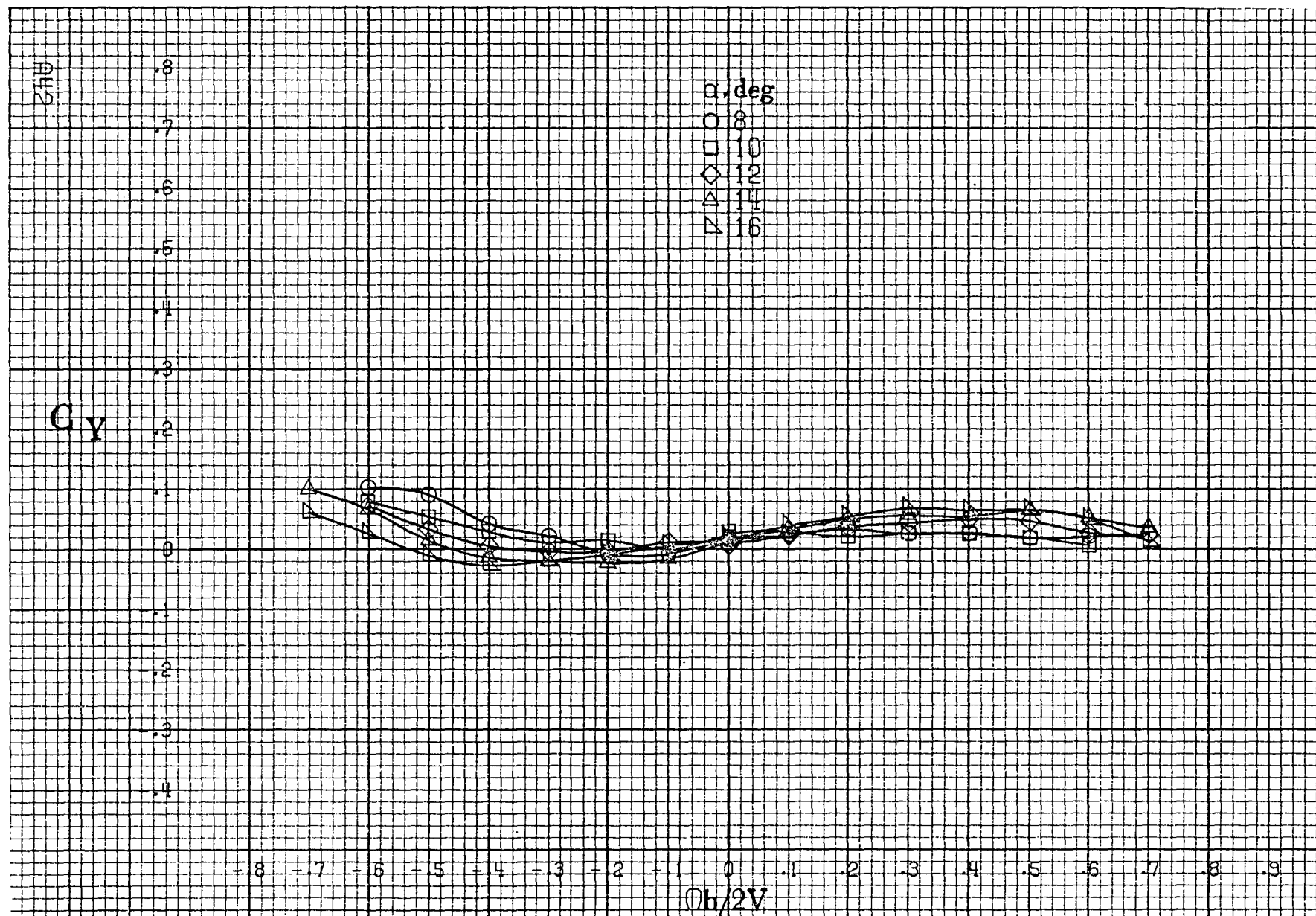






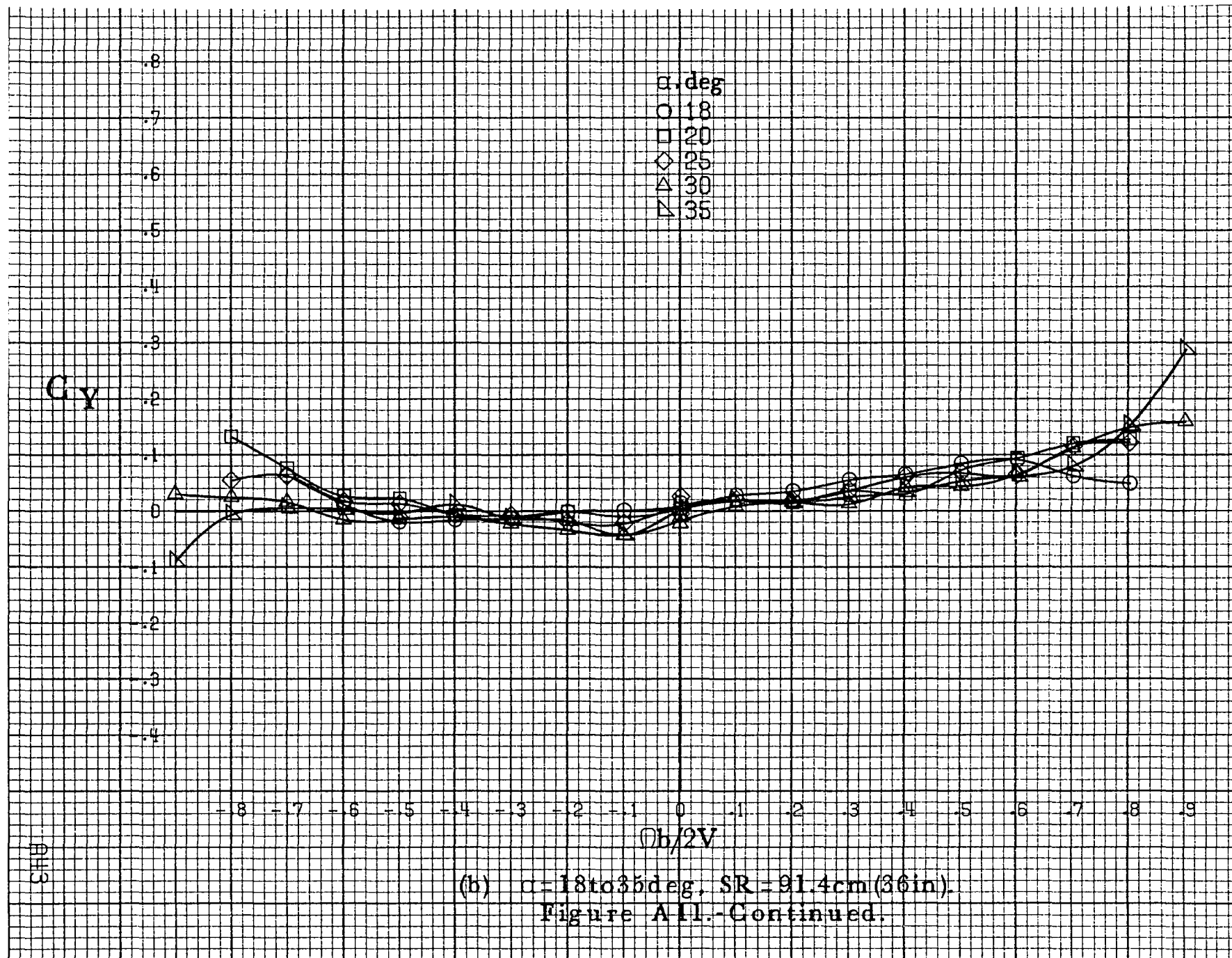
(c) $\alpha = 30$ to 50° , $SR = 0$.
Figure A10.-Continued.

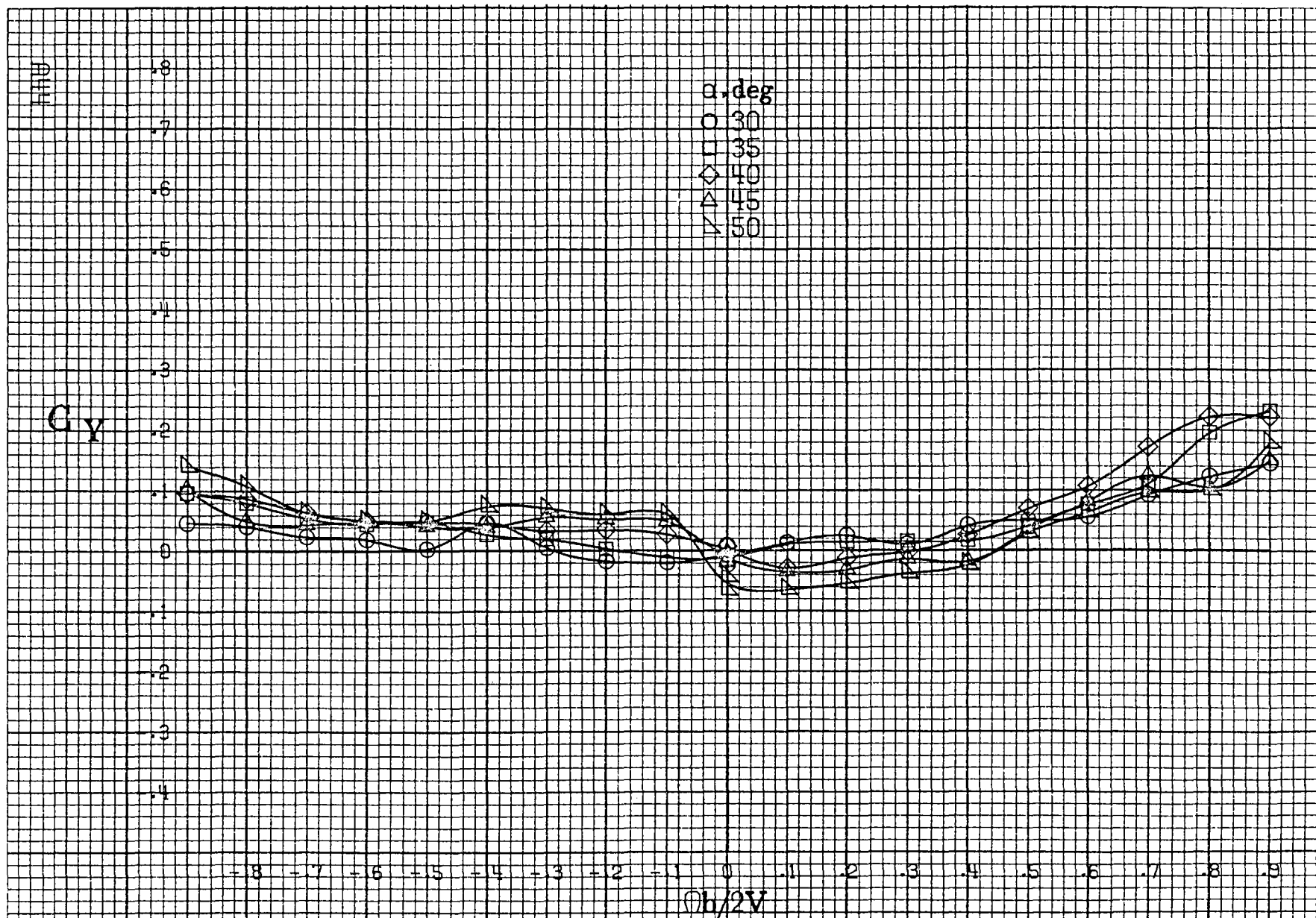




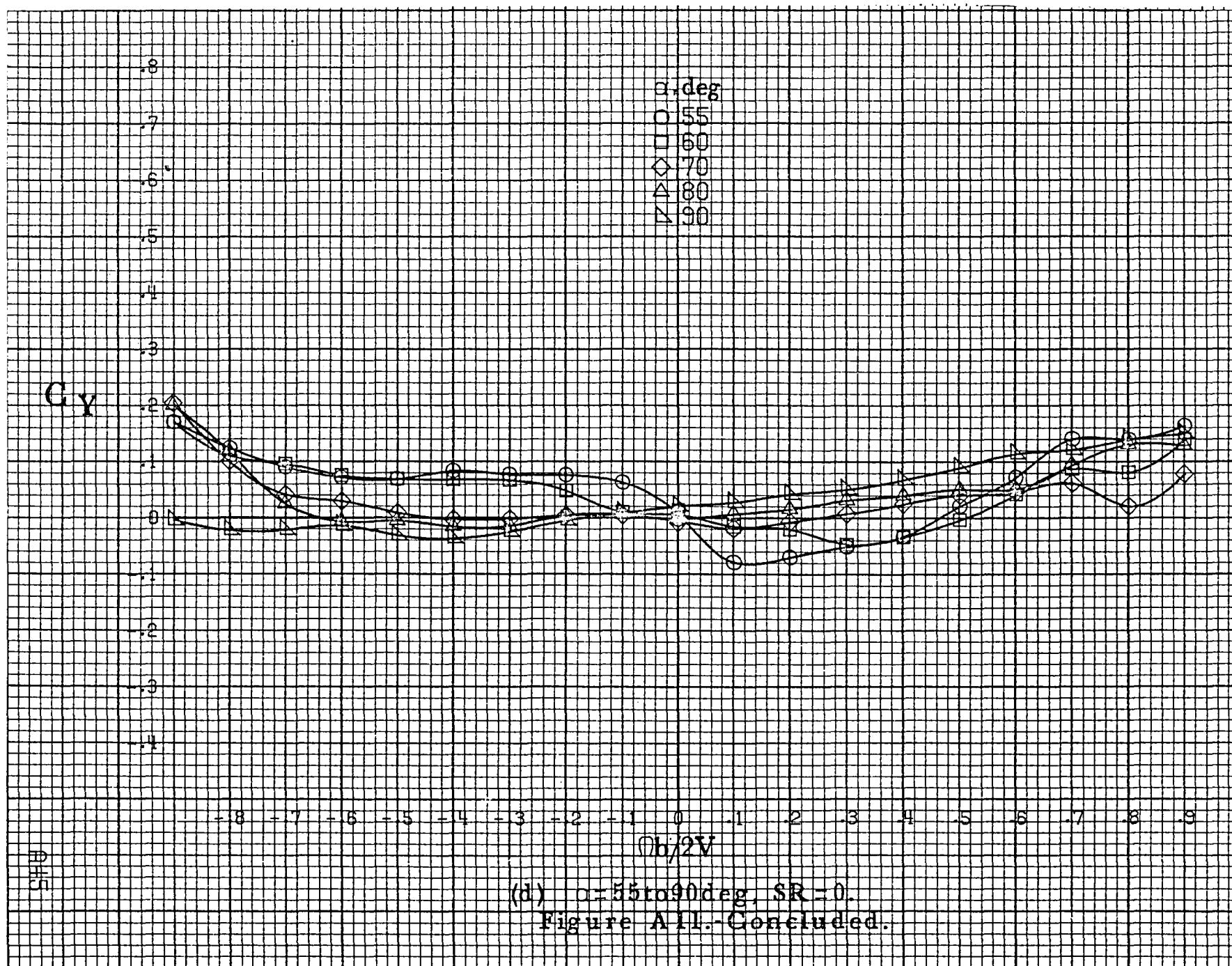
(a) $\alpha = 8$ to 16 deg, $SR = 91.4 \text{ cm (36 in.)}$.

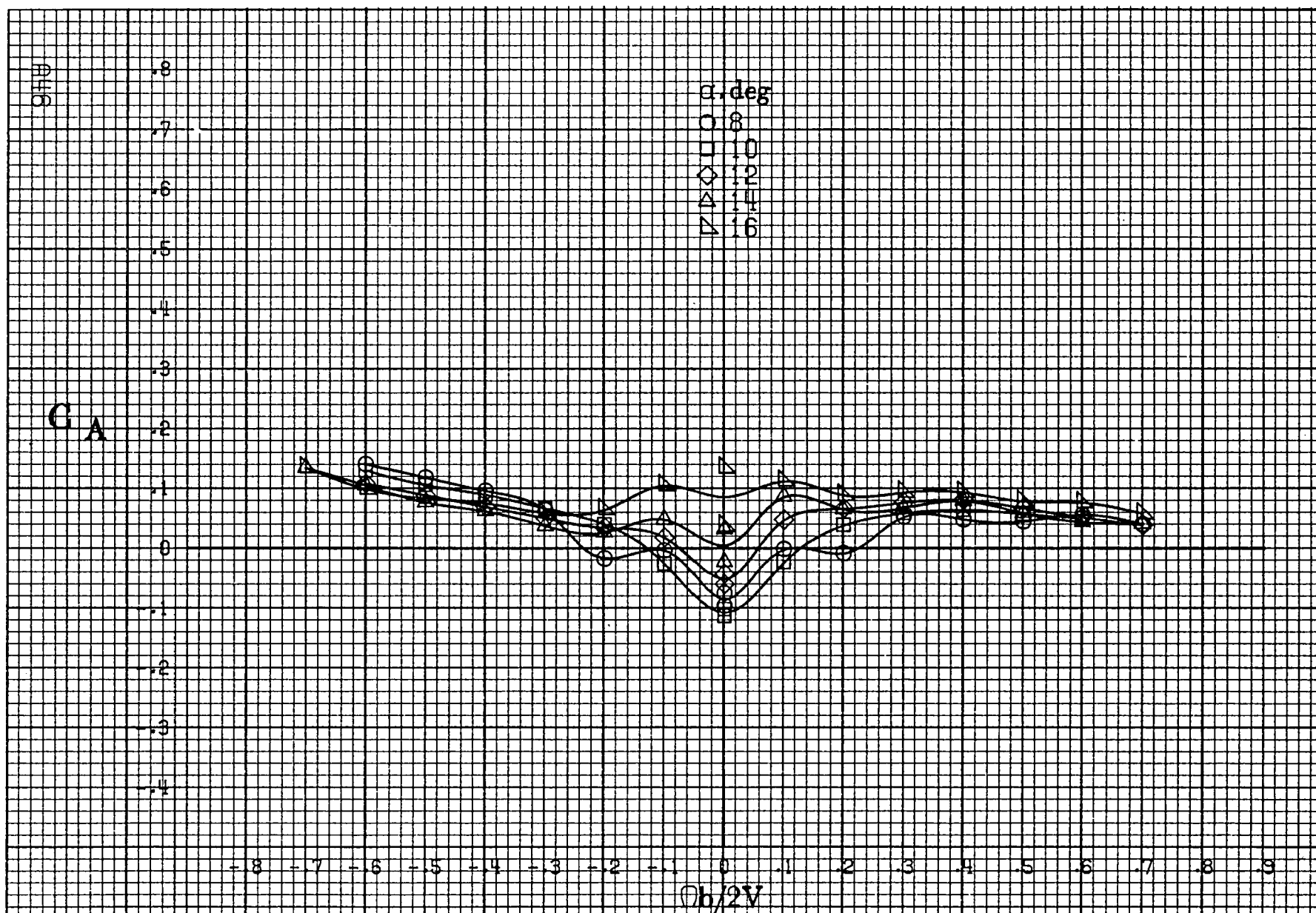
Figure A11 - Effect of rotation rate and angle of attack on side-force coefficient for short body, low wing, tail 2 configuration. $\delta_e = 0^\circ$, $\delta_a = 0^\circ$, $\delta_r = 0^\circ$, $\beta = 0^\circ$.





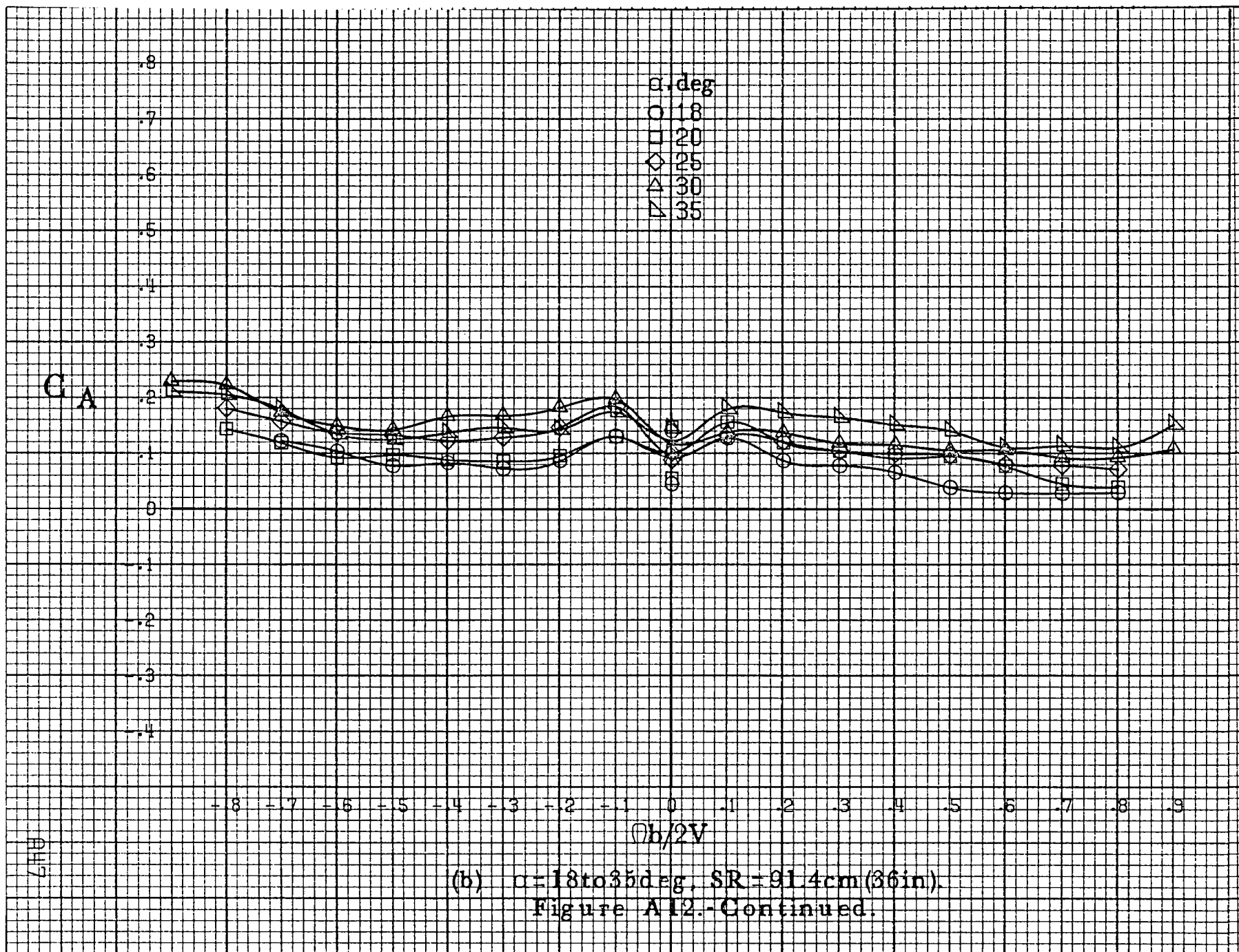
(c) $\alpha = 30$ to 50° , $SR = 0$.
Figure A11.-Continued.

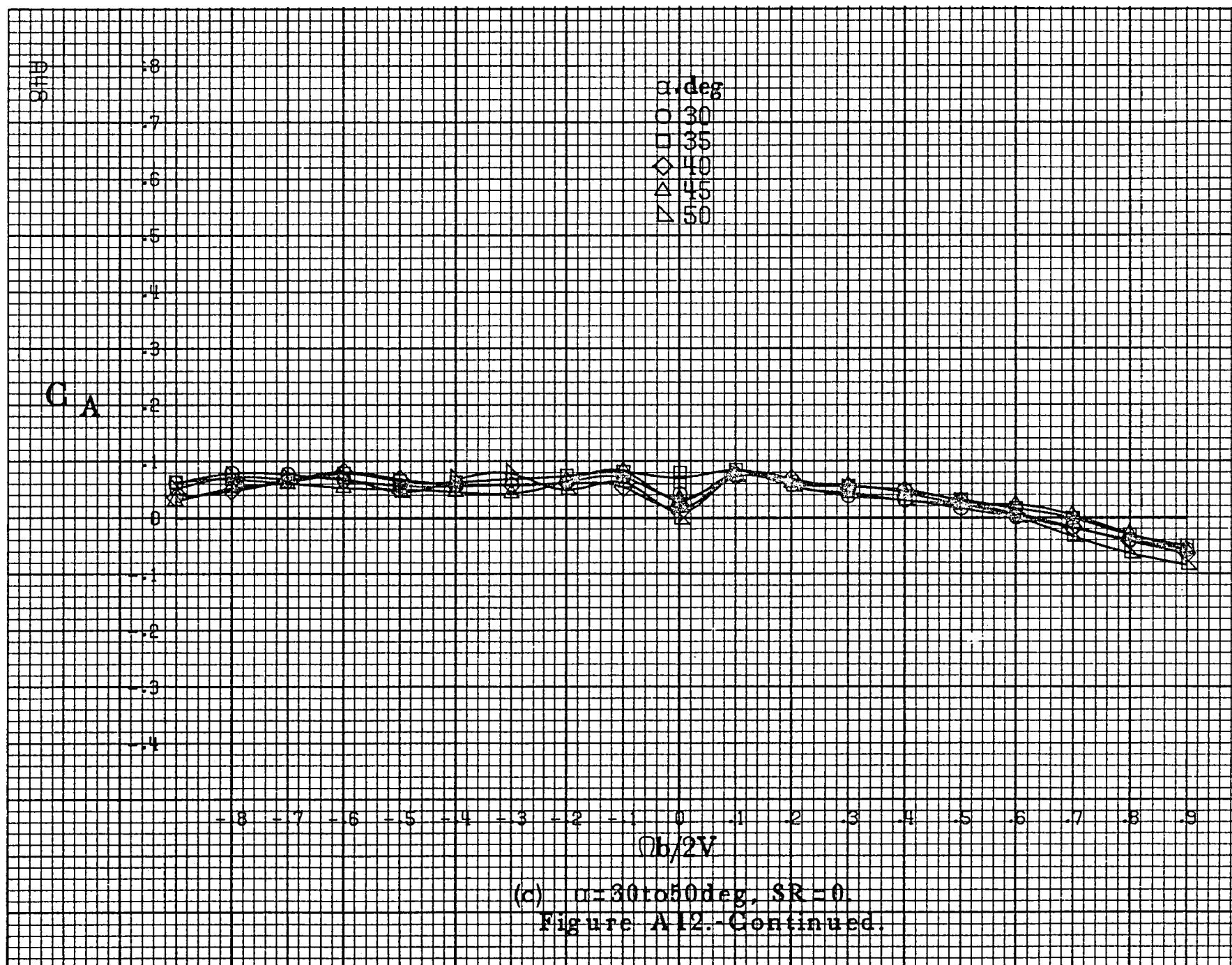


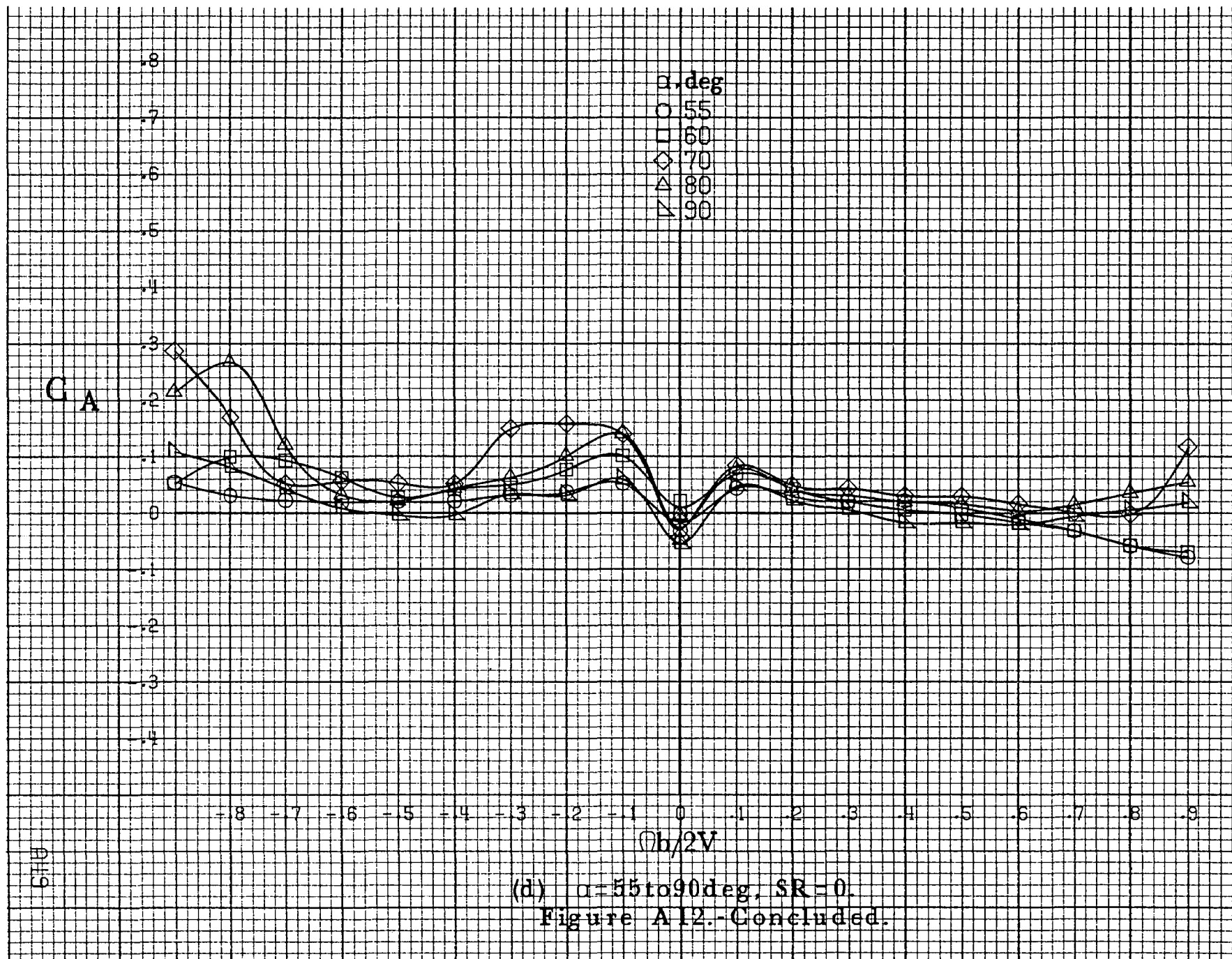


(a) $\alpha = 8$ to 16° , $SR = 91.4\text{cm (36in.)}$.

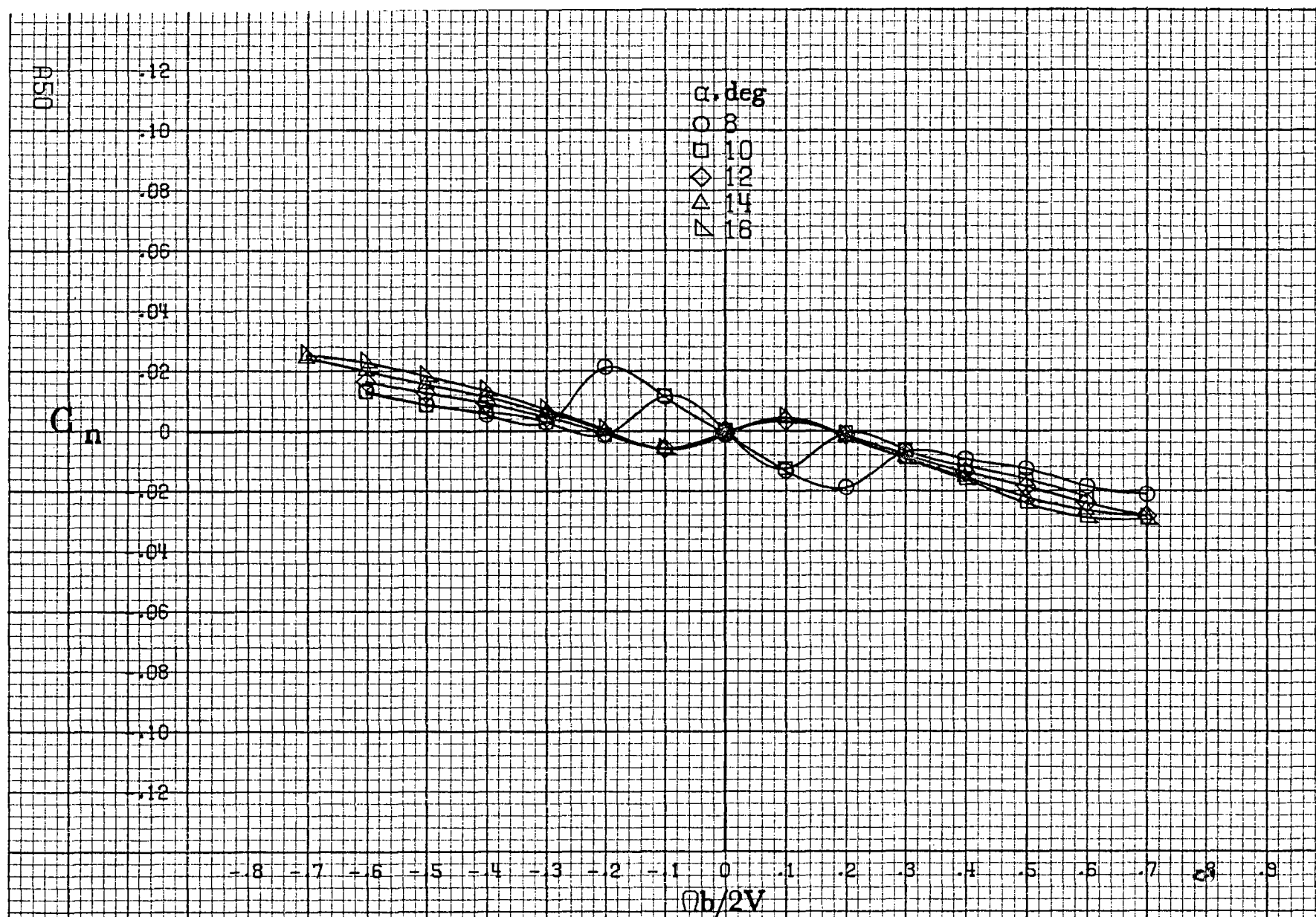
Figure A12.-Effect of rotation rate and angle of attack on axial-force coefficient for short body, low wing, tail 2 configuration. $\delta_e = 0^\circ$, $\delta_a = 0^\circ$, $\delta_r = 0^\circ$, $\beta = 0^\circ$.







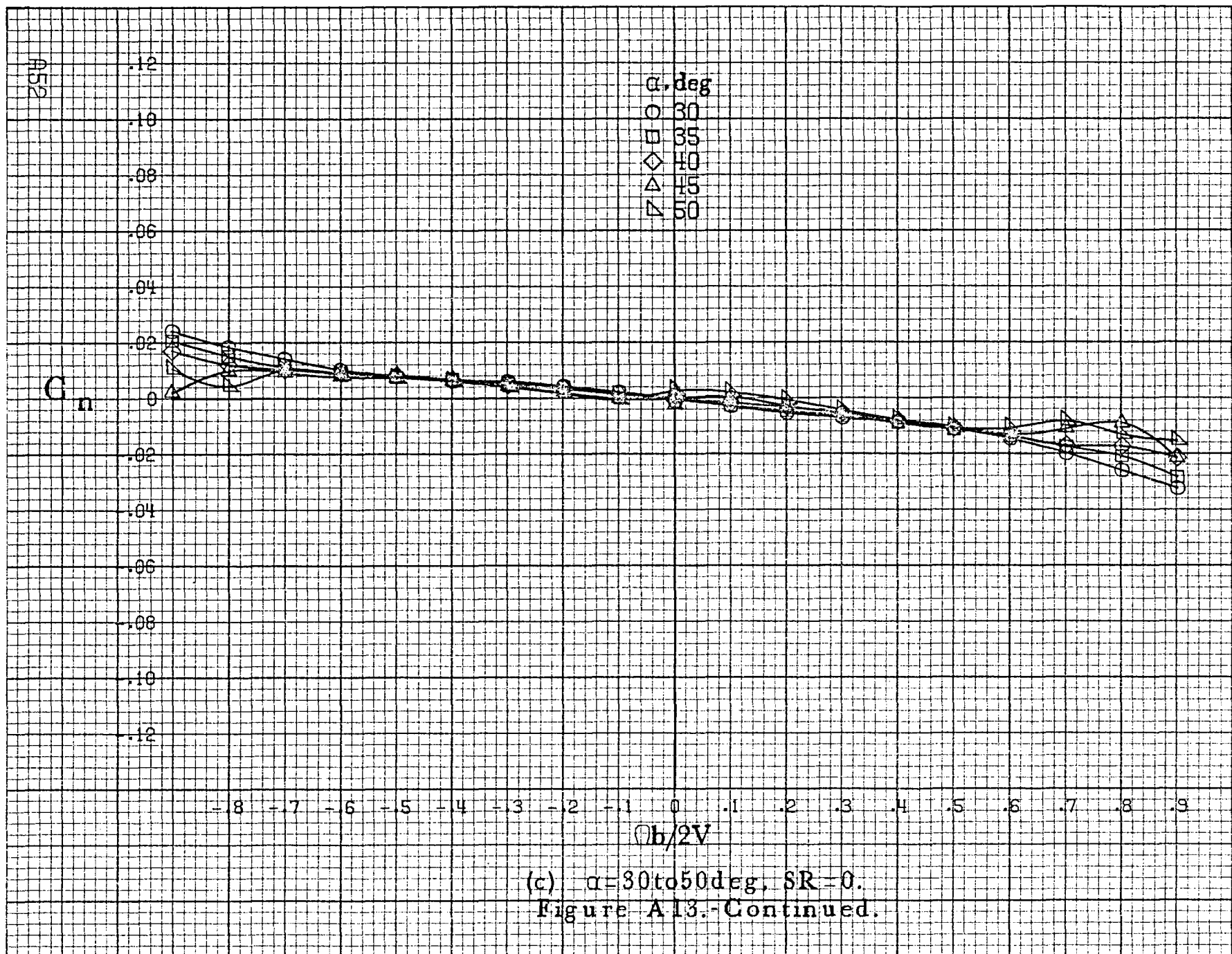
(d) $\alpha = 55$ to 90 deg, $SR = 0$.
Figure A12.- Concluded.

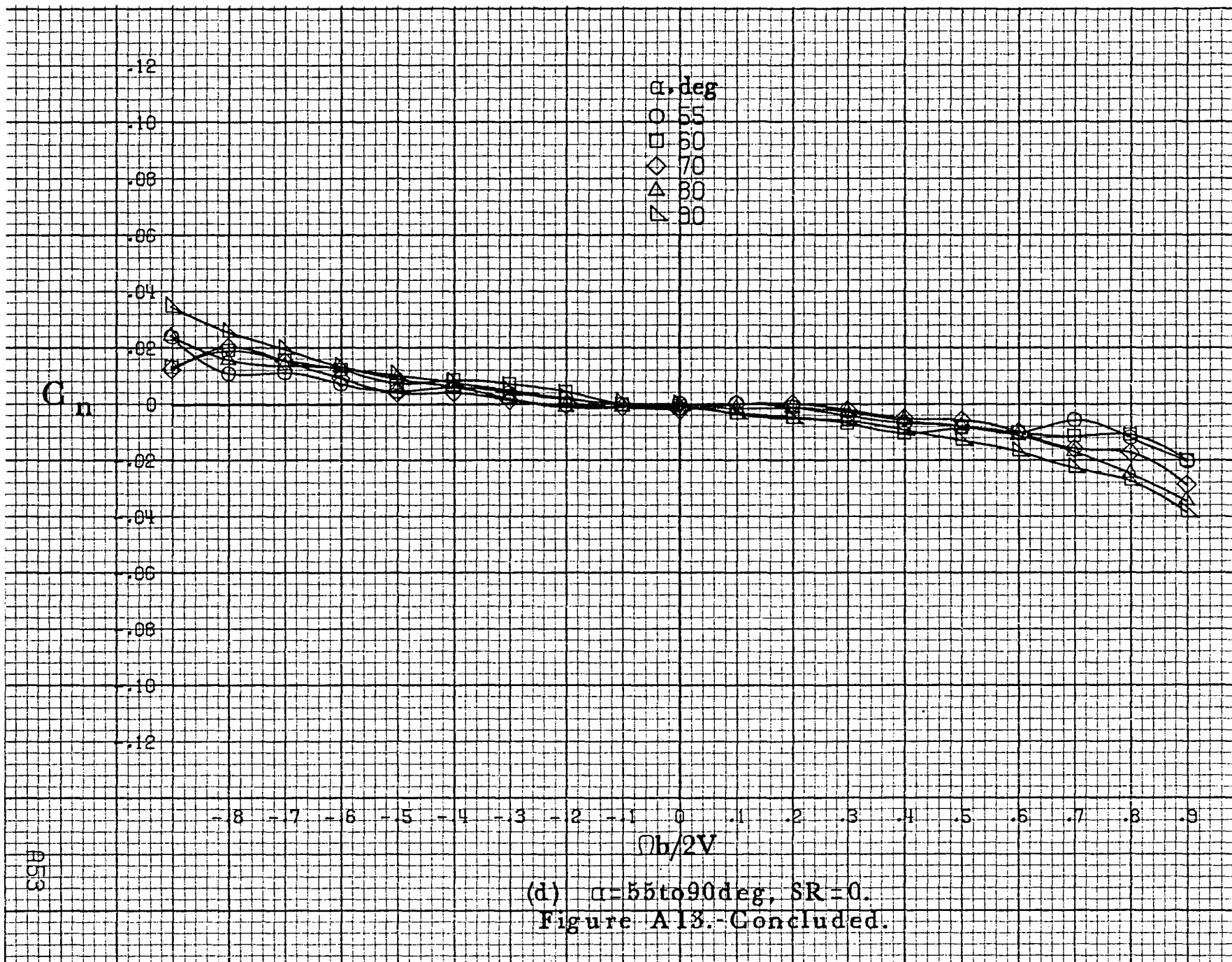


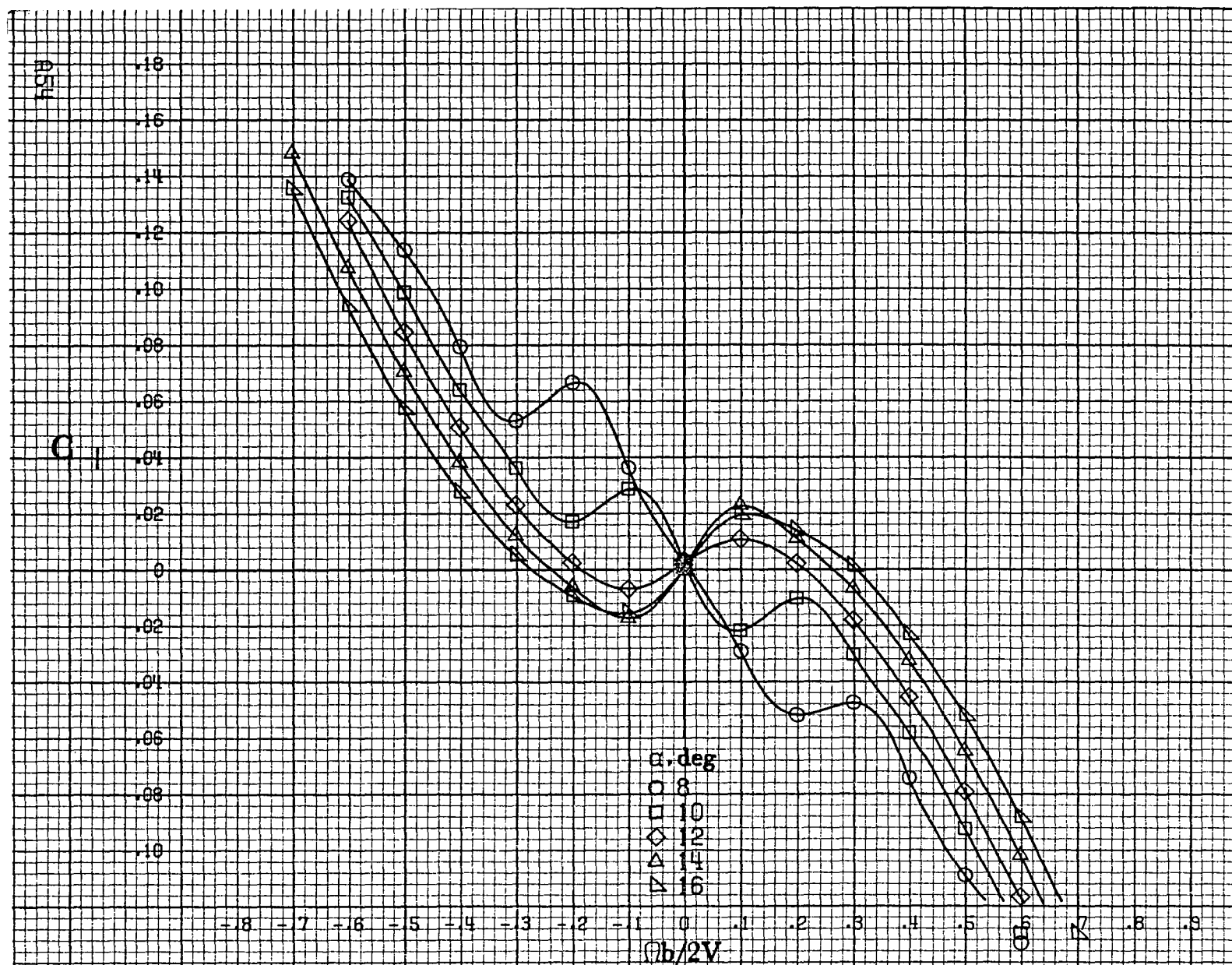
(a) $\alpha = 8$ to 16° , $SR = 91.4\text{cm (36in.)}$.

Figure A13.-Effect of rotation rate and angle of attack on yawing-moment coefficient for complete short body, low wing configuration. $\delta_e = 0^\circ$, $\delta_a = 0^\circ$, $\delta_r = 0^\circ$, $\beta = 0^\circ$.



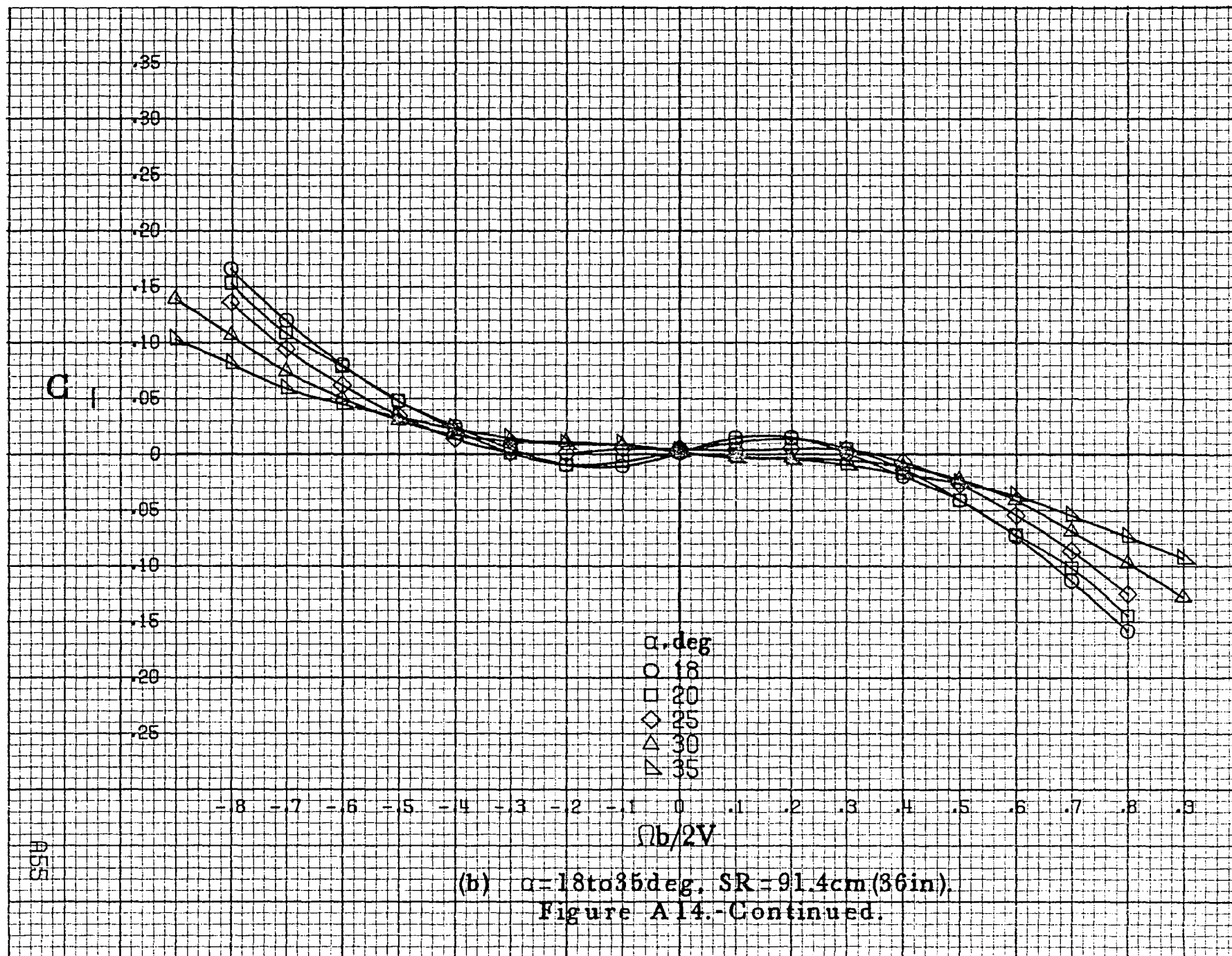


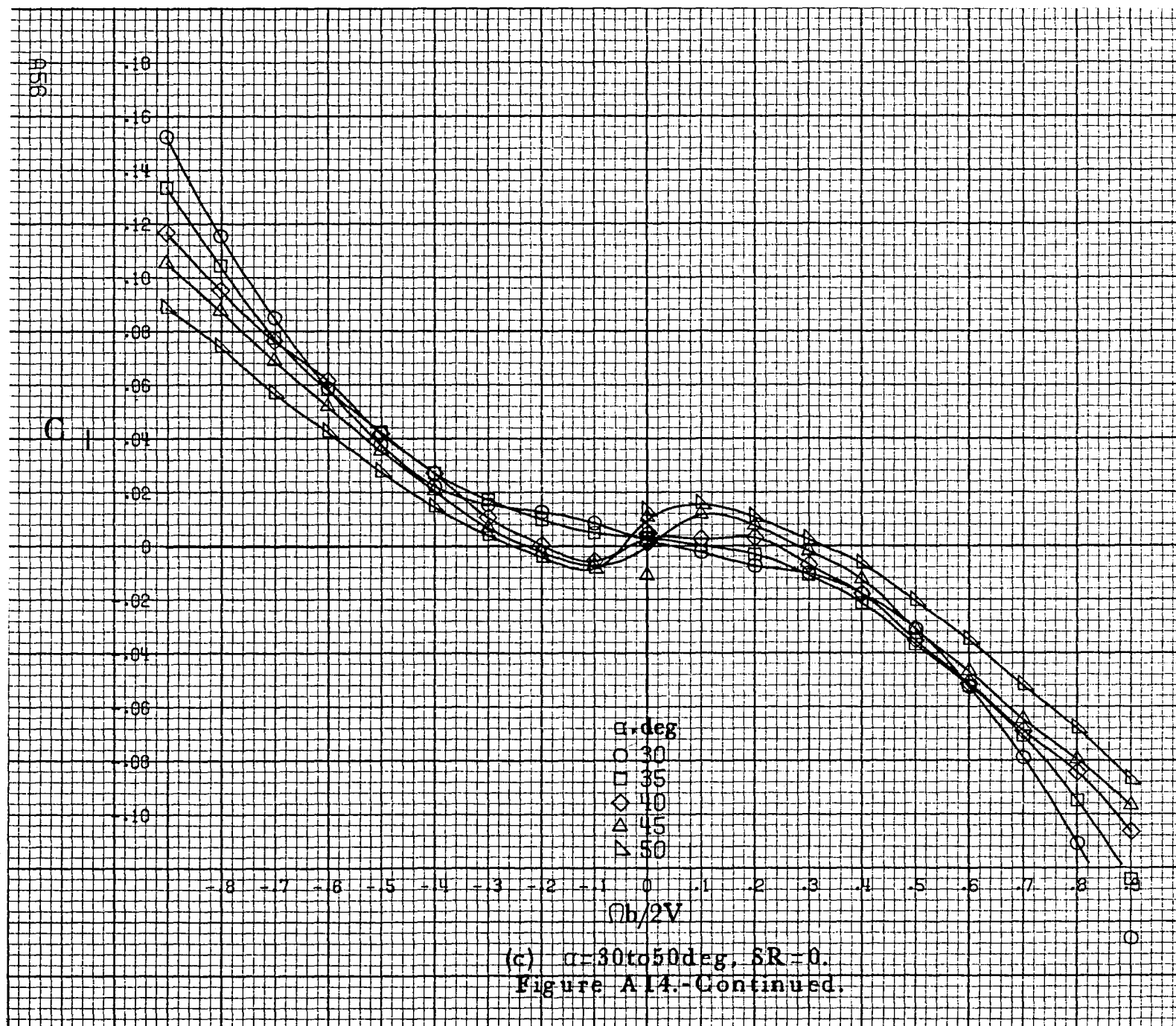


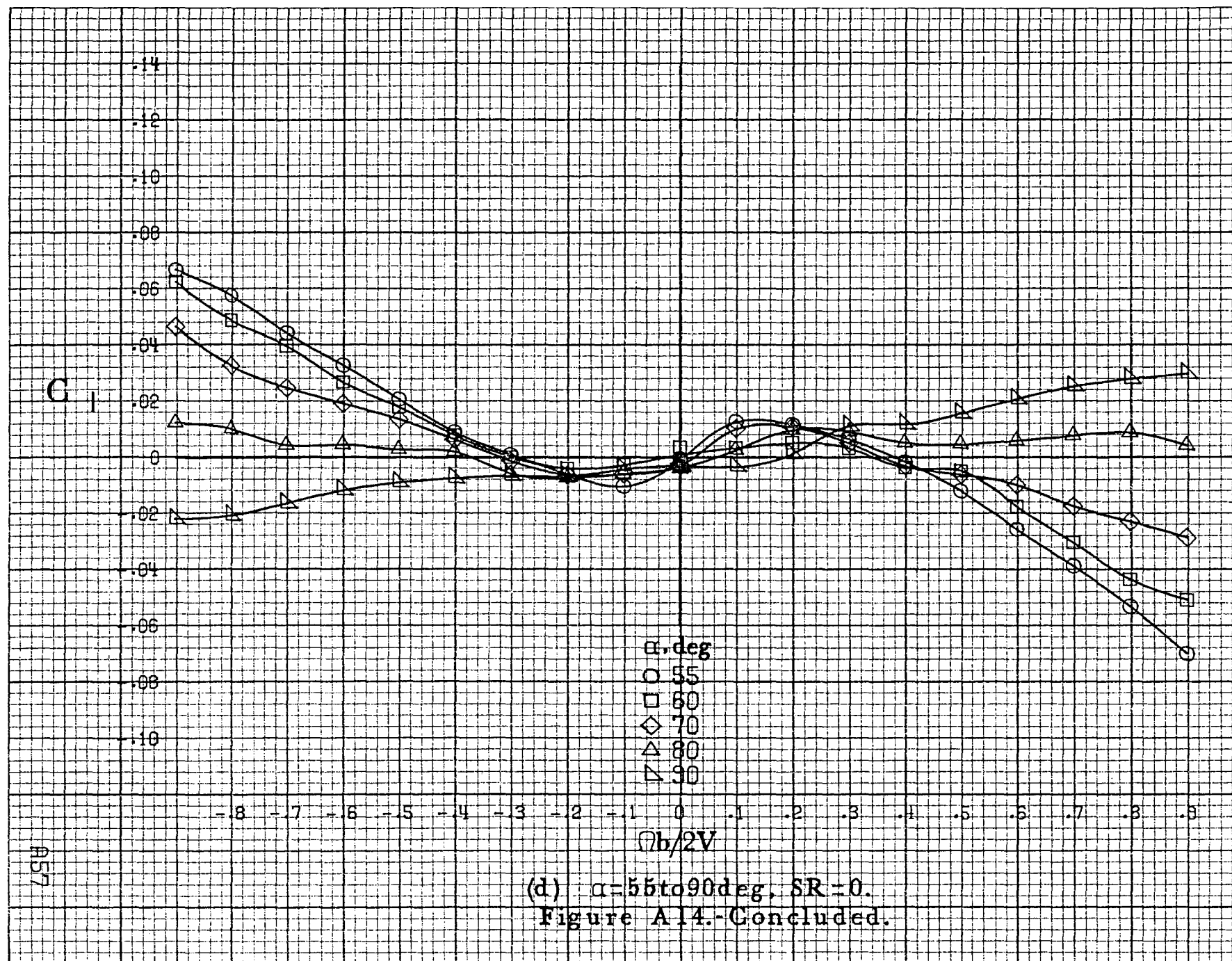


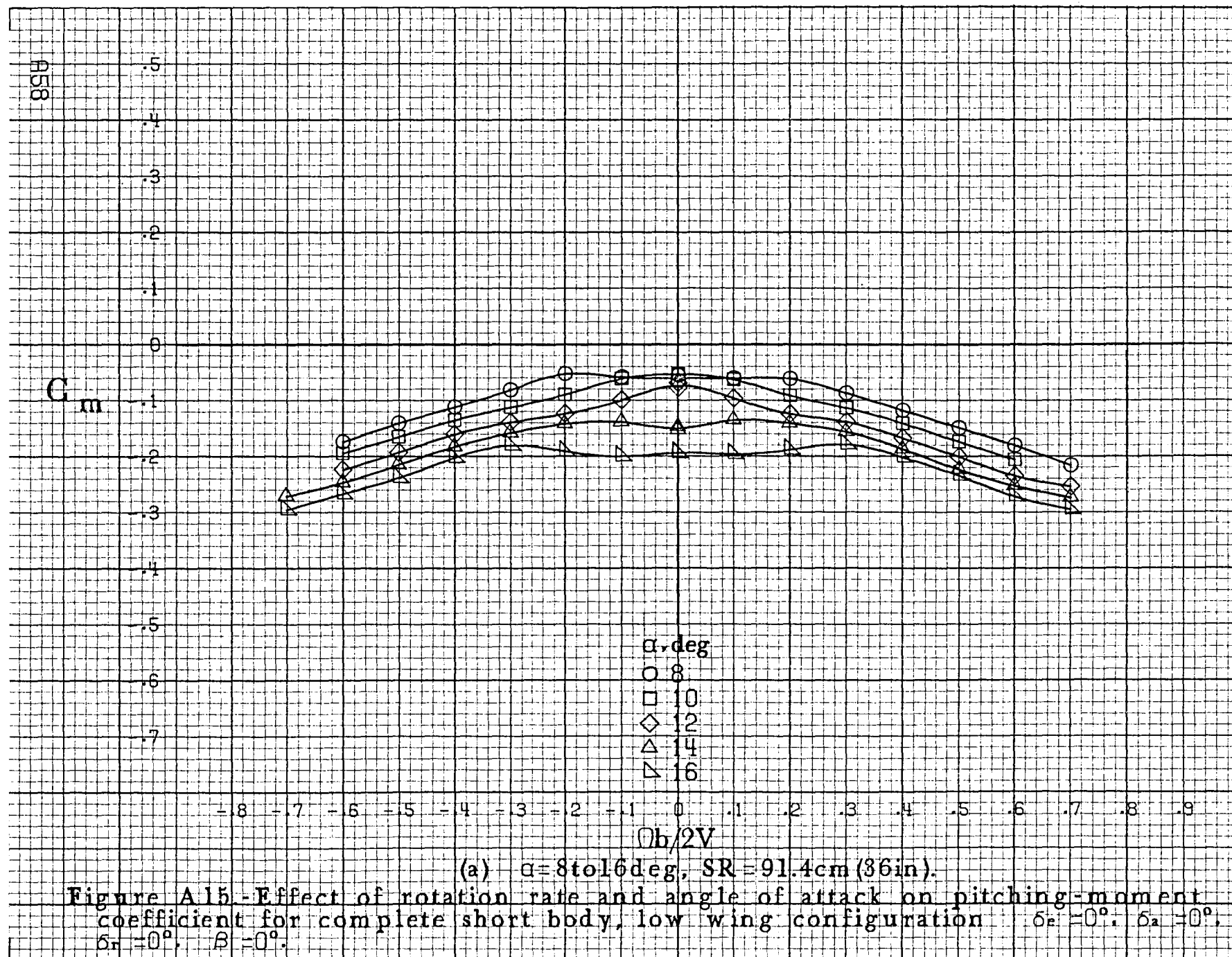
(a) $\alpha = 8$ to 16° , $SR = 91.4\text{cm} (36\text{in})$.

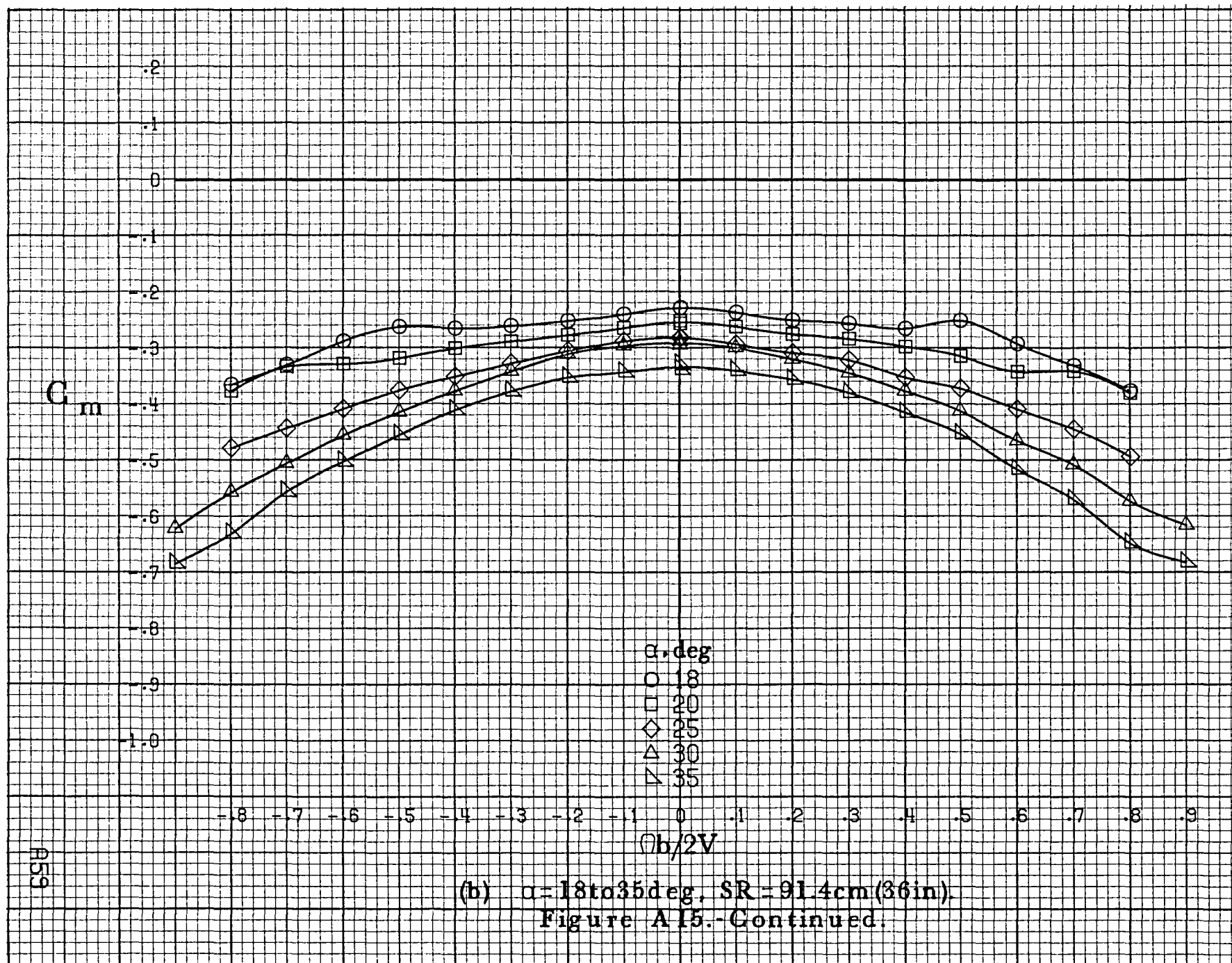
Figure A14 - Effect of rotation rate and angle of attack on rolling-moment coefficient for complete short body, low wing configuration. $\delta_r = 0^\circ$, $\delta_a = 0^\circ$, $\delta = 0^\circ$.



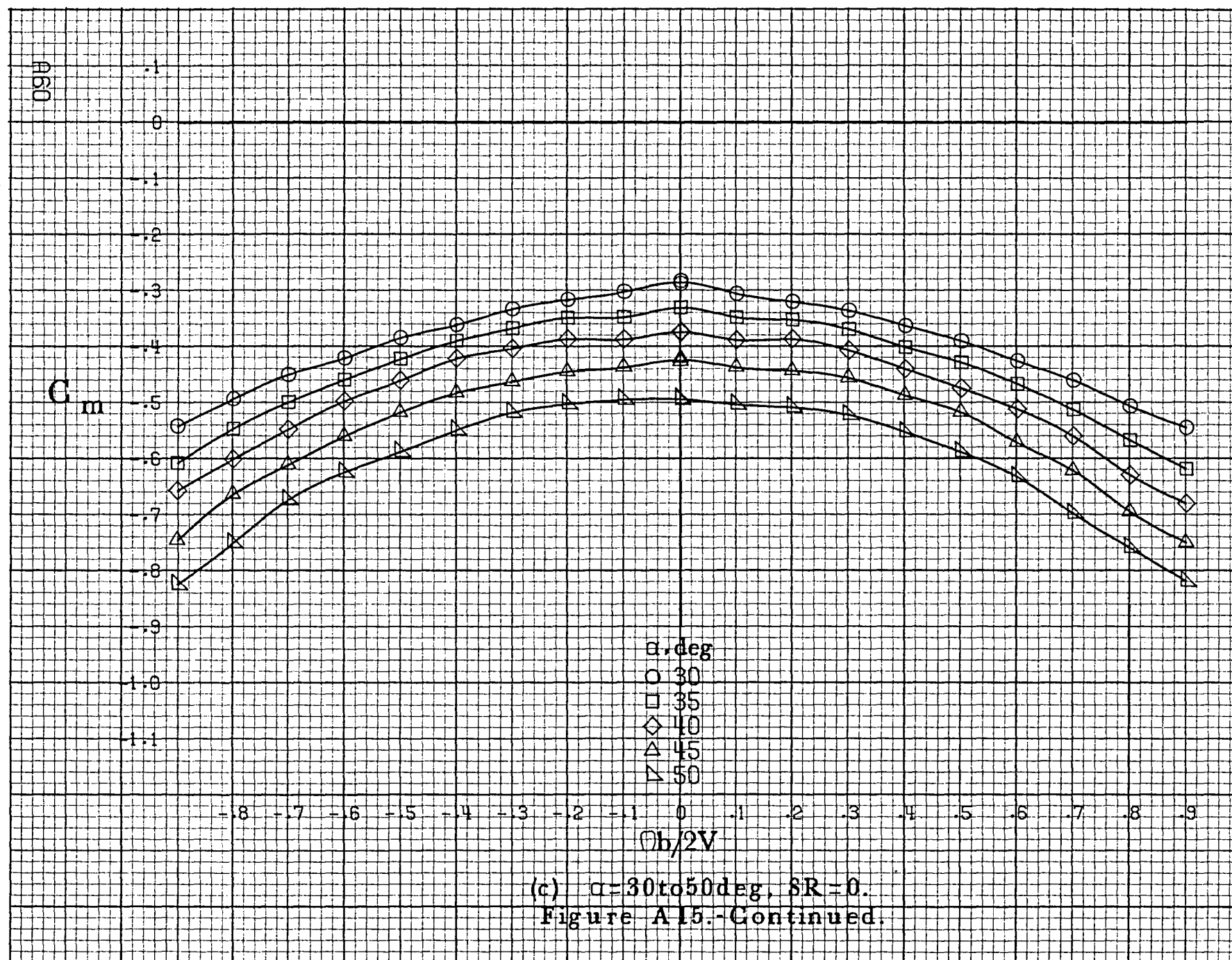


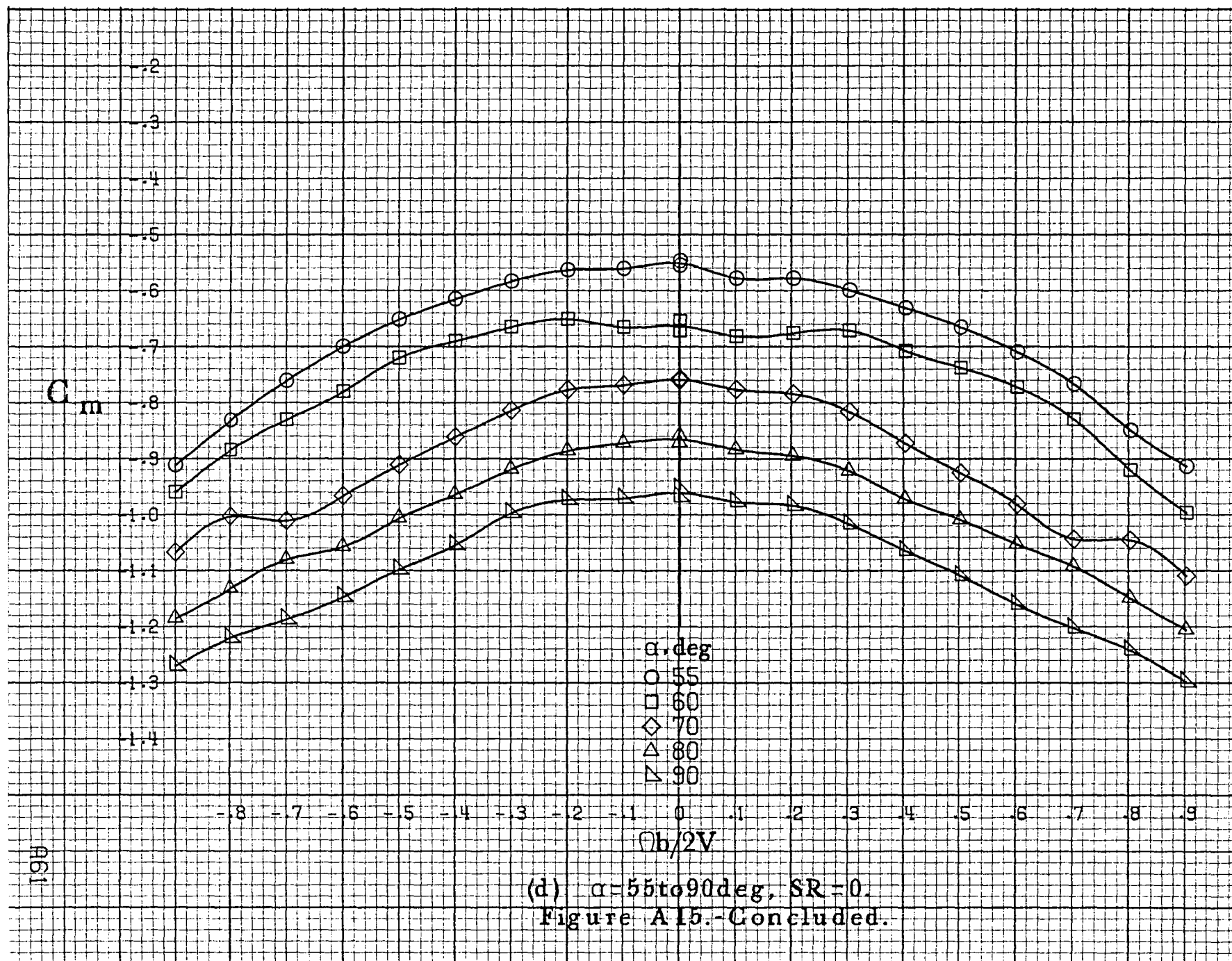


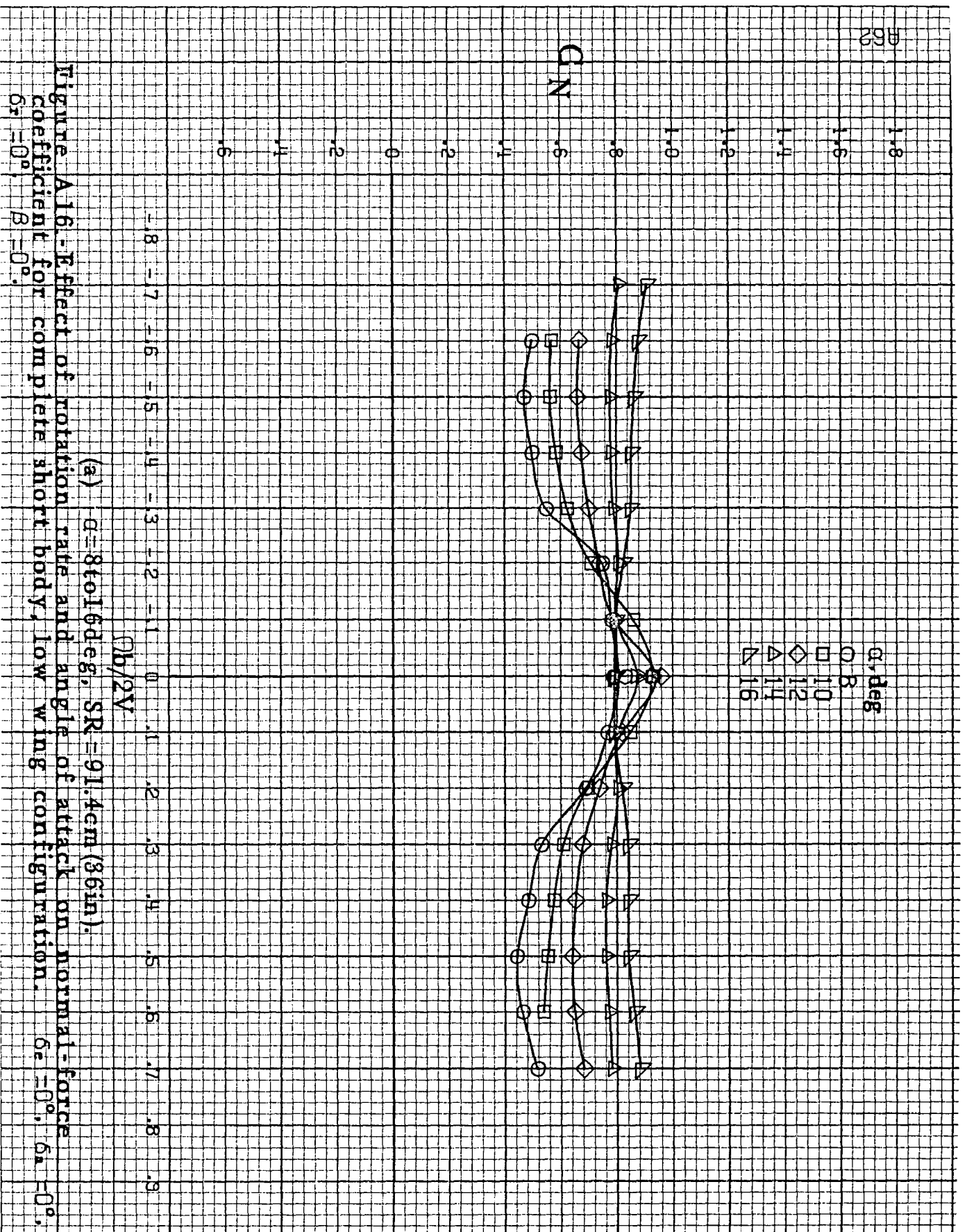


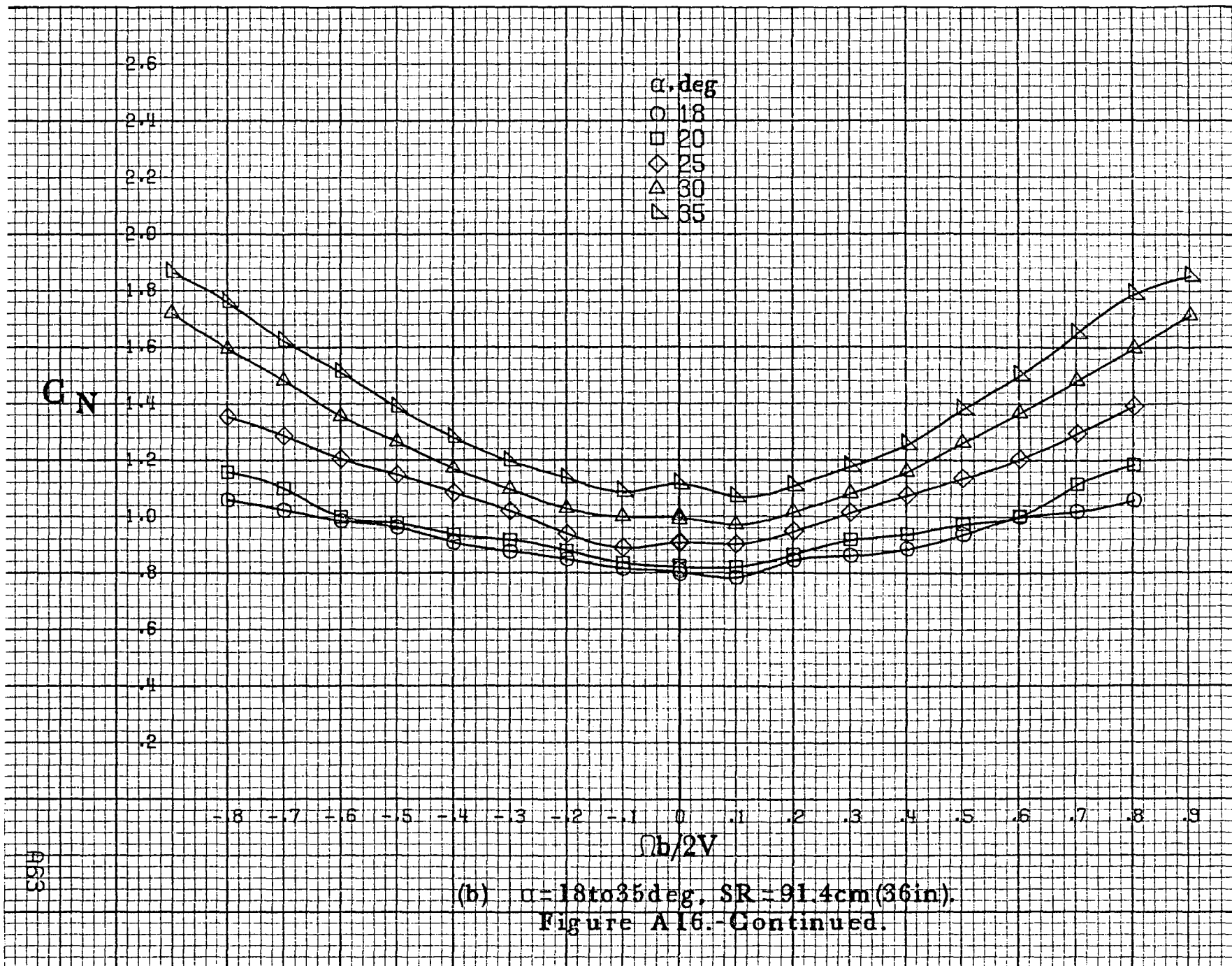


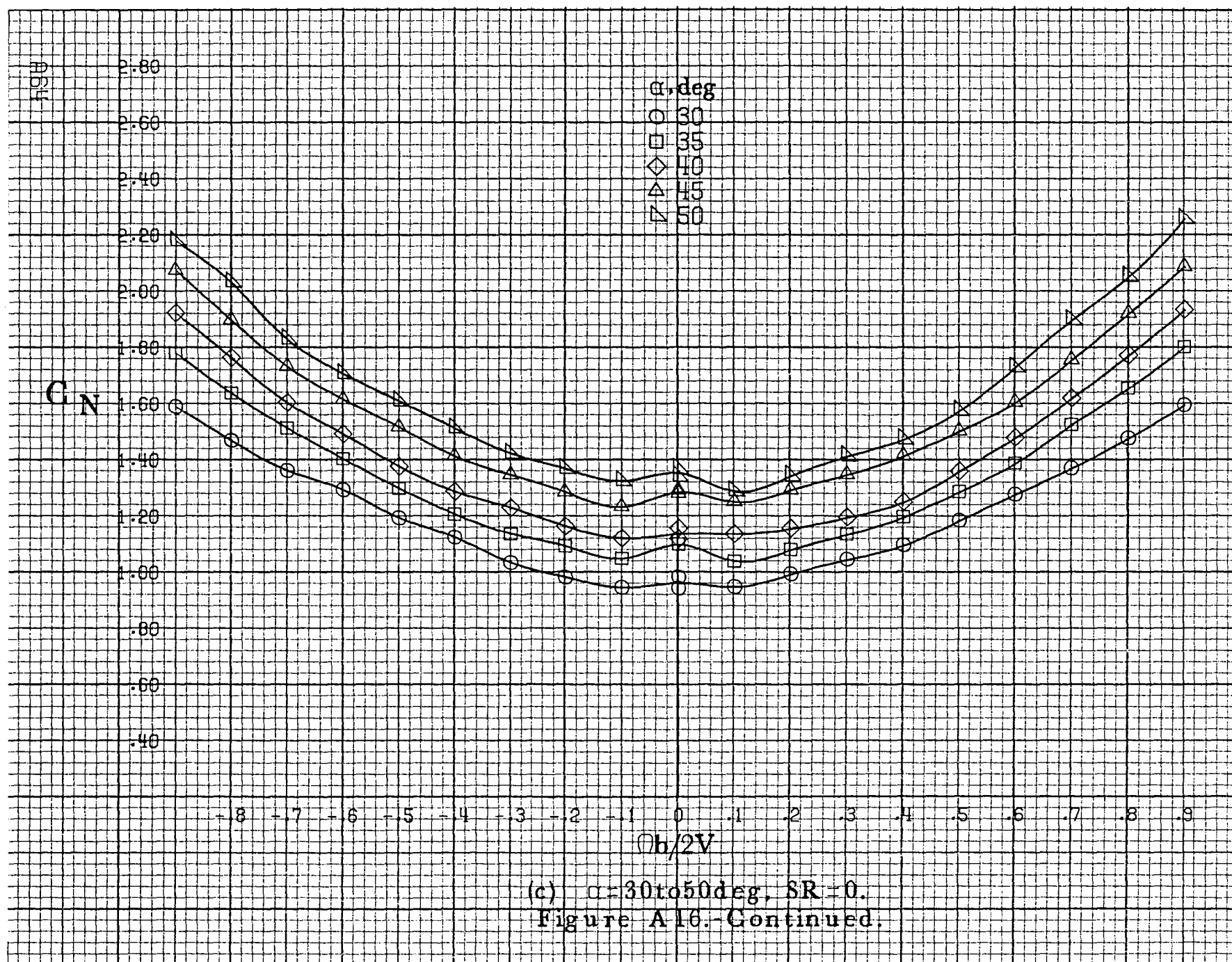
(b) $\alpha=18$ to 35° , SR=91.4cm(36in).
Figure A 15.-Continued.

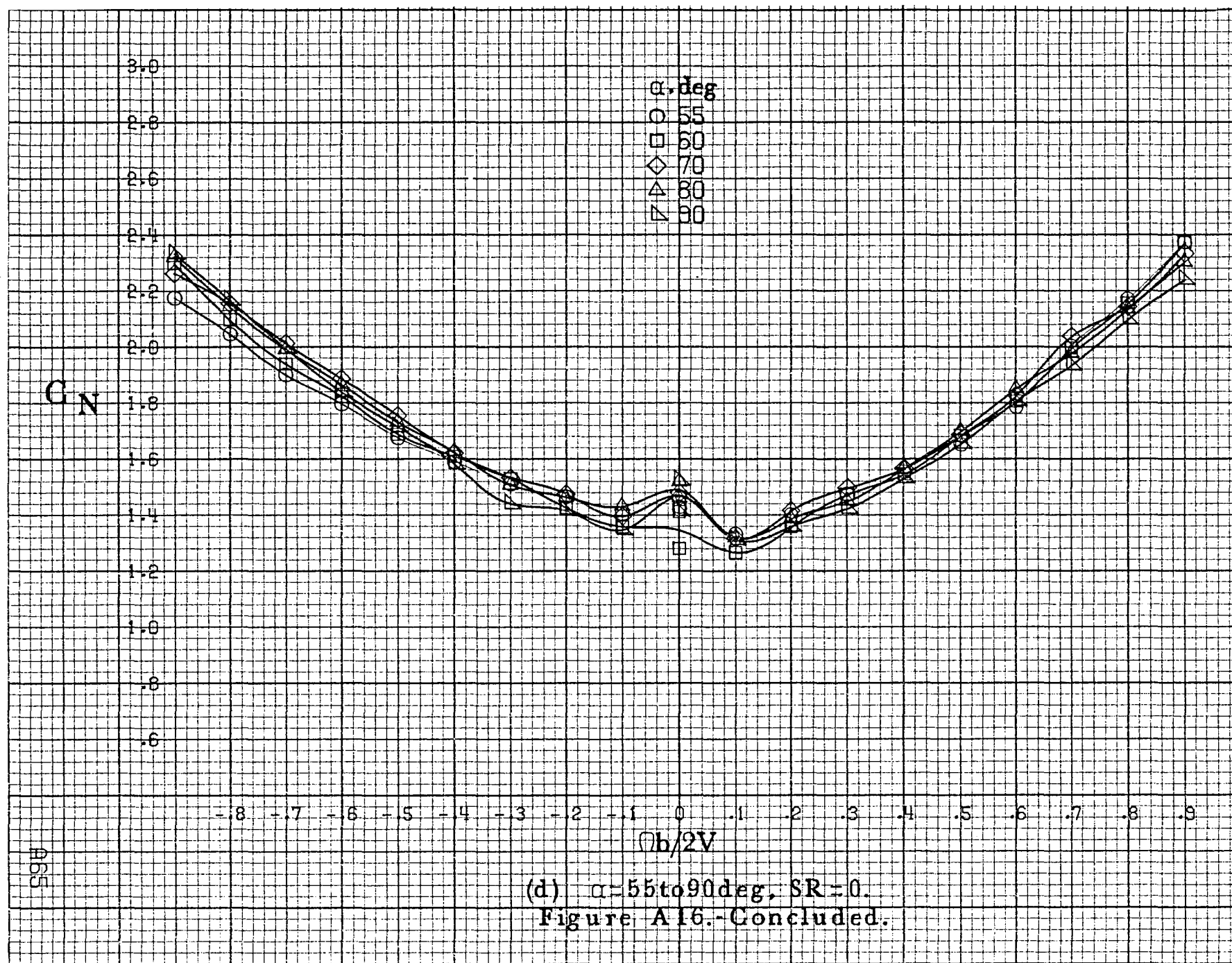


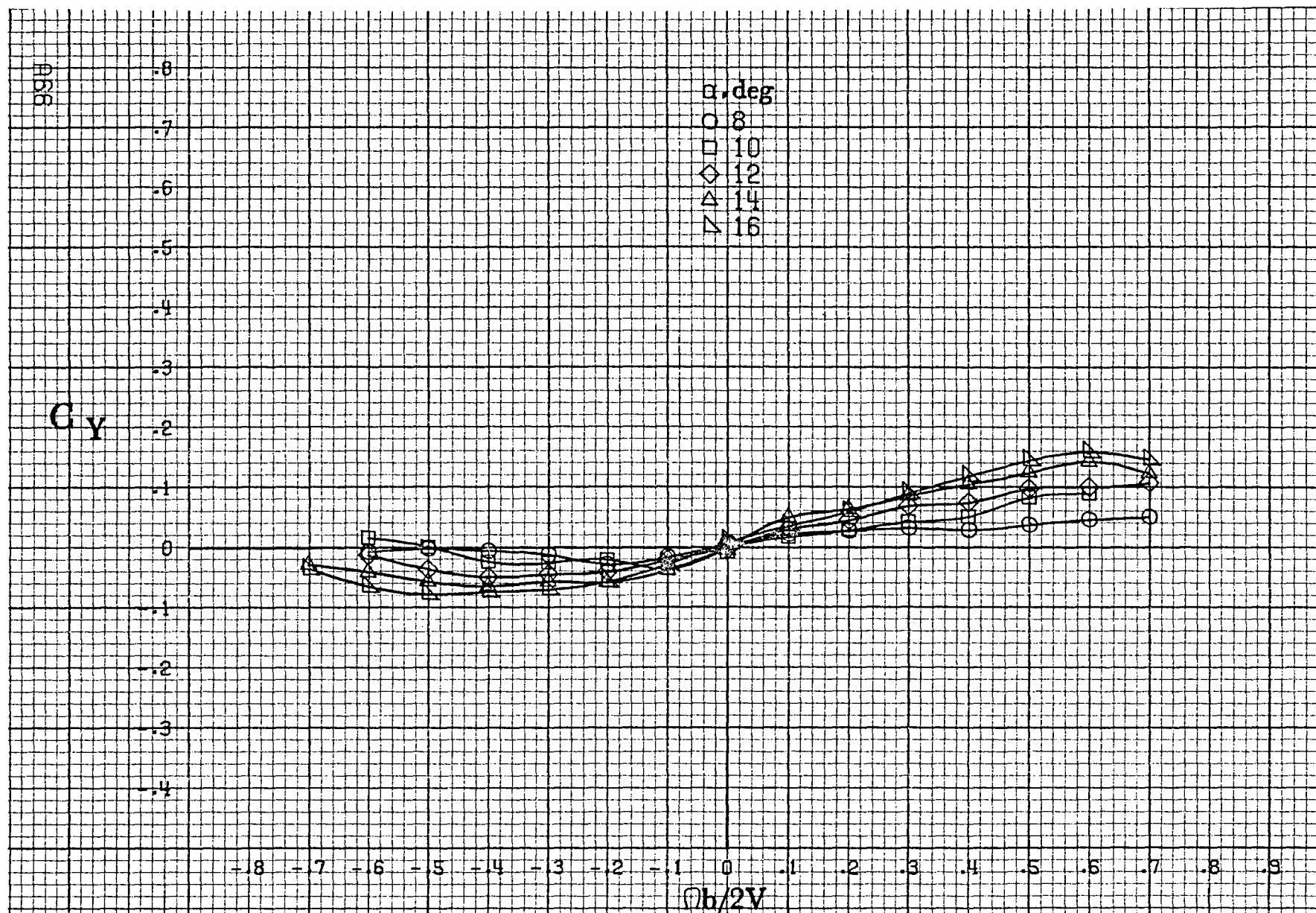






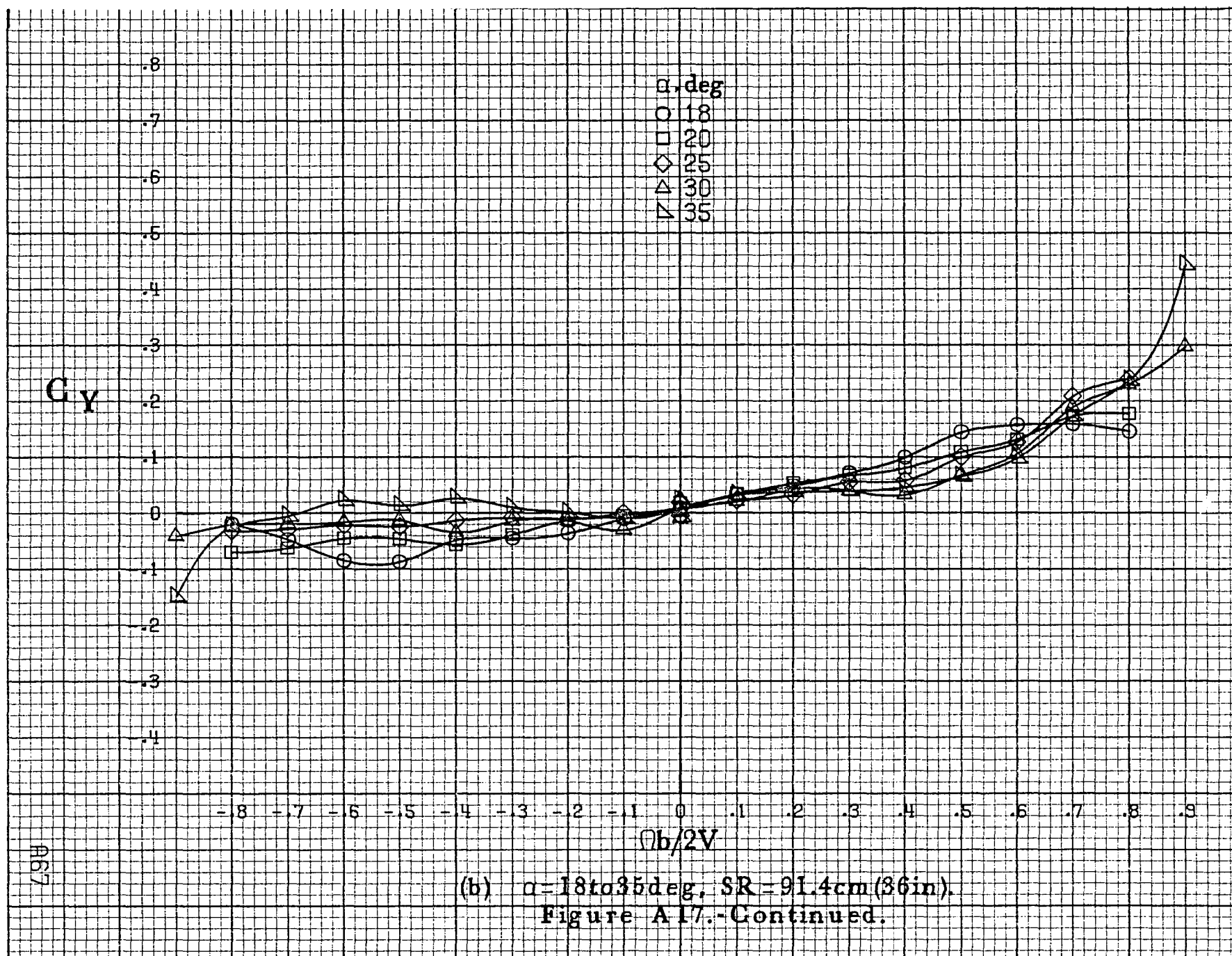






(a) $\alpha = 8$ to 16° , $SR = 91.4\text{cm} (36\text{in})$.

Figure A17.-Effect of rotation rate and angle of attack on side-force coefficient for complete short body, low wing configuration. $\delta_c = 0^\circ$, $\delta_a = 0^\circ$, $\delta_r = 0^\circ$, $\beta = 0^\circ$.



868

C_y

α, deg

- 30
- 35
- ◇ 40
- △ 45
- ▽ 50

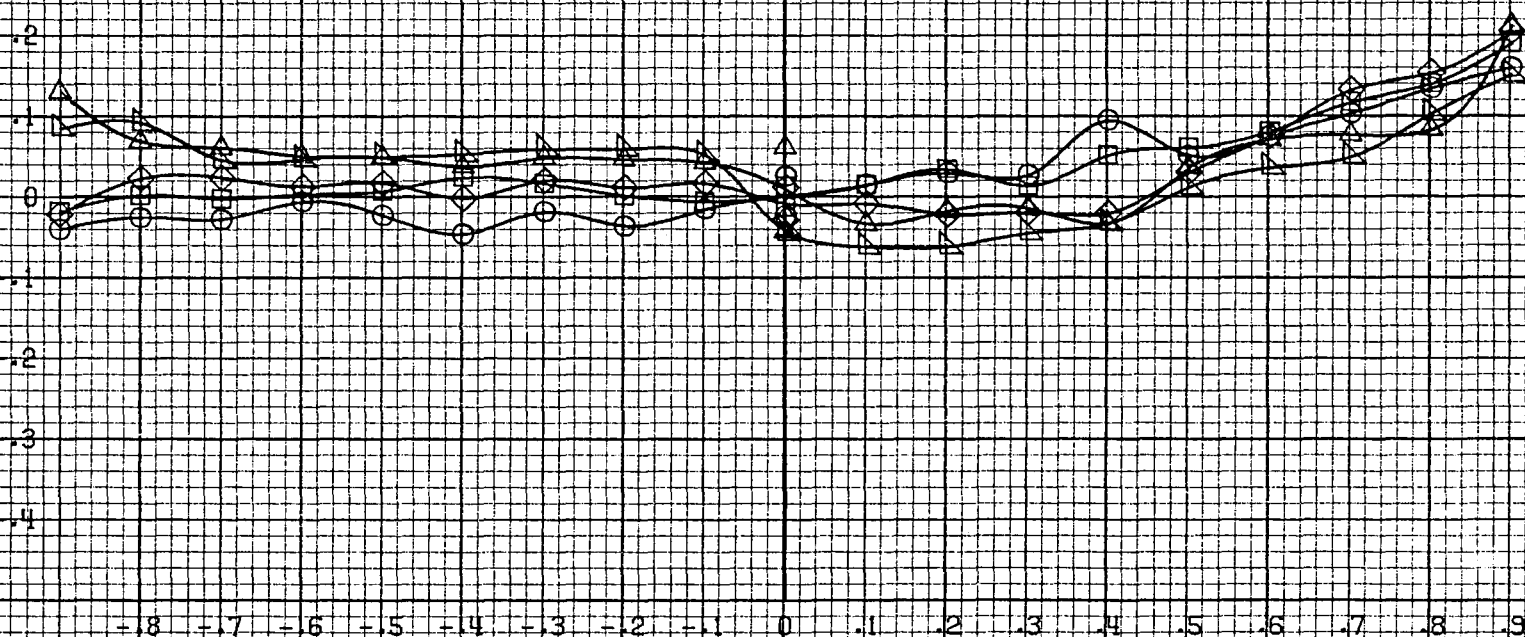
.8
.7
.6
.5
.4
.3
.2
.1
0
-.1
-.2
-.3
-.4

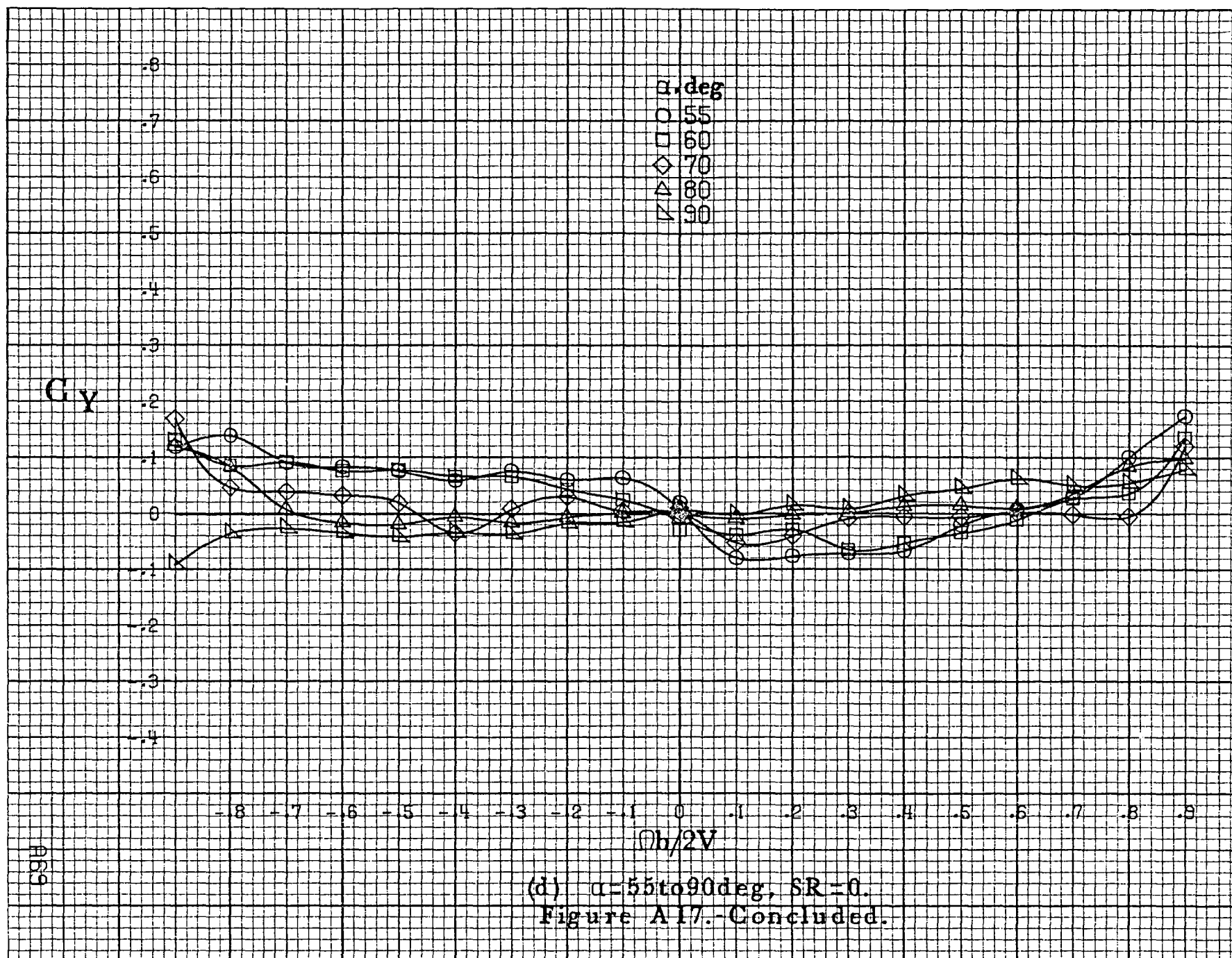
-.8 -.7 -.6 -.5 -.4 -.3 -.2 -.1 0 .1 .2 .3 .4 .5 .6 .7 .8 .9

$Ob/2V$

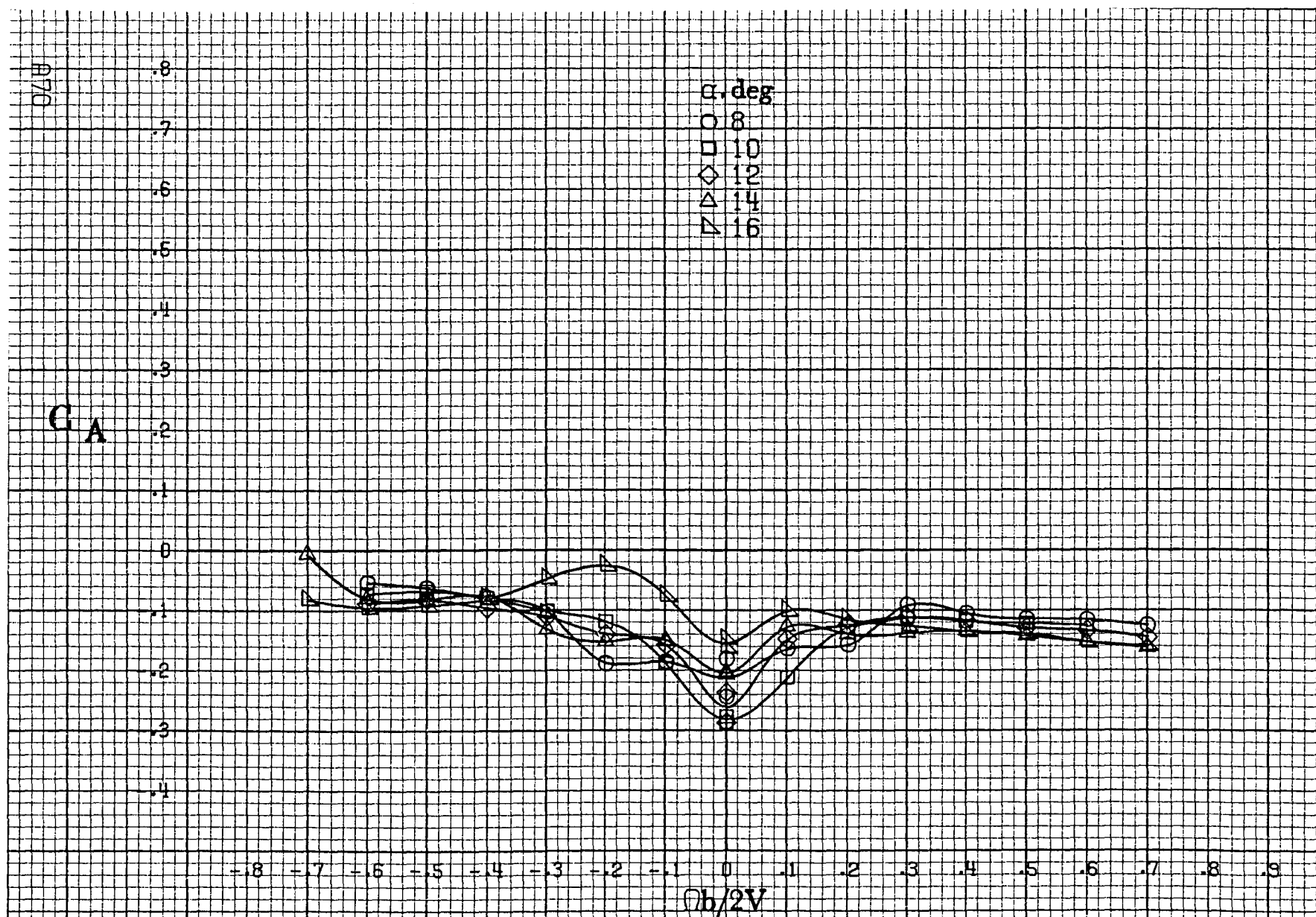
(c) $\alpha=30\text{to}50\text{deg}$, $SR=0$.

Figure A17.-Continued.



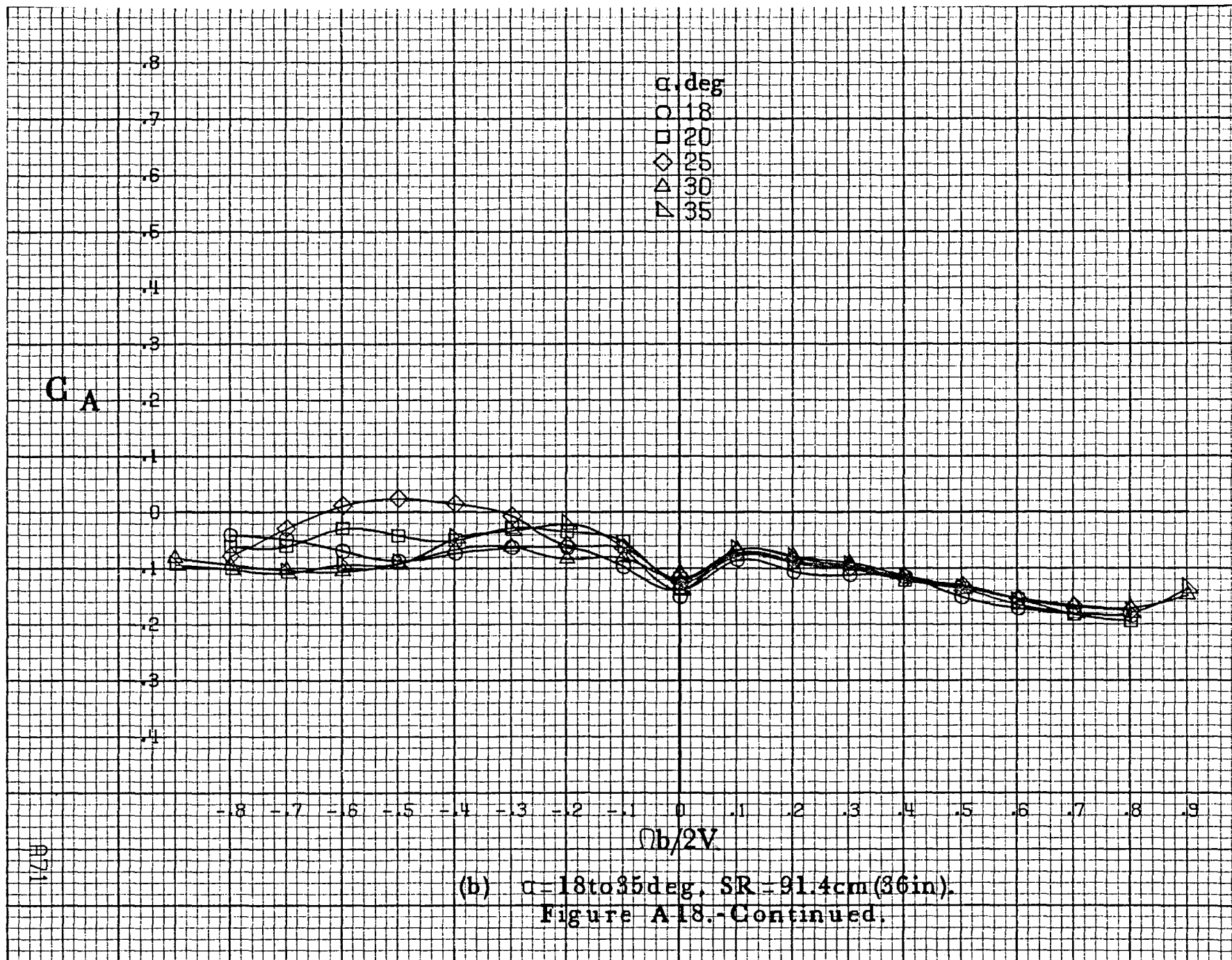


(d) $\alpha=55$ to 90° , $SR=0$.
Figure A17.-Concluded.



(a) $\alpha = 8$ to 16° , $SR = 91.4\text{cm} (36\text{in})$.

Figure A18.-Effect of rotation rate and angle of attack on axial-force coefficient for complete short body, low wing configuration. $\delta_e = 0^\circ$, $\delta_a = 0^\circ$, $\delta_r = 0^\circ$, $\beta = 0^\circ$.



C_A α, deg

- 30
- 35
- ◇ 40
- △ 45
- ▽ 50

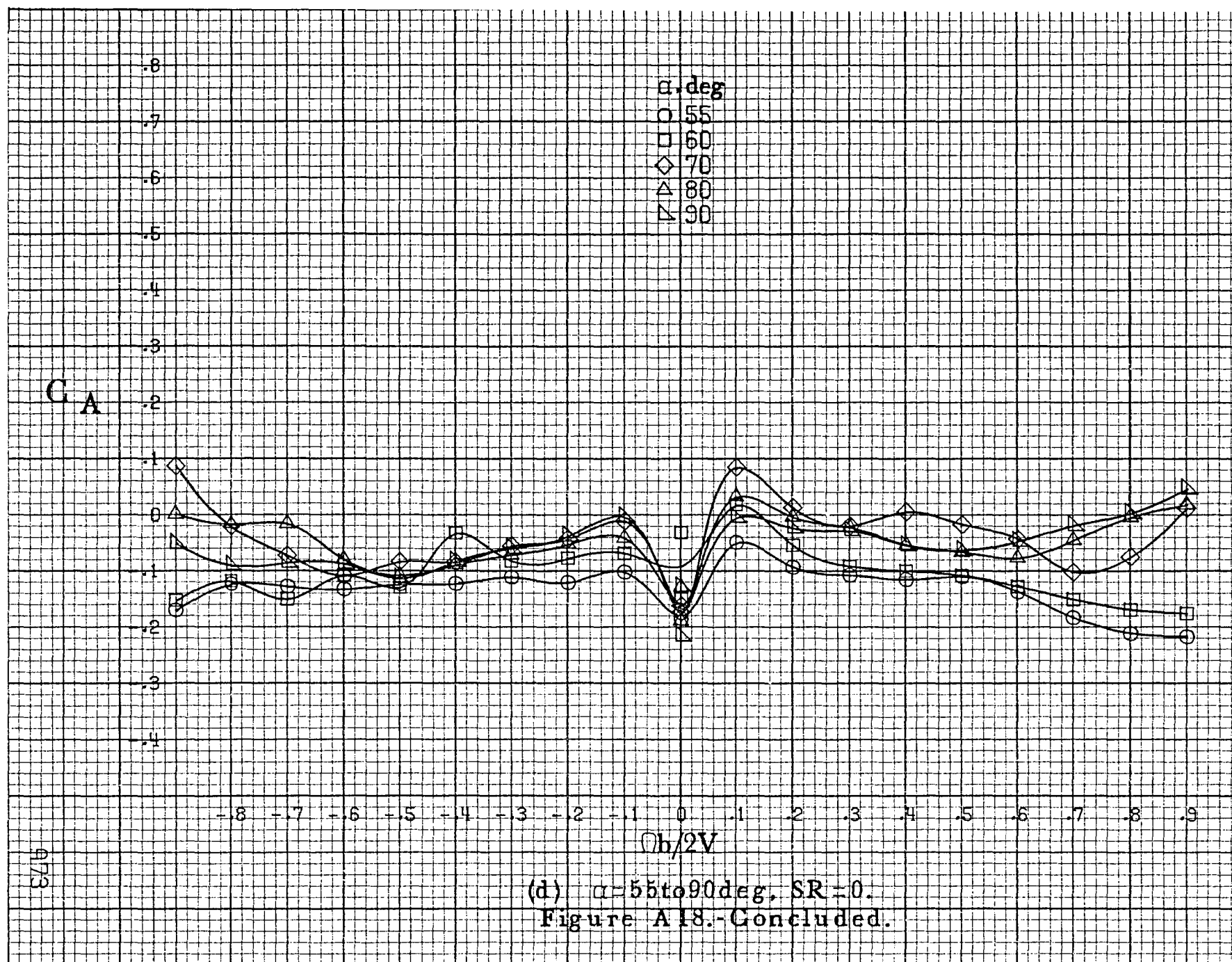
0.8
0.7
0.6
0.5
0.4
0.3
0.2
0.1
0
-0.1
-0.2
-0.3
-0.4

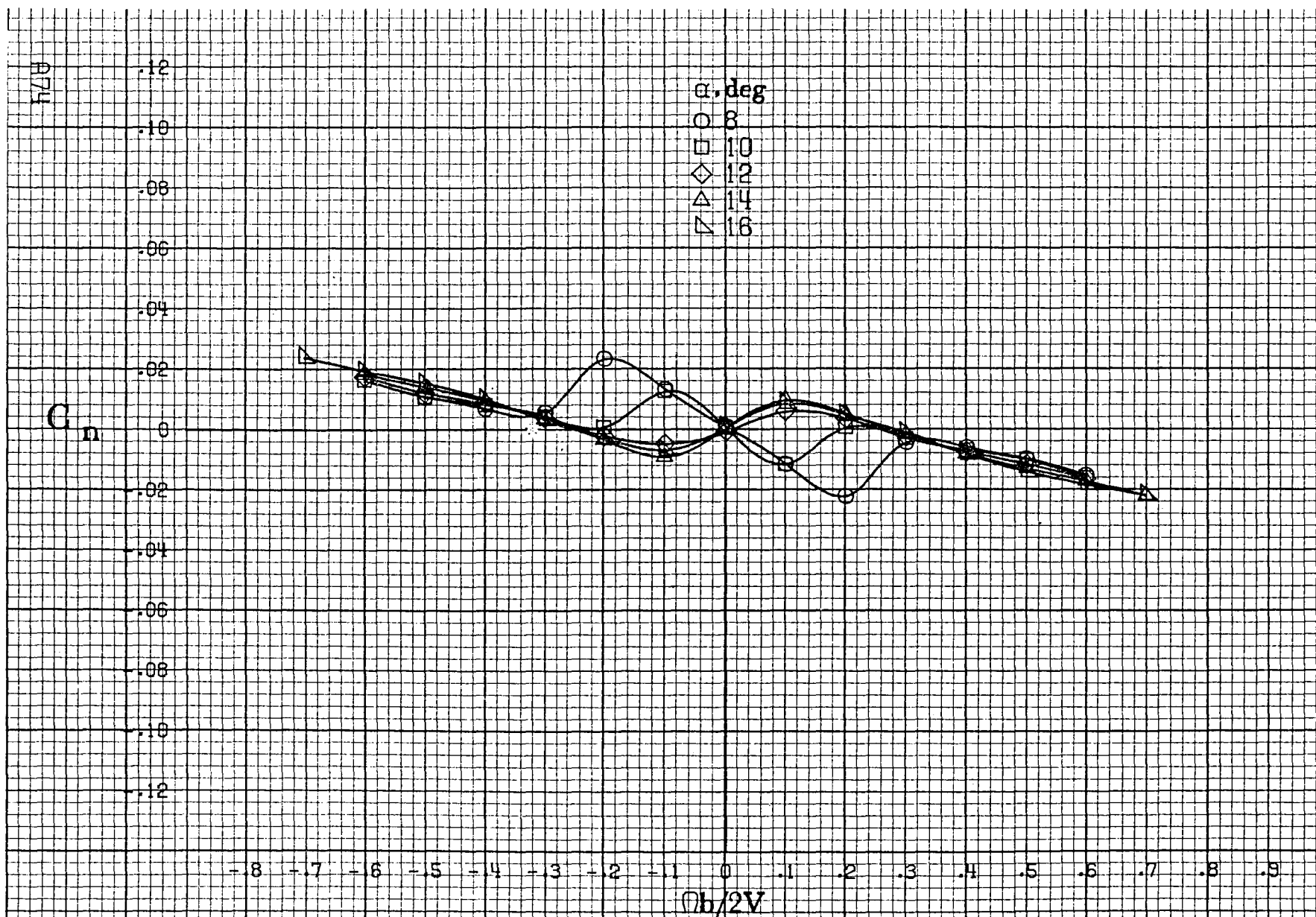
-0.8 -0.7 -0.6 -0.5 -0.4 -0.3 -0.2 -0.1 0 0.1 0.2 0.3 0.4 0.5 0.6 0.7 0.8 0.9

 $Ob/2V$

(c) $\alpha=30$ to 50 deg, $SR=0$.

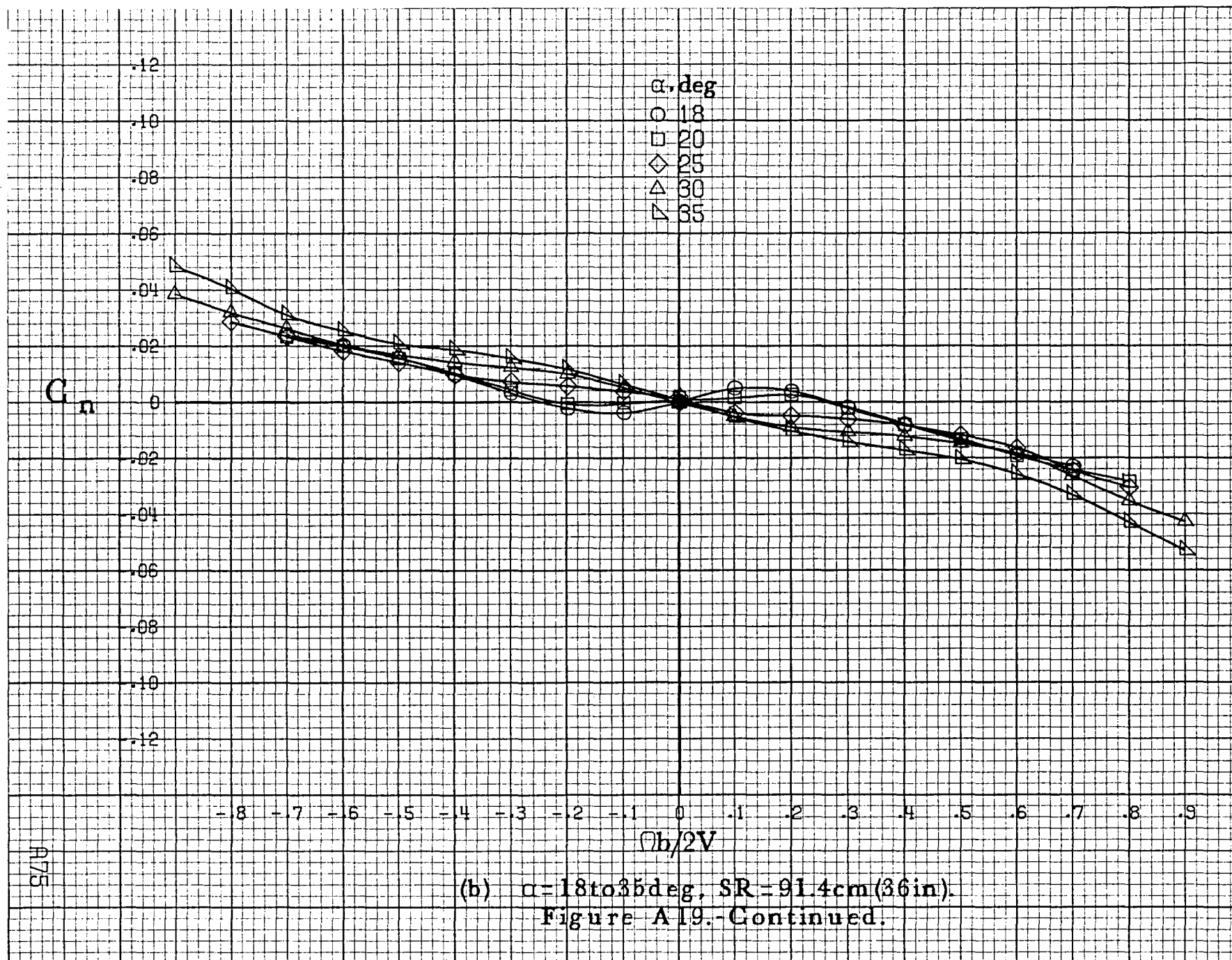
Figure A18.-Continued.

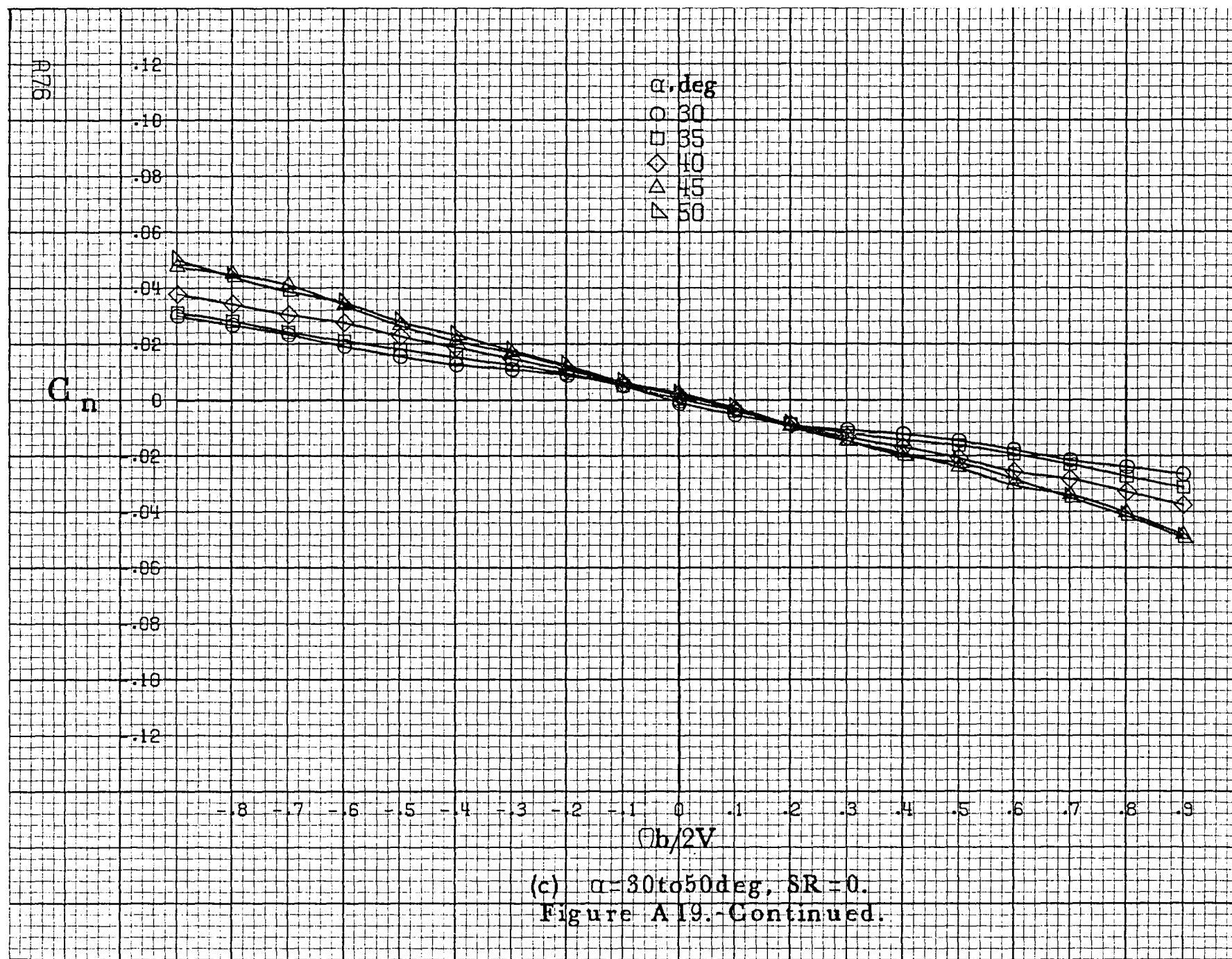


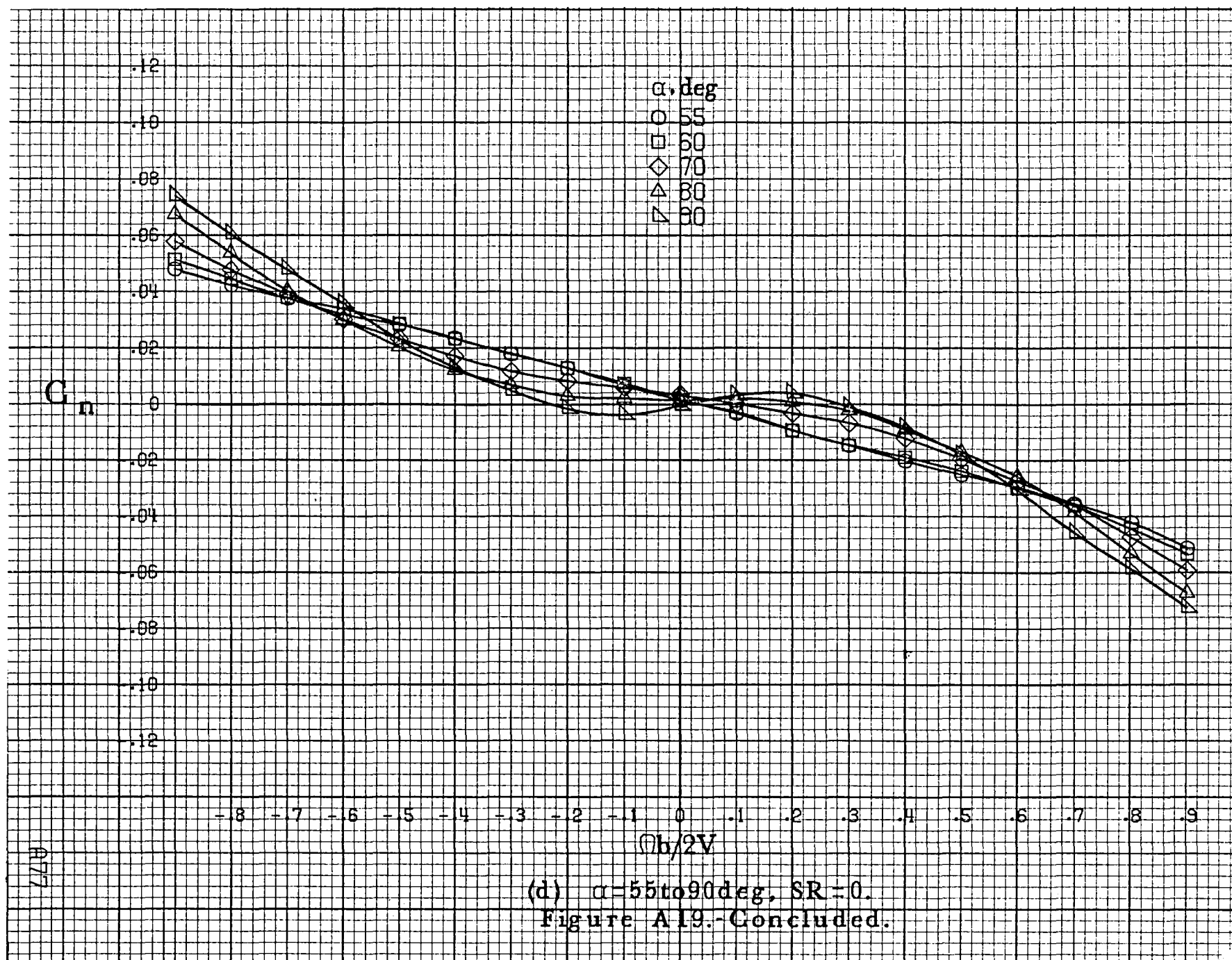


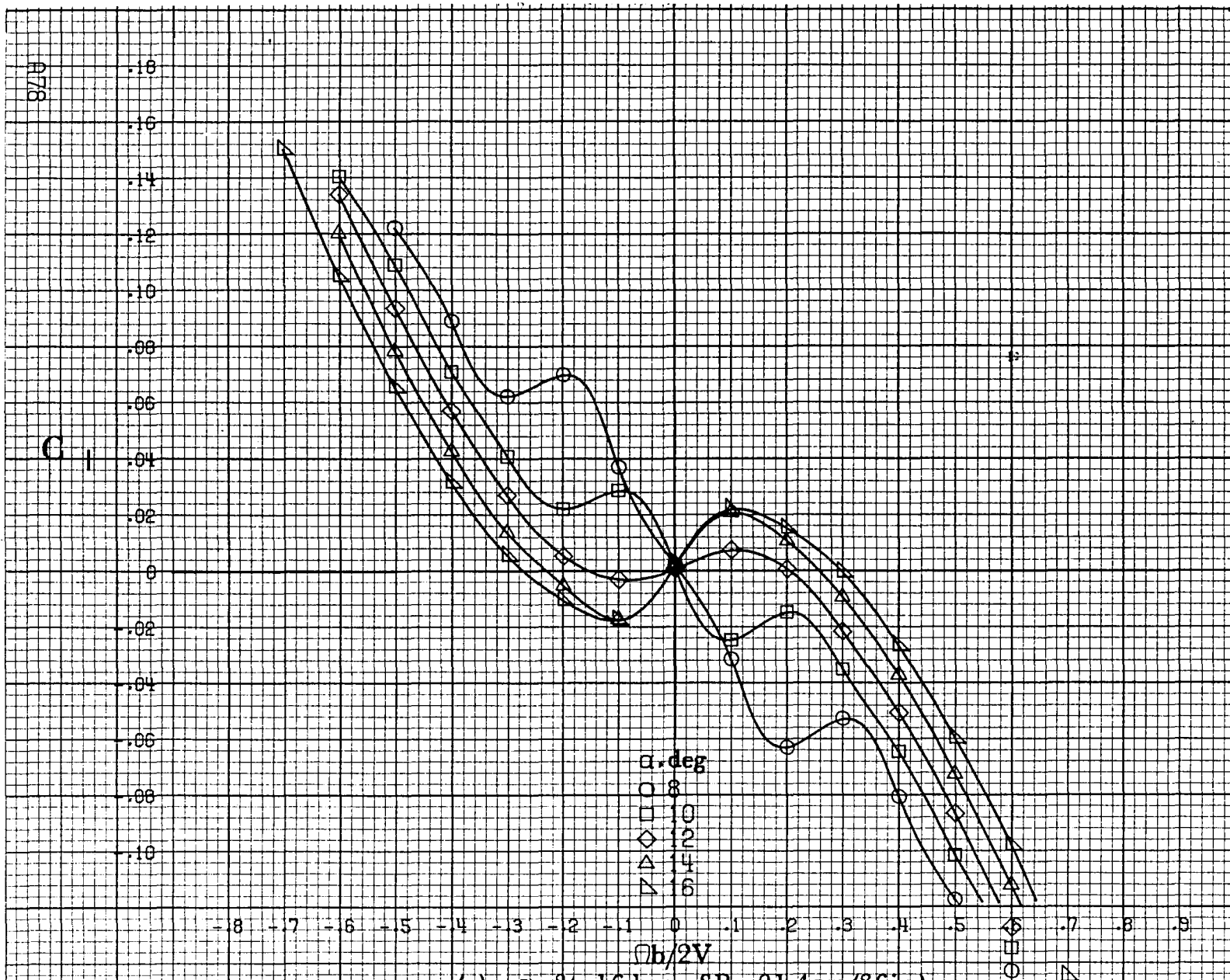
(a) $\alpha = 8$ to 16° , $SR = 91.4 \text{ cm (36 in.)}$.

Figure A19.-Effect of rotation rate and angle of attack on yawing-moment coefficient for short body, high wing, vertical configuration $\delta_e = 0^\circ$, $\delta_a = 0^\circ$, $\delta_r = 0^\circ$, $\beta = 0^\circ$.

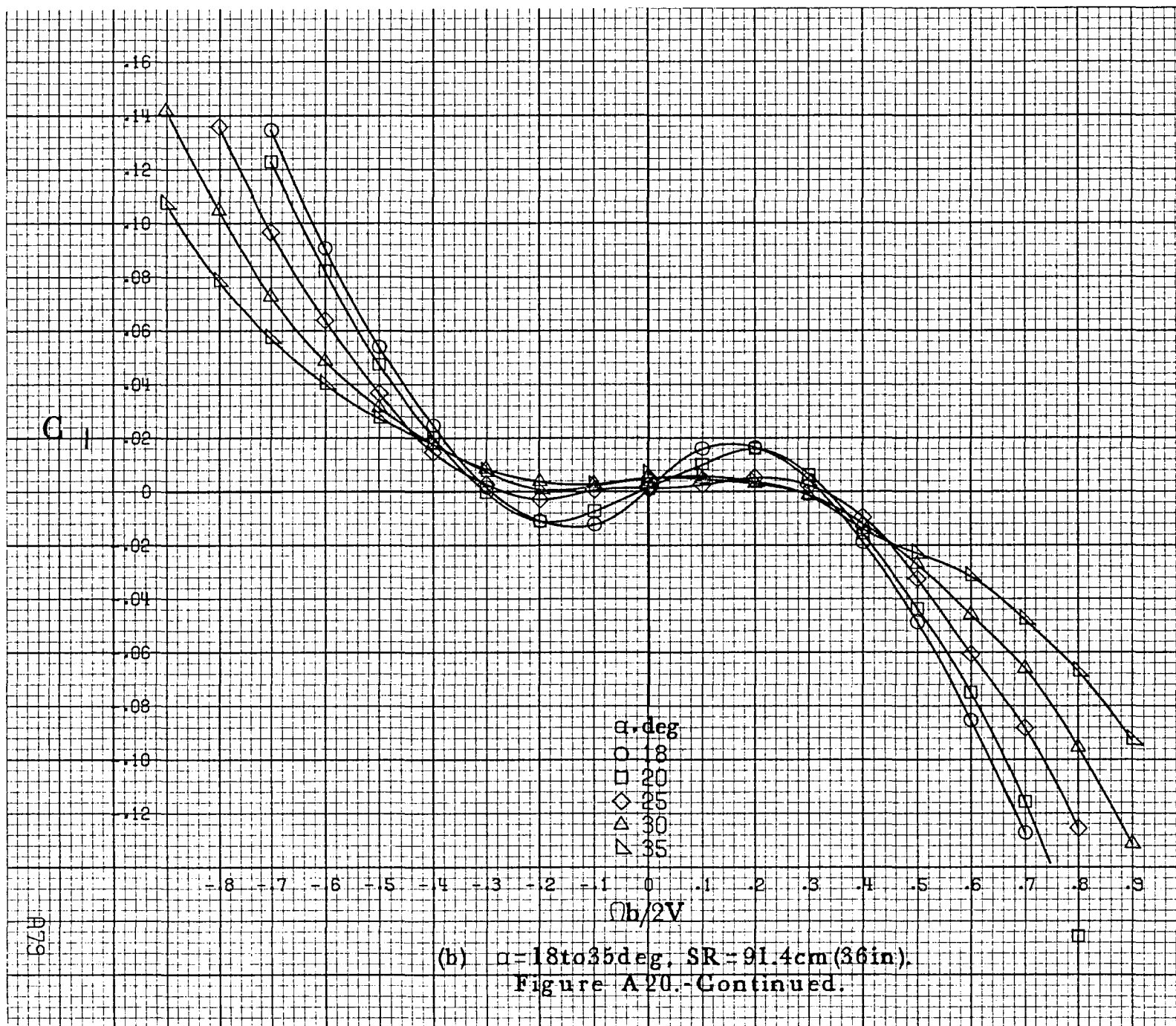


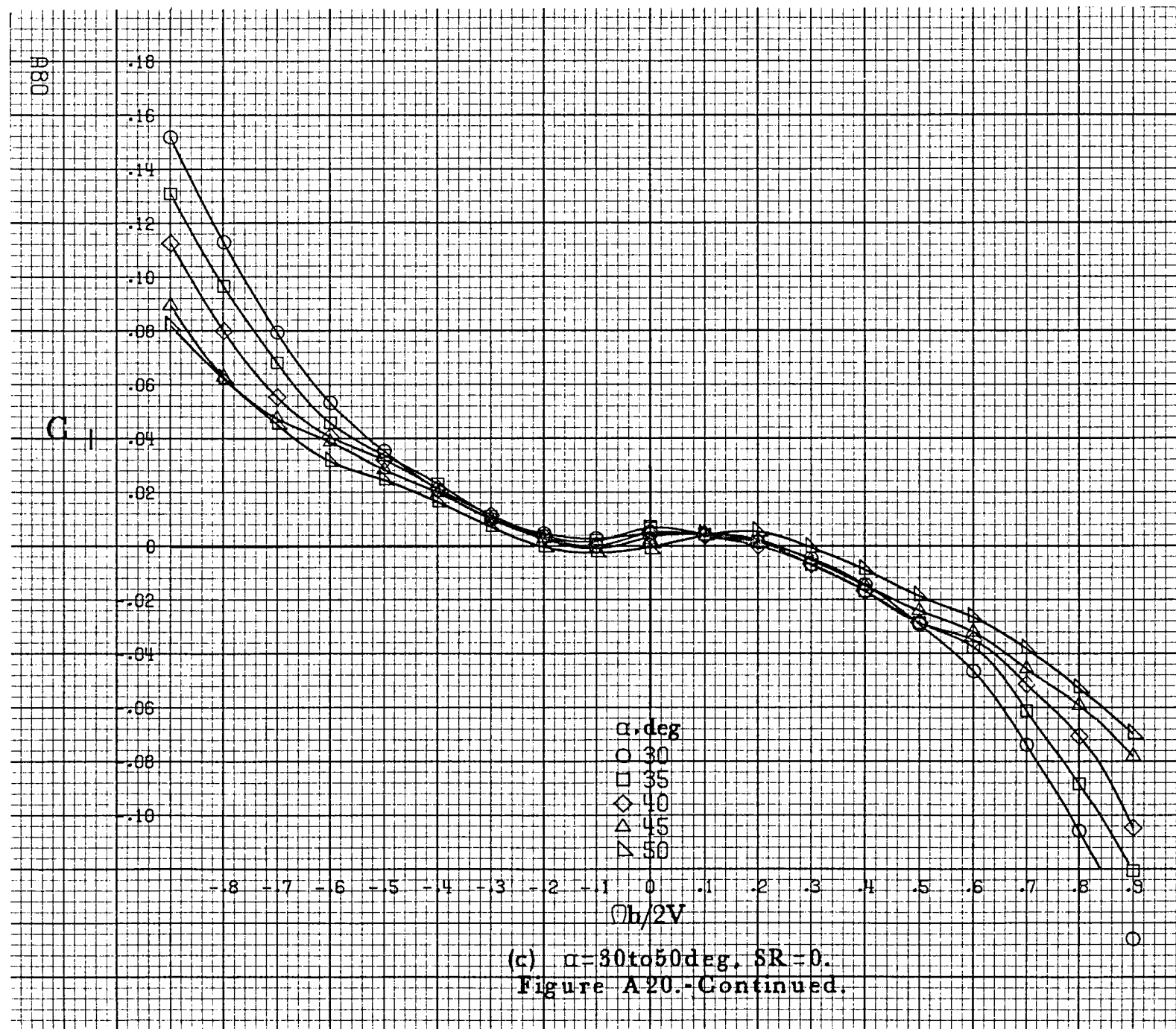


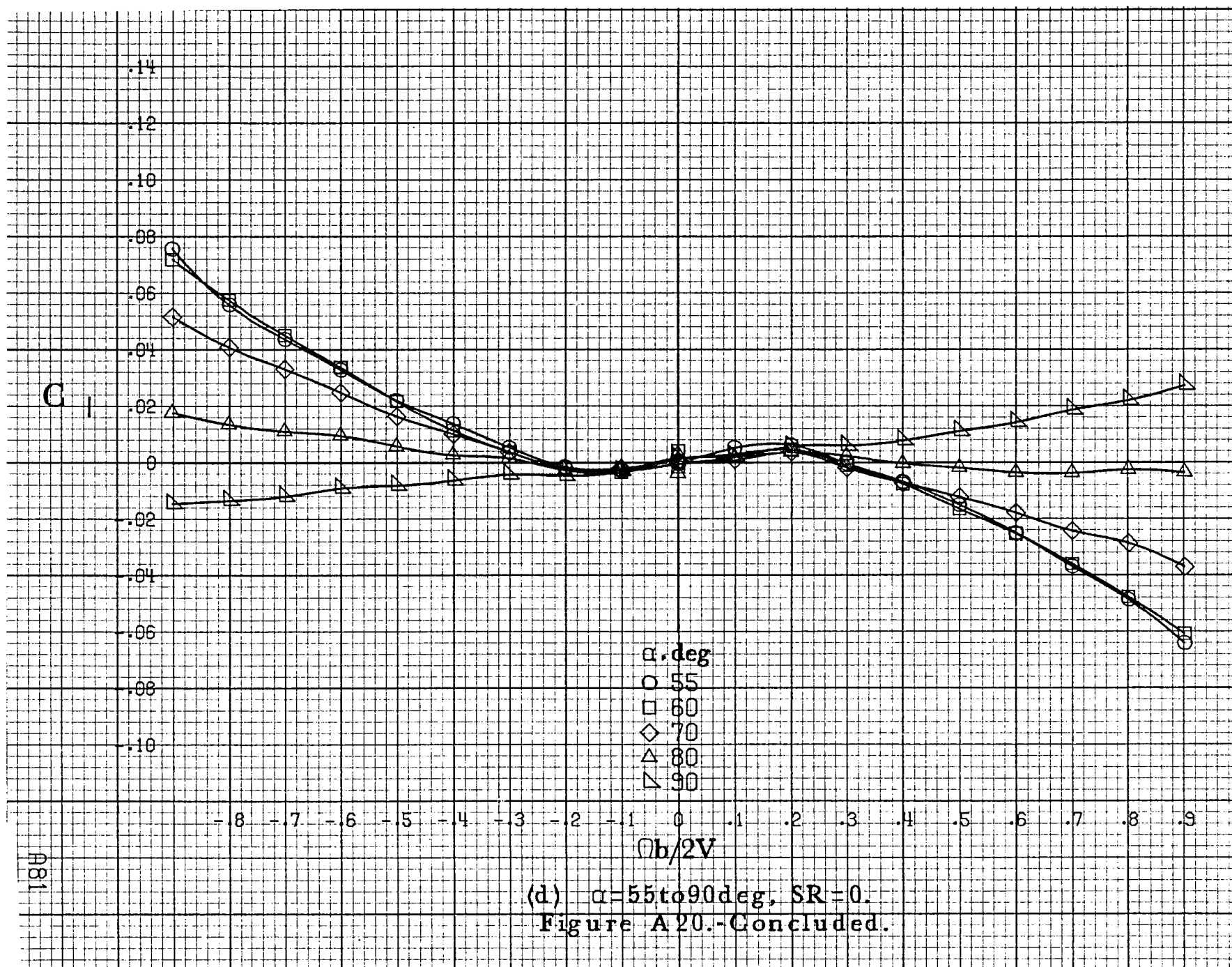


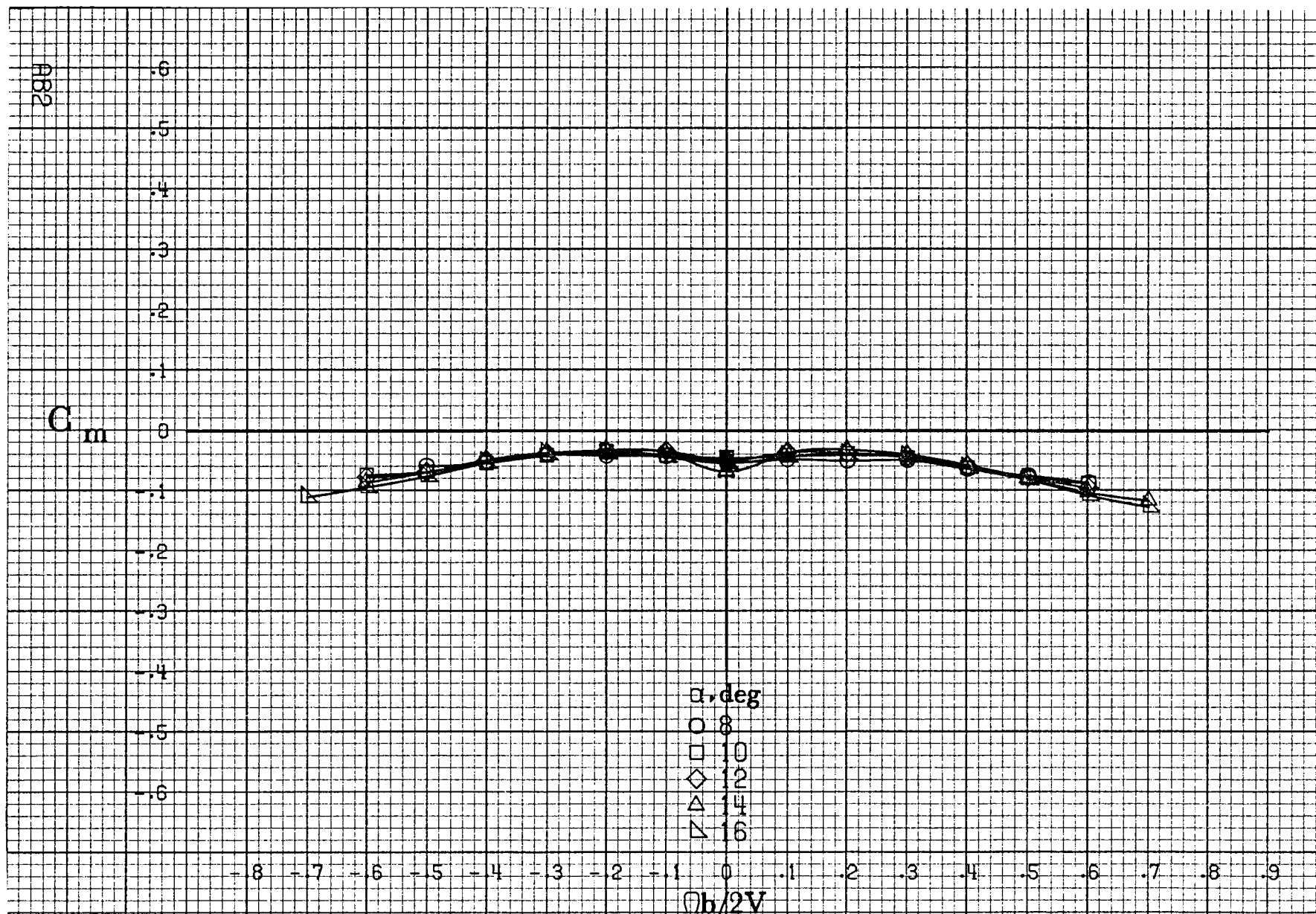


(a) $\alpha = 8$ to 16° , $SR = 91.4\text{cm (36in.)}$.
 Figure A20.-Effect of rotation rate and angle of attack on rolling-moment coefficient for short body, high wing, vertical configuration $\delta_r = 0^\circ$, $\delta_a = 0^\circ$, $\delta_e = 0^\circ$, $\beta = 0^\circ$.



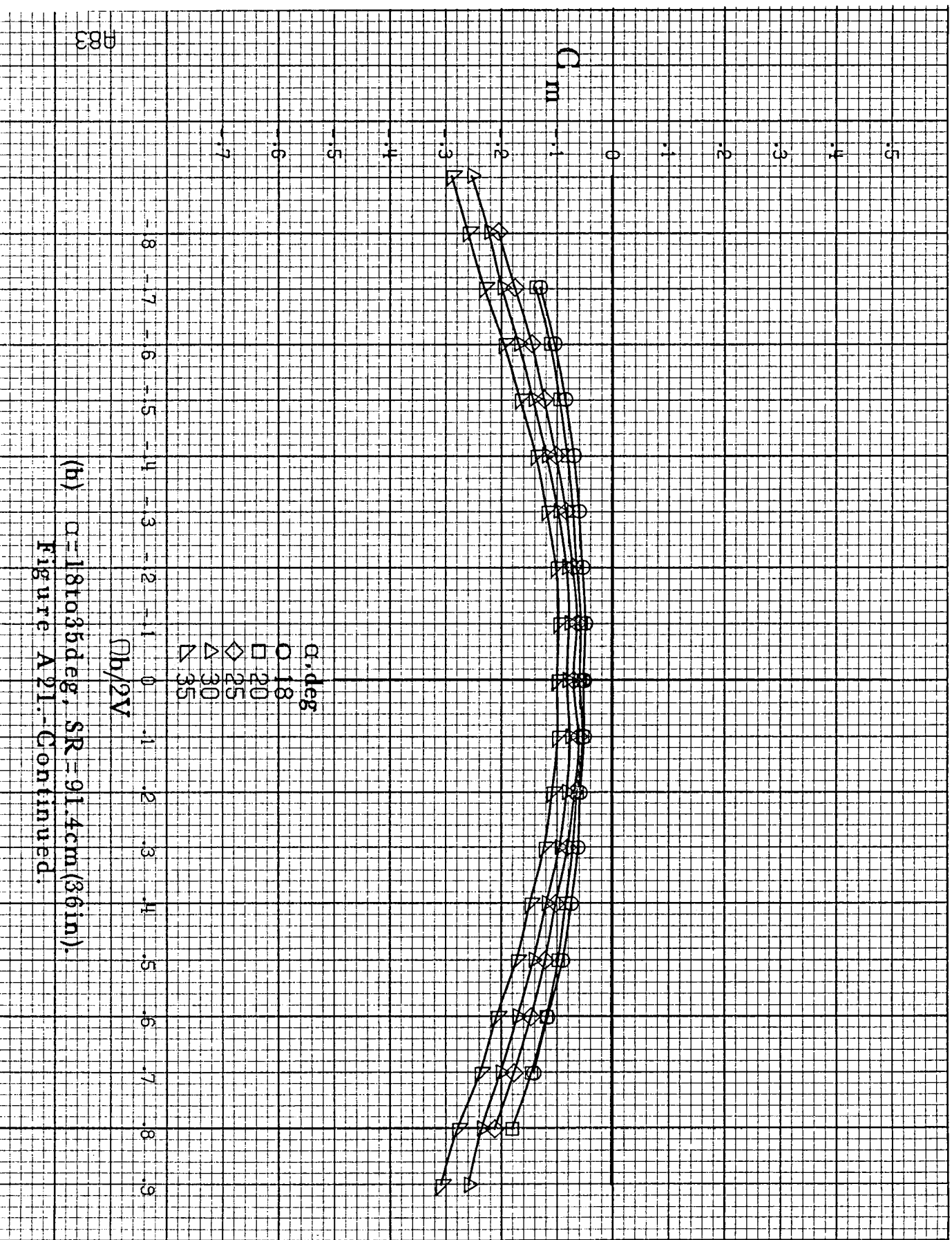






(a) $\alpha=8\text{ to }16^\circ$, $SR=91.4\text{cm}(36\text{in})$.

Figure A21.-Effect of rotation rate and angle of attack on pitching-moment coefficient for short body, high wing, vertical configuration. $\delta_e=0^\circ$, $\delta_a=0^\circ$, $\delta_r=0^\circ$, $\beta=0^\circ$.



(b) $\alpha=18$ to 35° deg, $SR=91.4\text{cm}(36\text{in})$.
 Figure A21. Continued.

884

C_m

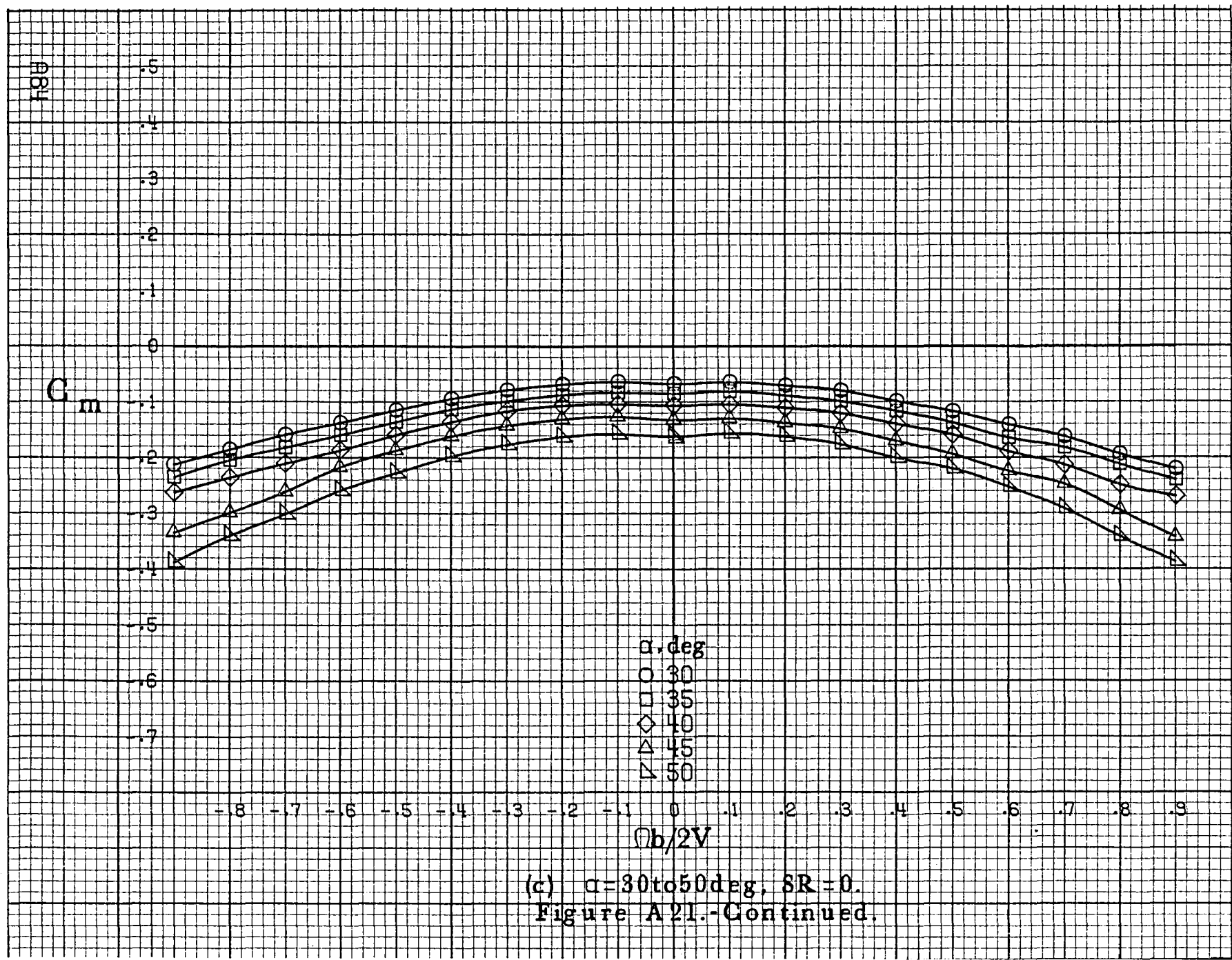
0.5
0.4
0.3
0.2
0.1
0
-0.1
-0.2
-0.3
-0.4
-0.5
-0.6
-0.7

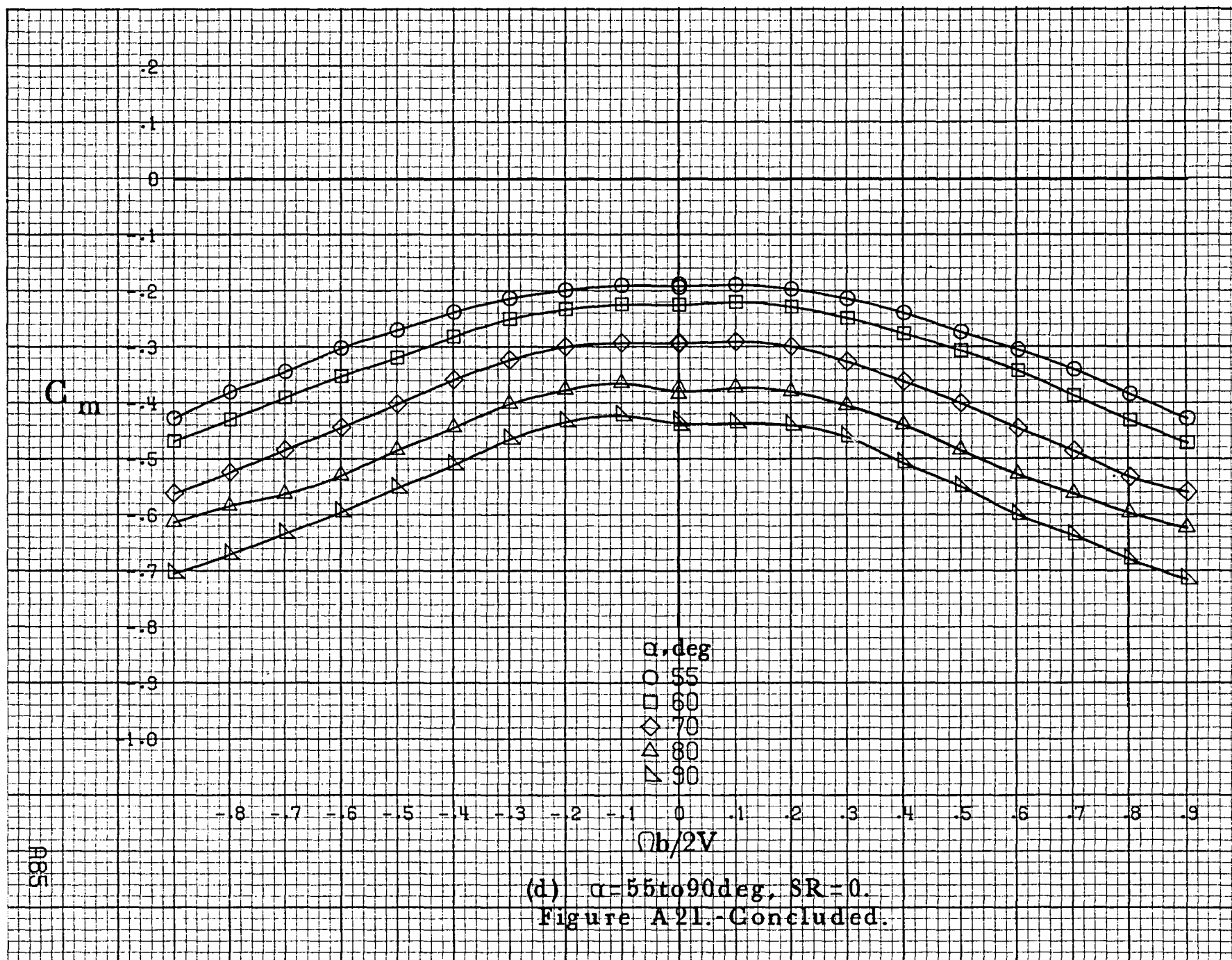
-0.8 -0.7 -0.6 -0.5 -0.4 -0.3 -0.2 -0.1 0 0.1 0.2 0.3 0.4 0.5 0.6 0.7 0.8 0.9

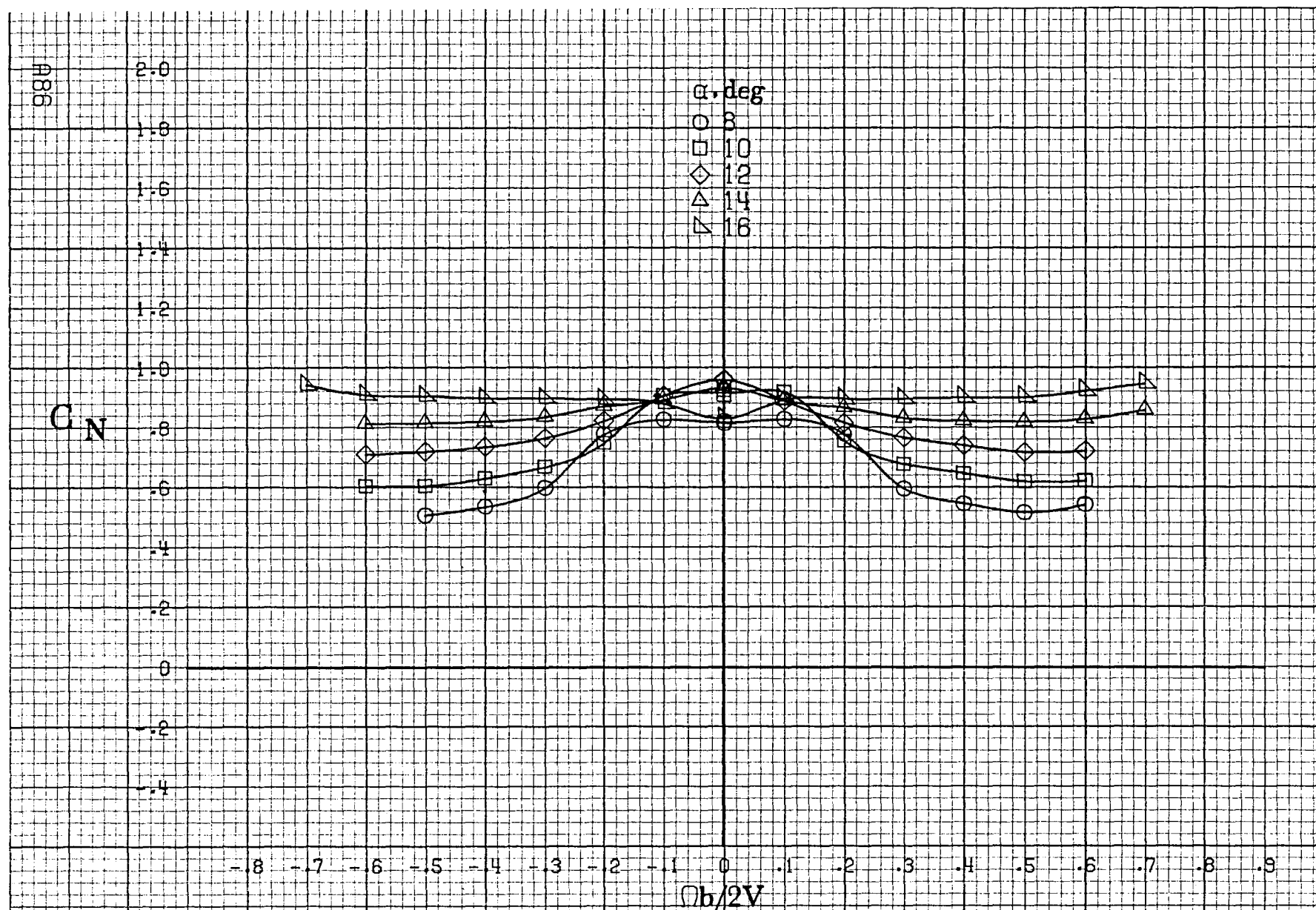
α, deg
 O 30
 □ 35
 ◇ 40
 △ 45
 ▽ 50

$Ob/2V$

(c) $\alpha=30\text{to}50\text{deg}$, $SR=0$.
 Figure A21.-Continued.

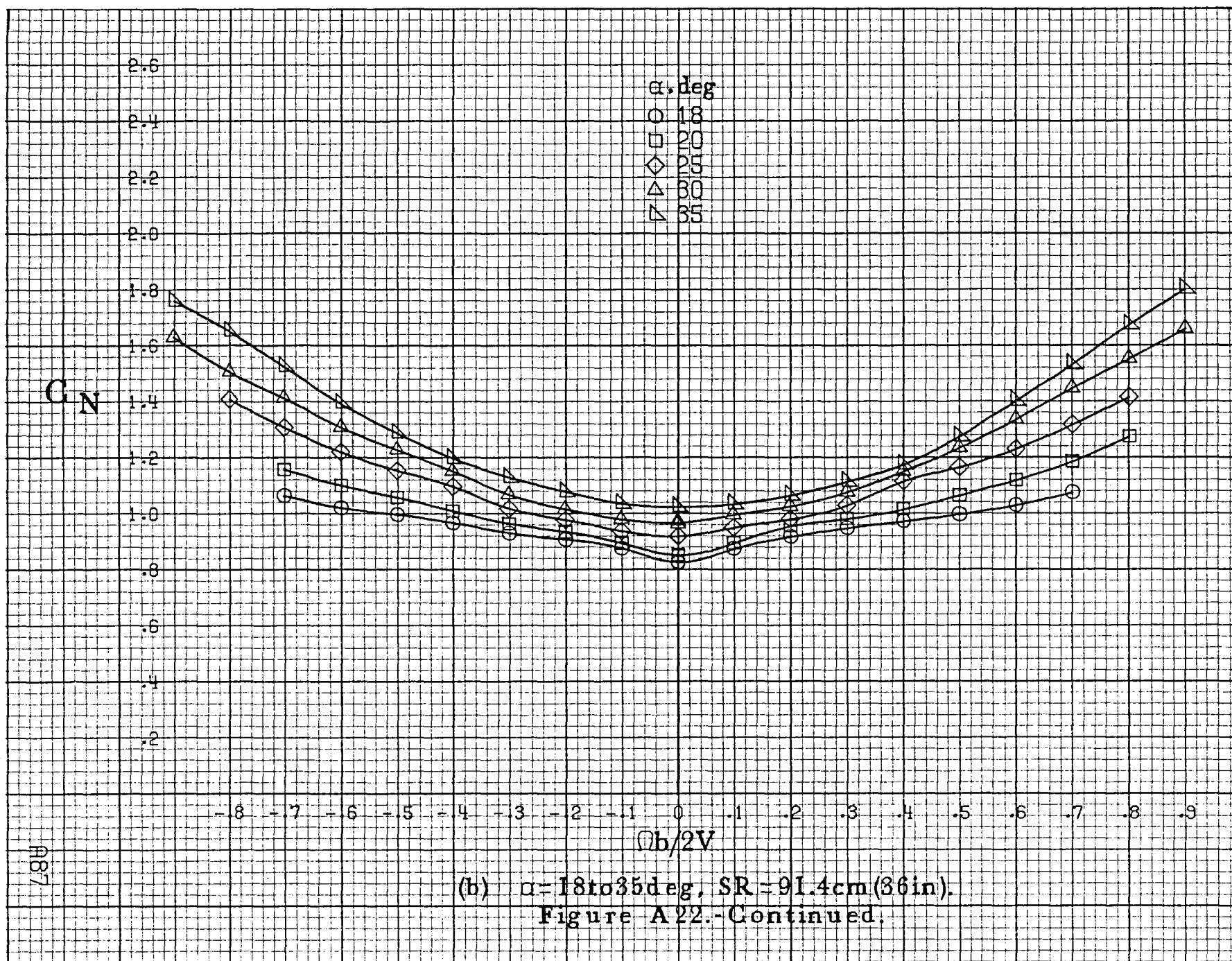


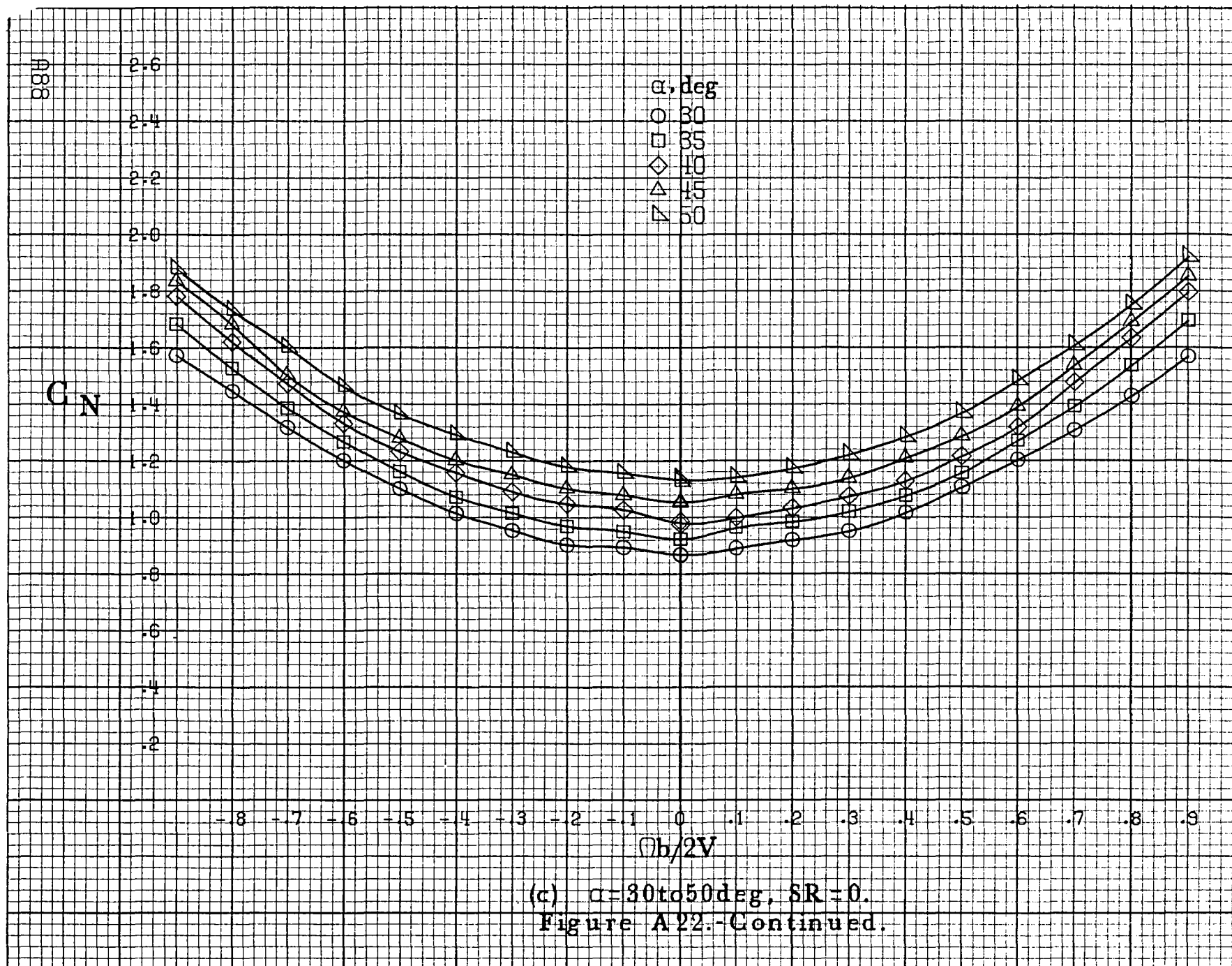


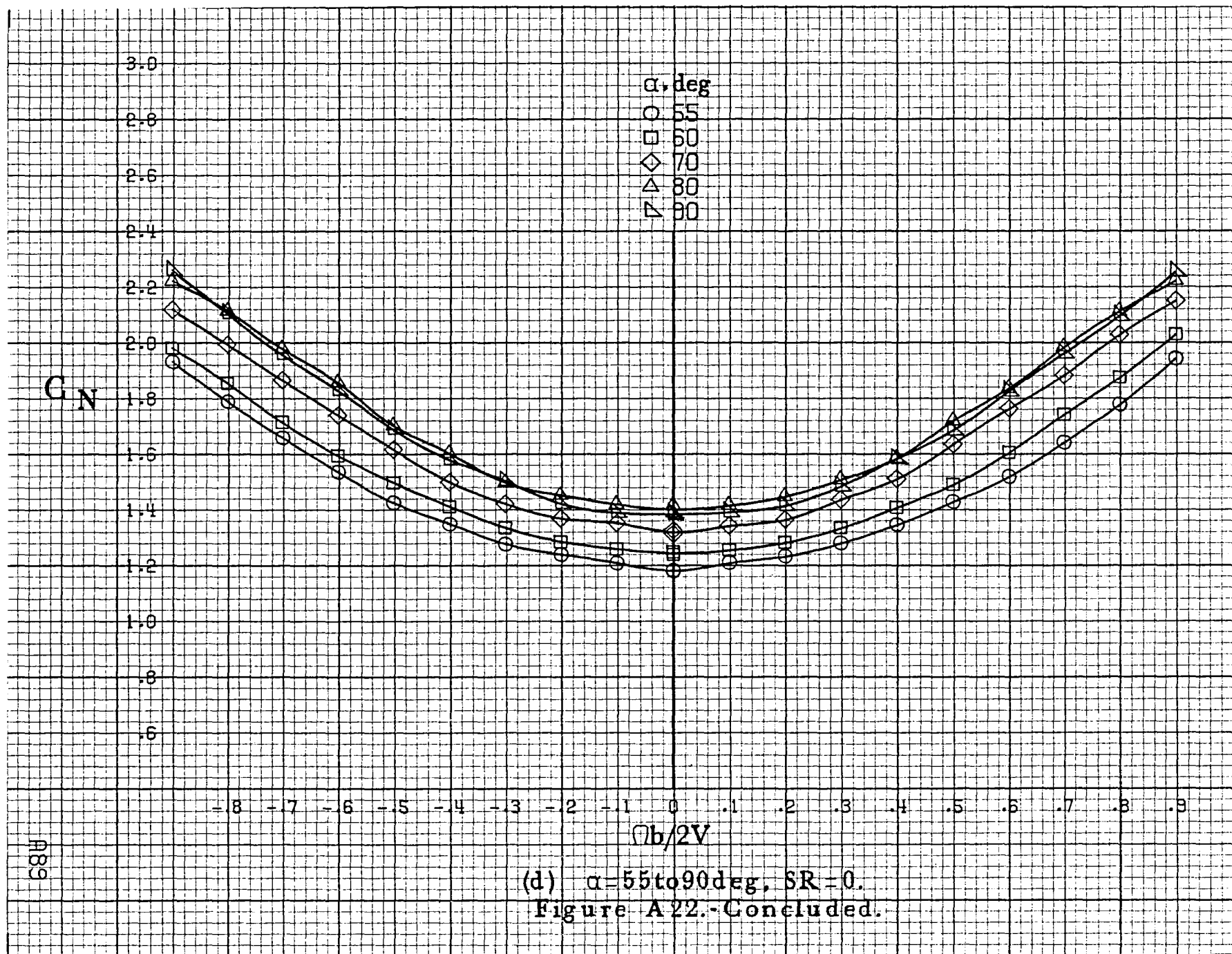


(a) $\alpha=8$ to 16° , $SR=91.4\text{cm}(36\text{in})$.

Figure A22 - Effect of rotation rate and angle of attack on normal-force coefficient for short body, high wing, vertical configuration $\delta_e=0^\circ$, $\delta_a=0^\circ$, $\delta_r=0^\circ$, $\beta=0^\circ$.







0.6B

C_y

α , deg
 O 8
 □ 10
 ◇ 12
 △ 14
 ▽ 16

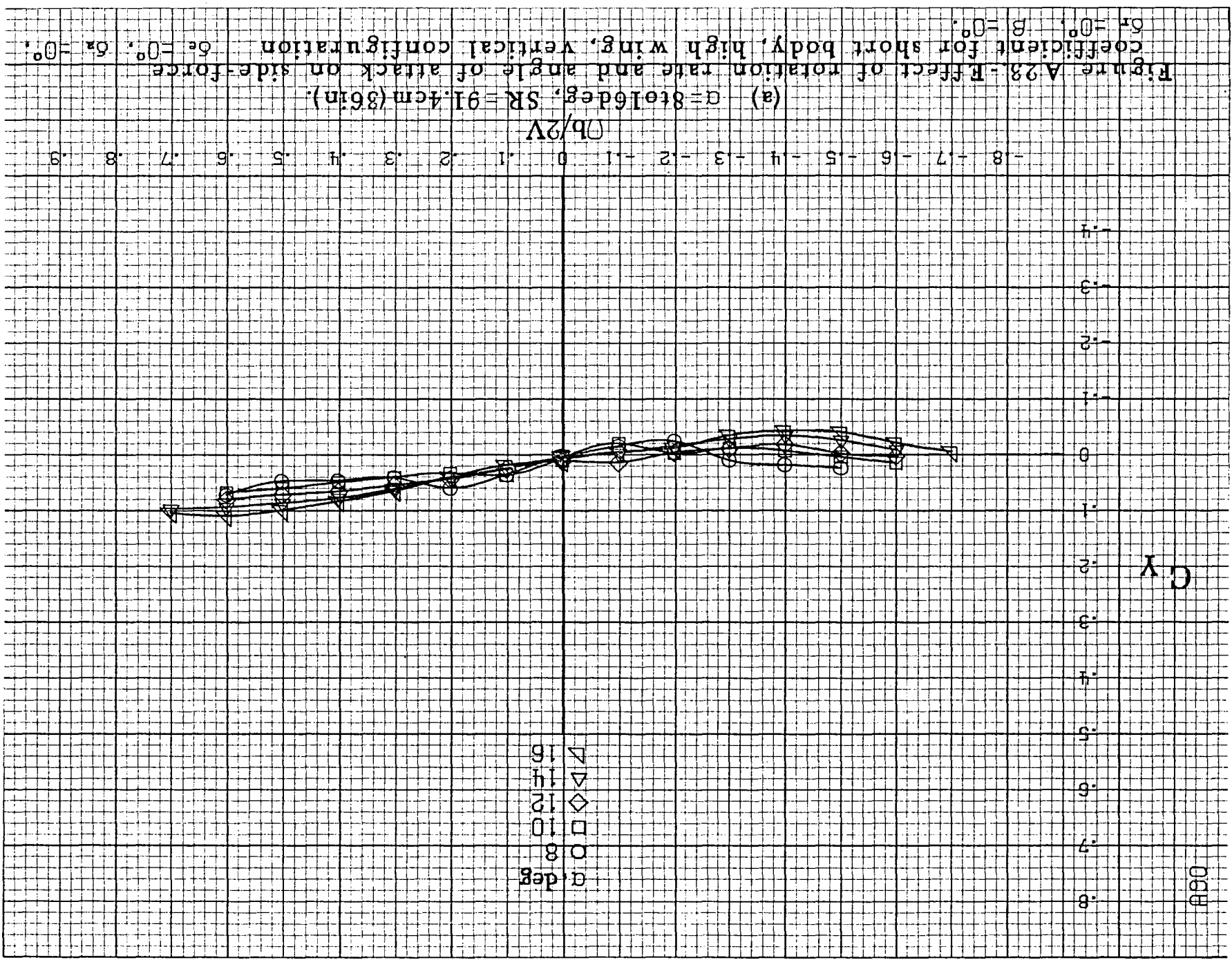
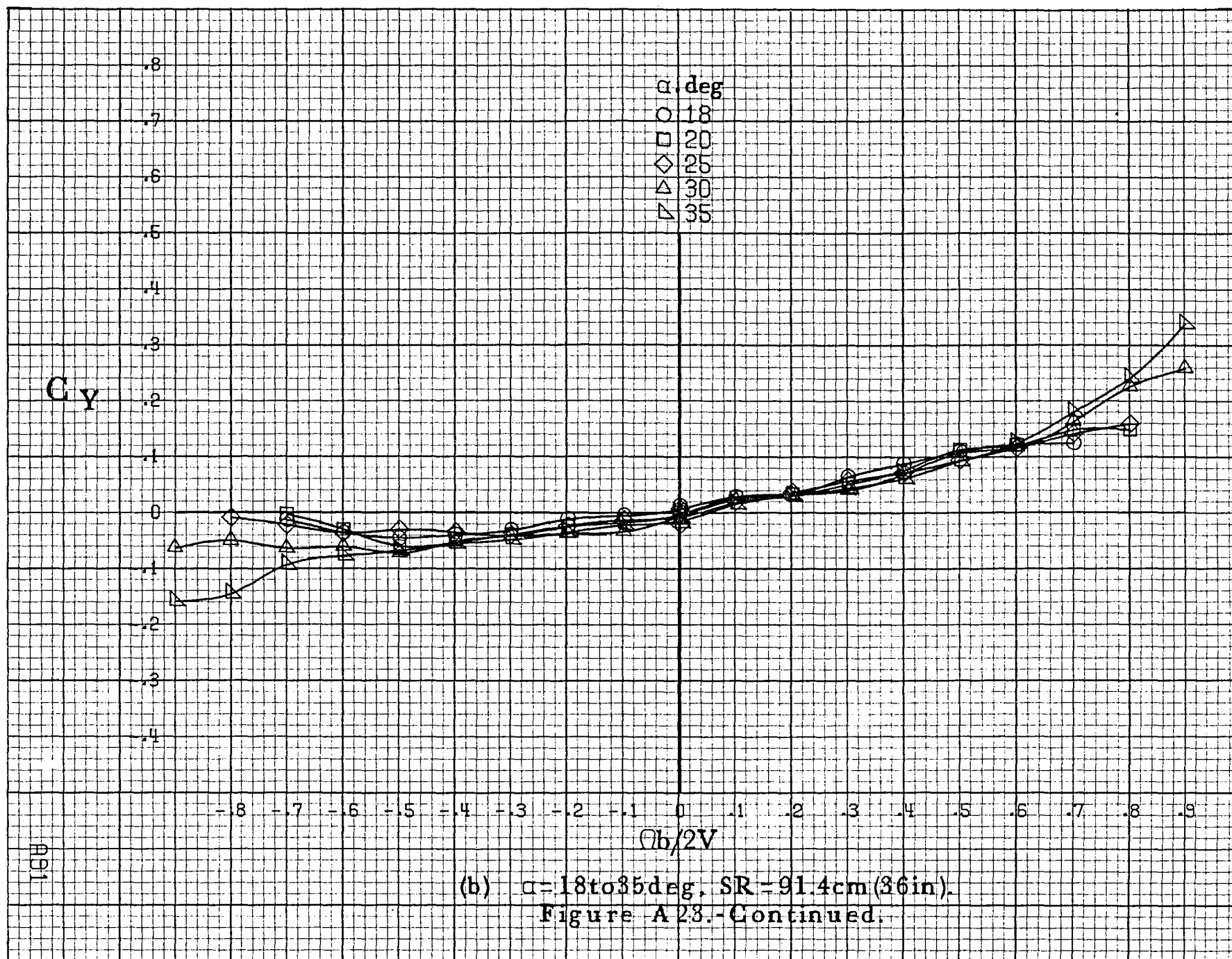
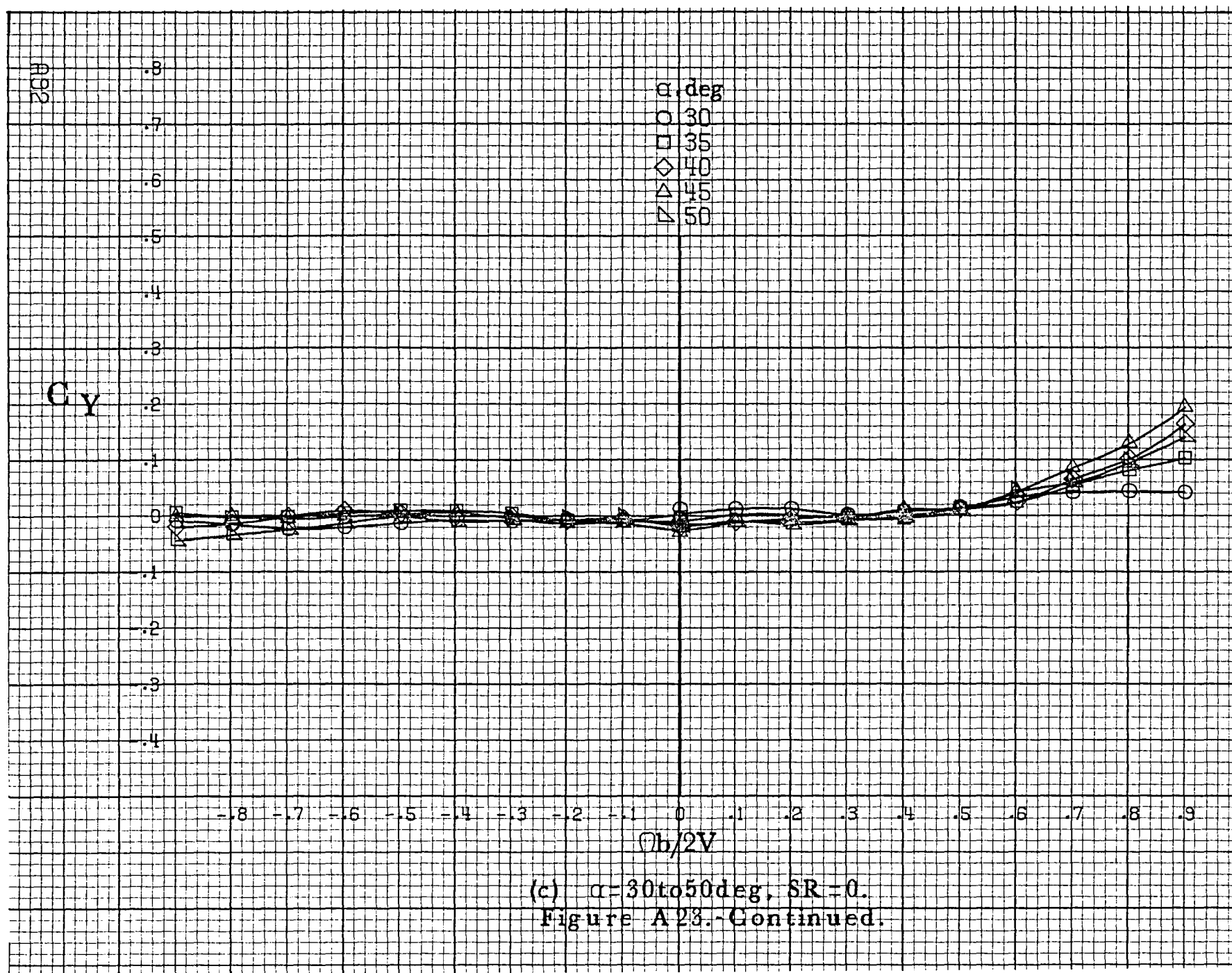
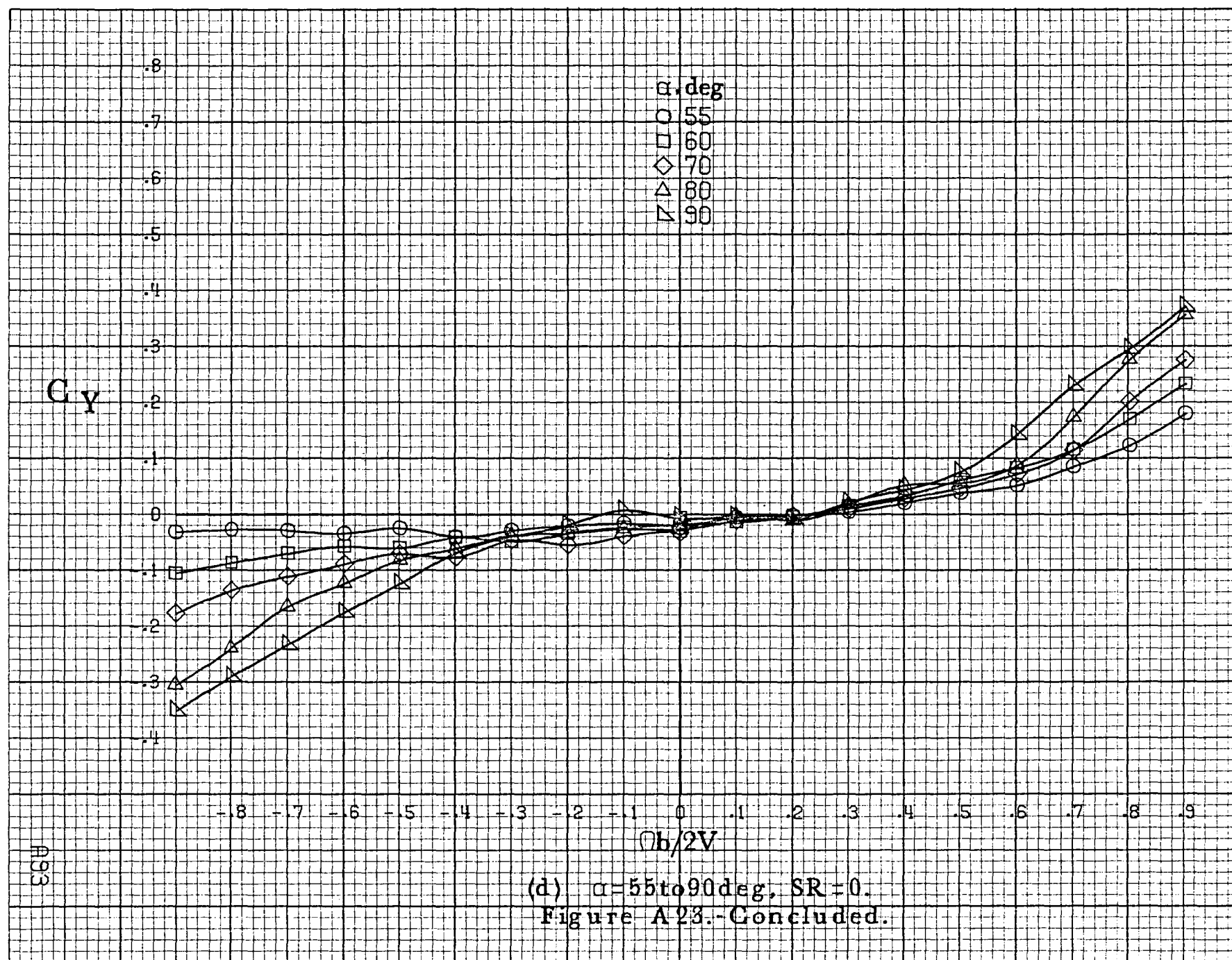


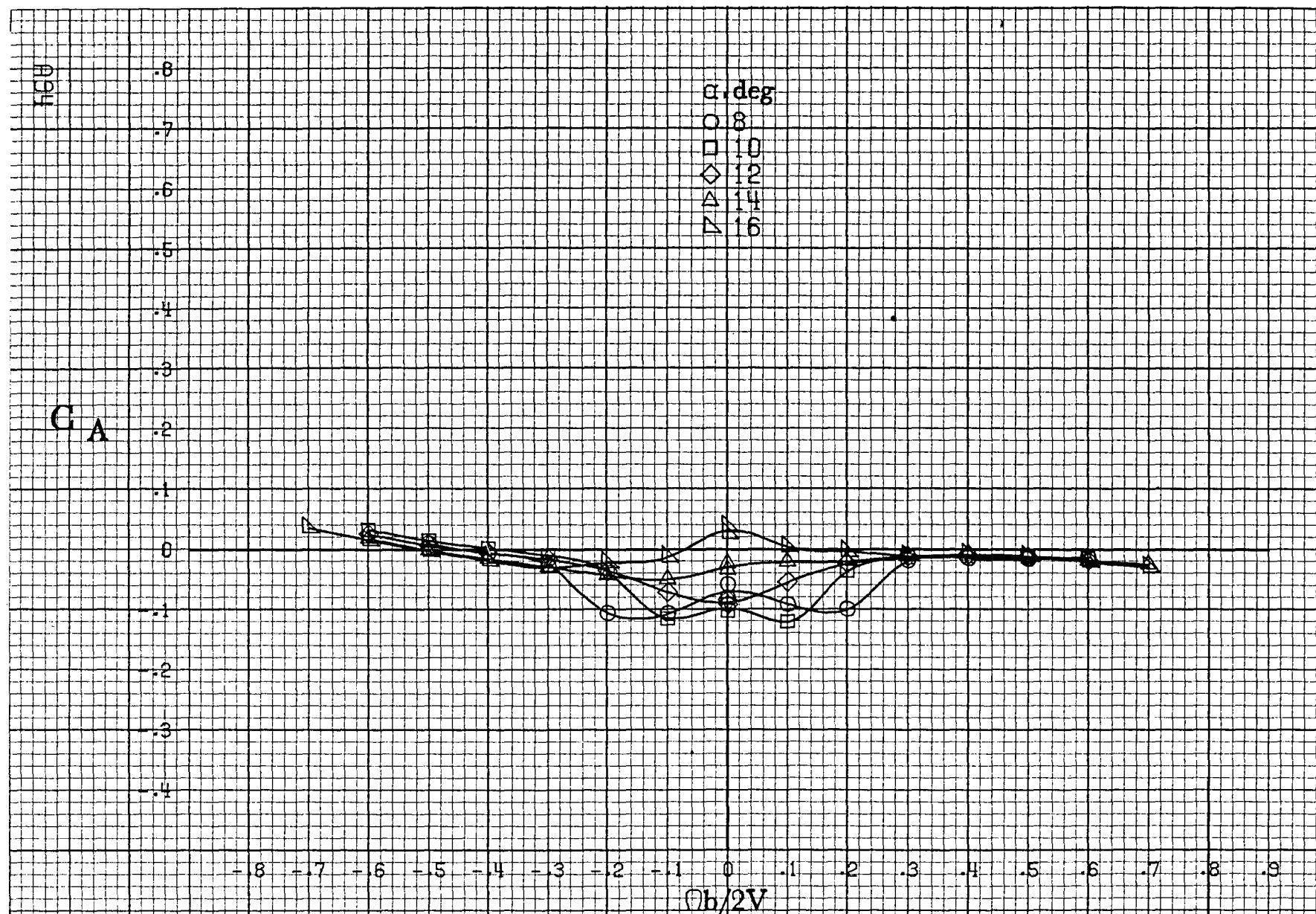
Figure A-23 - Effect of rotation rate and angle of attack on side-force coefficient for short body, high wing, vertical configuration $\dot{\alpha}=0^\circ$, $\beta=0^\circ$.
 (a) $\alpha=8$ to 16 deg, $SR=91.4$ cm (36 in).



(b) $\alpha = 18$ to 35° , $SR = 91.4 \text{ cm (36 in.)}$.
Figure A 23.-Continued.

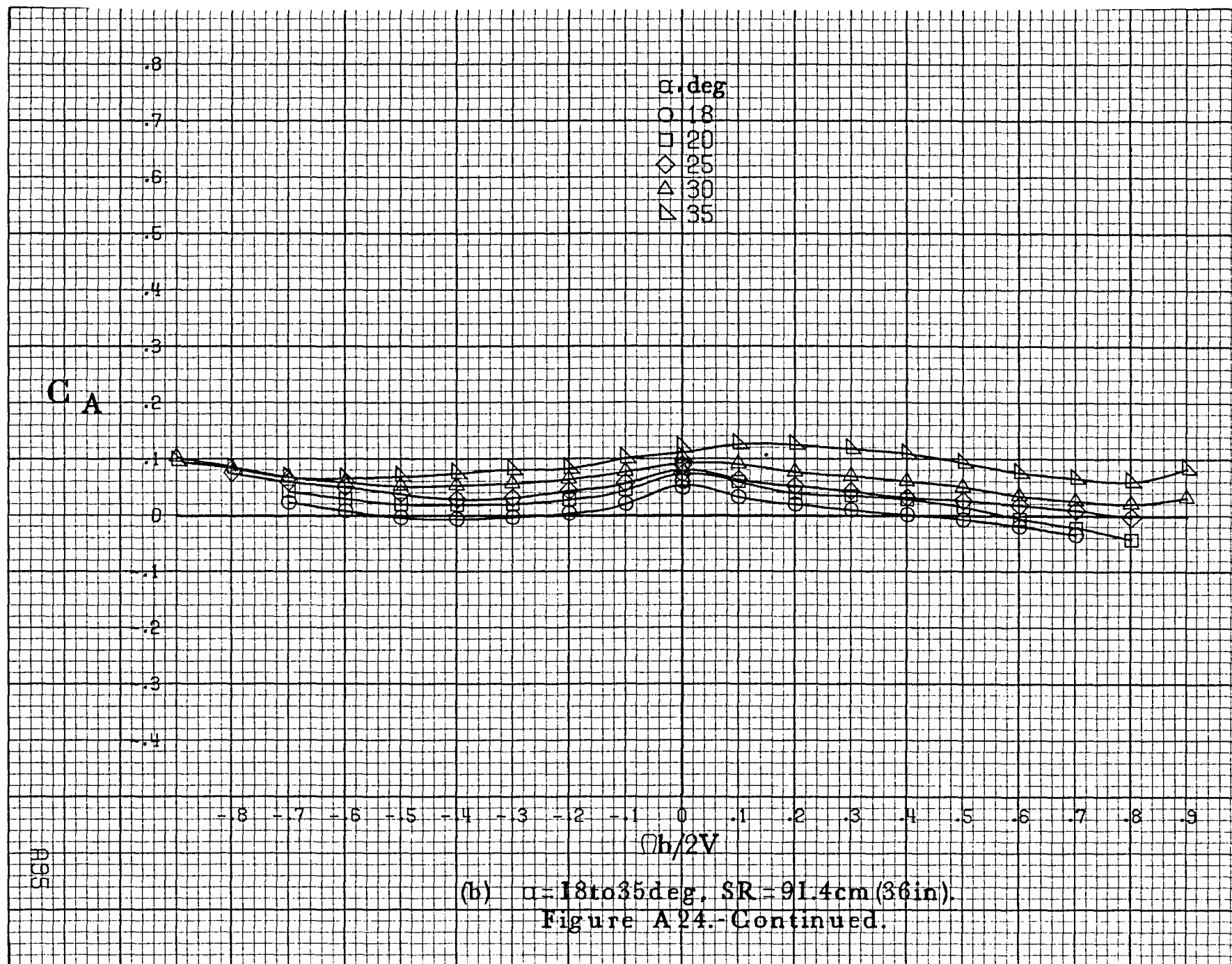


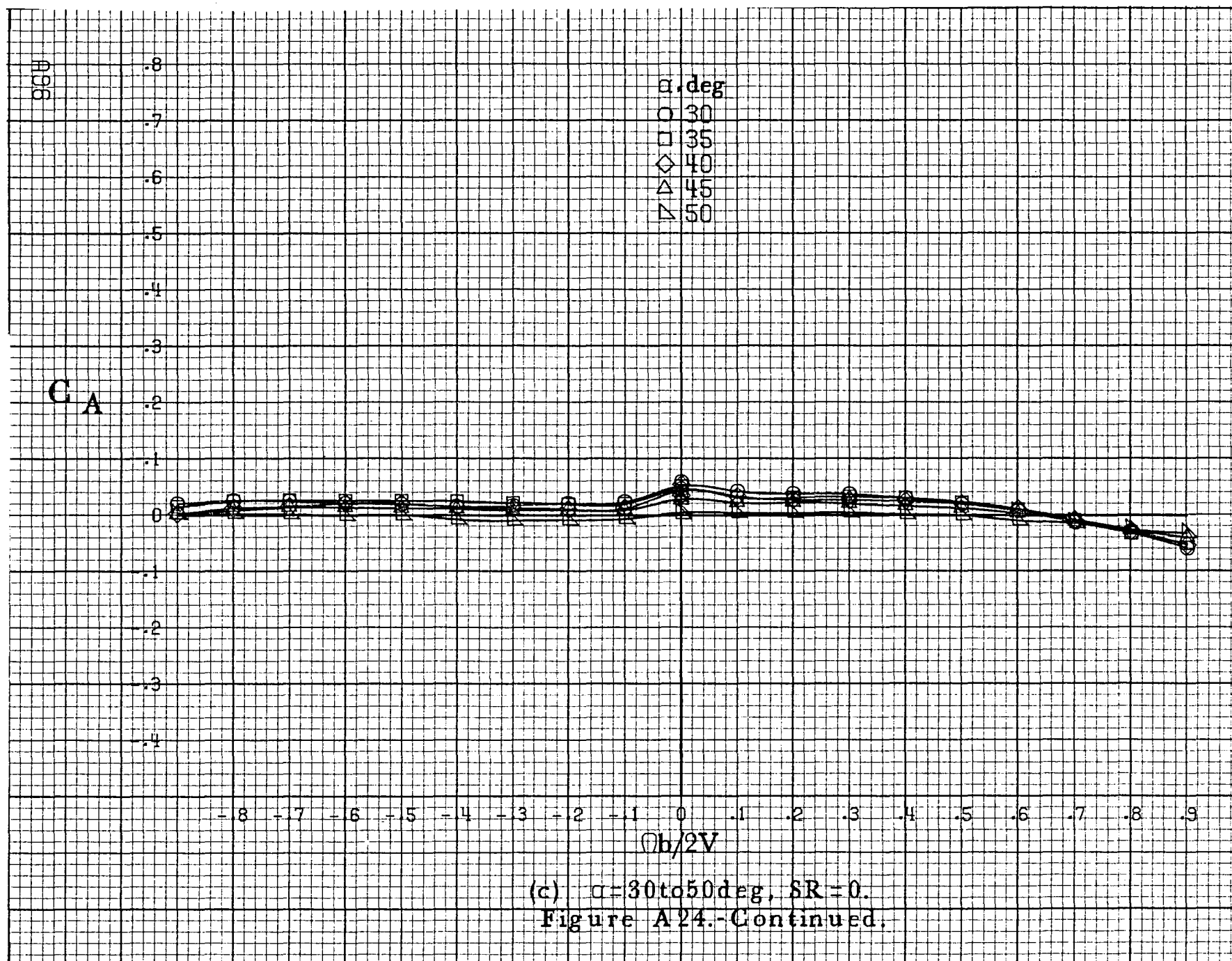




(a) $\alpha = 8$ to 16° , $SR = 91.4 \text{ cm (36 in.)}$.

Figure A24.-Effect of rotation rate and angle of attack on axial-force coefficient for short body, high wing, vertical configuration $\delta_e = 0^\circ$, $\delta_a = 0^\circ$, $\delta_r = 0^\circ$, $\beta = 0^\circ$.





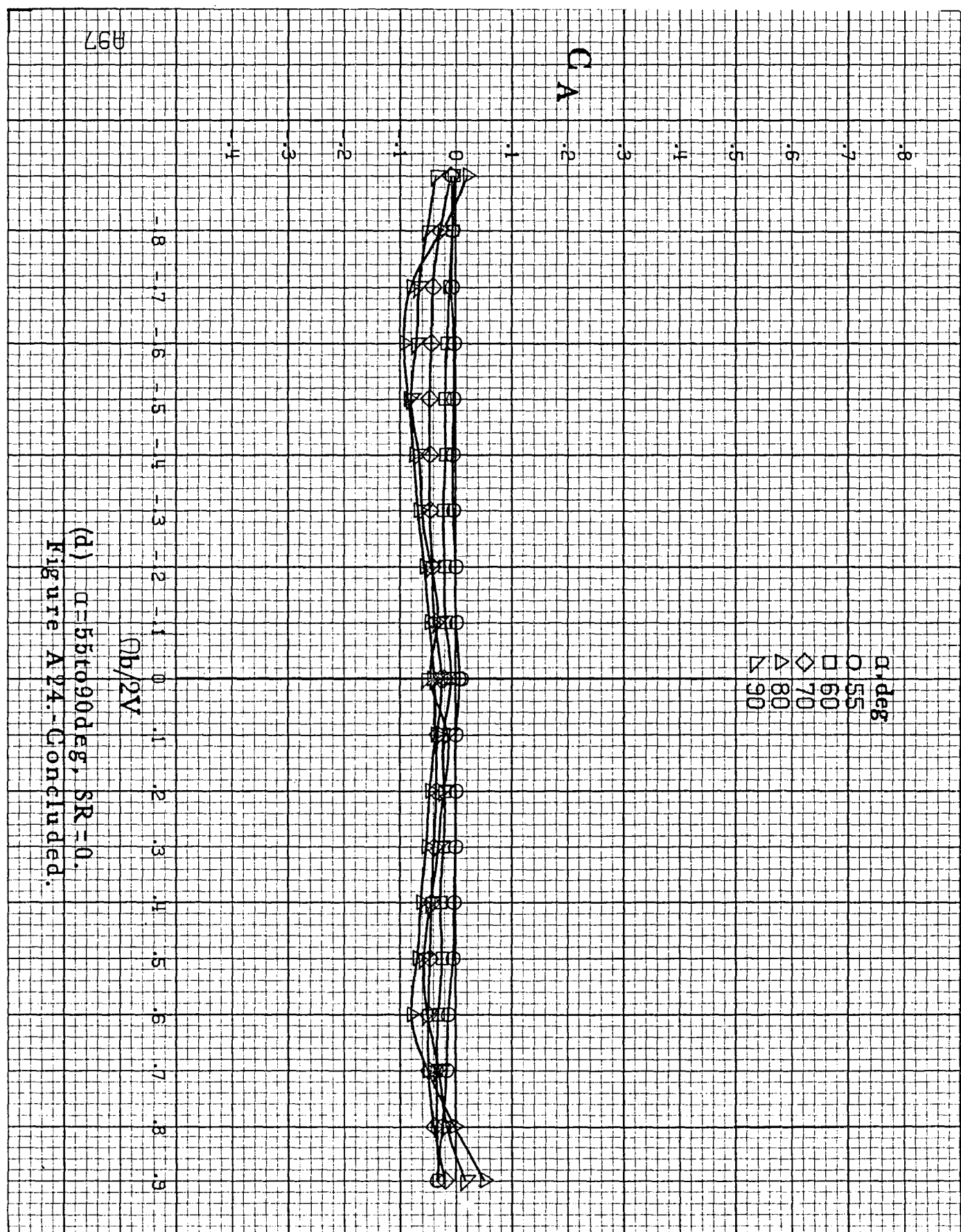
α , deg
 ○ 55
 □ 60
 ◇ 70
 △ 80
 ▽ 90

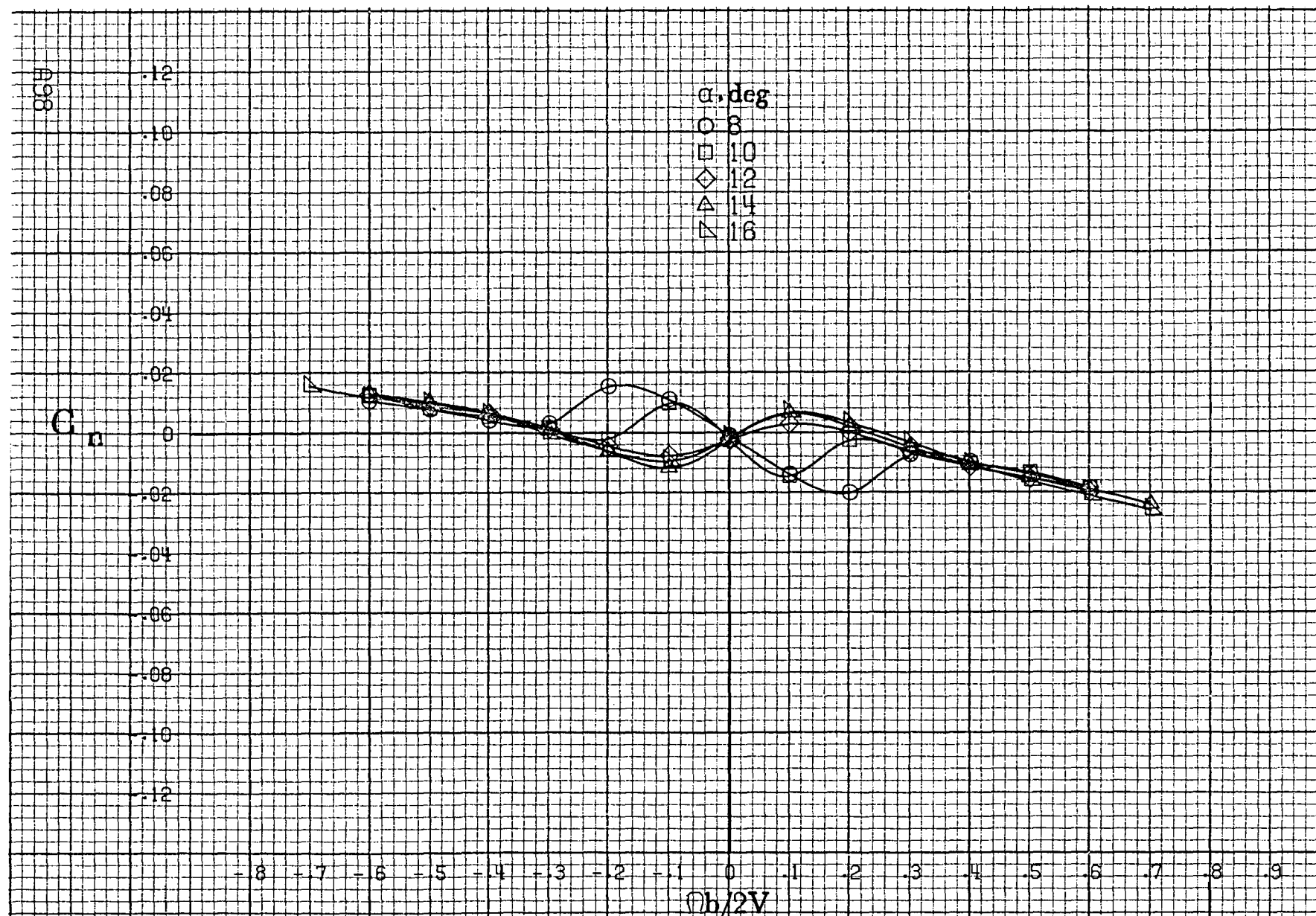
CA

0b/2V

(d) $\alpha=55$ to 90 deg, SR=0.
 Figure A24.-Concluded.

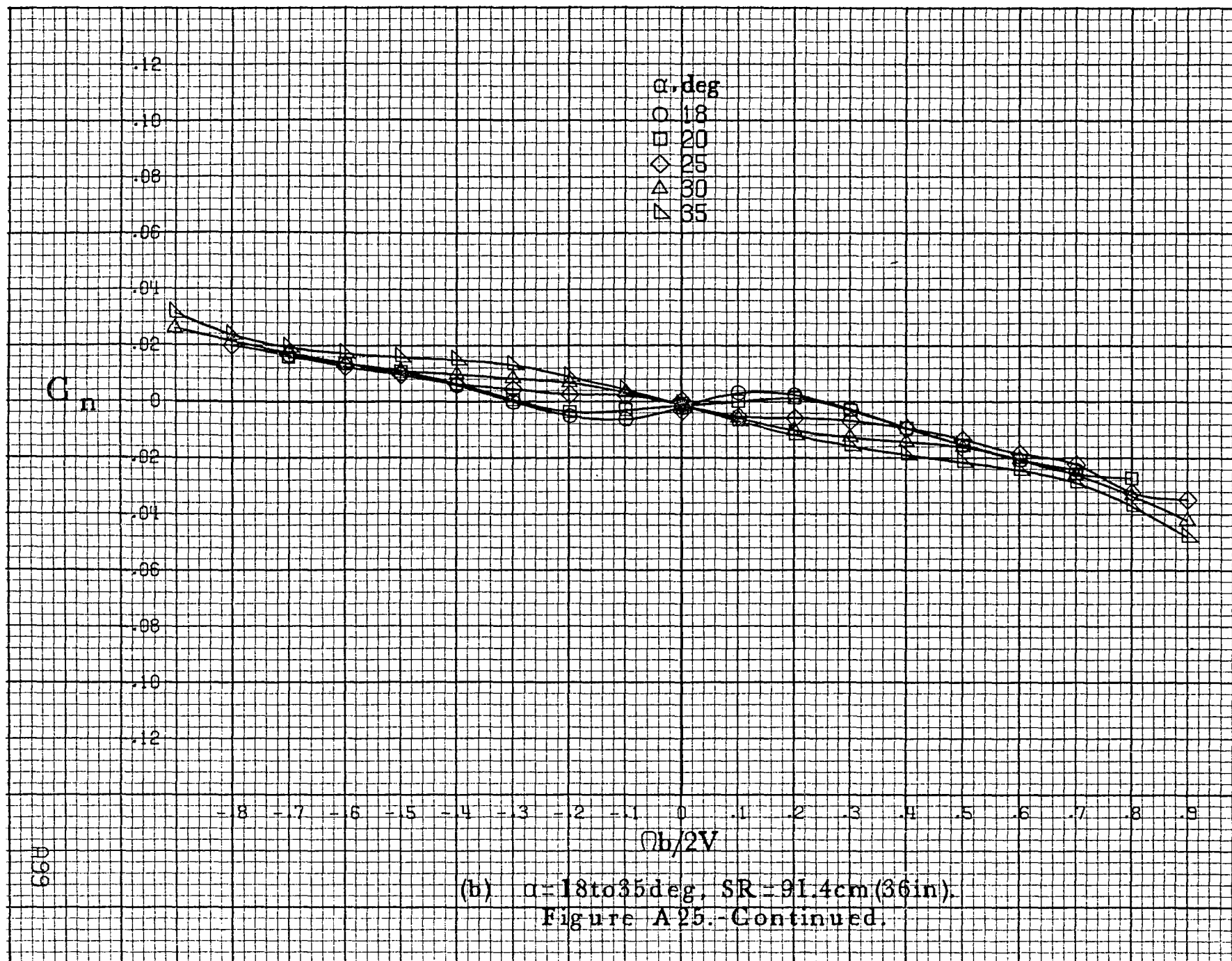
897

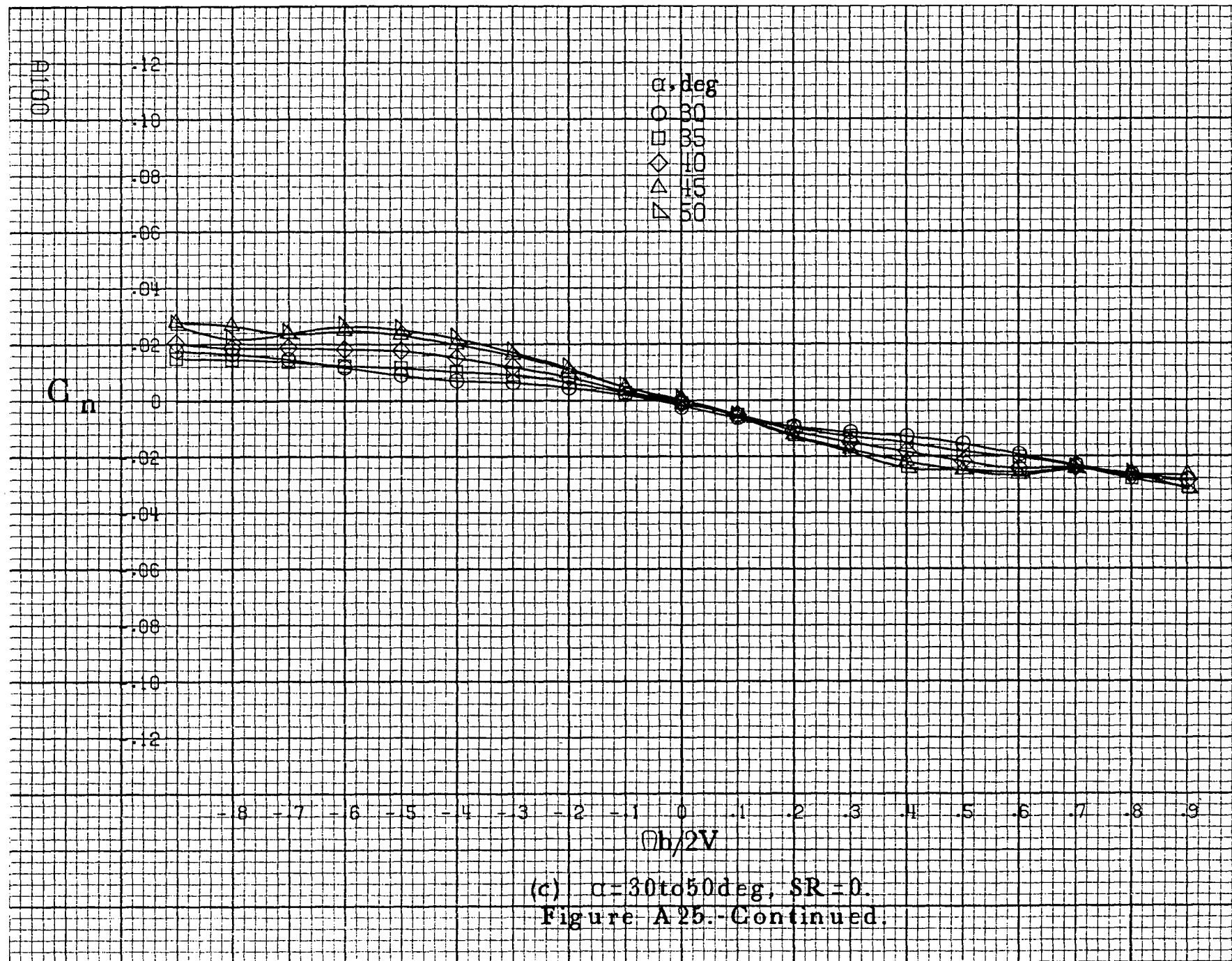


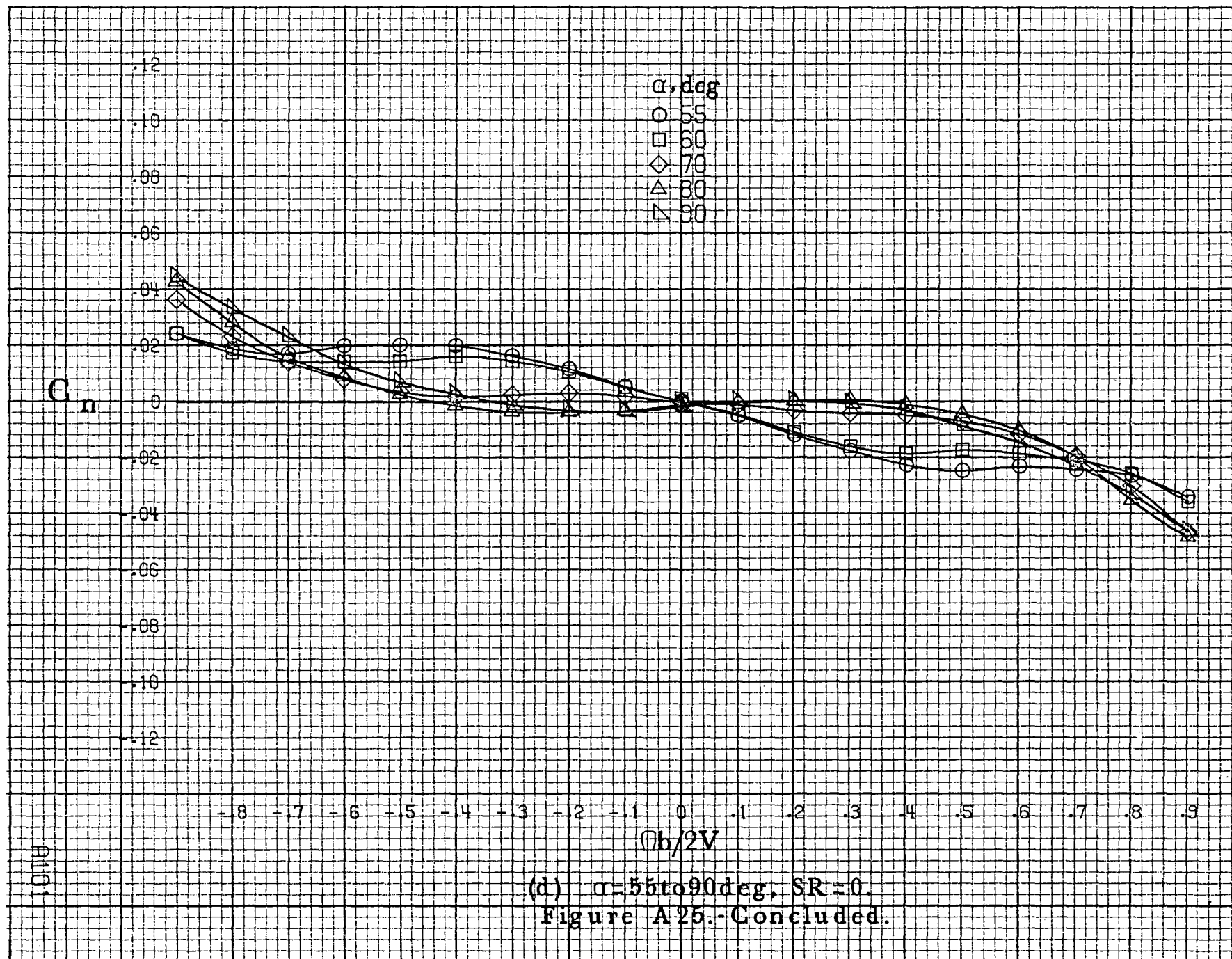


(a) $\alpha = 8$ to 16° , $SR = 91.4\text{cm (36in)}$.

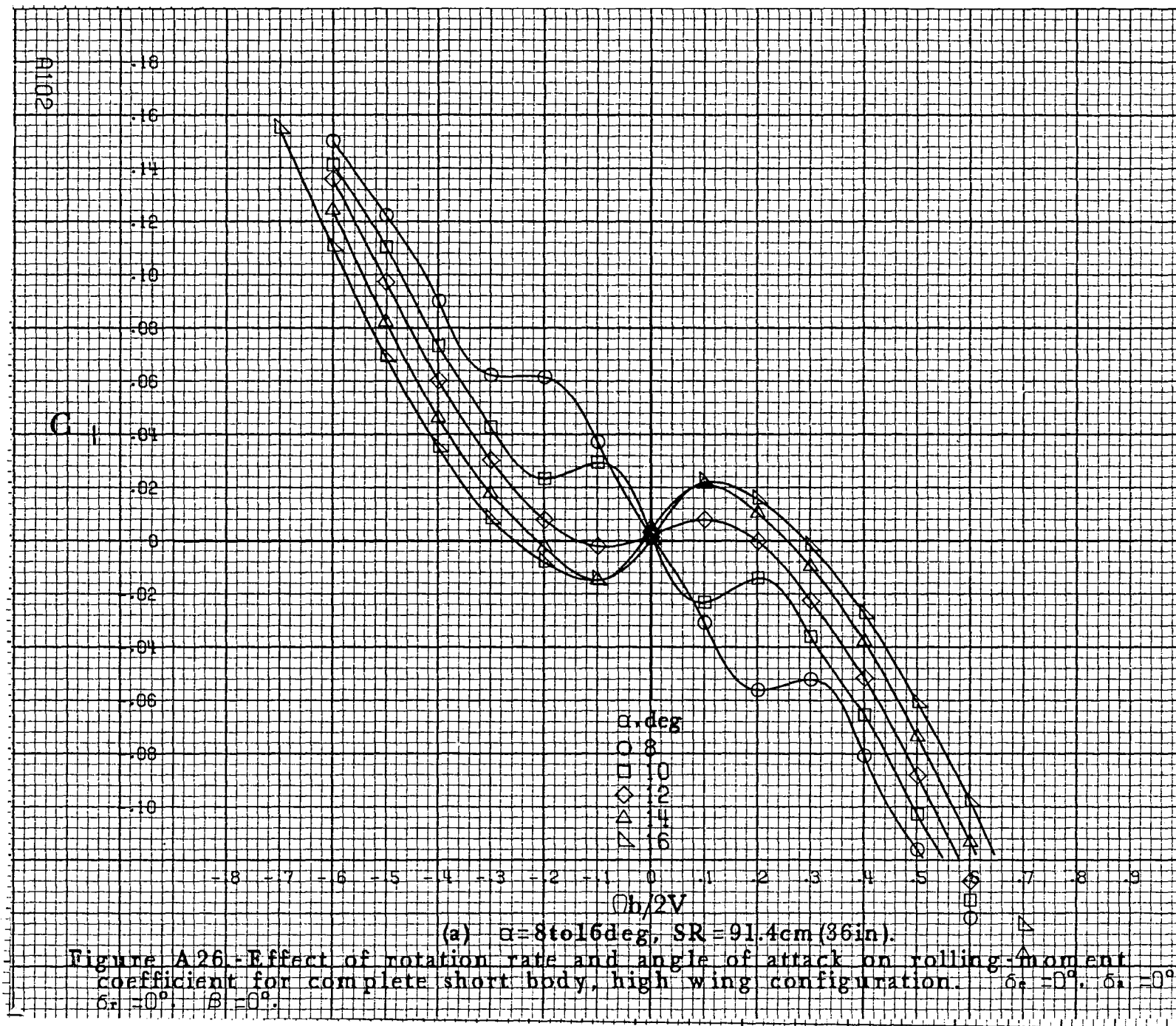
Figure A25 - Effect of rotation rate and angle of attack on yawing-moment coefficient for complete short body, high wing configuration. $\delta_r = 0^\circ$, $\delta_a = 0^\circ$, $\delta_r = 0^\circ$, $\beta = 0^\circ$.

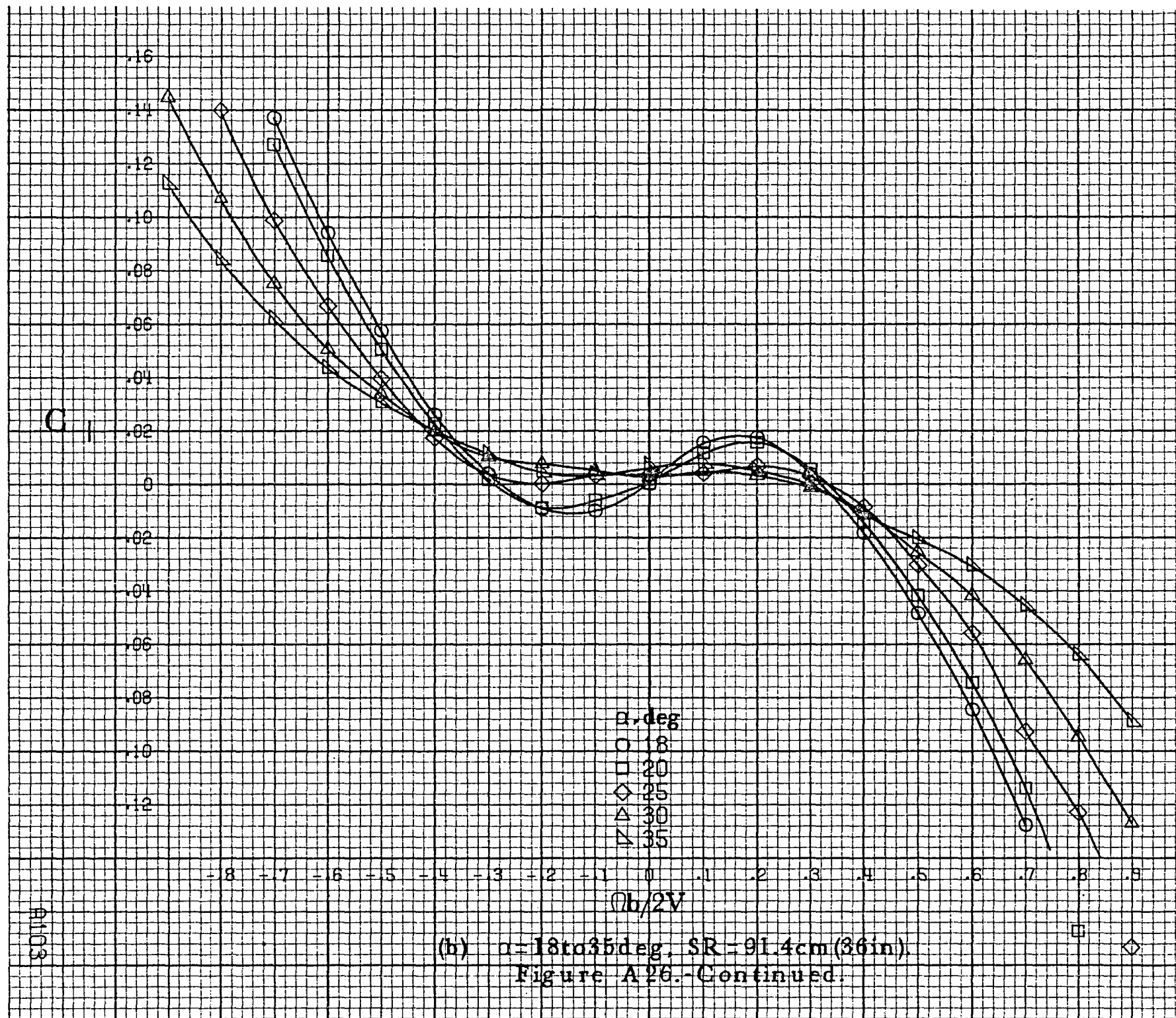


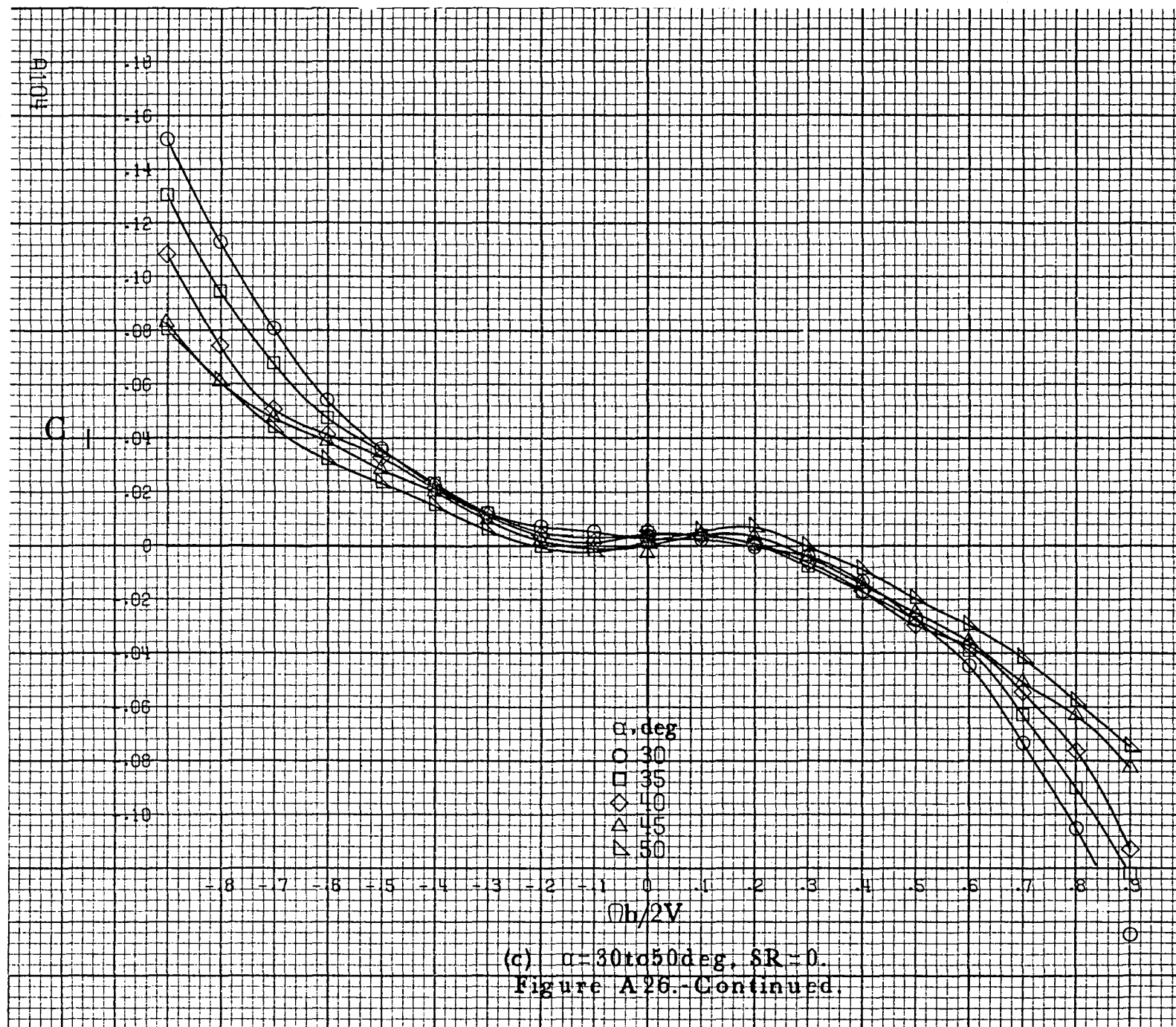


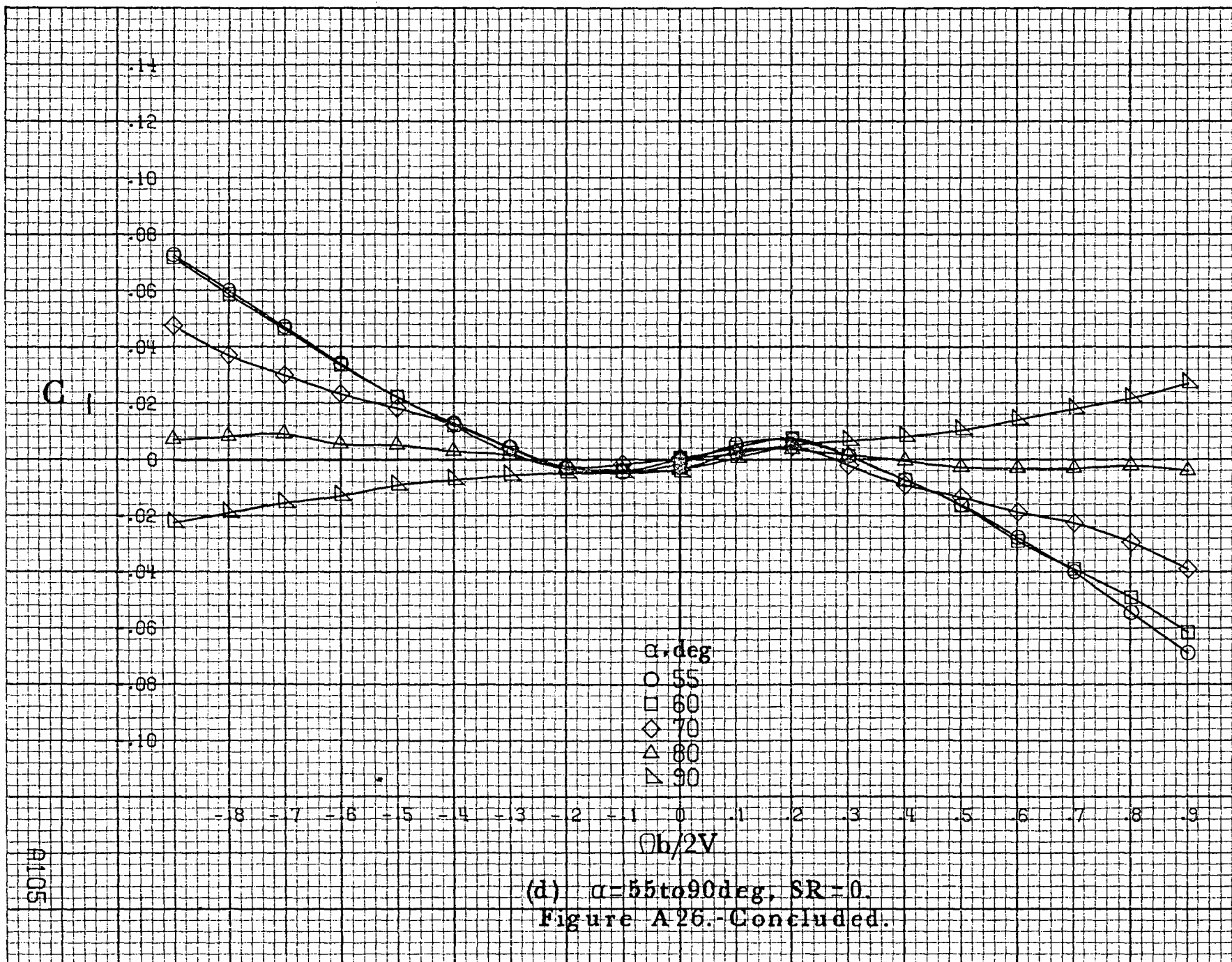


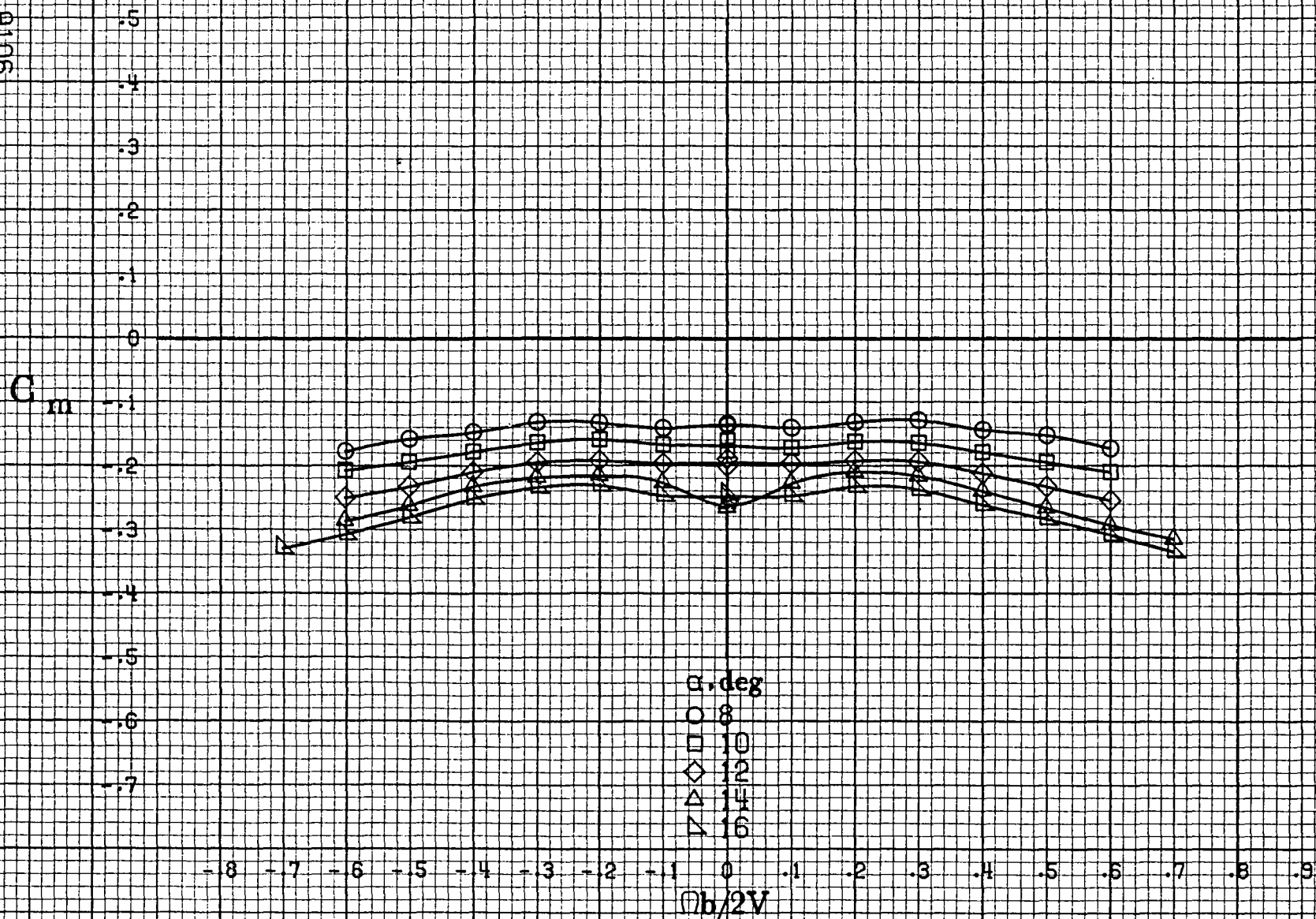
9101





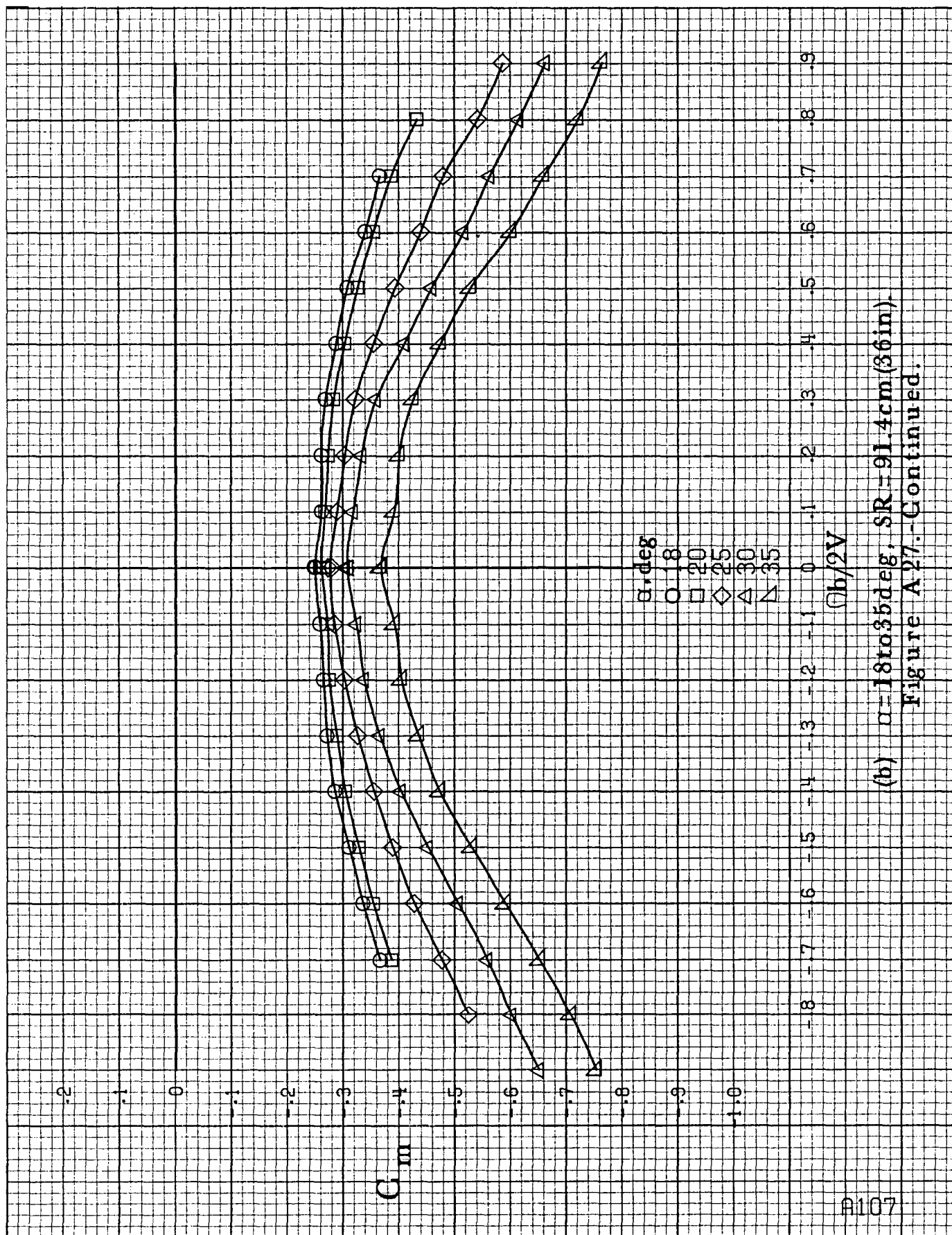






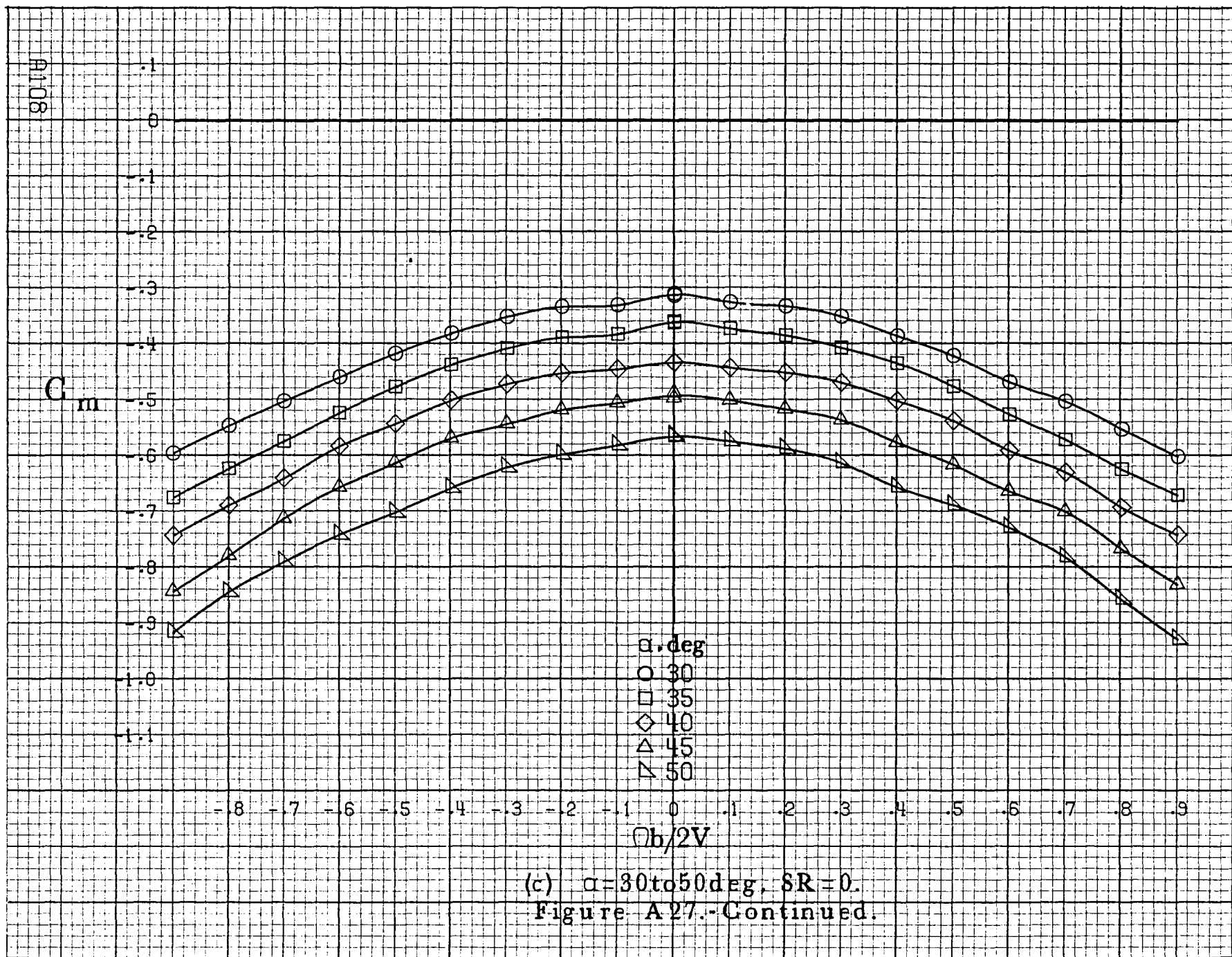
(a) $\alpha = 8$ to 16° , $SR = 91.4\text{cm (36in)}$.

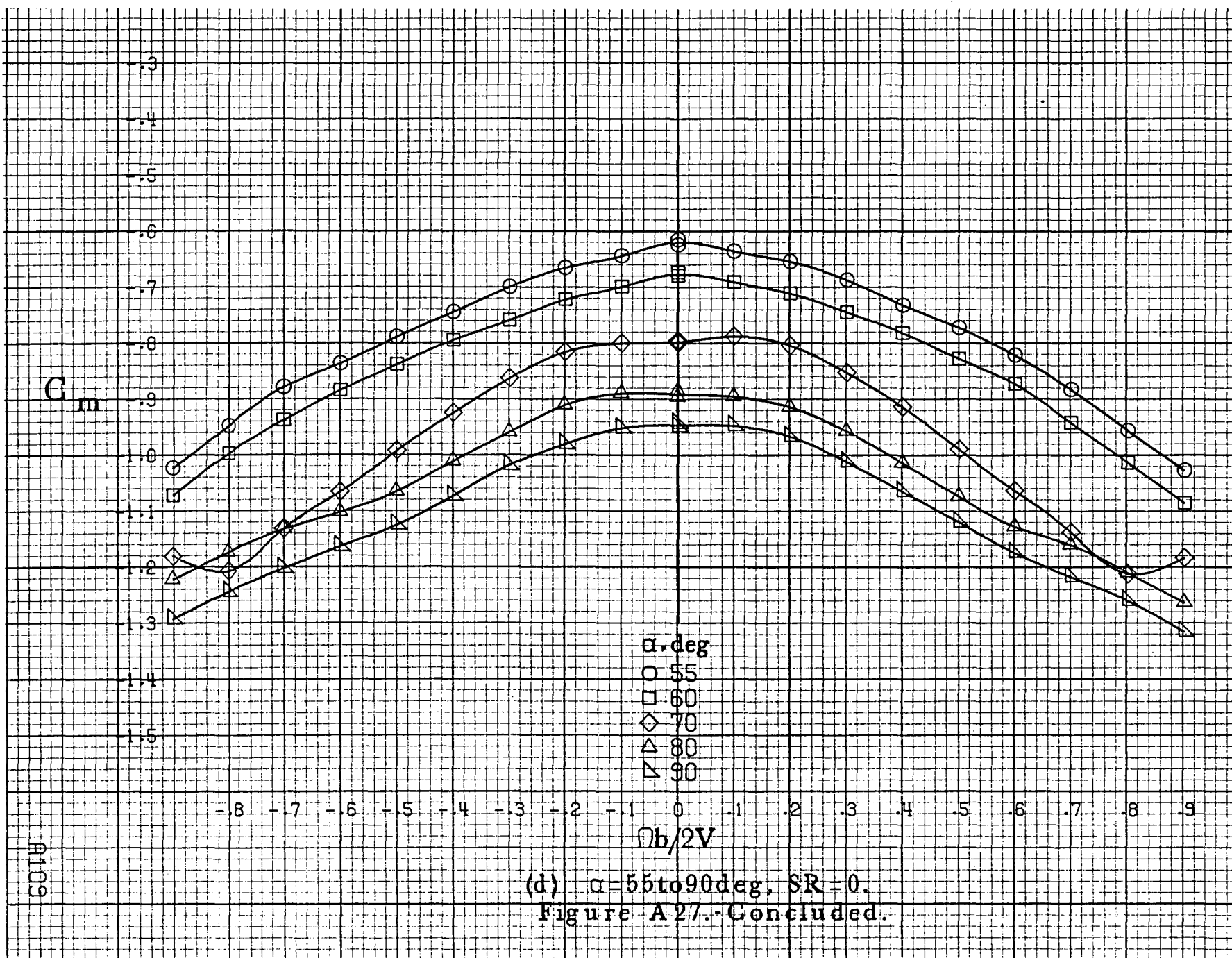
Figure A27.-Effect of rotation rate and angle of attack on pitching-moment coefficient for complete short body, high wing configuration. $\delta_r = 0^\circ$, $\delta_a = 0^\circ$, $\delta_r = 0^\circ$, $\beta = 0^\circ$.

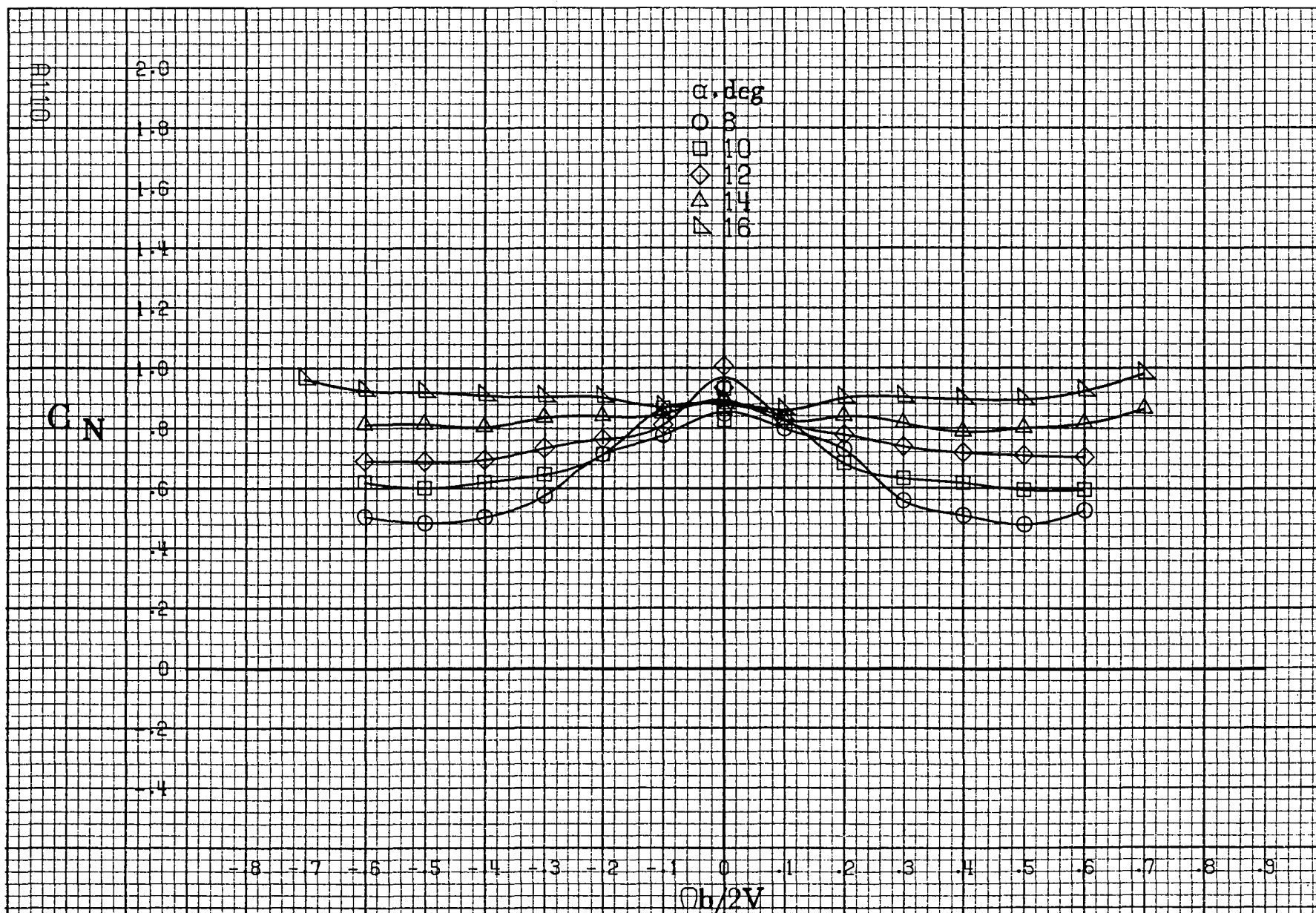


(b) $\alpha=18$ to 35° , $SR=91.4\text{cm}(36\text{in})$.

Figure A 27.-Continued.

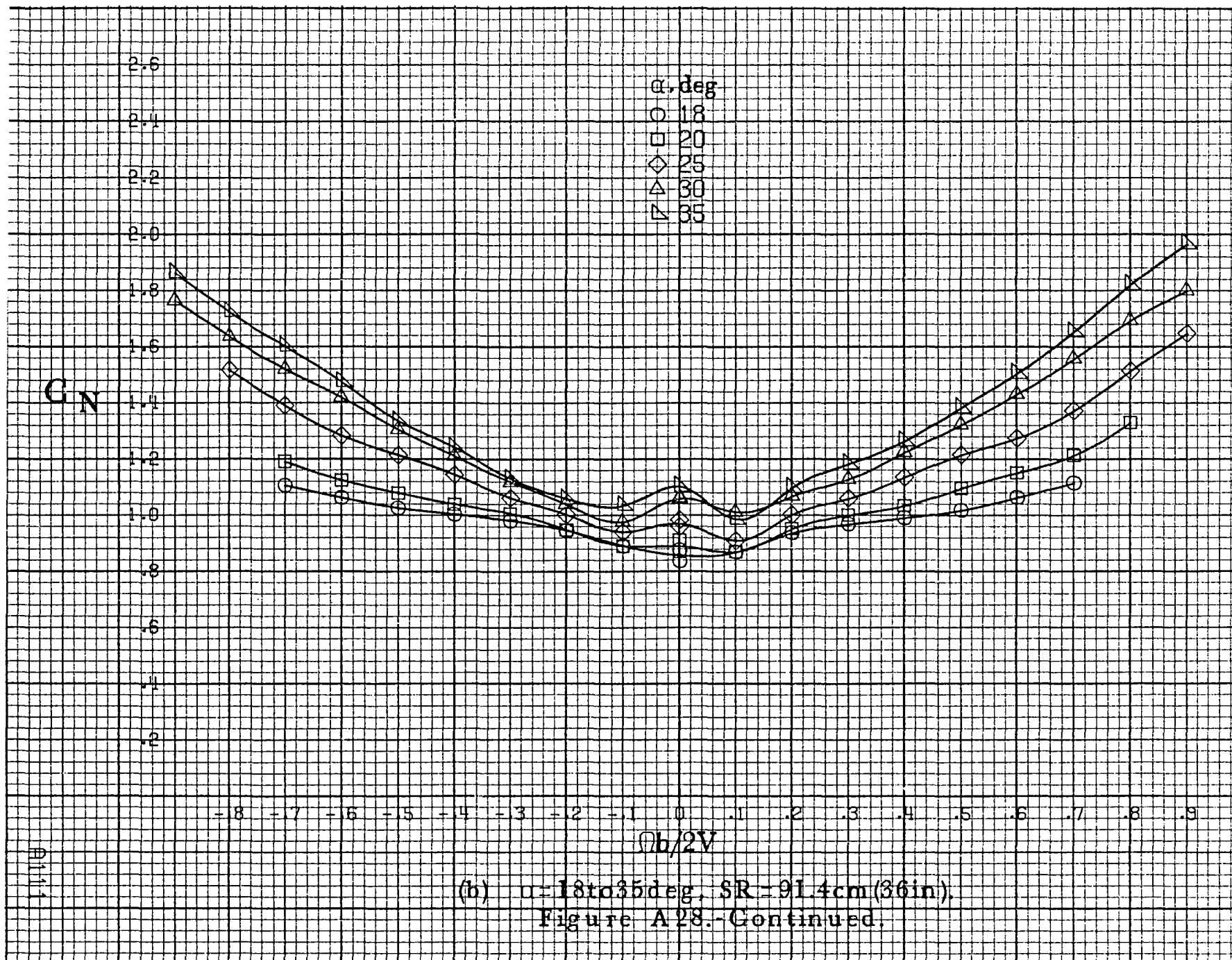


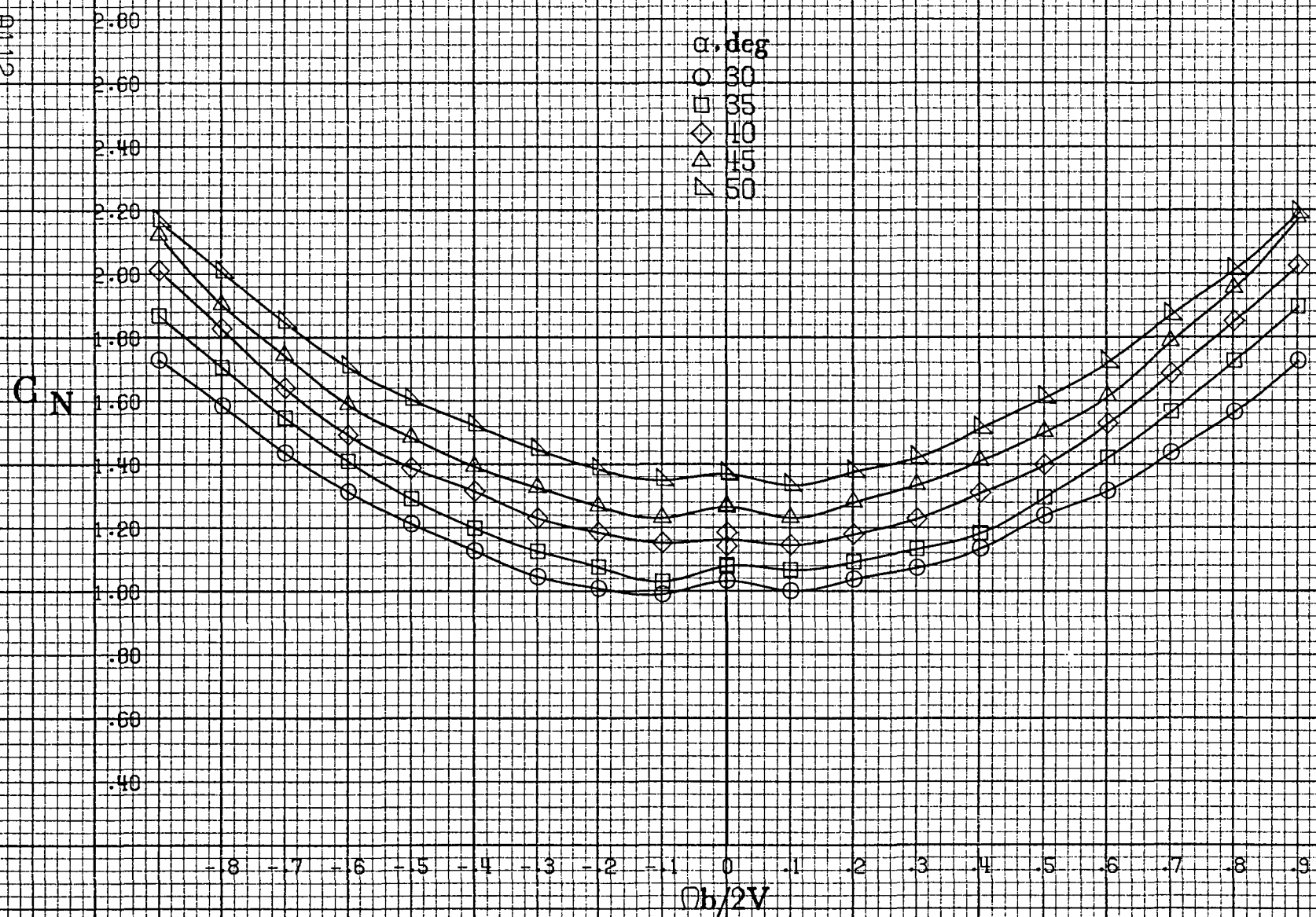




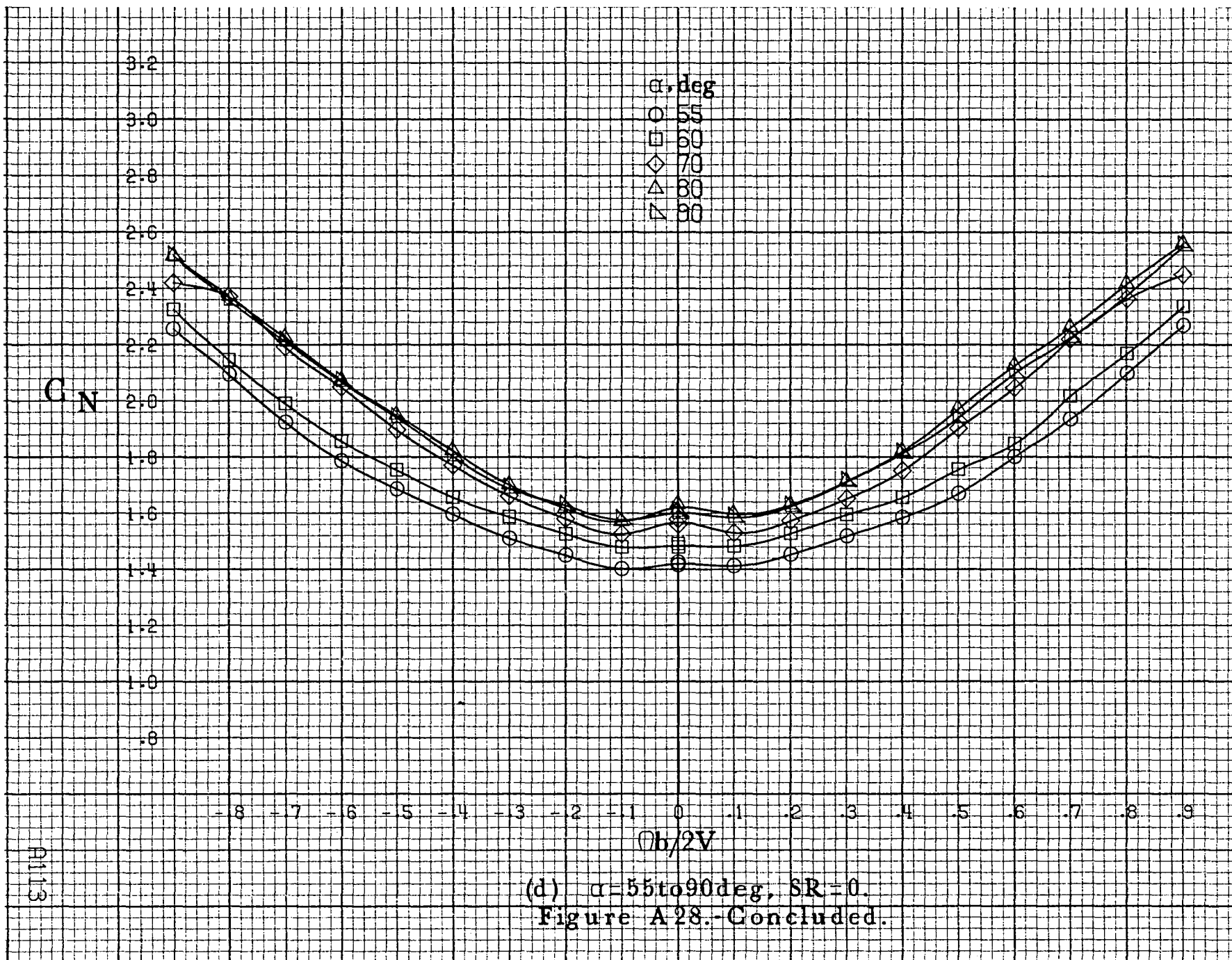
(a) $\alpha = 8$ to 16° , $SR = 91.4\text{cm (36in)}$.

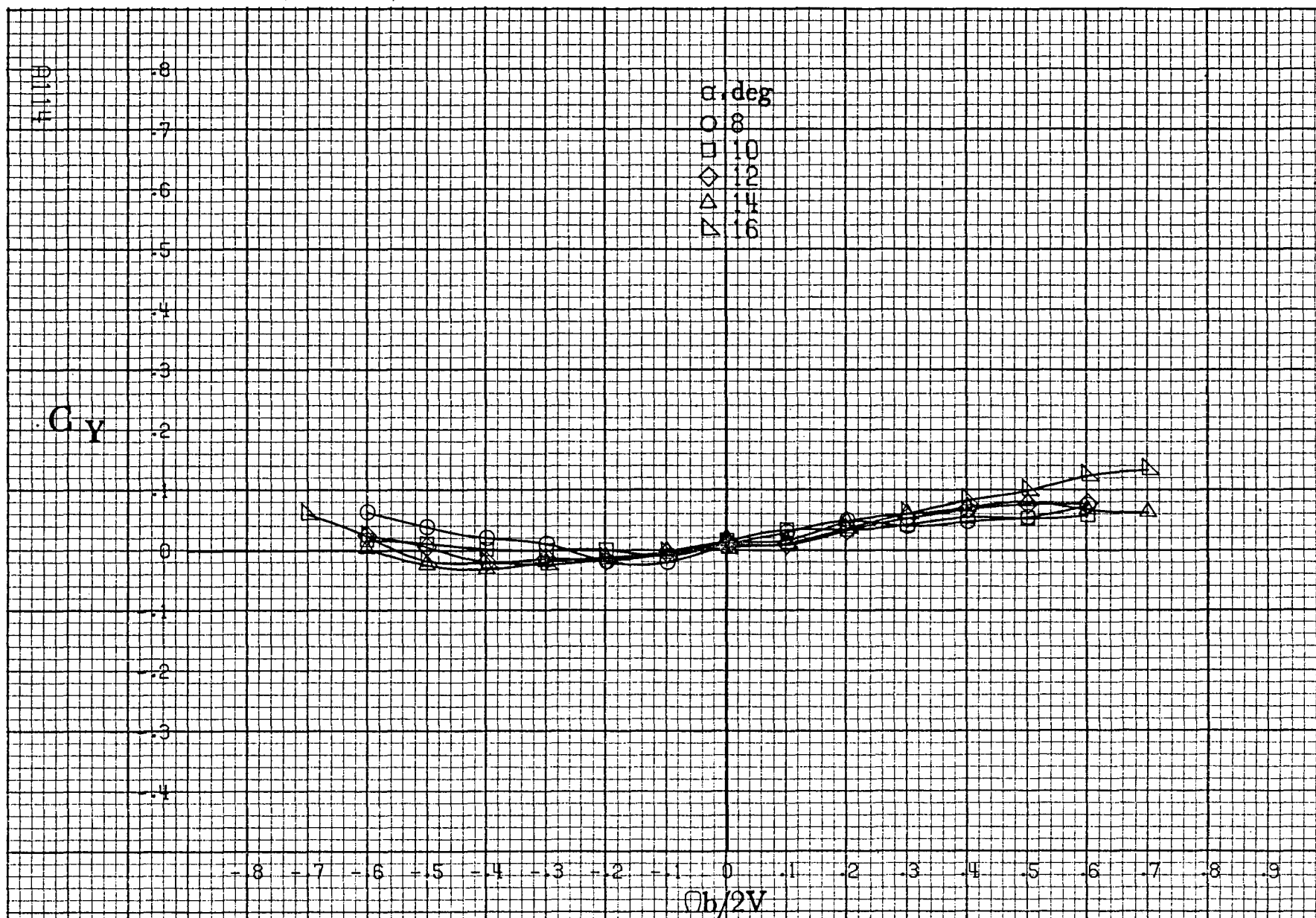
Figure A28 - Effect of rotation rate and angle of attack on normal-force coefficient for complete short body, high wing configuration. $\delta_c = 0^\circ$, $\delta_a = 0^\circ$, $\delta_r = 0^\circ$, $\beta = 0^\circ$.





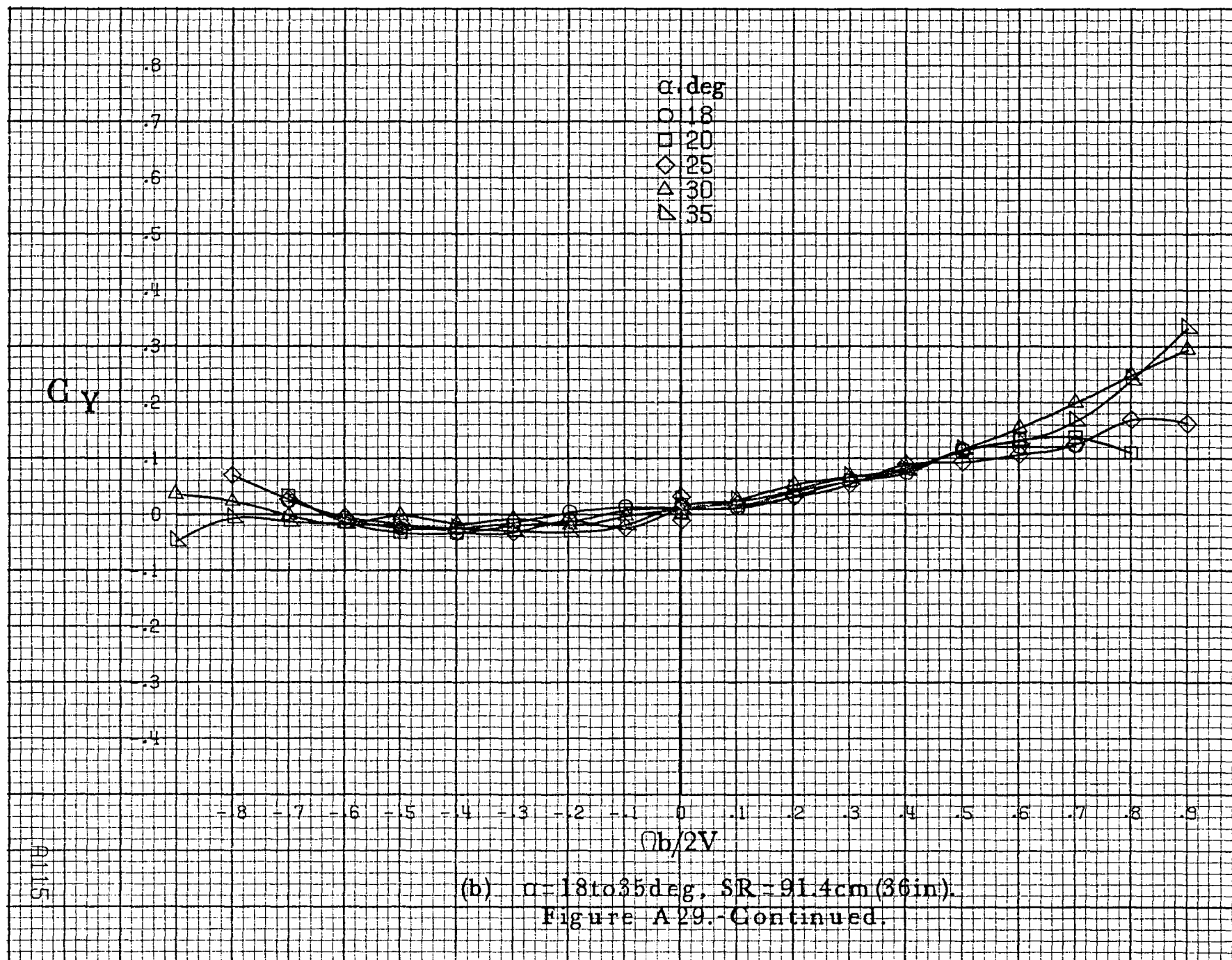
(c) $\alpha=30$ to 50 deg, $SR=0$.
Figure A28.-Continued.

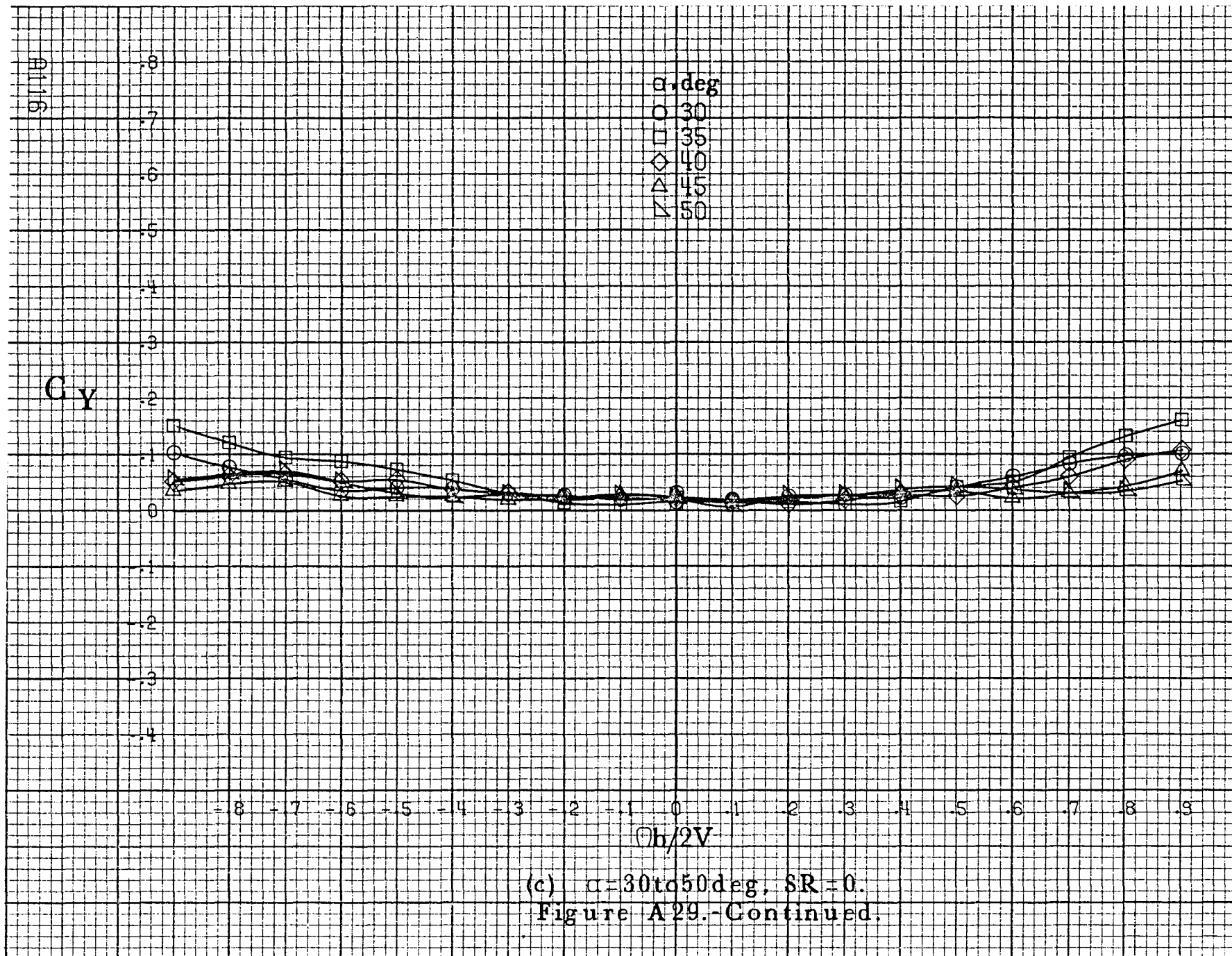


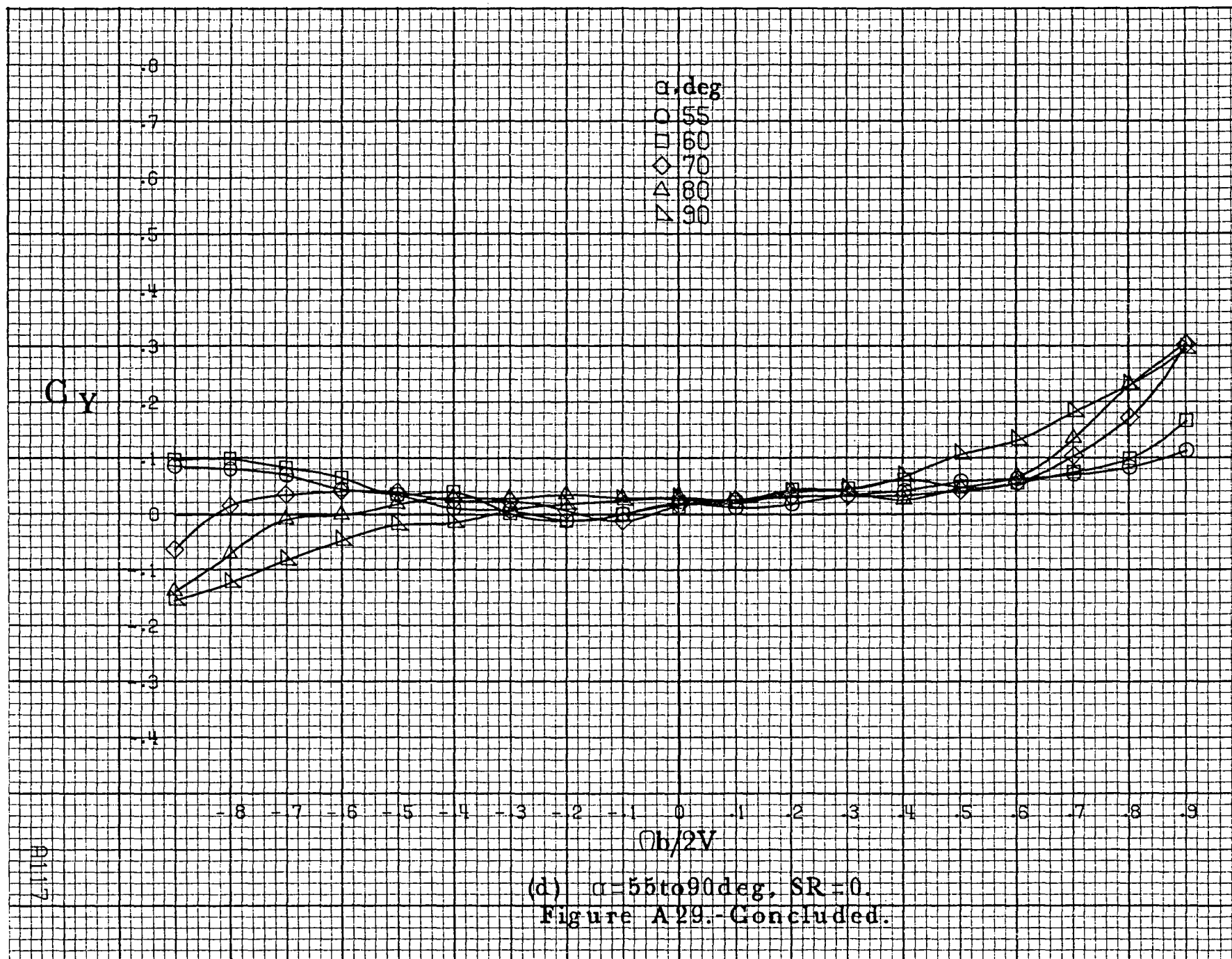


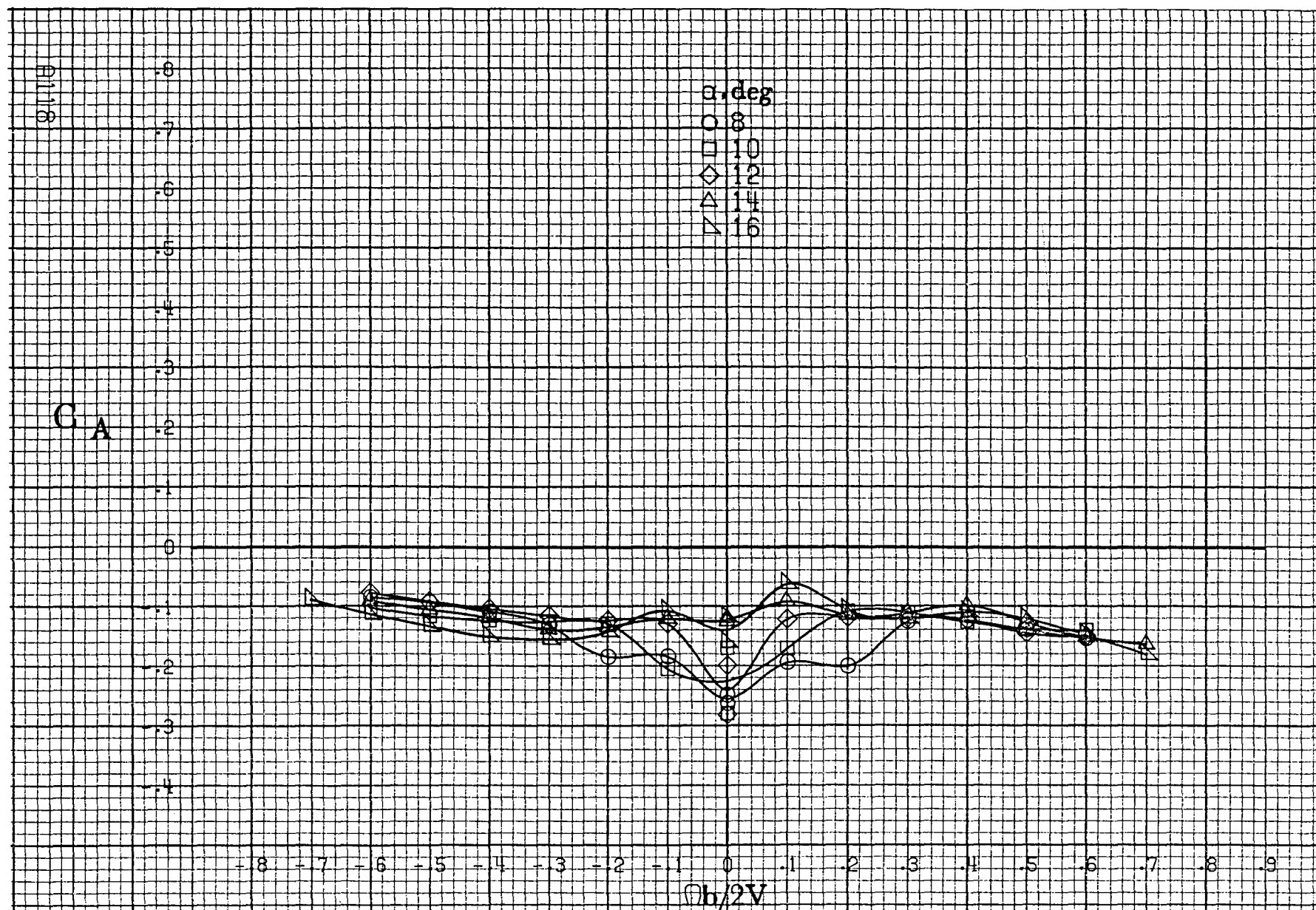
(a) $\alpha = 8$ to 16 deg, $SR = 91.4$ cm (36 in).

Figure A29 - Effect of rotation rate and angle of attack on side-force coefficient for complete short body, high wing configuration. $\delta_e = 0^\circ$, $\delta_a = 0^\circ$, $\delta_r = 0^\circ$, $\beta = 0^\circ$.



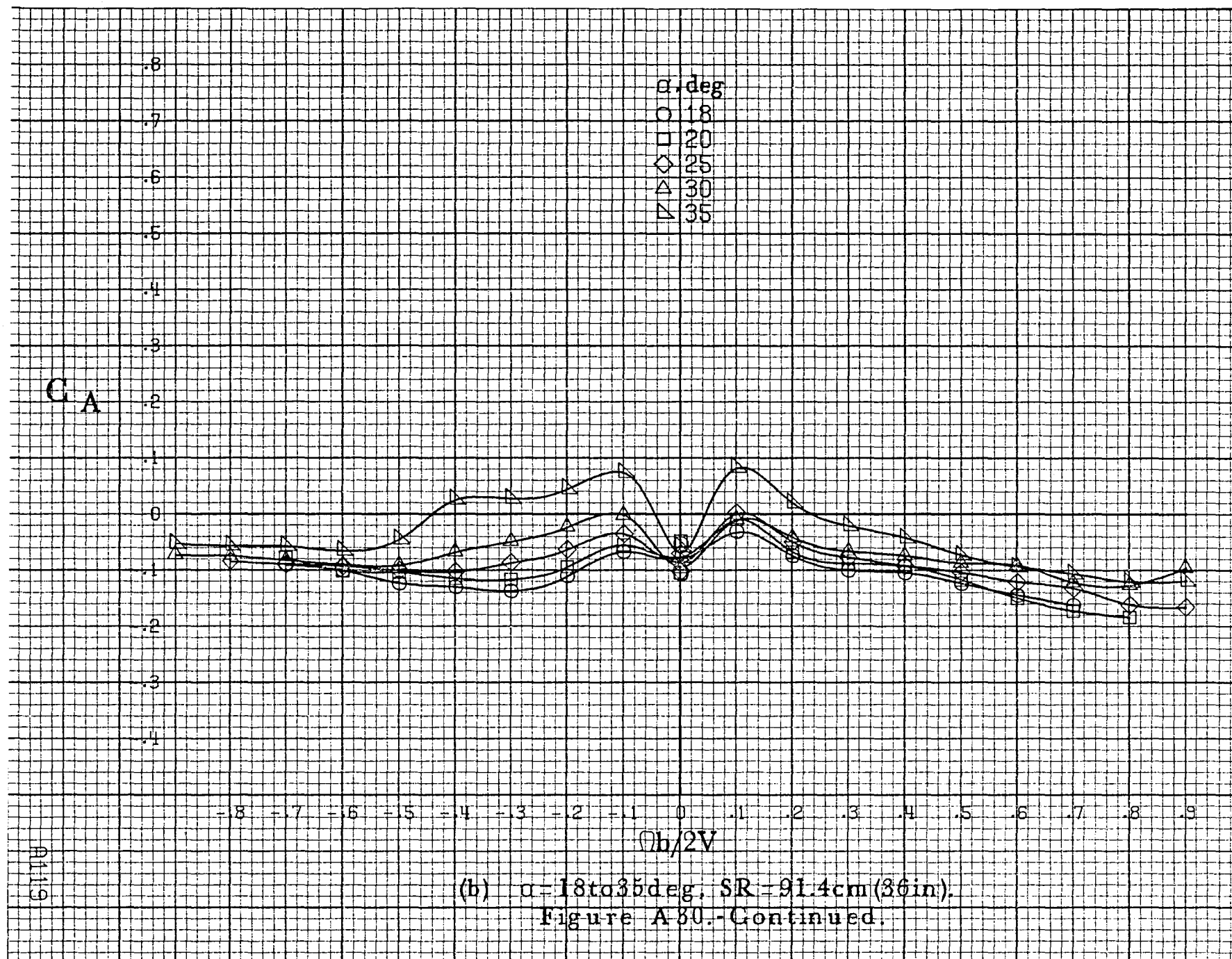


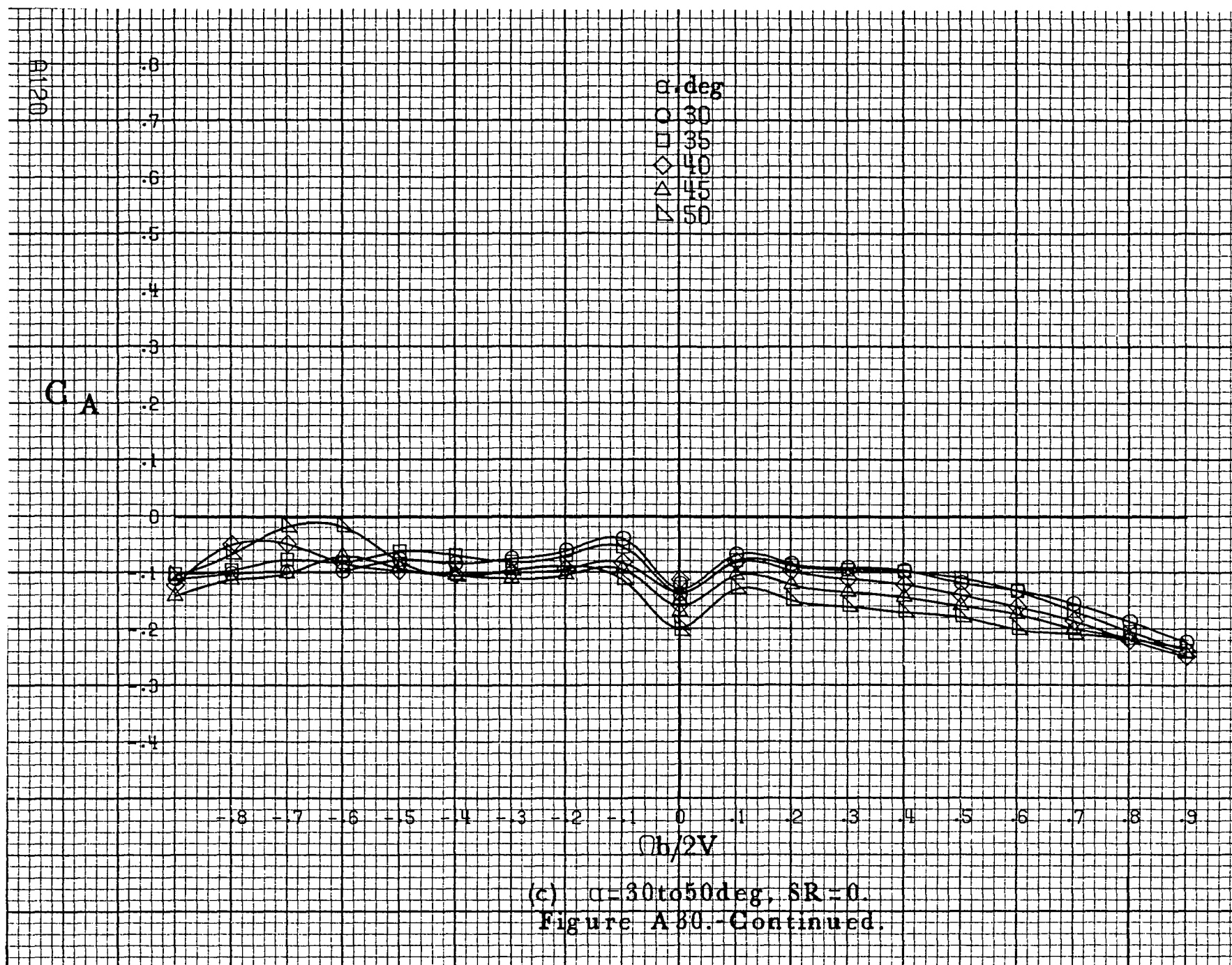


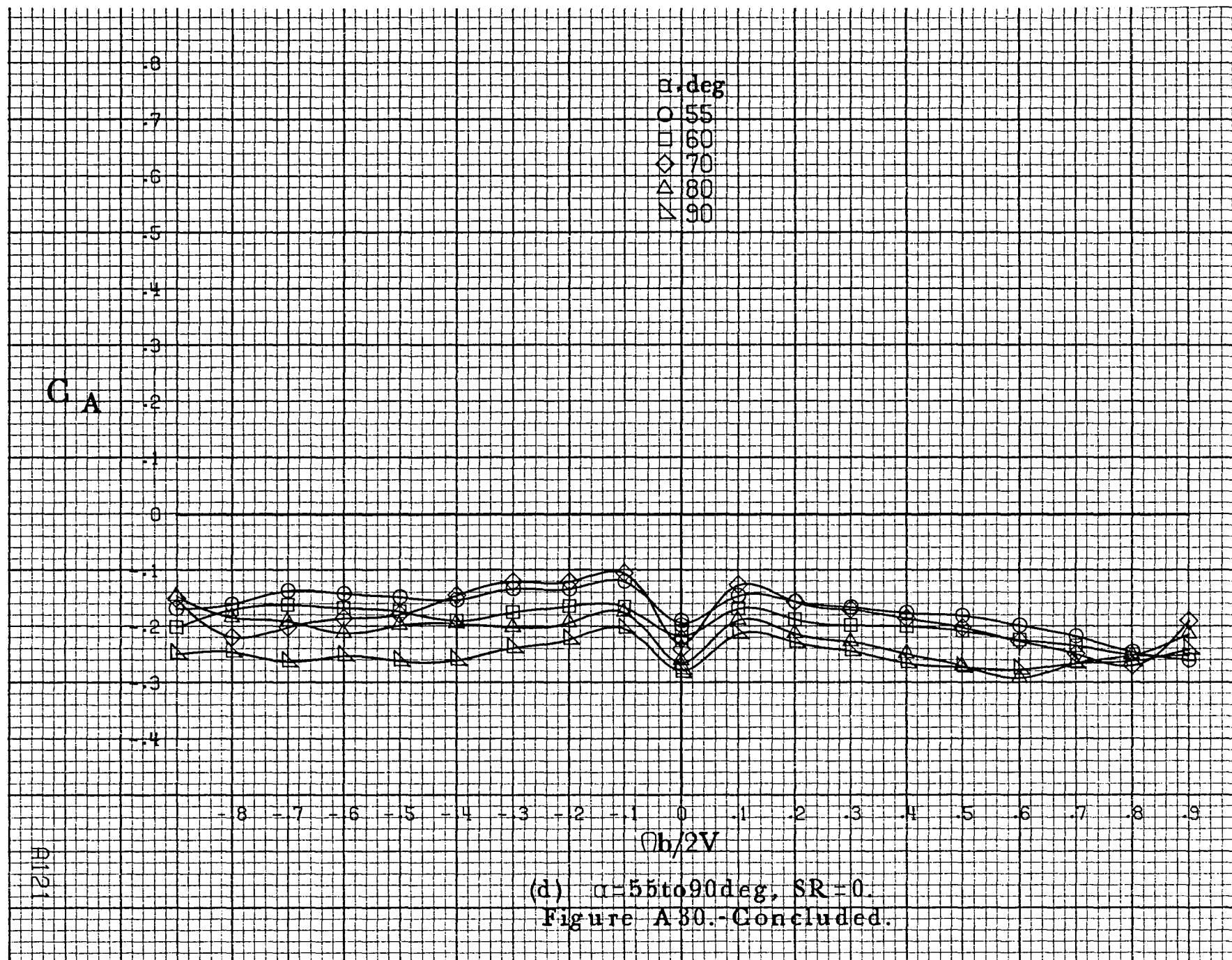


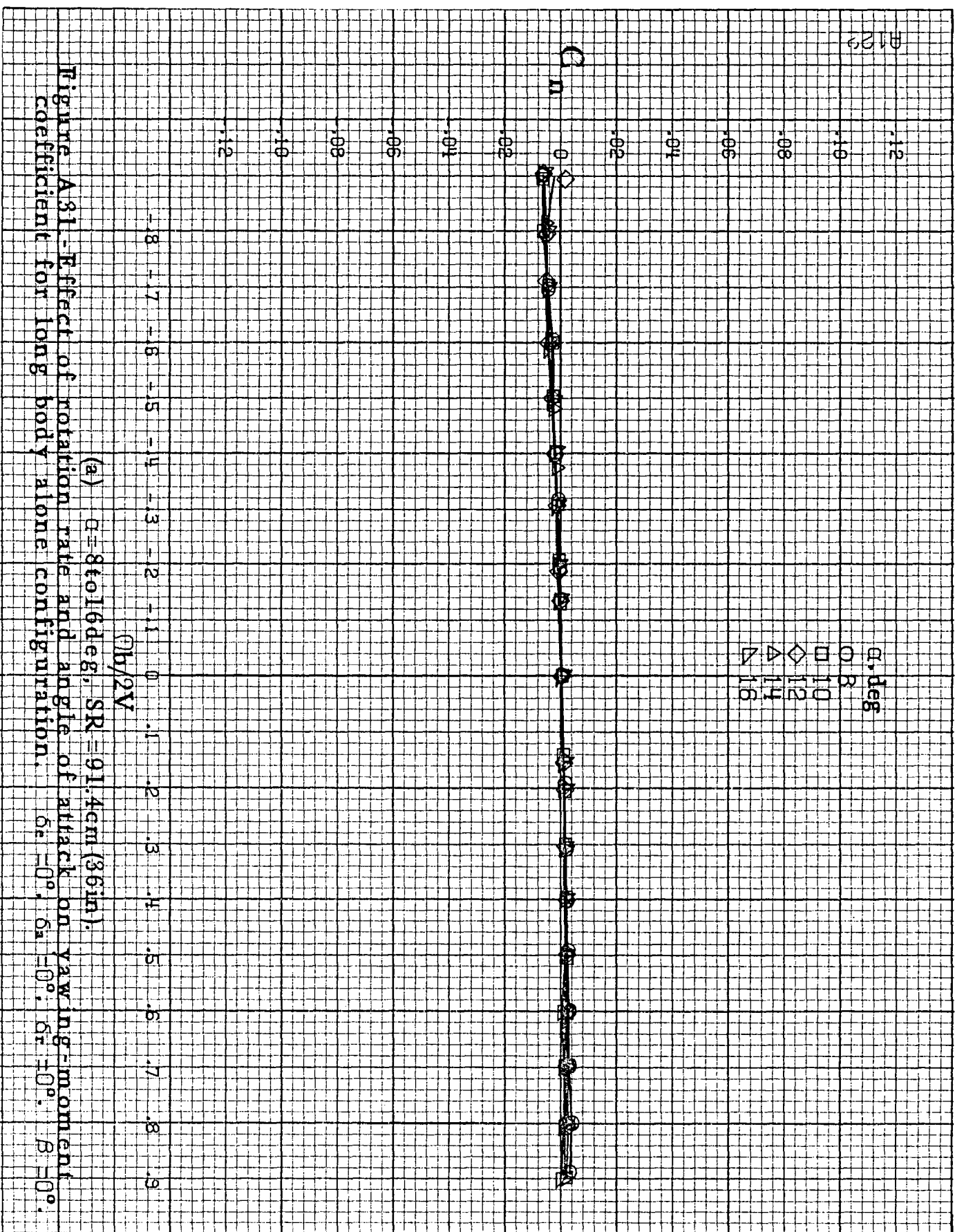
(a) $\alpha = 8$ to 16 deg, $SR = 91.4 \text{ cm (36 in.)}$.

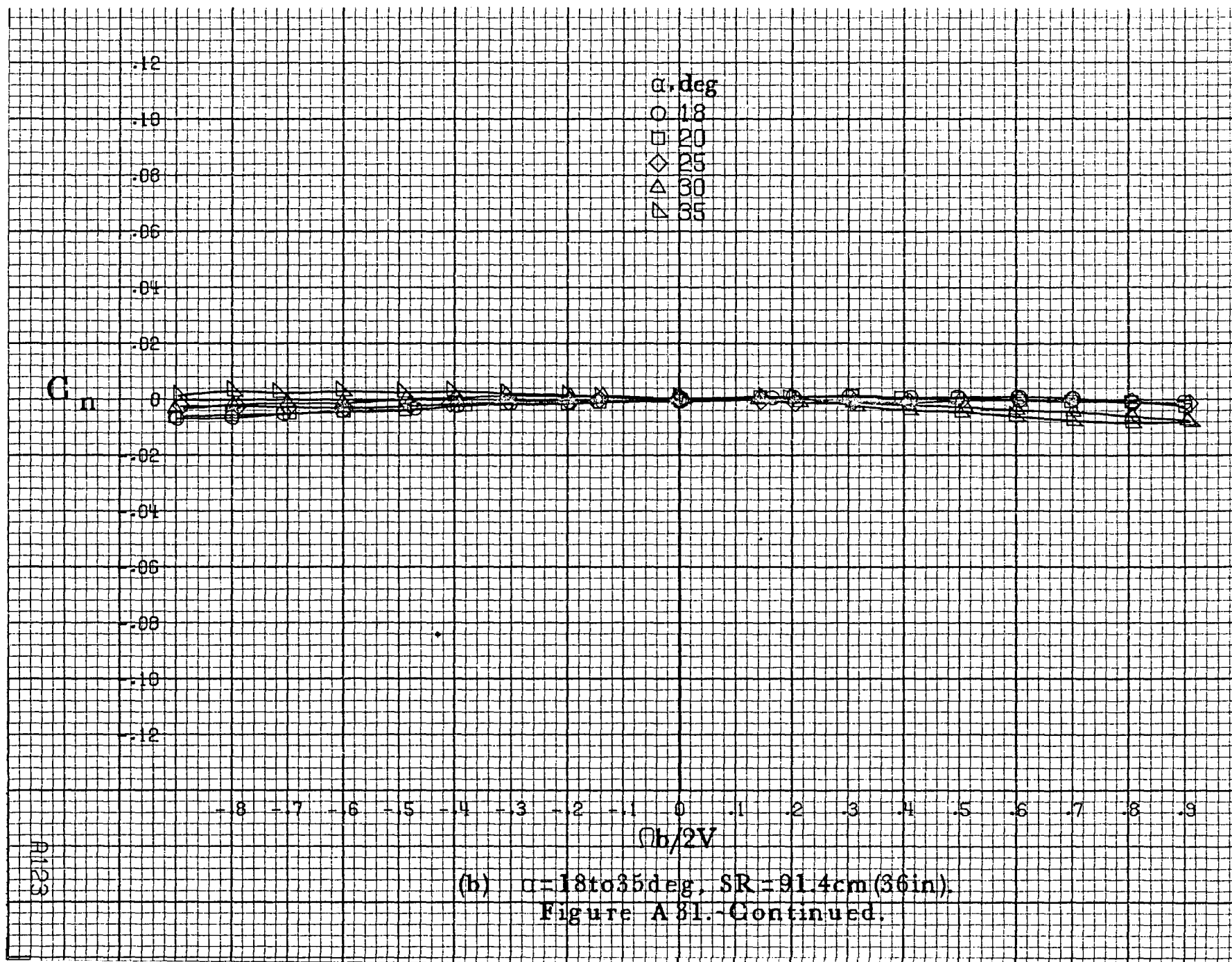
Figure A30.-Effect of rotation rate and angle of attack on axial-force coefficient for complete short body, high wing configuration. $\delta_e = 0^\circ$, $\delta_a = 0^\circ$, $\delta_r = 0^\circ$, $B = 0^\circ$.

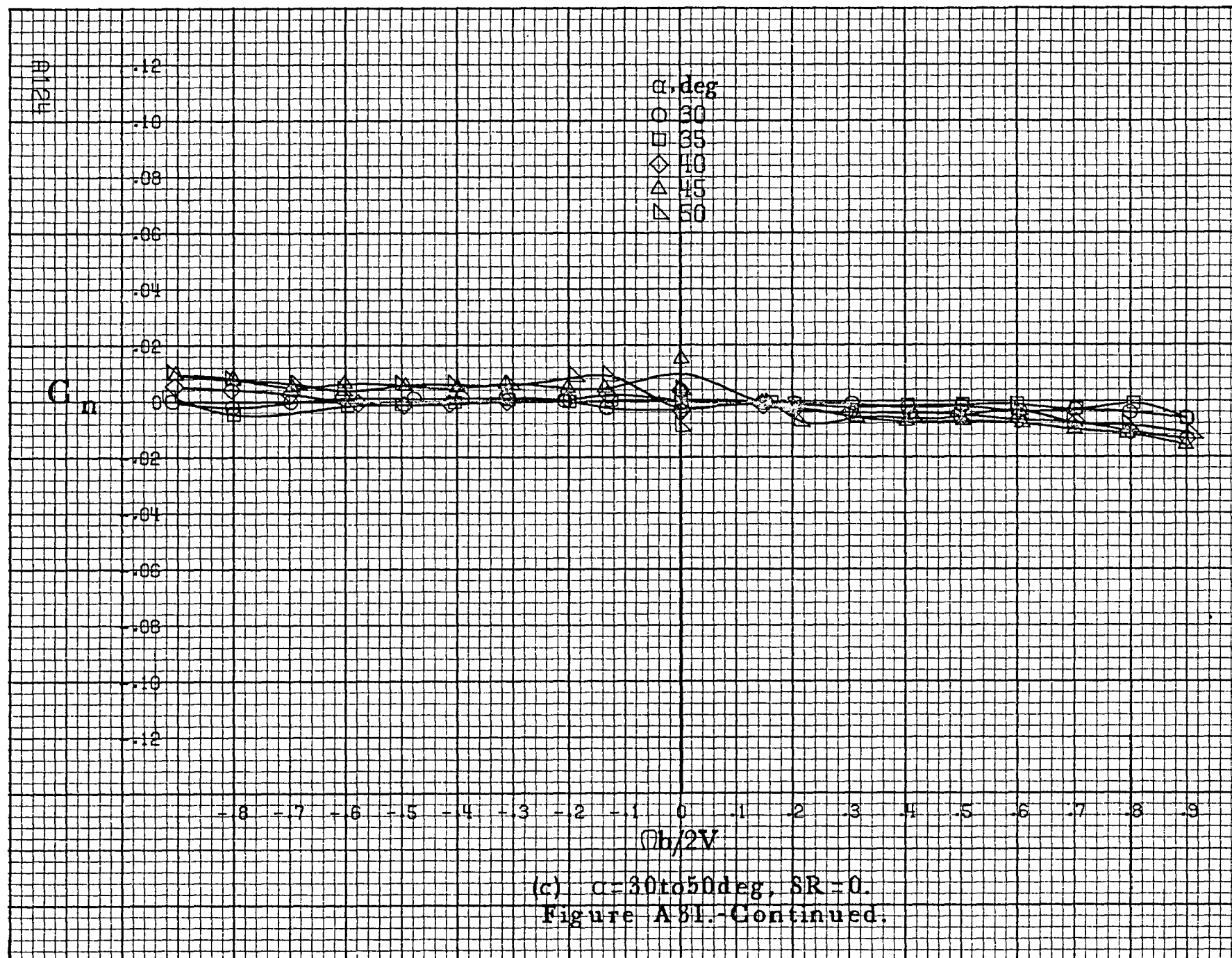


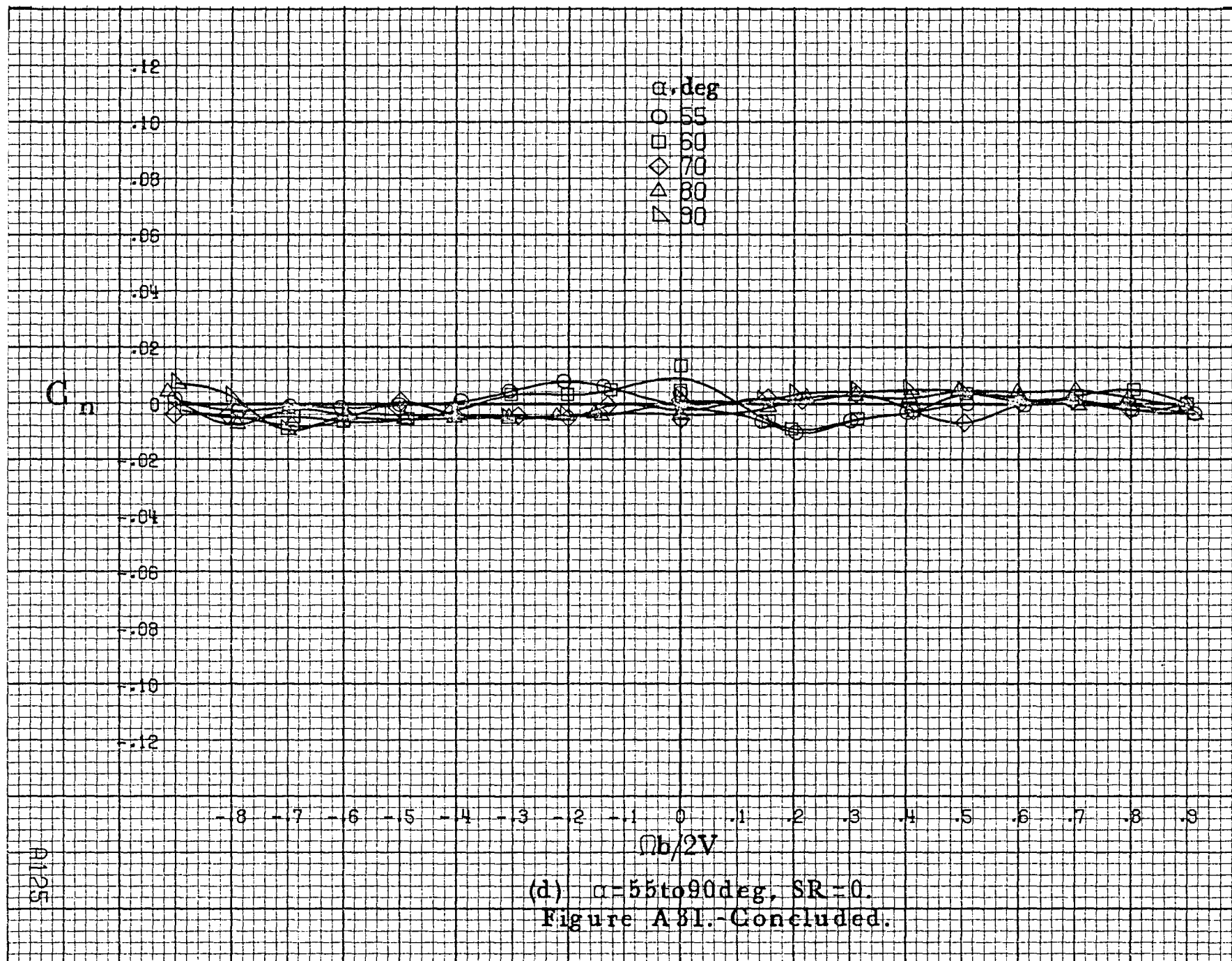


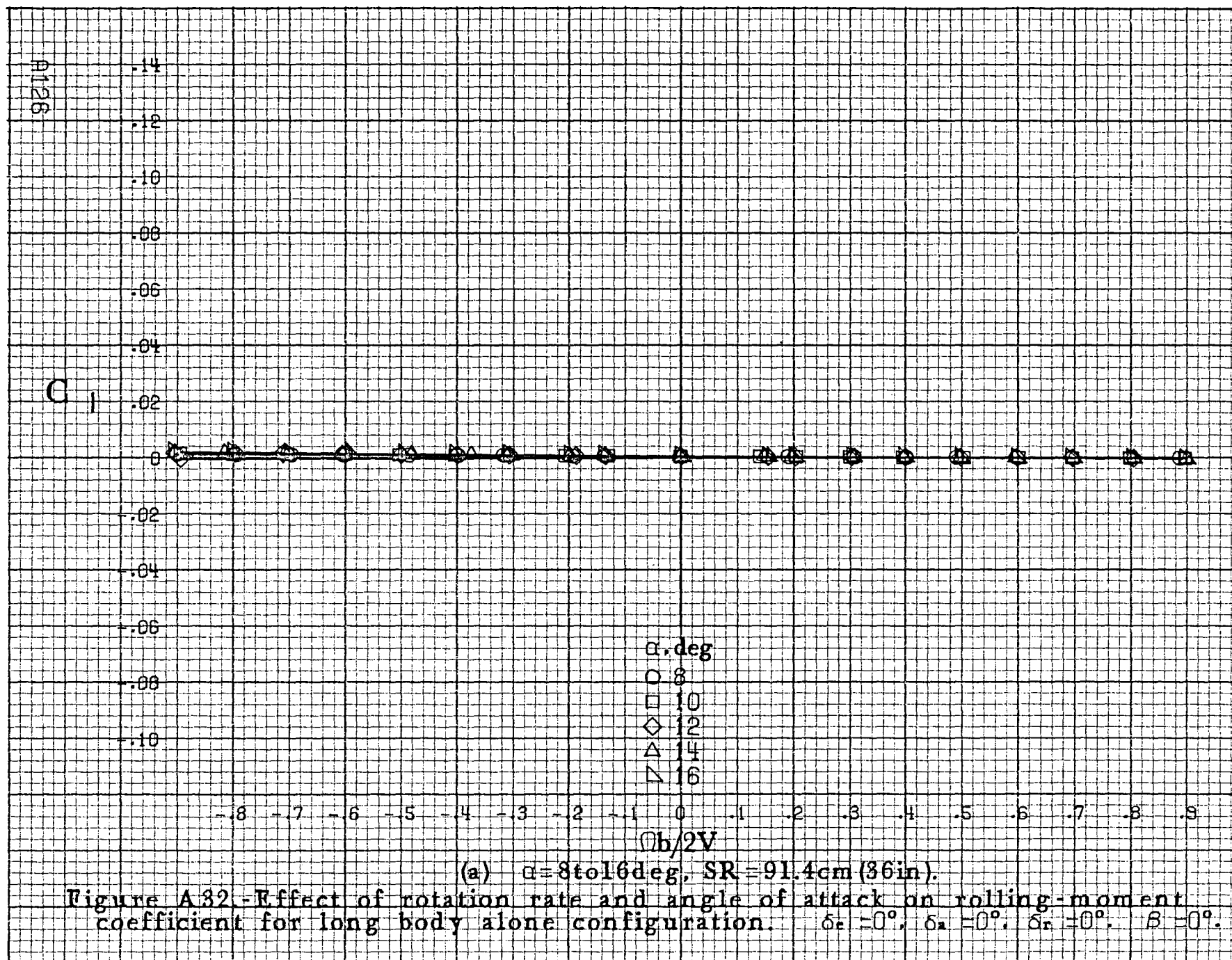












C₁

.14
.12
.10
.08
.06
.04
.02
0
-.02
-.04
-.06
-.08
-.10

α , deg
○ 18
□ 20
◇ 25
△ 30
▽ 35

- .8 - .7 - .6 - .5 - .4 - .3 - .2 - .1 0 .1 .2 .3 .4 .5 .6 .7 .8 .9

$\Omega b/2V$

(b) $\alpha=18$ to 35 deg, SR=91.4cm(36in).
Figure A32.-Continued.

A127

A128

C₁

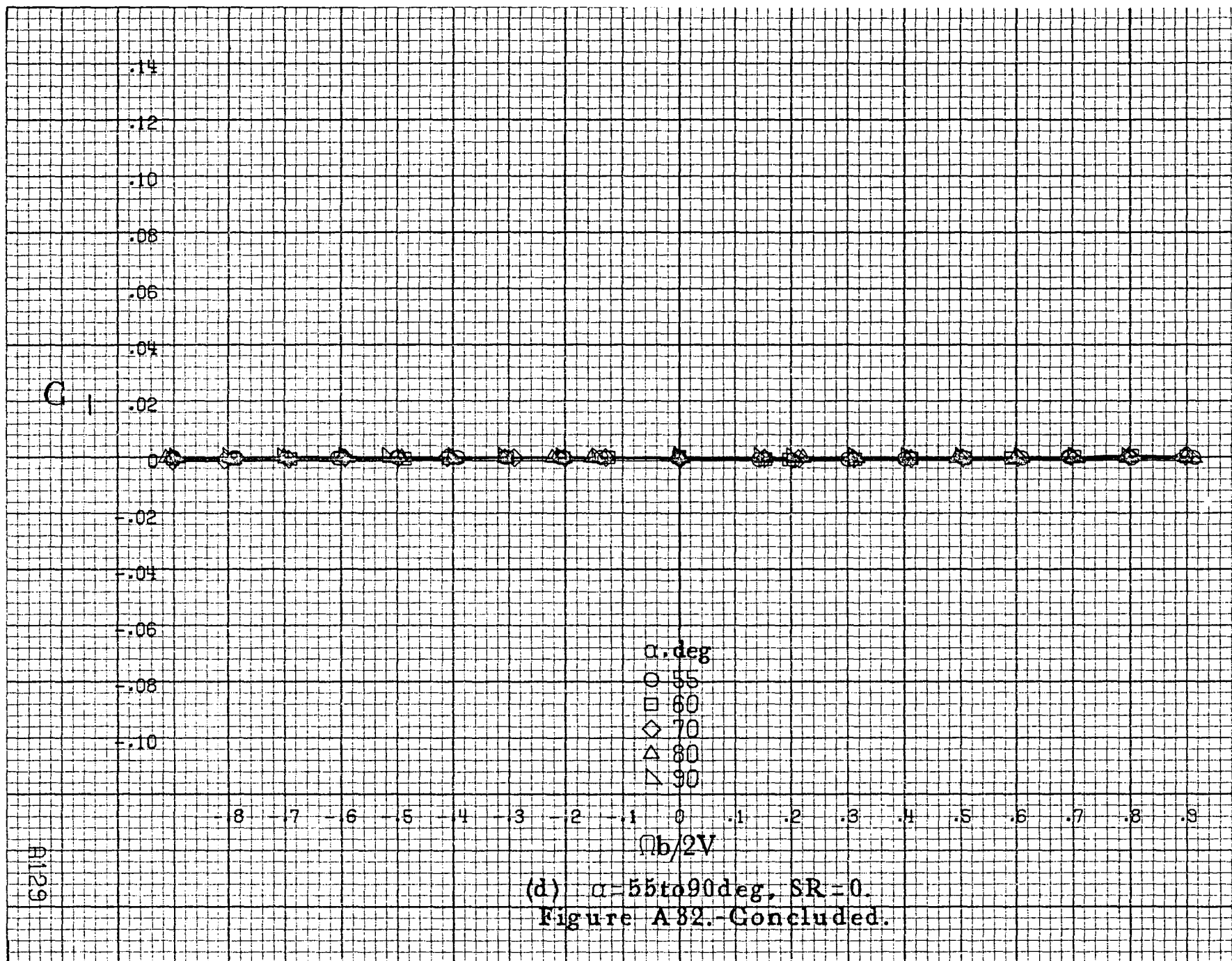
.14
.12
.10
.08
.06
.04
.02
0
-.02
-.04
-.06
-.08
-.10

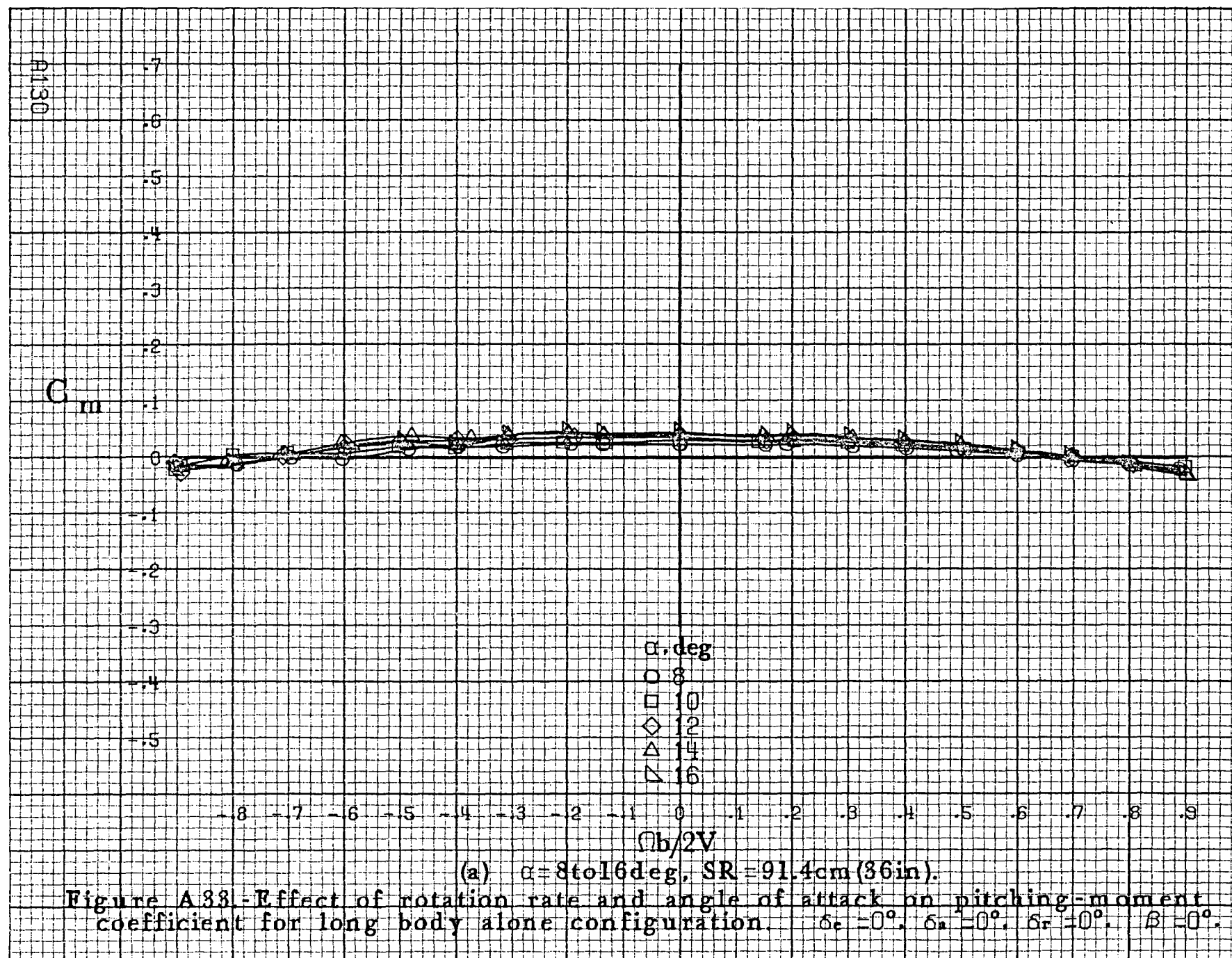
α, deg
○ 30
□ 35
◇ 40
△ 45
▽ 50

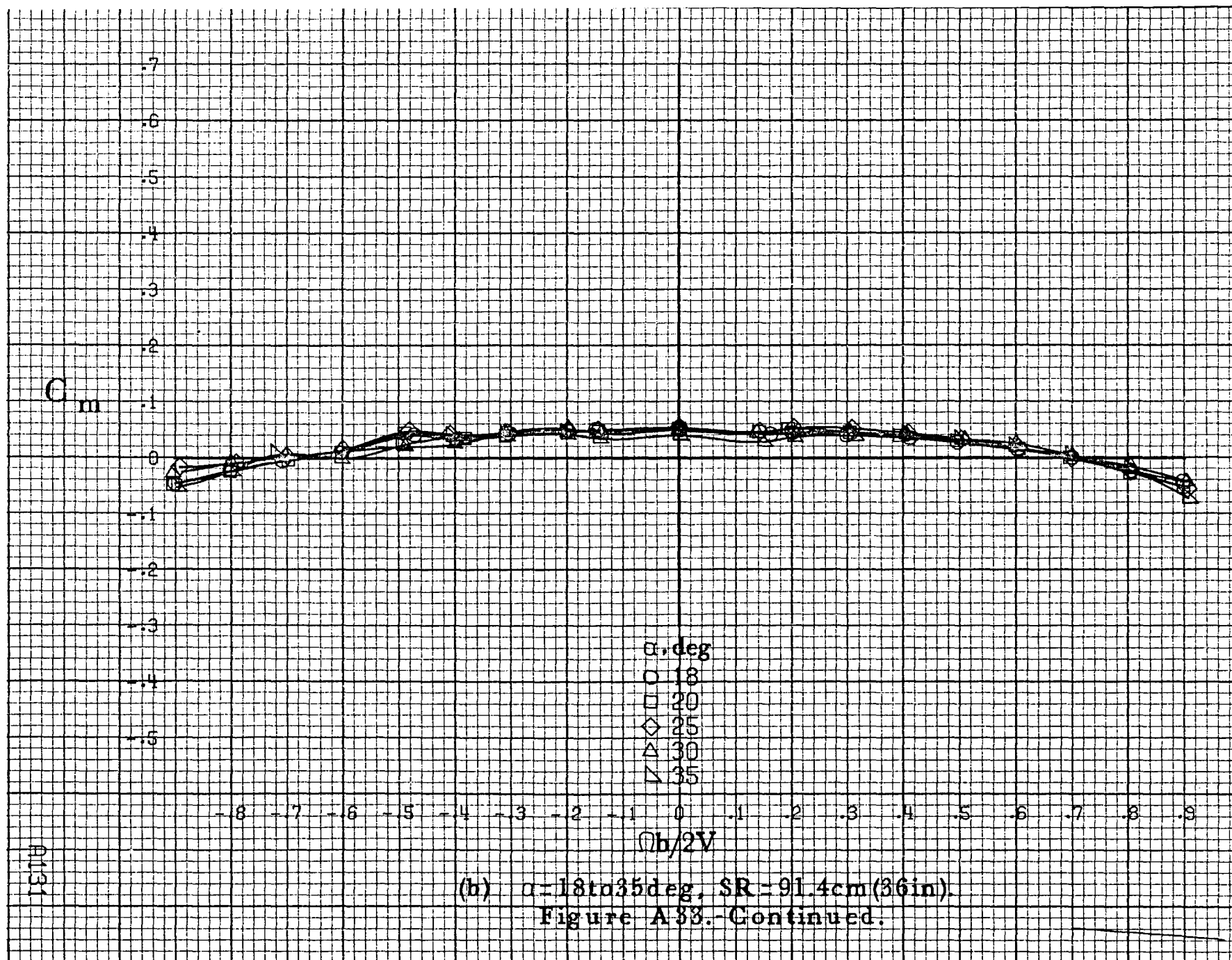
-.8 -.7 -.6 -.5 -.4 -.3 -.2 -.1 0 .1 .2 .3 .4 .5 .6 .7 .8 .9

 $Ob/2V$

(c) $\alpha=30\text{ to }50\text{ deg, SR}=0$.
Figure A 82.-Continued.







C_m

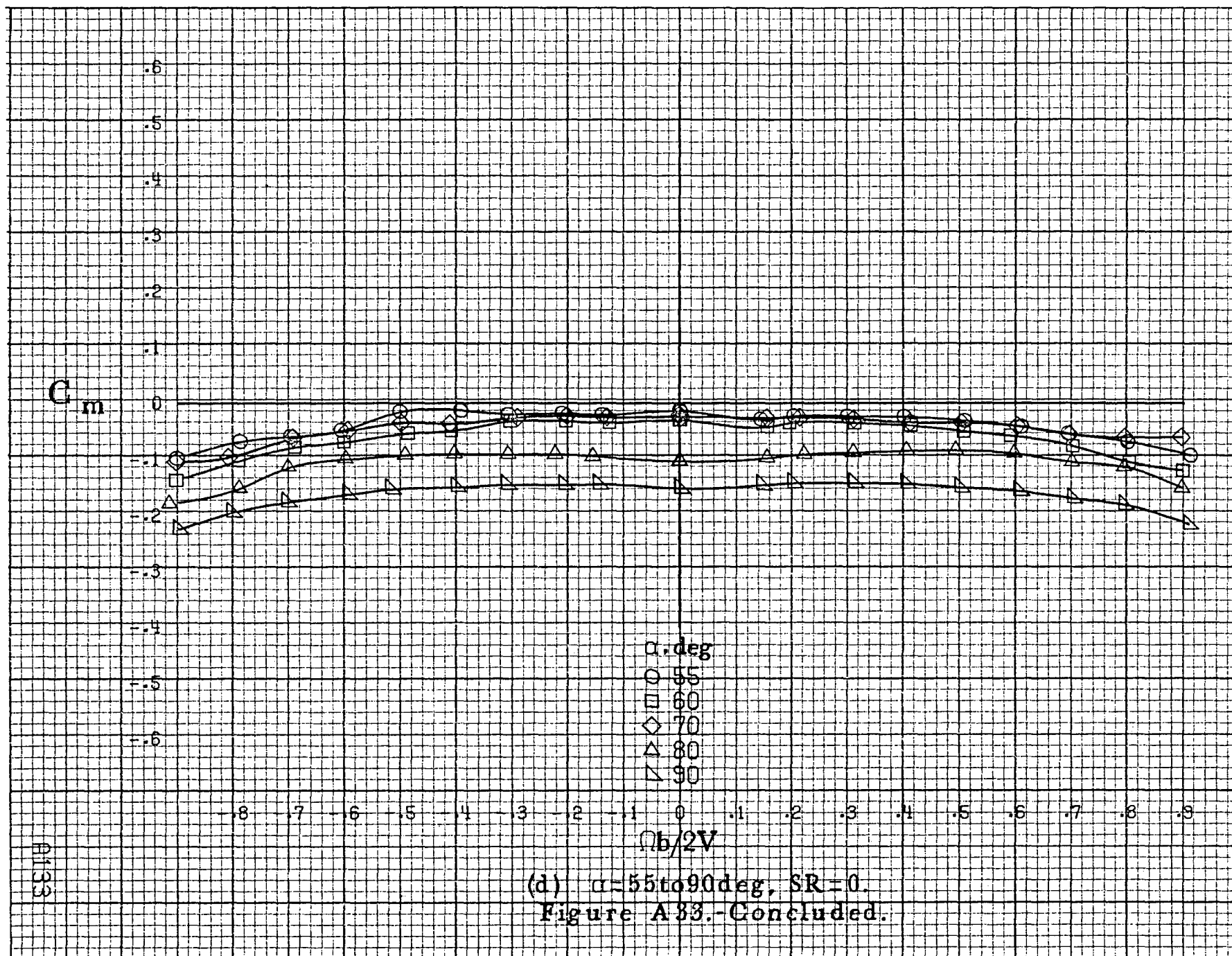
.7
.6
.5
.4
.3
.2
.1
0
-.1
-.2
-.3
-.4
-.5

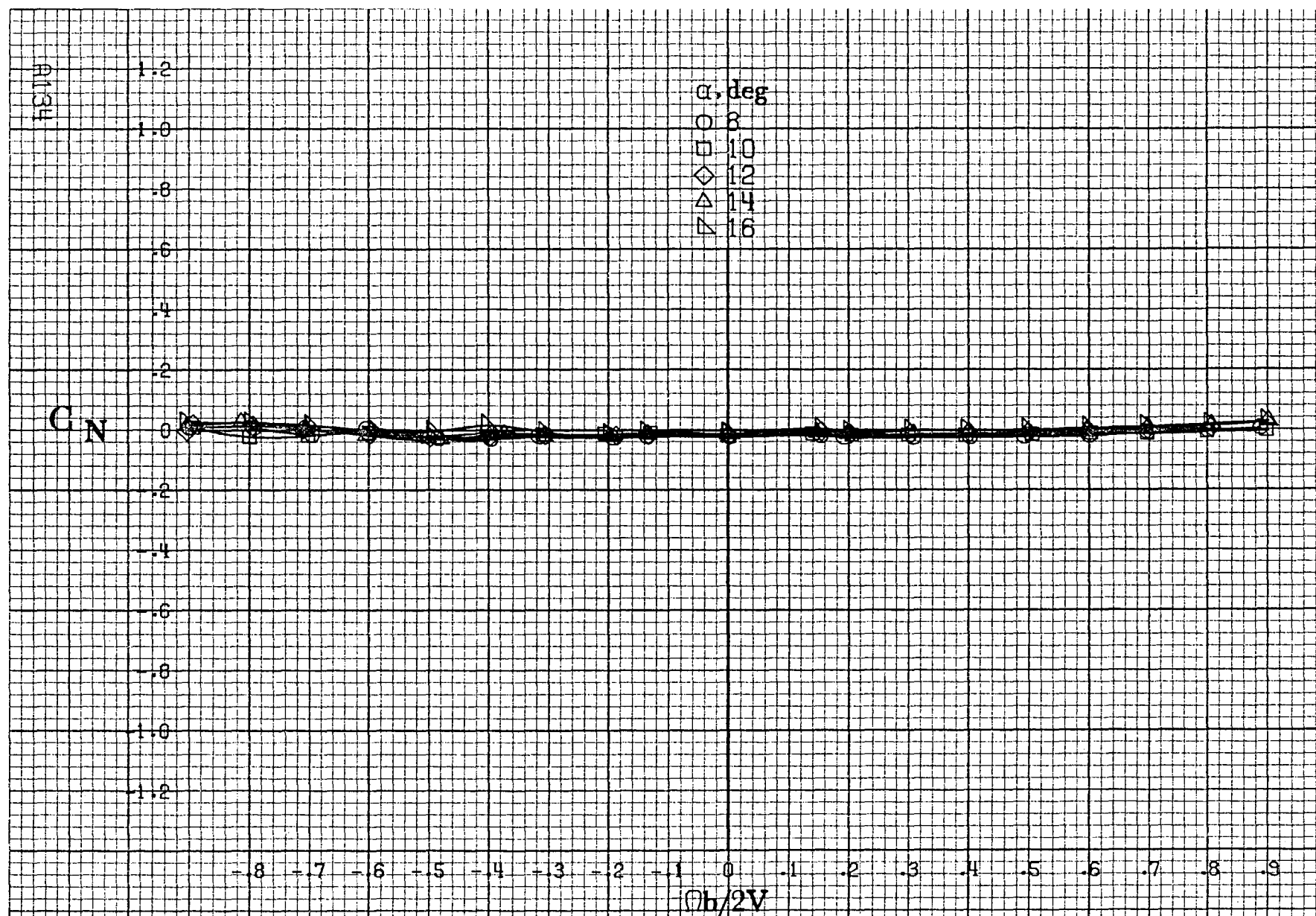
α, deg
○ 30
□ 35
◇ 40
△ 45
▽ 50

-.8 -.7 -.6 -.5 -.4 -.3 -.2 -.1 0 .1 .2 .3 .4 .5 .6 .7 .8 .9

 $b/2V$

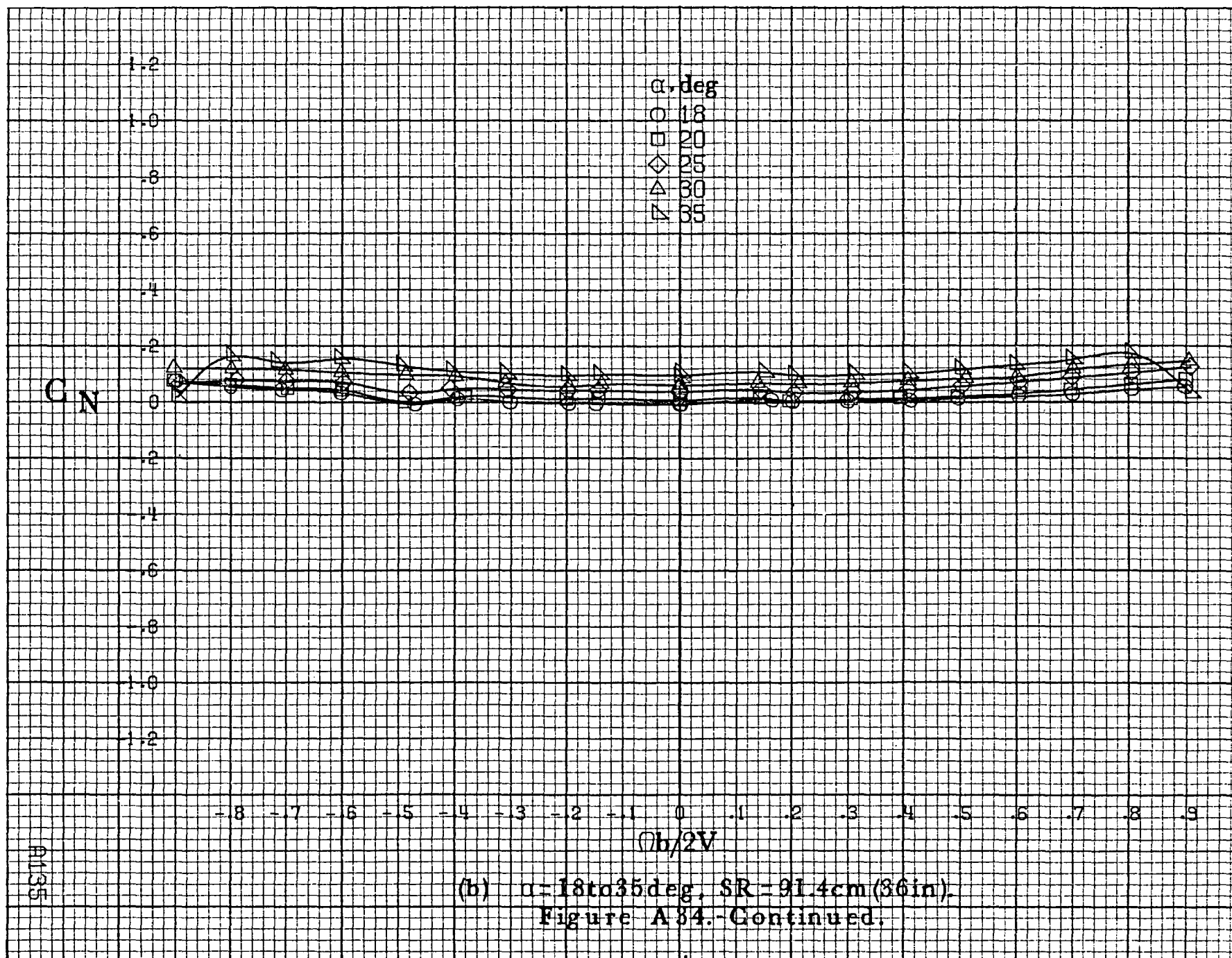
(c) $\alpha=30$ to 50 deg. $SR=0$.
Figure A33.-Continued.

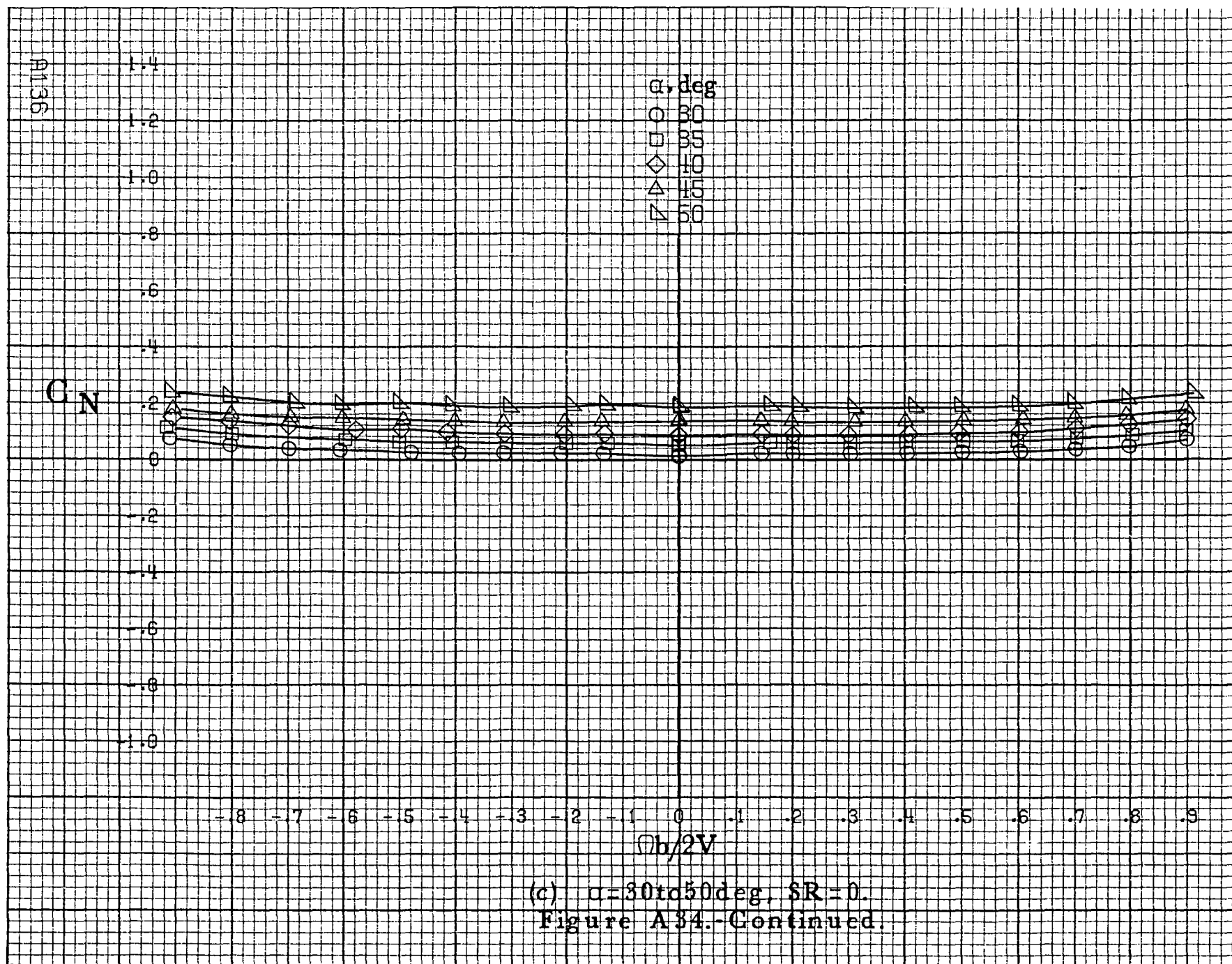


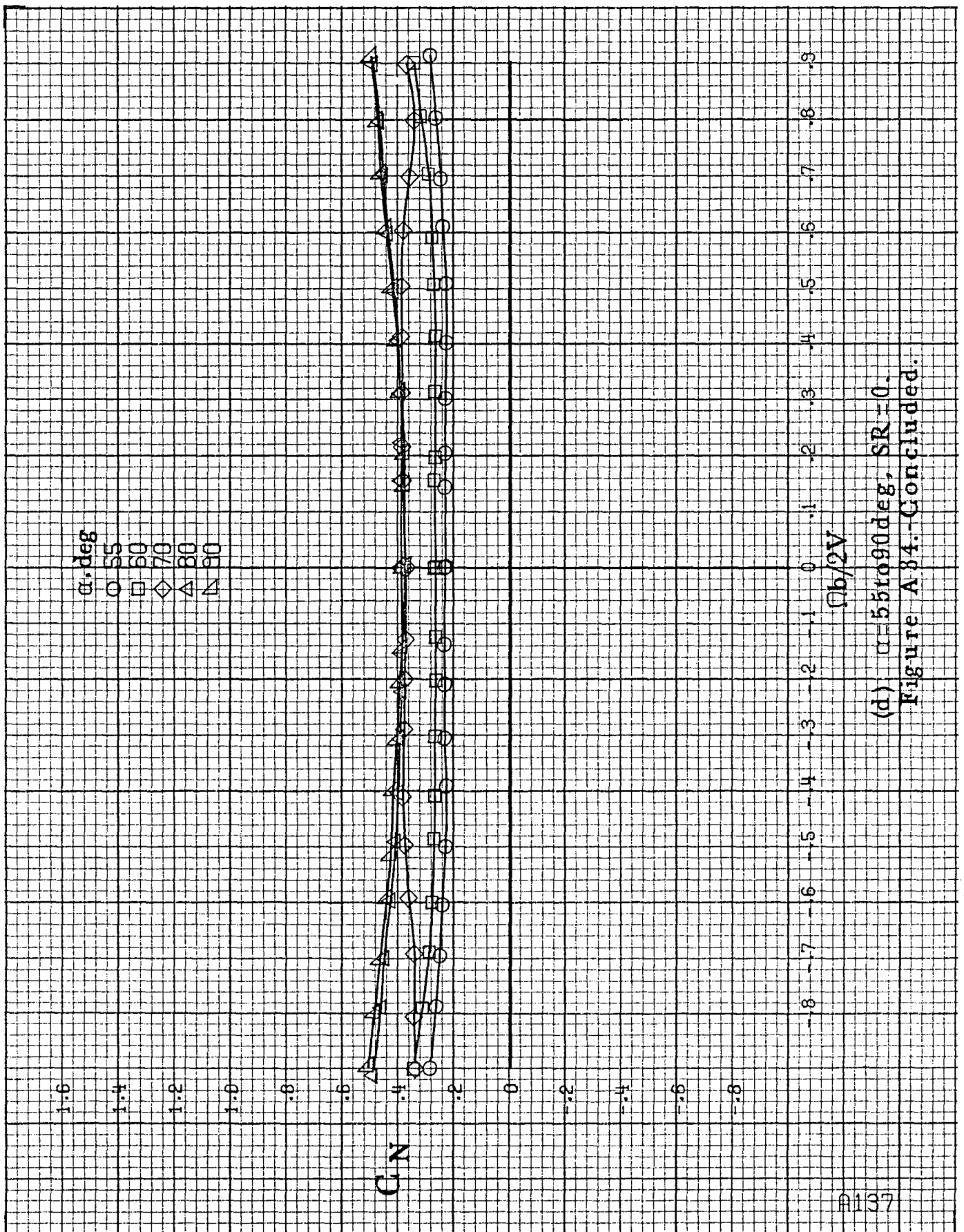


(a) $\alpha=8$ to 16° , $SR=91.4\text{cm}(36\text{in})$.

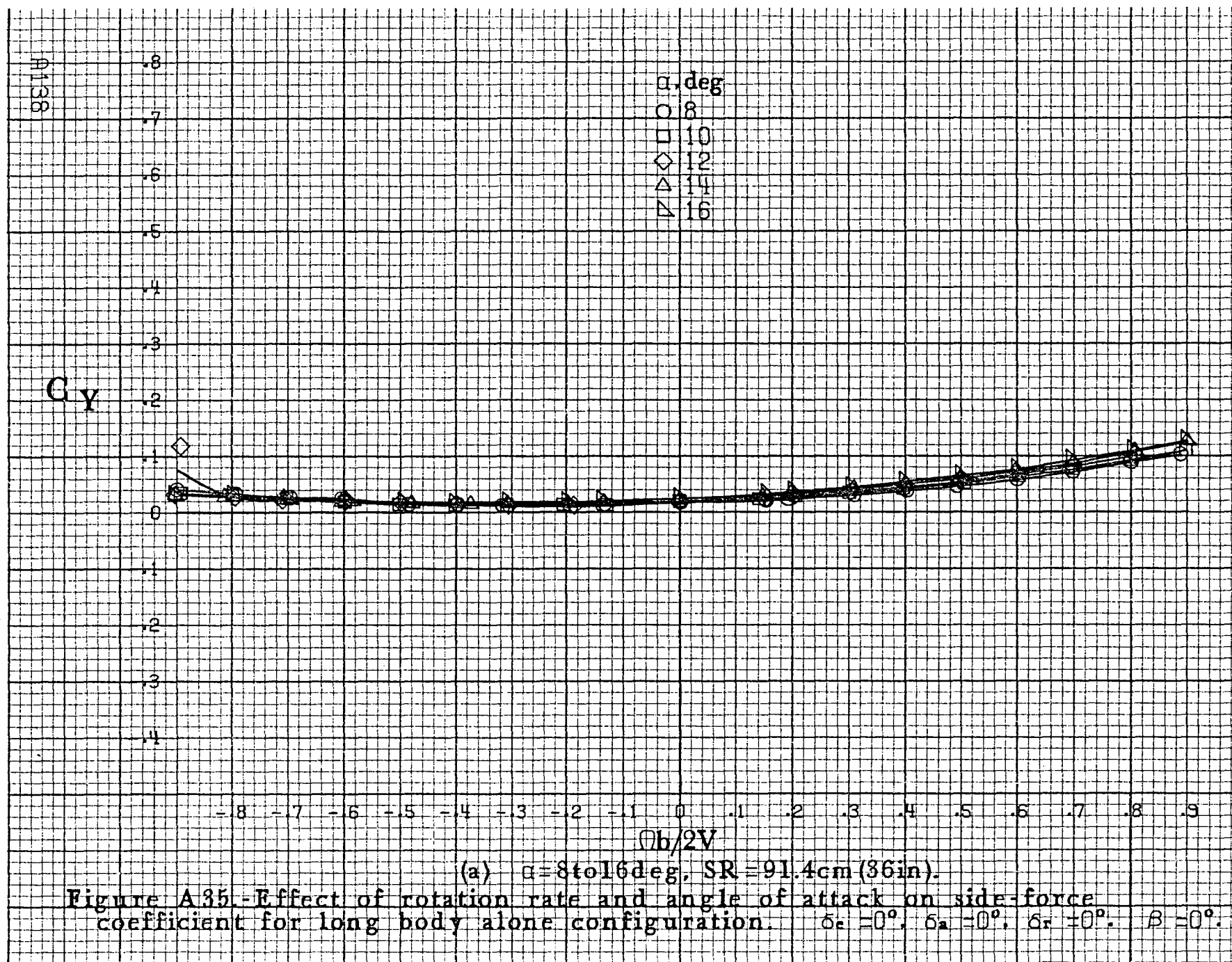
Figure A34 - Effect of rotation rate and angle of attack on normal-force coefficient for long body alone configuration. $\delta_c=0^\circ$, $\delta_a=0^\circ$, $\delta_r=0^\circ$, $\beta=0^\circ$.

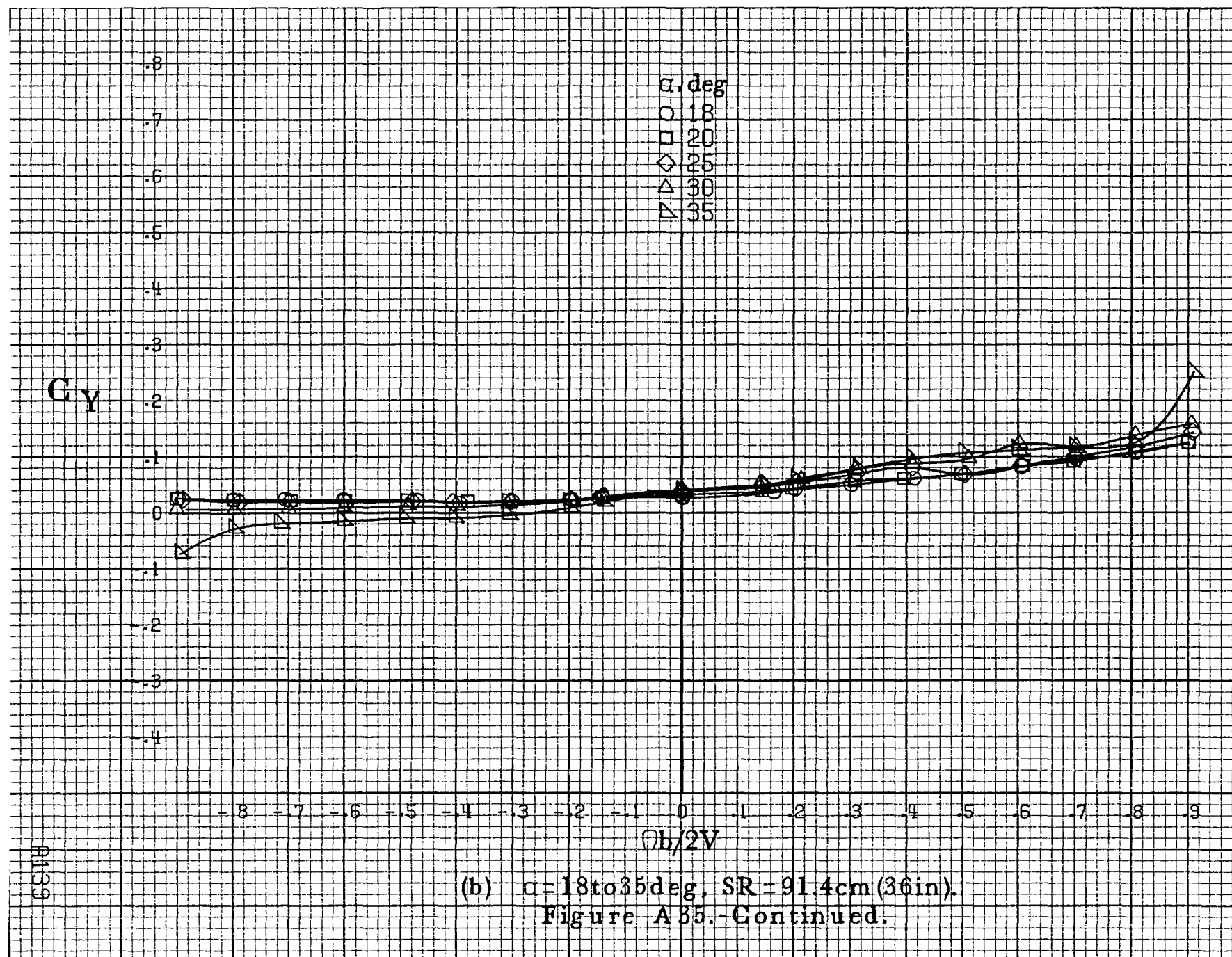


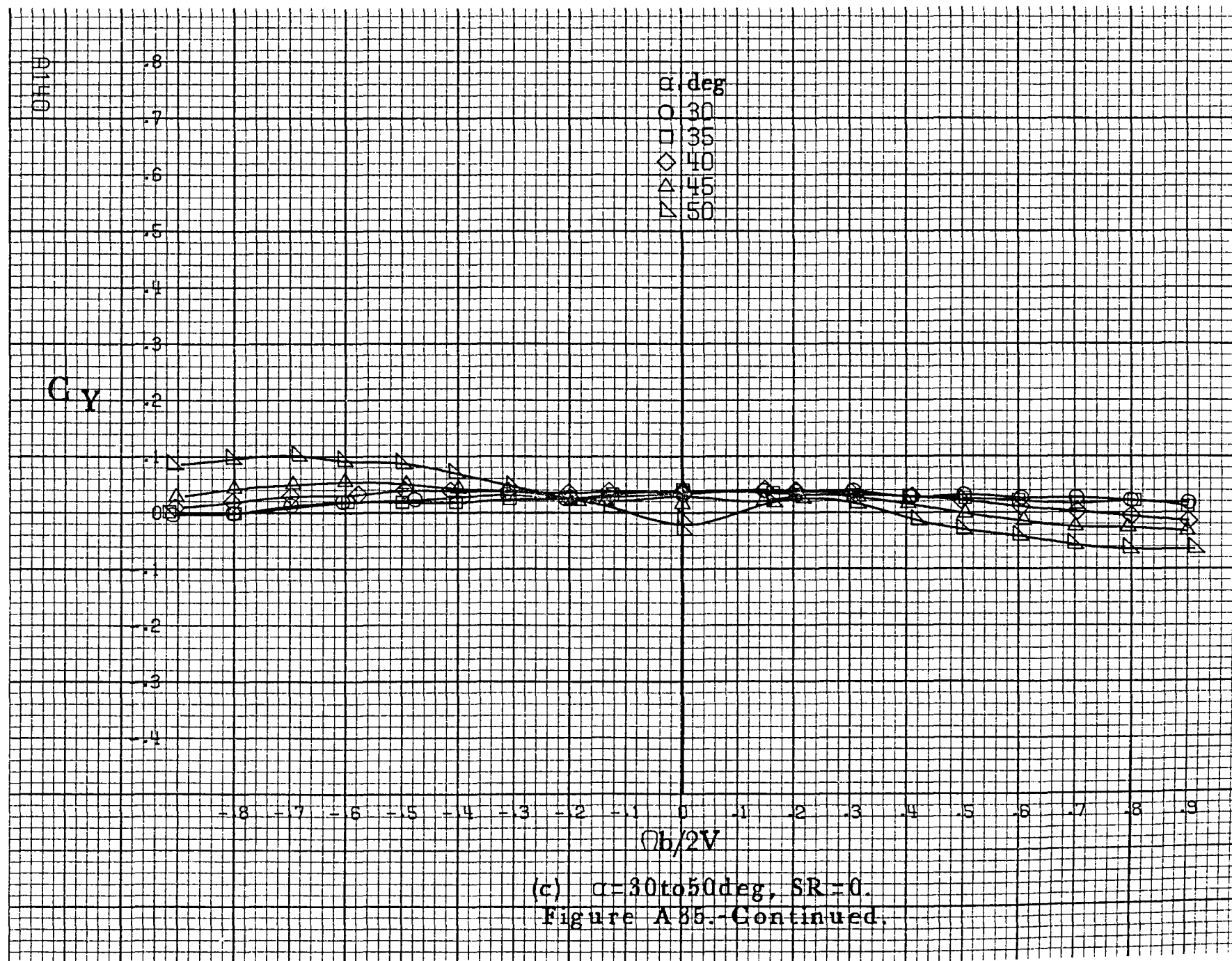


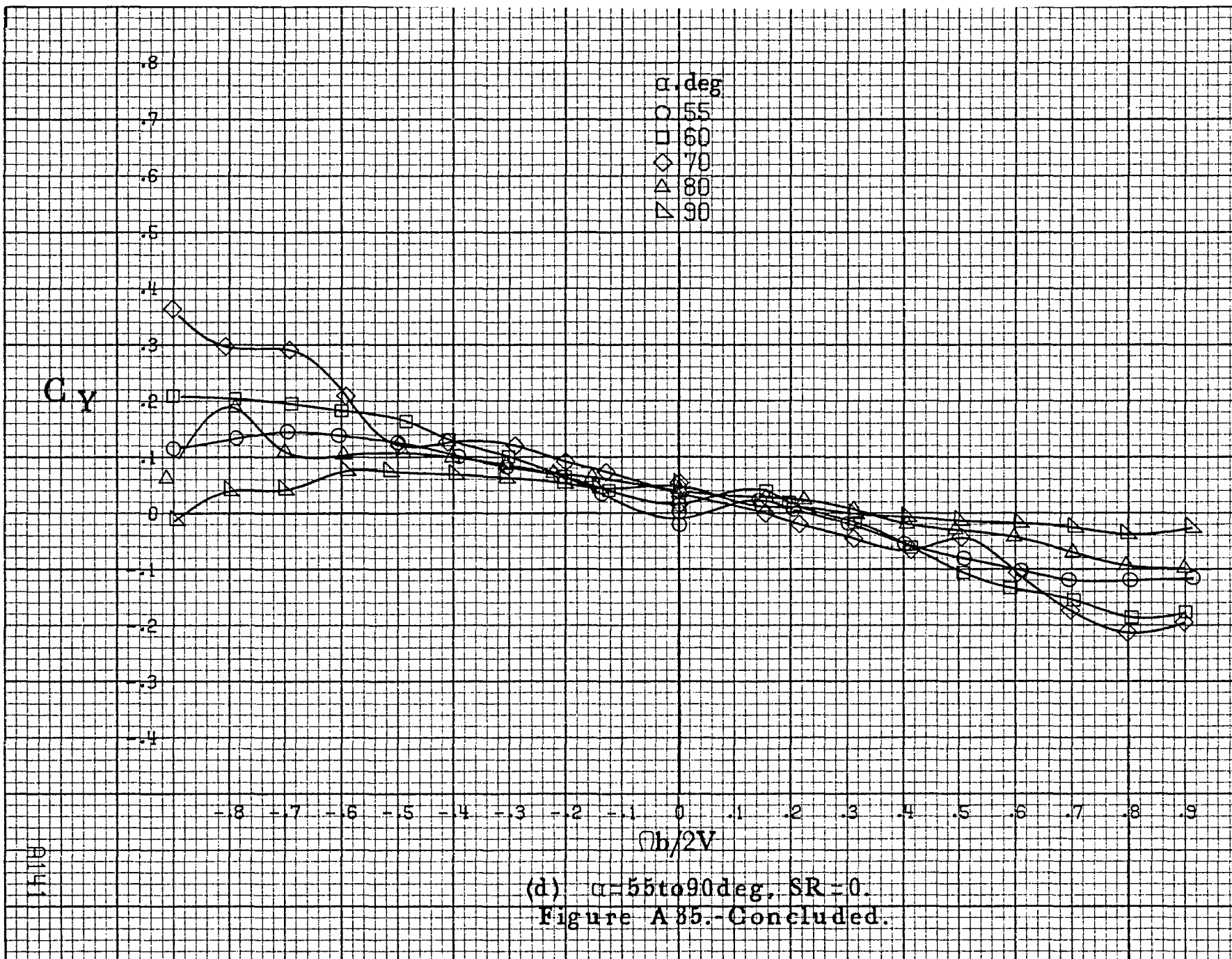


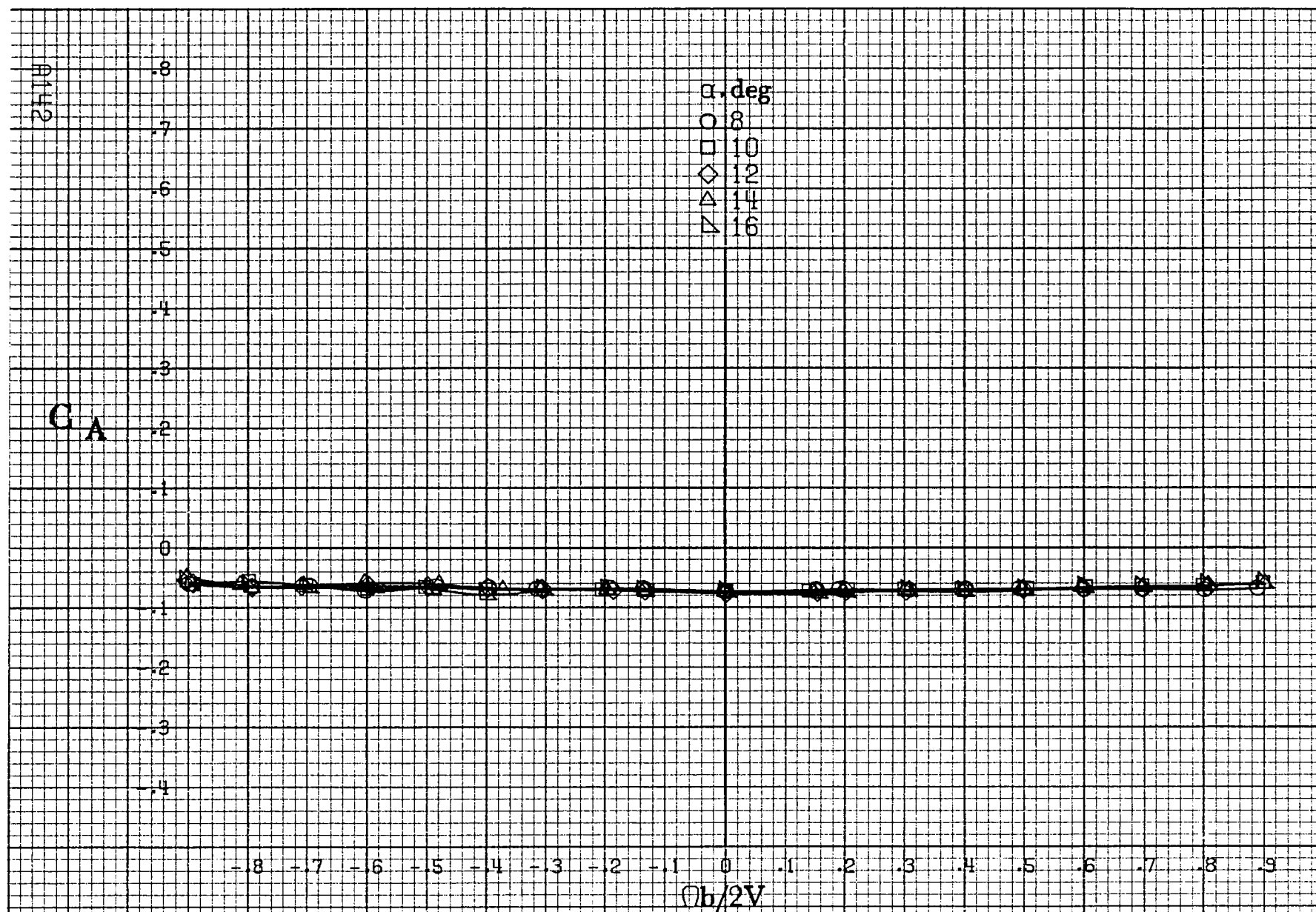
(d) $\alpha=55$ to 90° , $SR=0$.
Figure A 84.-Concluded.





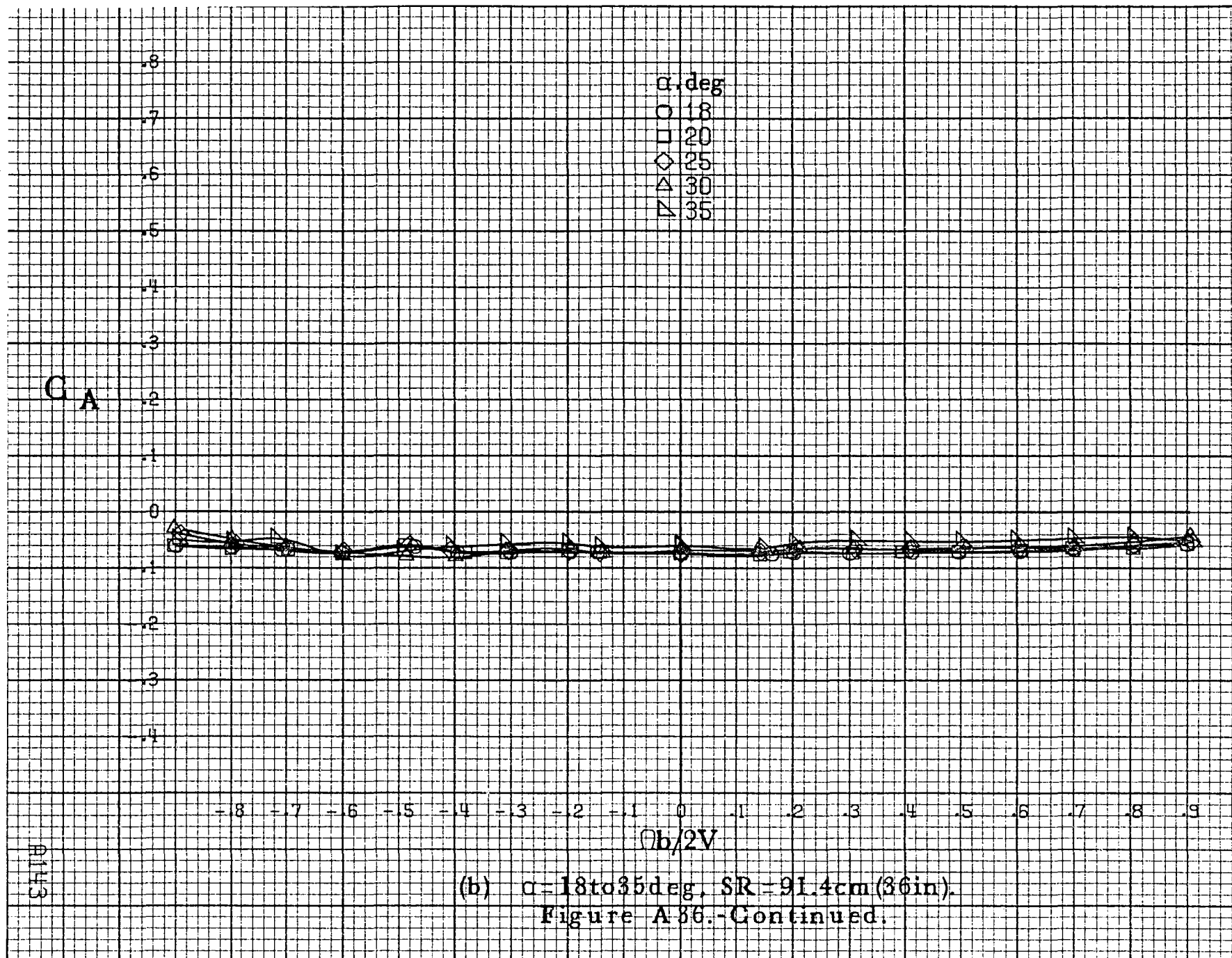


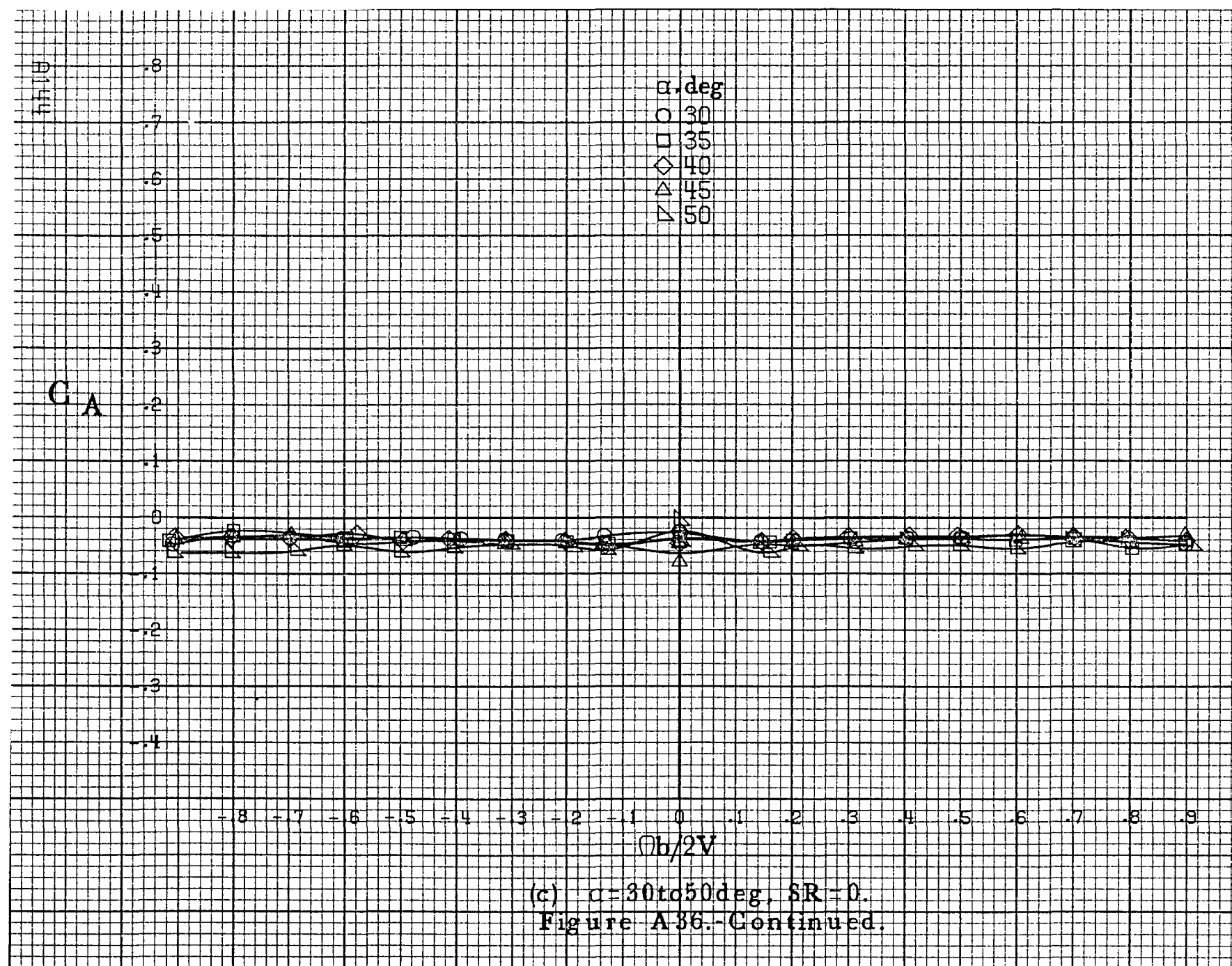


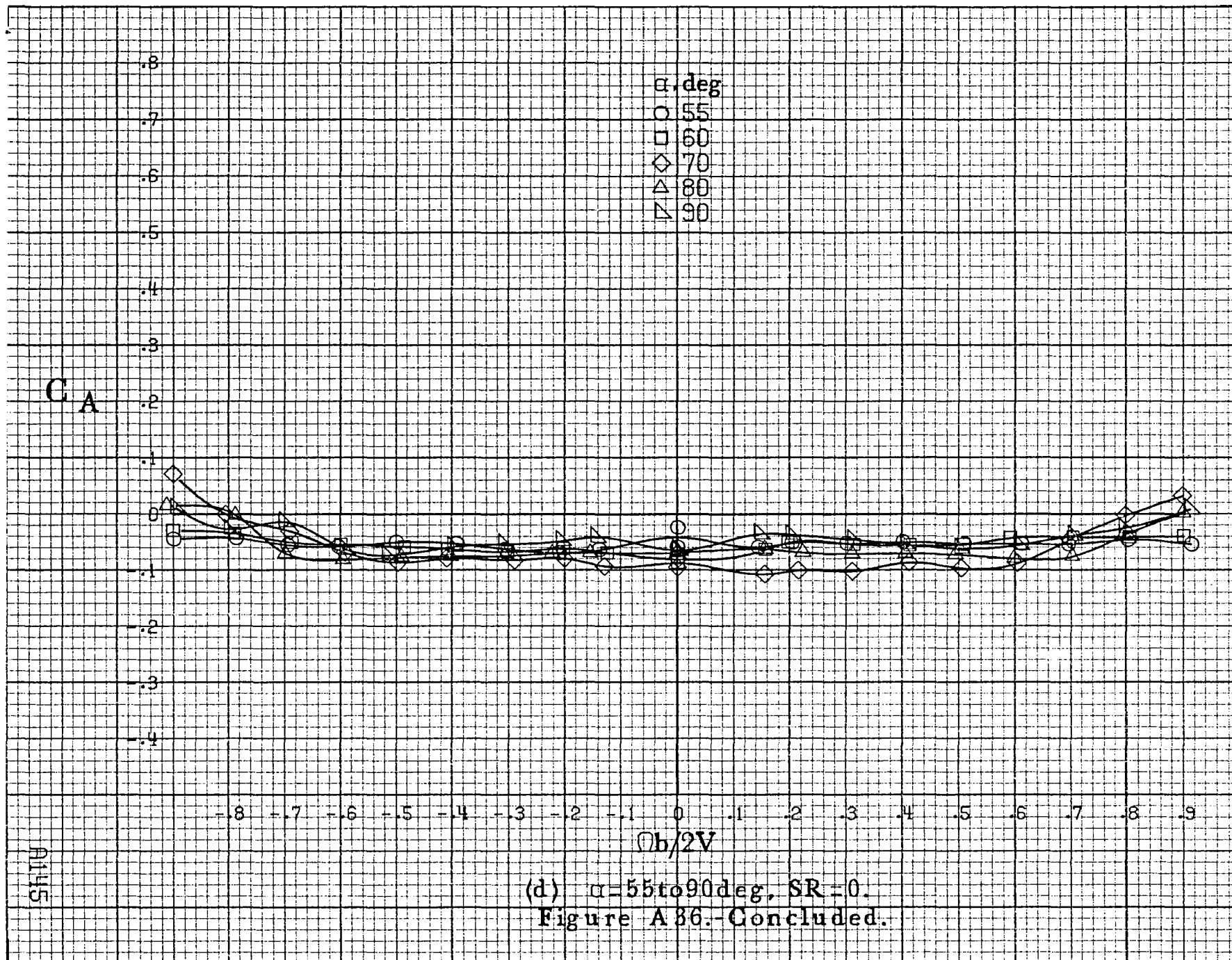


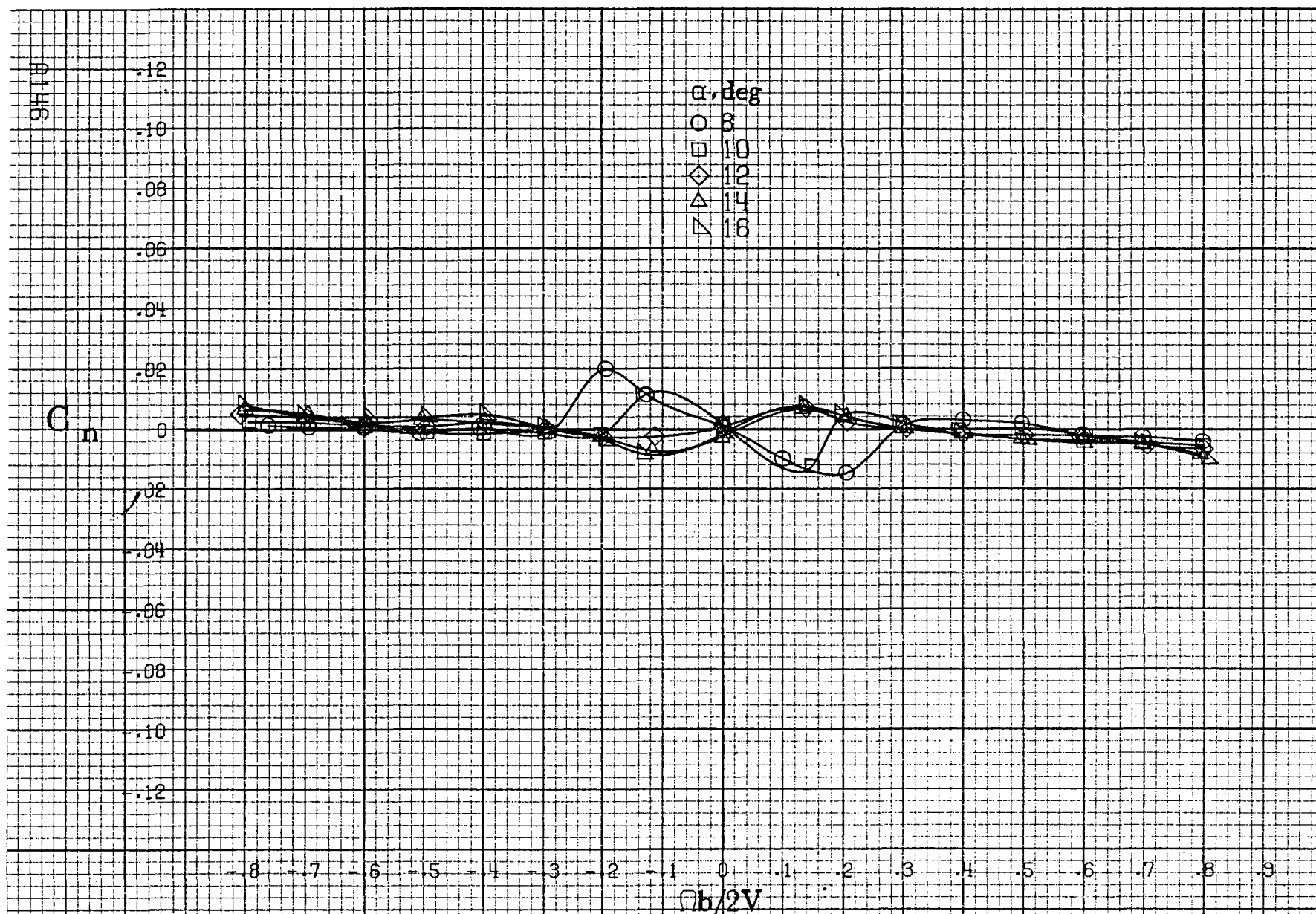
(a) $\alpha=8$ to 16° , $SR=91.4\text{cm}(36\text{in})$.

Figure A36.-Effect of rotation rate and angle of attack on axial-force coefficient for long body alone configuration. $\delta_c=0^\circ$, $\delta_a=0^\circ$, $\delta_r=0^\circ$, $\beta=0^\circ$.



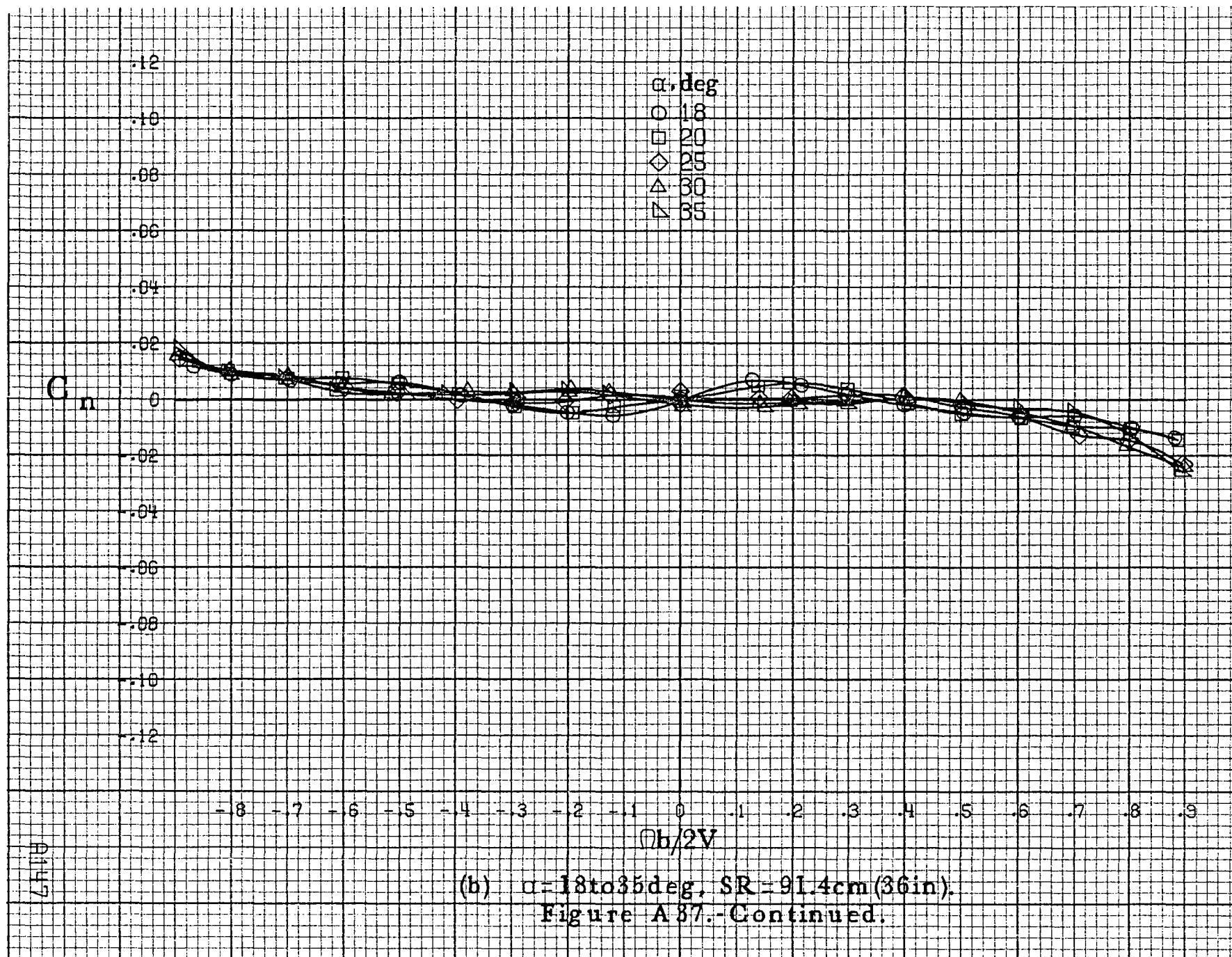






(a) $\alpha = 8$ to 16° , $SR = 91.4\text{cm}$ (36in).

Figure A37 - Effect of rotation rate and angle of attack on yawing-moment coefficient for long body, low wing configuration. $\delta_e = 0^\circ$, $\delta_a = 0^\circ$, $\delta_r = 0^\circ$, $\beta = 0^\circ$.



0418

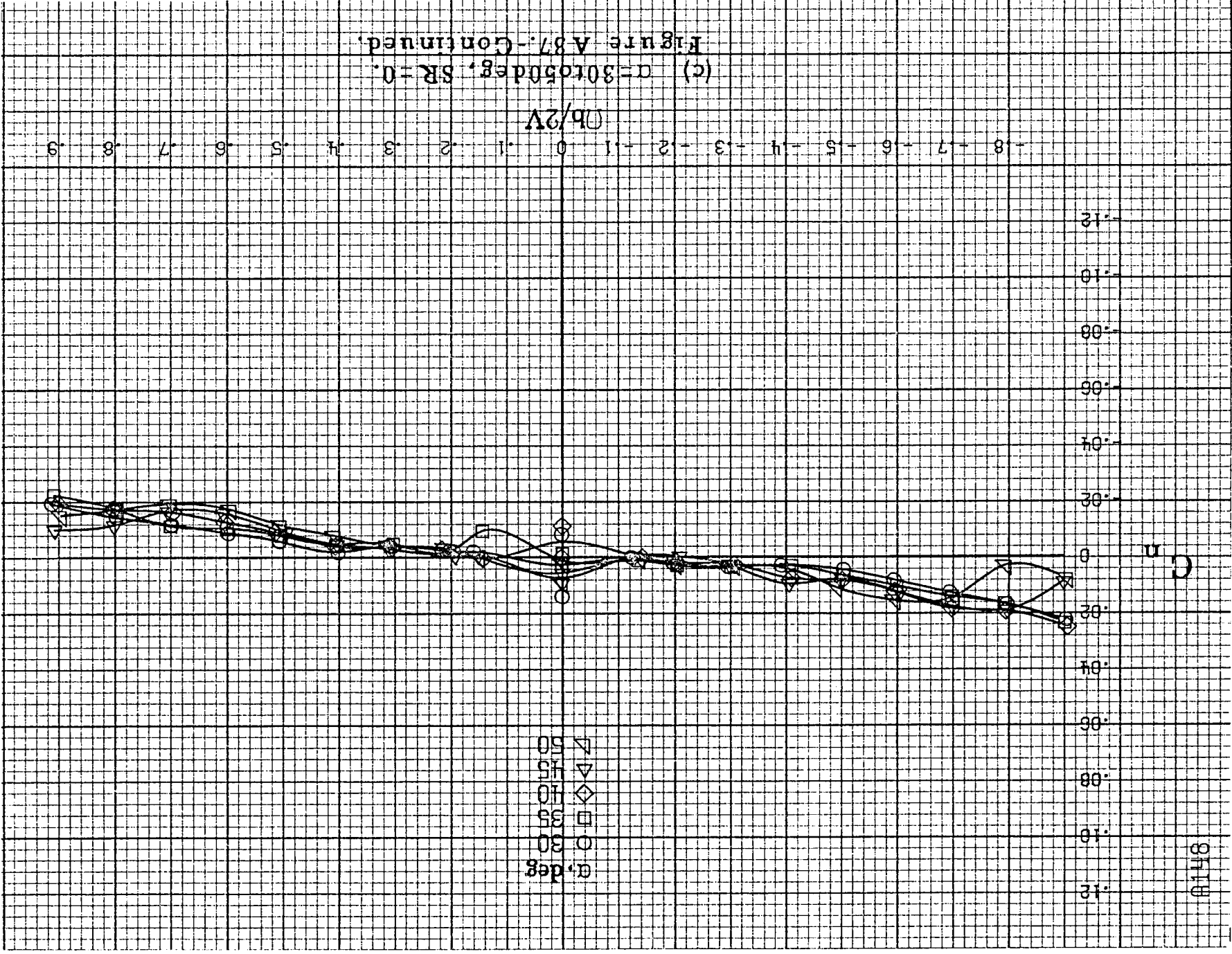
C_n

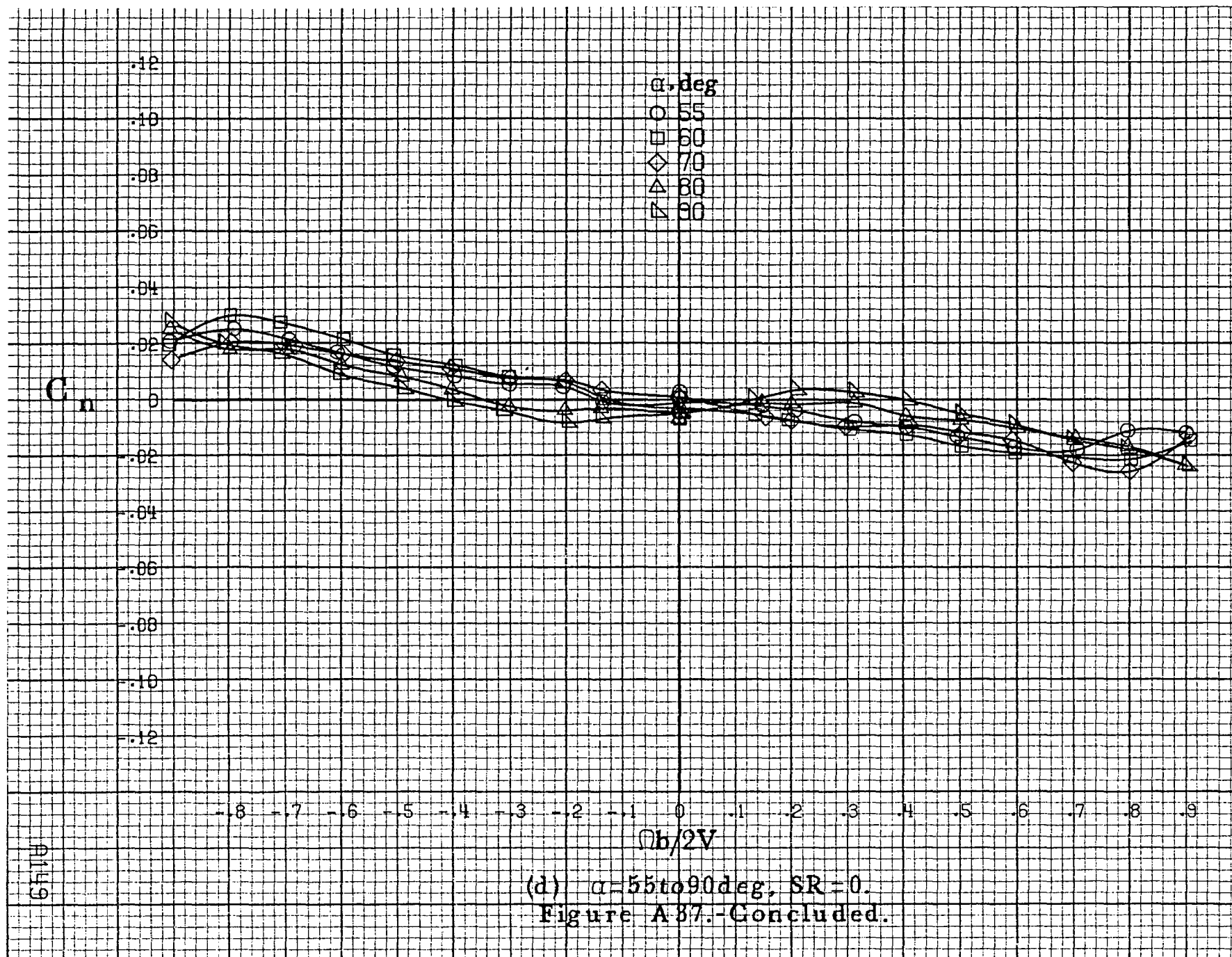
α, deg

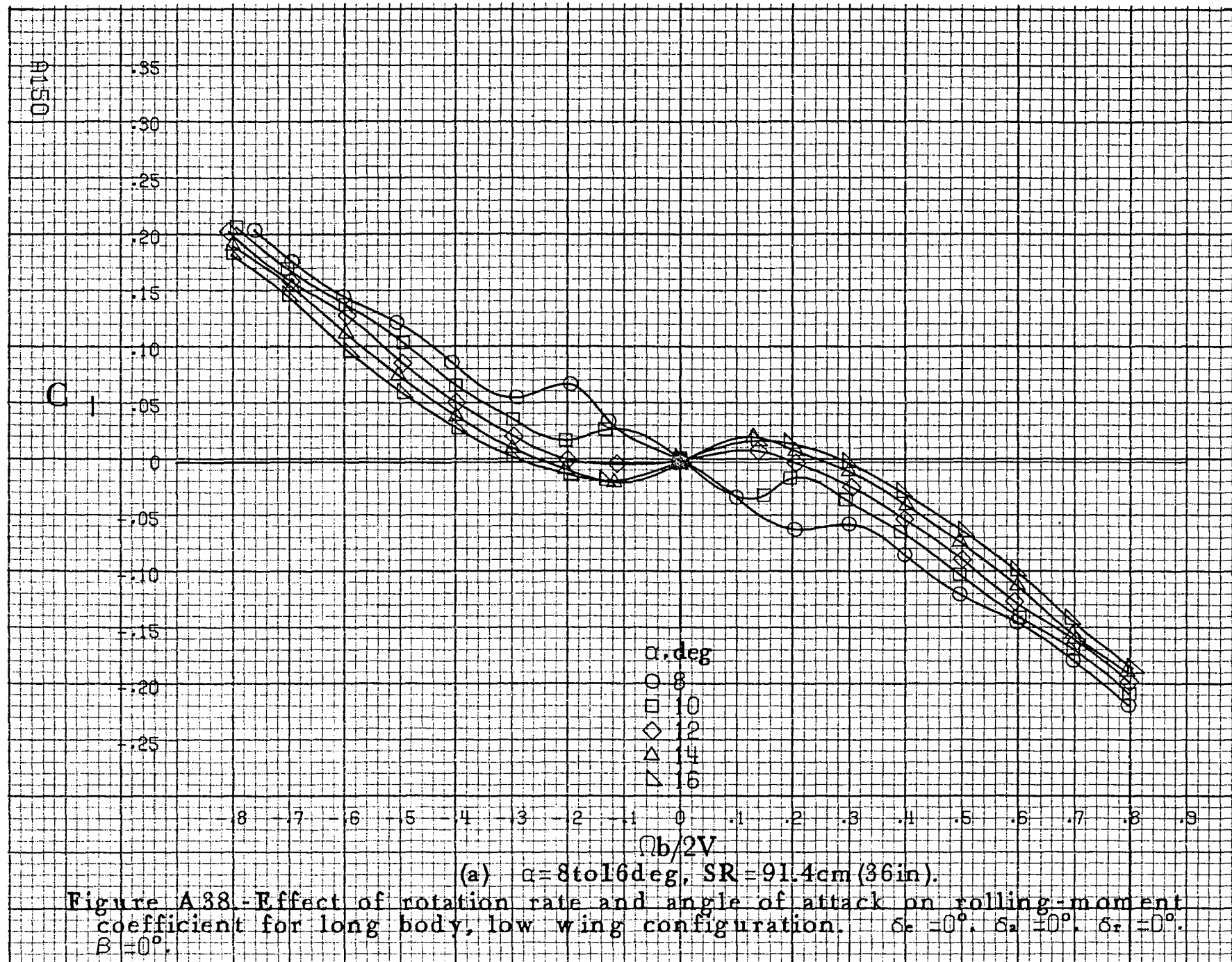
30
35
40
45
50

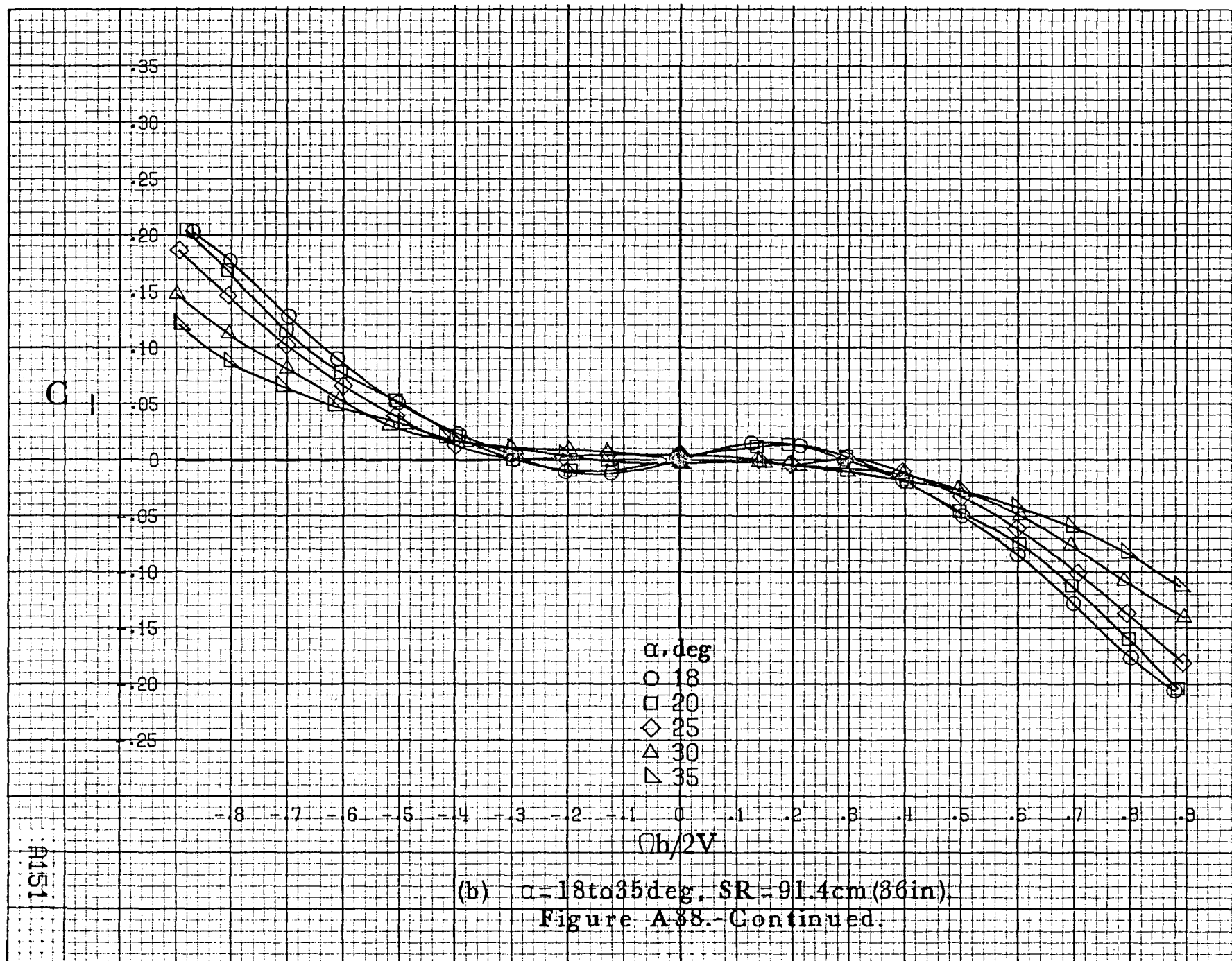
0b/2V

(c) $\alpha=30$ to 50 deg, $SR=0$.
Figure A 87.-Continued.









A152

C₁

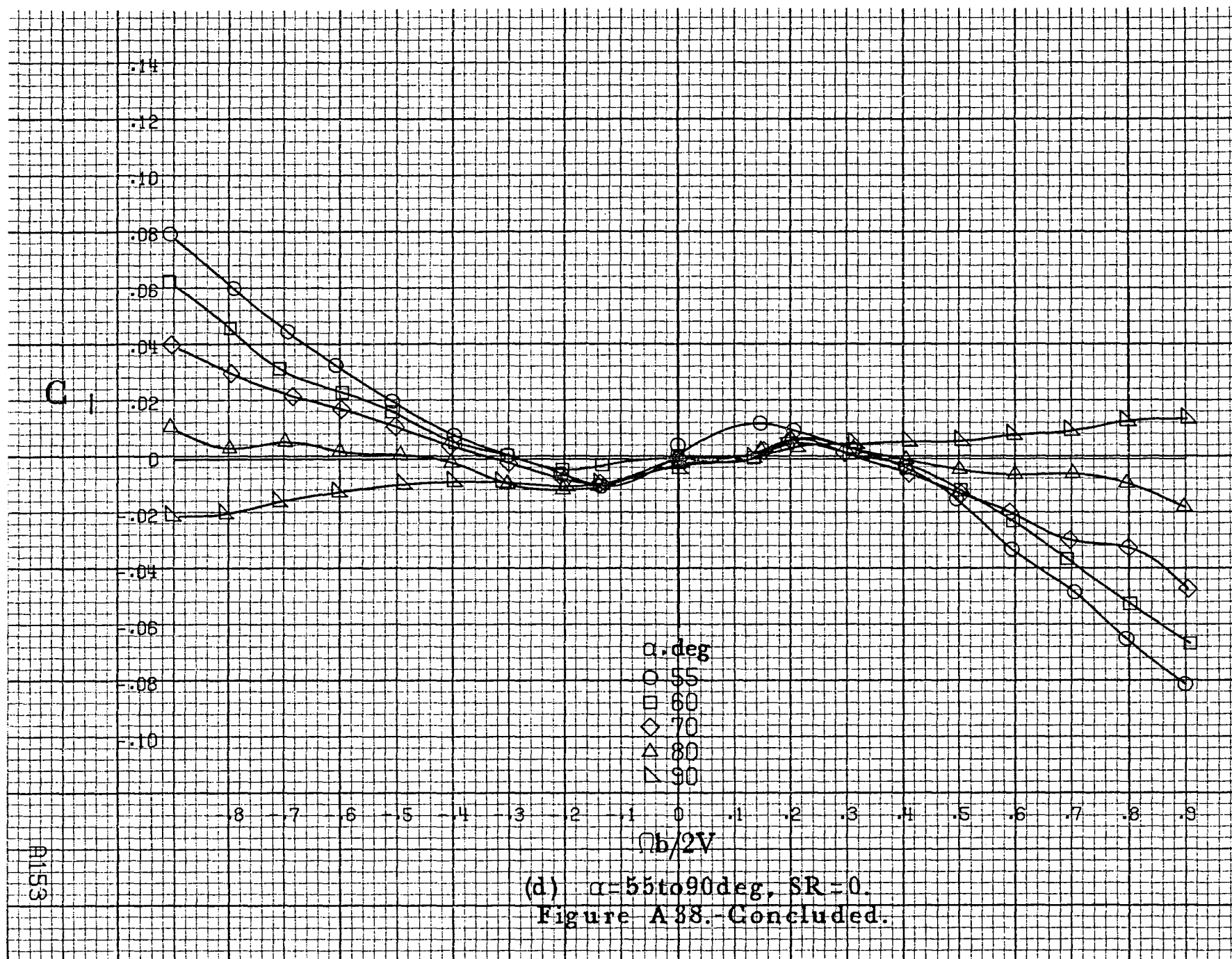
.35
.30
.25
.20
.15
.10
.05
0
-.05
-.10
-.15
-.20
-.25

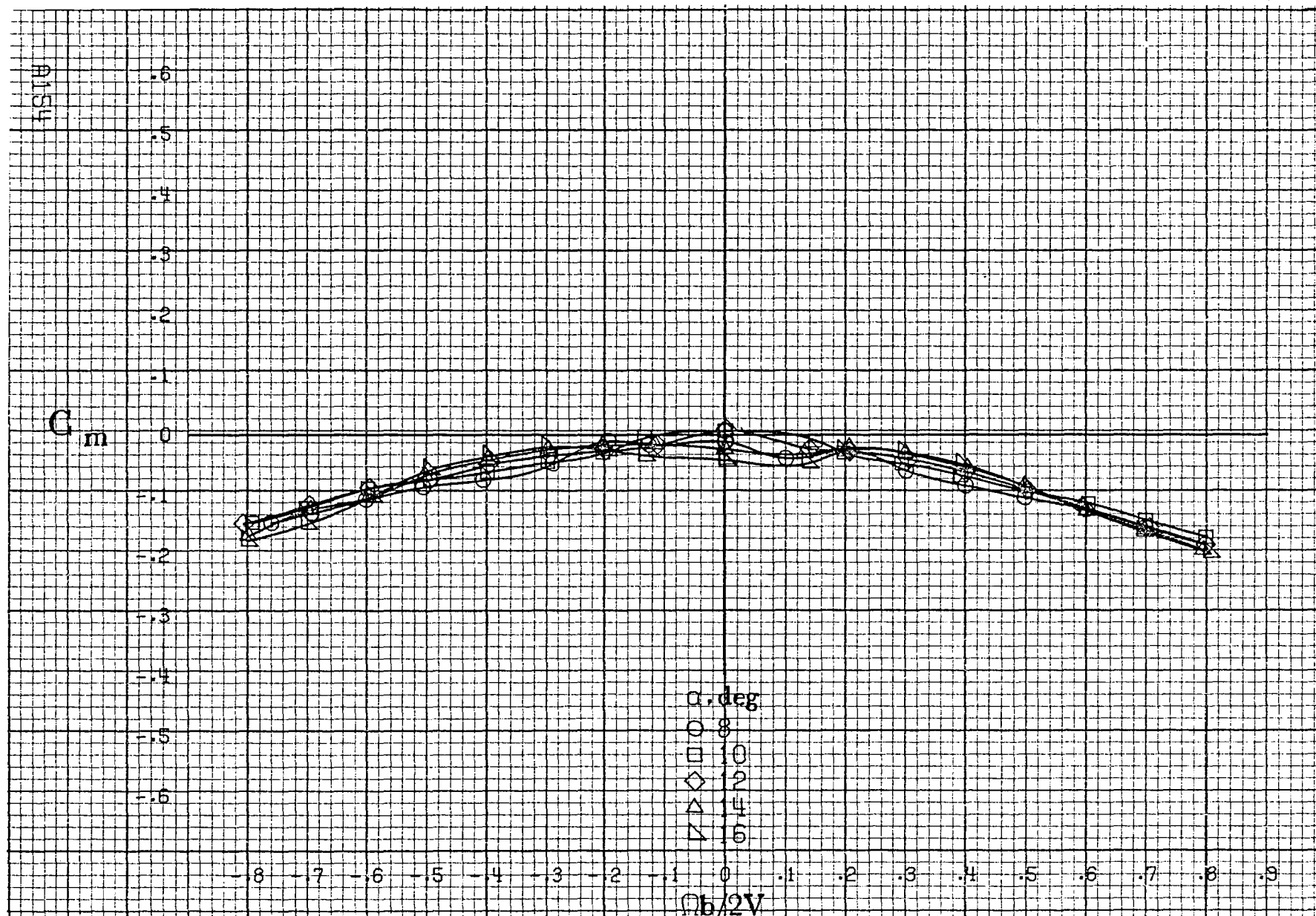
α, deg
○ 30
□ 35
◇ 40
△ 45
▽ 50

 $\Omega b/2V$

(c) $\alpha=30\text{ to }50\text{deg}$, $SR=0$.
Figure A38.-Continued.

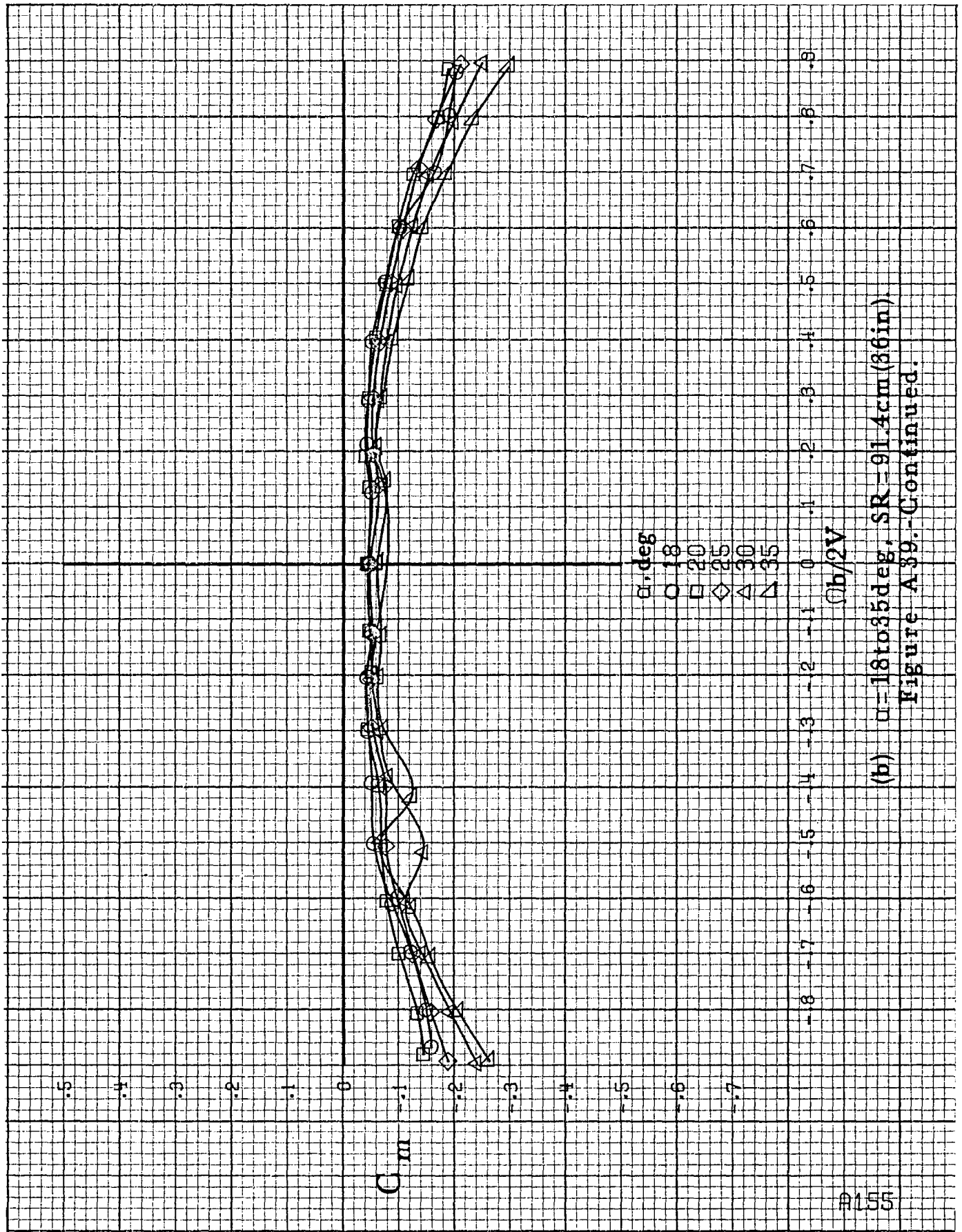
-8 -7 -6 -5 -4 -3 -2 -1 0 .1 .2 .3 .4 .5 .6 .7 .8 .9





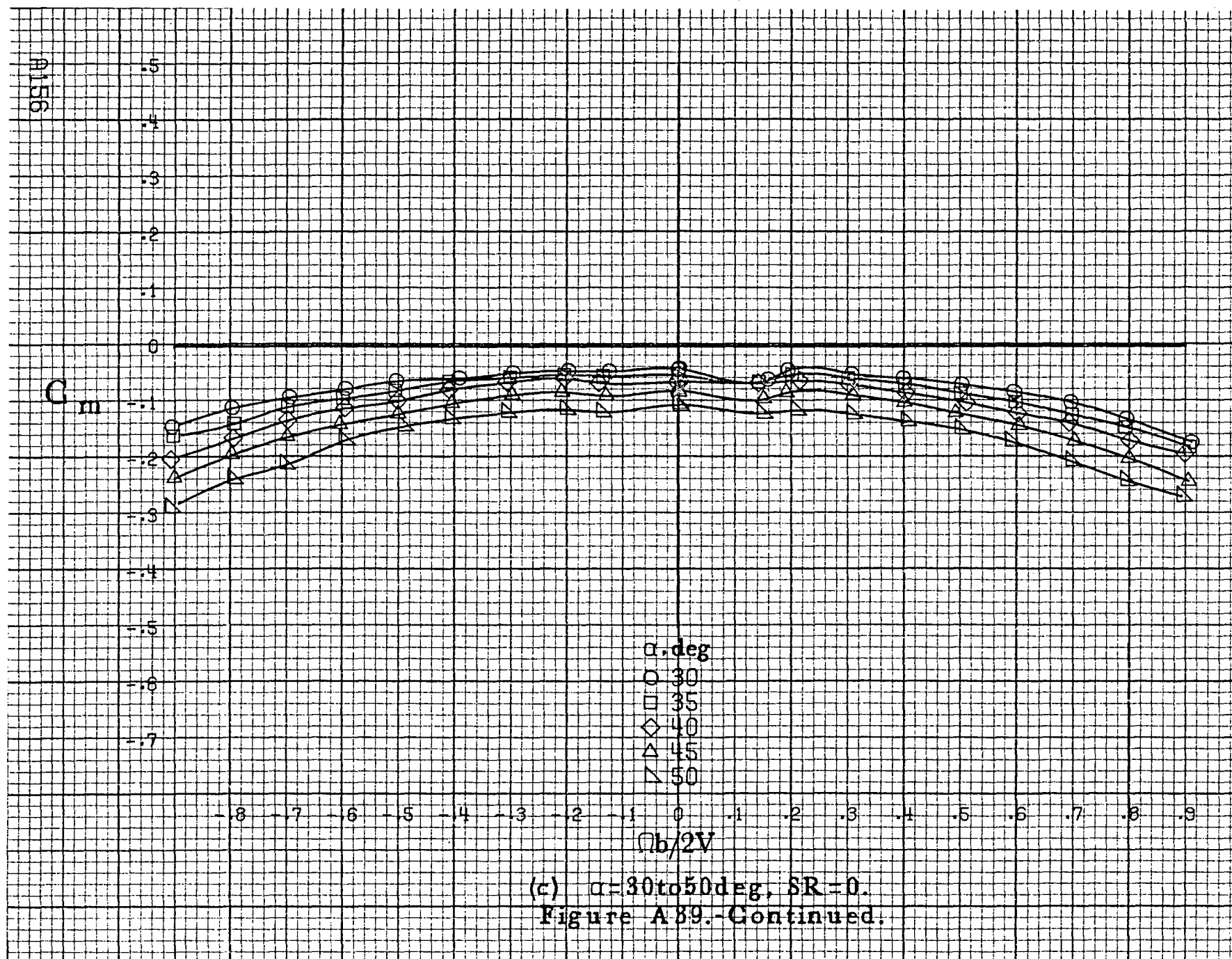
(a) $\alpha = 8$ to 16° , $SR = 91.4\text{cm (36in.)}$.

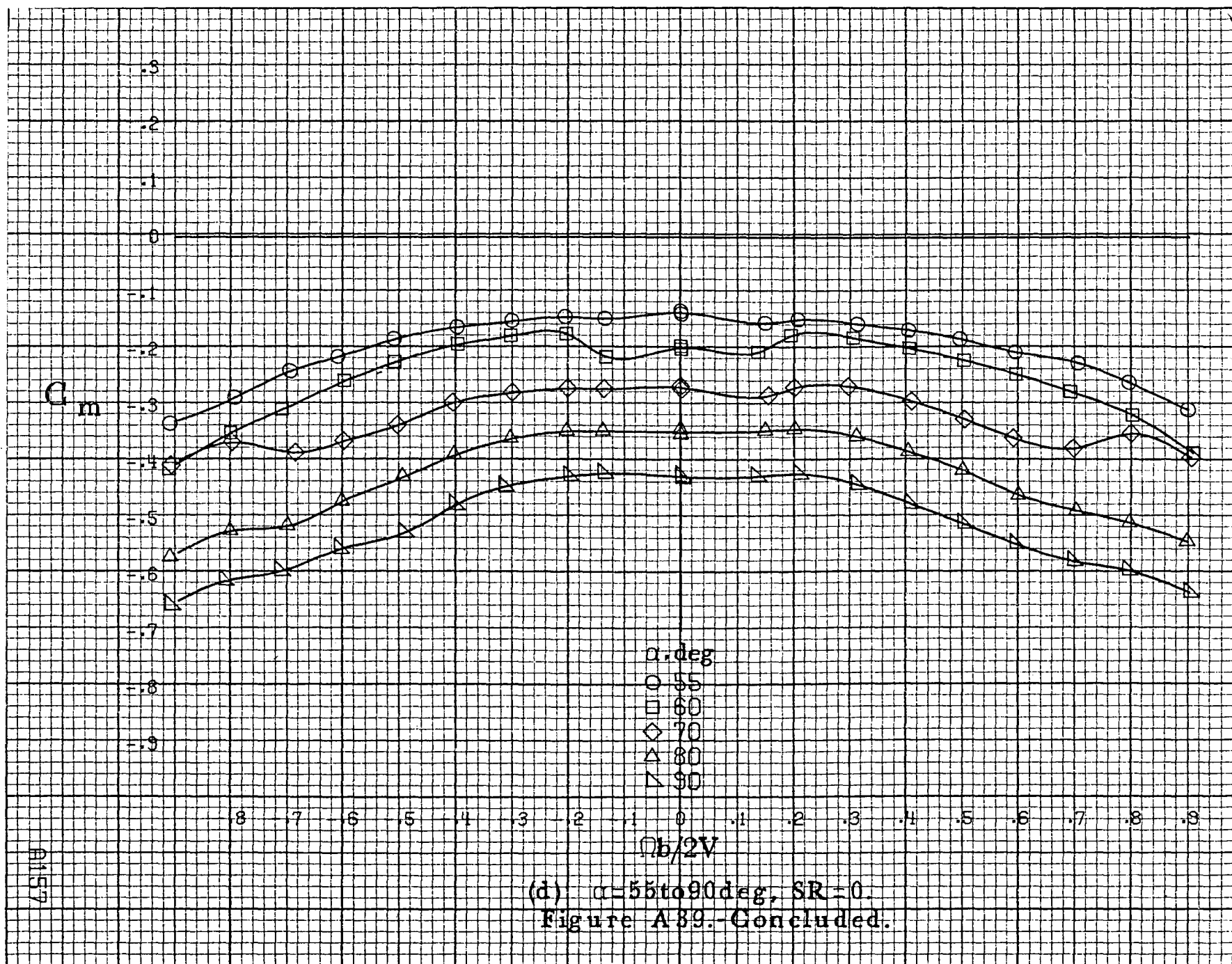
Figure A39.-Effect of rotation rate and angle of attack on pitching-moment coefficient for long body, low wing configuration. $\delta_e = 0^\circ$, $\delta_a = 0^\circ$, $\delta_r = 0^\circ$, $\beta = 0^\circ$.

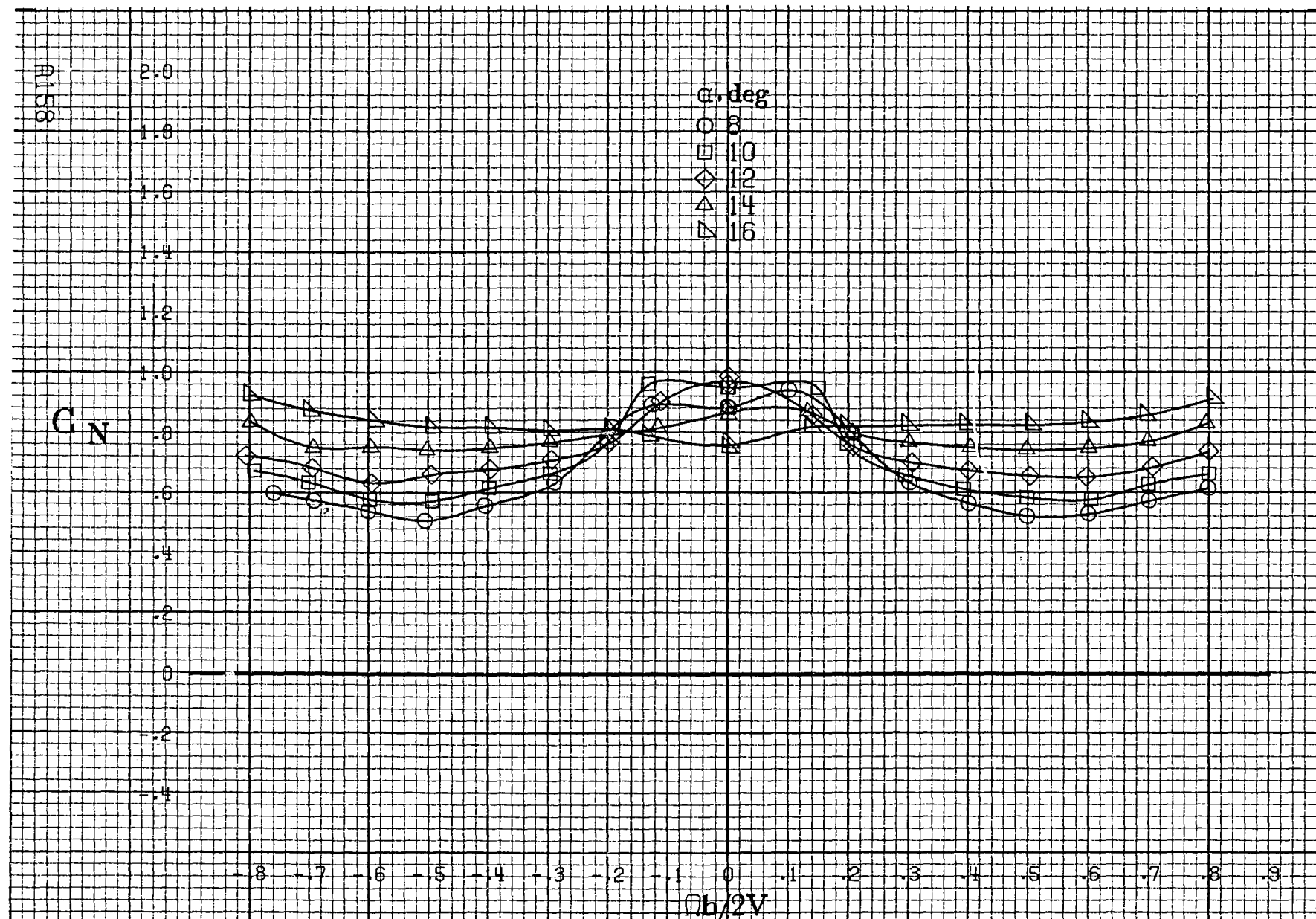


(b) $\alpha=18$ to 35° , SR-91.4cm (36in).

Figure A39.-Continued.

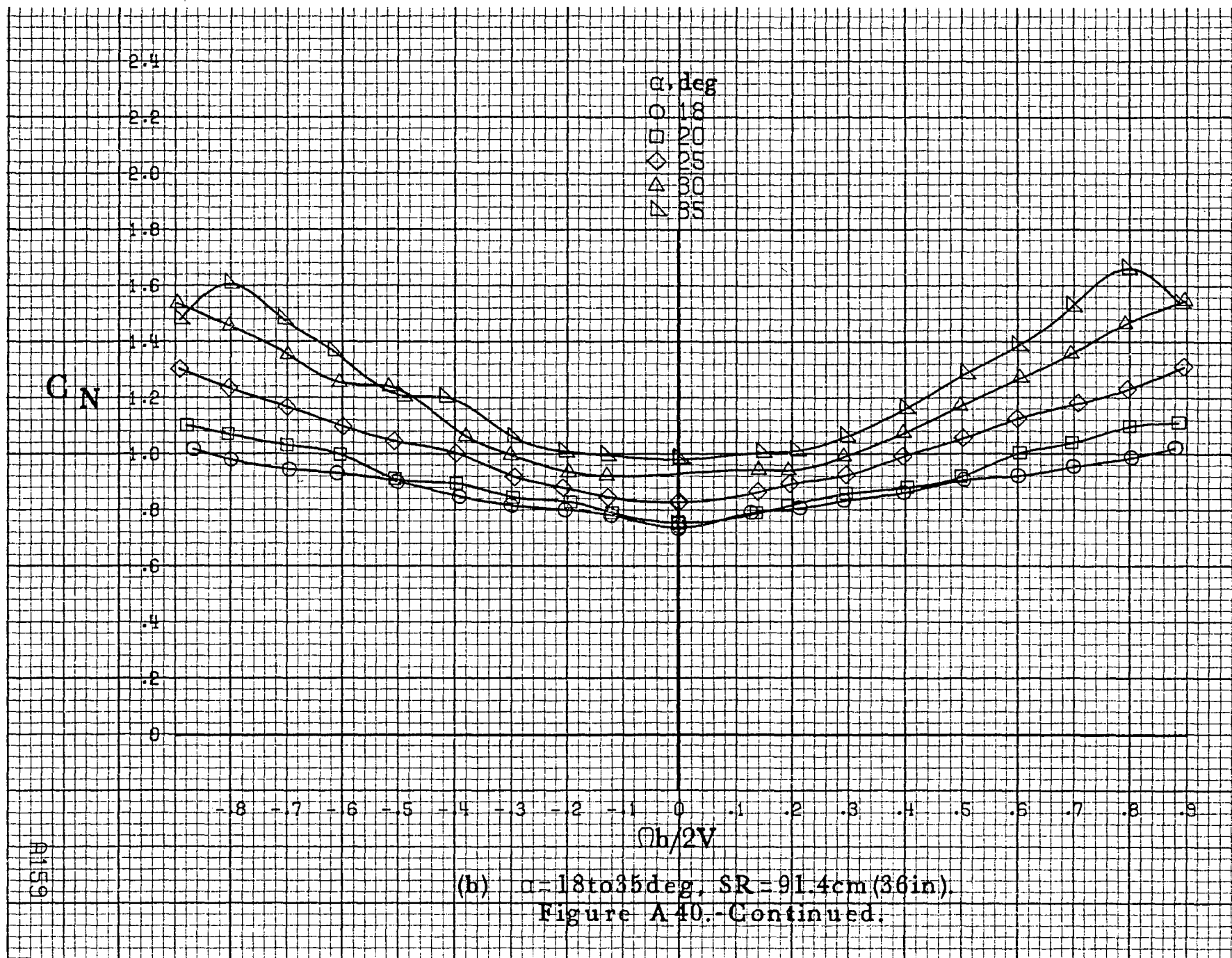


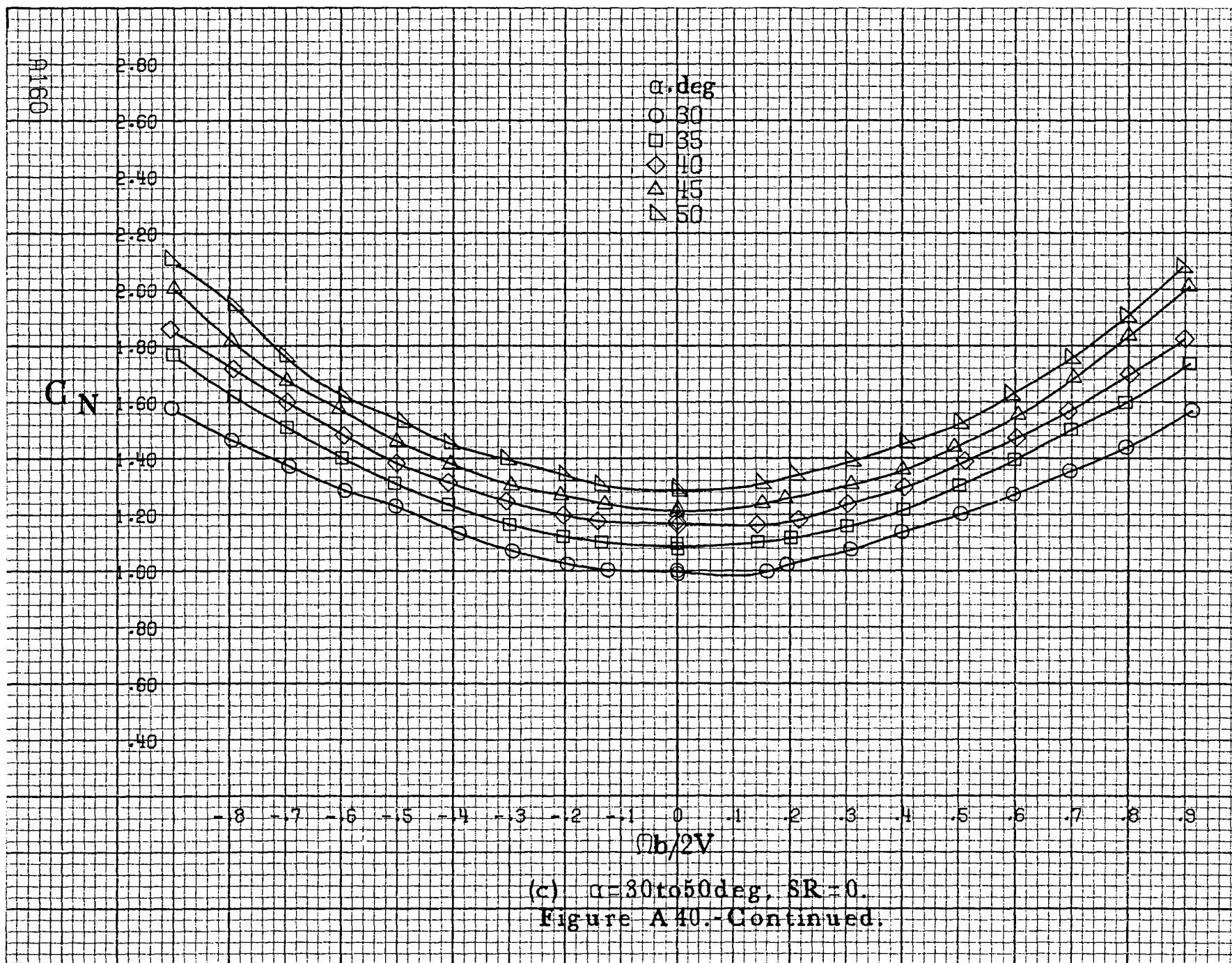


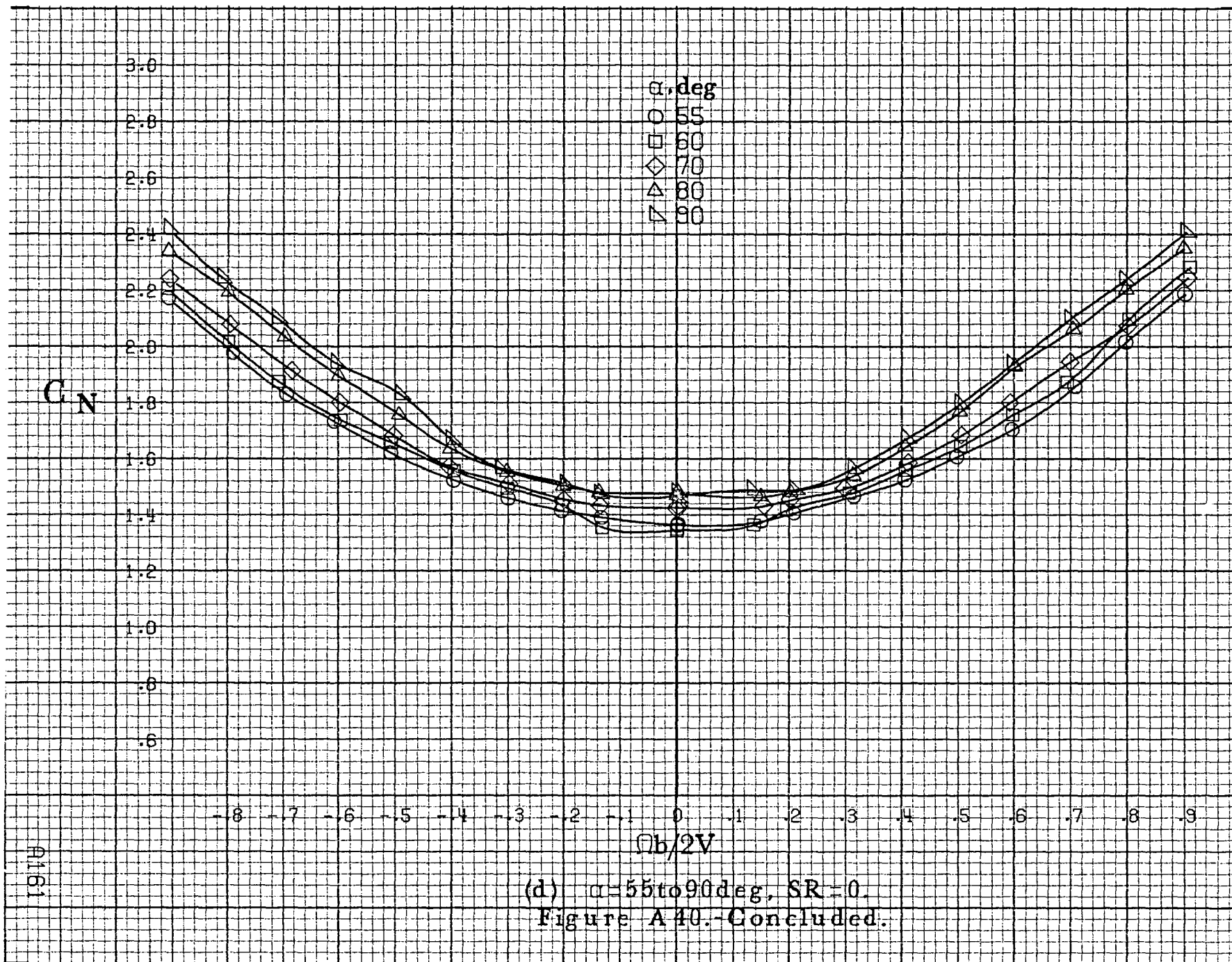


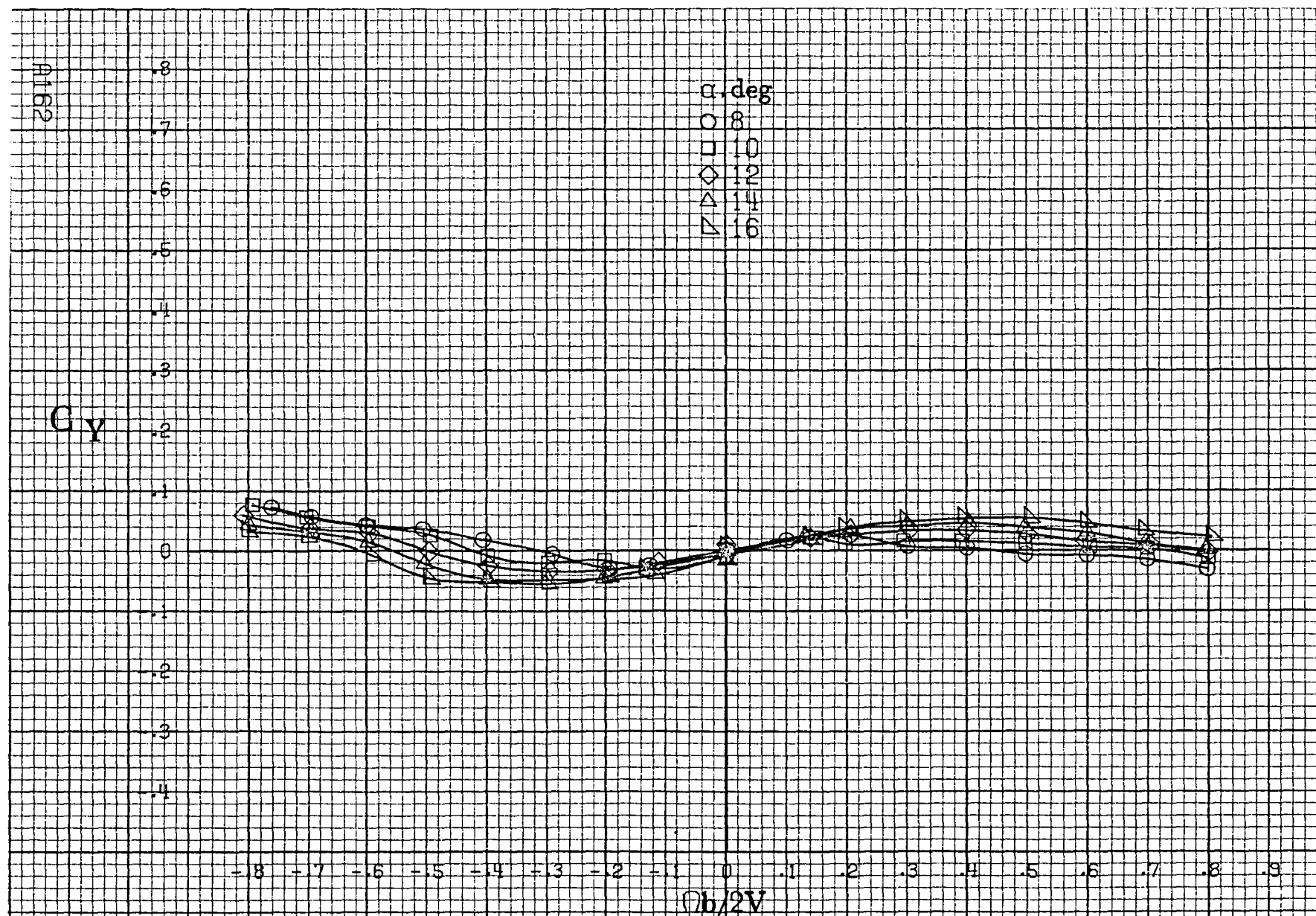
(a) $\alpha = 8$ to 16 deg, $SR = 91.4$ cm (36 in).

Figure A40.-Effect of rotation rate and angle of attack on normal-force coefficient for long body, low wing configuration. $\delta_c = 0^\circ$, $\delta_a = 0^\circ$, $\delta_r = 0^\circ$, $\delta = 0^\circ$.



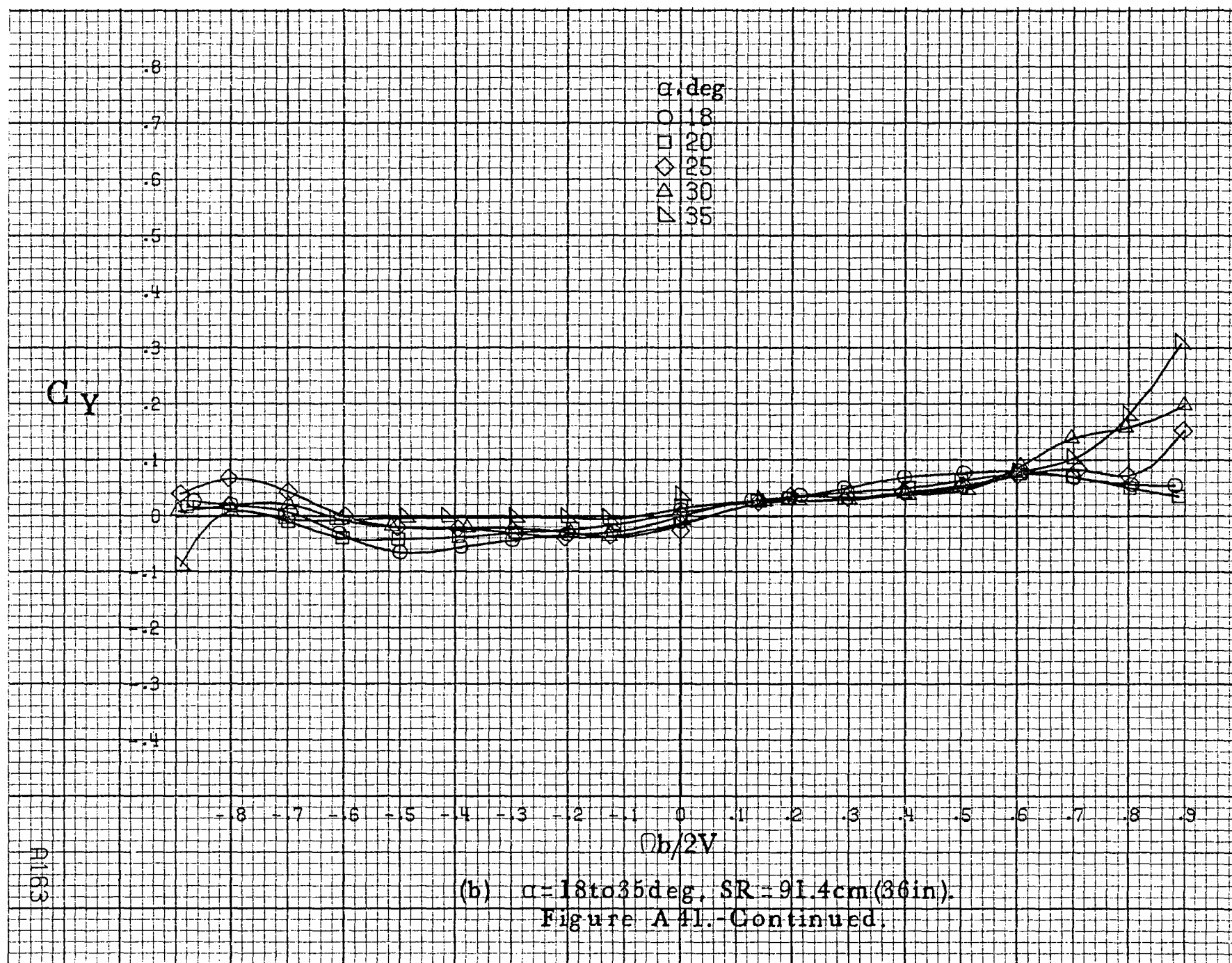


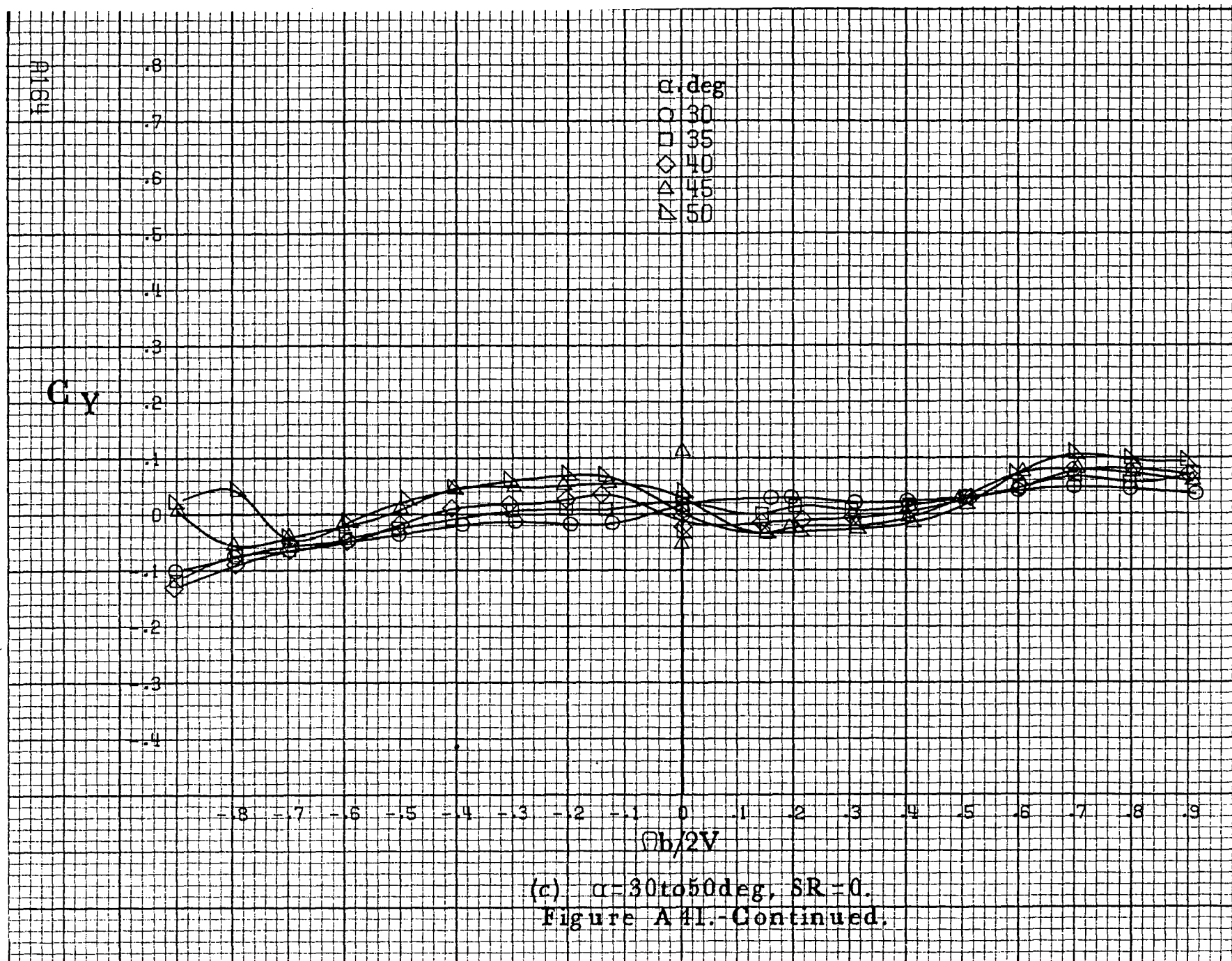




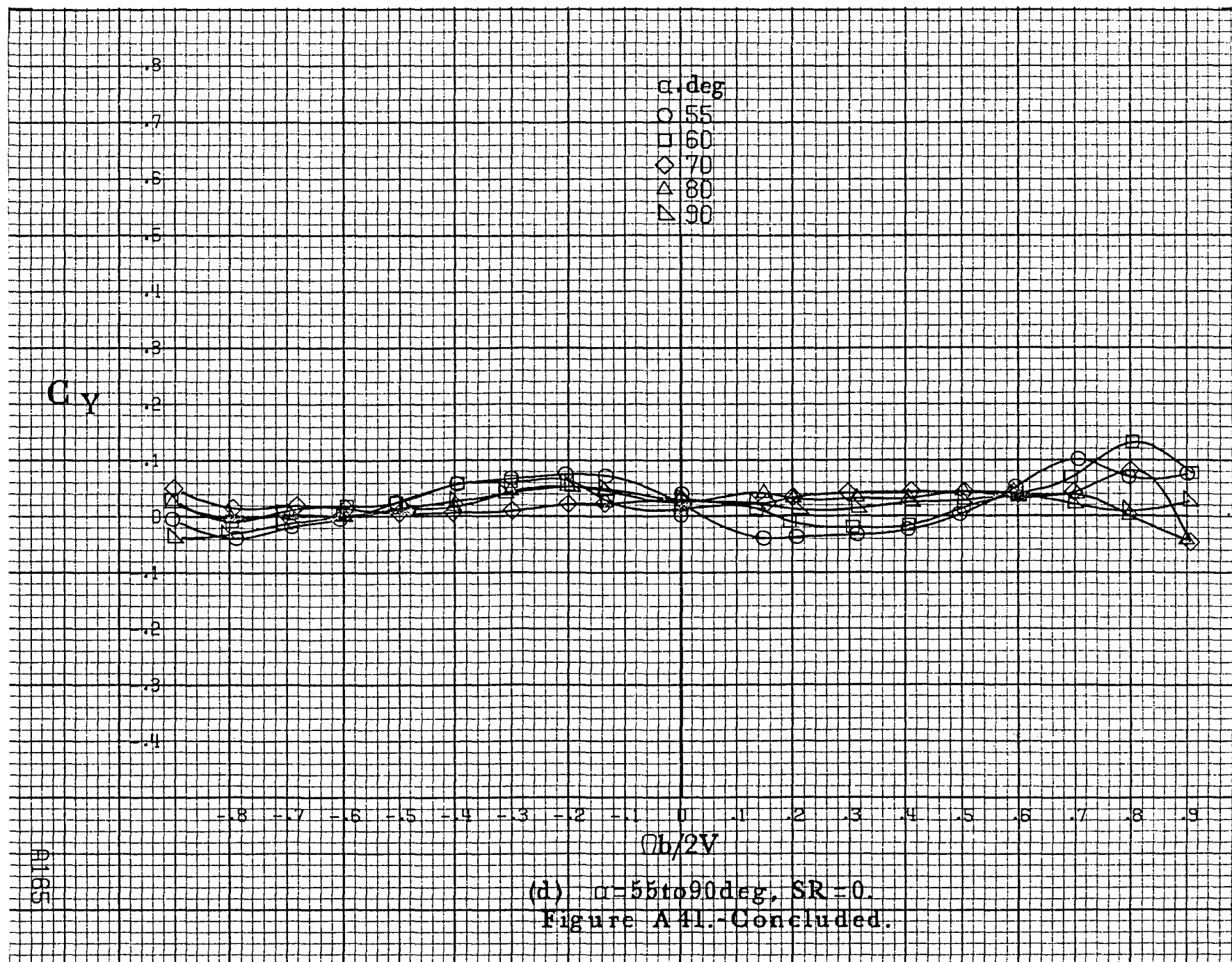
(a) $\alpha = 8 \text{ to } 16 \text{ deg}$, $SR = 91.4 \text{ cm (36 in)}$.

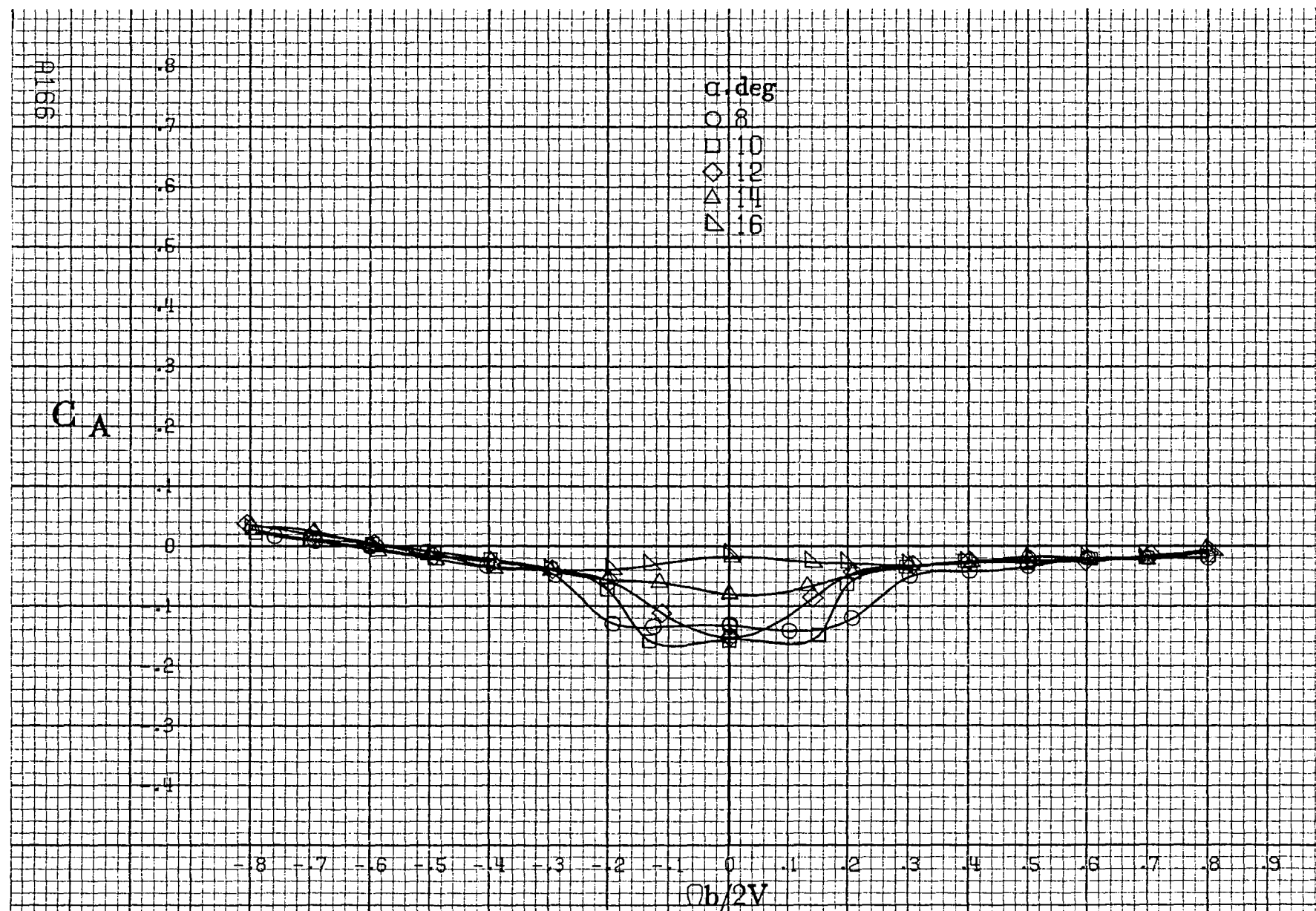
Figure A41.-Effect of rotation rate and angle of attack on side-force coefficient for long body, low wing configuration. $\delta_c = 0^\circ$, $\delta_w = 0^\circ$, $\delta_r = 0^\circ$. $\beta = 0^\circ$.





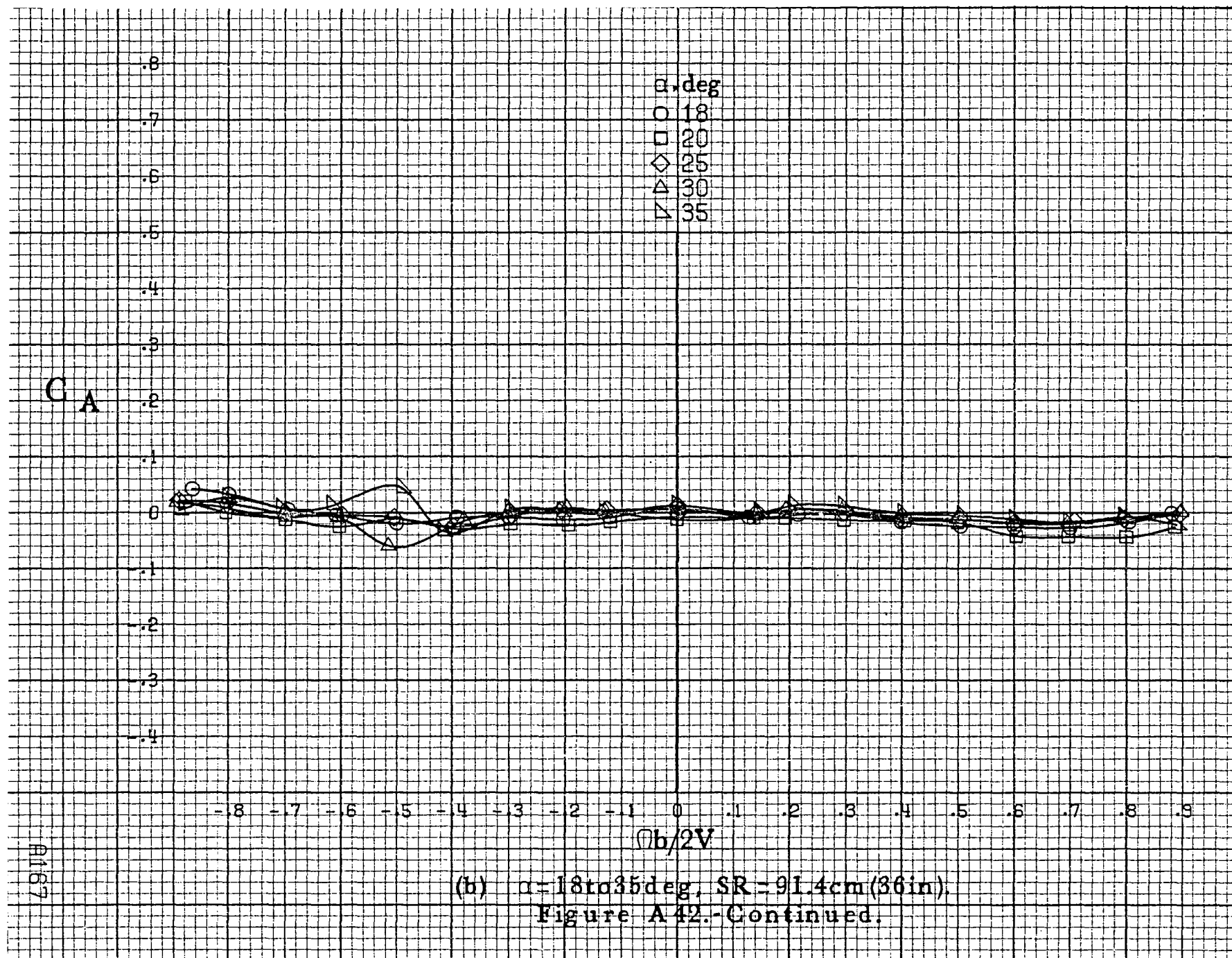
(c) $\alpha=30$ to 50 deg, $SR=0$.
Figure A41.-Continued.

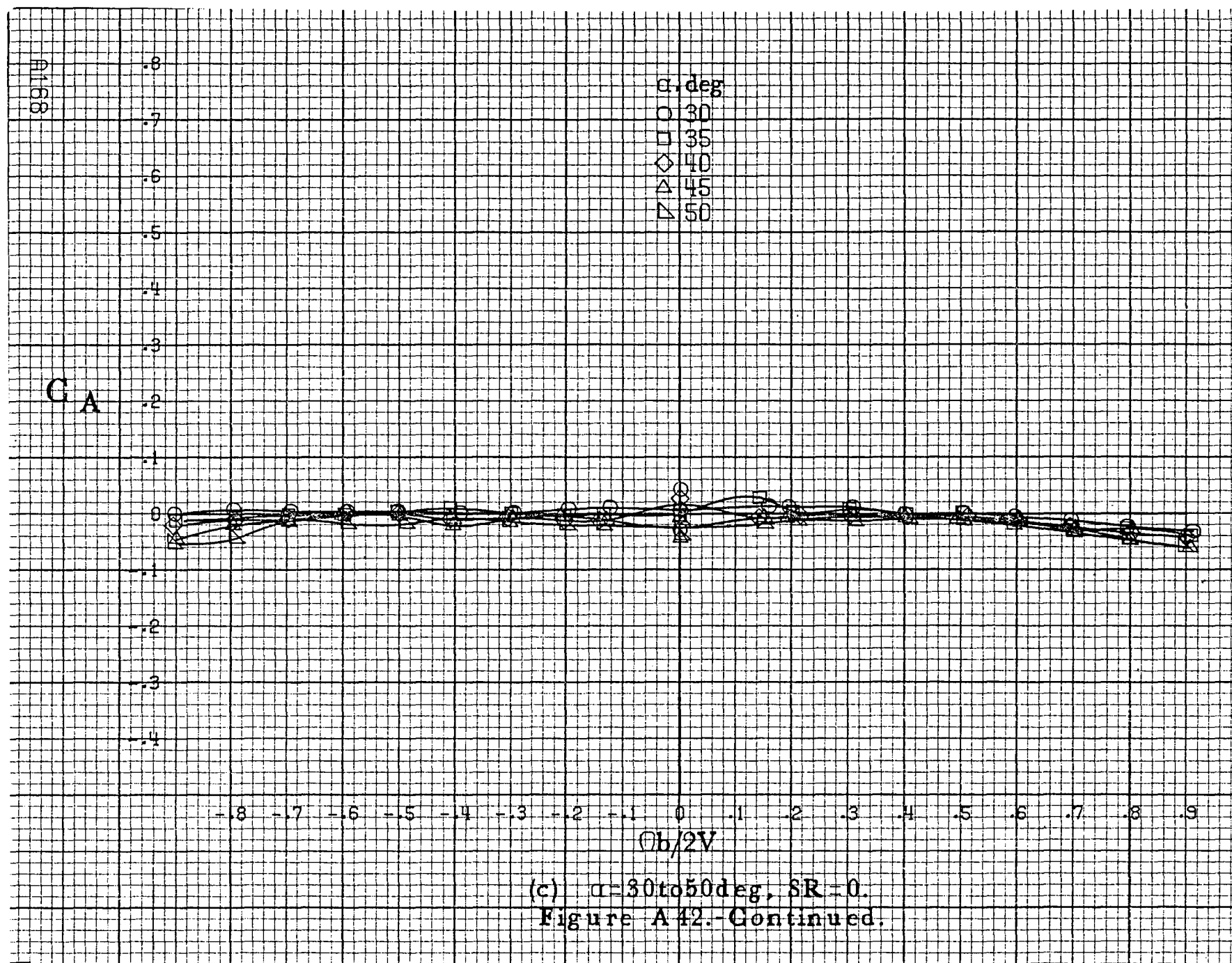


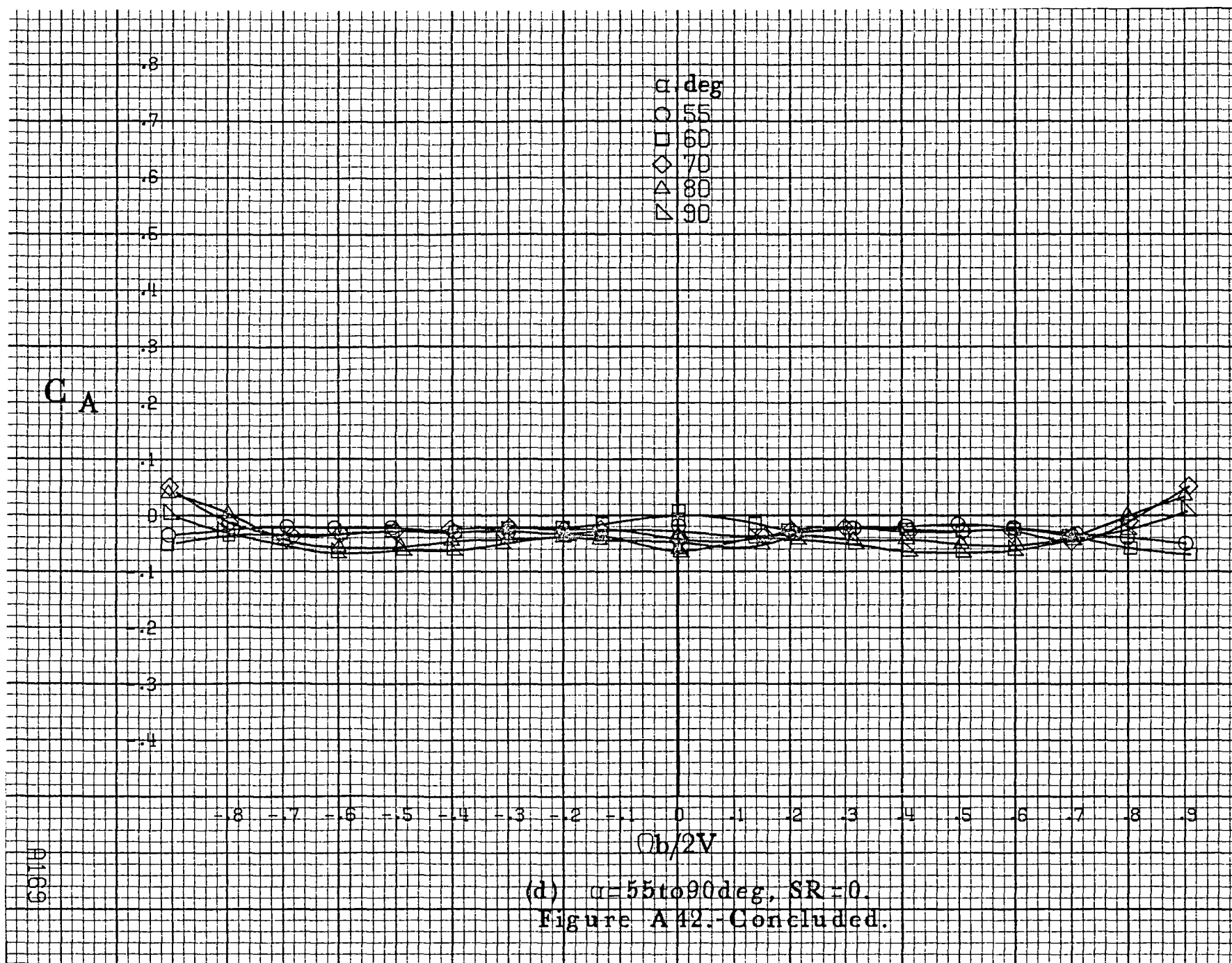


(a) $\alpha=8$ to 16° , $SR=91.4\text{cm}(36\text{in})$.

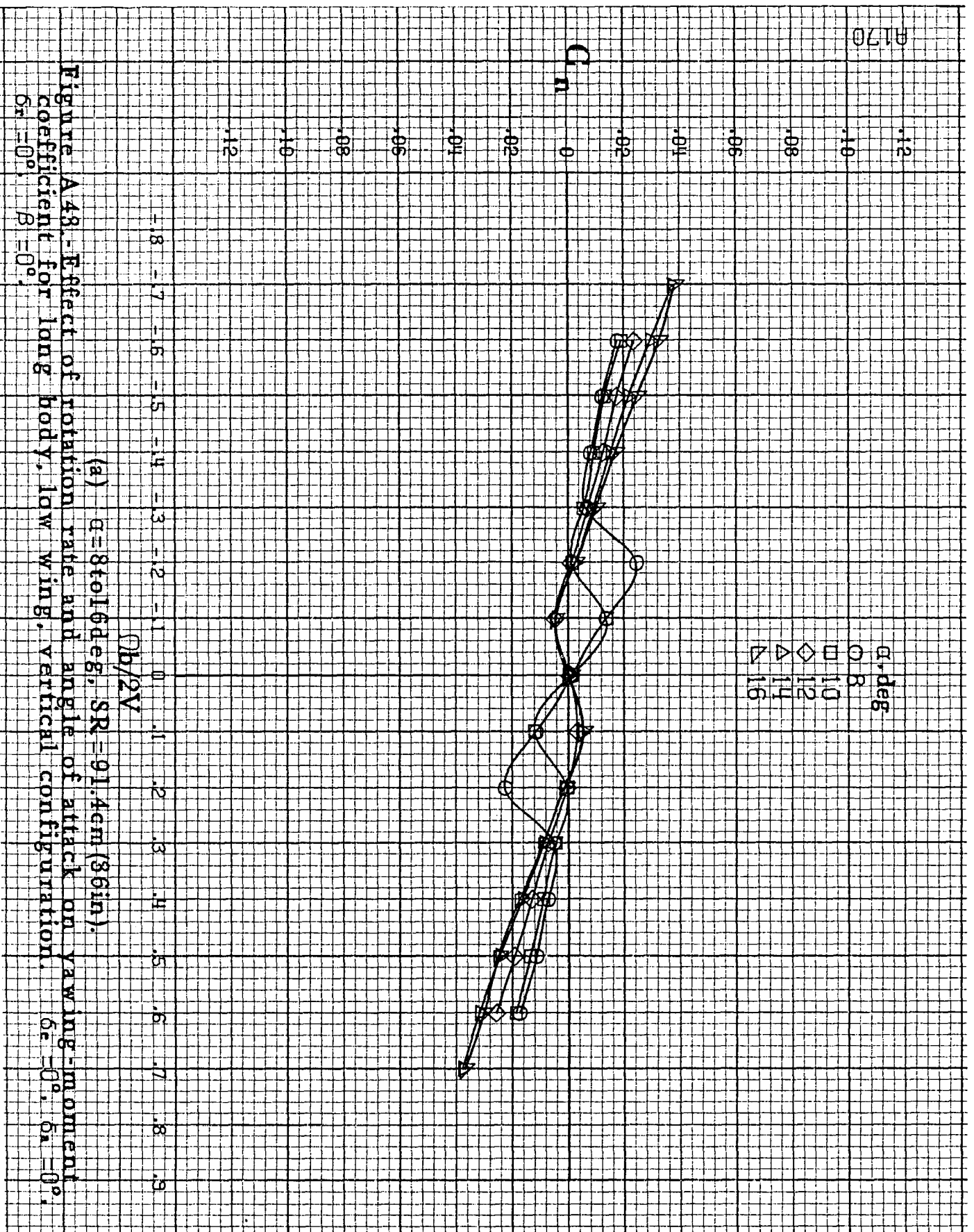
Figure A42 - Effect of rotation rate and angle of attack on axial-force coefficient for long body, low wing configuration. $\delta_e=0^\circ$, $\delta_r=0^\circ$, $\delta_t=0^\circ$, $\delta=0^\circ$.

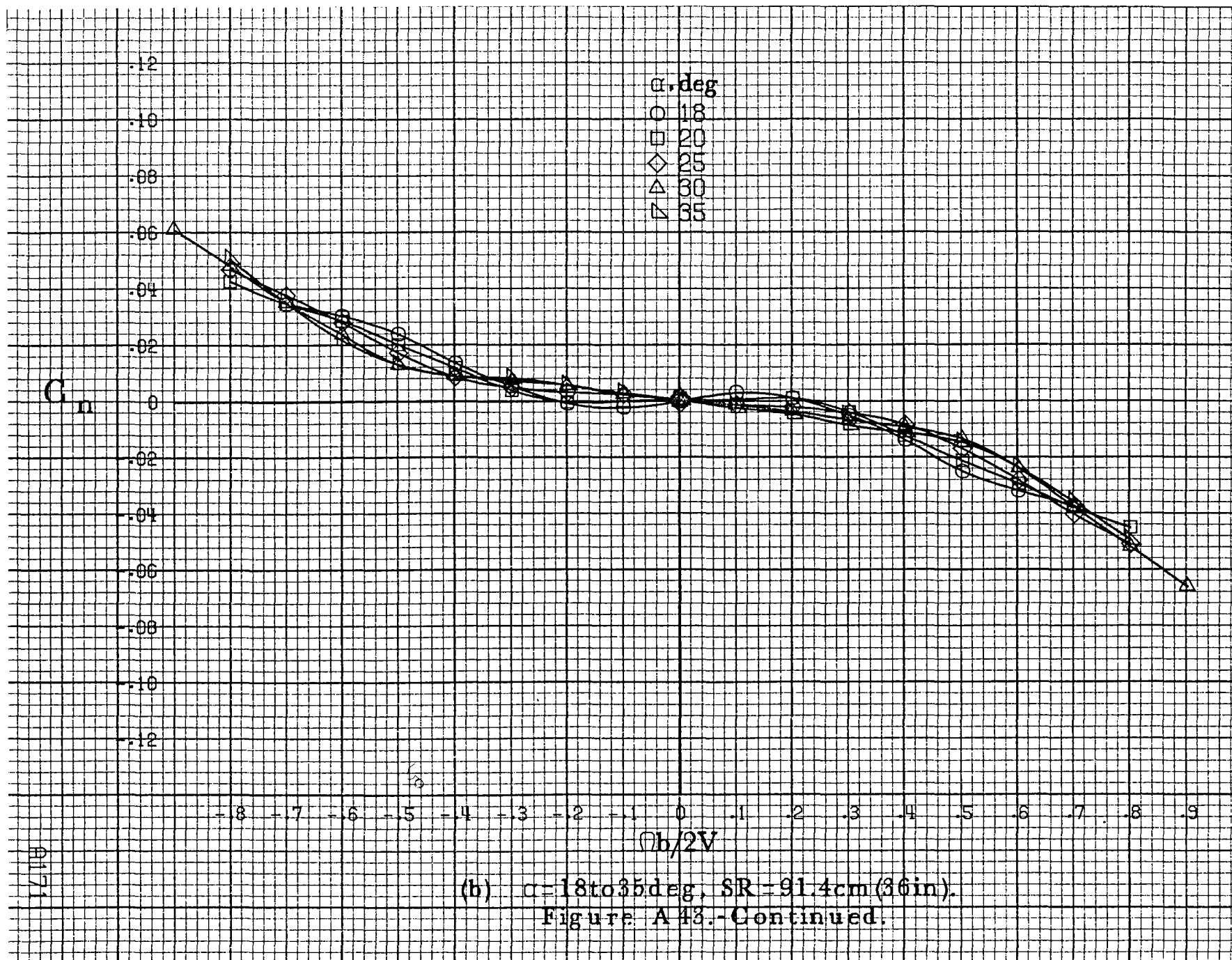






(d) $\alpha = 55$ to 90° , $SR = 0$.
Figure A 42.-Concluded.





8172

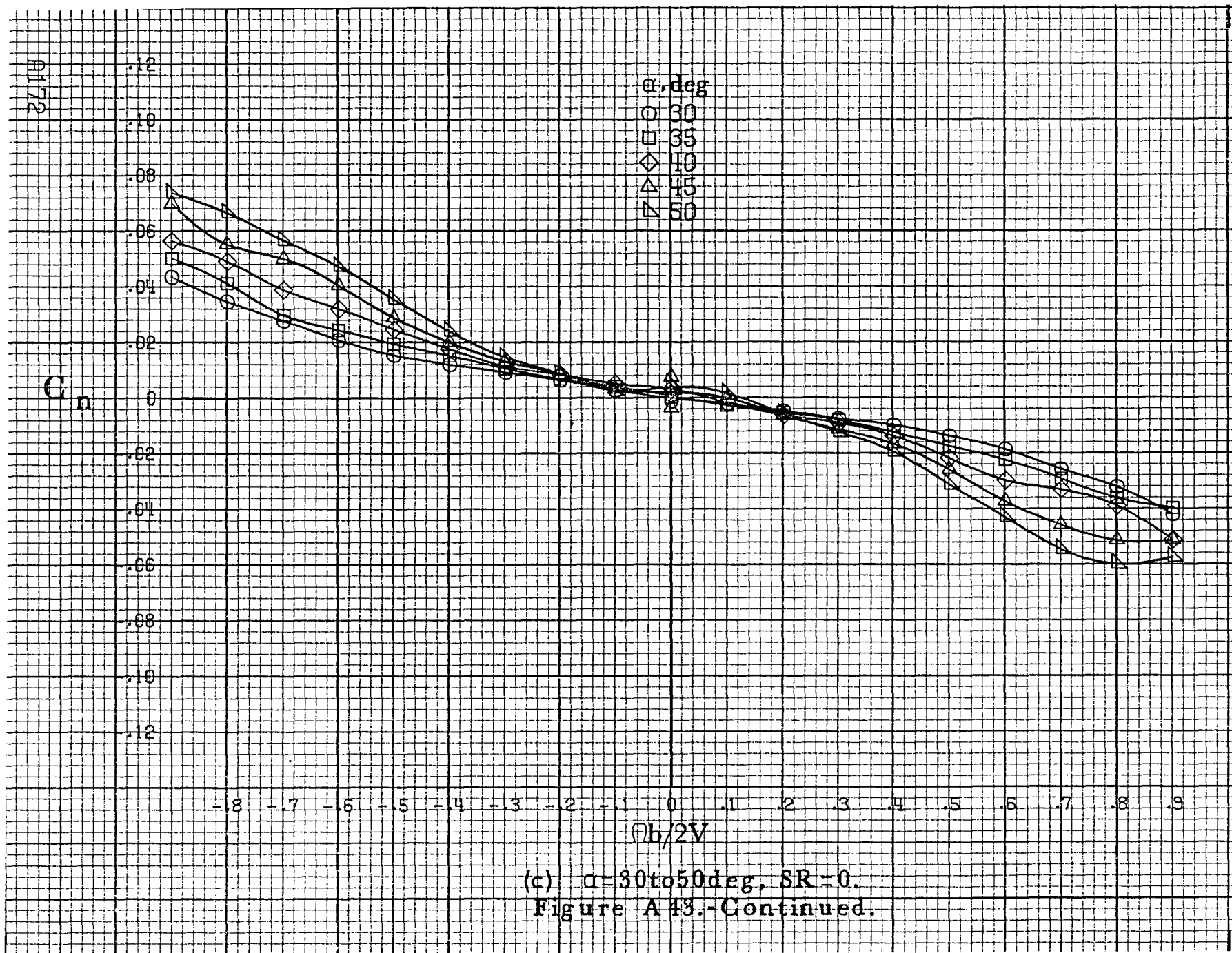
C_n

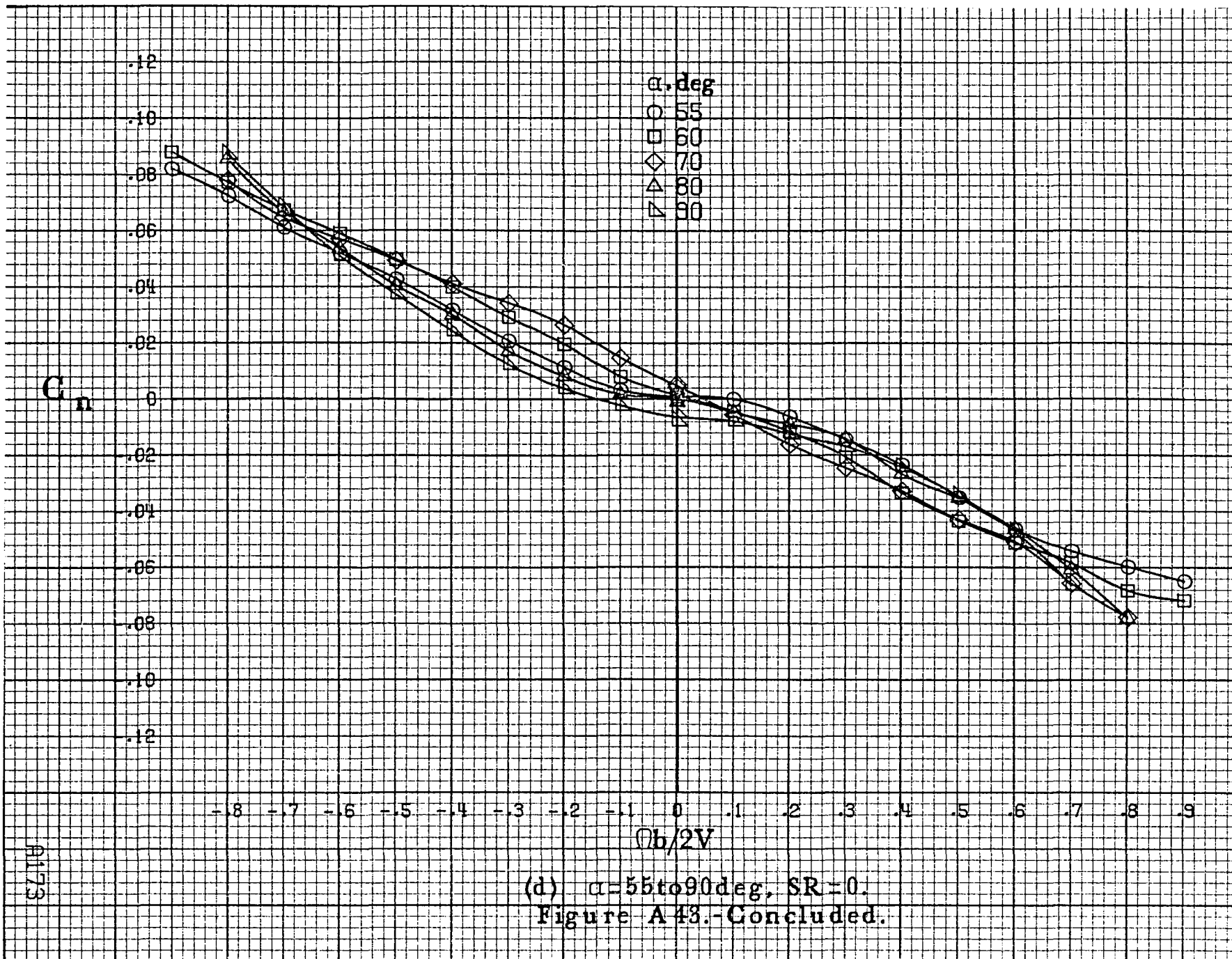
.12
.10
.08
.06
.04
.02
0
-.02
-.04
-.06
-.08
-.10
-.12

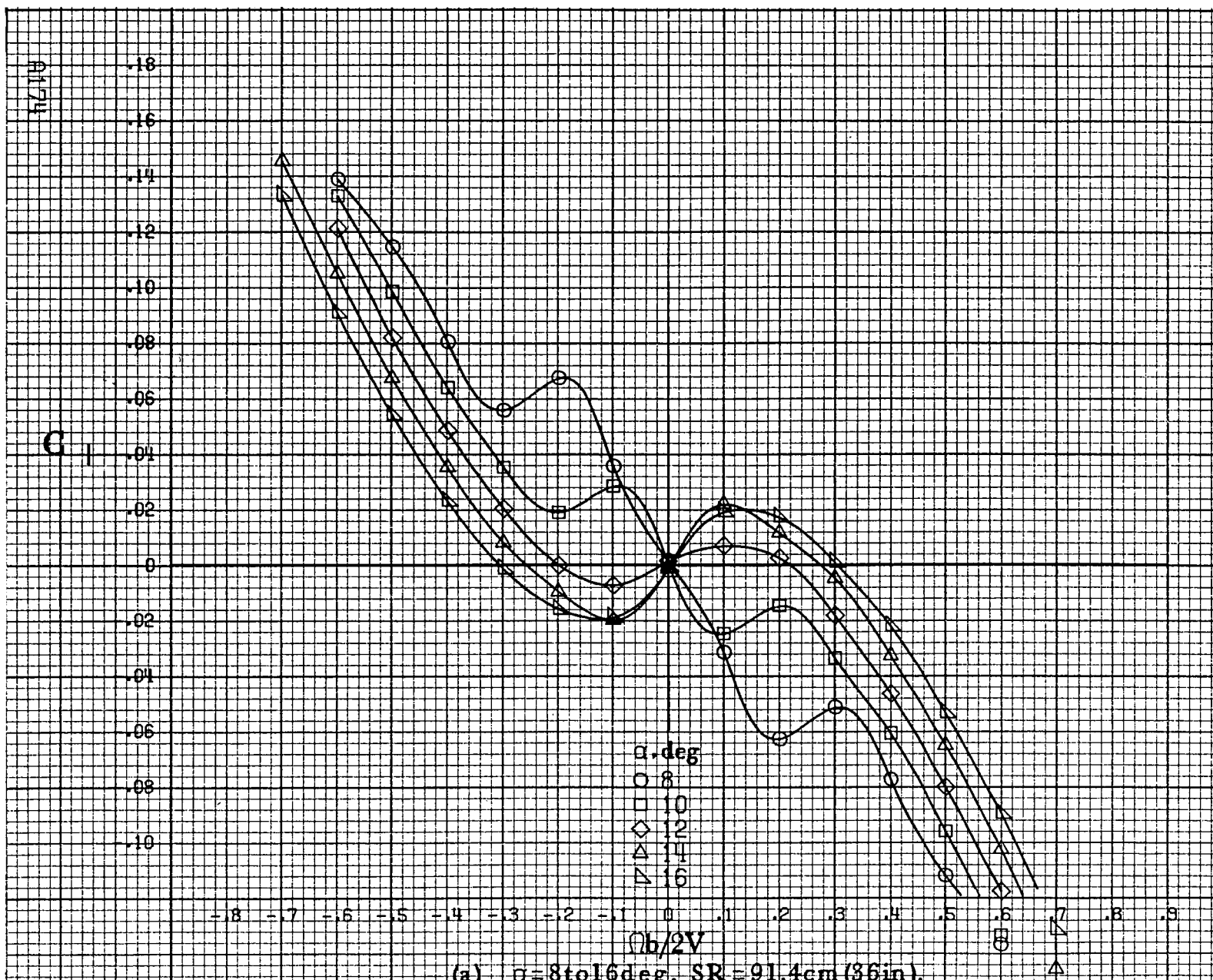
α, deg
○ 30
□ 35
◇ 40
△ 45
▽ 50

-0.8 -0.7 -0.6 -0.5 -0.4 -0.3 -0.2 -0.1 0 0.1 0.2 0.3 0.4 0.5 0.6 0.7 0.8 0.9
 $\phi b/2V$

(c) $\alpha=30\text{ to }50\text{deg}$, $SR=0$.
Figure A43.-Continued.

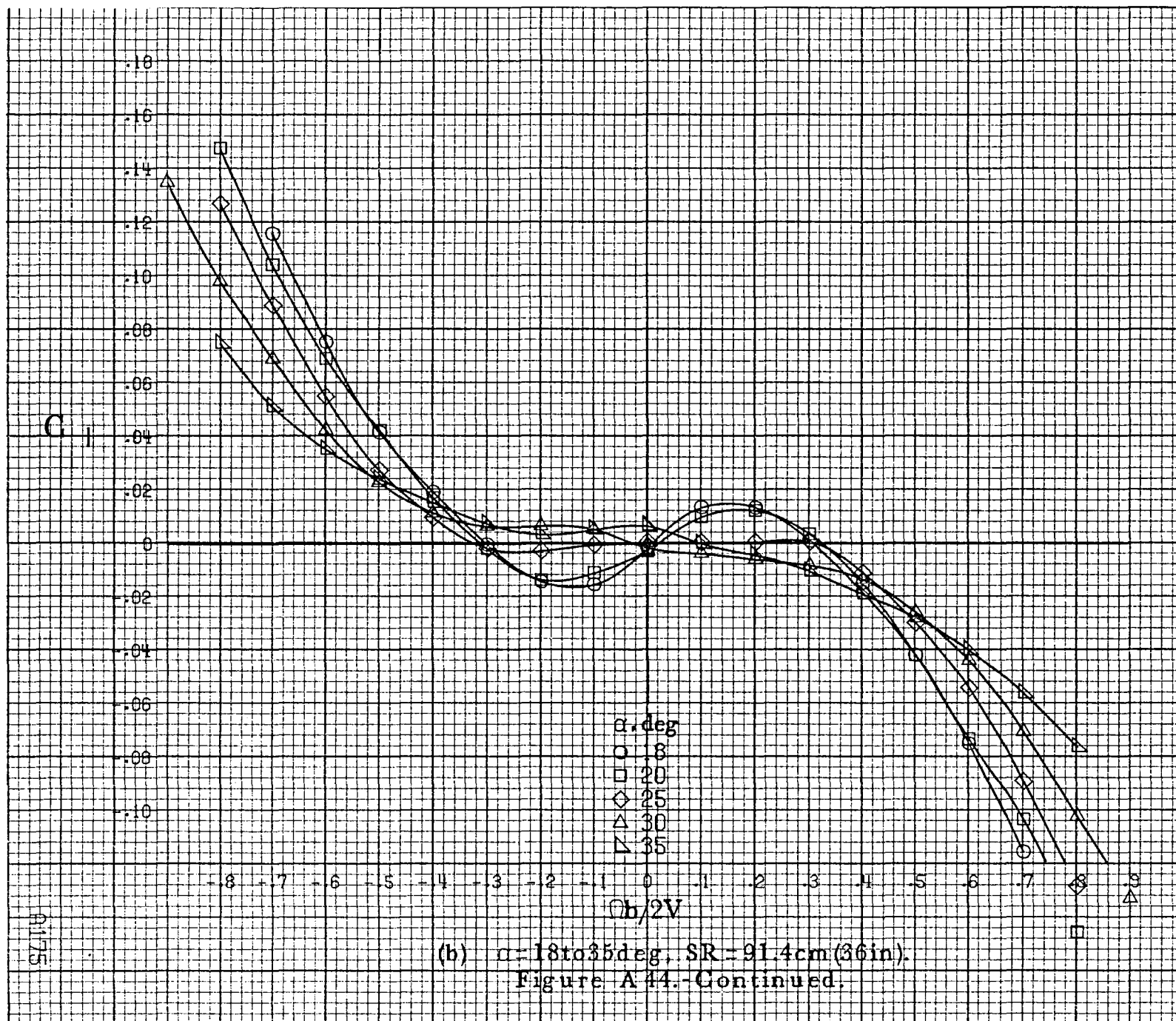


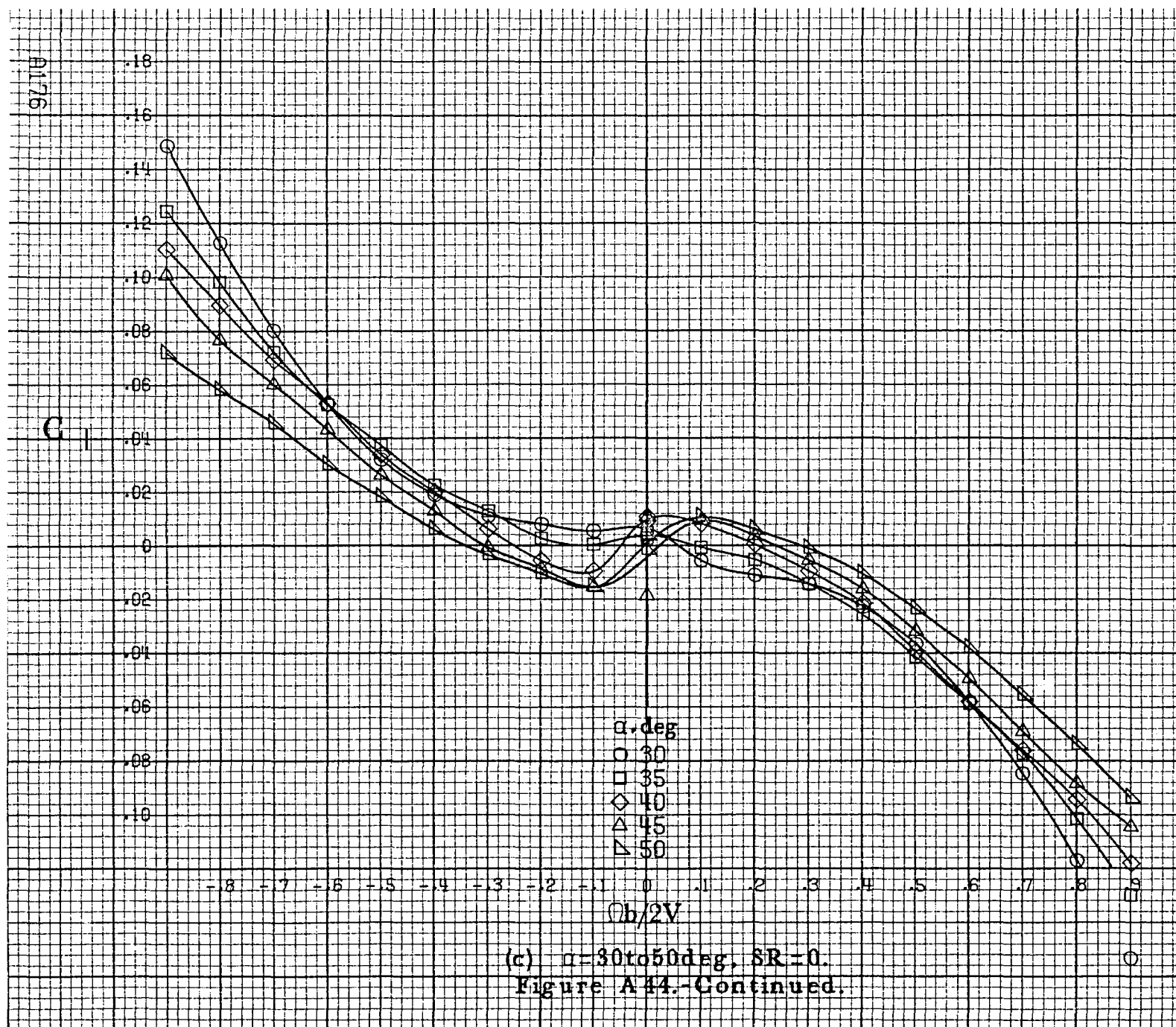


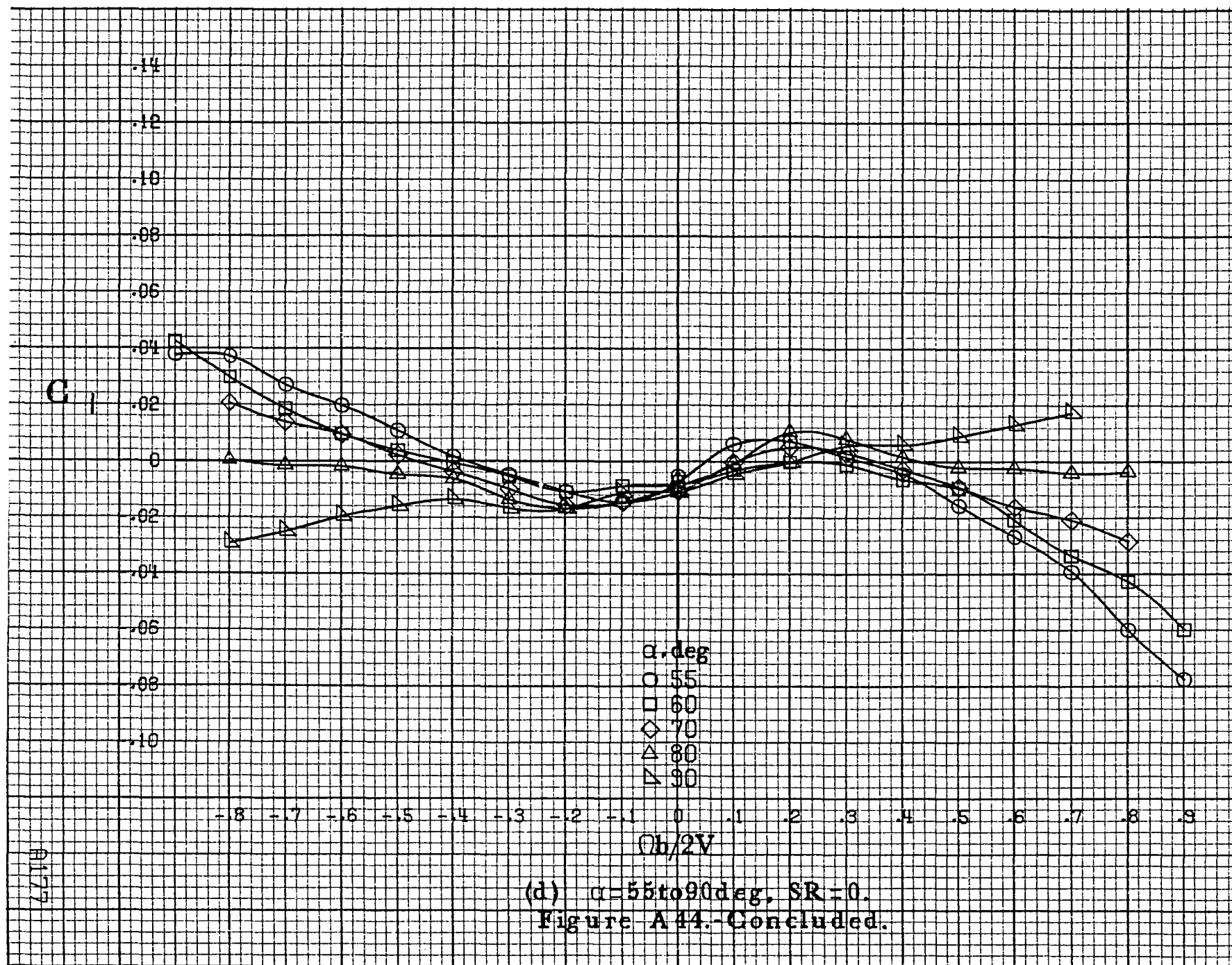


(a) $\alpha = 8 \text{ to } 16 \text{ deg}$, $SR = 91.4 \text{ cm (36 in.)}$.

Figure A44.-Effect of rotation rate and angle of attack on rolling-moment coefficient for long body, low wing, vertical configuration. $\delta_c = 0^\circ$, $\delta_a = 0^\circ$, $\delta_r = 0^\circ$, $\beta = 0^\circ$.







(d) $\alpha = 55$ to 90° , $SR = 0$.
Figure A 44. - Concluded.

8178

C_m

.6
.5
.4
.3
.2
.1
0
-.1
-.2
-.3
-.4
-.5
-.6

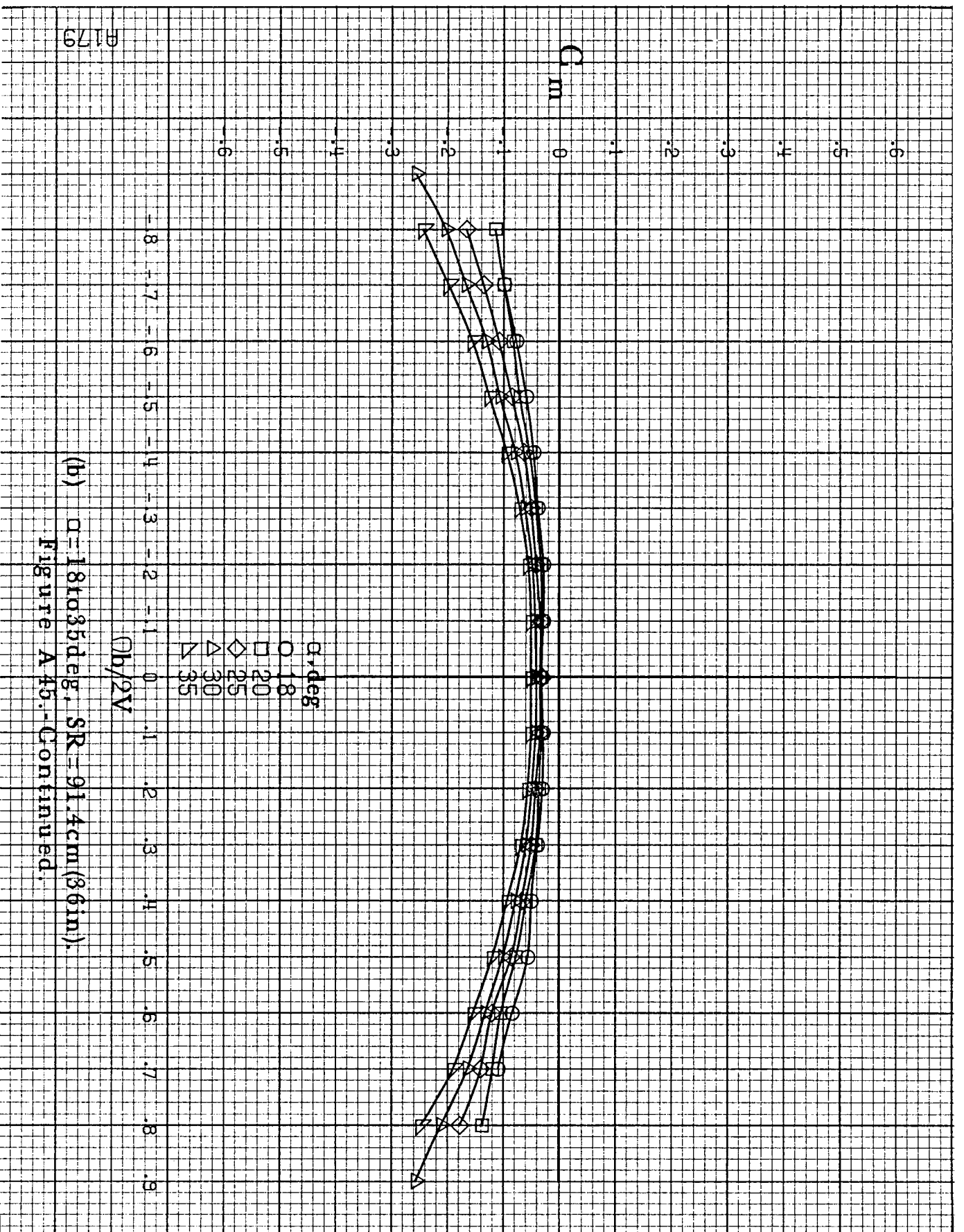
α, deg
○ 8
□ 10
◇ 12
△ 14
▽ 16

-.8 -.7 -.6 -.5 -.4 -.3 -.2 -.1 0 .1 .2 .3 .4 .5 .6 .7 .8 .9

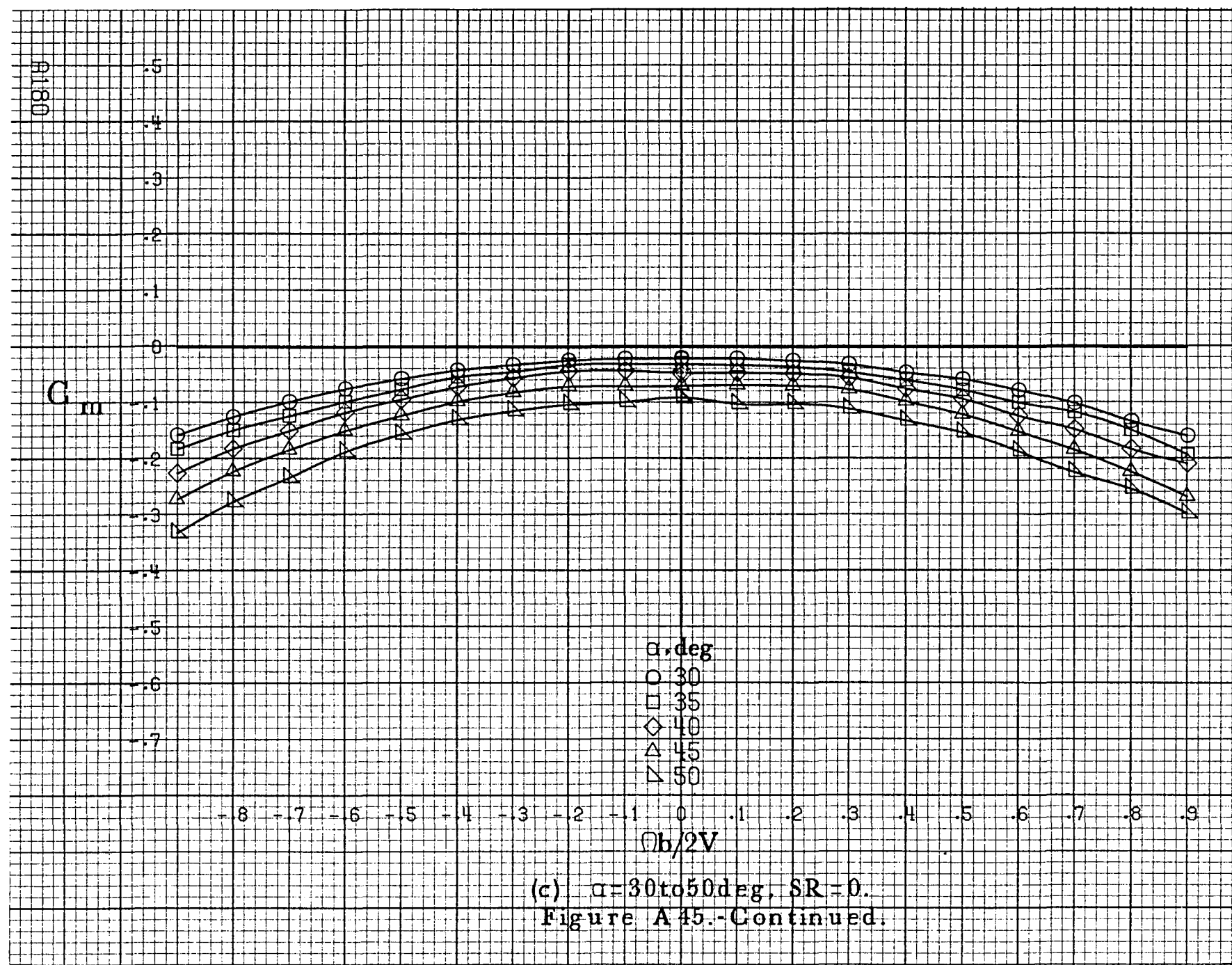
$\Omega b/2V$

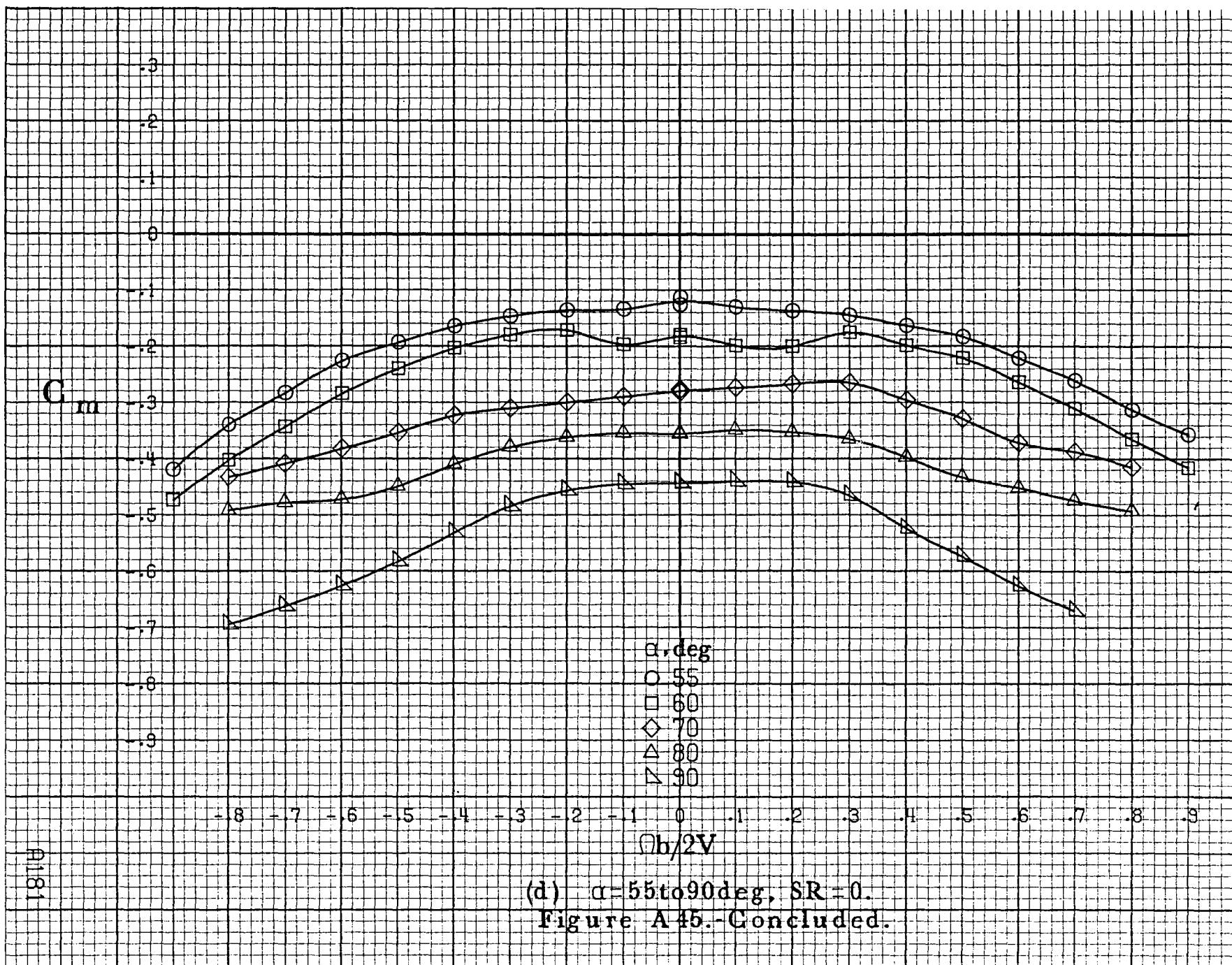
(a) $\alpha = 8 \text{ to } 16 \text{ deg}$, $SR = 91.4 \text{ cm (36 in)}$.

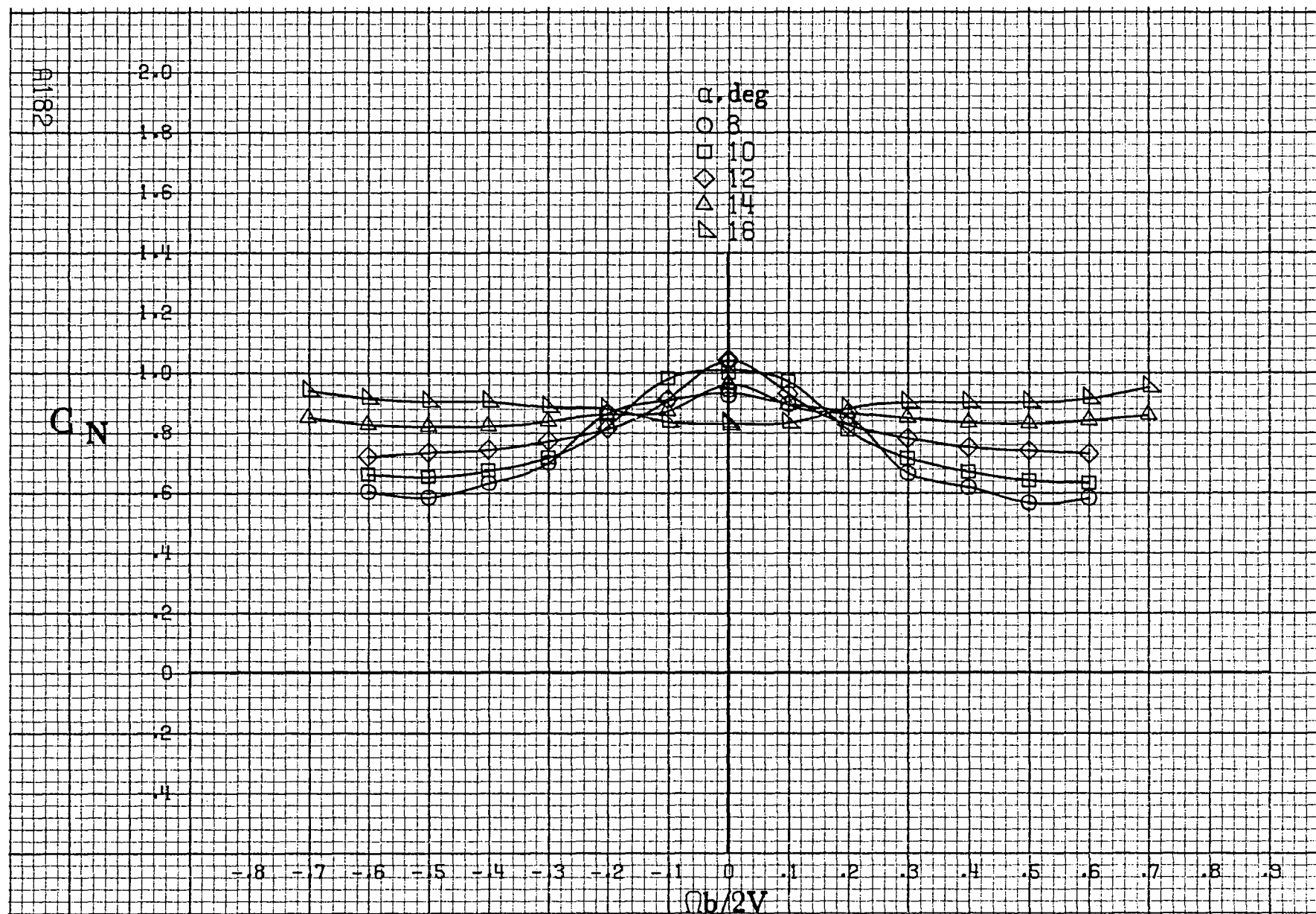
Figure A 45.- Effect of rotation rate and angle of attack on pitching-moment coefficient for long body, low wing, vertical configuration. $\delta_e = 0^\circ$, $\delta_a = 0^\circ$, $\delta_r = 0^\circ$, $\beta = 0^\circ$.



A179

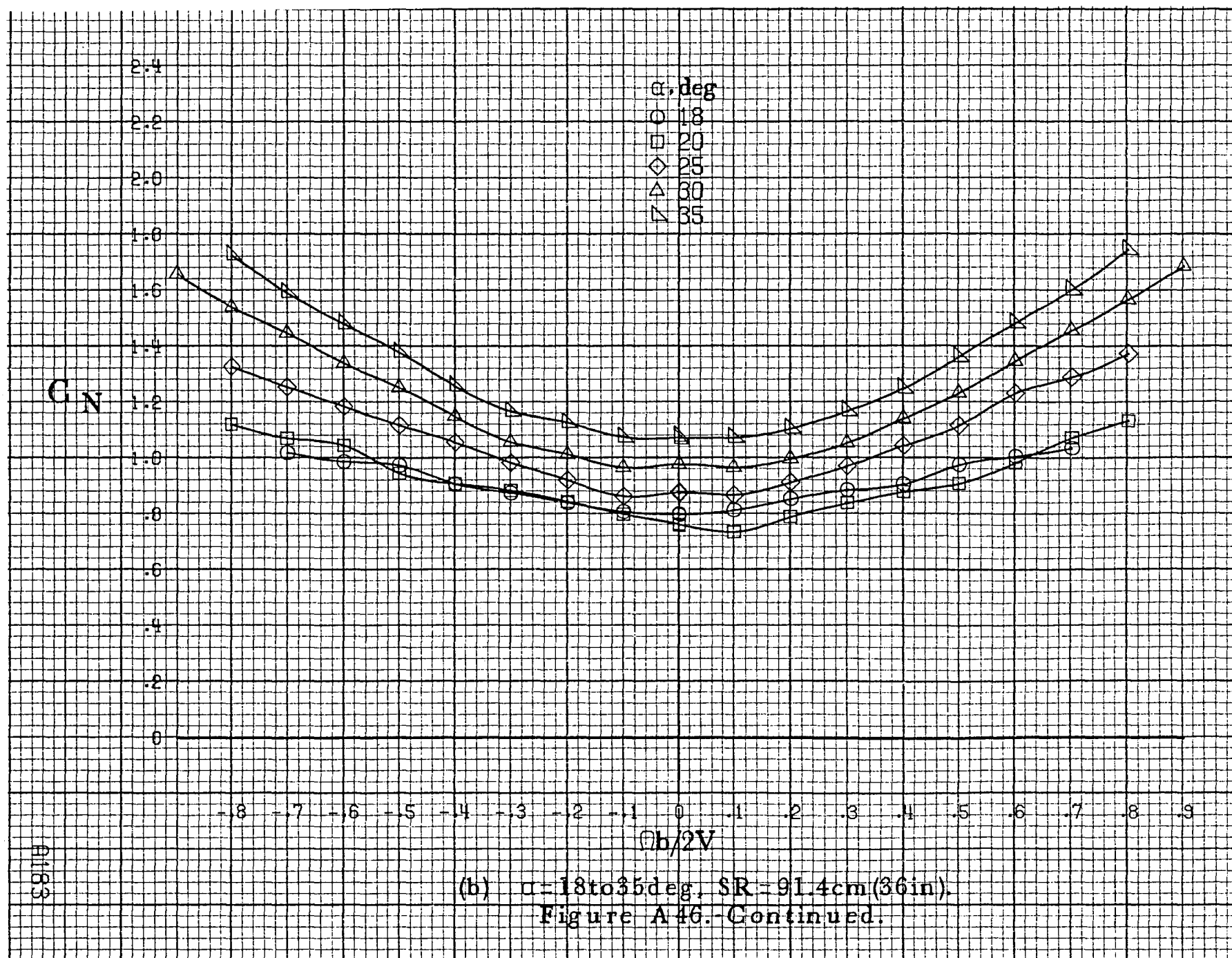


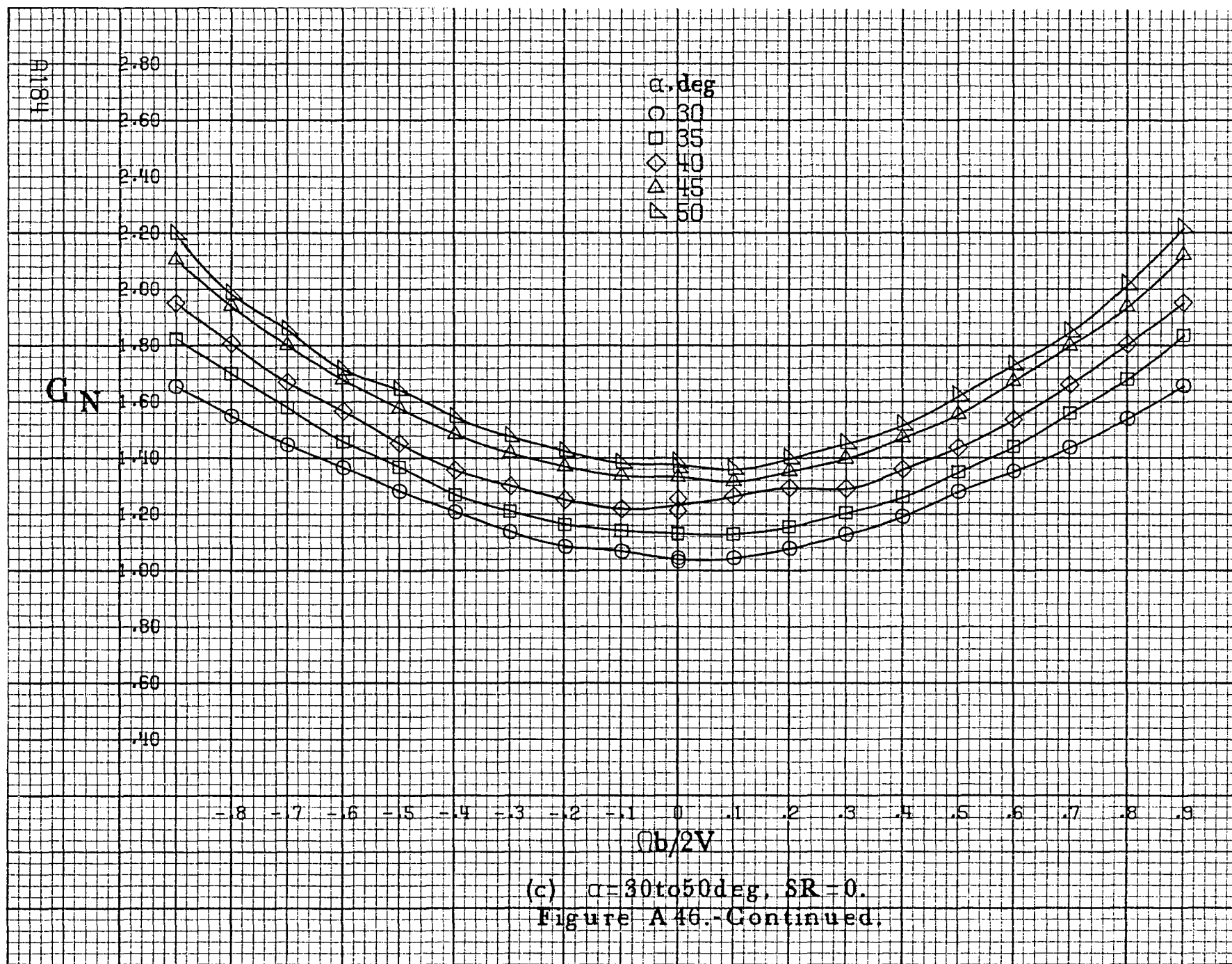


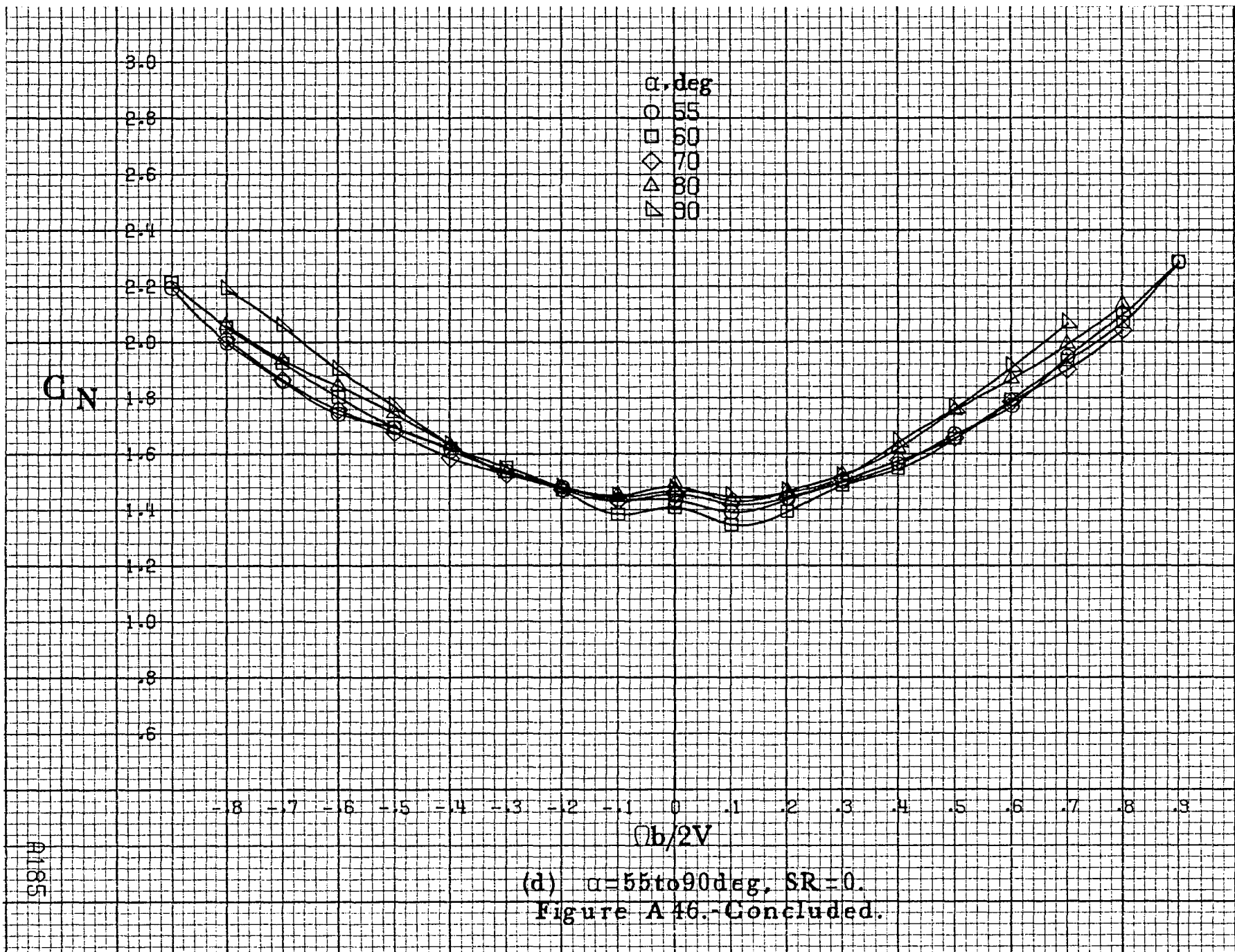


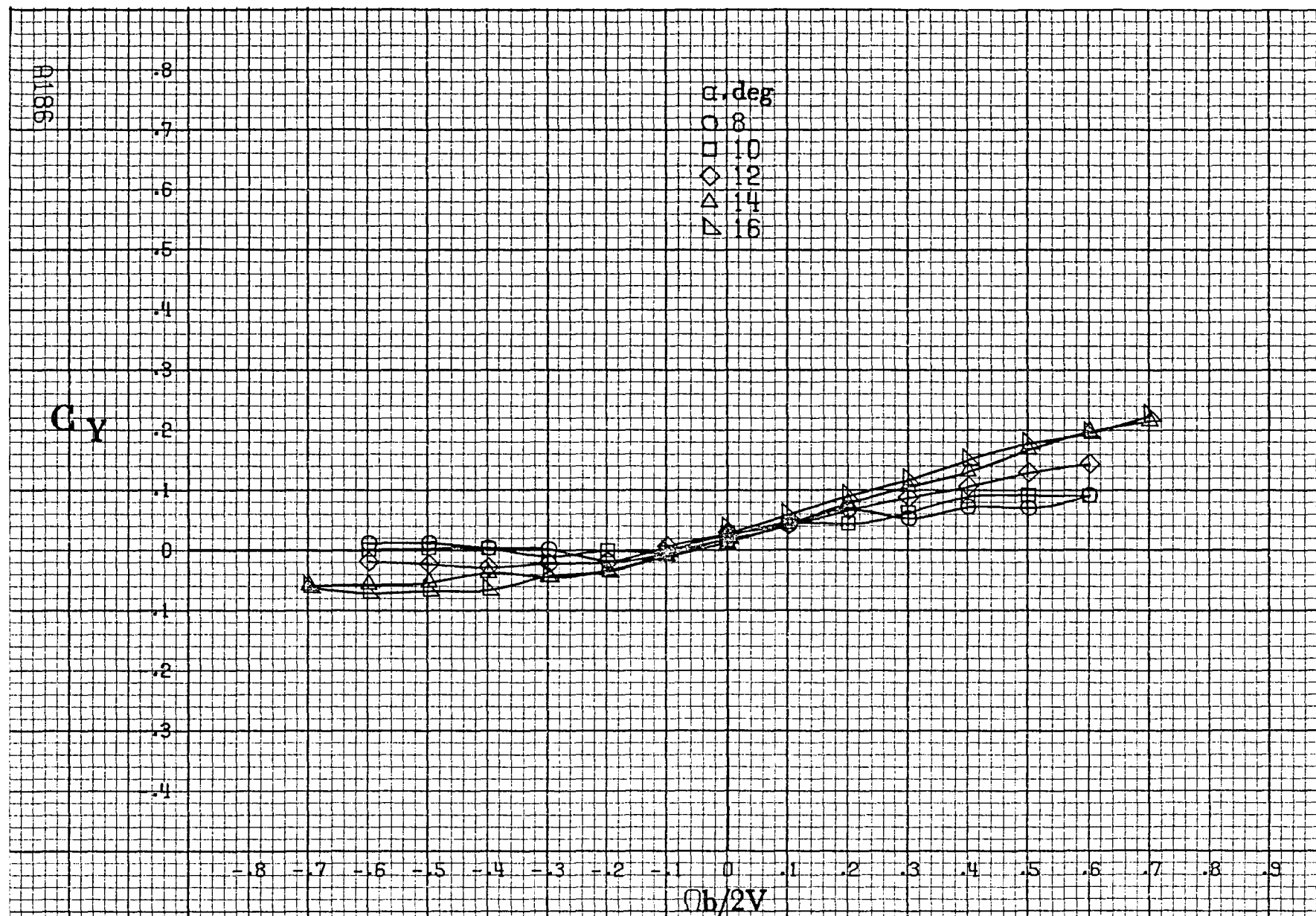
(a) $\alpha = 8$ to 16 deg, $SR = 91.4$ cm (36 in).

Figure A46.-Effect of rotation rate and angle of attack on normal-force coefficient for long body, low wing, vertical configuration. $\delta_e = 0^\circ$, $\delta_a = 0^\circ$, $\delta_r = 0^\circ$, $\beta = 0^\circ$.



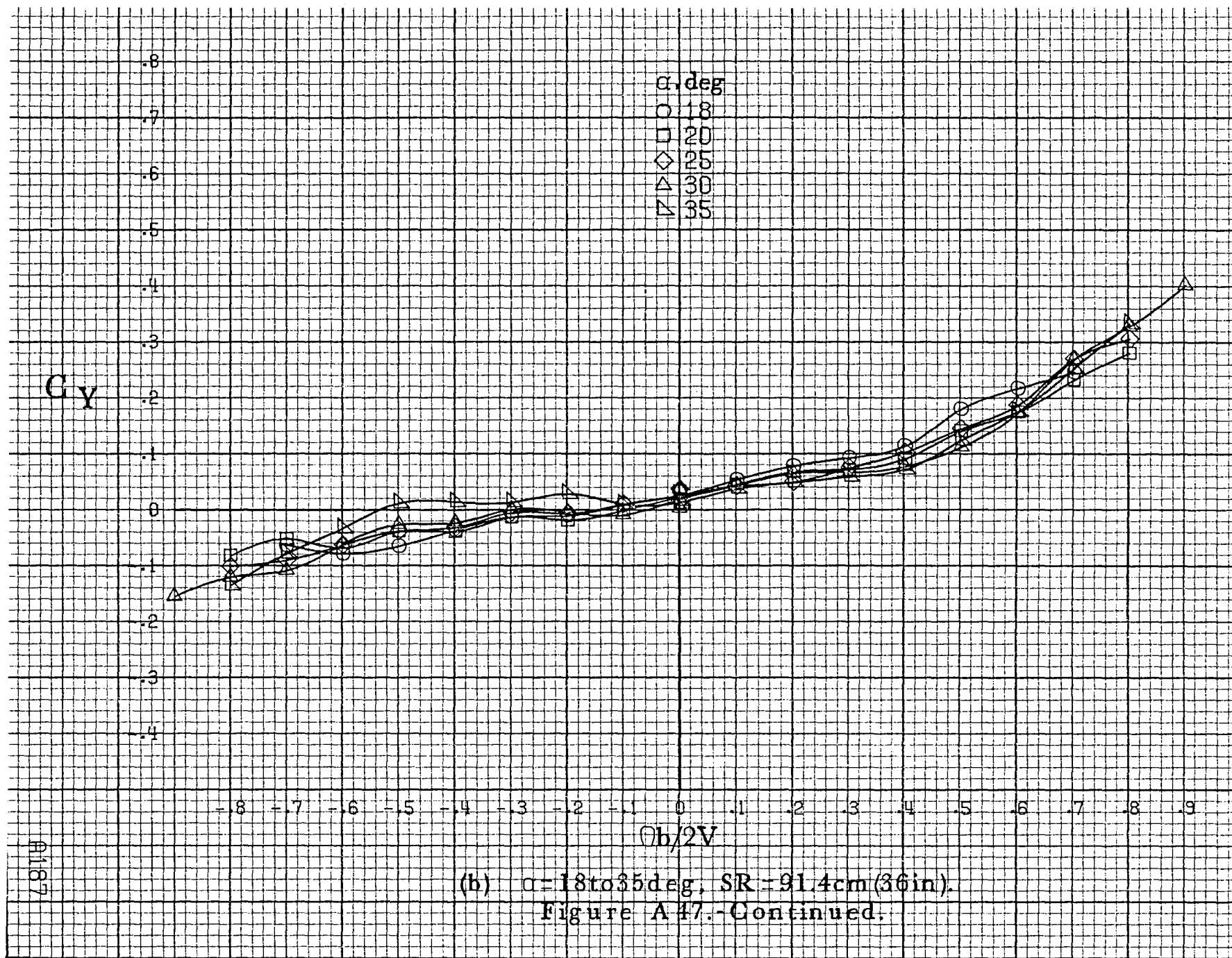




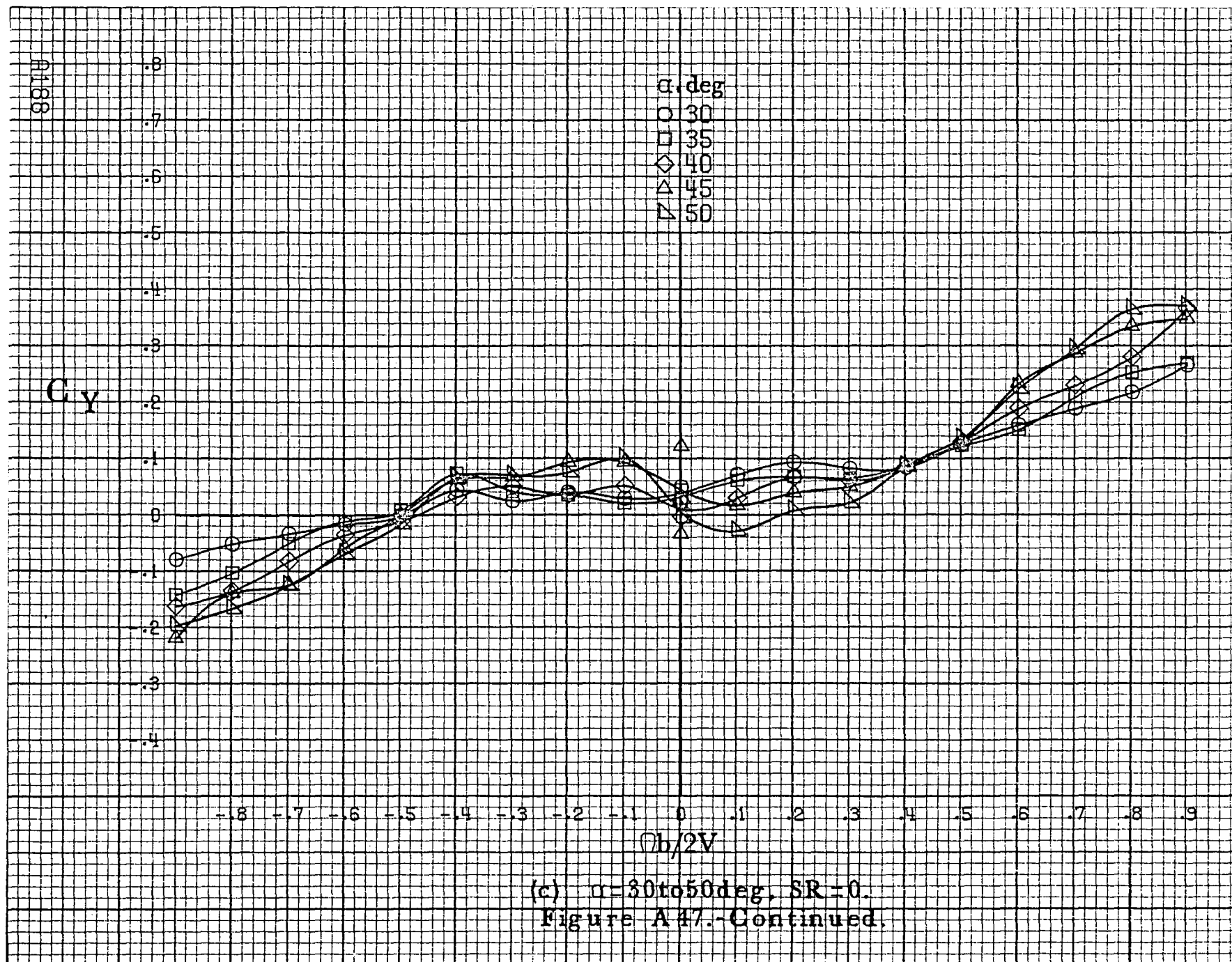


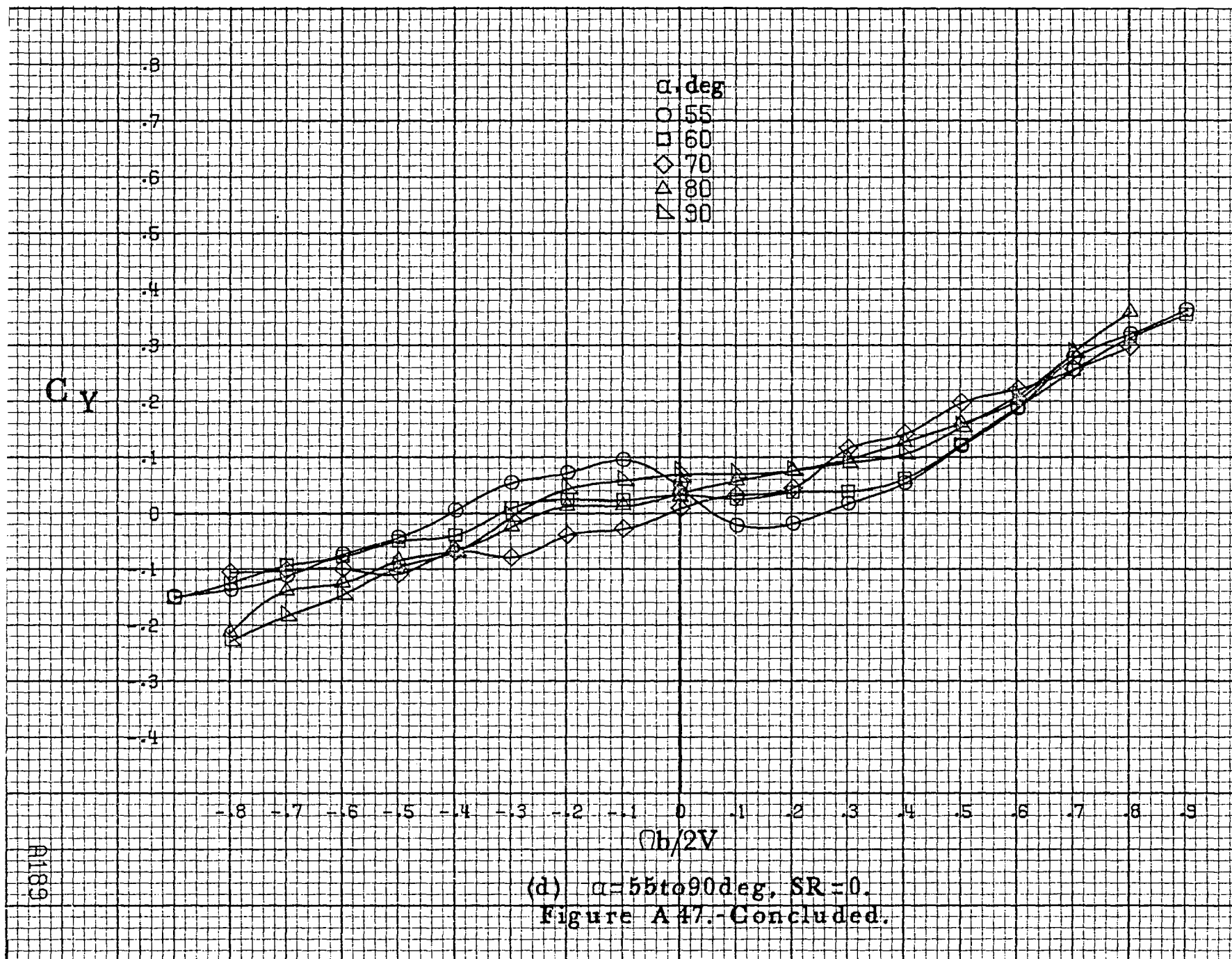
(a) $\alpha=8$ to 16° , $SR=91.4\text{cm}(36\text{in})$.

Figure A47.-Effect of rotation rate and angle of attack on side-force coefficient for long body, low wing, vertical configuration. $\delta_c=0^\circ$, $\delta_a=0^\circ$, $\delta_r=0^\circ$, $\beta=0^\circ$.

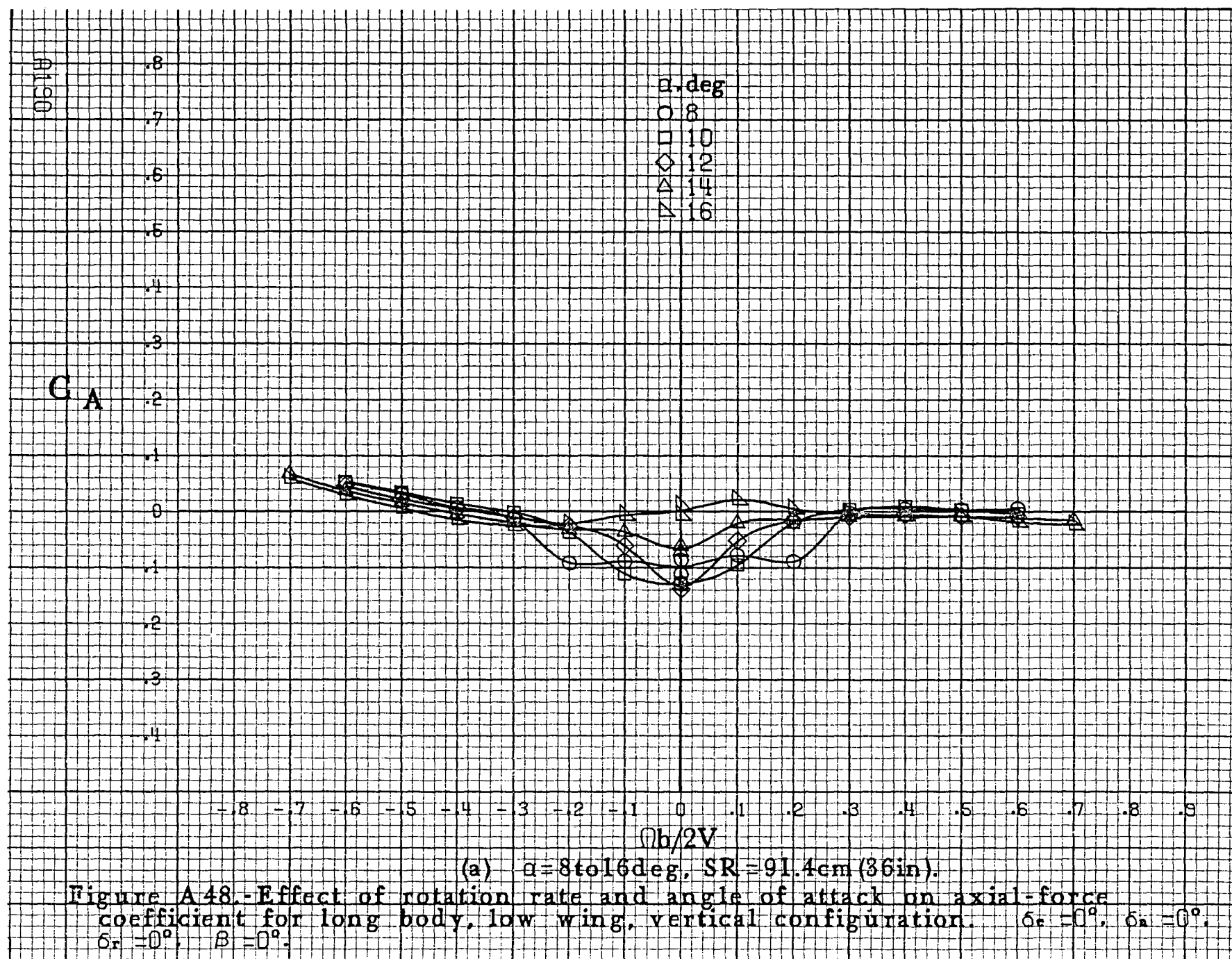


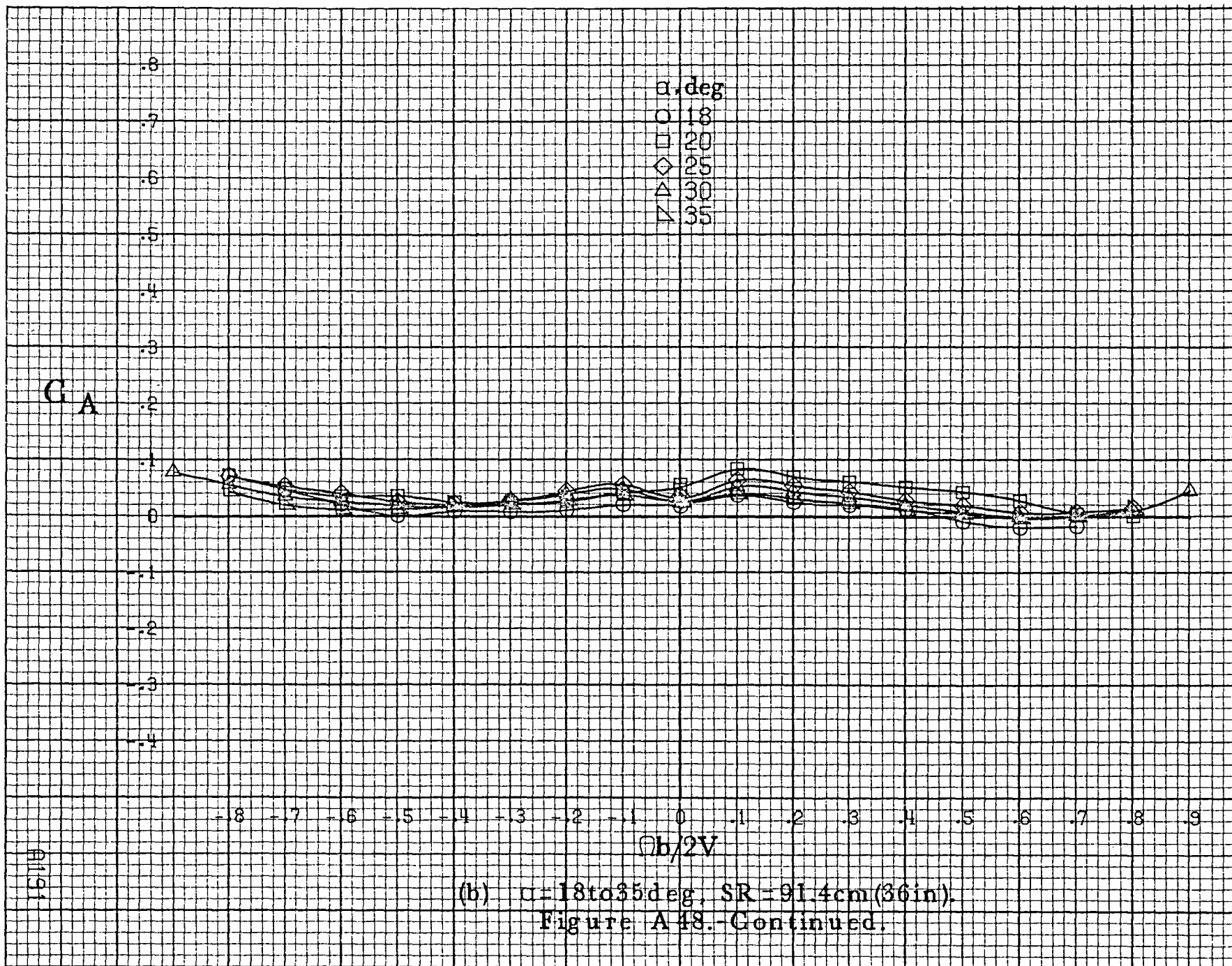
(b) $\alpha = 18$ to 35° , SR = 91.4 cm (36 in).
Figure A 47.-Continued.

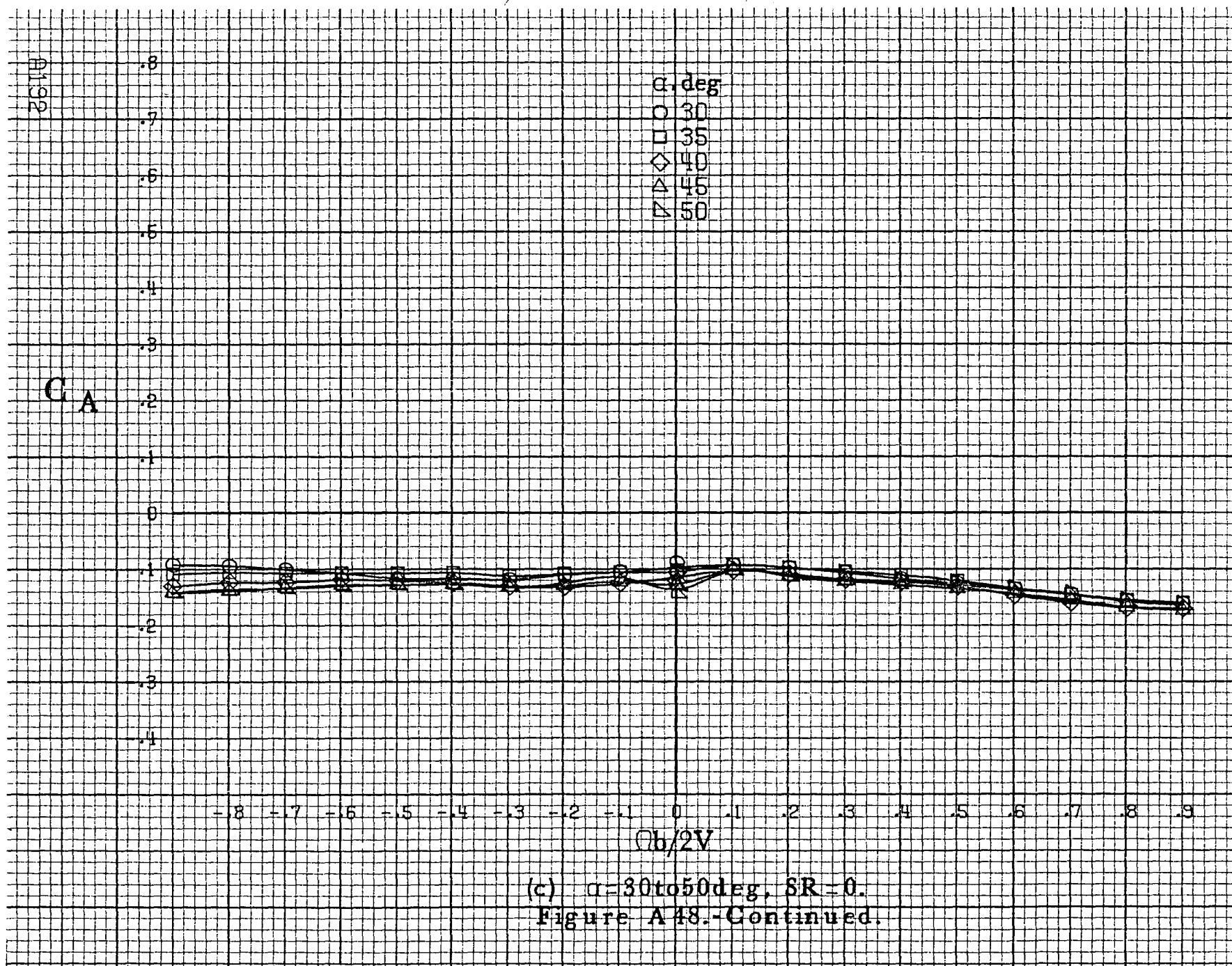


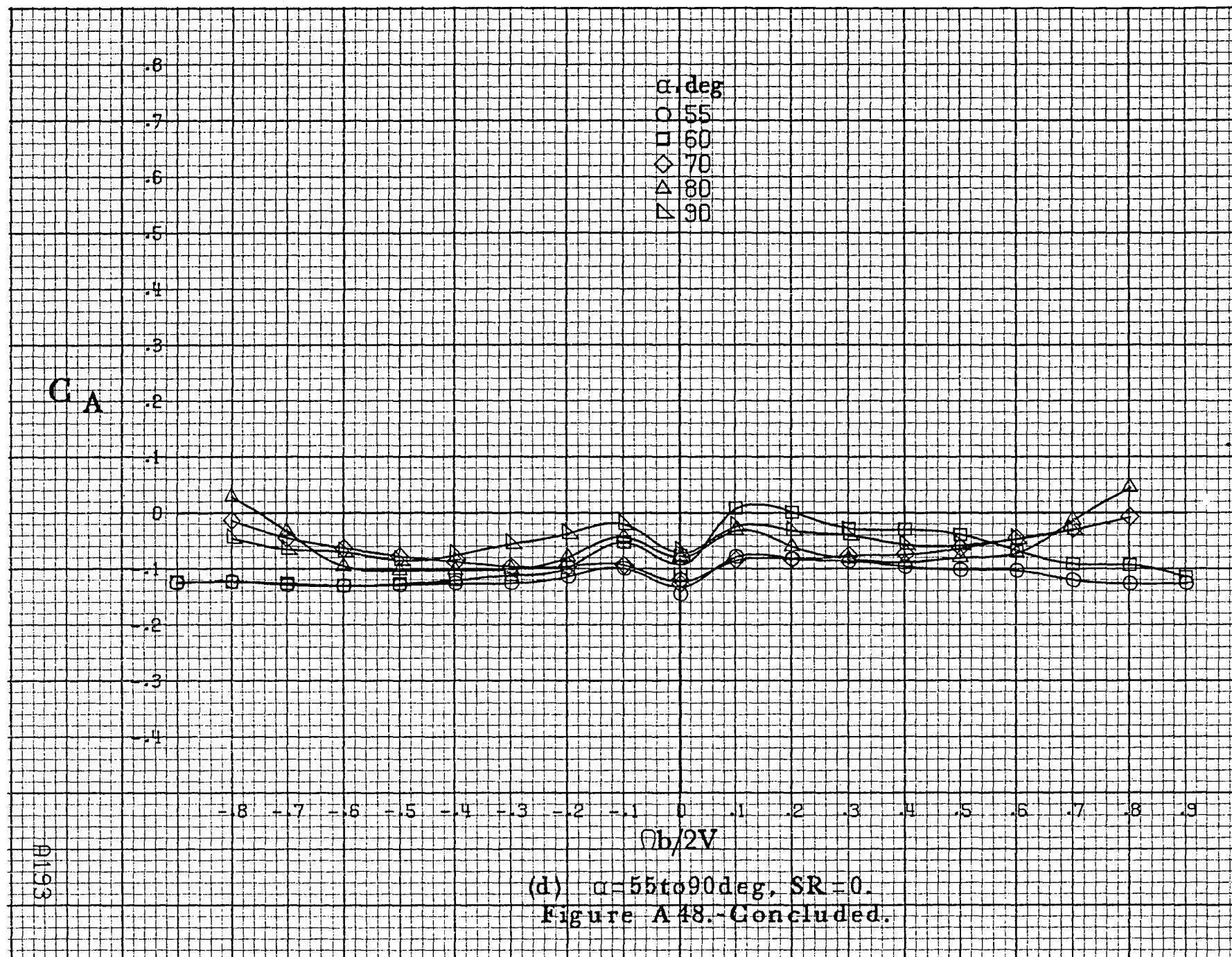


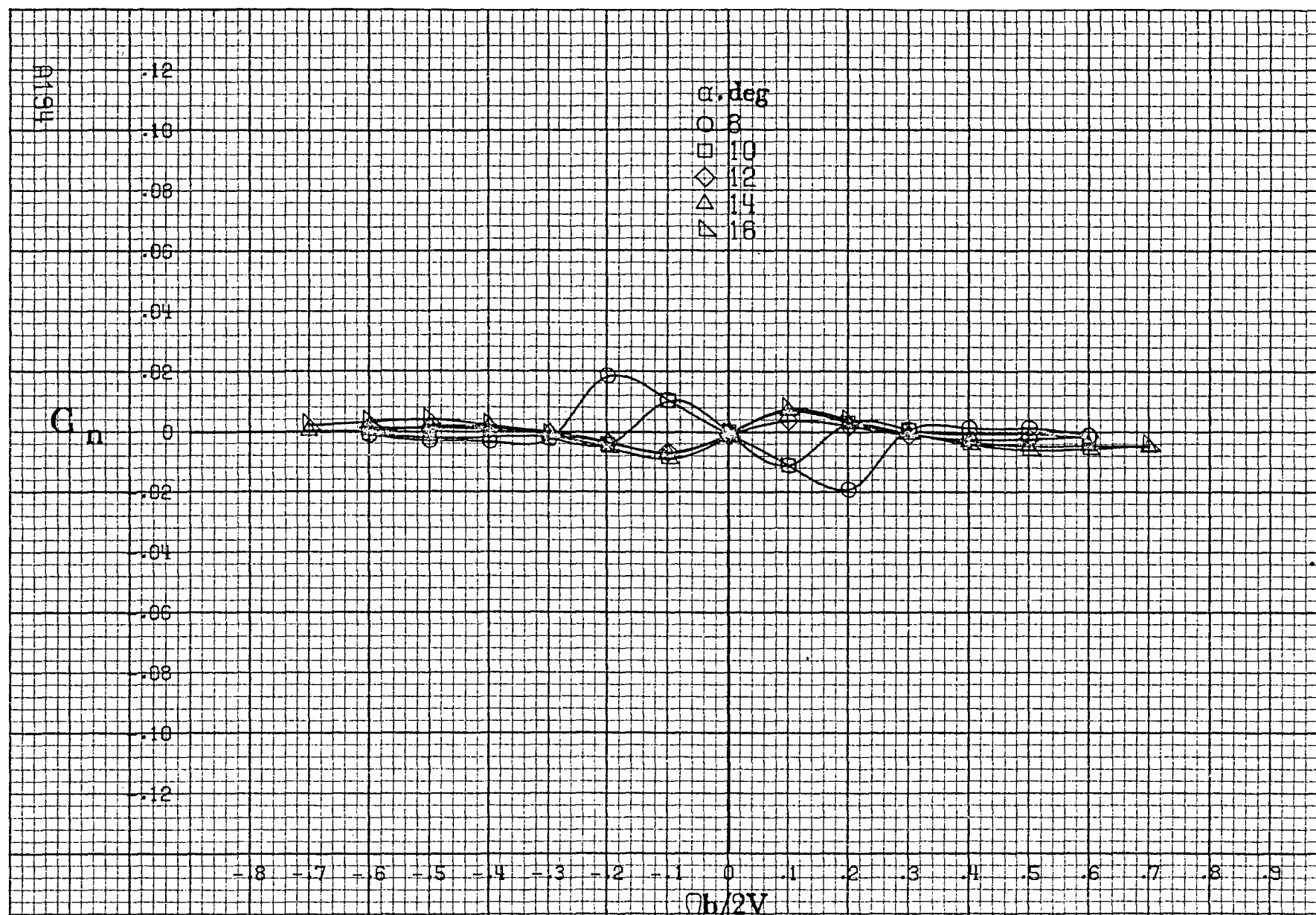
(d) $\alpha=55$ to 90° , $SR=0$.
Figure A 47.-Concluded.





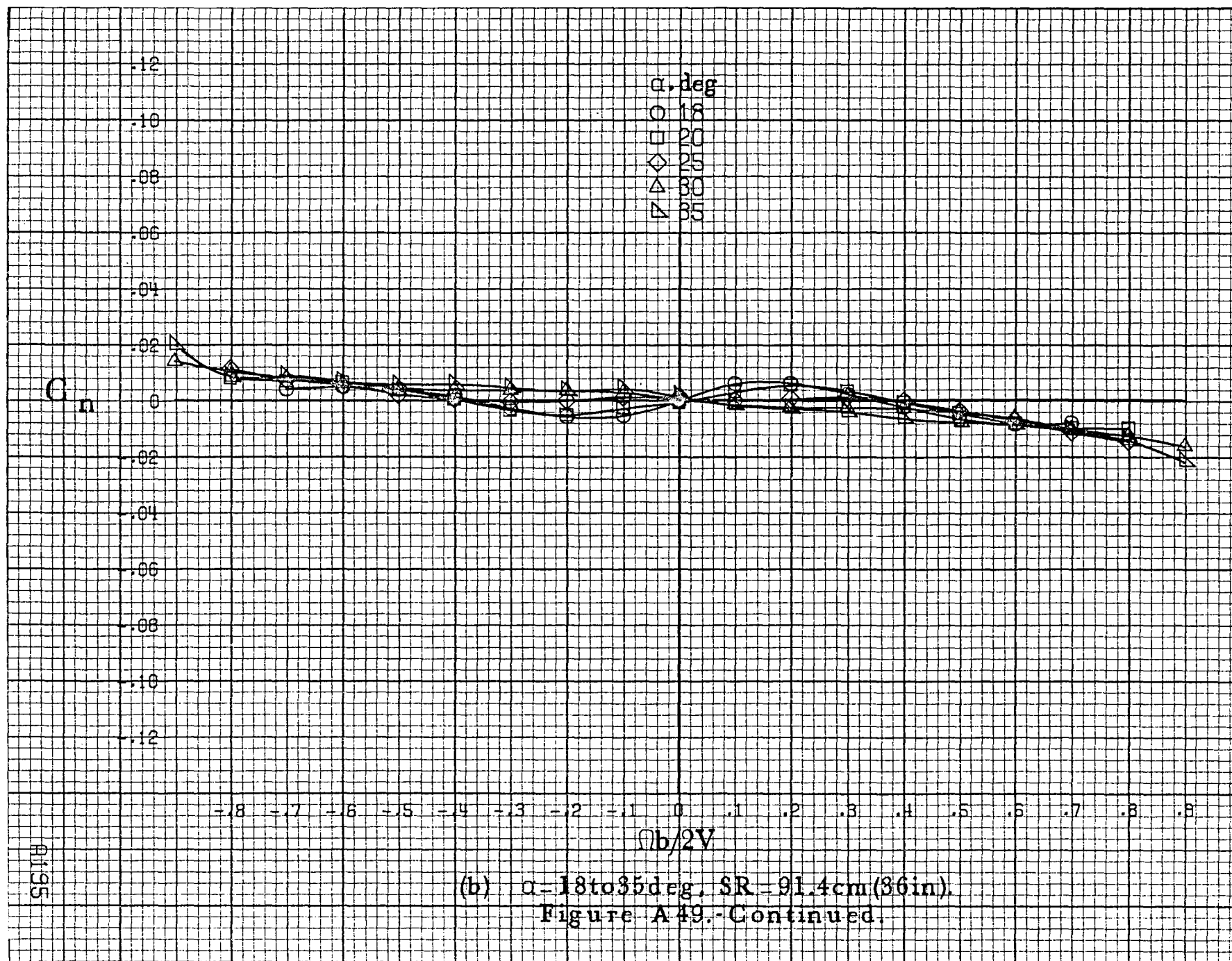


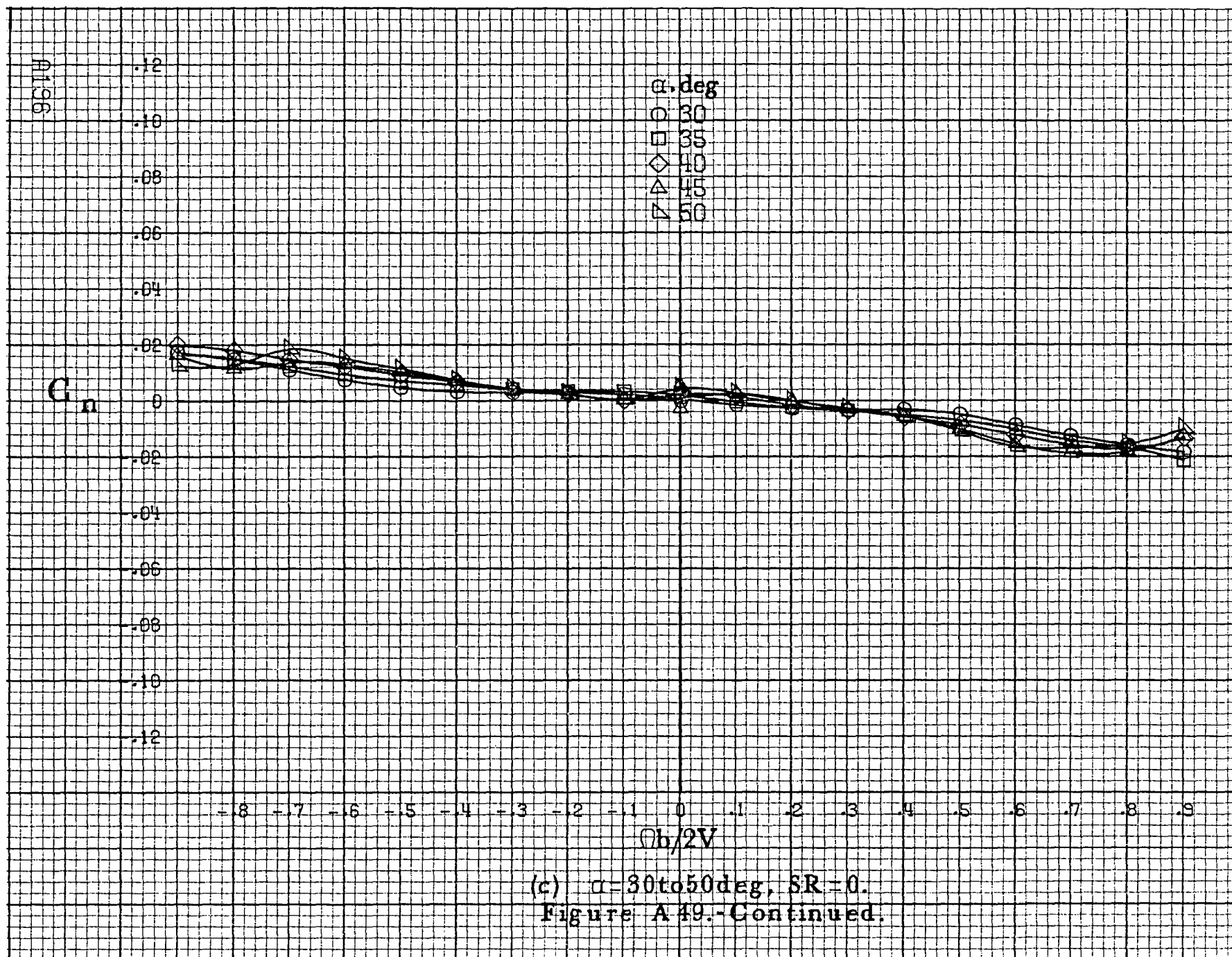


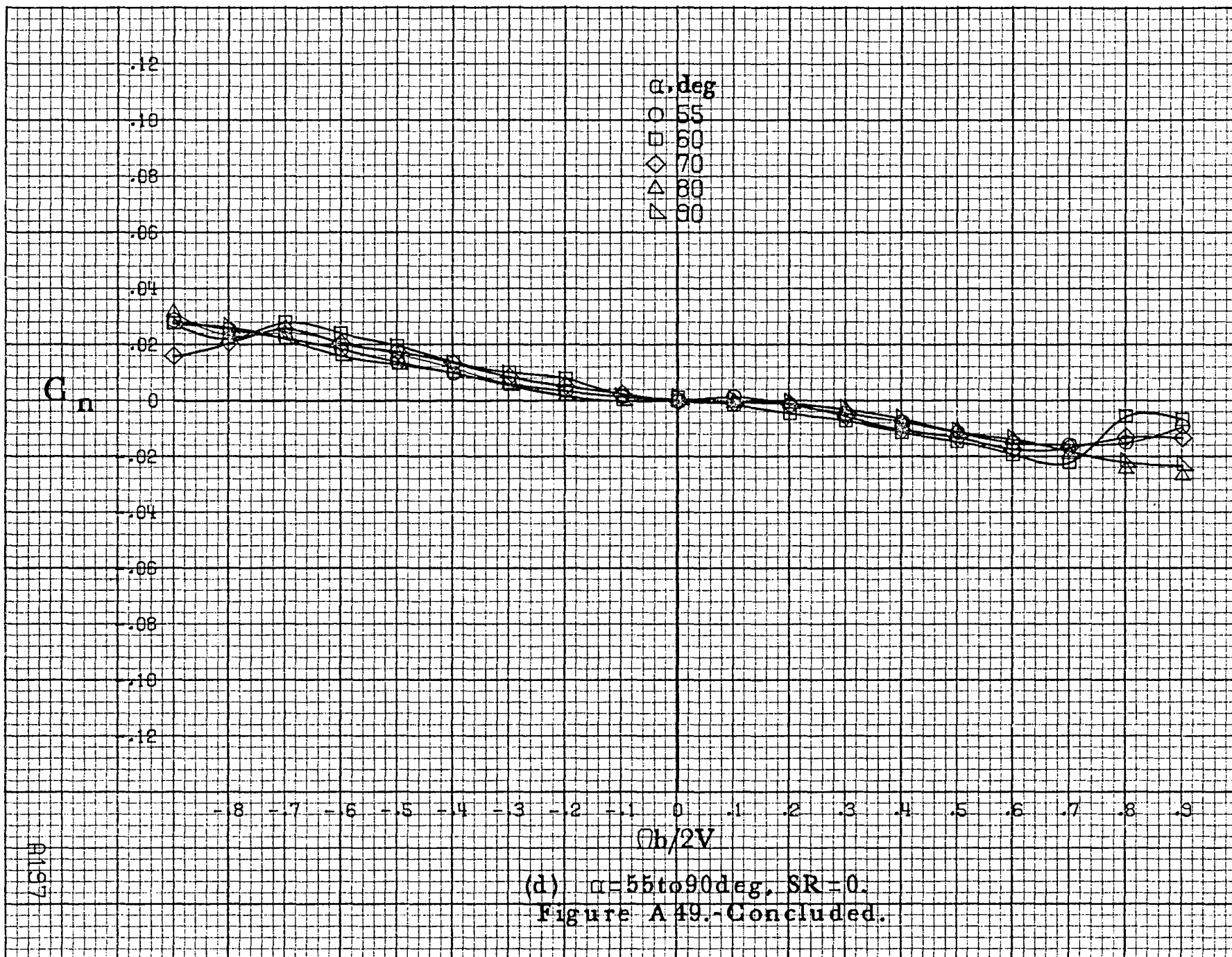


(a) $\alpha=8$ to 16° , $SR=91.4\text{cm}$ (36in).

Figure A49 - Effect of rotation rate and angle of attack on yawing-moment coefficient for long body, low wing, horizontal configuration. $\delta_r=0^\circ$, $\delta_a=0^\circ$, $\beta=0^\circ$.







(d) $\alpha = 55$ to 90° , $SR = 0$.
Figure A 49.-Concluded.

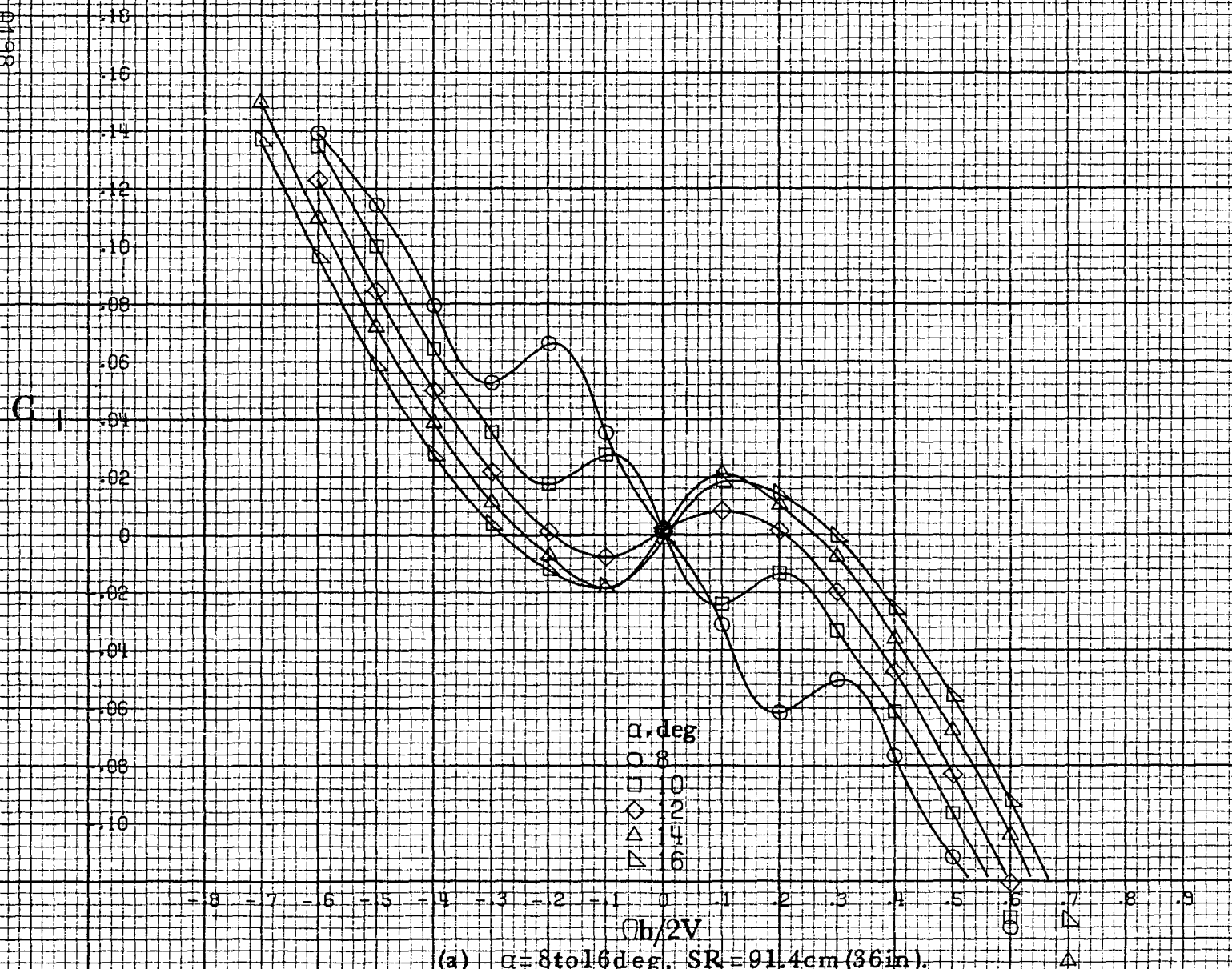
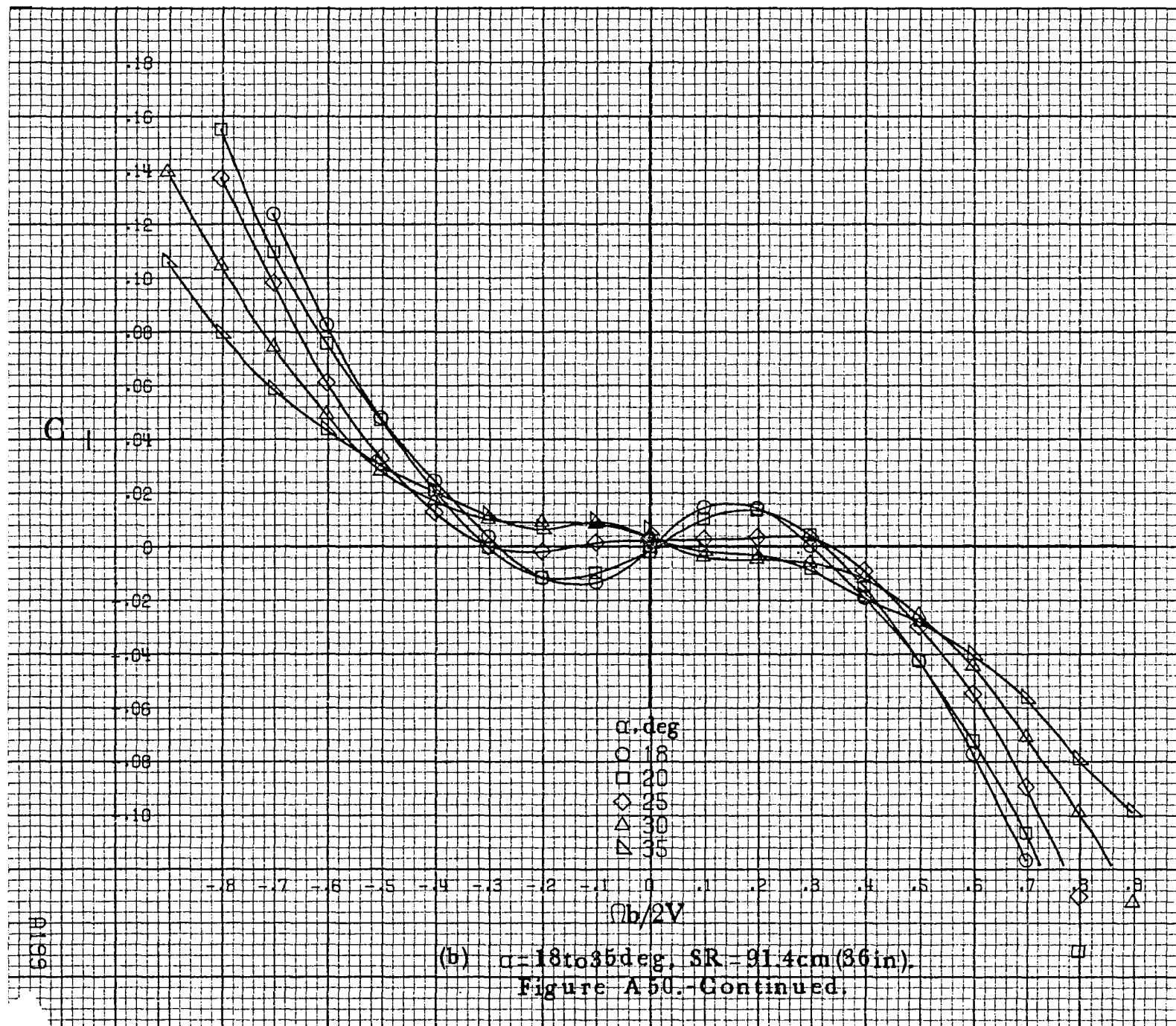
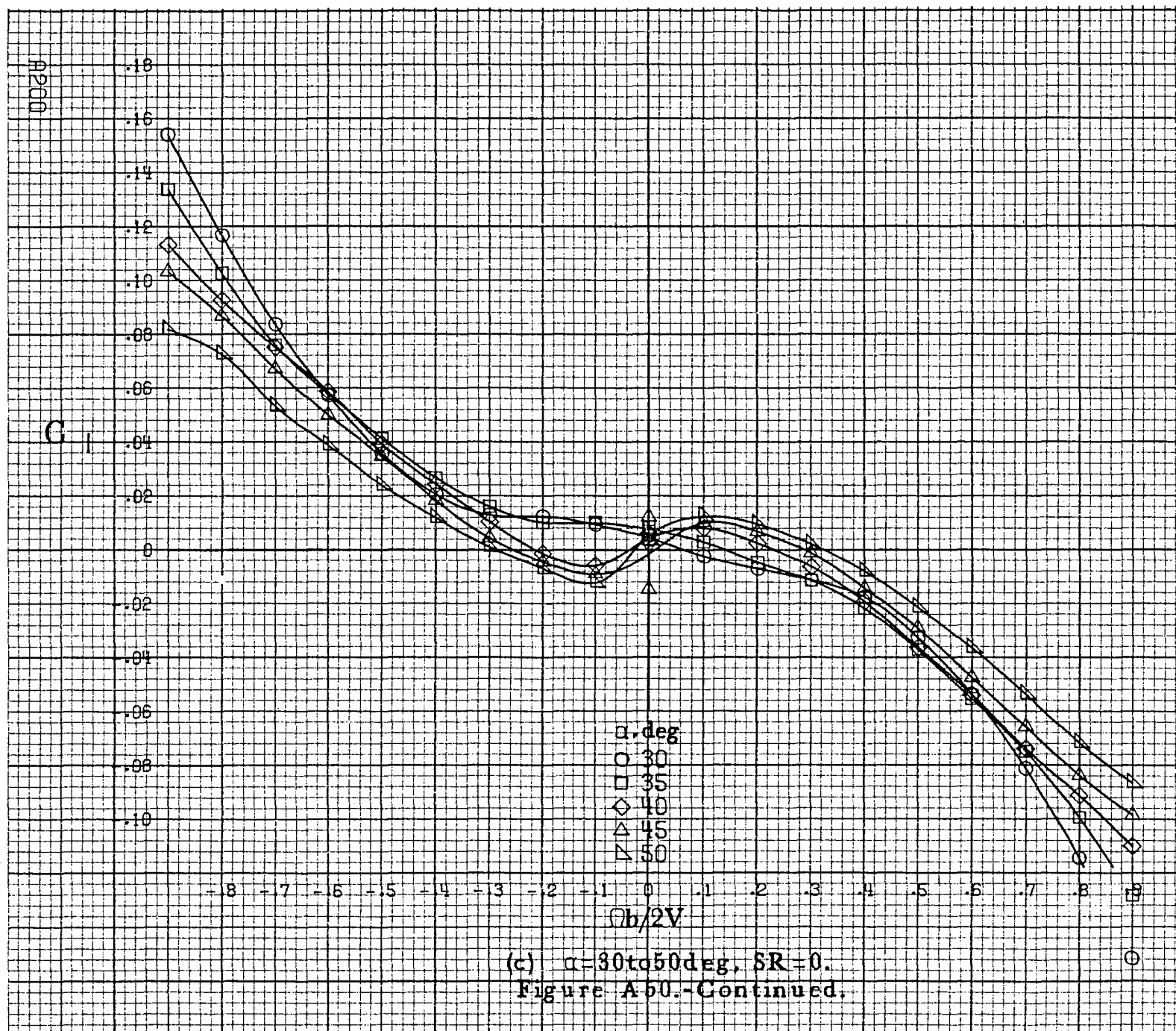
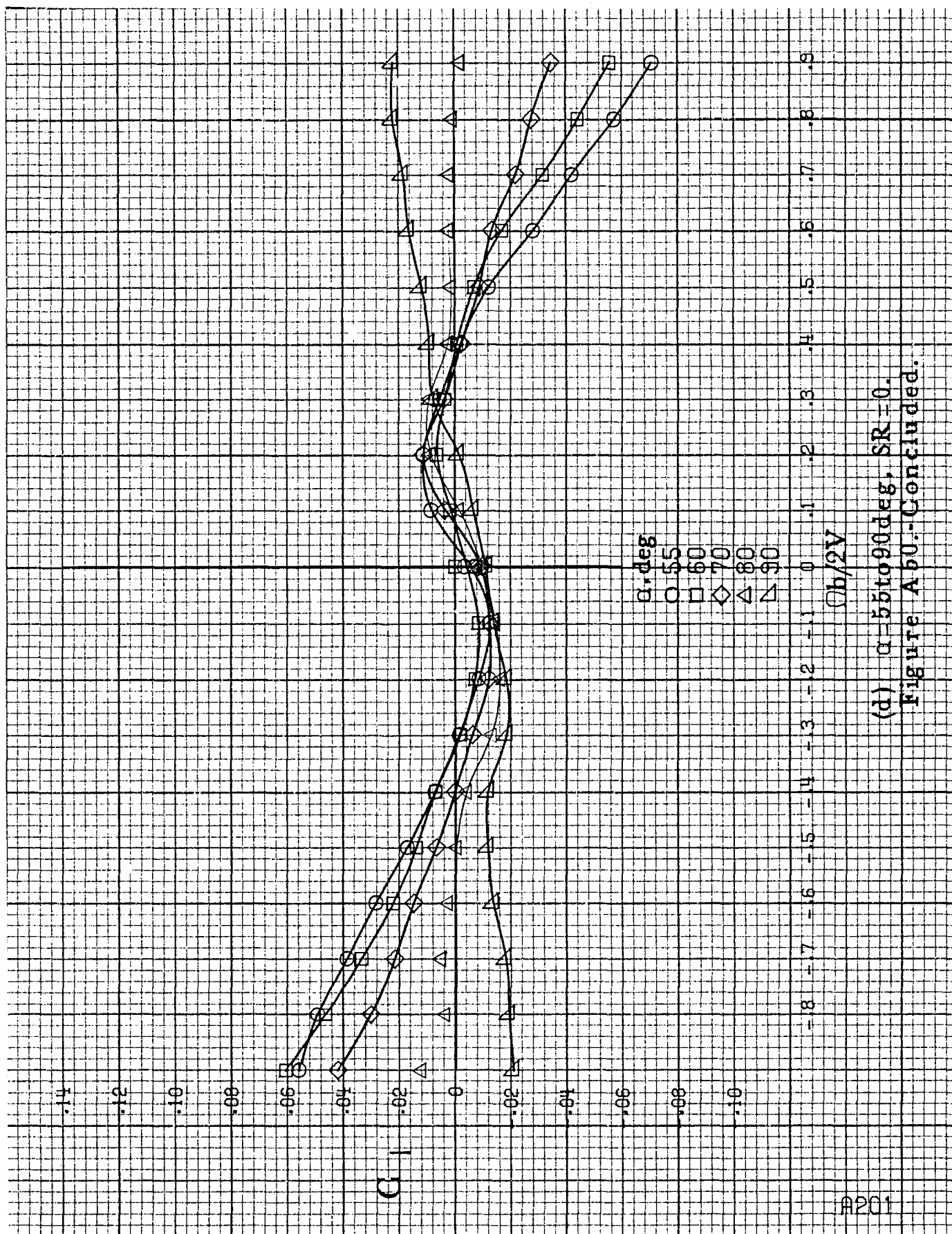


Figure A50.-Effect of rotation rate and angle of attack on rolling-moment coefficient for long body, low wing, horizontal configuration. $\delta_r = 0^\circ$, $\delta_a = 0^\circ$, $\beta = 0^\circ$.







(d) $\alpha=55$ to 90° , $SR=0$.
Figure A60.-Concluded.

C_m

.5
 .4
 .3
 .2
 .1
 0
 -.1
 -.2
 -.3
 -.4
 -.5
 -.6
 -.7

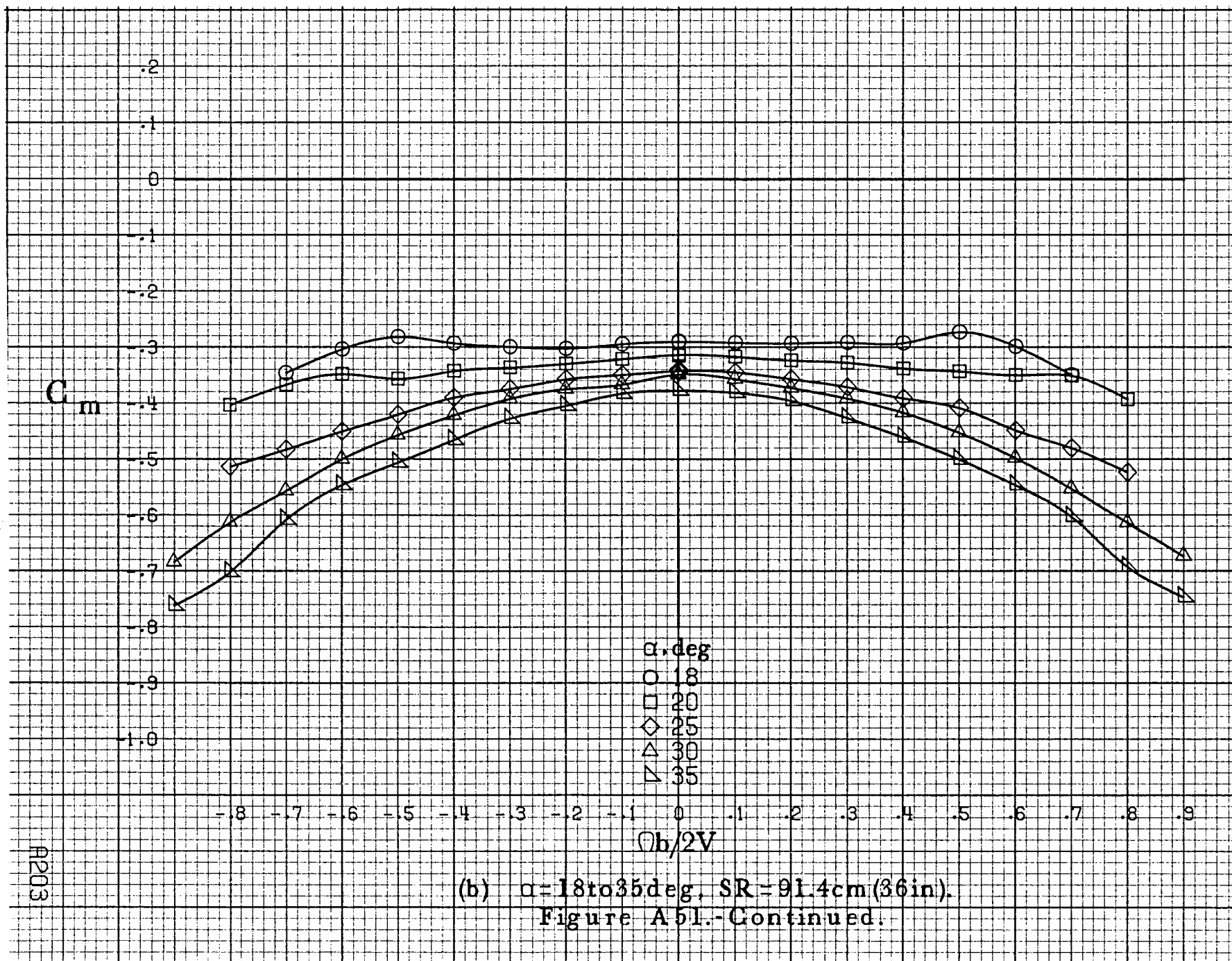
α , deg
 ○ 8
 □ 10
 ◇ 12
 △ 14
 ▽ 16

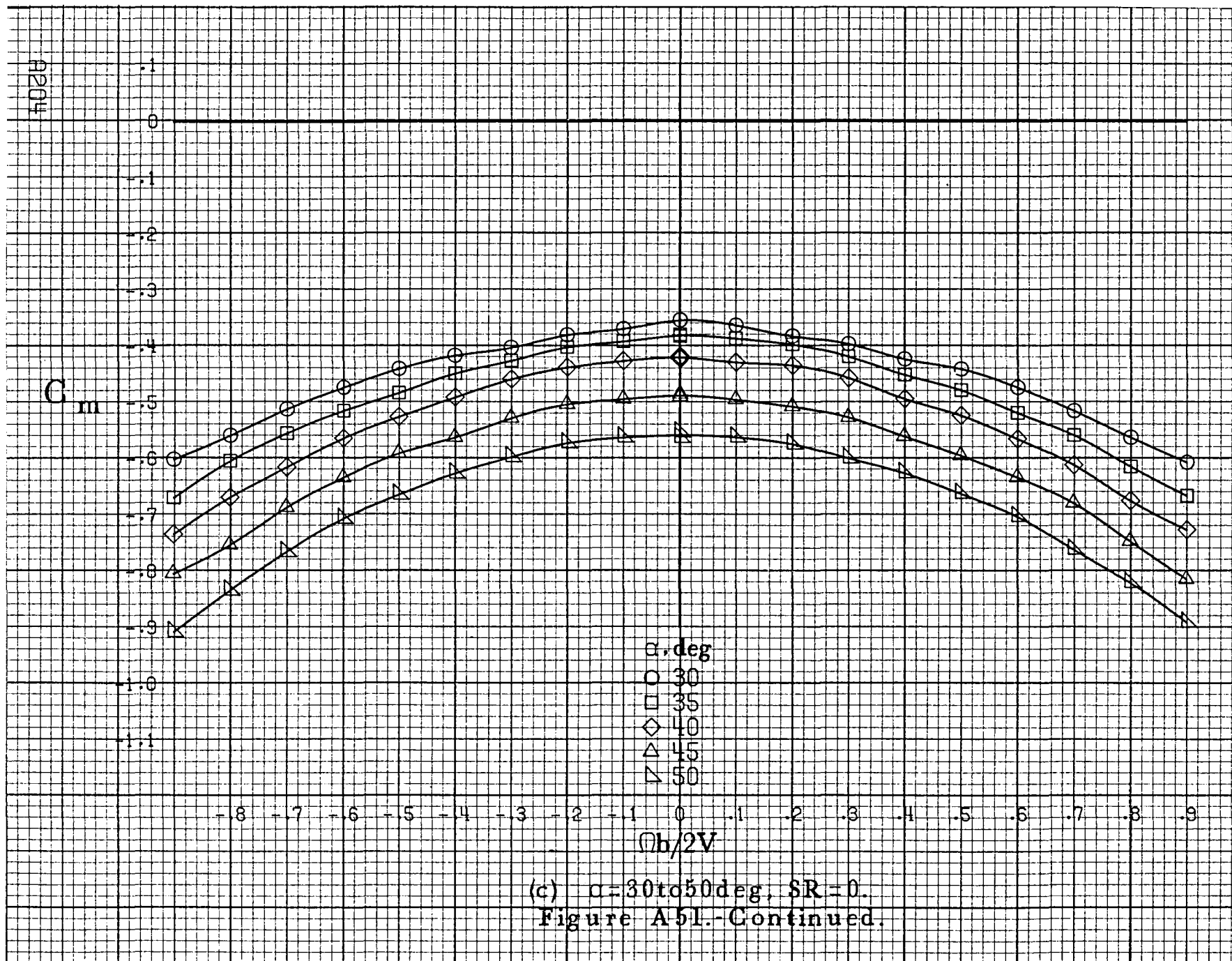
 $\Omega b/2V$

-.8 -.7 -.6 -.5 -.4 -.3 -.2 -.1 0 .1 .2 .3 .4 .5 .6 .7 .8 .9

(a) $\alpha = 8$ to 16 deg, $SR = 91.4$ cm (36 in).

Figure A51 - Effect of rotation rate and angle of attack on pitching-moment coefficient for long body, low wing, horizontal configuration. $\delta_e = 0^\circ$, $\delta_a = 0^\circ$, $\delta_r = 0^\circ$, $\beta = 0^\circ$.





C_m

α, deg

○ 55

□ 60

◇ 70

△ 80

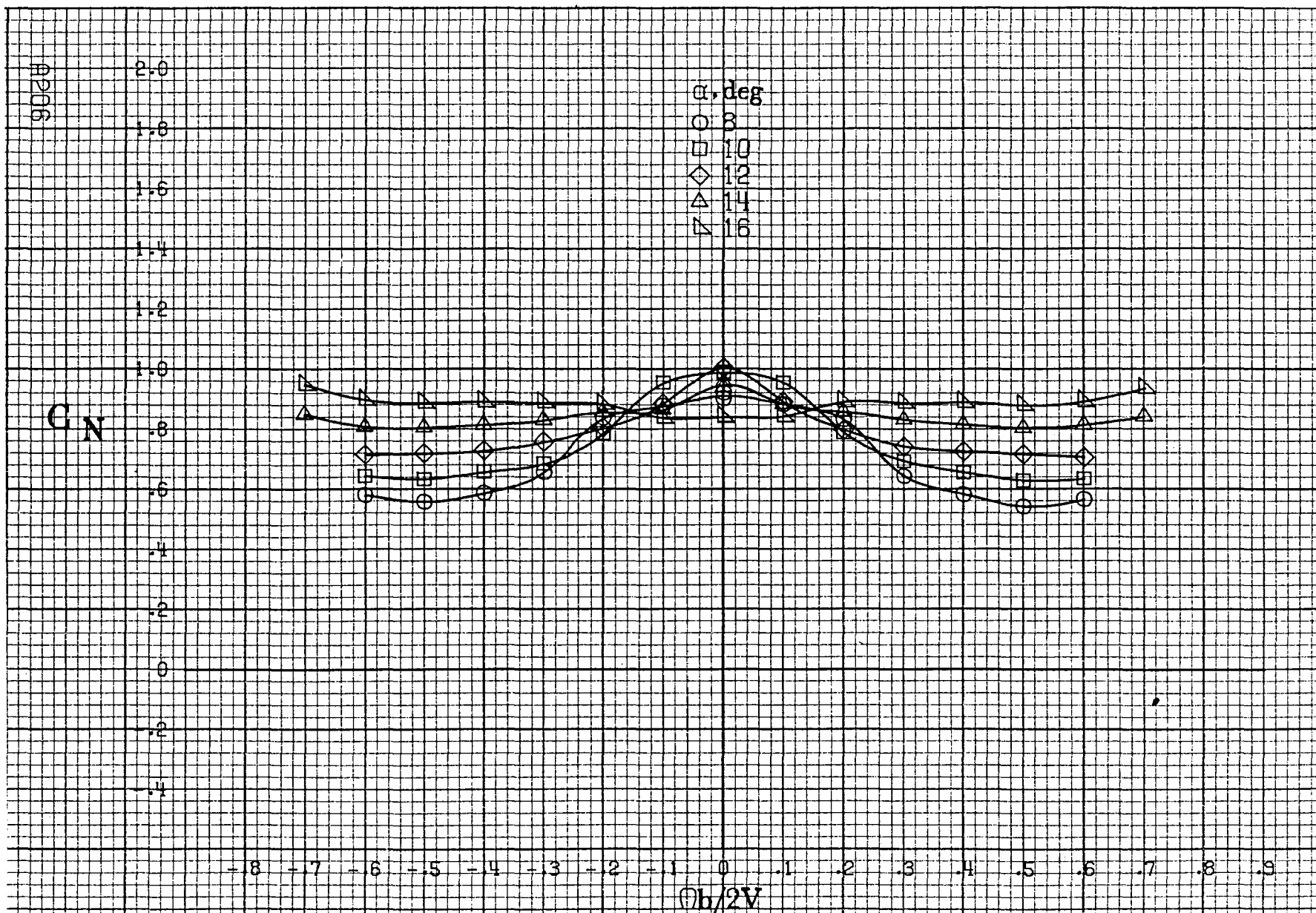
▽ 90

$b/2V$

(d) $\alpha=55$ to 90 deg, $SR=0$.

Figure A51.-Concluded.

A205



(a) $\alpha = 8$ to 16° , $SR = 91.4\text{cm (36in)}$.

Figure A52.- Effect of rotation rate and angle of attack on normal-force coefficient for long body, low wing, horizontal configuration. $\delta_r = 0^\circ$, $\delta_a = 0^\circ$, $\delta_r = 0^\circ$, $\beta = 0^\circ$.

C_N

α, deg

○ 18

□ 20

◇ 25

△ 30

▽ 35

2.6

2.4

2.2

2.0

1.8

1.6

1.4

1.2

1.0

.8

.6

.4

.2

-.8

-.7

-.6

-.5

-.4

-.3

-.2

-.1

0

.1

.2

.3

.4

.5

.6

.7

.8

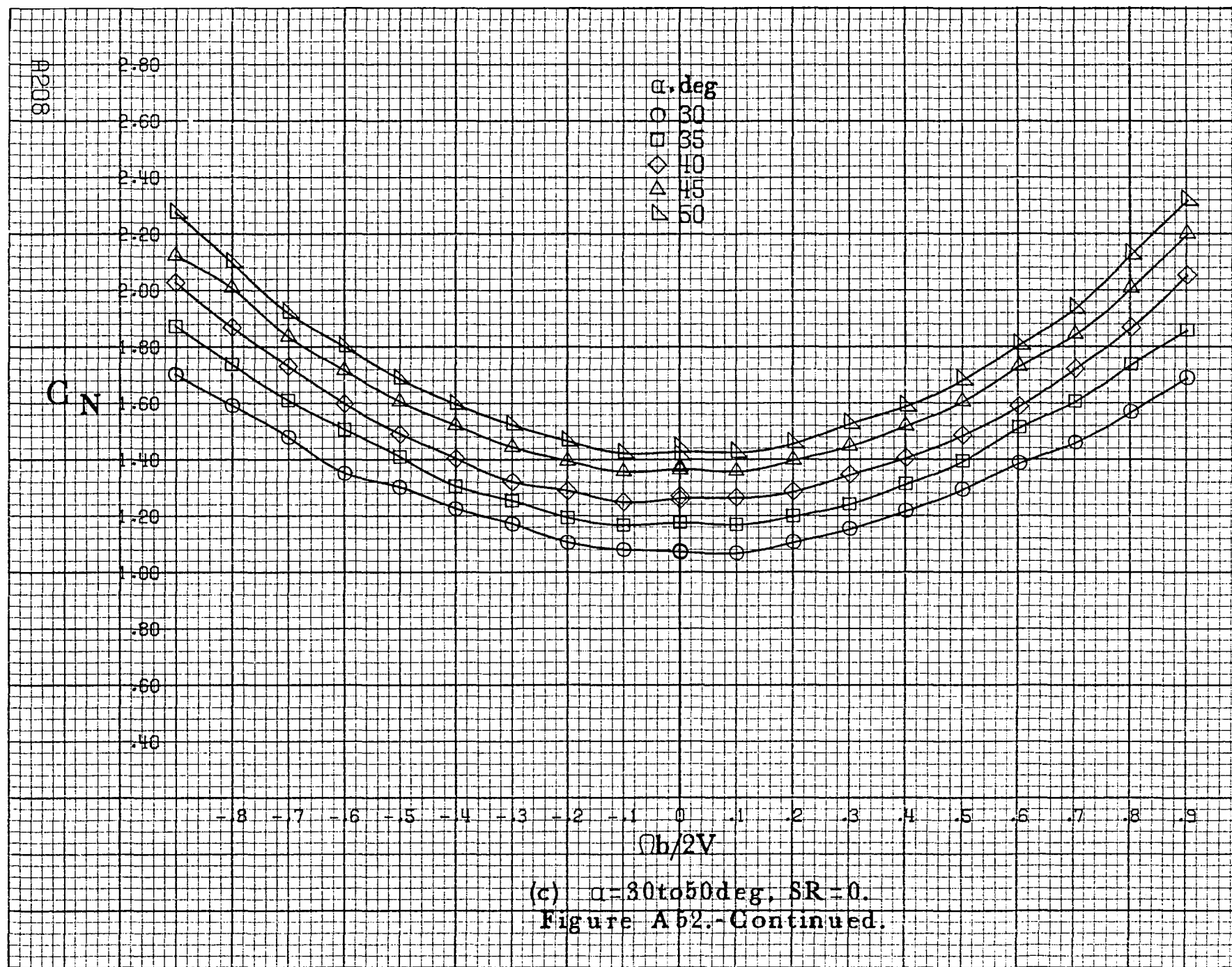
.9

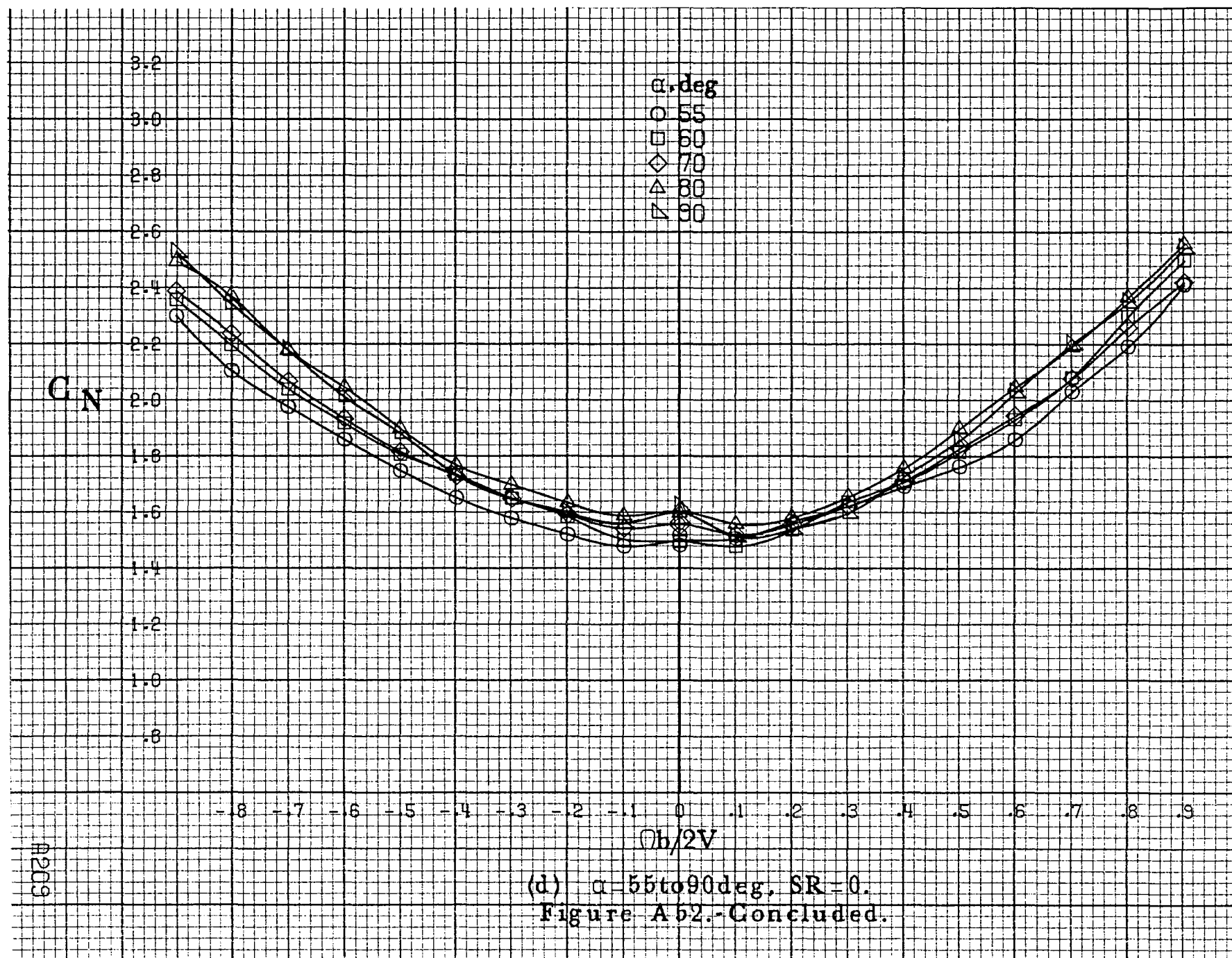
$b/2V$

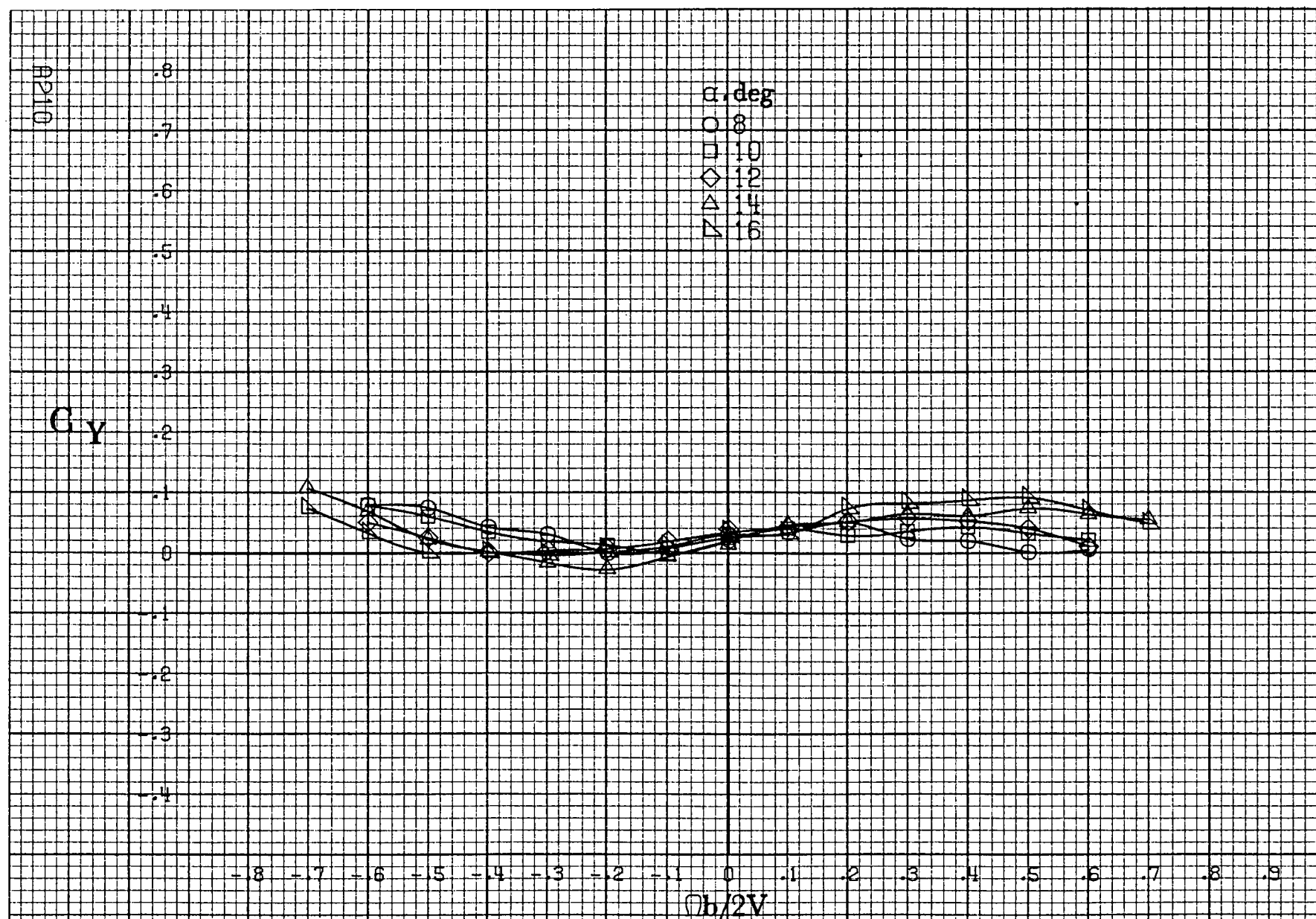
(b) $\alpha=18$ to 35 deg, SR=91.4cm (36in).

Figure A 52.-Continued.

A207

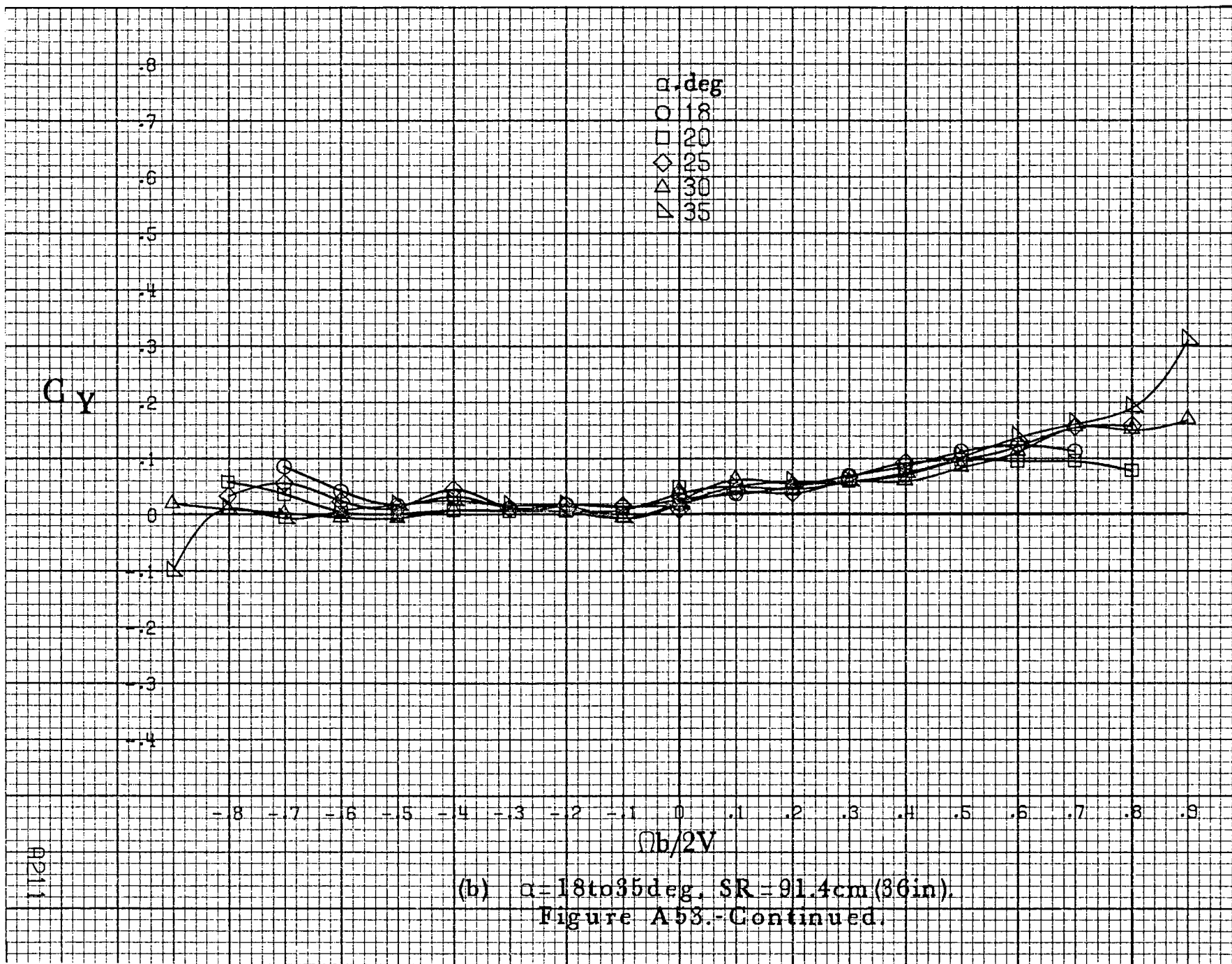






(a) $\alpha=8\text{ to }16^\circ$, $SR=91.4\text{cm}(36\text{in})$.

Figure A53 - Effect of rotation rate and angle of attack on side-force coefficient for long body, low wing, horizontal configuration. $\delta_e=0^\circ$, $\delta_a=0^\circ$, $\delta_r=0^\circ$, $\beta=0^\circ$.



8212

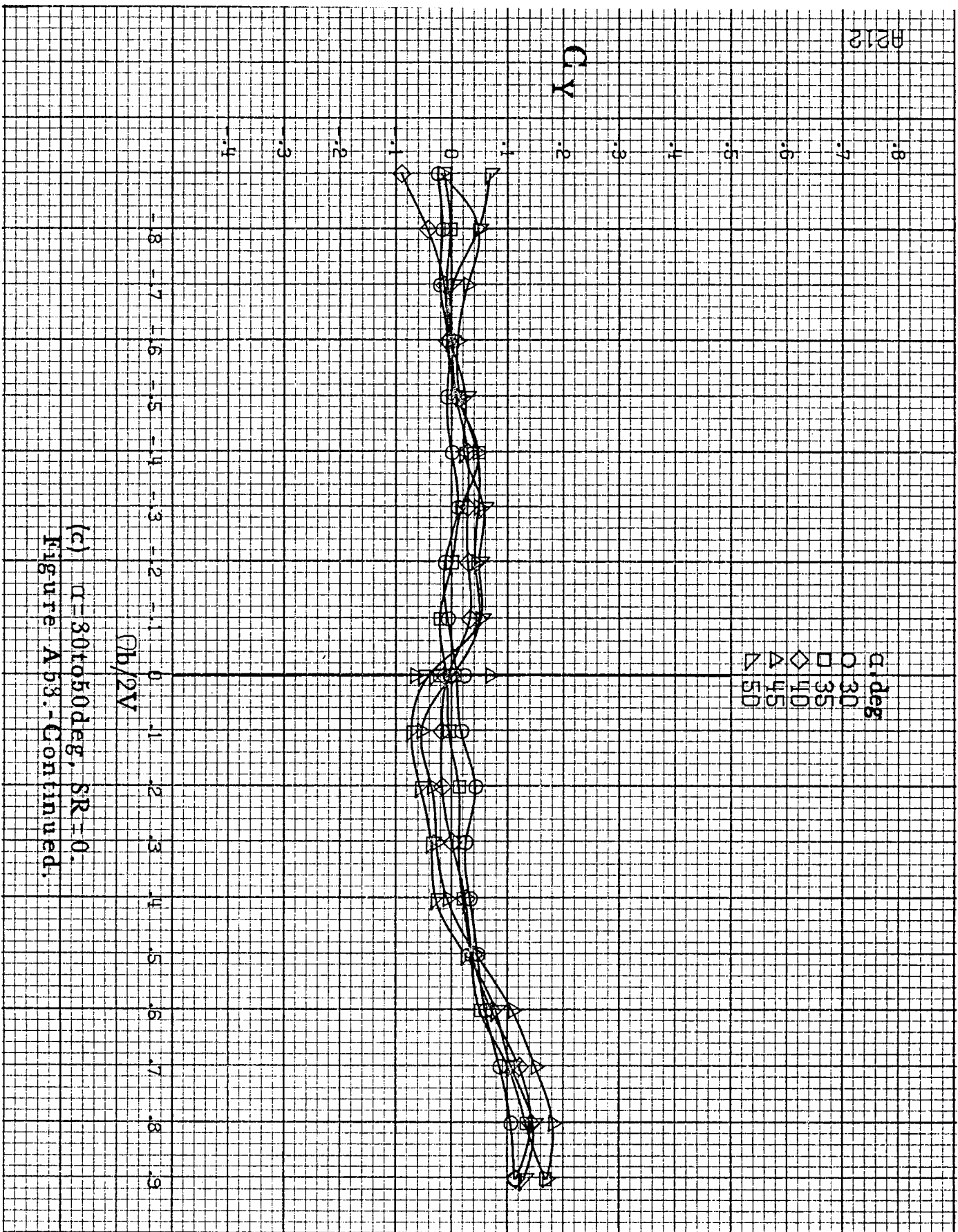
C_Y

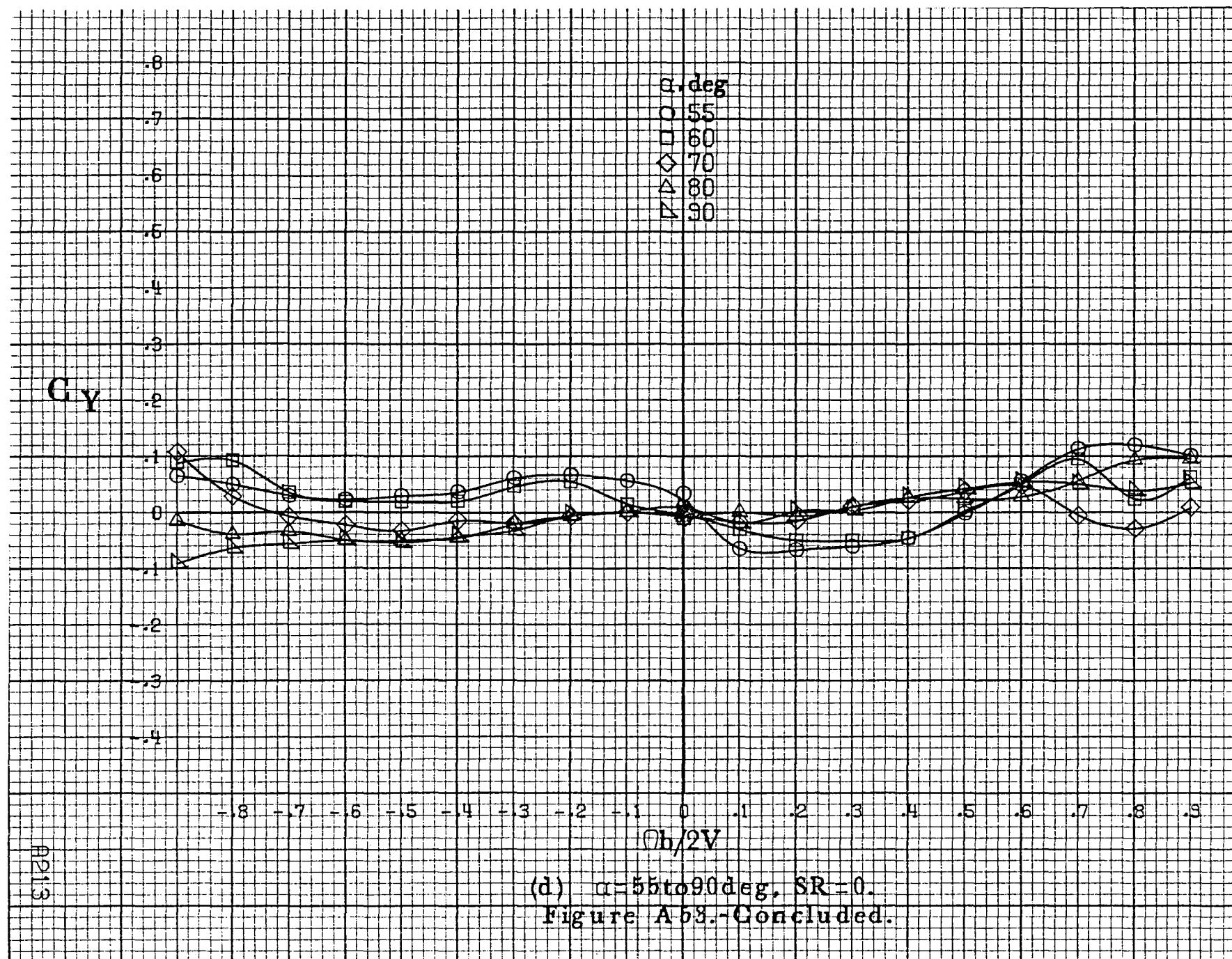
α, deg
 ○ 30
 □ 35
 ◇ 40
 △ 45
 ▲ 50

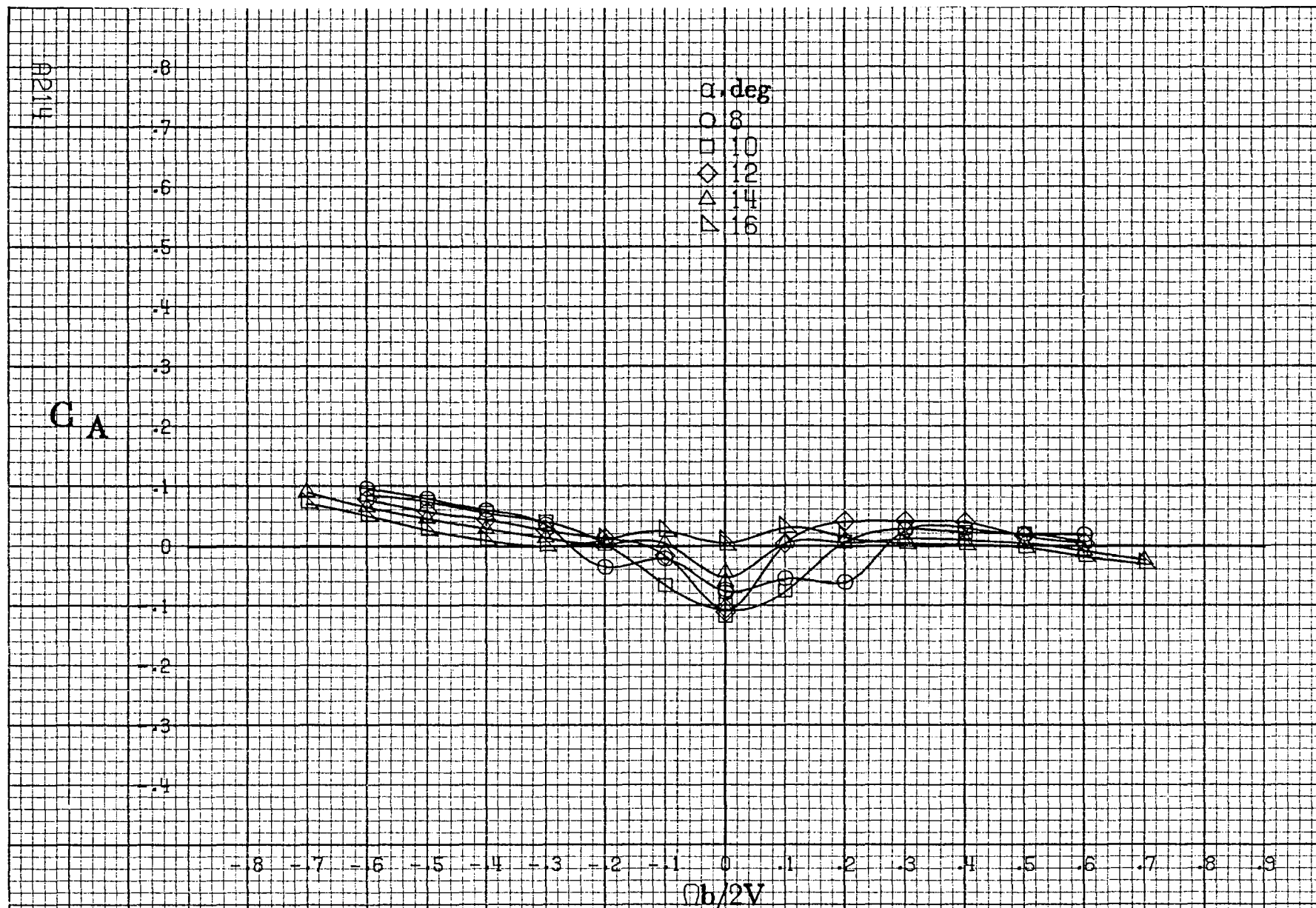
$b/2V$

(c) $\alpha=30$ to 50 deg, $SR=0$.

Figure A53.-Continued.

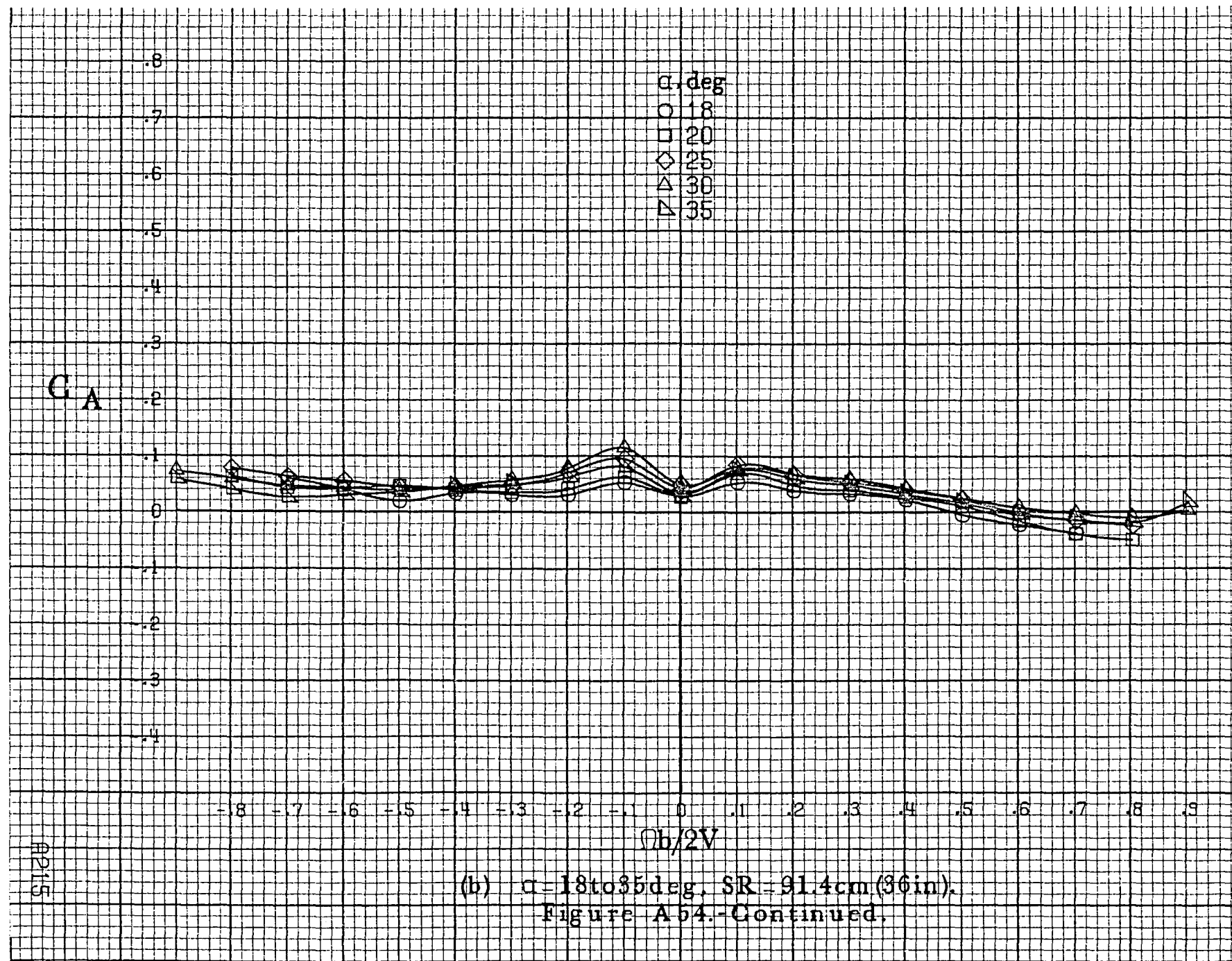




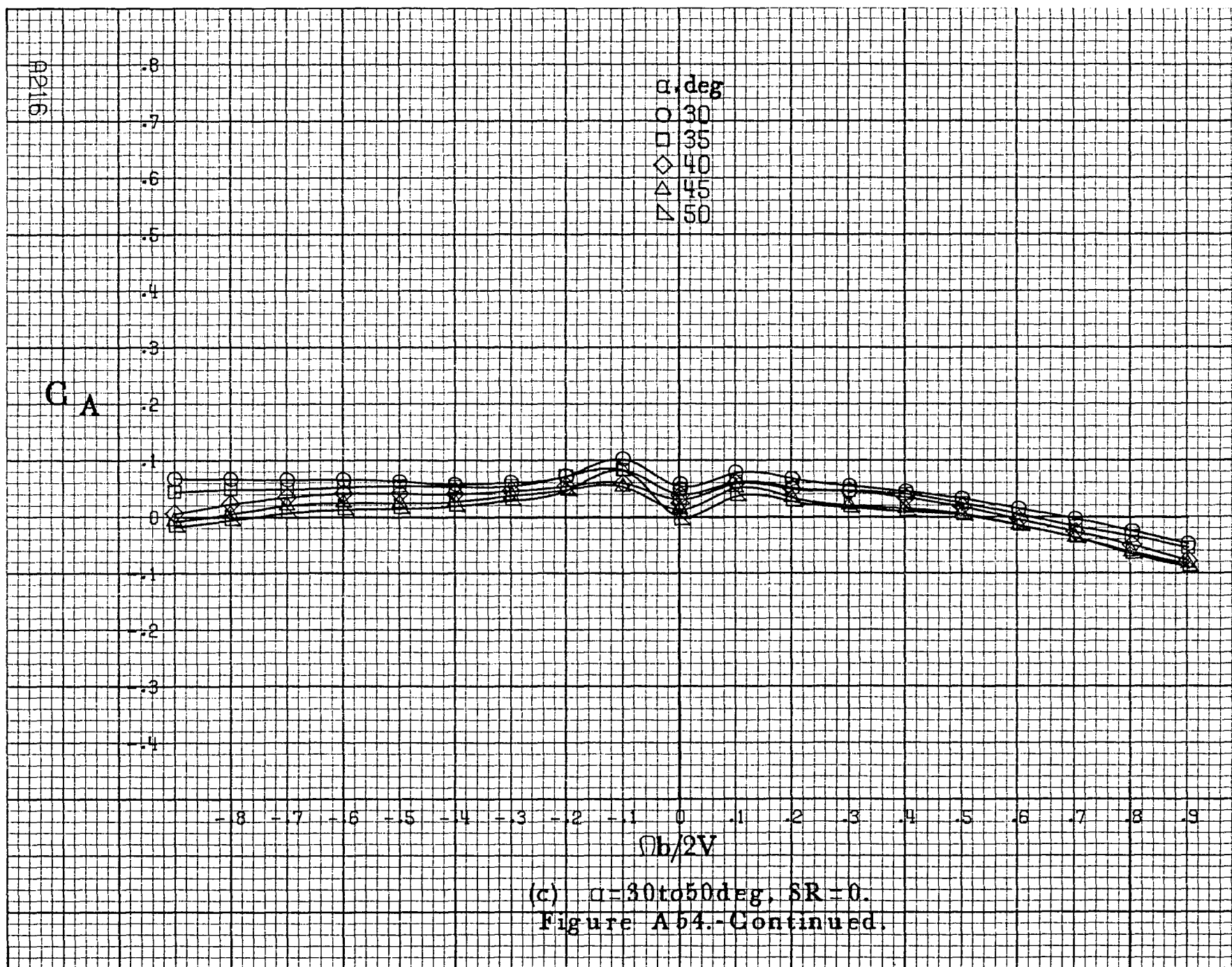


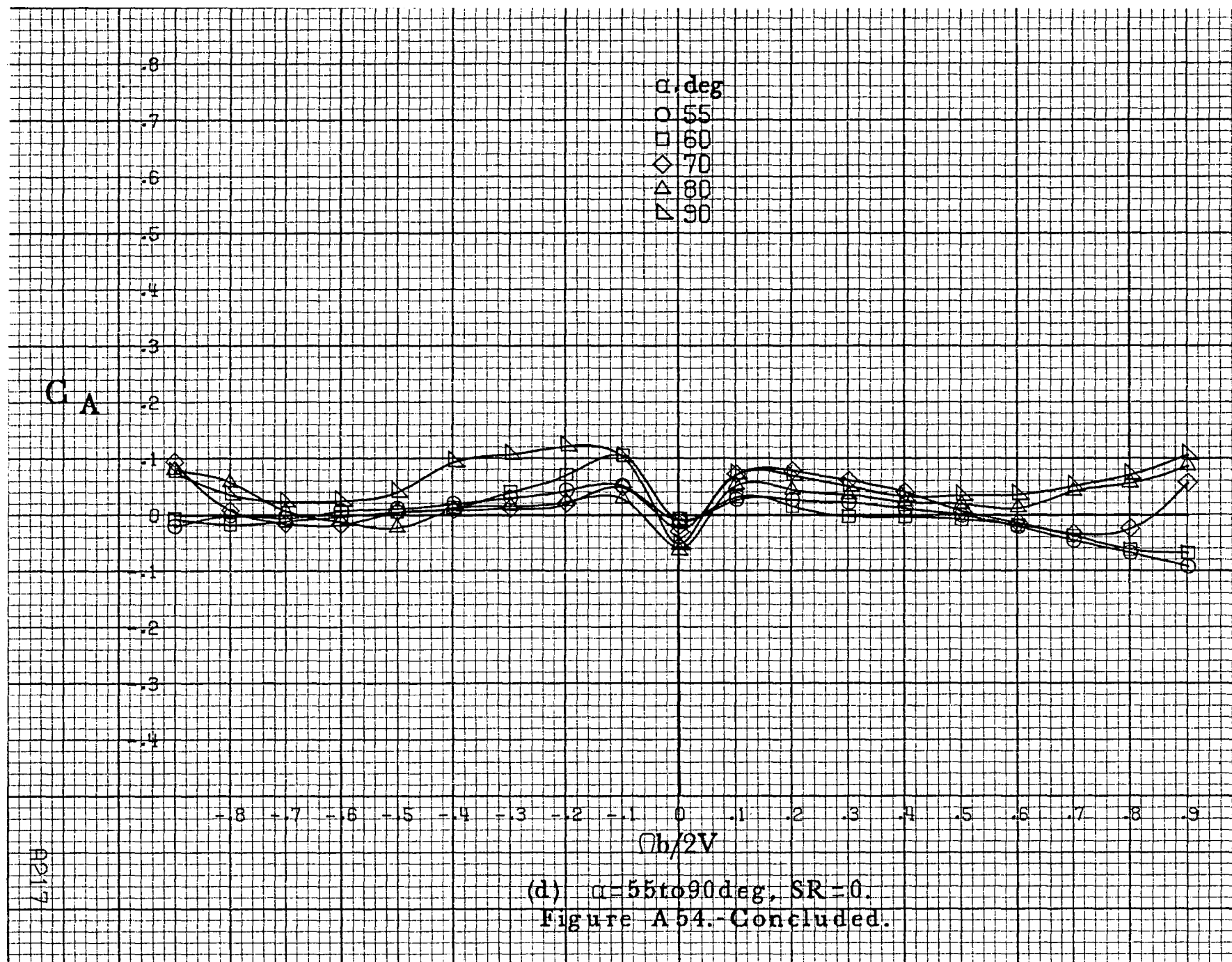
(a) $\alpha = 8 \text{ to } 16 \text{ deg}$, $SR = 91.4 \text{ cm (36 in)}$.

Figure A54 - Effect of rotation rate and angle of attack on axial-force coefficient for long body, low wing, horizontal configuration. $\delta_r = 0^\circ$, $\delta_a = 0^\circ$, $\delta_r = 0^\circ$, $\beta = 0^\circ$.

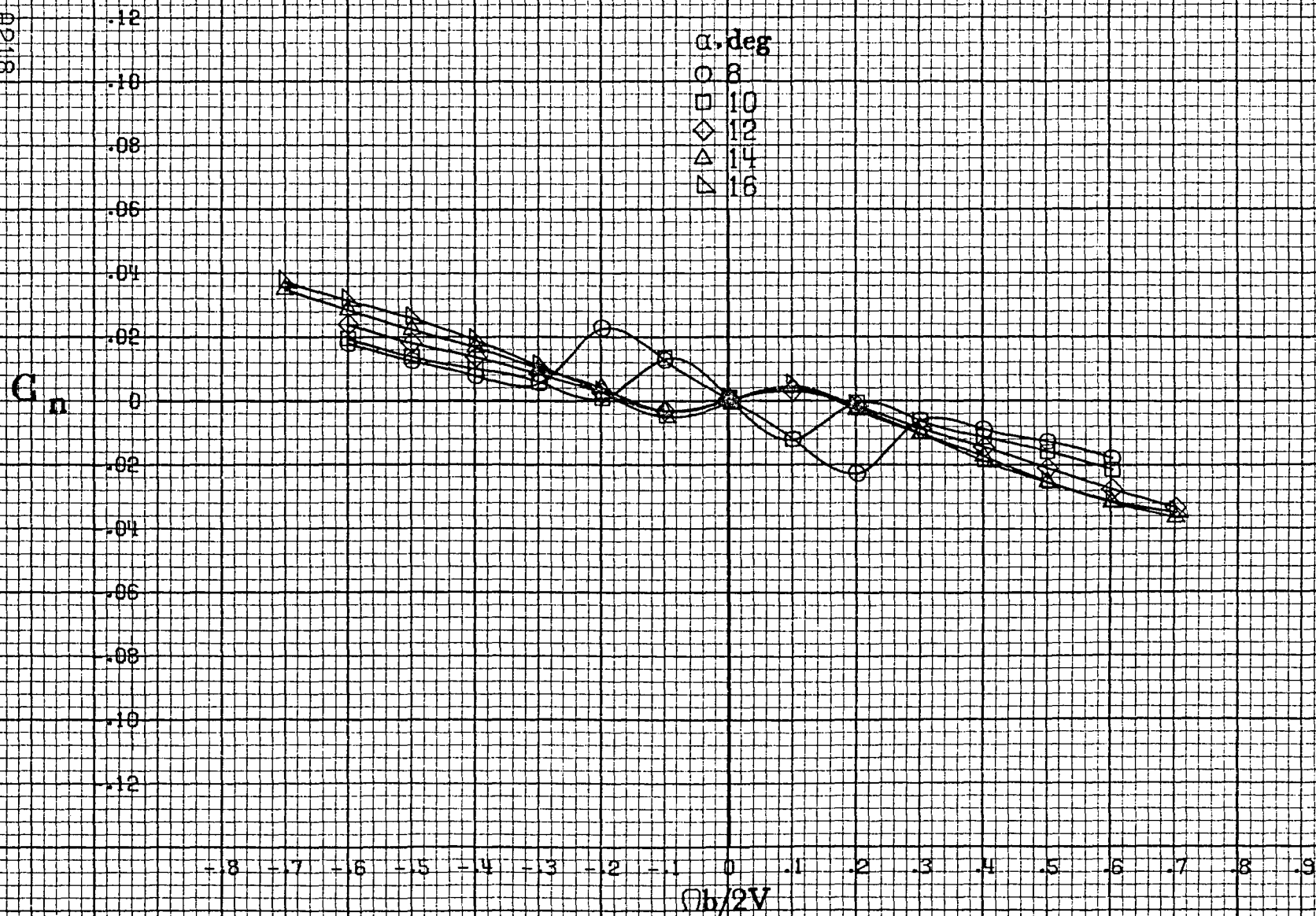


(b) $\alpha = 18$ to 35° , $SR = 91.4 \text{ cm (36 in.)}$.
Figure A54.-Continued.





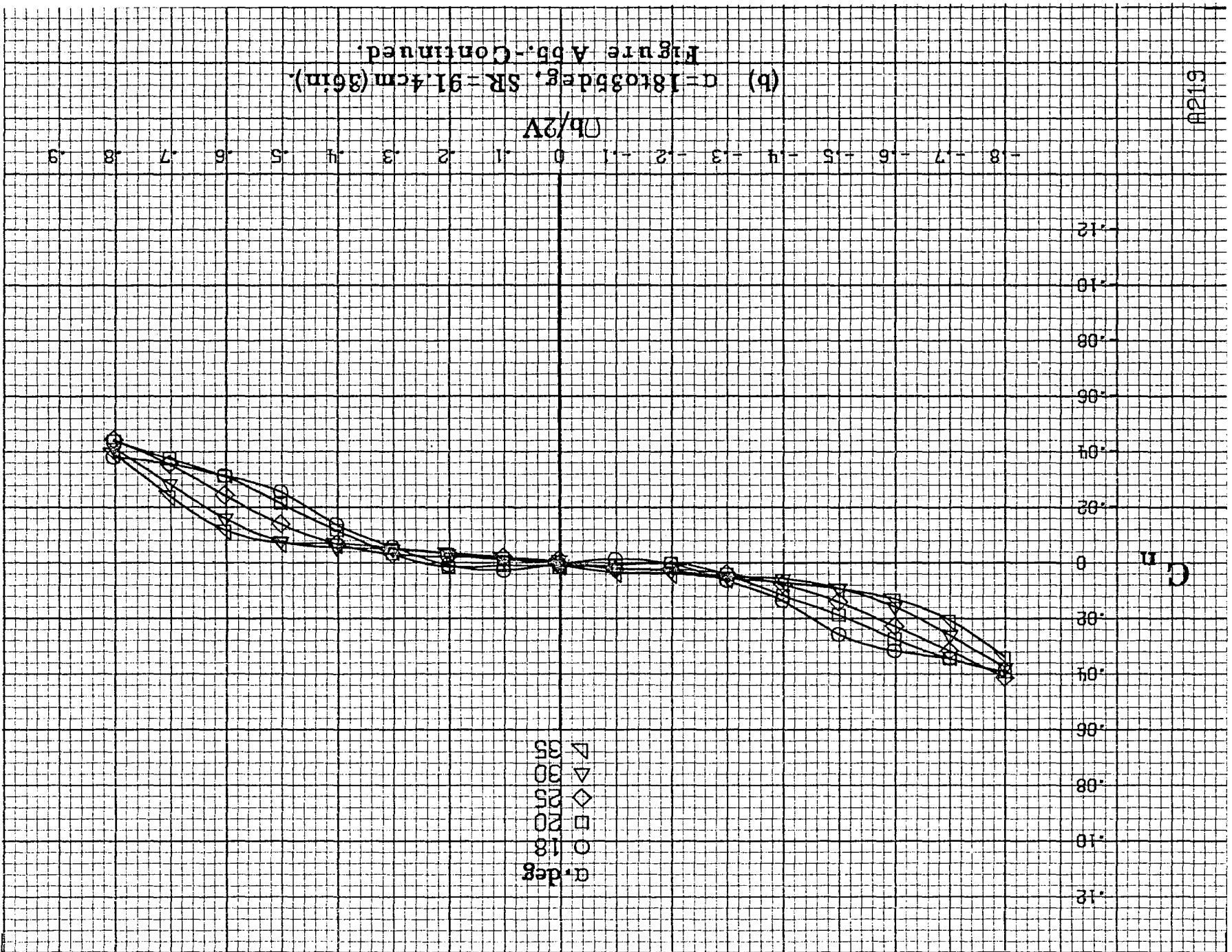
A218

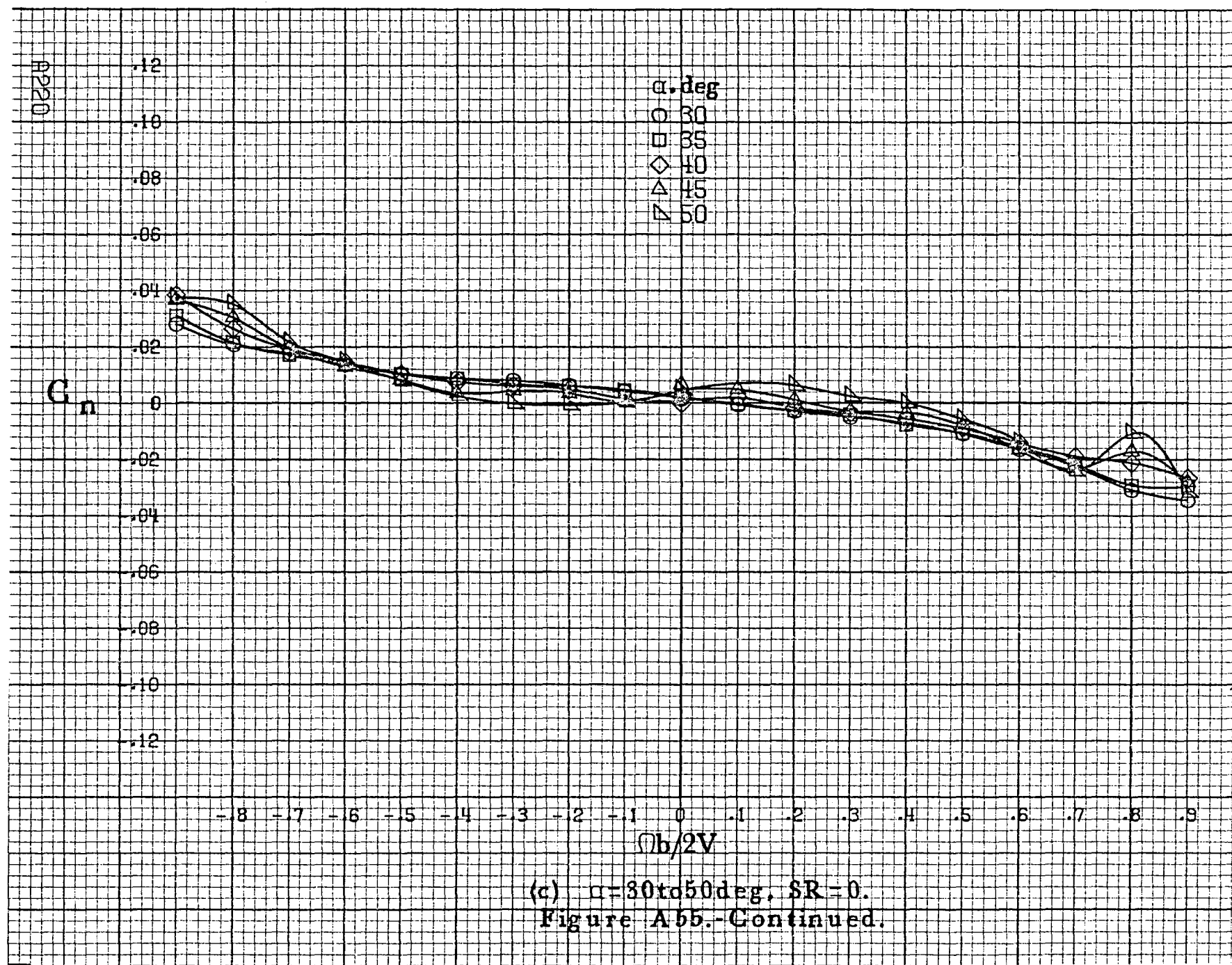


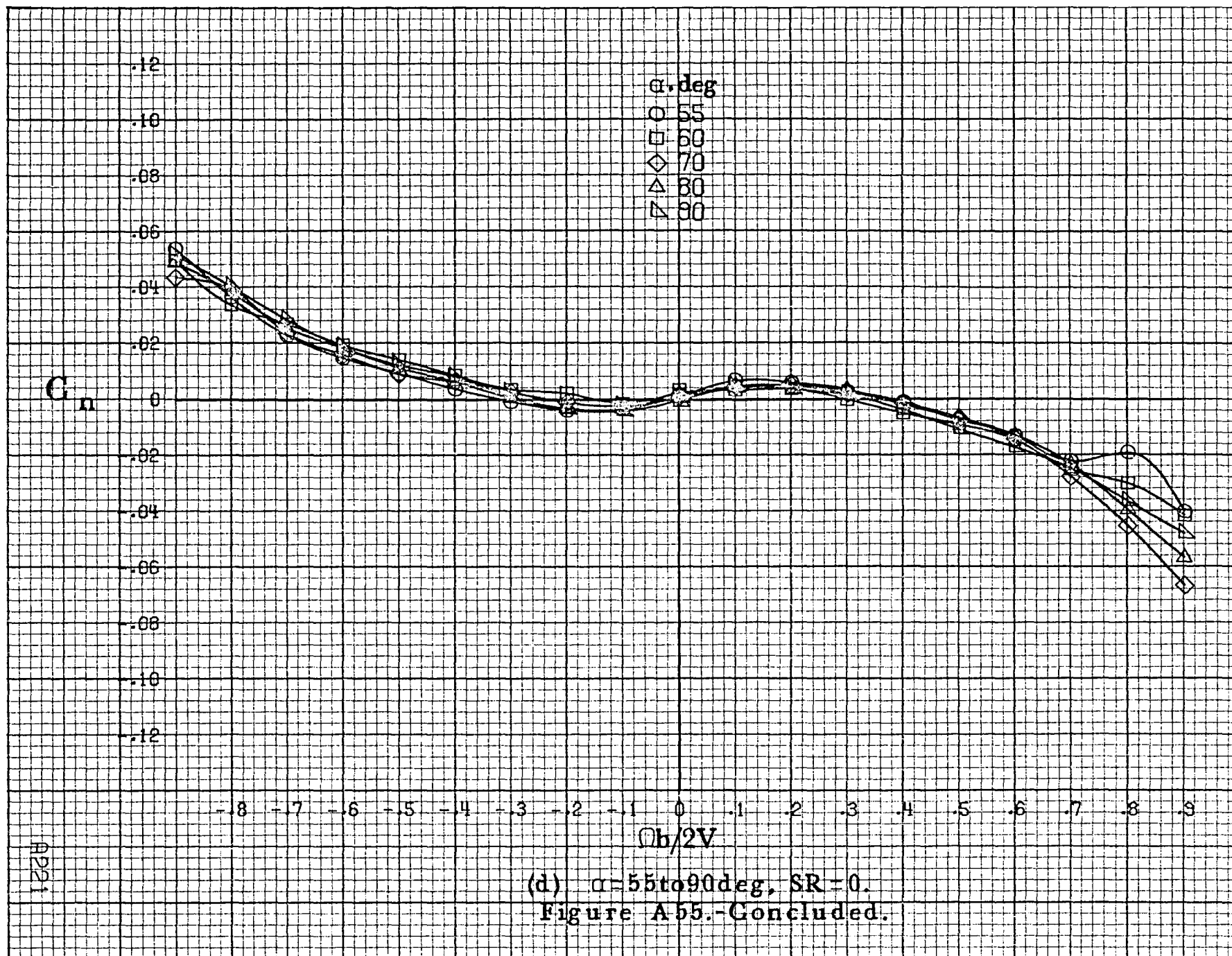
(a) $\alpha = 8$ to 16 deg, $SR = 91.4$ cm (36 in).

Figure A55.- Effect of rotation rate and angle of attack on yawing-moment coefficient for complete long body, low wing configuration. $\delta_r = 0^\circ$, $\delta_a = 0^\circ$, $\delta_r = 0^\circ$, $\beta = 0^\circ$.

(b) $\alpha = 18.035^\circ$, $SR = 91.4 \text{ cm (36 in.)}$
Figure A55.-Continued.







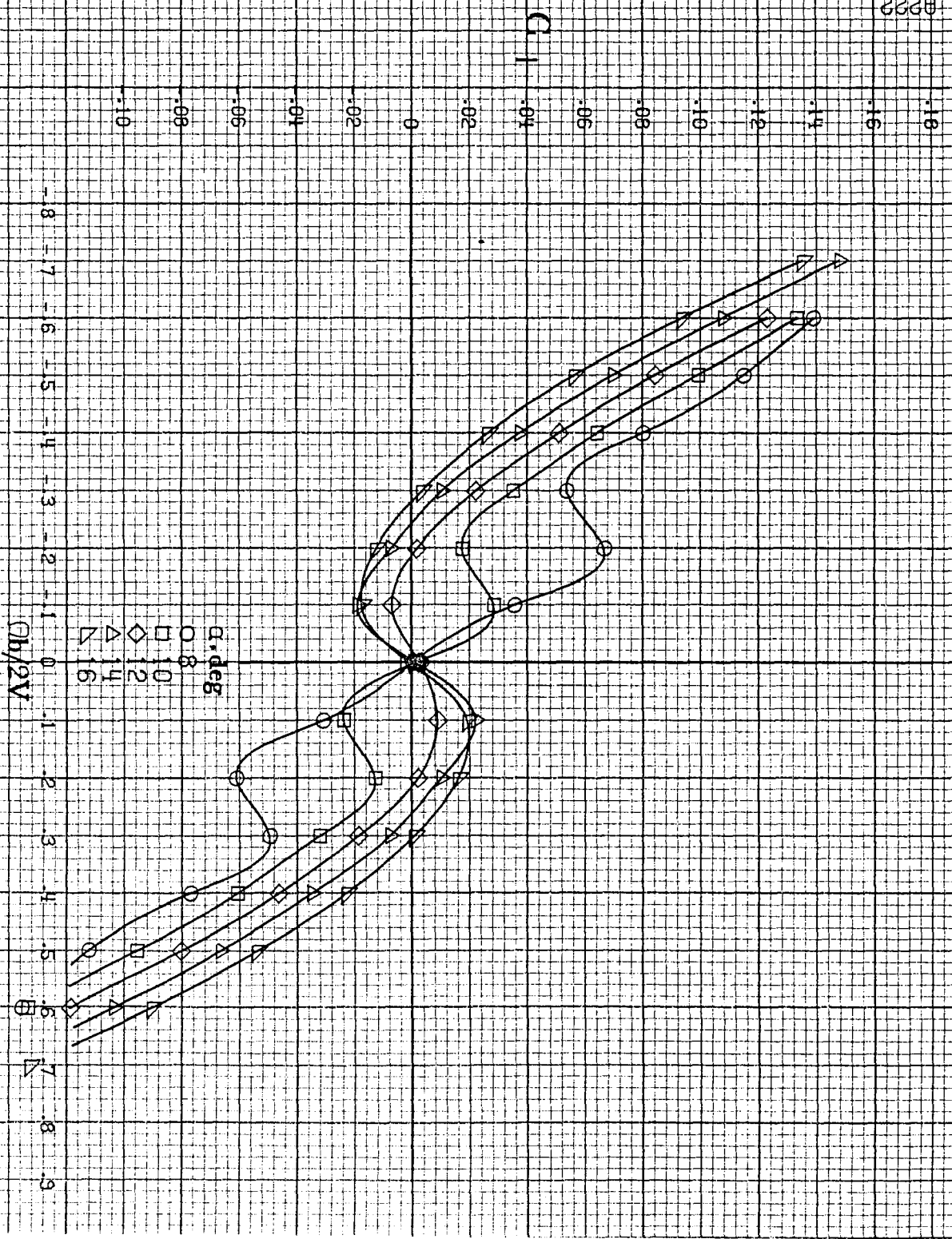
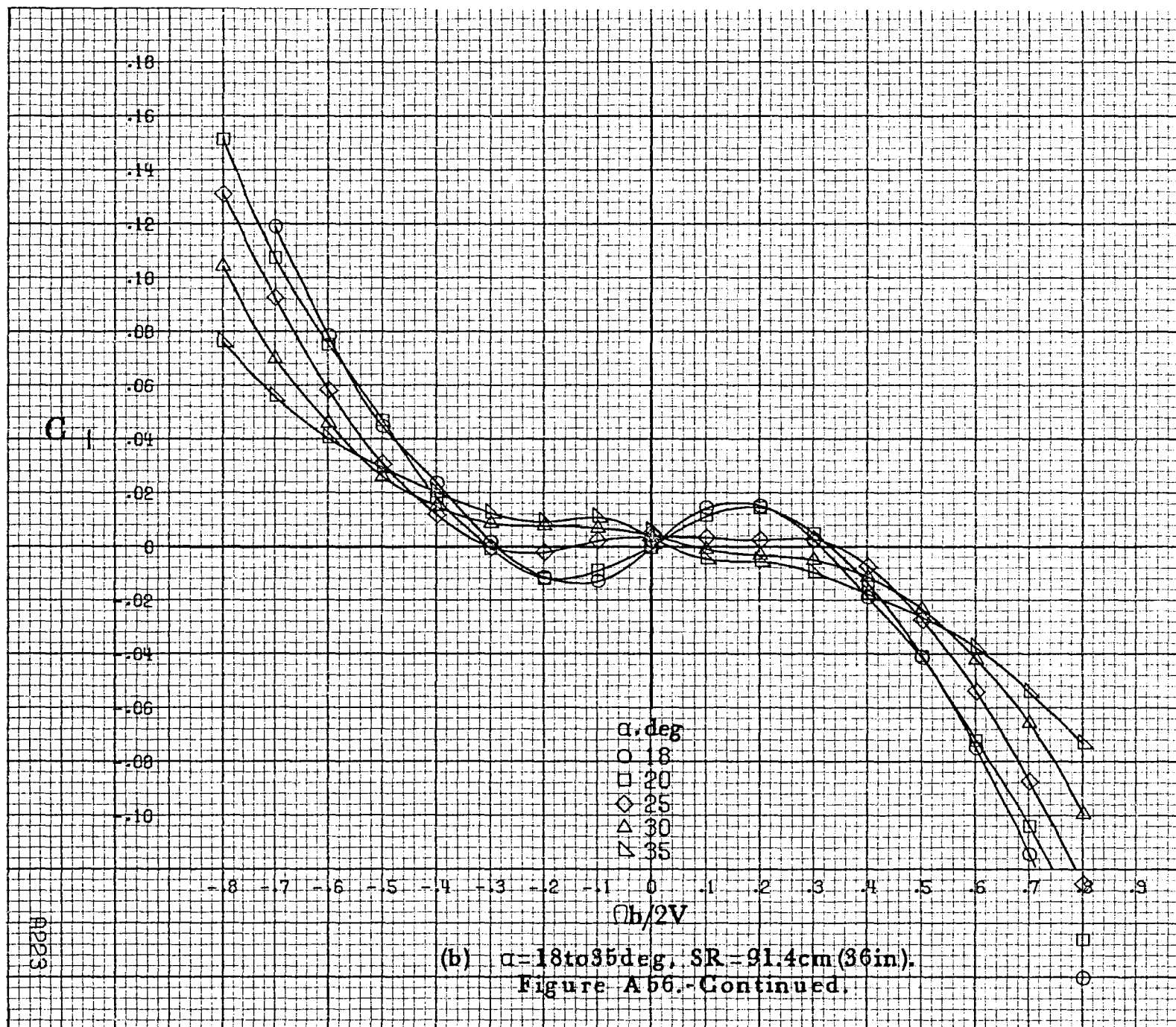


Figure A56 Effect of rotation rate and angle of attack on rolling-moment coefficient for complete long body, low wing configuration. $\delta = 0^\circ$. $\delta\alpha = 0^\circ$.



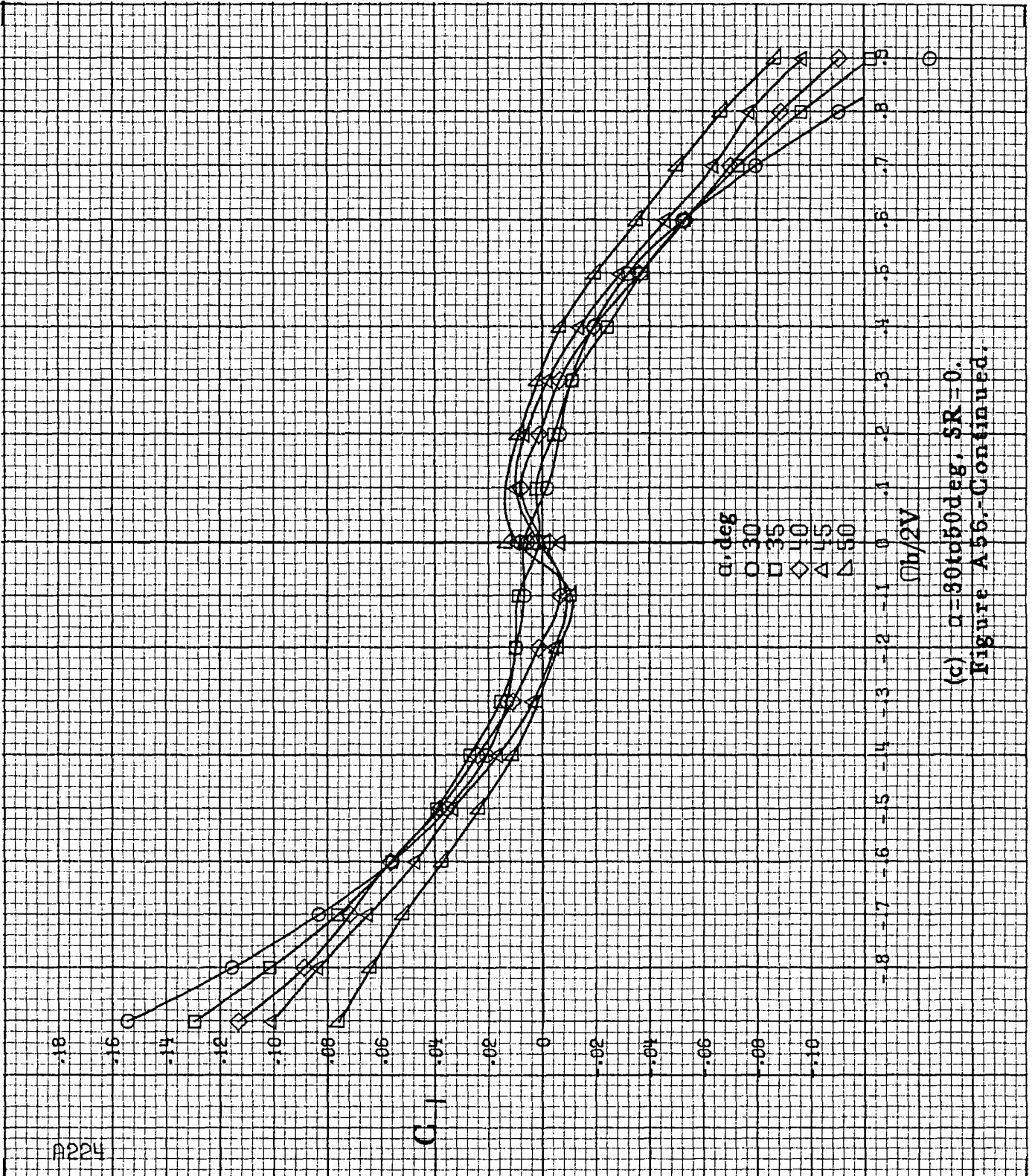
A224

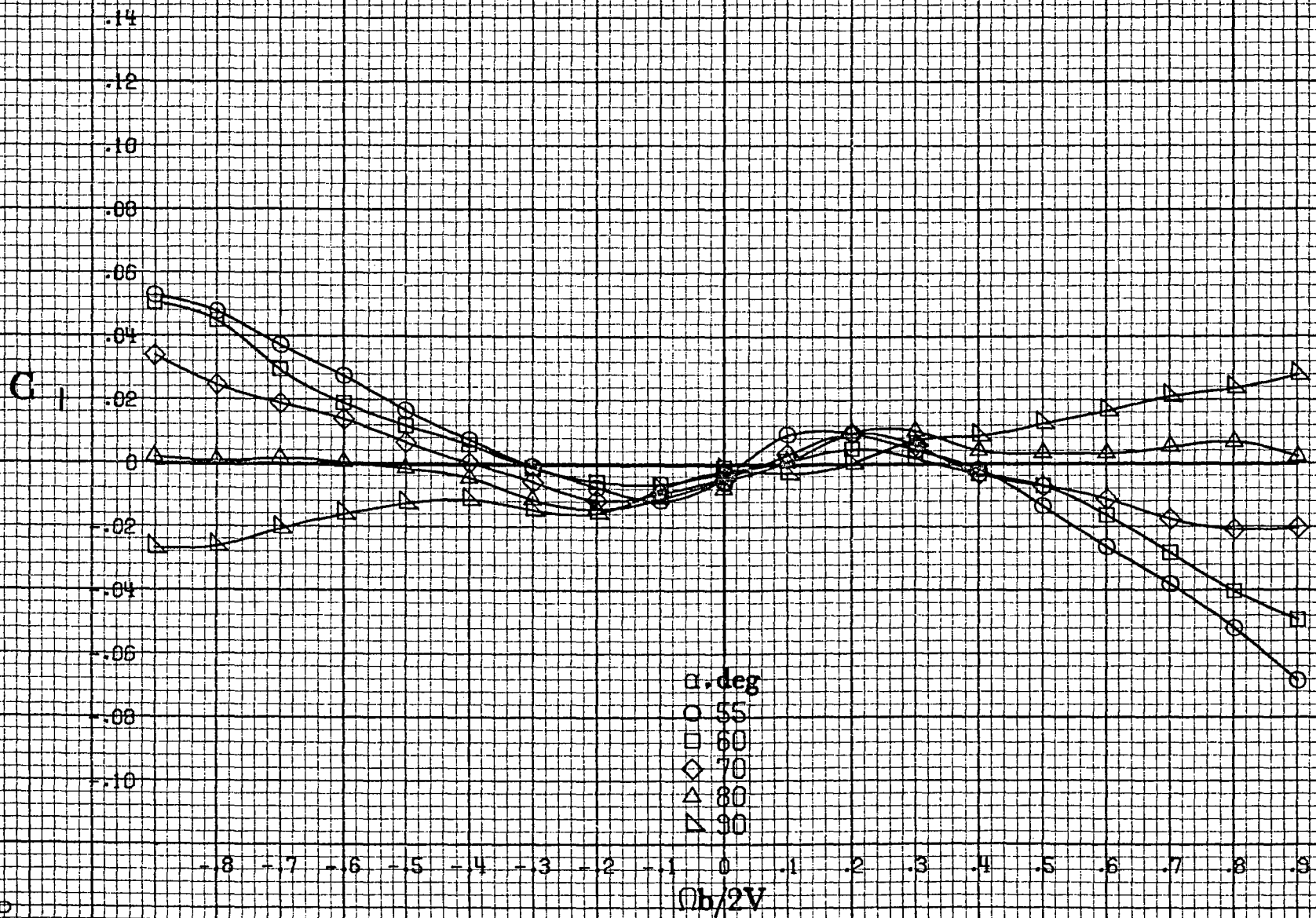
C_1

α, deg
 $\circ 30$
 $\square 35$
 $\diamond 40$
 $\triangle 45$
 $\nabla 50$

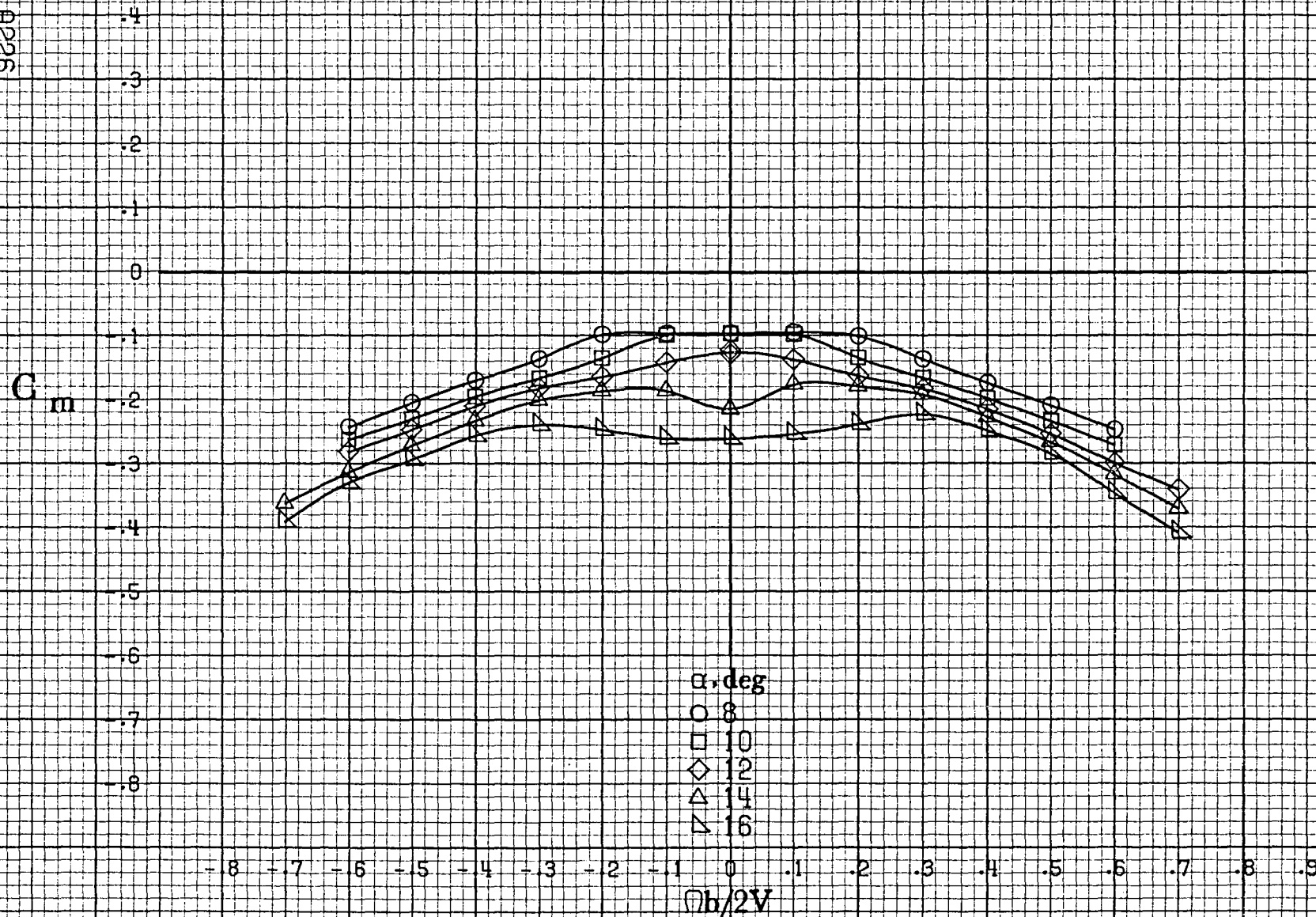
$\eta h/2V$

(c) $\alpha = 30 \text{ to } 50 \text{ deg}$, $SR = 0$.
 Figure A56.-Continued.



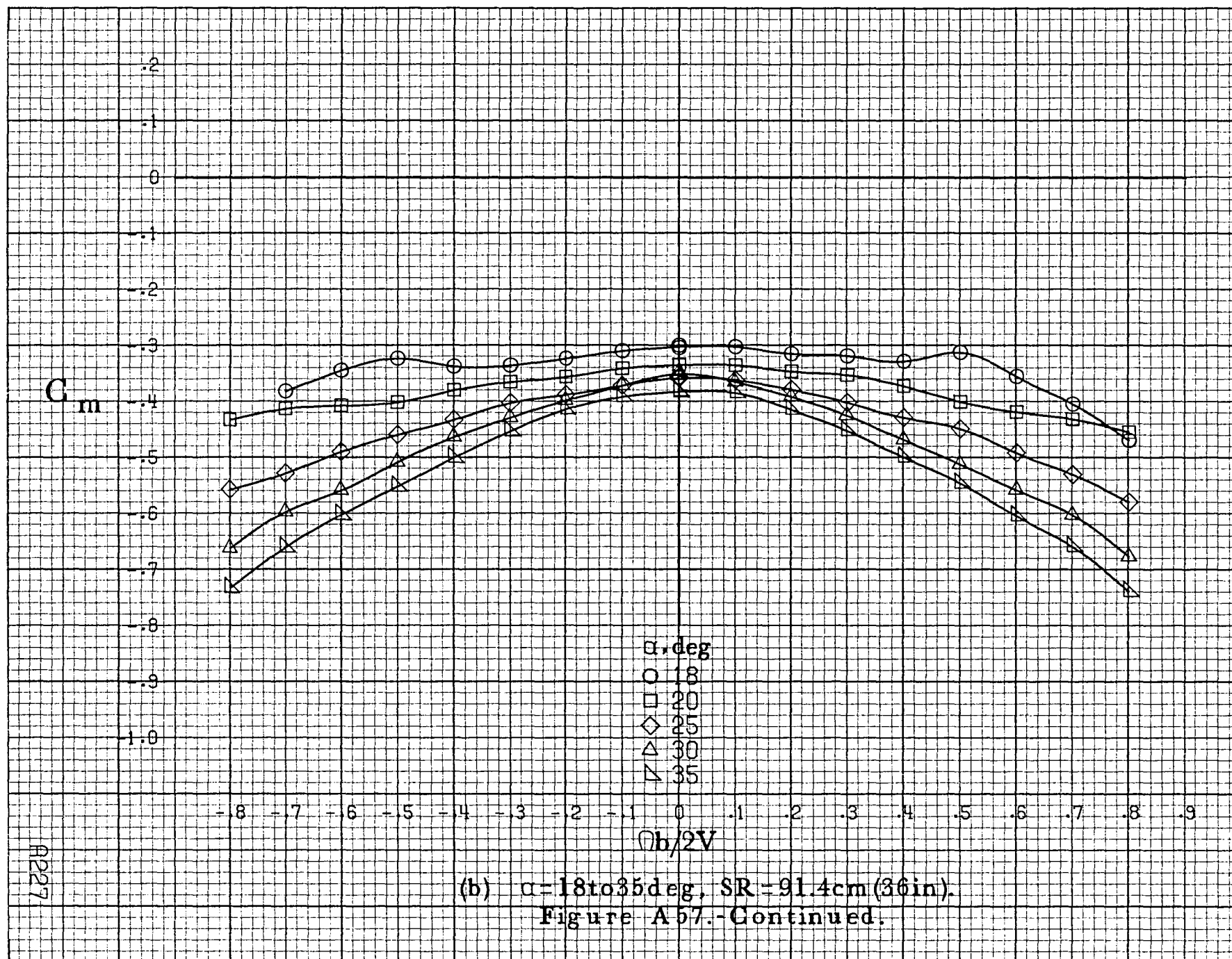


(d) $\alpha=55$ to 90 deg, $SR=0$.
Figure A56.-Concluded.



(a) $\alpha = 8$ to 16° , $SR = 91.4\text{cm (36in.)}$.

Figure A57.-Effect of rotation rate and angle of attack on pitching-moment coefficient for complete long body, low wing configuration. $\delta_r = 0^\circ$, $\delta_a = 0^\circ$, $\delta_r = 0^\circ$, $\beta = 0^\circ$.



AP226

C_m

-1
0
-1
-2
-3
-4
-5
-6
-7
-8
-9
-1.0
-1.1

α, deg

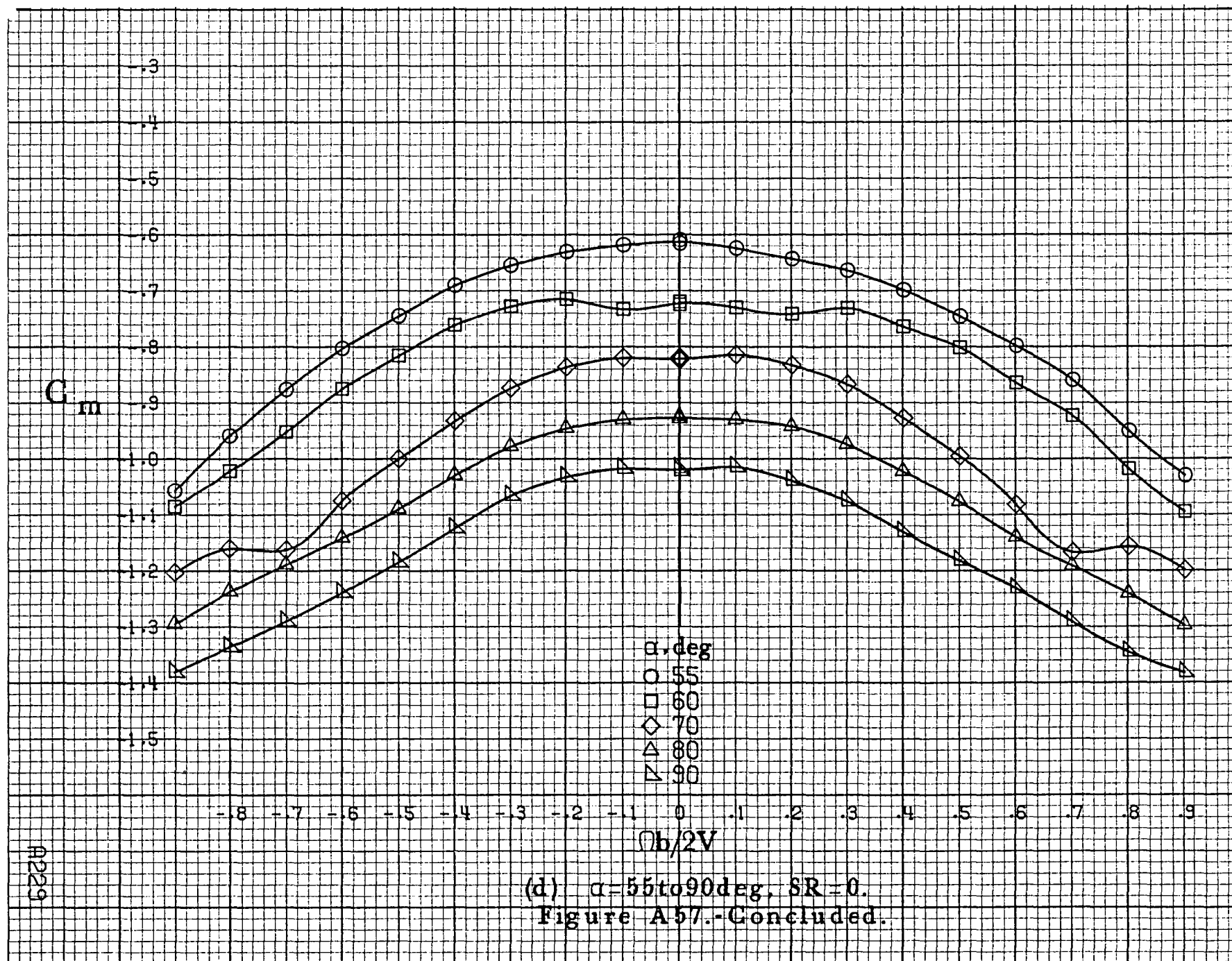
○ 30
□ 35
◇ 40
△ 45
▽ 50

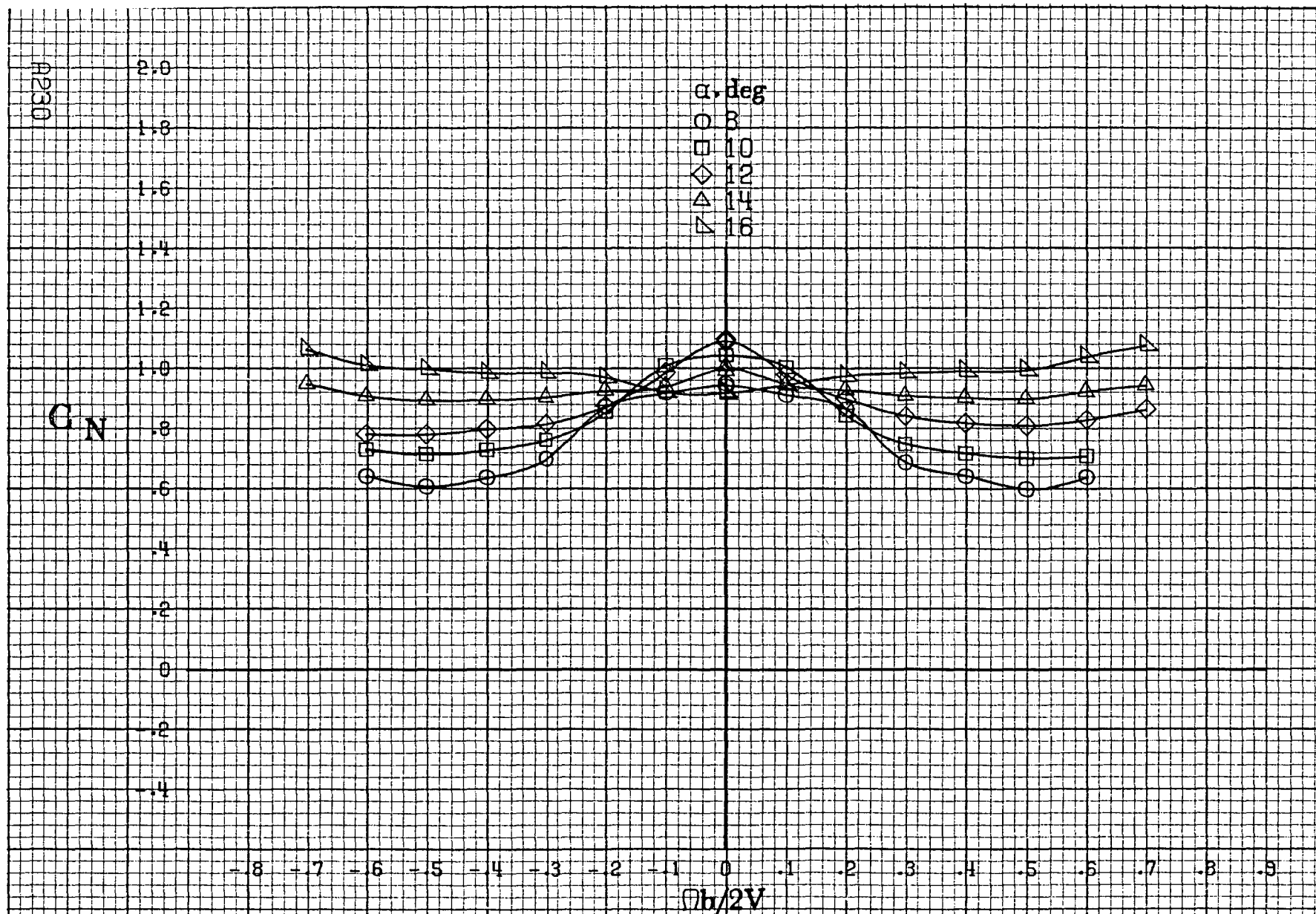
-8 -7 -6 -5 -4 -3 -2 -1 0 .1 .2 .3 .4 .5 .6 .7 .8 .9

$b/2V$

(c) $\alpha=30\text{ to }50\text{deg}$, $SR=0$.

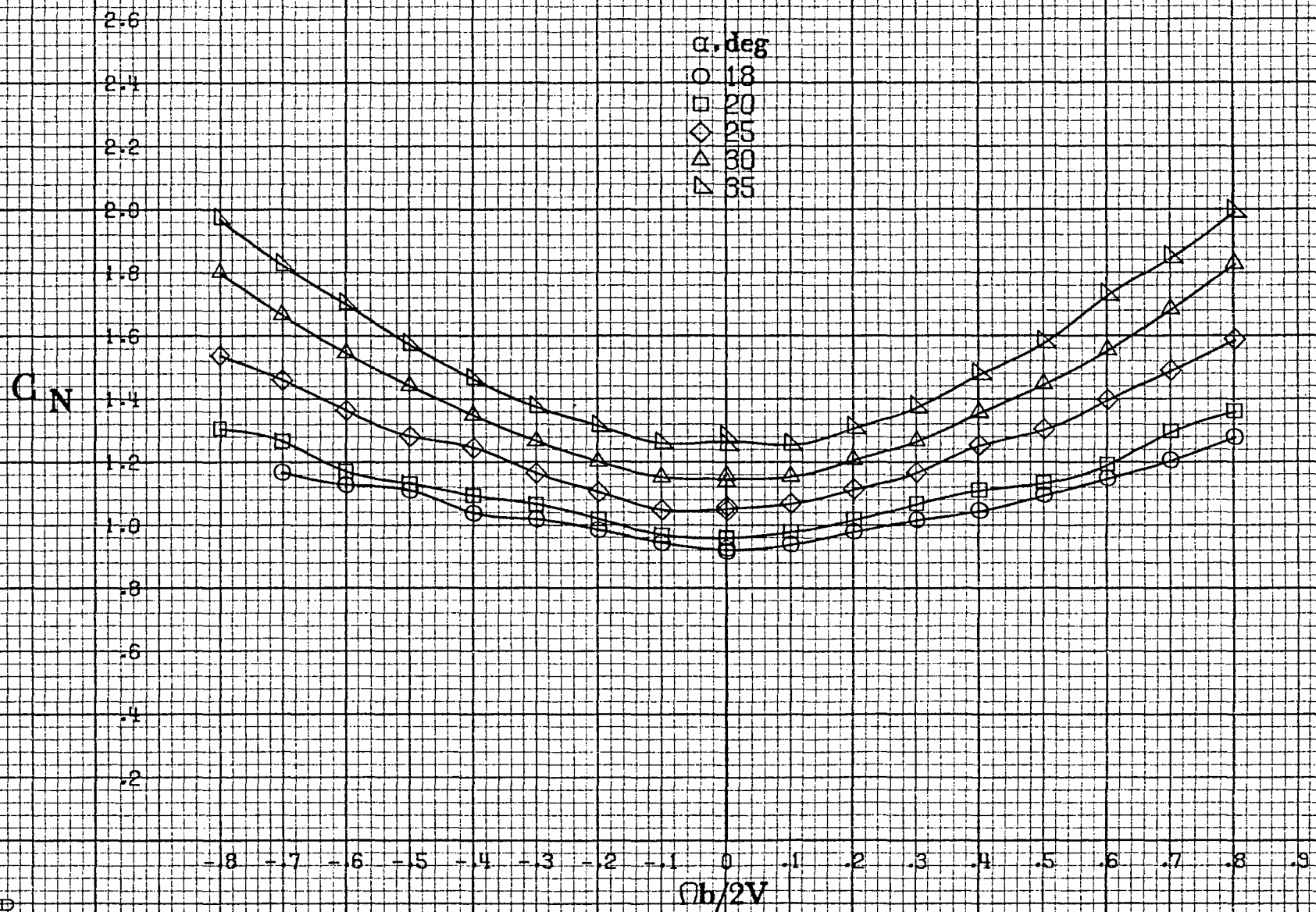
Figure A67.-Continued.



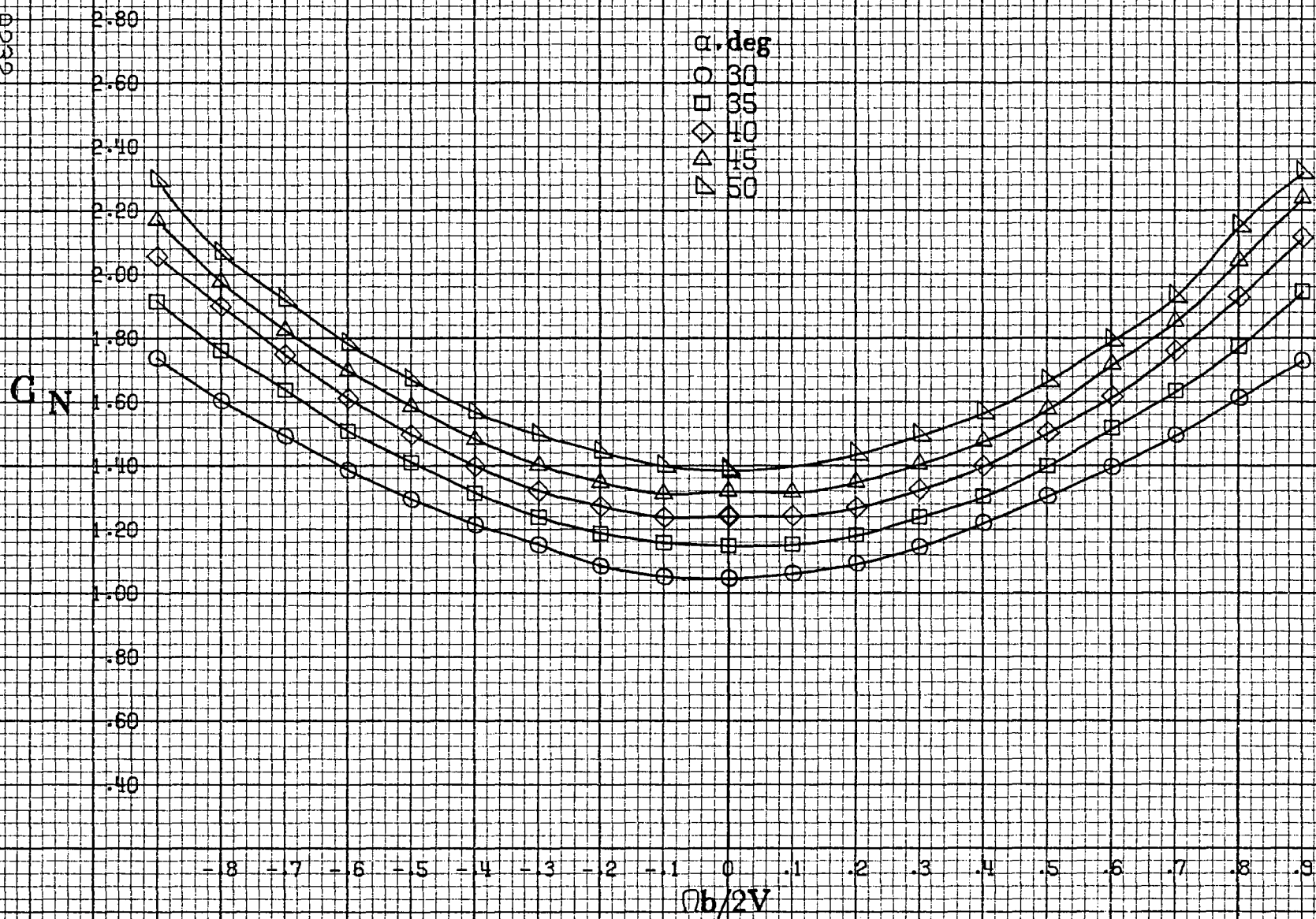


(a) $\alpha = 8$ to 16 deg, $SR = 91.4$ cm (36 in).

Figure A58 - Effect of rotation rate and angle of attack on normal-force coefficient for complete long body, low wing configuration. $\delta_c = 0^\circ$, $\delta_n = 0^\circ$, $\delta_r = 0^\circ$, $\beta = 0^\circ$.

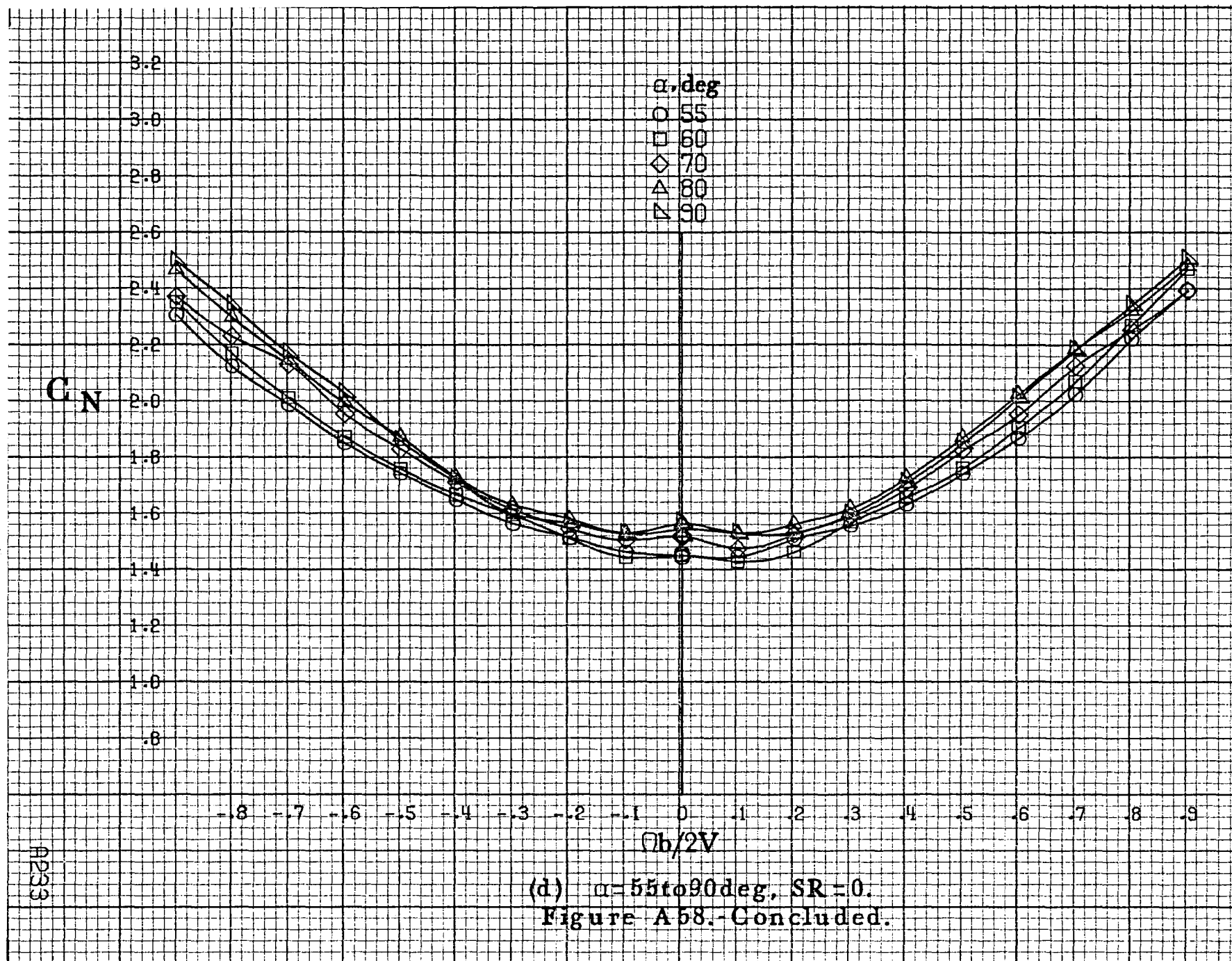


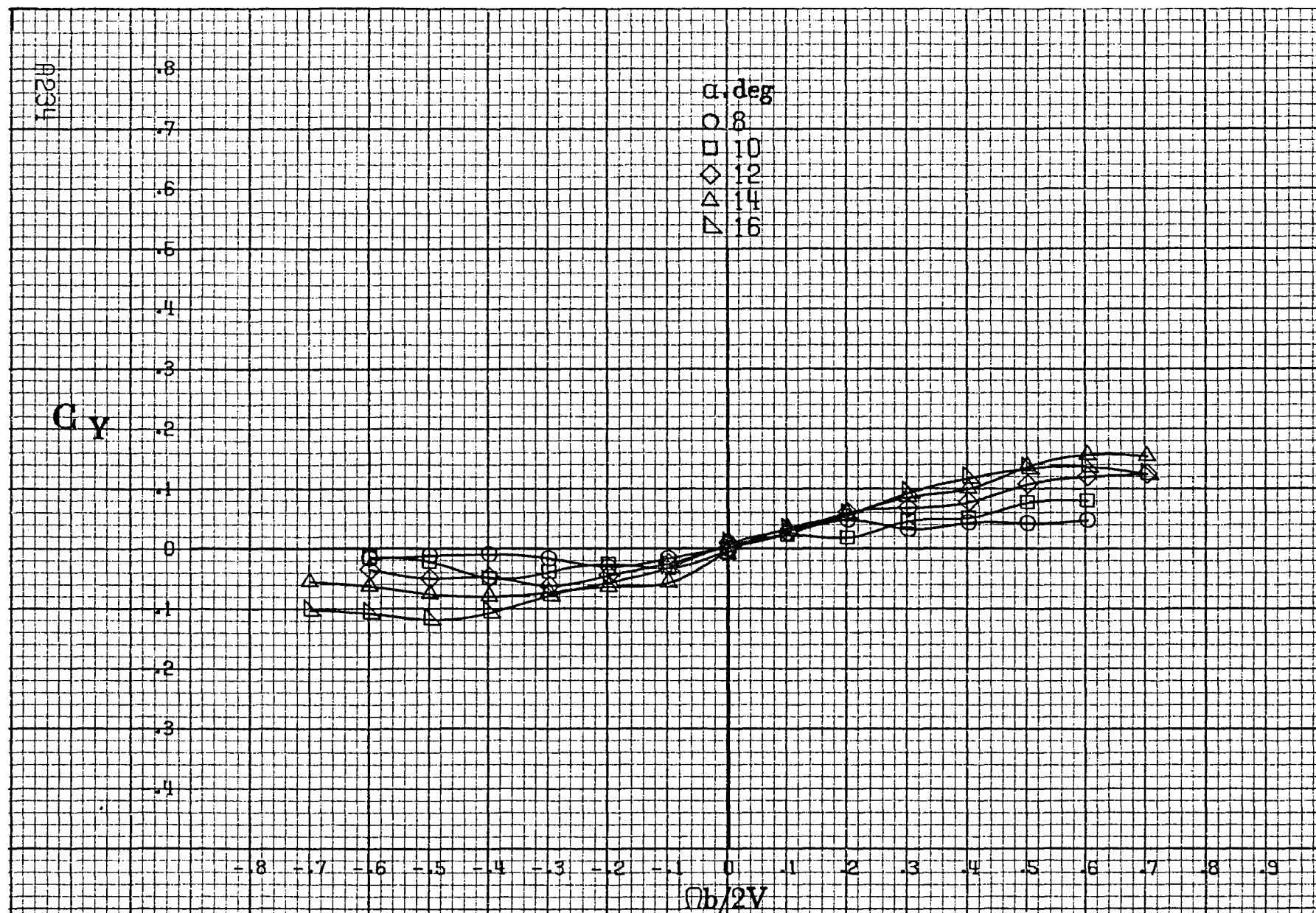
(b) $\alpha = 18$ to 35 deg, $SR = 91.4$ cm (36 in).
Figure A 58.-Continued.



(c) $\alpha = 30$ to 50° , $SR = 0$.

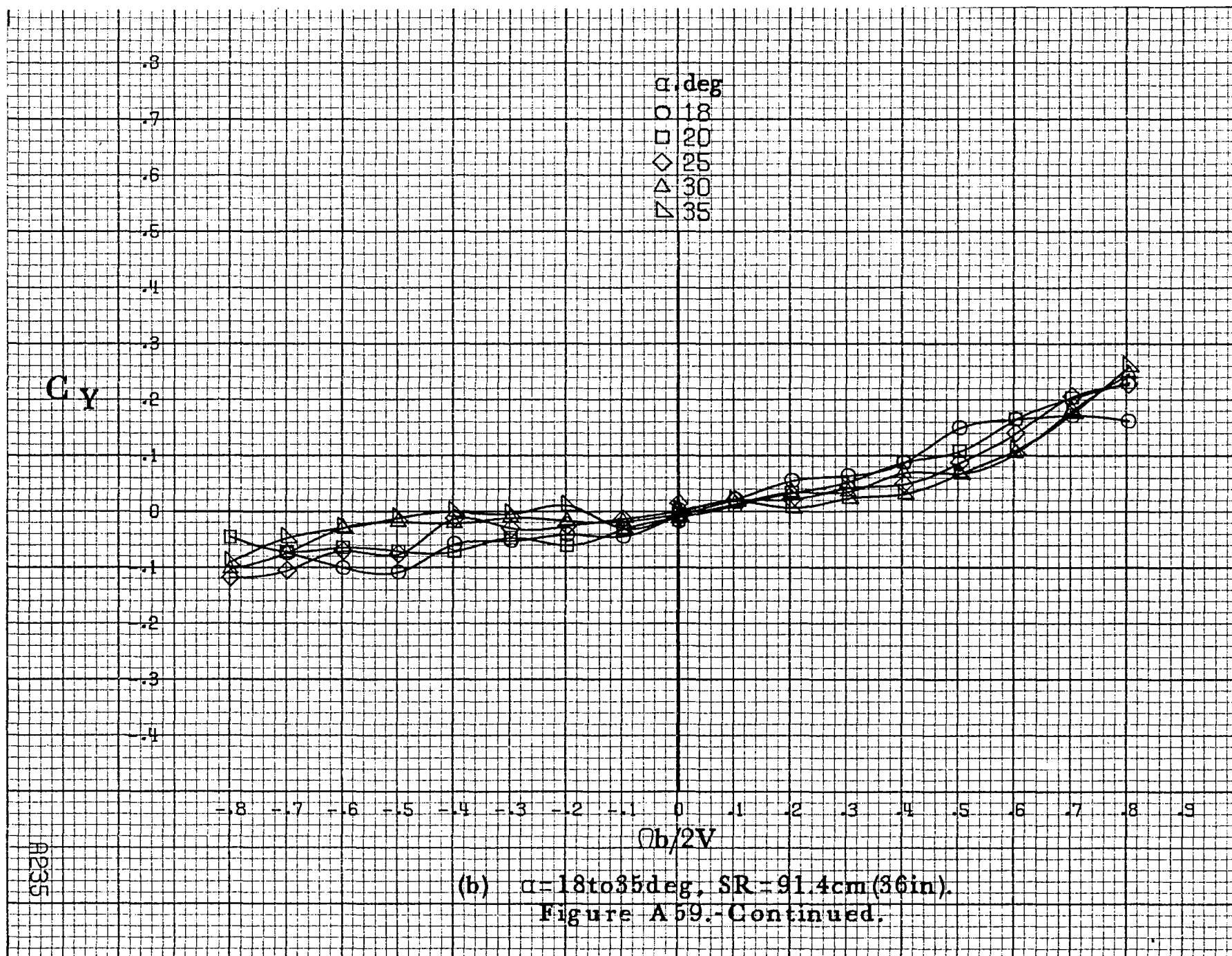
Figure A 58.-Continued.

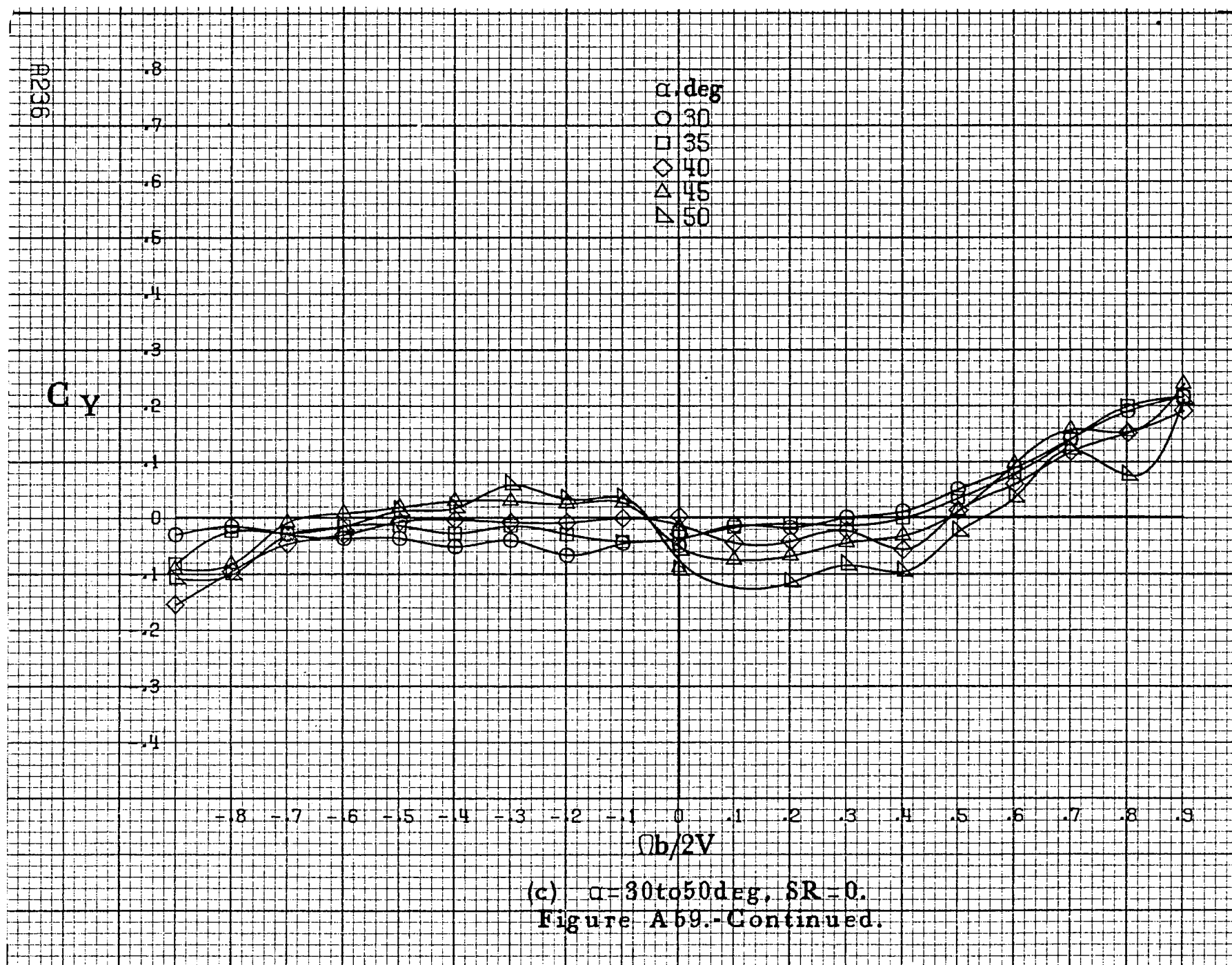


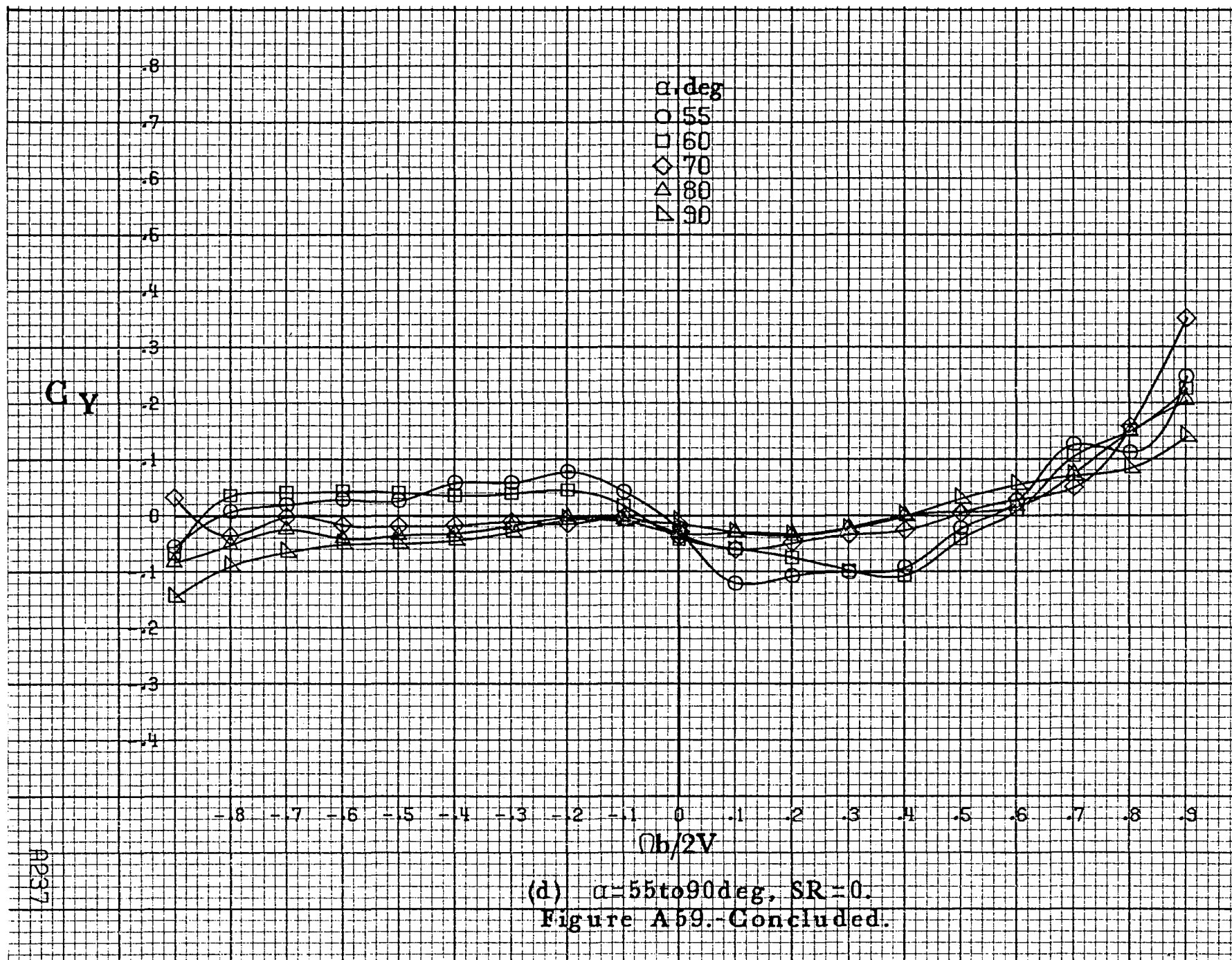


(a) $\alpha=8\text{ to }16\text{deg}$, $SR=91.4\text{cm}(36\text{in})$.

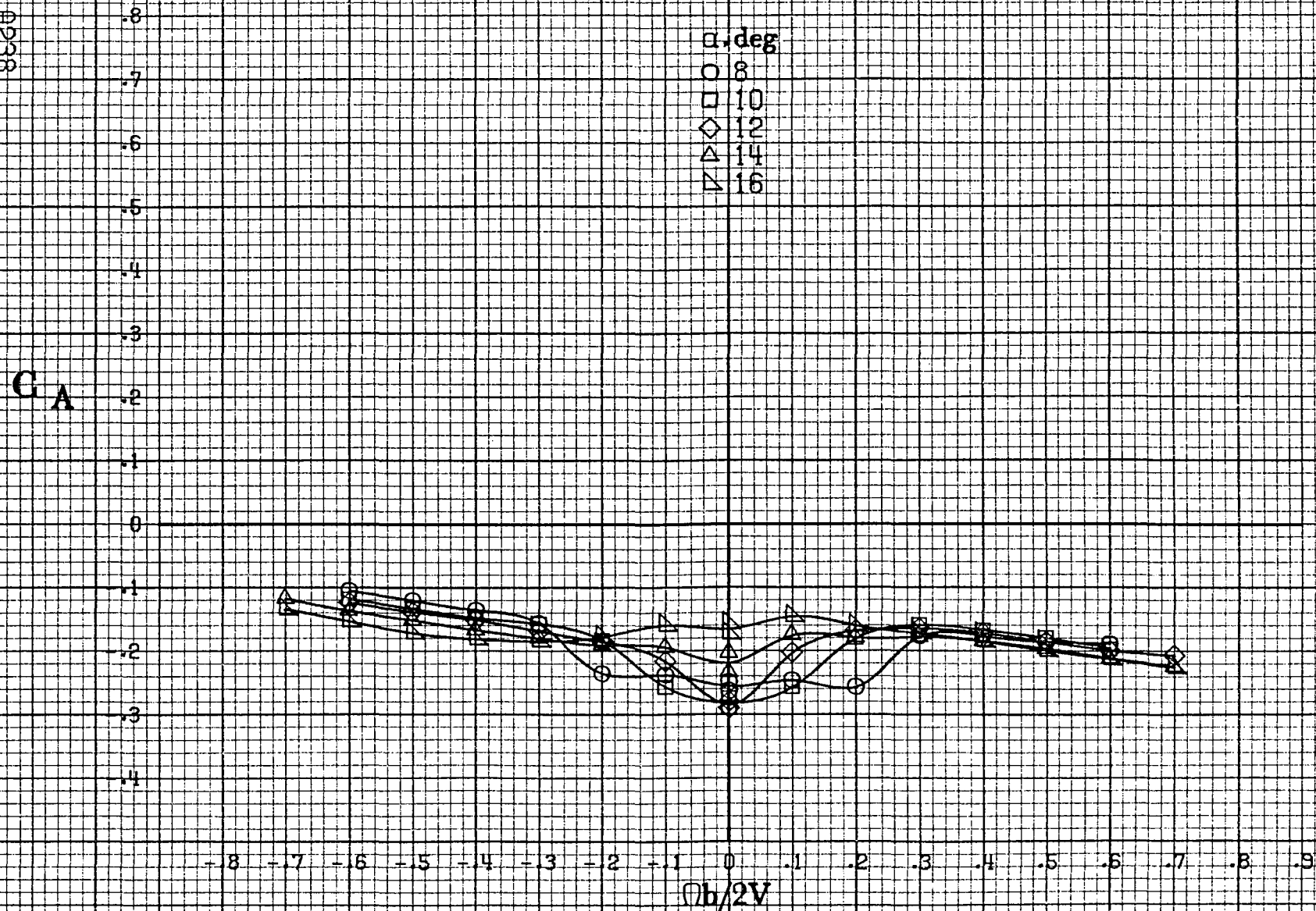
Figure A59.-Effect of rotation rate and angle of attack on side-force coefficient for complete long body, low wing configuration. $\delta_r=0^\circ$. $\delta_a=0^\circ$. $\delta_r=0^\circ$. $\beta=0^\circ$.





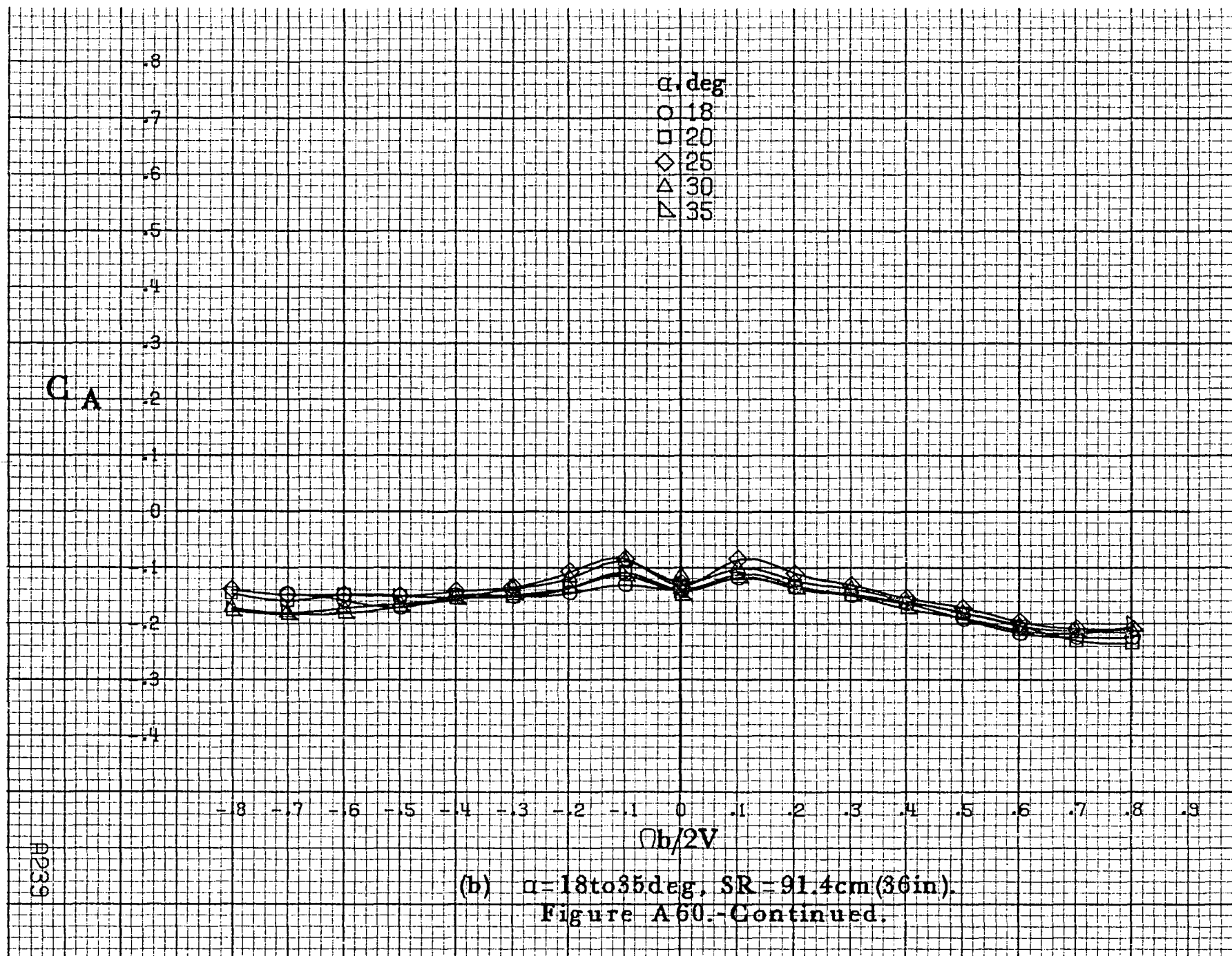


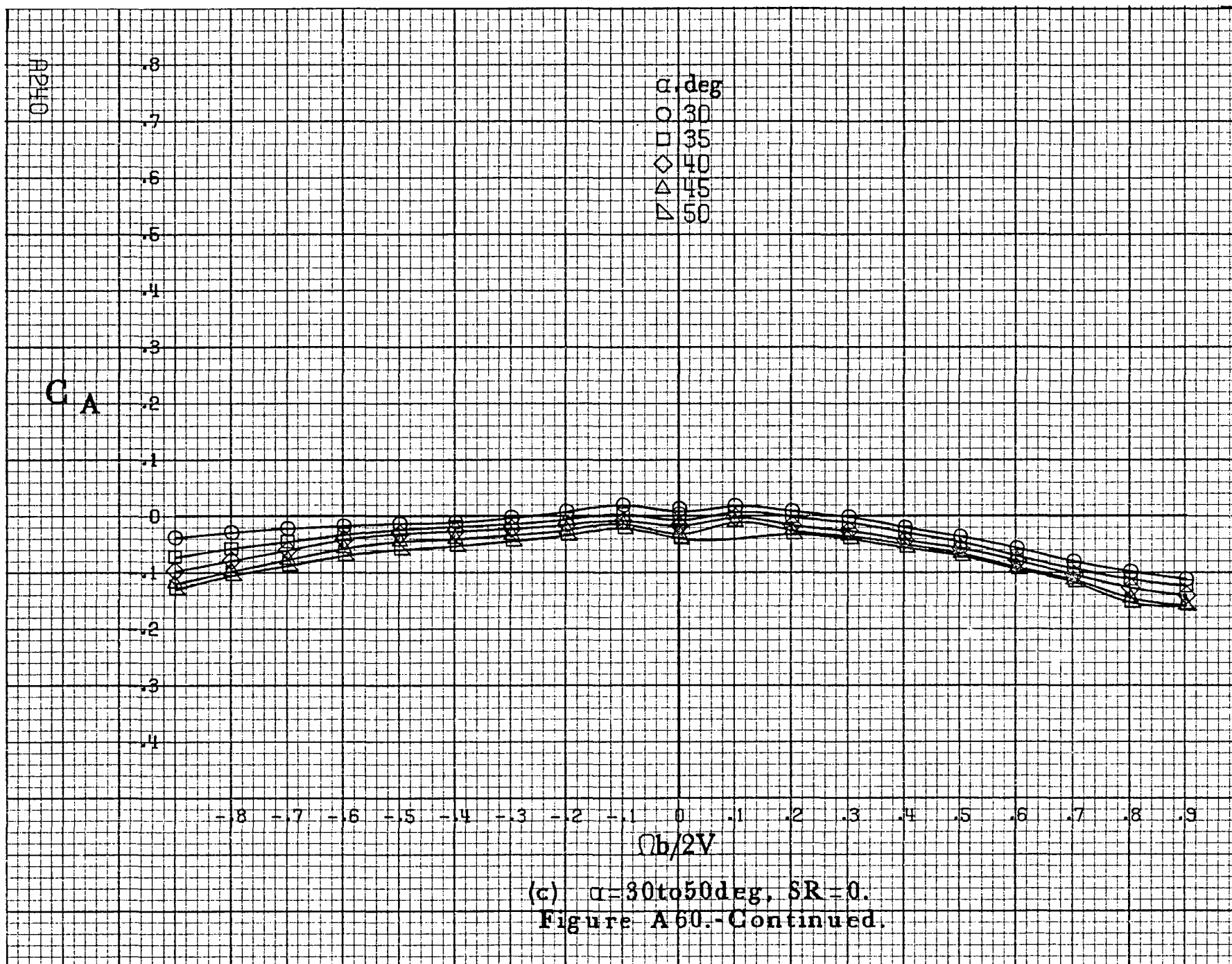
11238

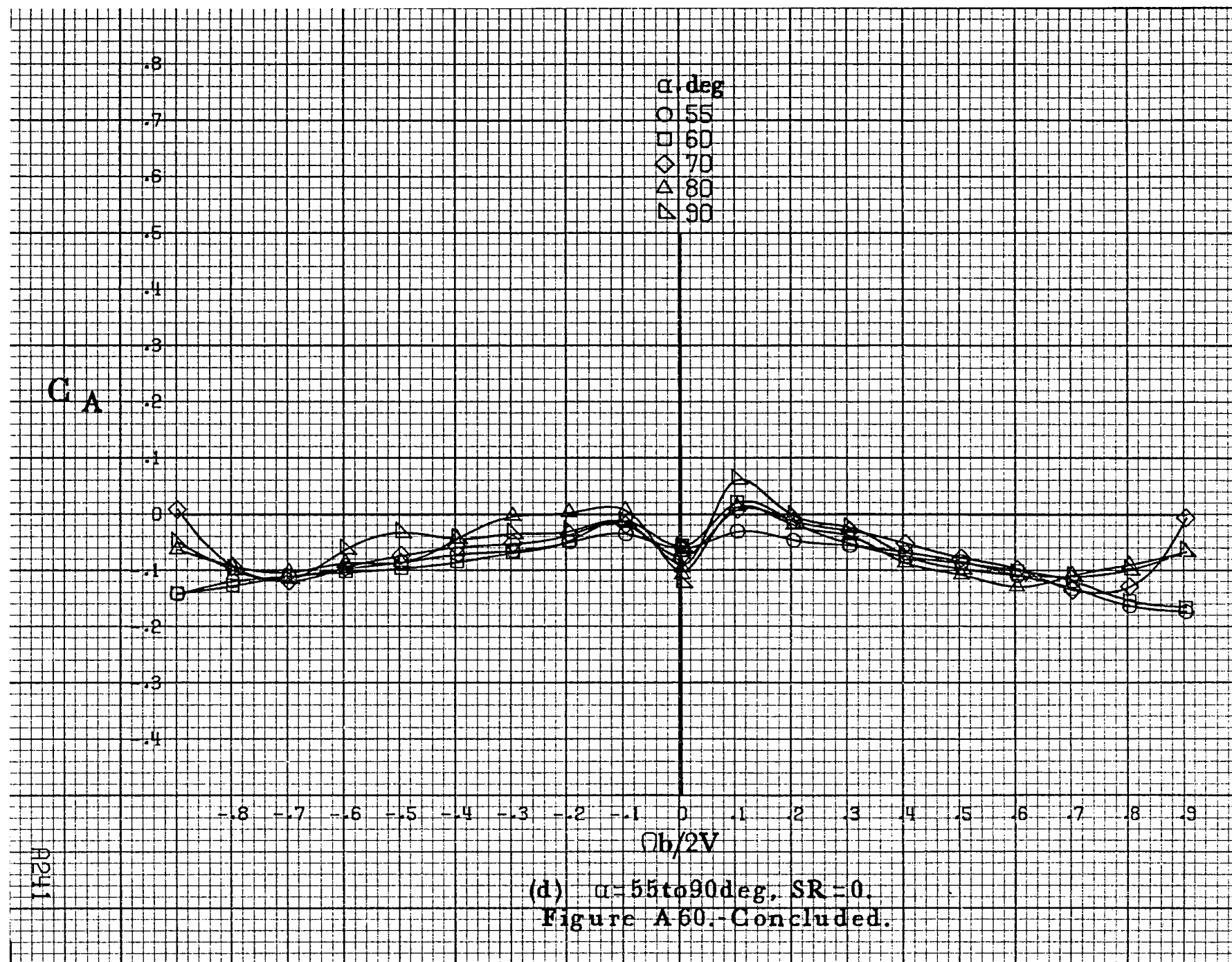


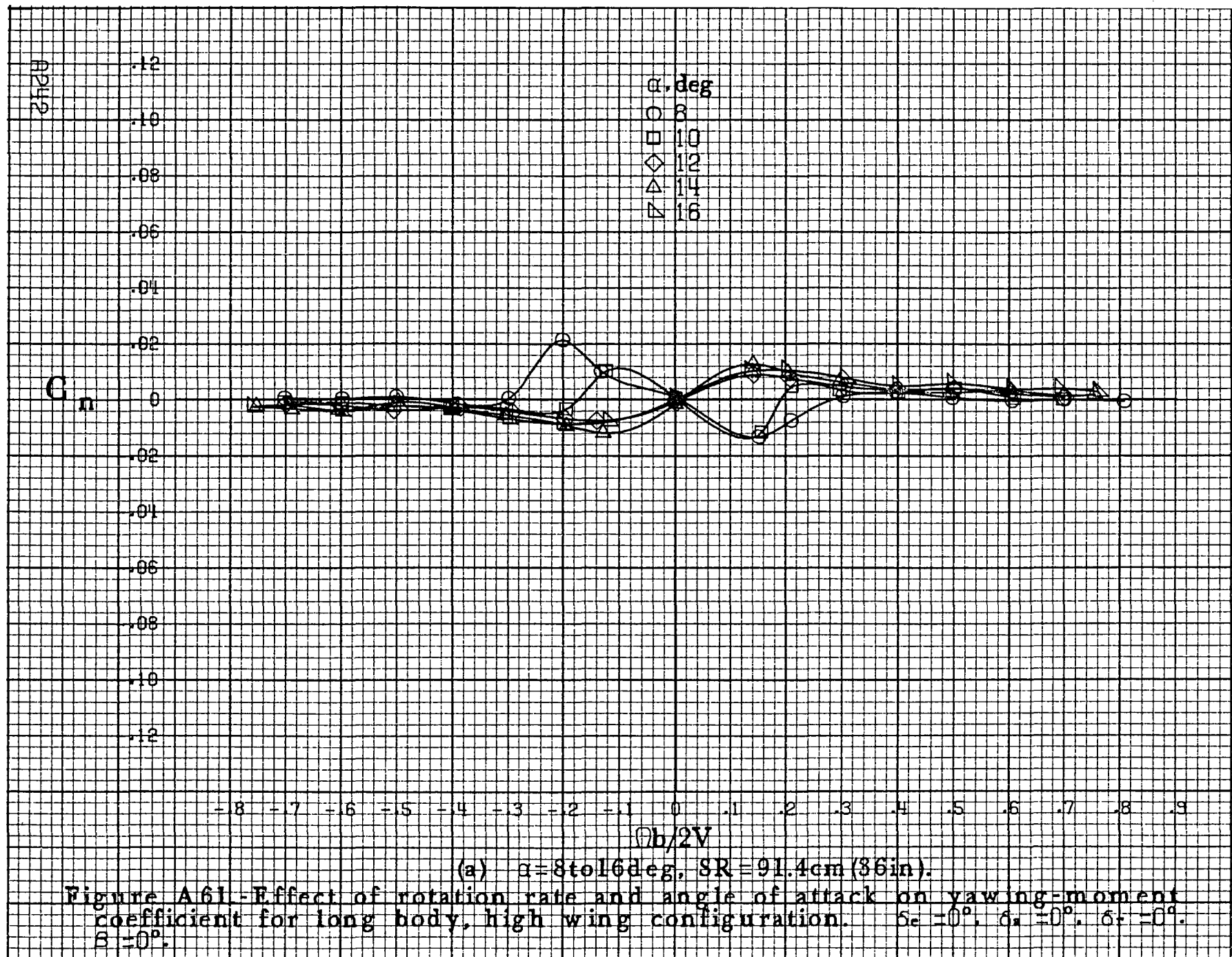
(a) $\alpha = 8$ to 16 deg, $SR = 91.4$ cm (36 in).

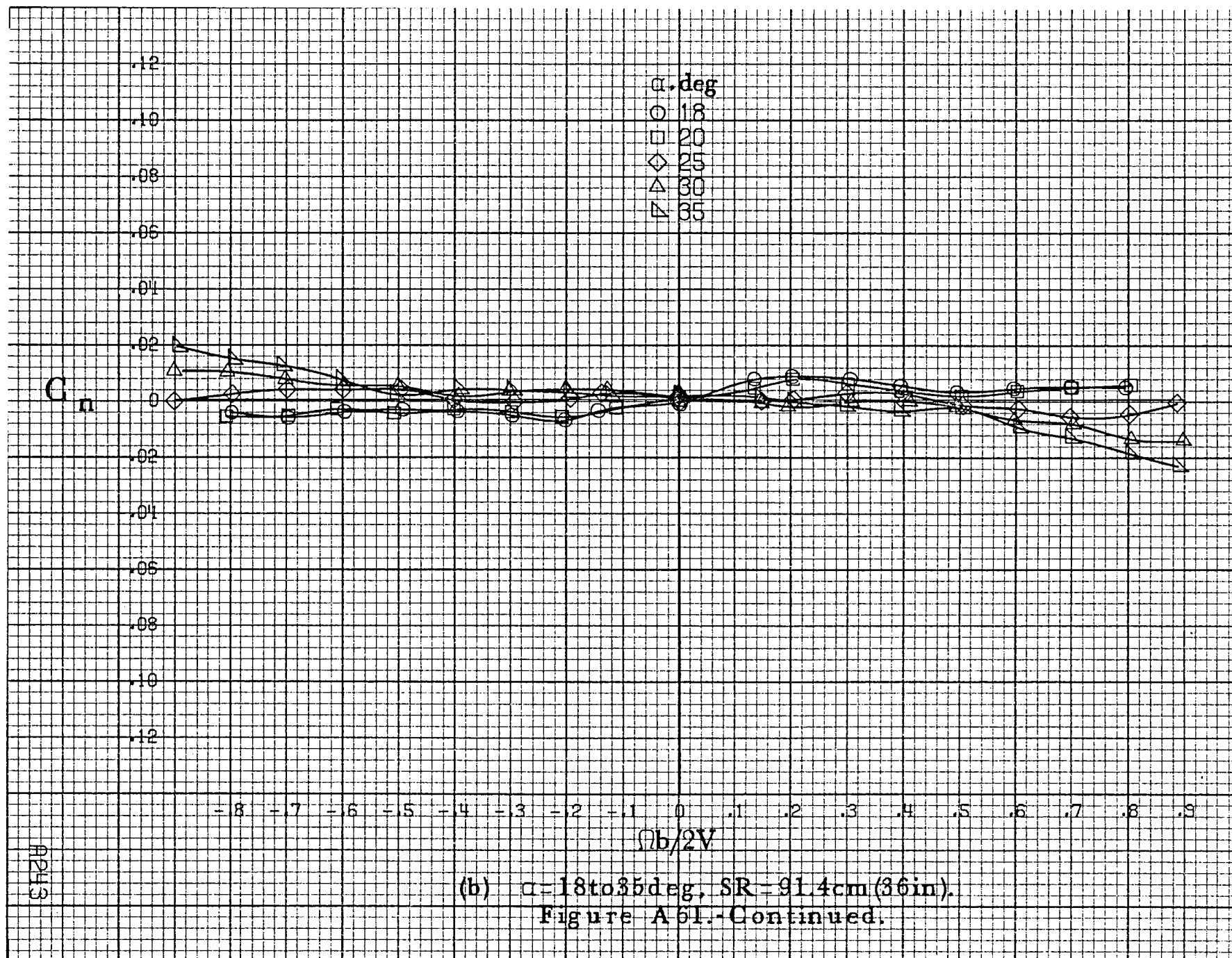
Figure A60.-Effect of rotation rate and angle of attack on axial-force coefficient for complete long body, low wing configuration. $\delta_c = 0^\circ$, $\delta_a = 0^\circ$, $\delta_r = 0^\circ$, $\beta = 0^\circ$.

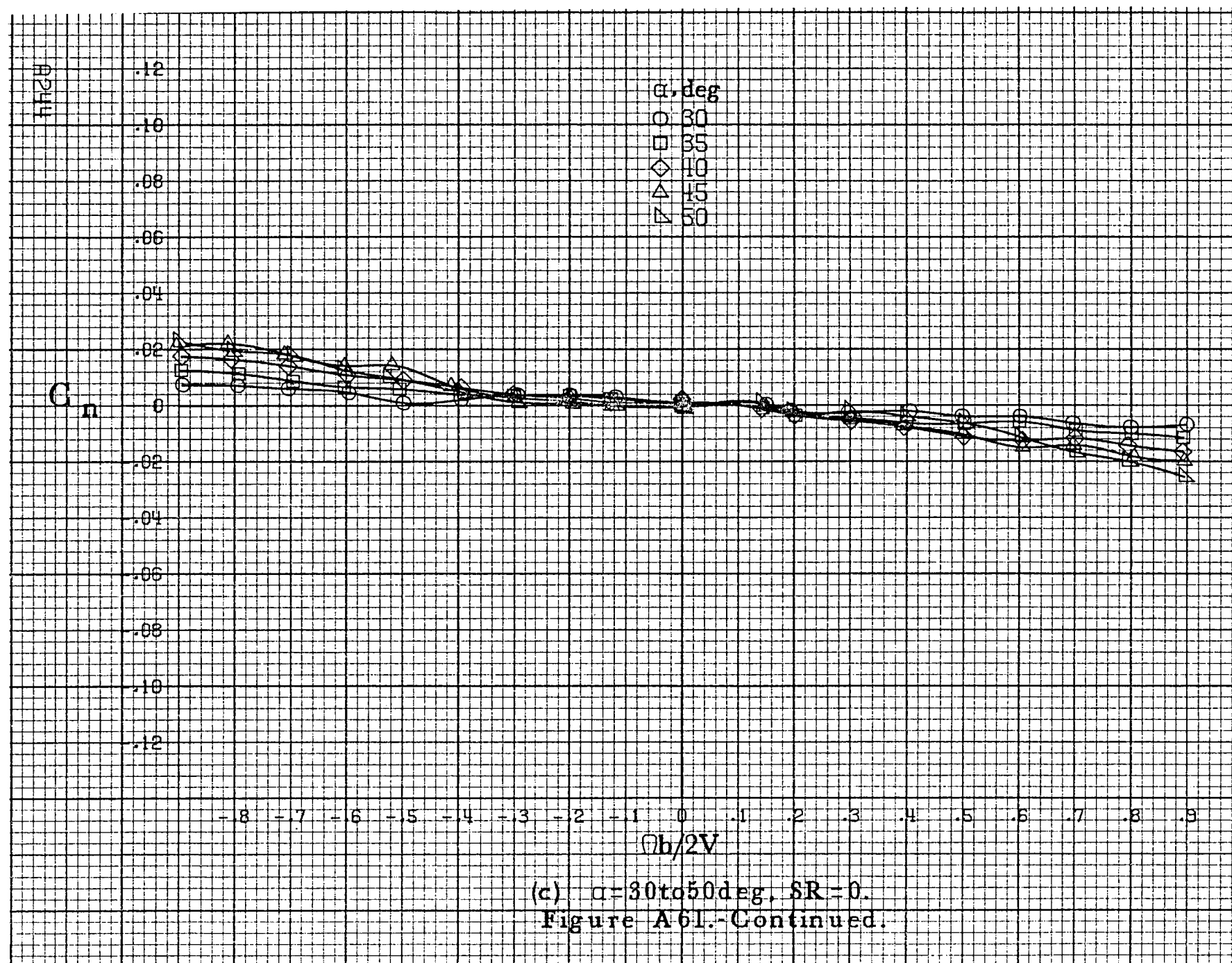


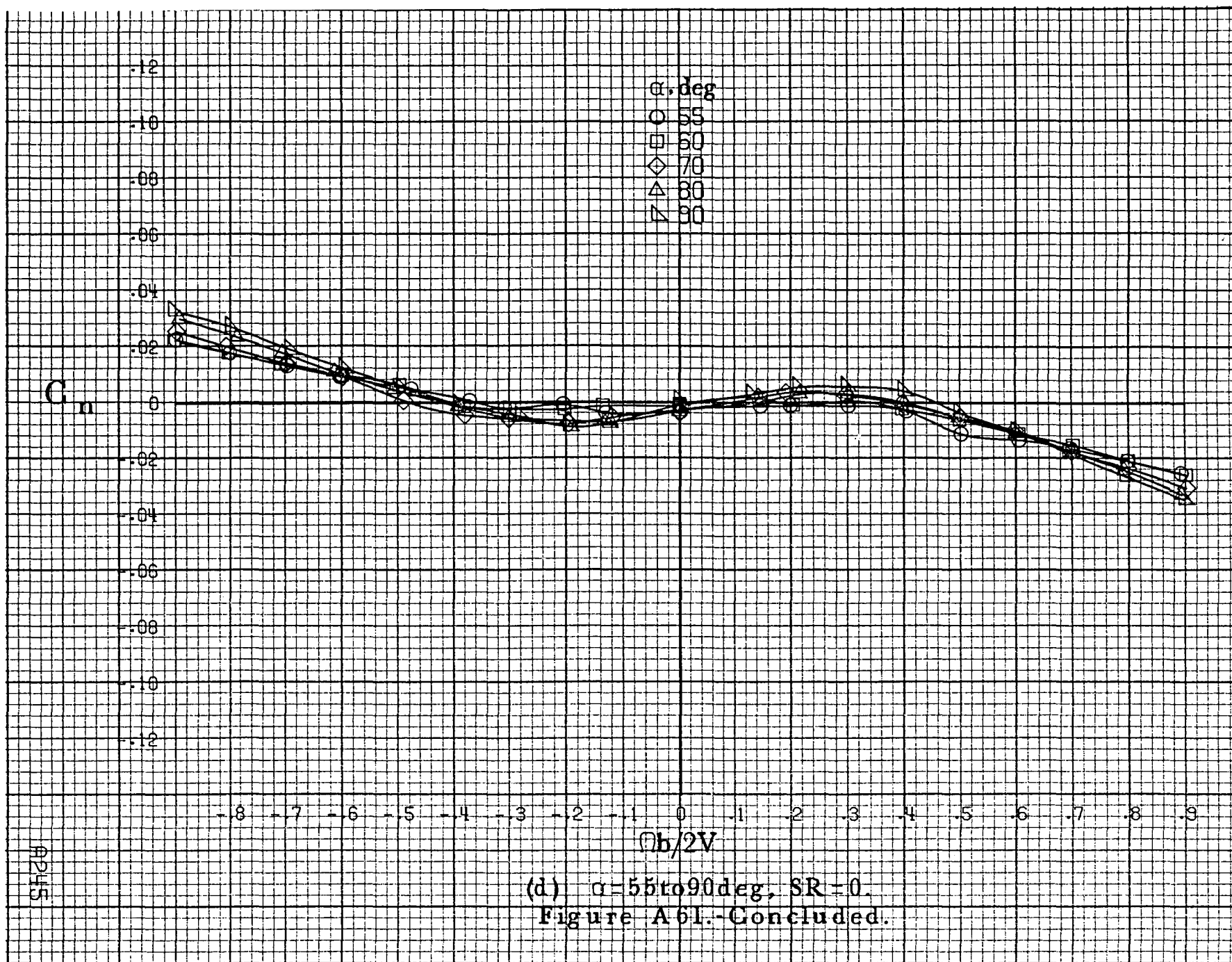












C

.35
.30
.25
.20
.15
.10
.05
0
.05
.10
.15
.20
.25

α , deg
○ 8
□ 10
◇ 12
△ 14
▽ 16

-0.8 -0.7 -0.6 -0.5 -0.4 -0.3 -0.2 -0.1 0 .1 .2 .3 .4 .5 .6 .7 .8 .9

$\Omega b/2V$

(a) $\alpha = 8$ to 16 deg, $SR = 91.4$ cm (36 in).

Figure A62.-Effect of rotation rate and angle of attack on rolling-moment coefficient for long body, high wing configuration. $\delta_c = 0^\circ$, $\delta_s = 0^\circ$, $\delta_r = 0^\circ$, $\beta = 0^\circ$.

C_I

.35
.30
.25
.20
.15
.10
.05
0
.05
.10
.15
.20
.25

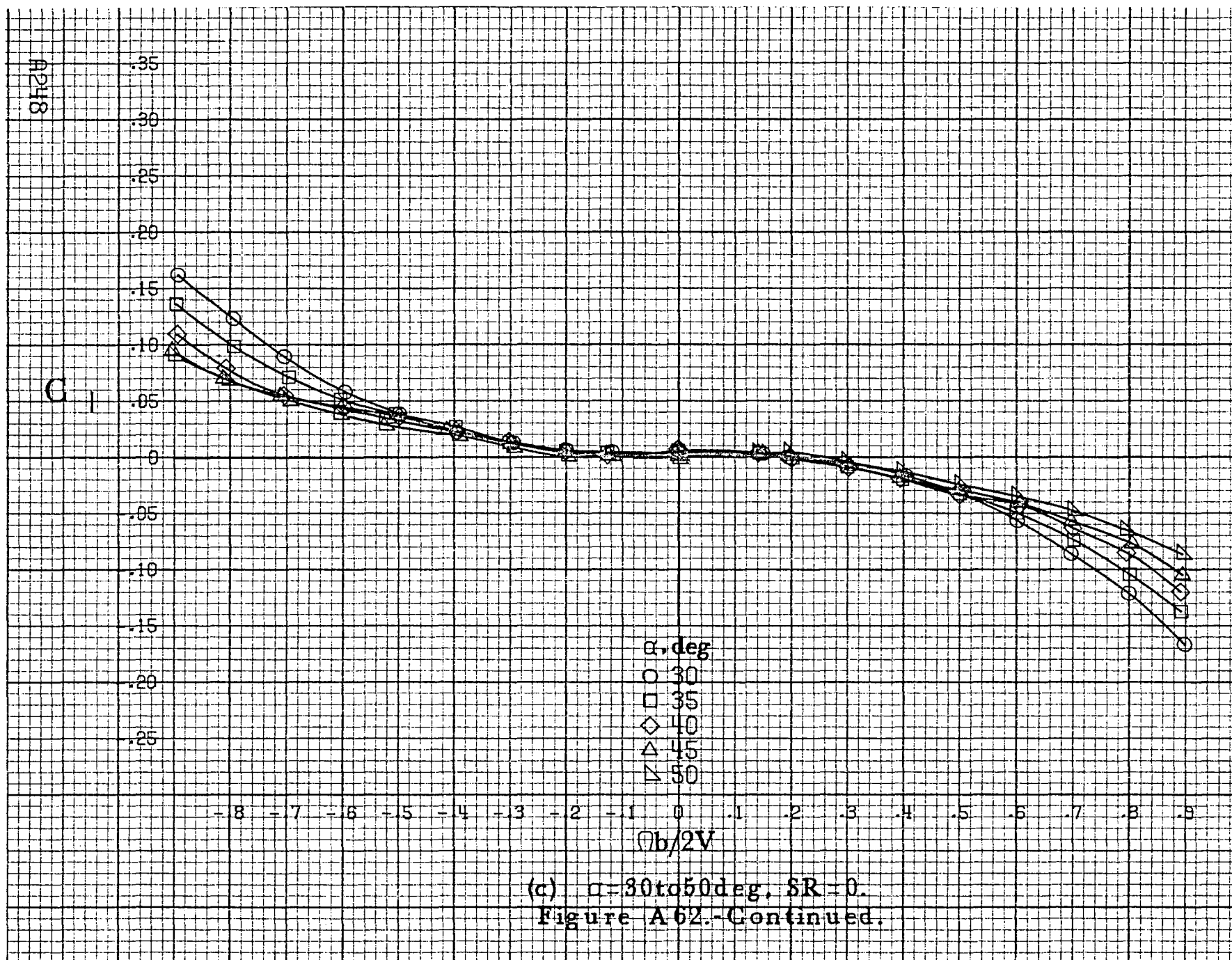
α, deg
○ 18
□ 20
◇ 25
△ 30
▽ 35

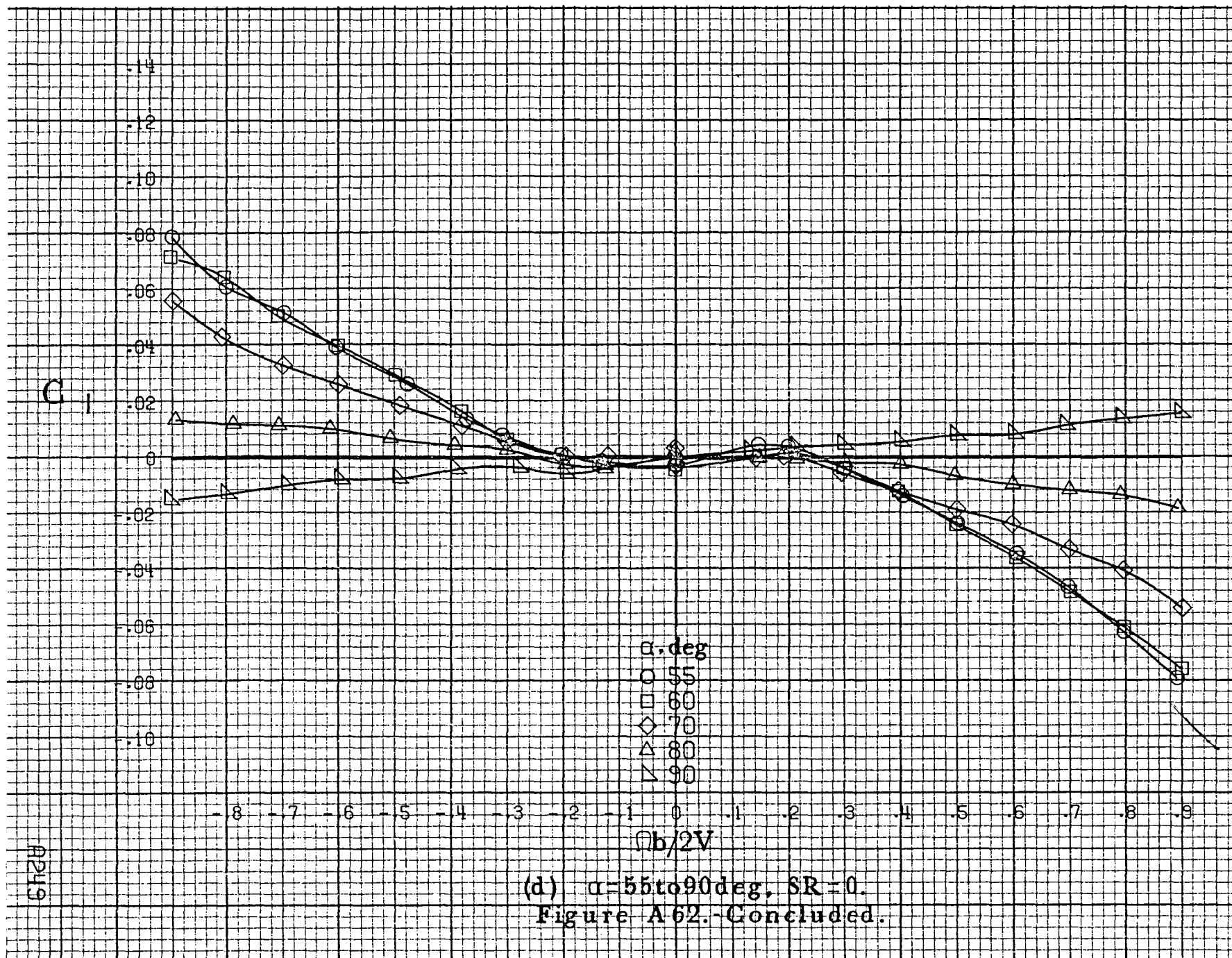
- .8 - .7 - .6 - .5 - .4 - .3 - .2 - .1 0 .1 .2 .3 .4 .5 .6 .7 .8 .9

$Ob/2V$

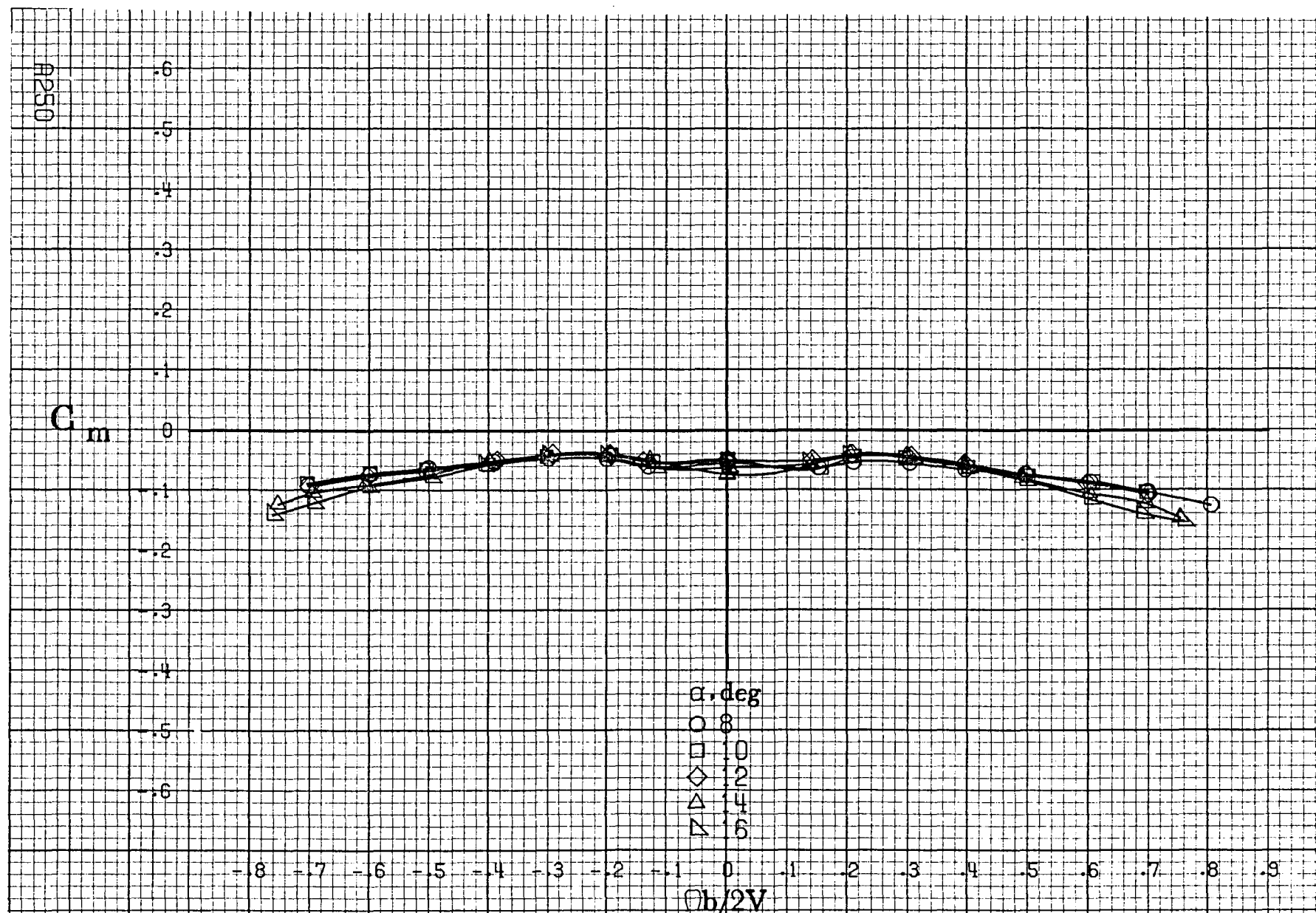
(b) $\alpha = 18 \text{ to } 35 \text{ deg}$, $SR = 91.4 \text{ cm (36 in.)}$.
Figure A 62.-Continued.

A247



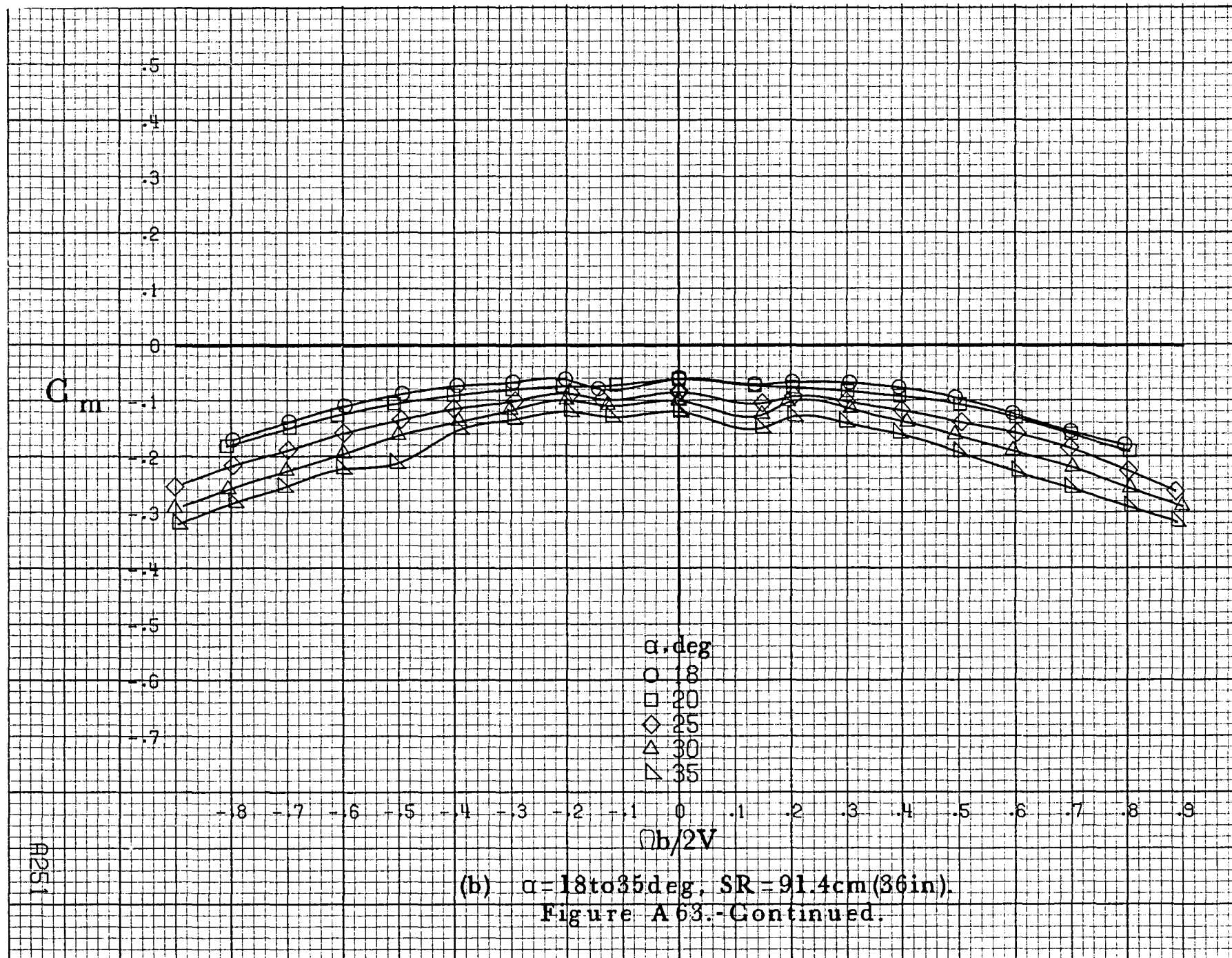


(d) $\alpha = 55$ to 90° , $SR = 0$.
Figure A 62.-Concluded.



(a) $\alpha=8$ to 6° , $SR=91.4\text{cm}(36\text{in})$.

Figure A63.- Effect of rotation rate and angle of attack on pitching-moment coefficient for long body, high wing configuration. $\delta_c=0^\circ$, $\delta_a=0^\circ$, $\delta_r=0^\circ$, $\beta=0^\circ$.



A251

C_m

4
3
2
1
0
-1
-2
-3
-4
-5
-6
-7
-8

α, deg
○ 30
□ 35
◇ 40
△ 45
▽ 50

-8 -7 -6 -5 -4 -3 -2 -1 0 -1 -2 -3 -4 -5 -6 -7 -8
 $\eta b/2V$

(c) $\alpha=30$ to 50 deg, $\delta R=0$.
Figure A 63.-Continued.

C_m

.2
.1
0
.1
.2
.3
.4
.5
.6
.7
.8
.9
1.0

α, deg
○ 55
□ 60
◇ 70
△ 80
▽ 90

-.8 -.7 -.6 -.5 -.4 -.3 -.2 -.1 0 .1 .2 .3 .4 .5 .6 .7 .8 .9
 $Ob/2V$

(d) $\alpha=55\text{to}90\text{deg}$, $SR=0$.
Figure A63.- Concluded.

A253

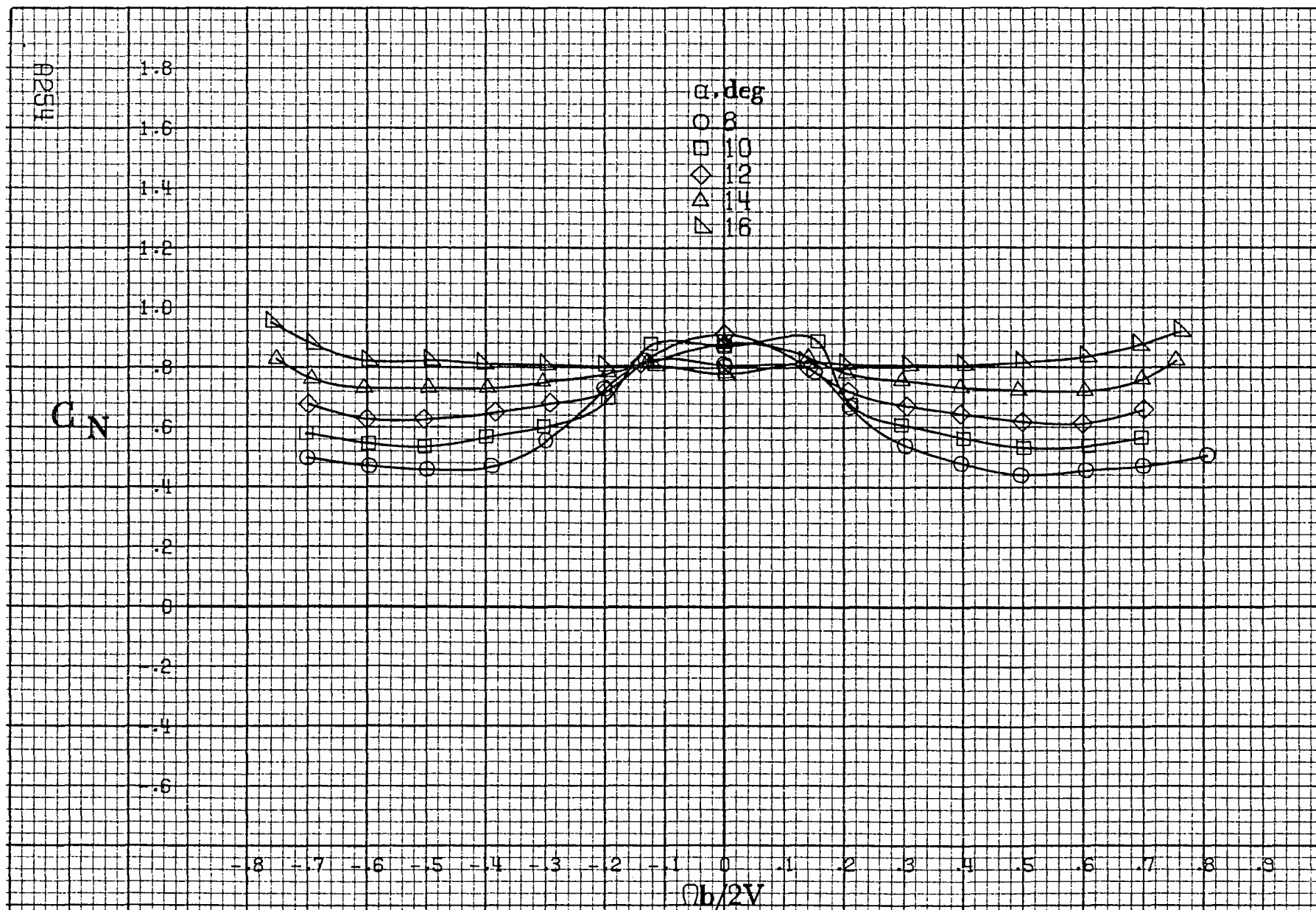
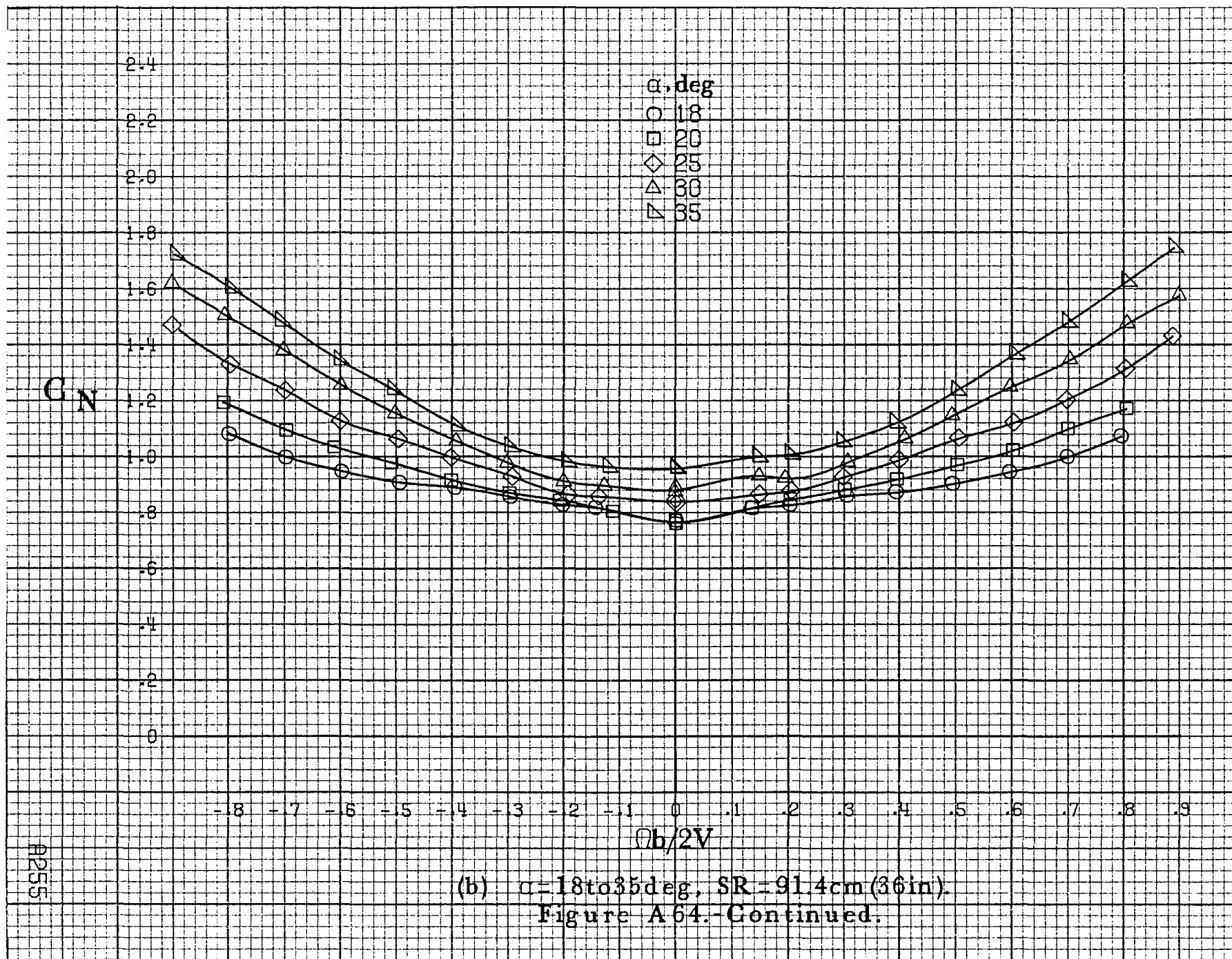
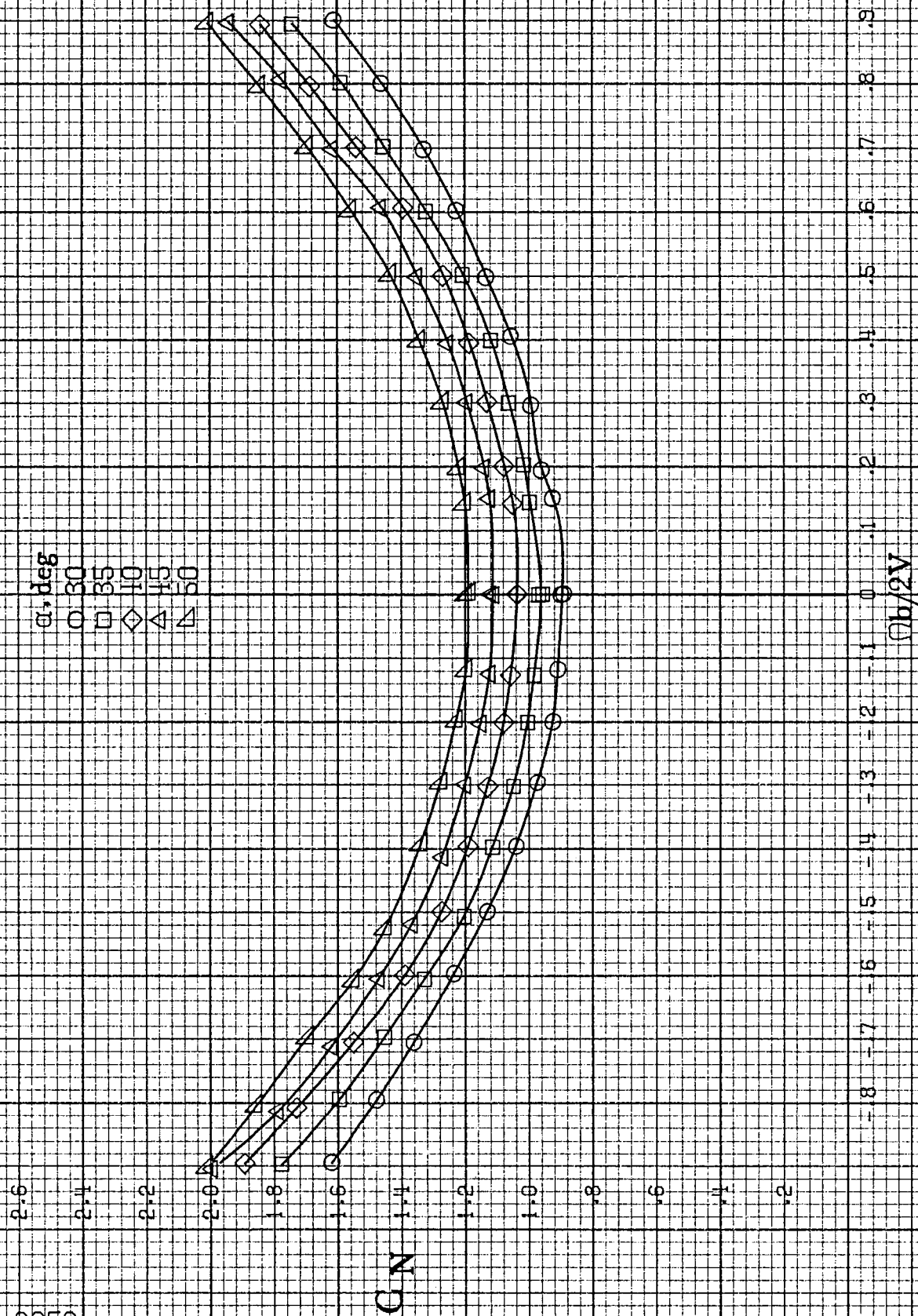


Figure A64.-Effect of rotation rate and angle of attack on normal-force coefficient for long body, high wing configuration. $\delta_c = 0^\circ$, $\delta_a = 0^\circ$, $\delta_r = 0^\circ$, $\beta = 0^\circ$.

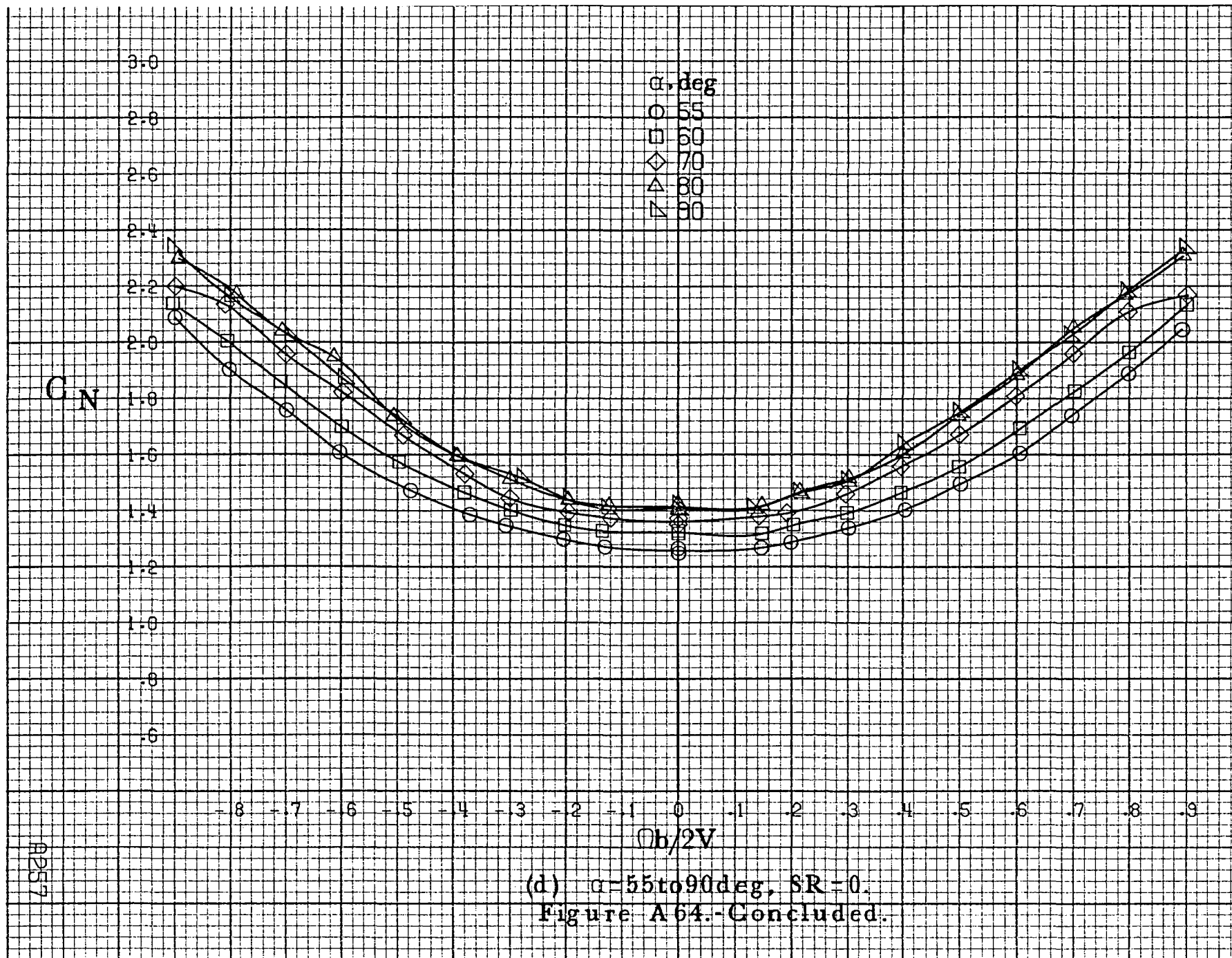


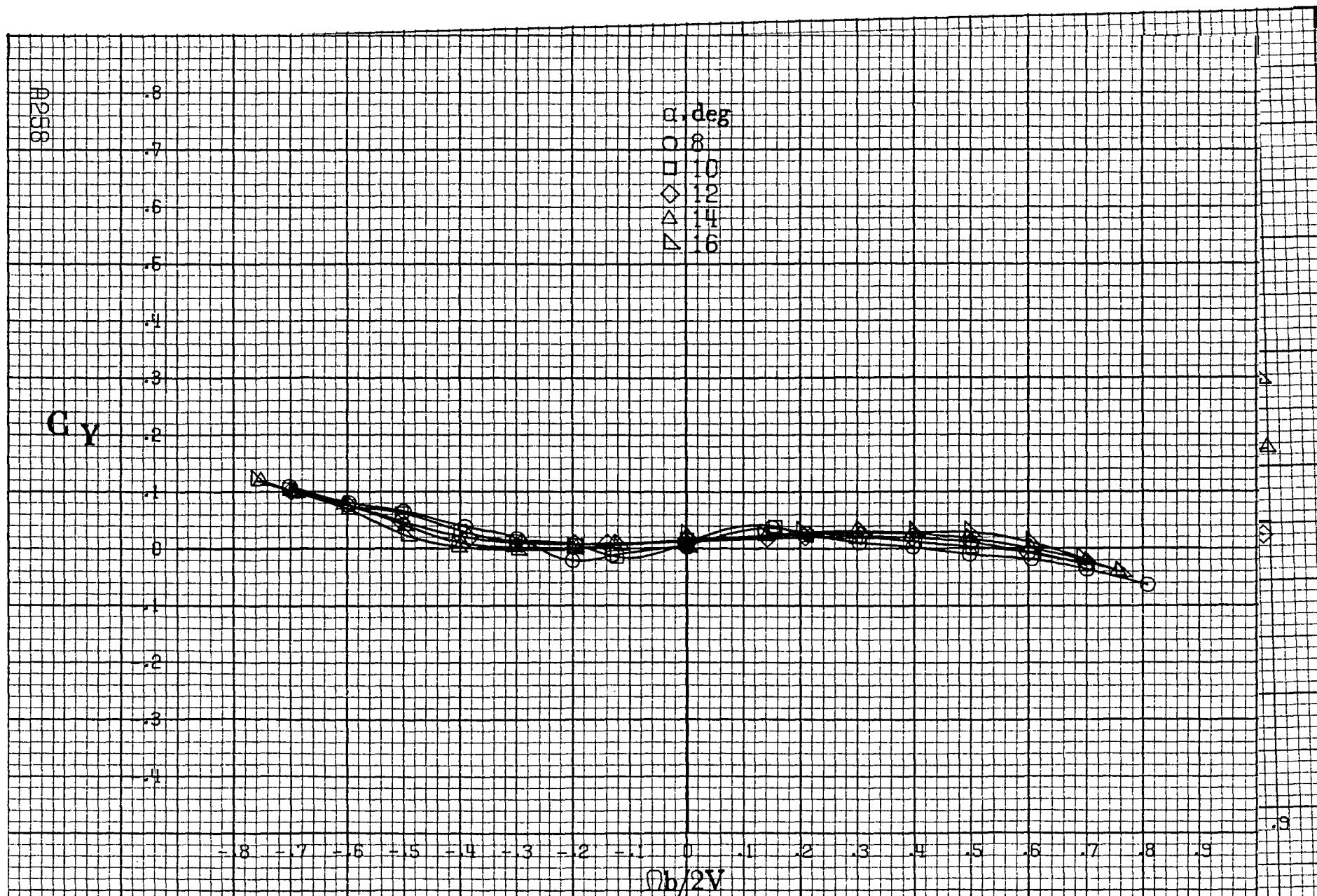
A256



(c) $\alpha = 30$ to 50 deg, $SR = 0$.

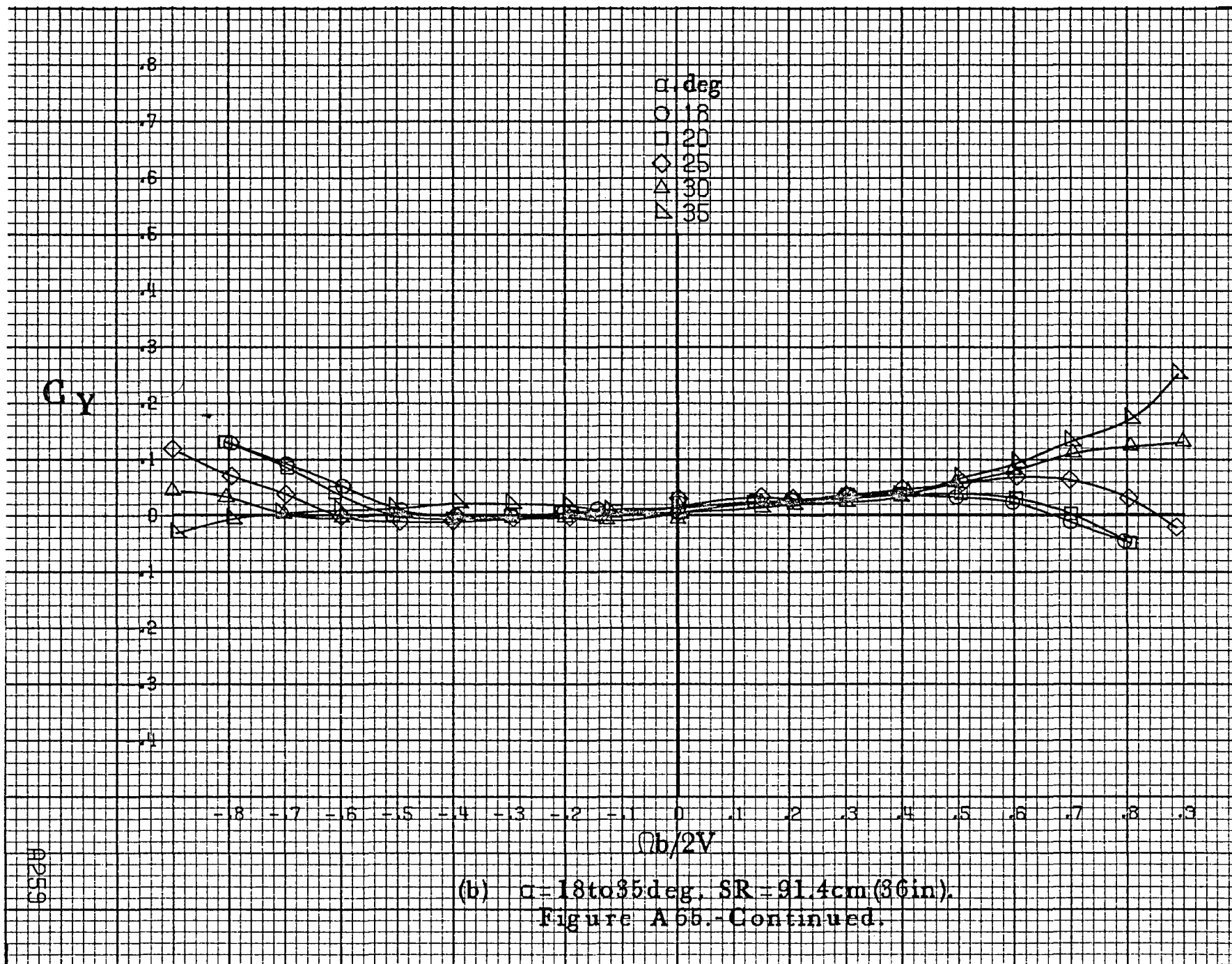
Figure A64.-Continued.



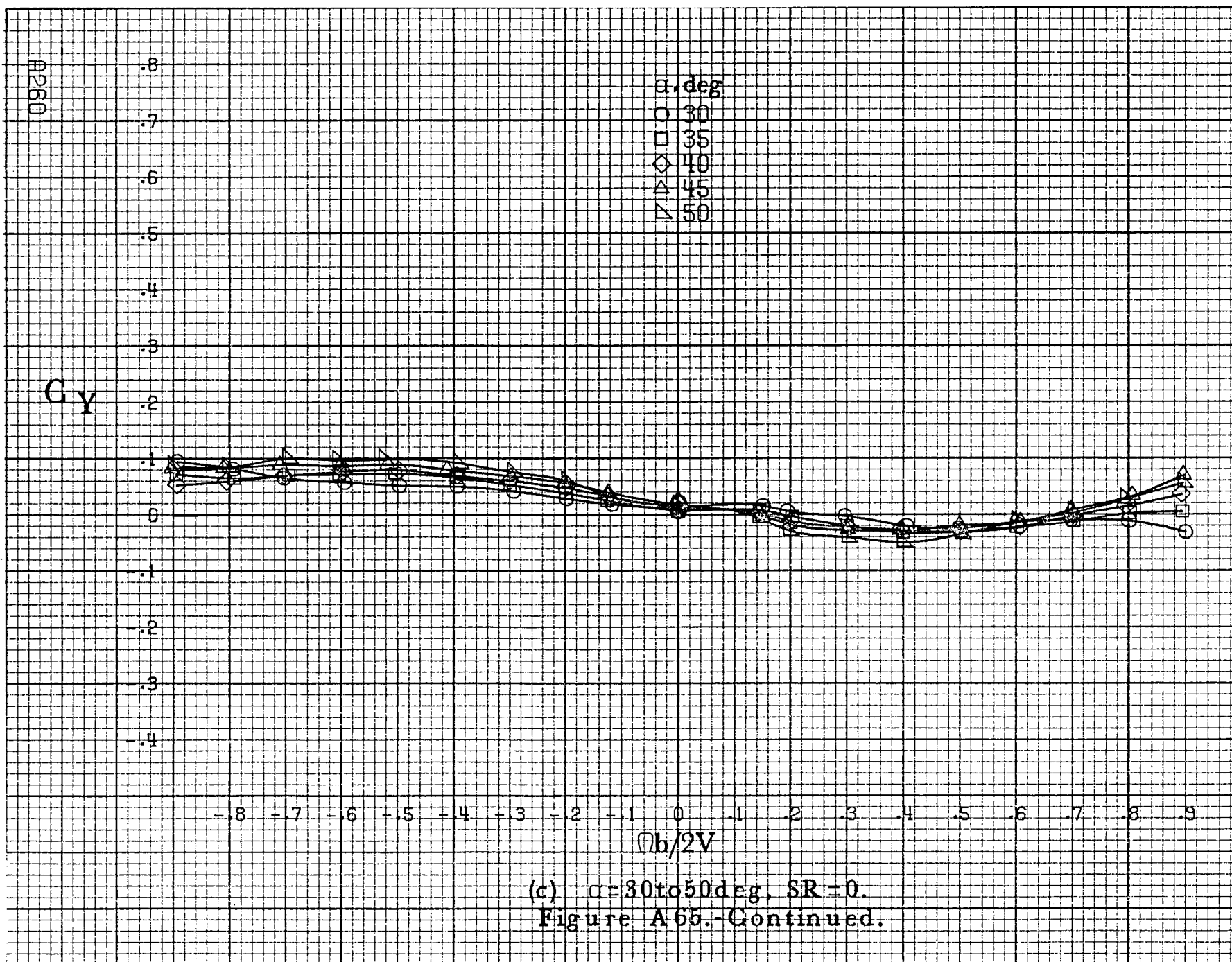


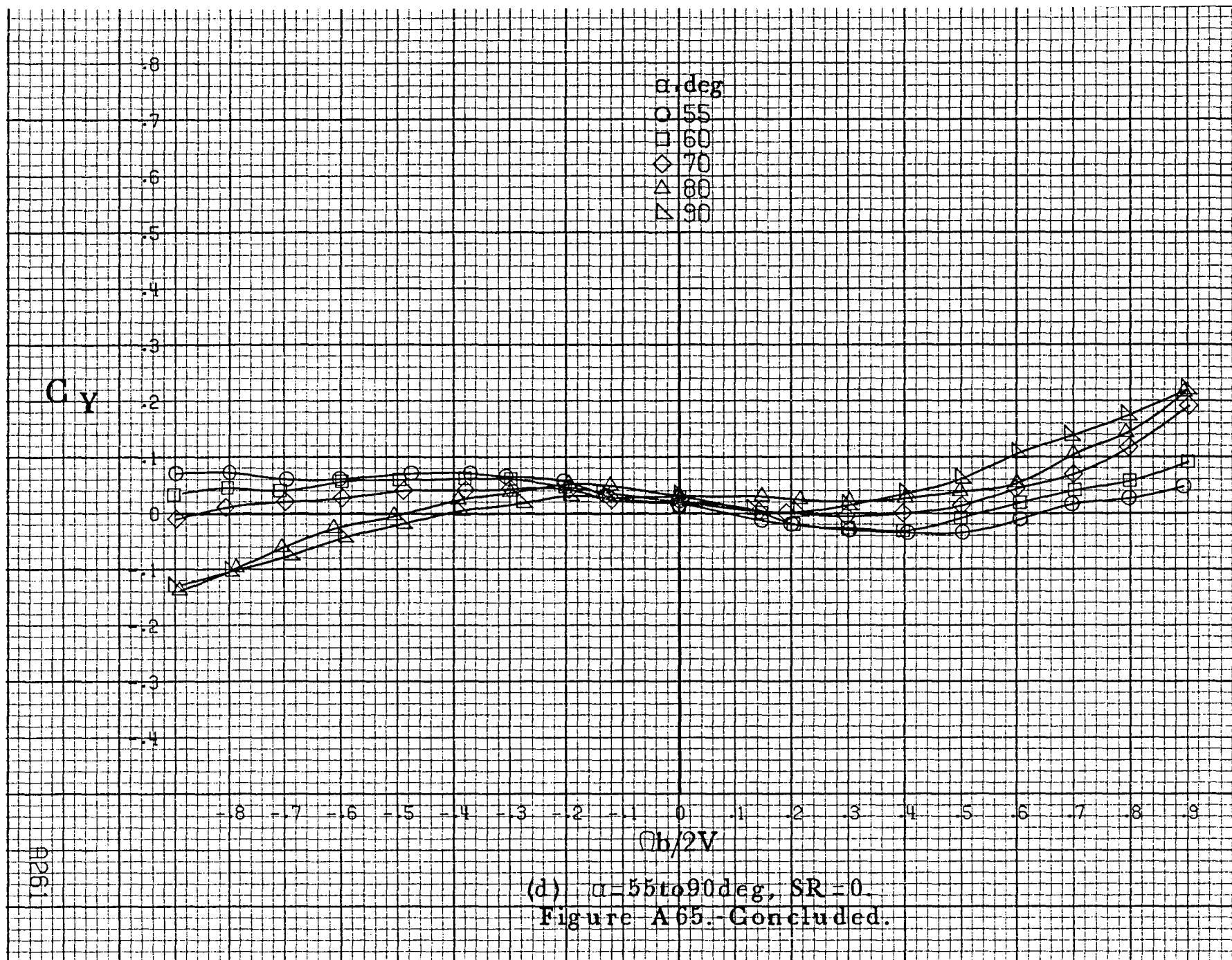
(a) $\alpha=8$ to 16° , $SR=91.4\text{cm}(36\text{in})$.

Figure A65.-Effect of rotation rate and angle of attack on side force coefficient for long body, high wing configuration. $\delta_c=0^\circ$, $\delta_s=0^\circ$, $\delta_t=0^\circ$, $\beta=0^\circ$.



(b) $\alpha = 18$ to 35° . $SR = 91.4\text{ cm (36 in.)}$.
Figure A 65.-Continued.





B262

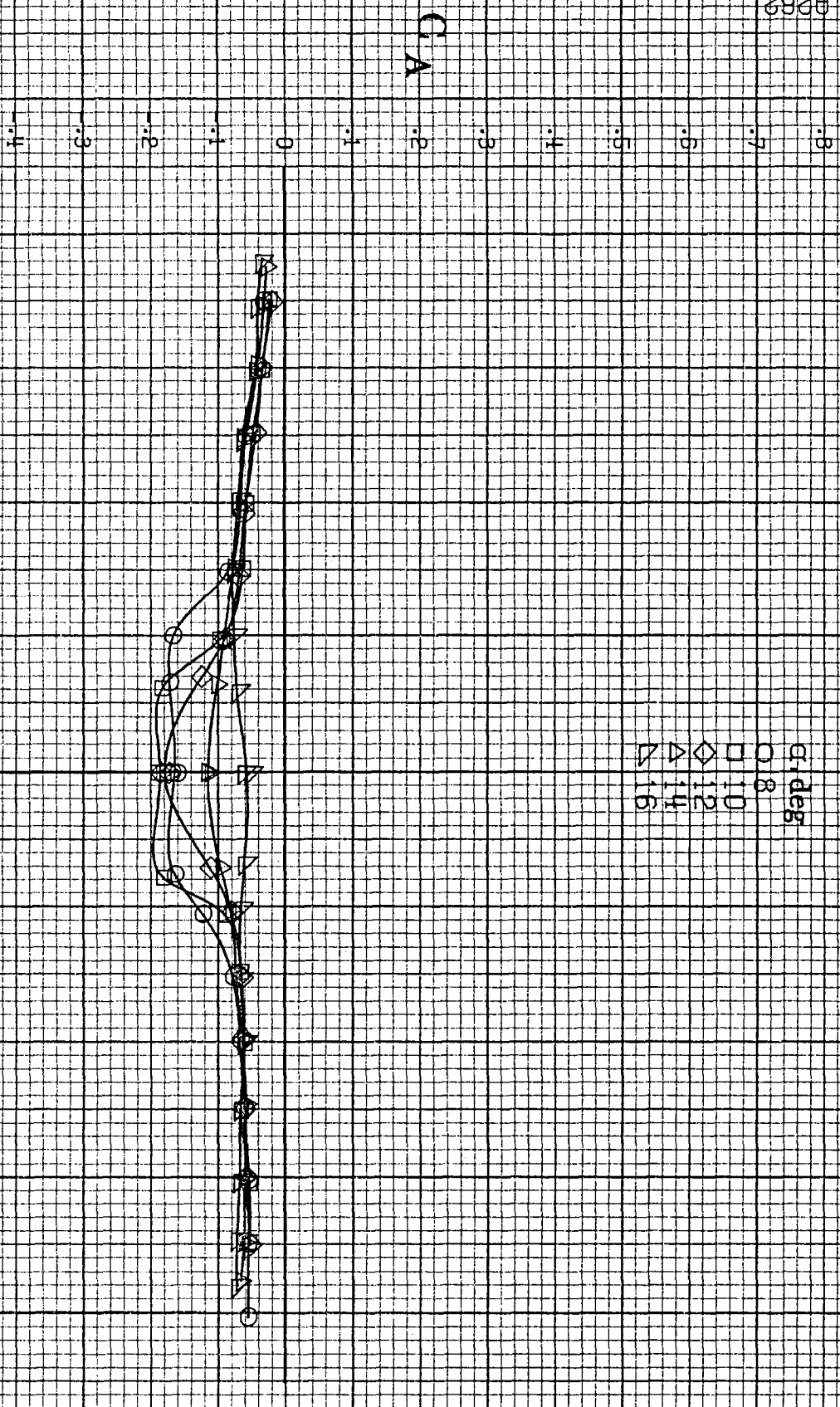
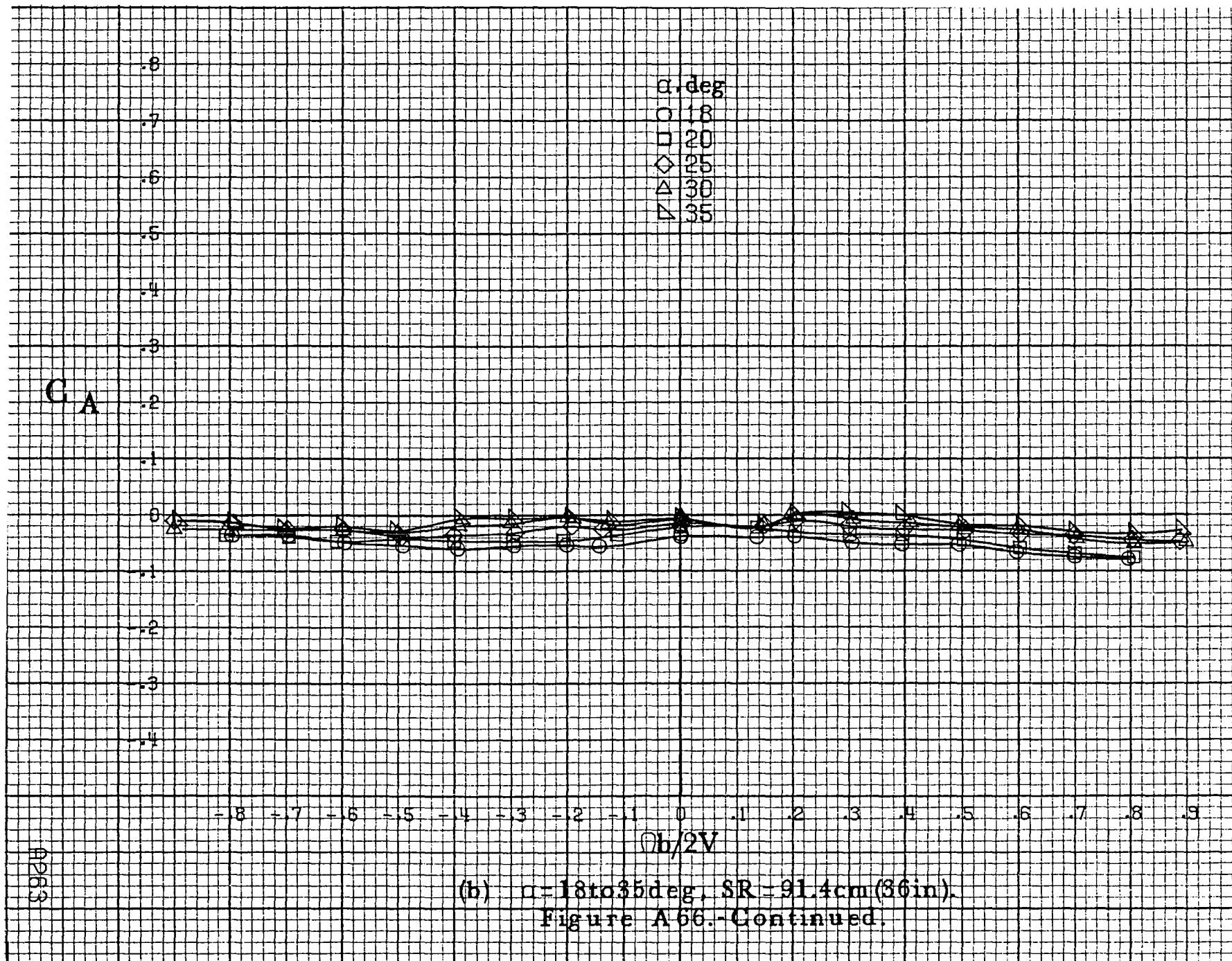
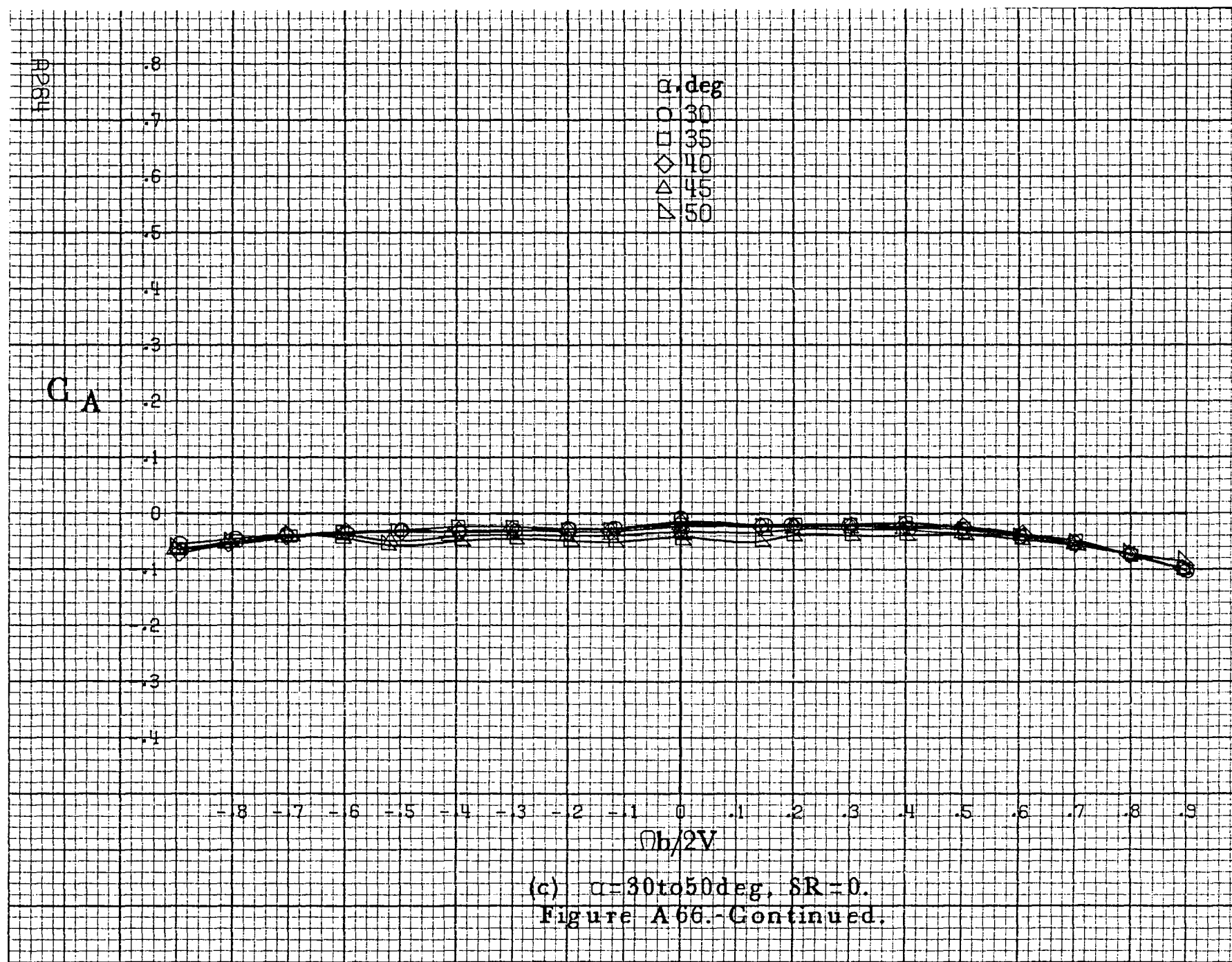
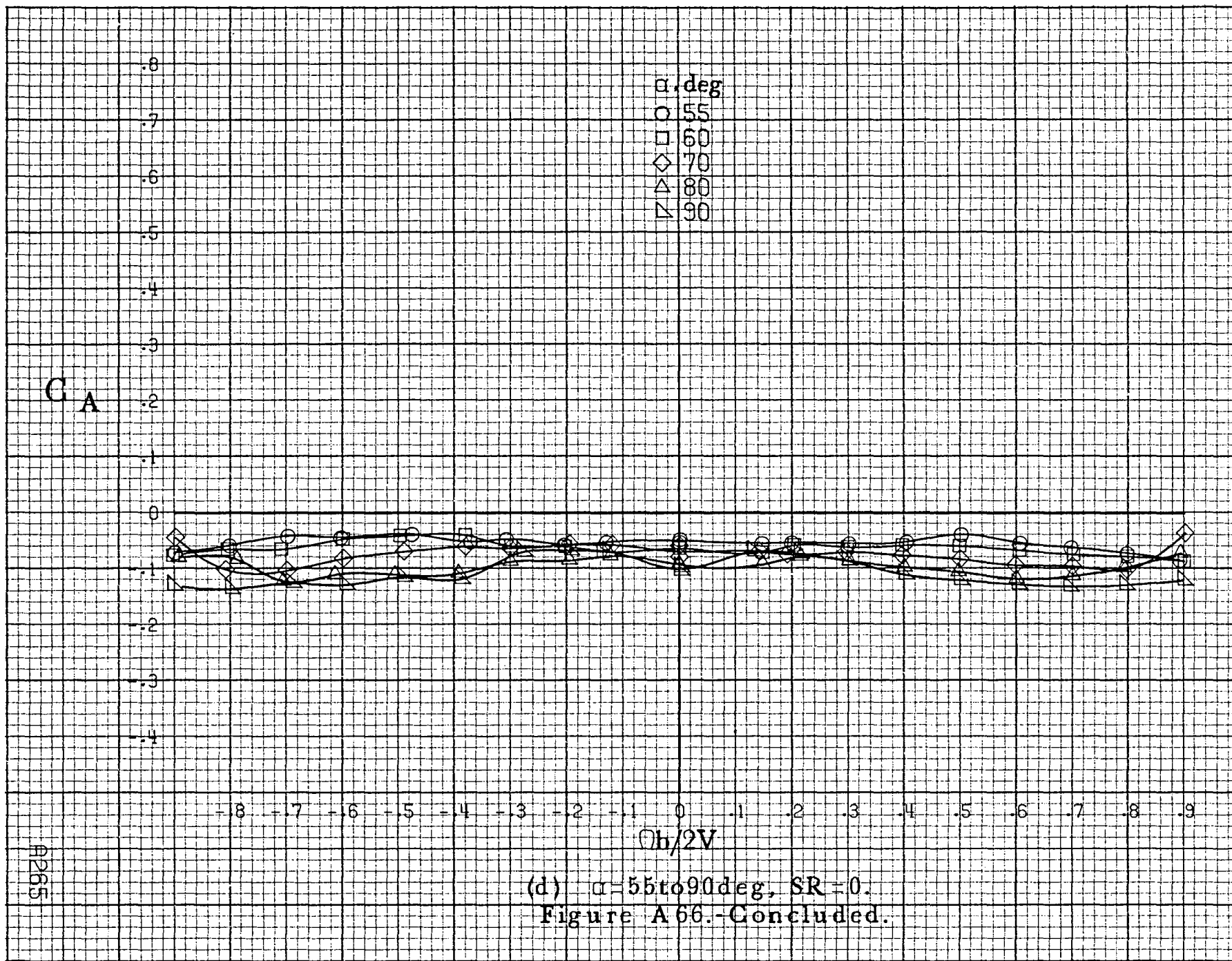
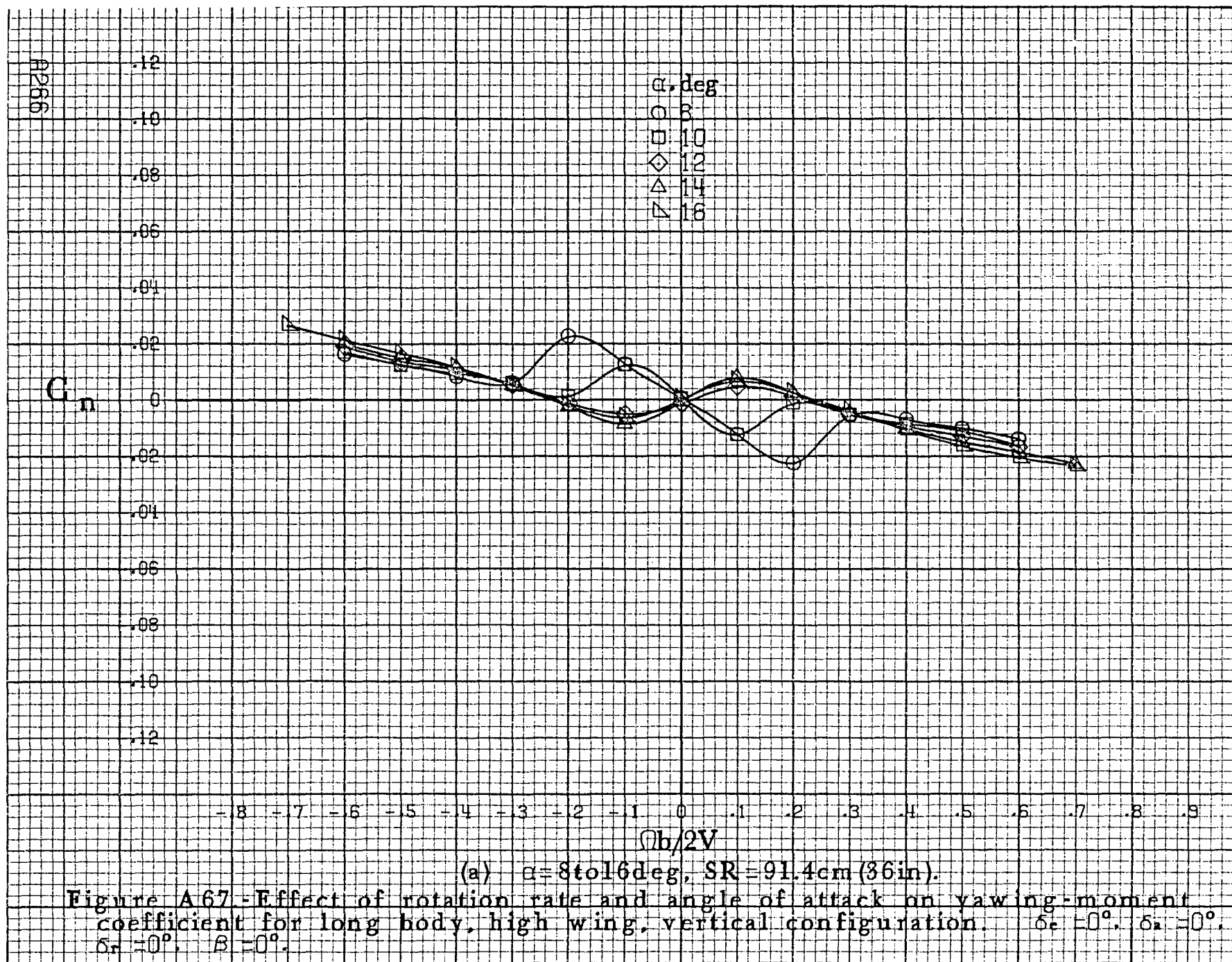


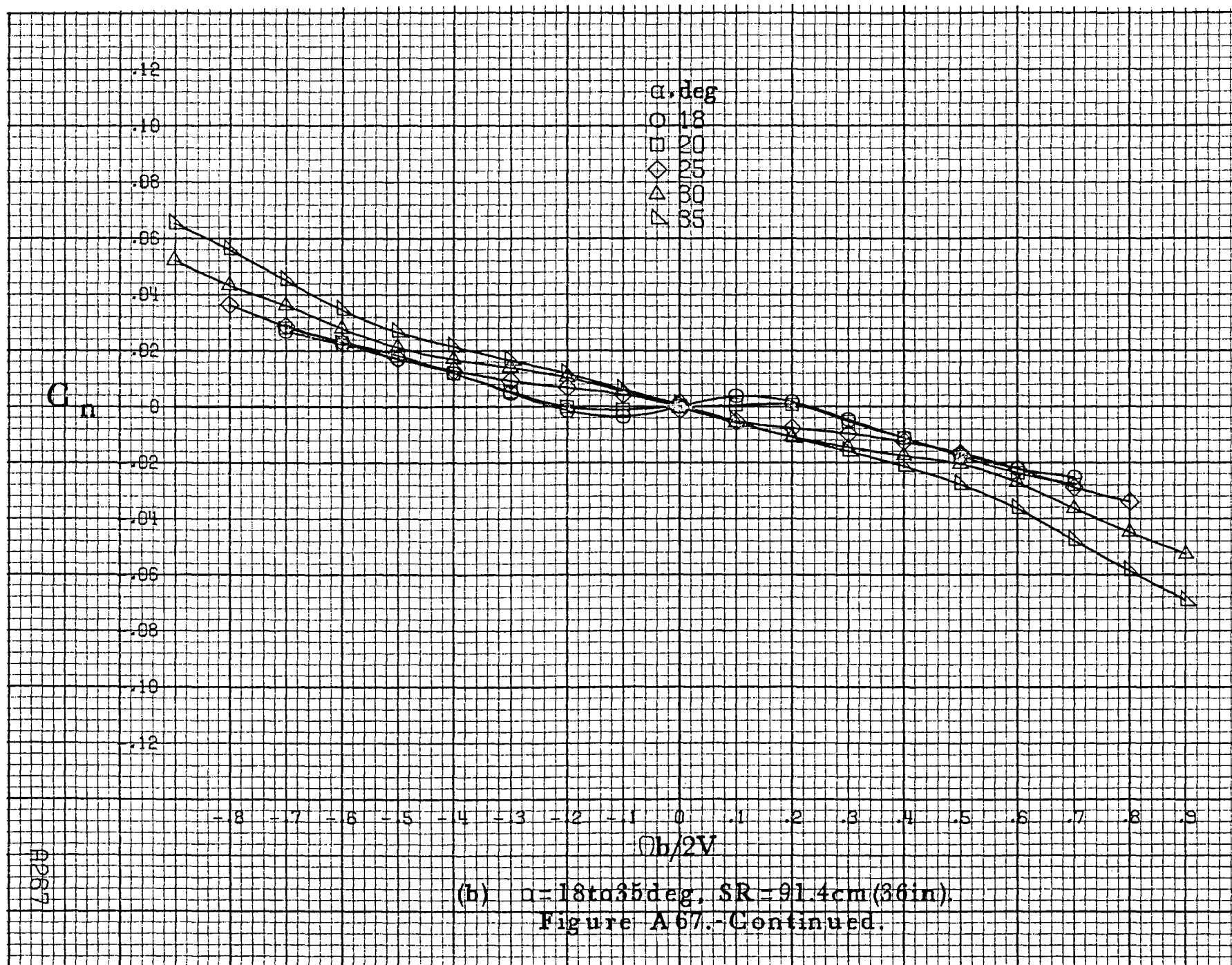
Figure A66. Effect of rotation rate and angle of attack on axial force coefficient for long body, high wing configuration. $\delta_e = 0^\circ$, $\delta_a = 0^\circ$, $\delta_r = 0^\circ$.











A268

 C_n α, deg

○ 30

□ 35

◇ 40

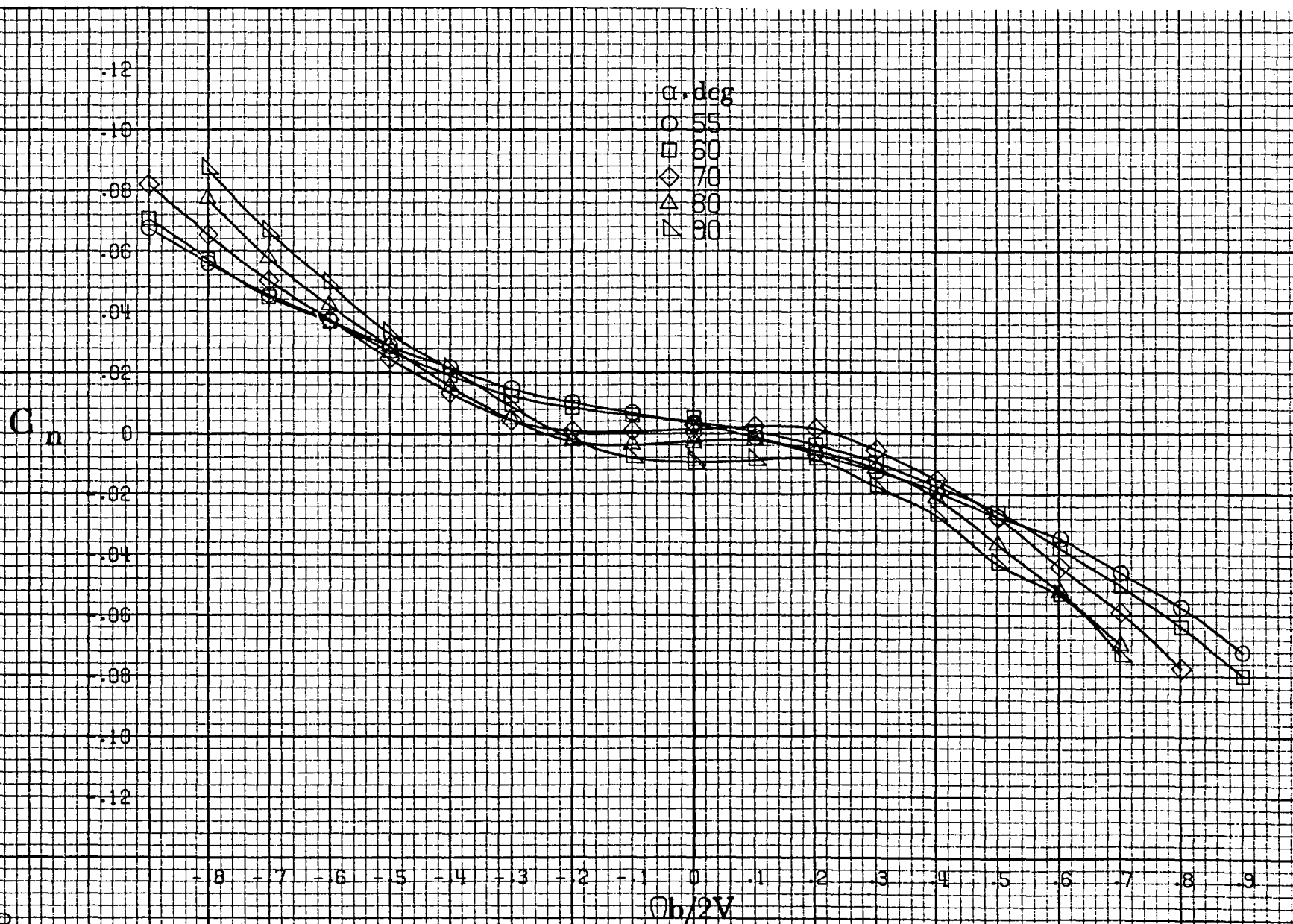
△ 45

▽ 50

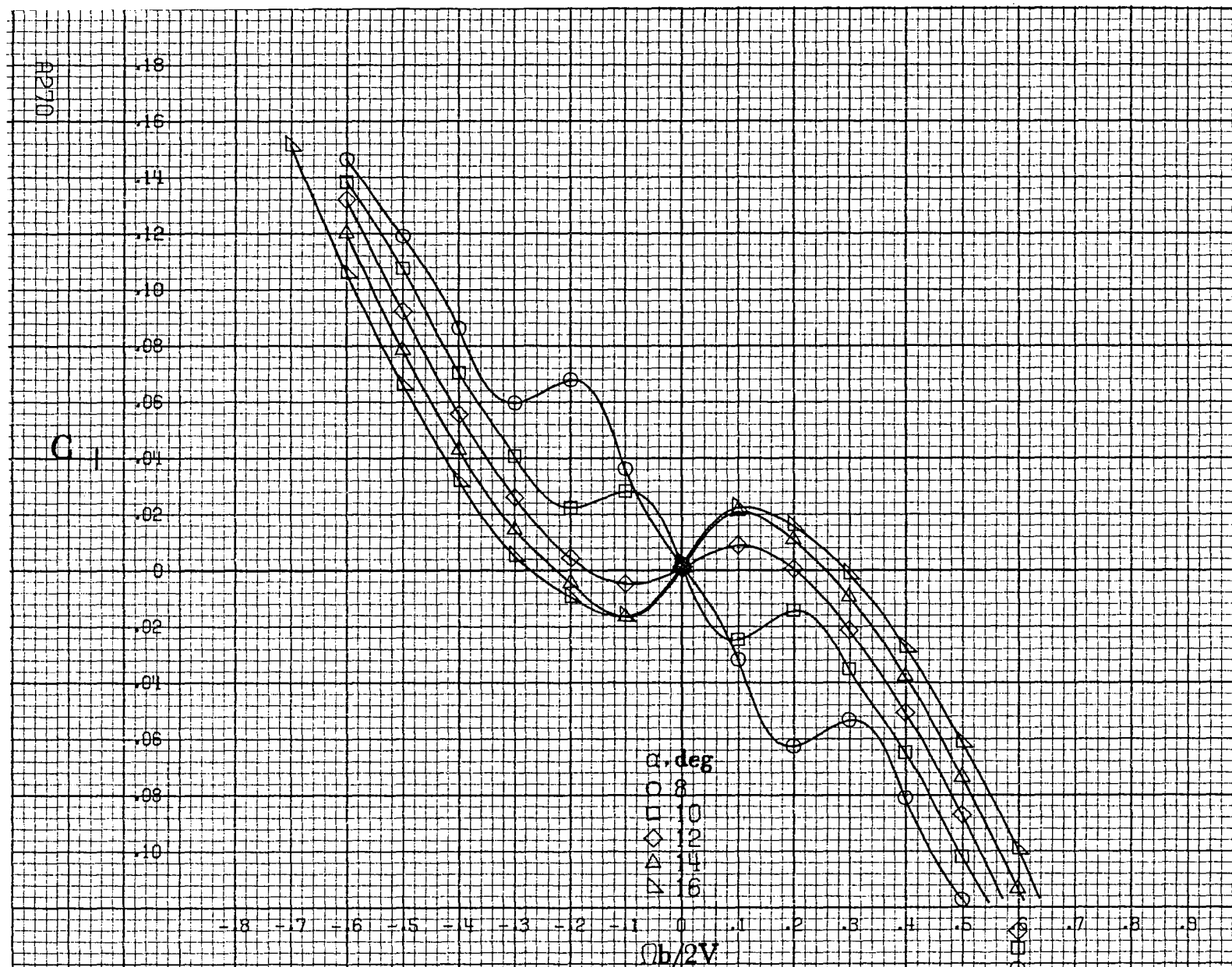
-8 -7 -6 -5 -4 -3 -2 -1 0 .1 .2 .3 .4 .5 .6 .7 .8 .9

 $b/2V$ (c) $\alpha=30$ to 50 deg, $SR=0$.

Figure A67.-Continued.



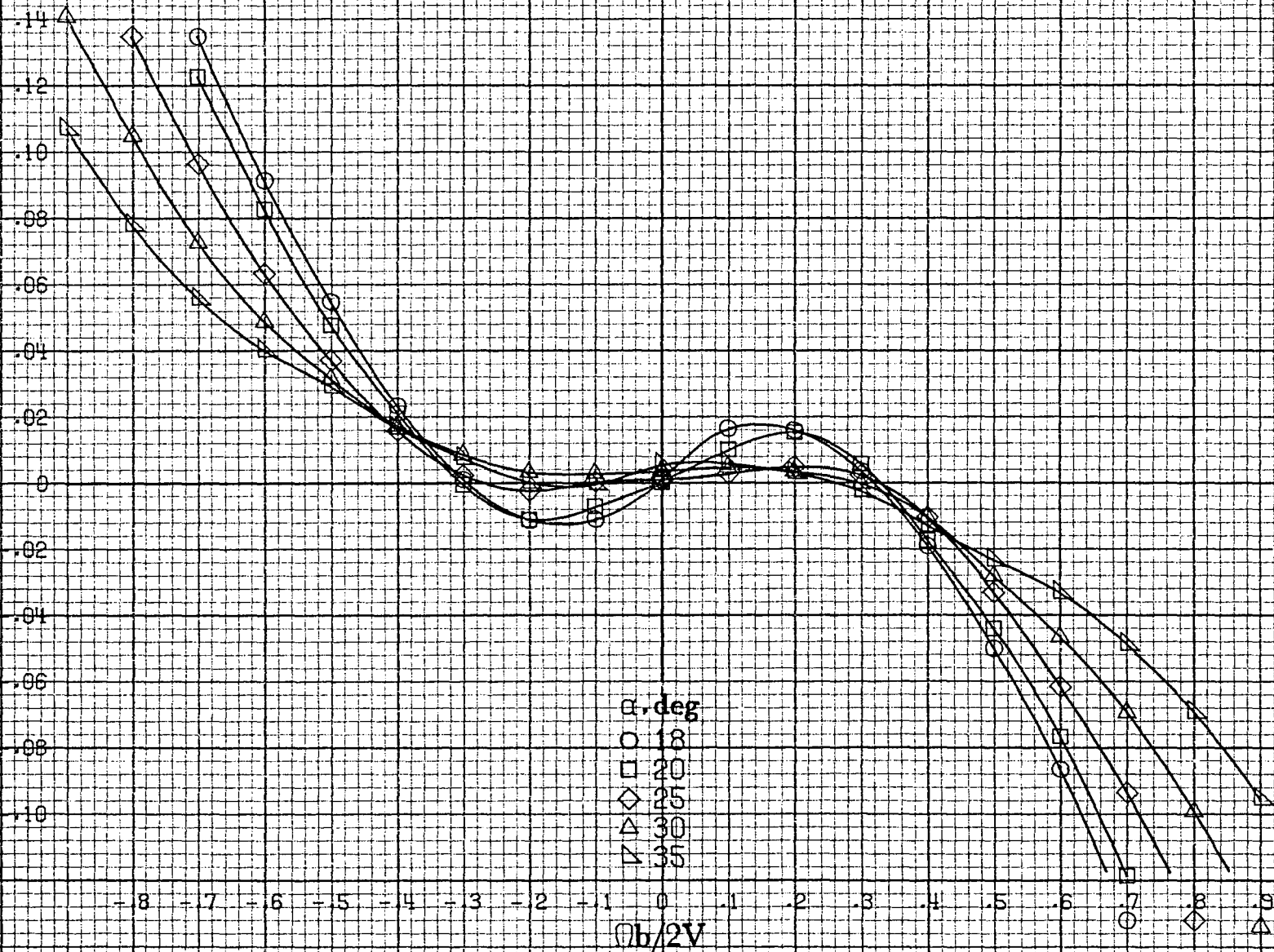
(d) $\alpha = 55$ to 90° , $SR = 0$.
Figure A 67.-Concluded.



(a) $\alpha = 8$ to 16° , $SR = 91.4 \text{ cm (36 in.)}$.

Figure A68.-Effect of rotation rate and angle of attack on rolling-moment coefficient for long body, high wing, vertical configuration. $\delta_e = 0^\circ$, $\delta_a = 0^\circ$, $\delta_r = 0^\circ$, $\beta = 0^\circ$.

C_1



(b) $\alpha = 18$ to 35° , $SR = 91.4 \text{ cm (36 in.)}$.
Figure A68.-Continued.

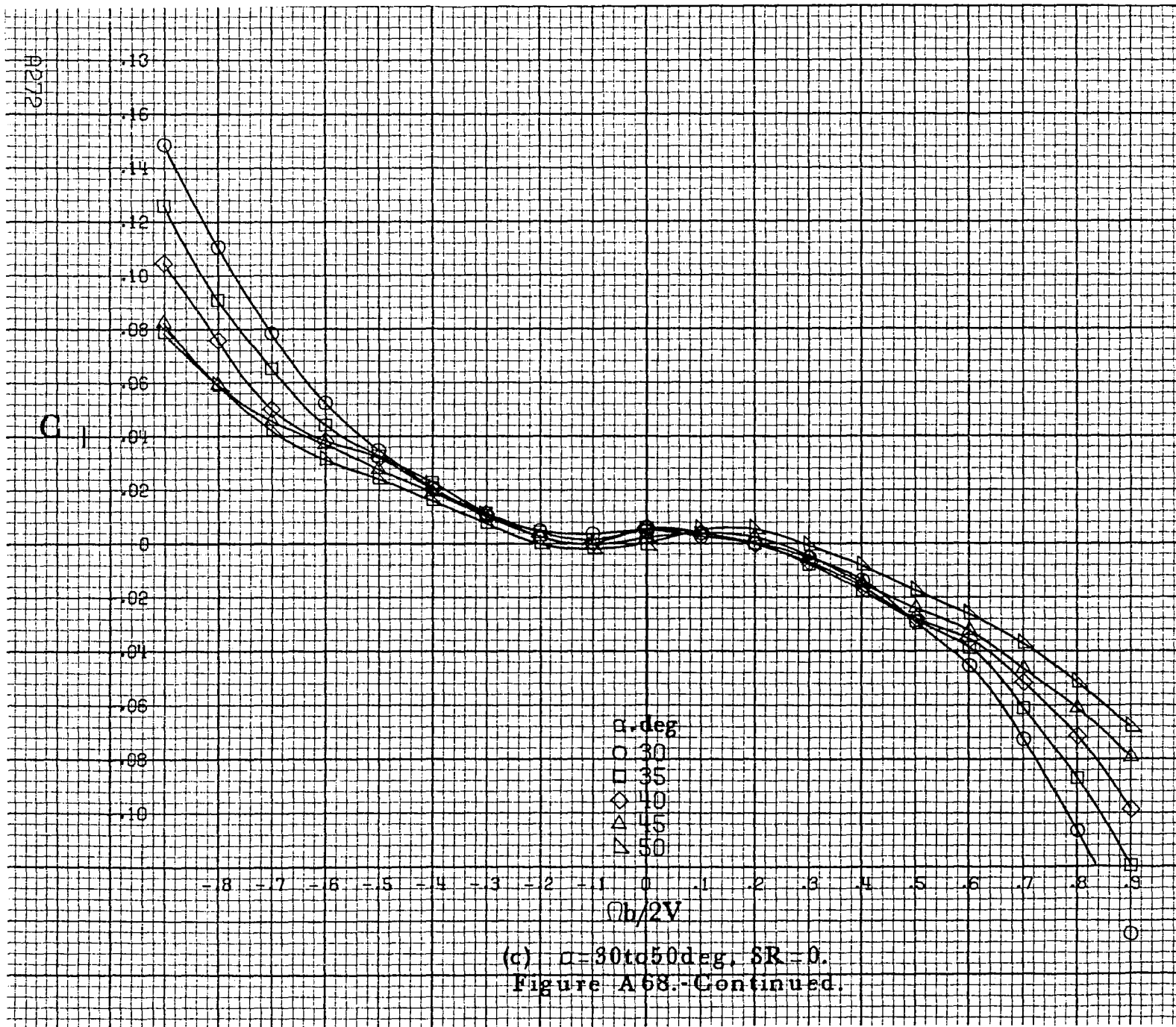
C_1

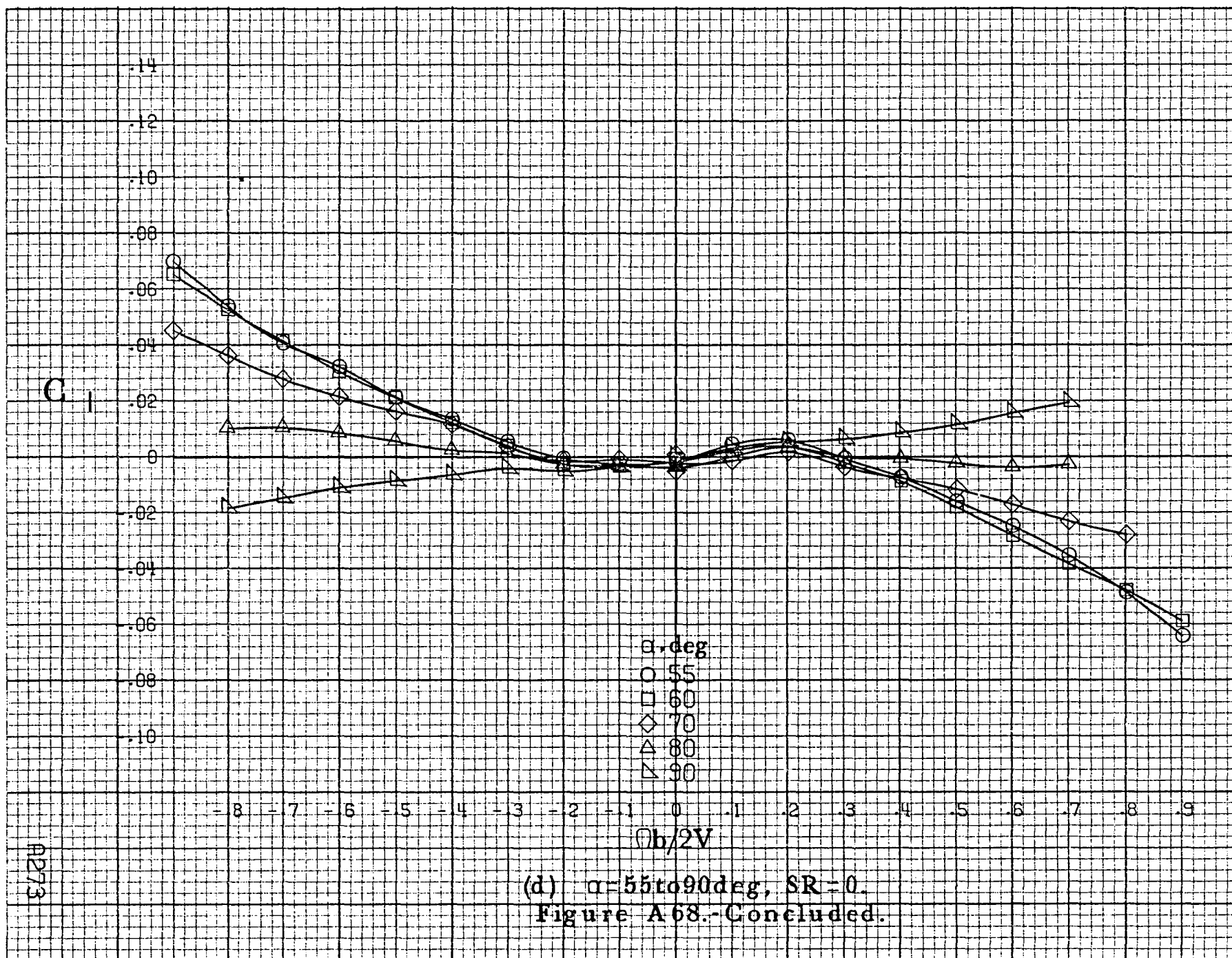
.13
.12
.11
.10
.09
.08
.07
.06
.05
.04
.03
.02
0
-.02
-.04
-.06
-.08
-.10

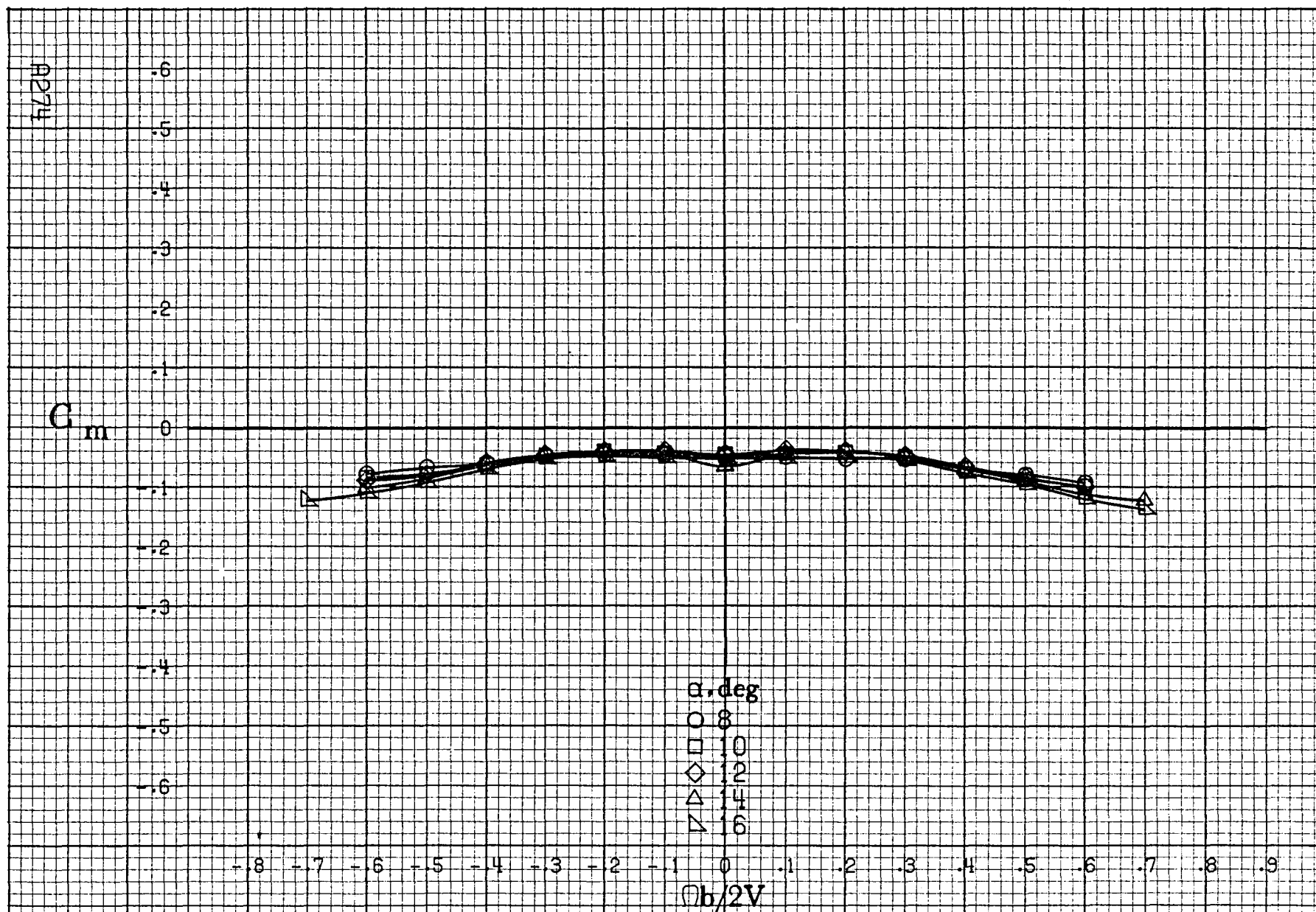
α, deg
○ 30
□ 35
◇ 40
△ 45
▽ 50

-8 -7 -6 -5 -4 -3 -2 -1 0 .1 .2 .3 .4 .5 .6 .7 .8 .9
 $Ob/2V$

(c) $\alpha=30$ to 50 deg, $SR=0$.
Figure A68.-Continued.

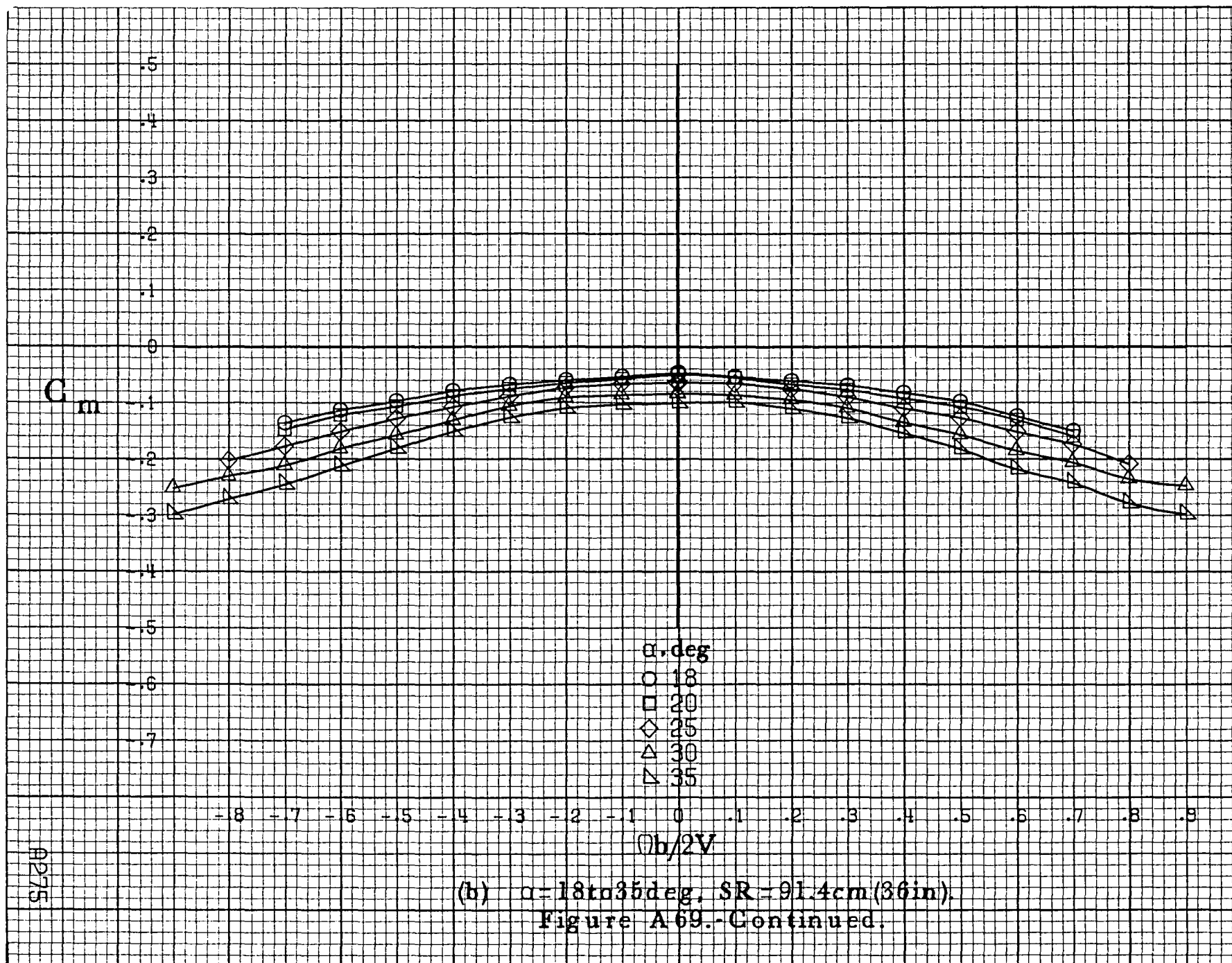


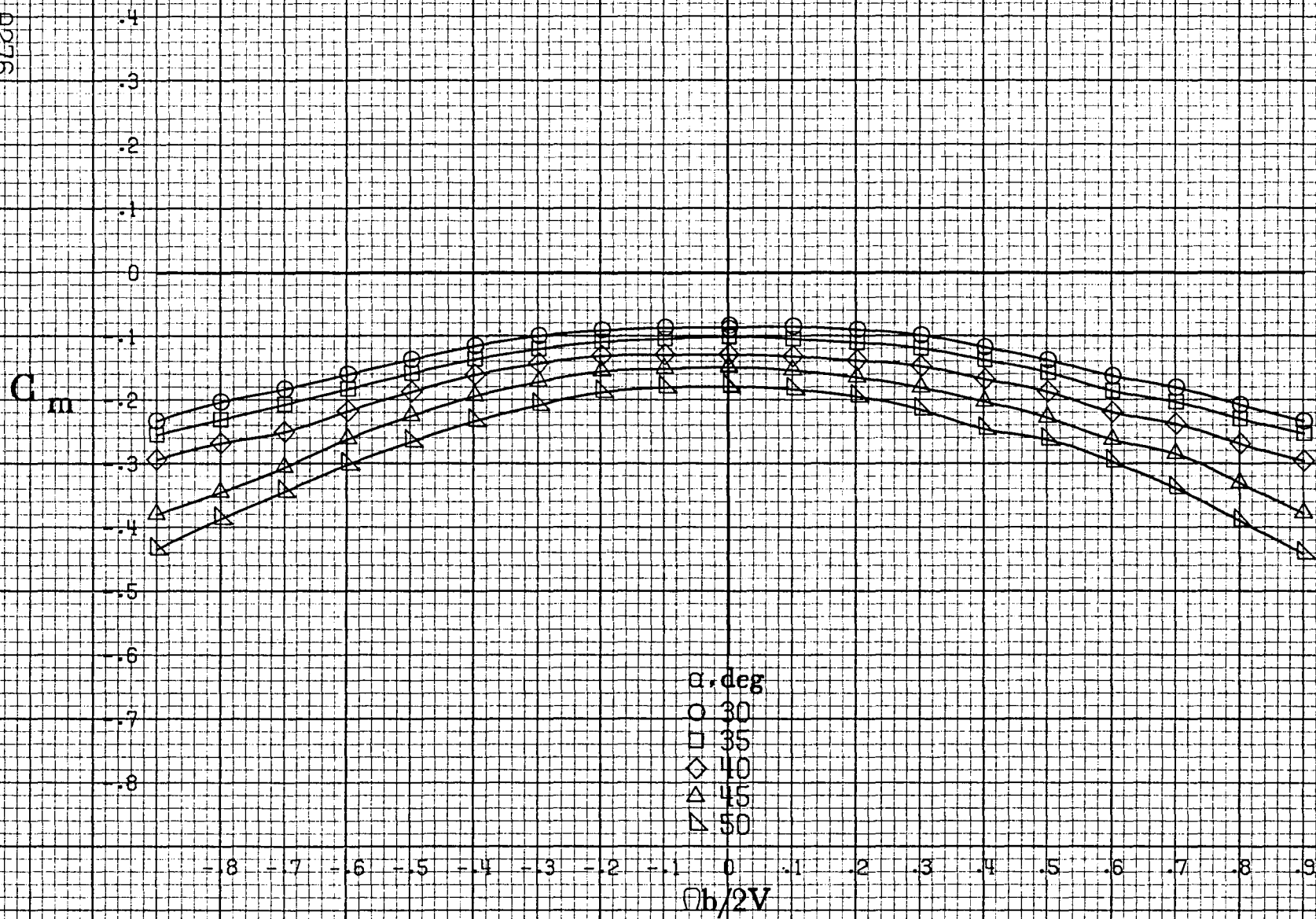




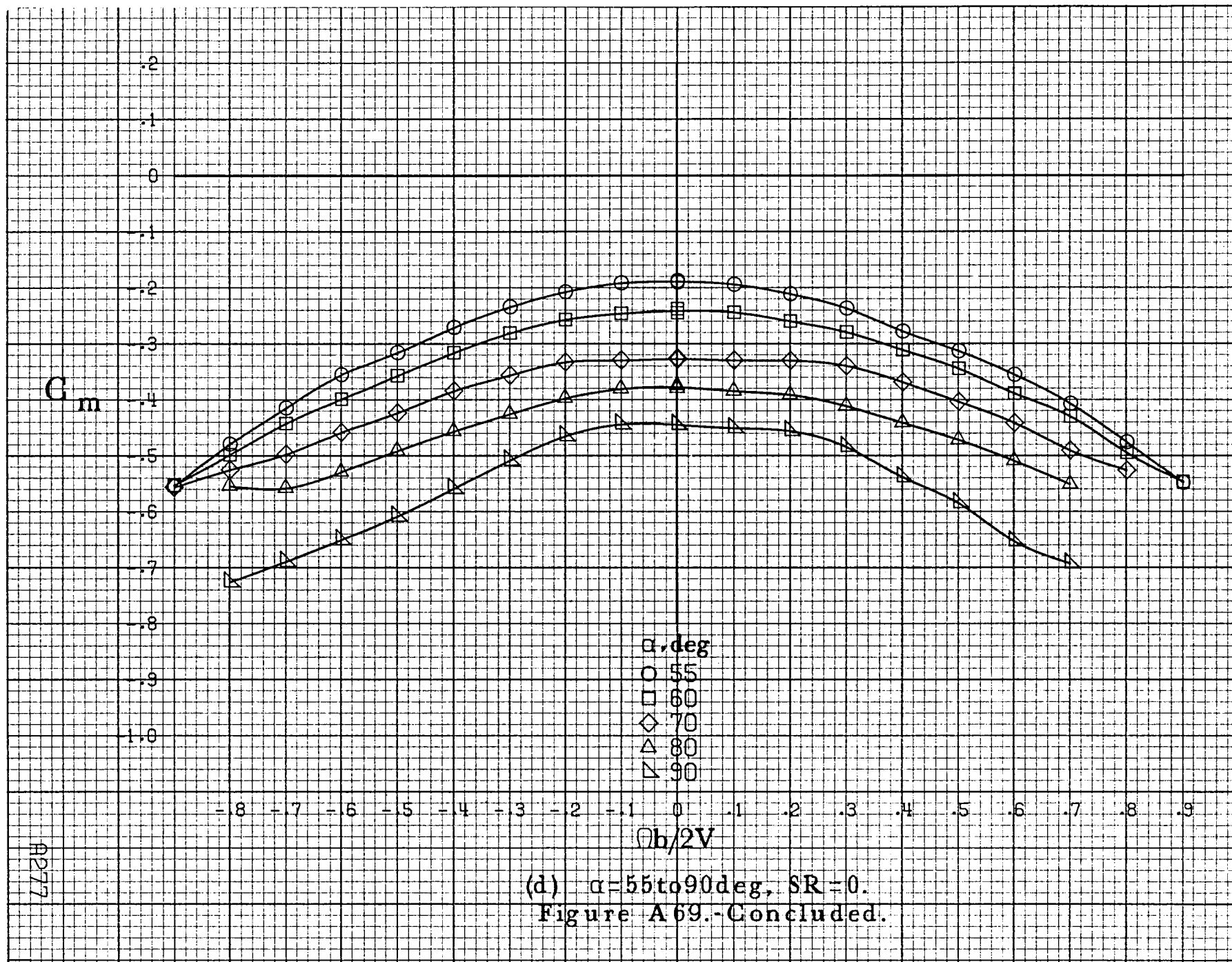
(a) $\alpha = 8$ to 16° , $SR = 91.4\text{cm}$ (36in).

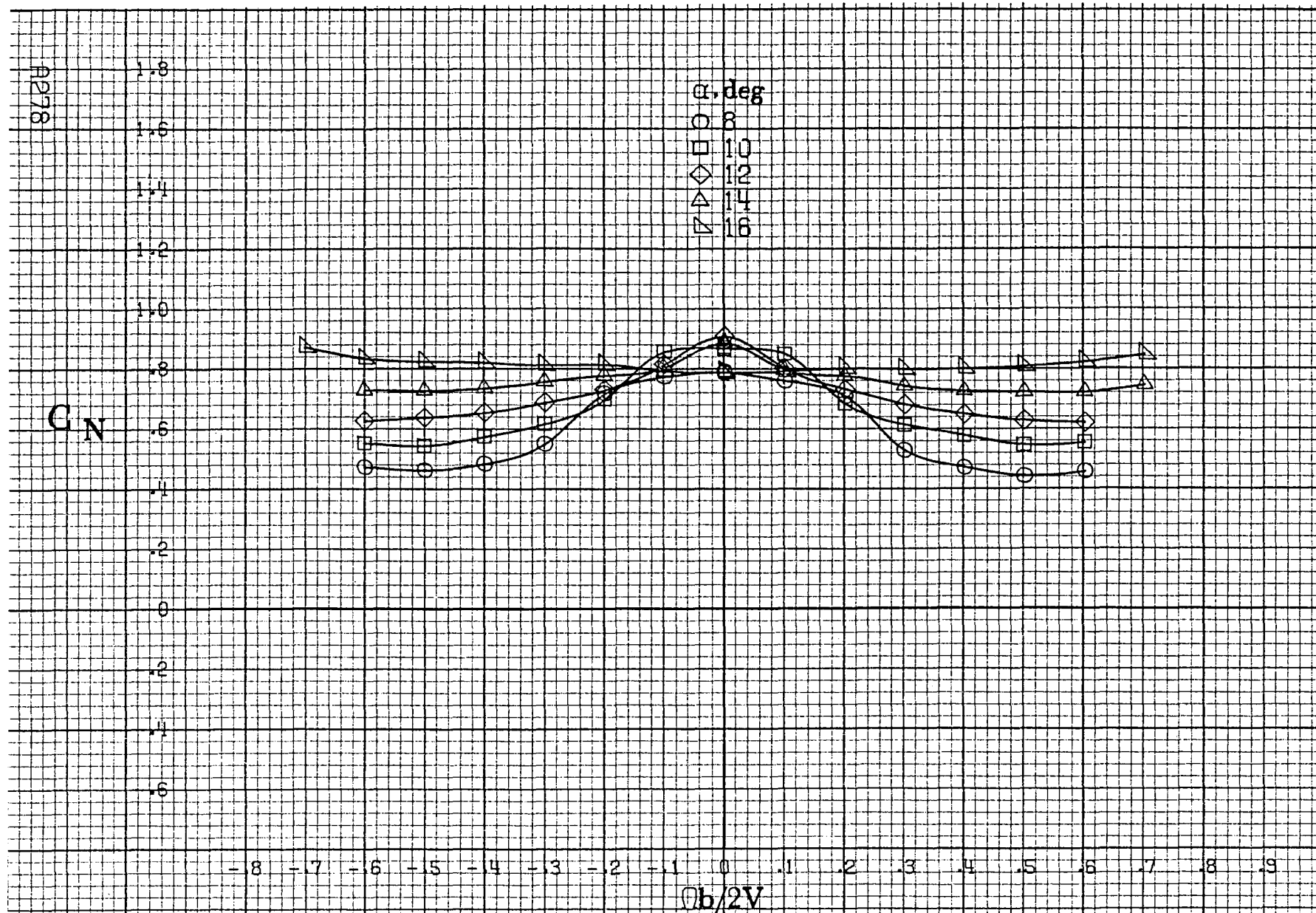
Figure A69.-Effect of rotation rate and angle of attack on pitching-moment coefficient for long body, high wing, vertical configuration. $\delta_e = 0^\circ$, $\delta_a = 0^\circ$, $\delta_r = 0^\circ$, $\beta = 0^\circ$.





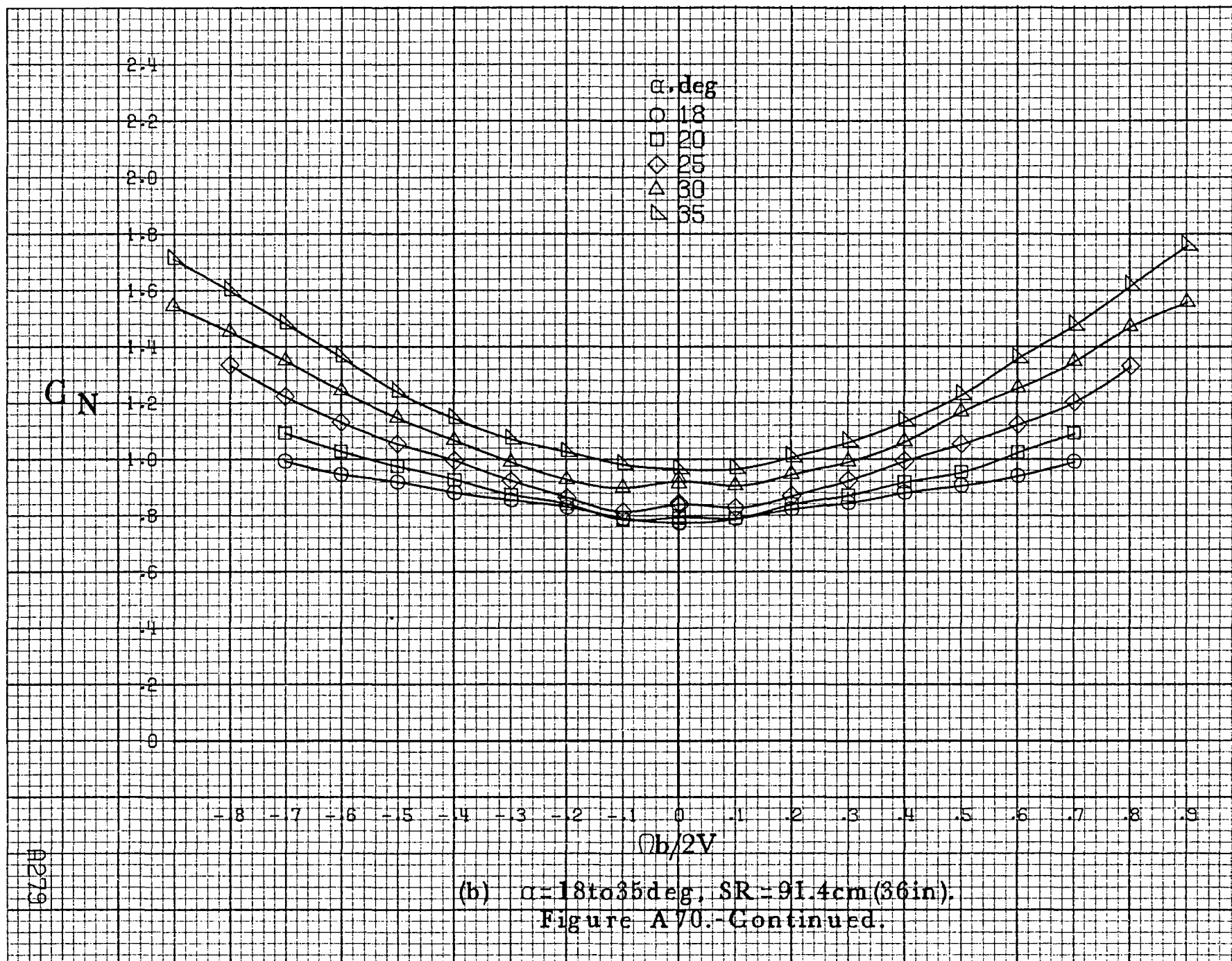
(c) $\alpha = 30$ to 50° , $SR = 0$.
Figure A 69.-Continued.



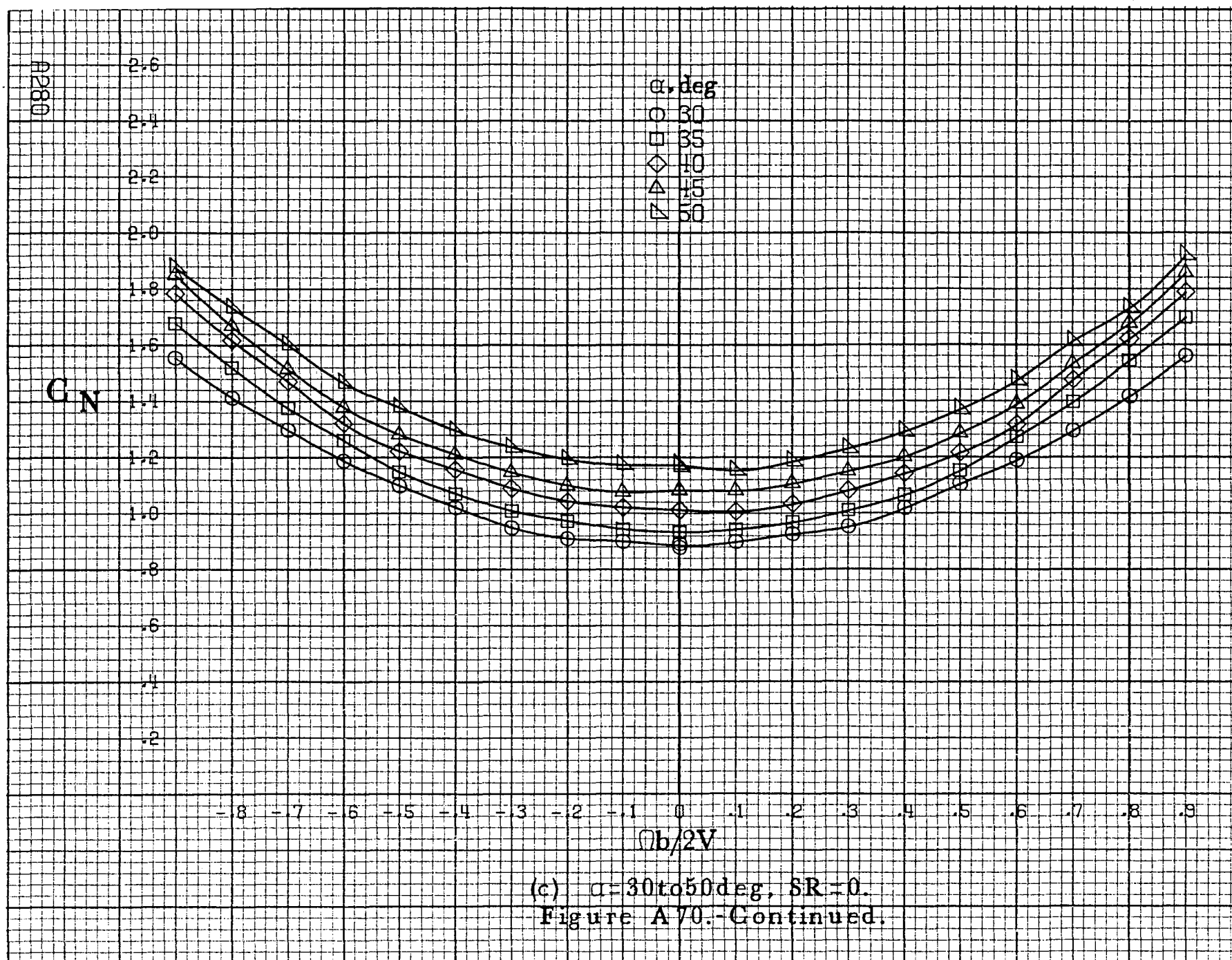


(a) $\alpha = 8 \text{ to } 16^\circ$, $SR = 91.4 \text{ cm (36 in)}$.

Figure A70 - Effect of rotation rate and angle of attack on normal-force coefficient for long body, high wing, vertical configuration. $\delta_c = 0^\circ$, $\delta_a = 0^\circ$, $\delta_r = 0^\circ$, $\beta = 0^\circ$.



(b) $\alpha=18$ to 35 deg, $SR=91.4$ cm (36 in).
Figure A70.-Continued.



C_N

α, deg

- 55
- 60
- ◇ 70
- △ 80
- ▽ 90

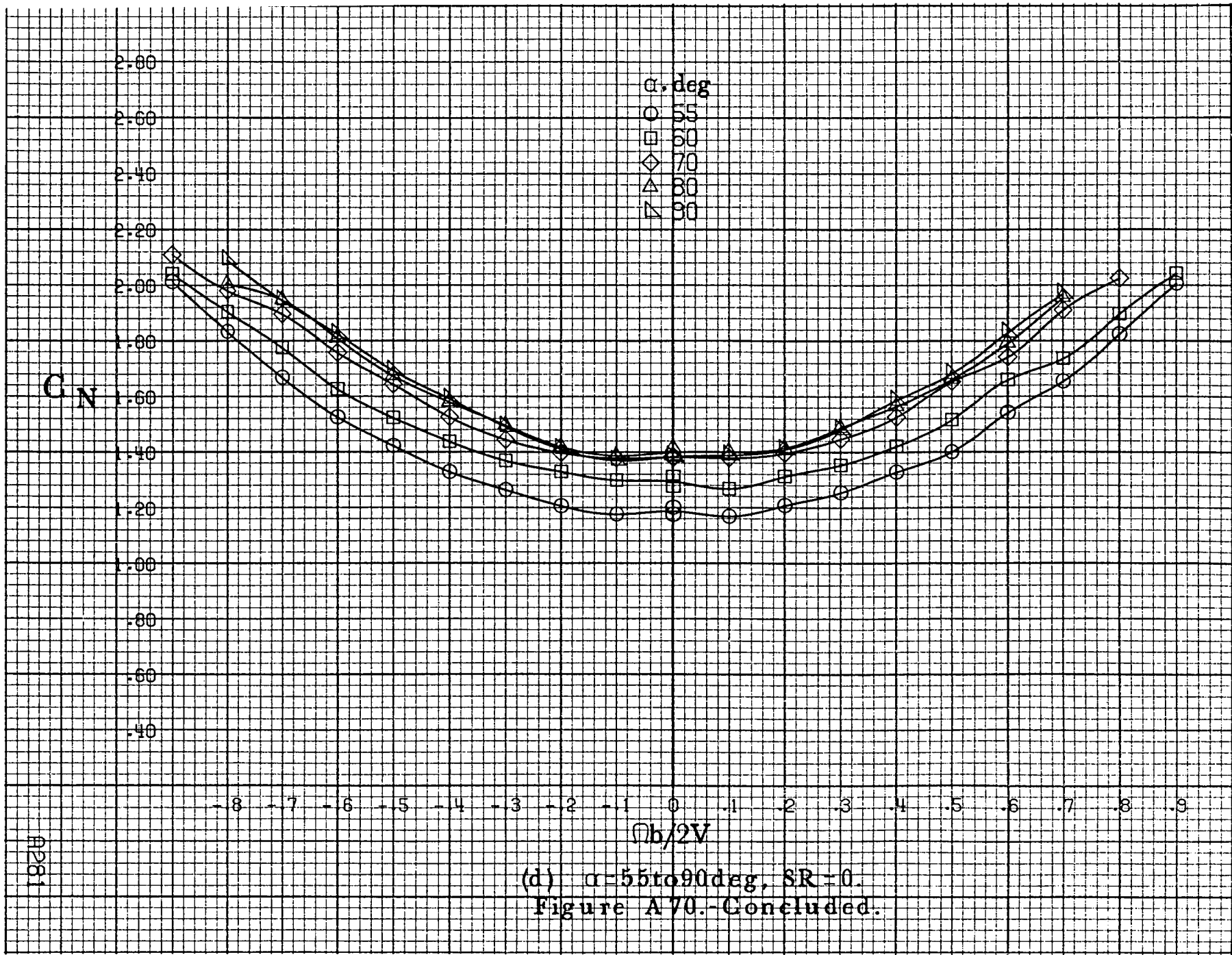
2.80
2.60
2.40
2.20
2.00
1.80
1.60
1.40
1.20
1.00
.80
.60
.40

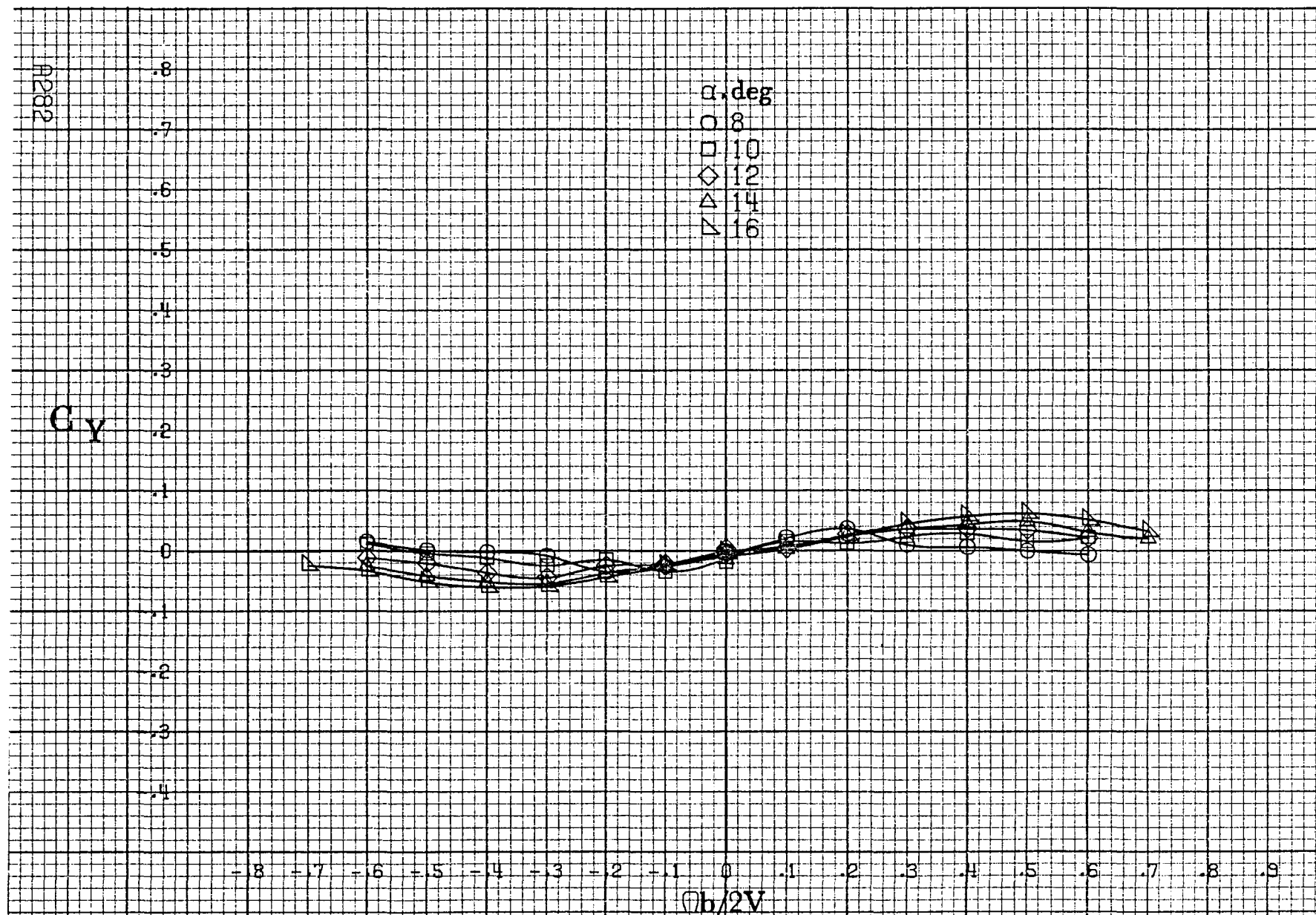
-.8 -.7 -.6 -.5 -.4 -.3 -.2 -.1 0 .1 .2 .3 .4 .5 .6 .7 .8 .9

$Ob/2V$

(d) $\alpha=55\text{to}90\text{deg}, SR=0.$
Figure A70.-Concluded.

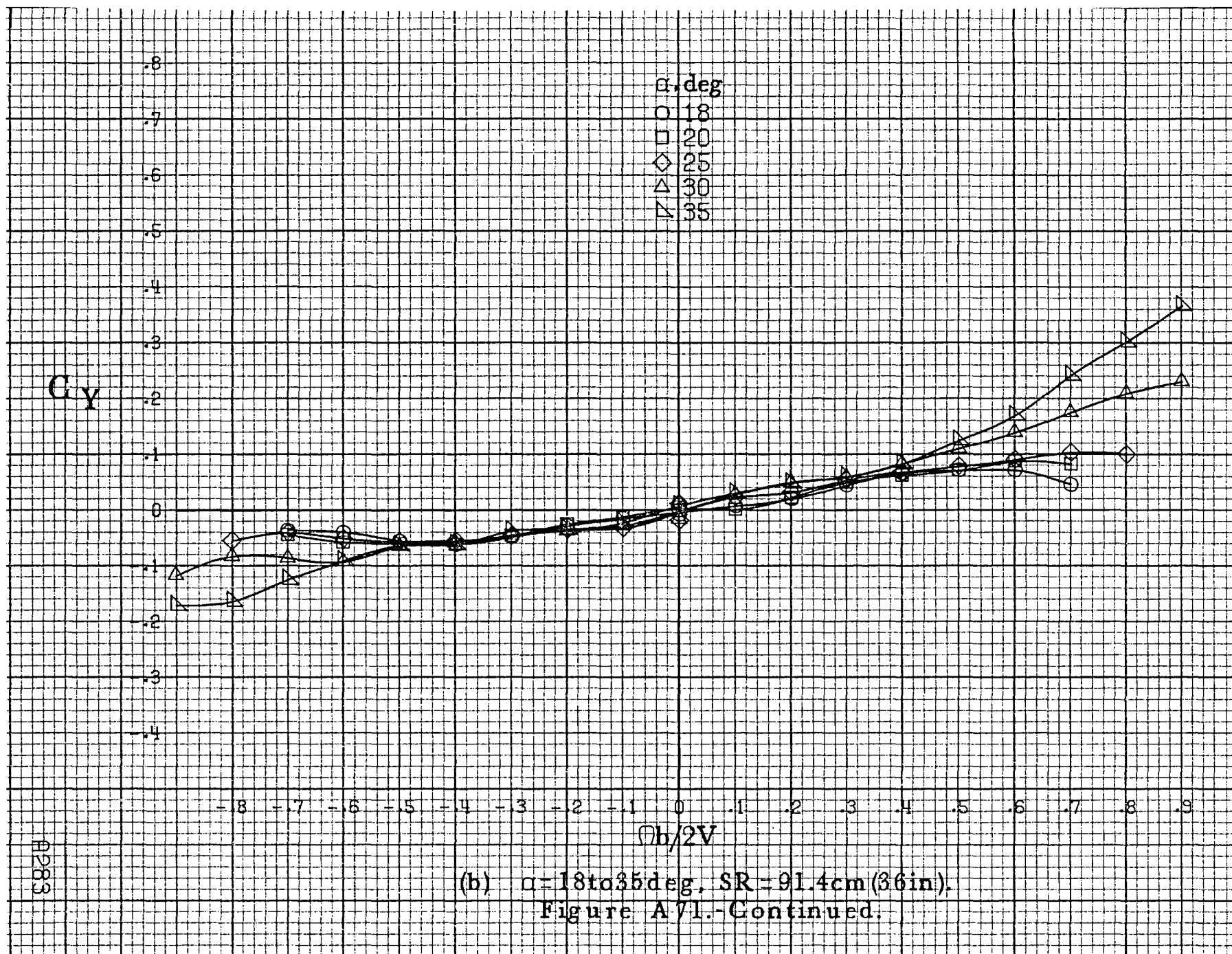
A281

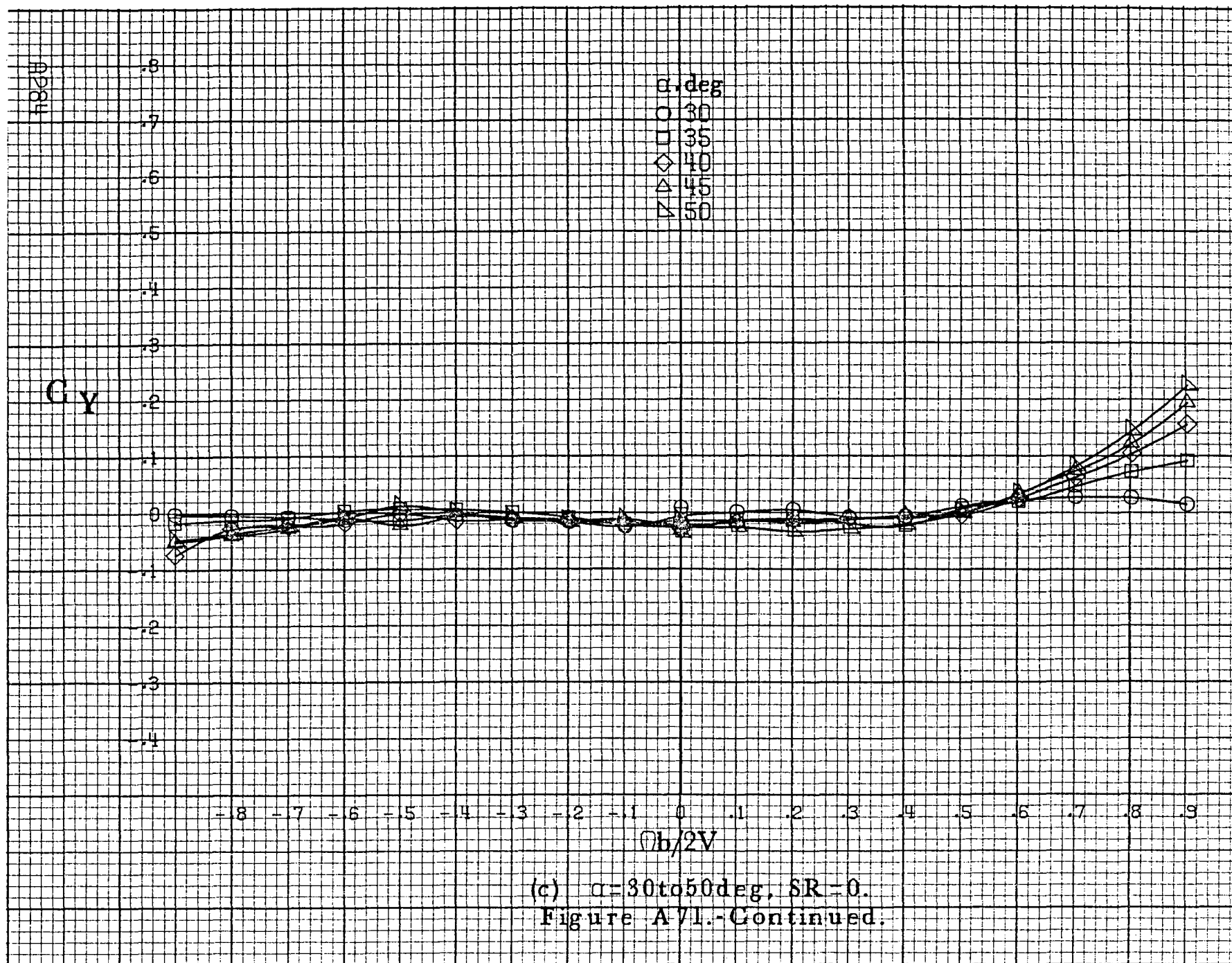


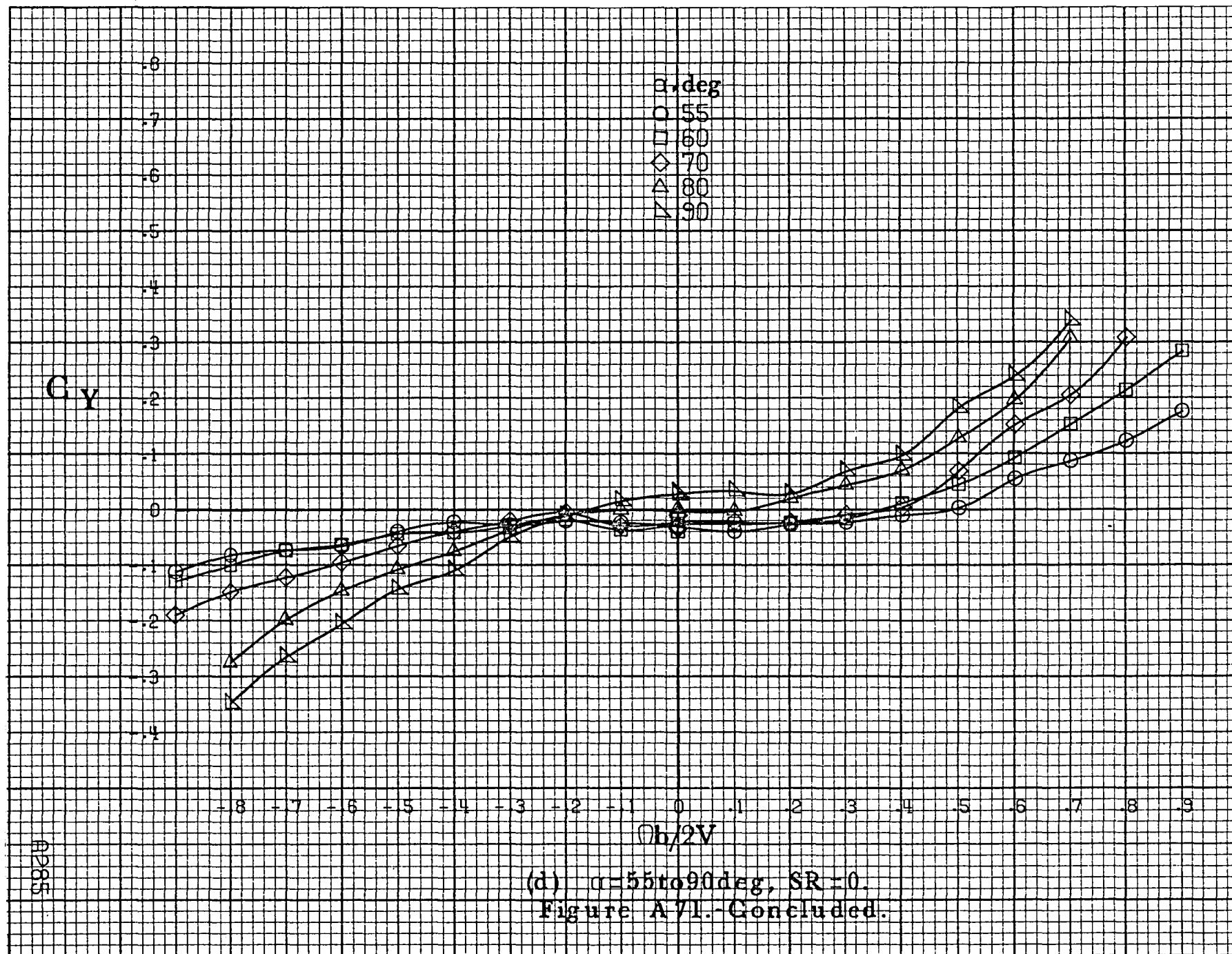


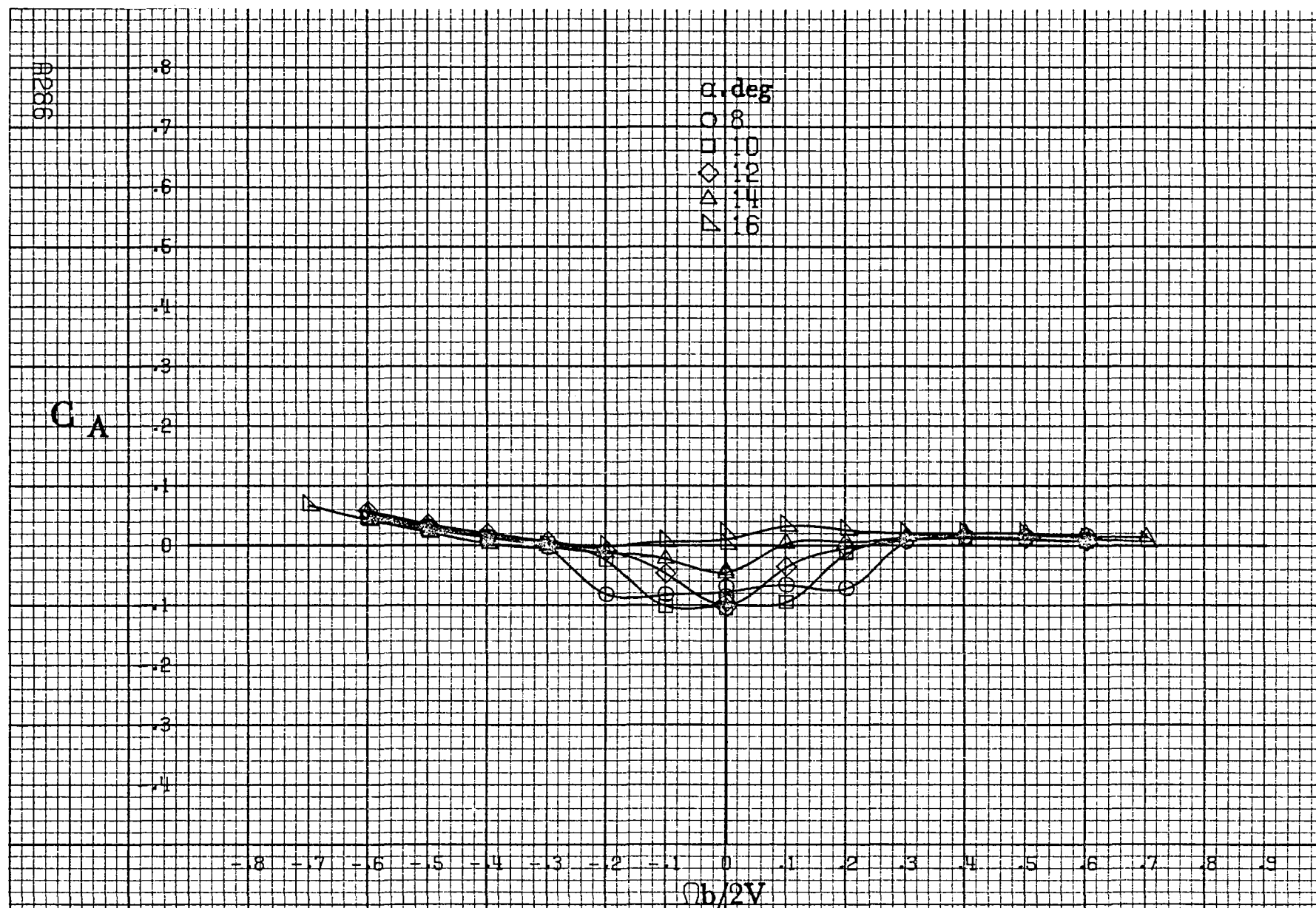
(a) $\alpha=8$ to 16° , $SR=91.4\text{cm}(36\text{in})$.

Figure A71.-Effect of rotation rate and angle of attack on side-force coefficient for long body, high wing, vertical configuration. $\delta_e=0^\circ$, $\delta_a=0^\circ$, $\delta_r=0^\circ$, $\beta=0^\circ$.



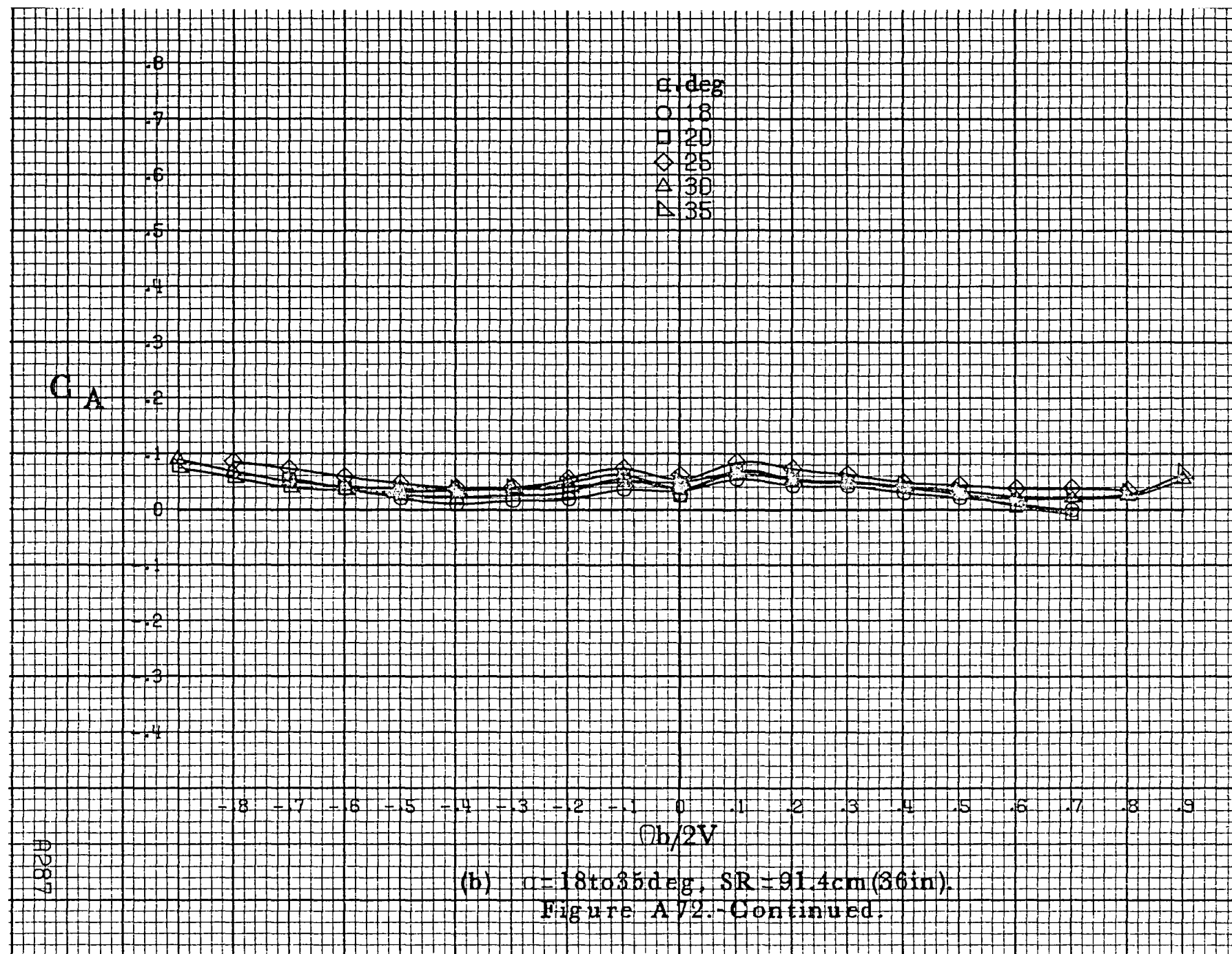




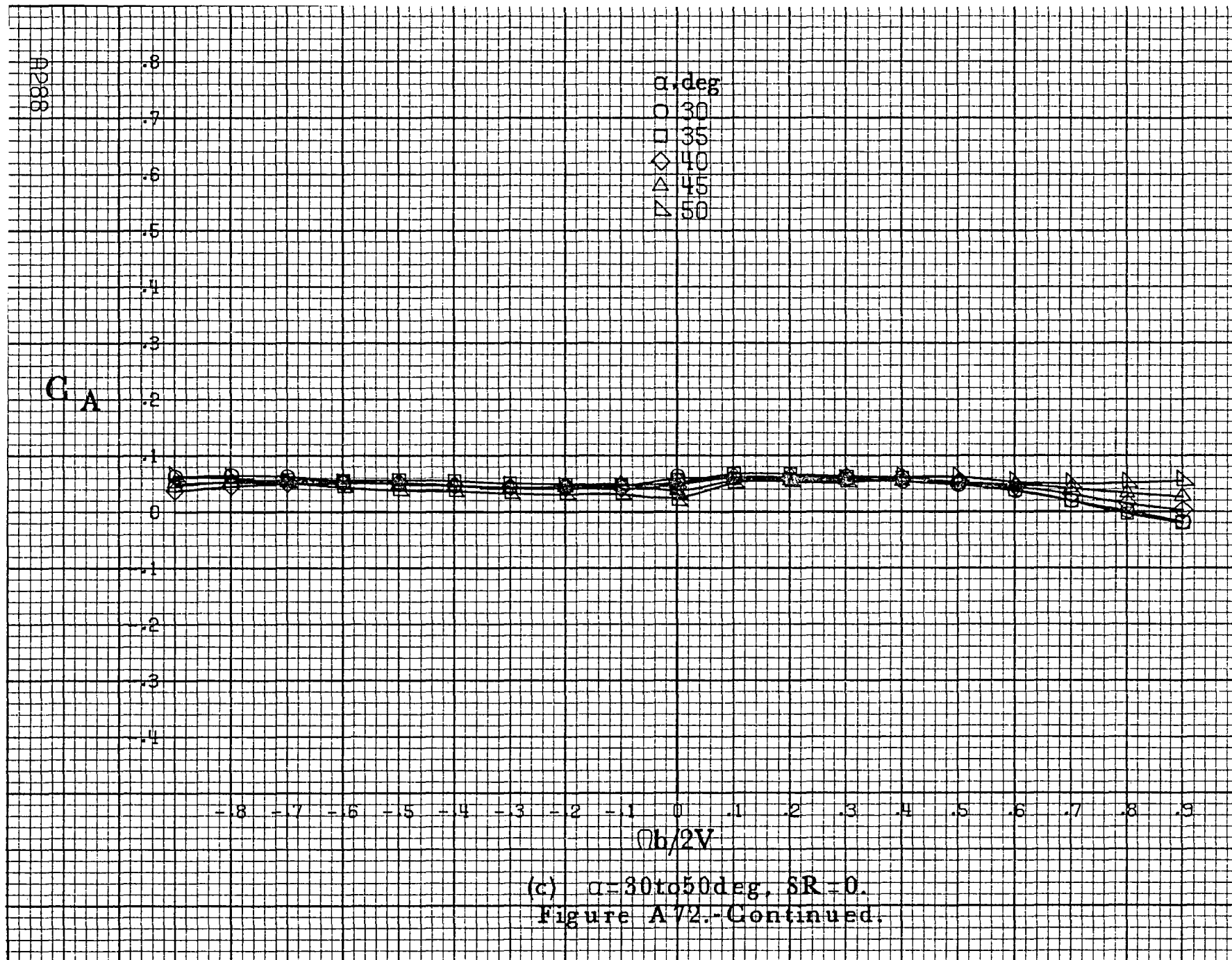


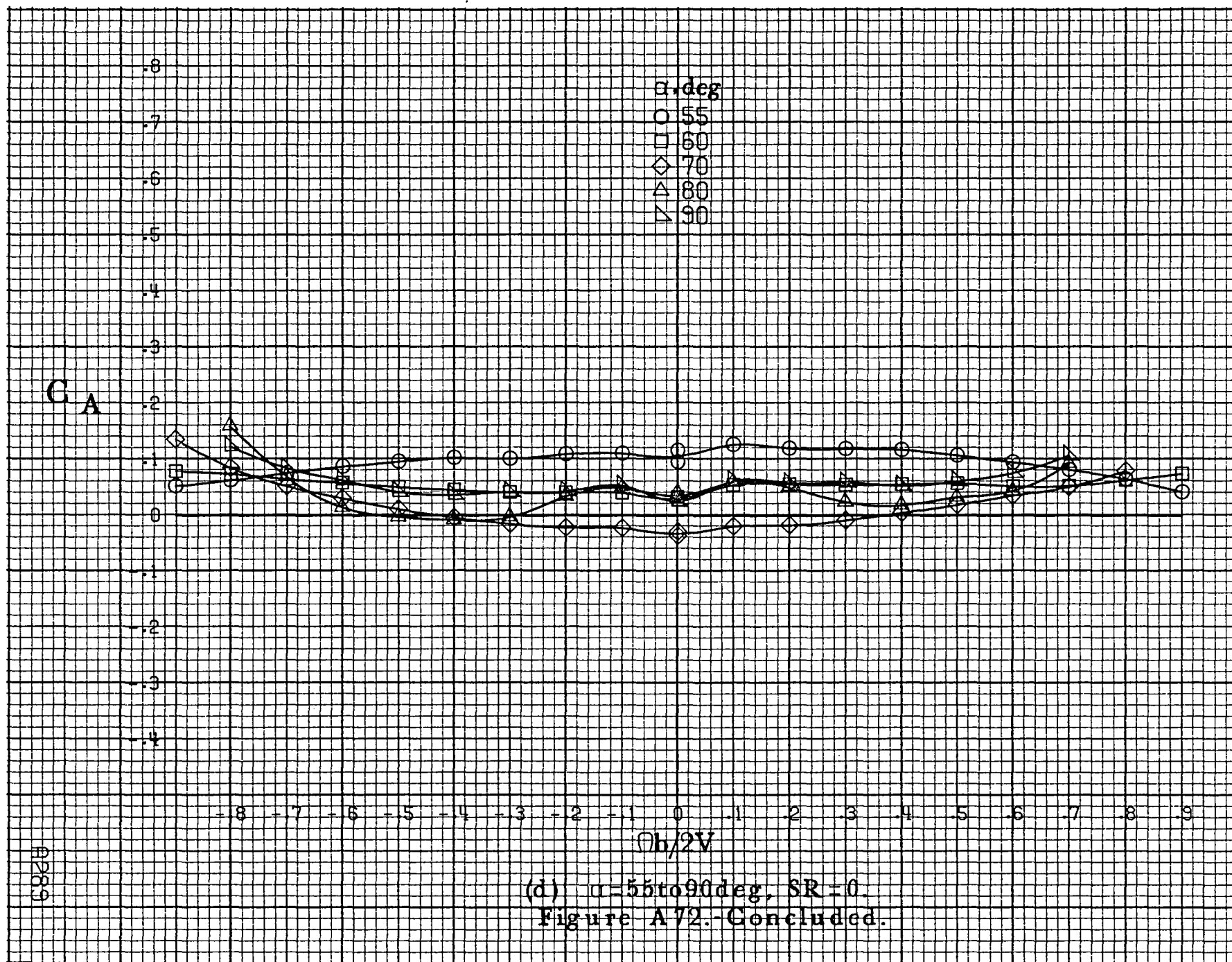
(a) $\alpha=8\text{ to }16^\circ$, $SR=91.4\text{ cm (36 in.)}$.

Figure A72.- Effect of rotation rate and angle of attack on axial-force coefficient for long body, high wing, vertical configuration. $\delta_r=0^\circ$, $\delta_a=0^\circ$, $\delta_r=0^\circ$, $\beta=0^\circ$.

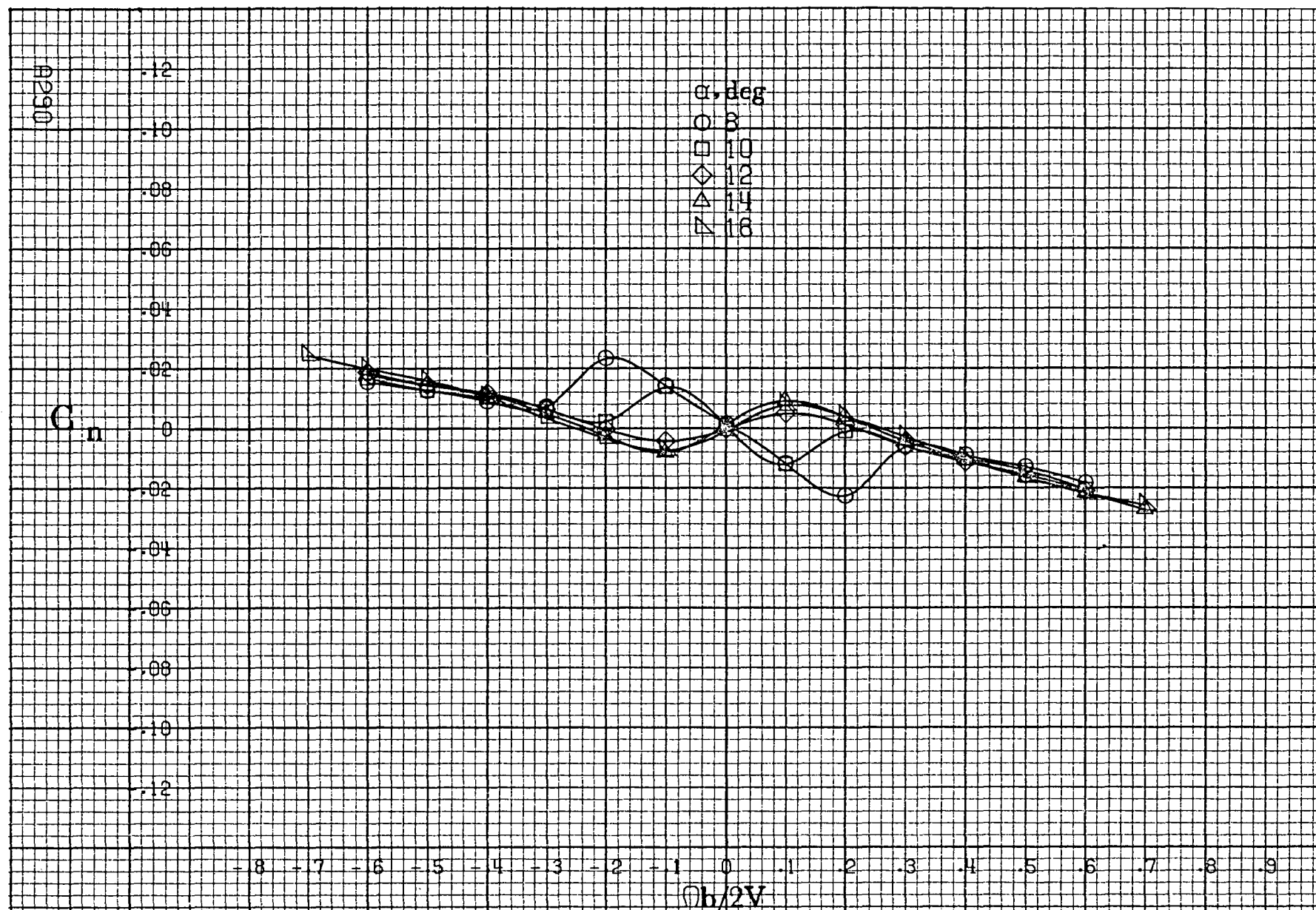


(b) $\alpha = 18$ to 35° , $SR = 91.4\text{cm (36in.)}$.
Figure A 72.-Continued.



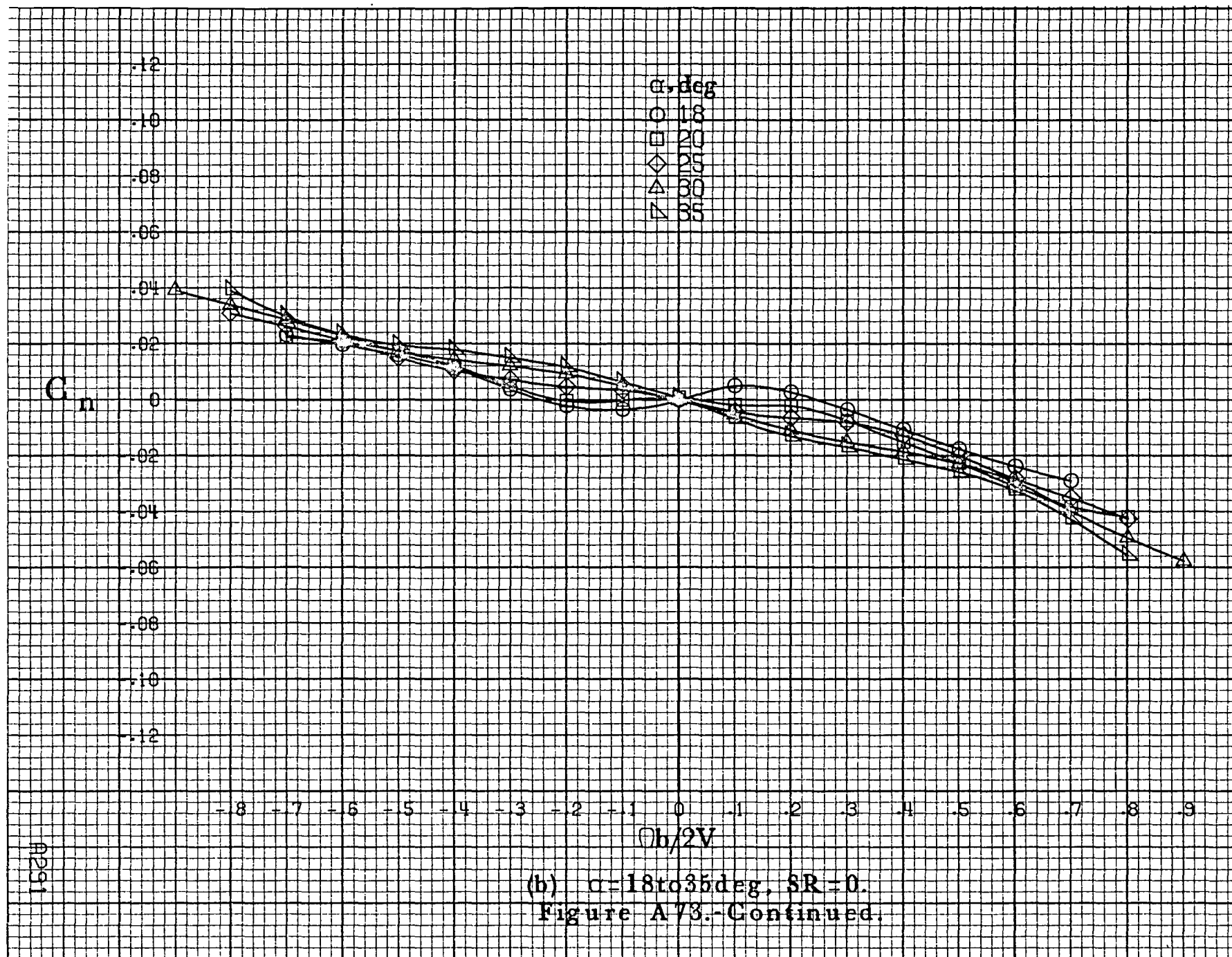


(d) $\alpha=55$ to 90 deg, $SR=0$.
Figure A72.-Concluded.



(a) $\alpha=8$ to 16° , $SR=91.4\text{cm}$ (36in).

Figure A73 - Effect of rotation rate and angle of attack on yawing-moment coefficient for complete long body, high wing configuration. $\delta_r=0^\circ$, $\delta_a=0^\circ$, $\delta_r=0^\circ$, $\beta=0^\circ$.



0292

C_n

α, deg

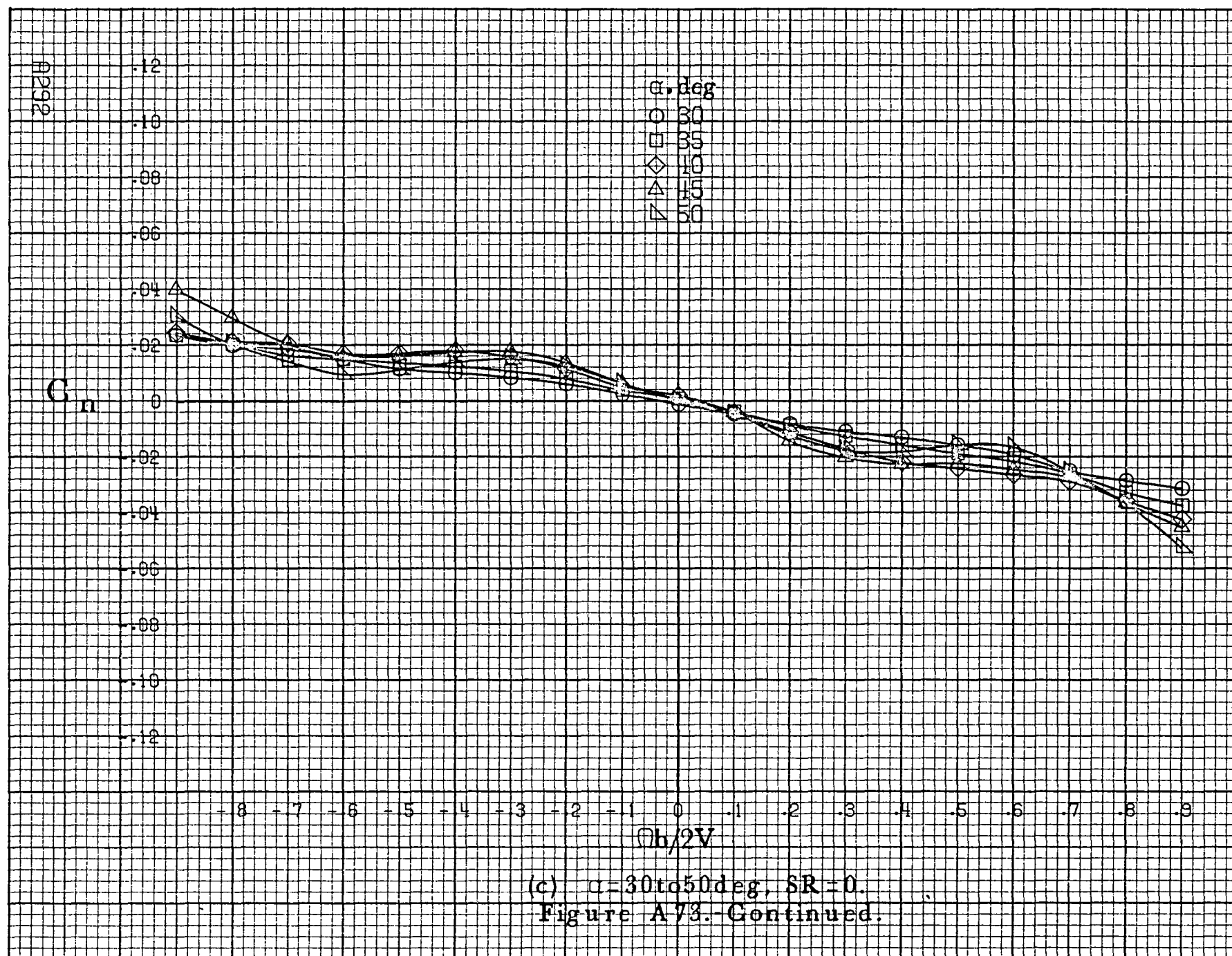
- 30
- 35
- ◇ 40
- △ 45
- ▽ 50

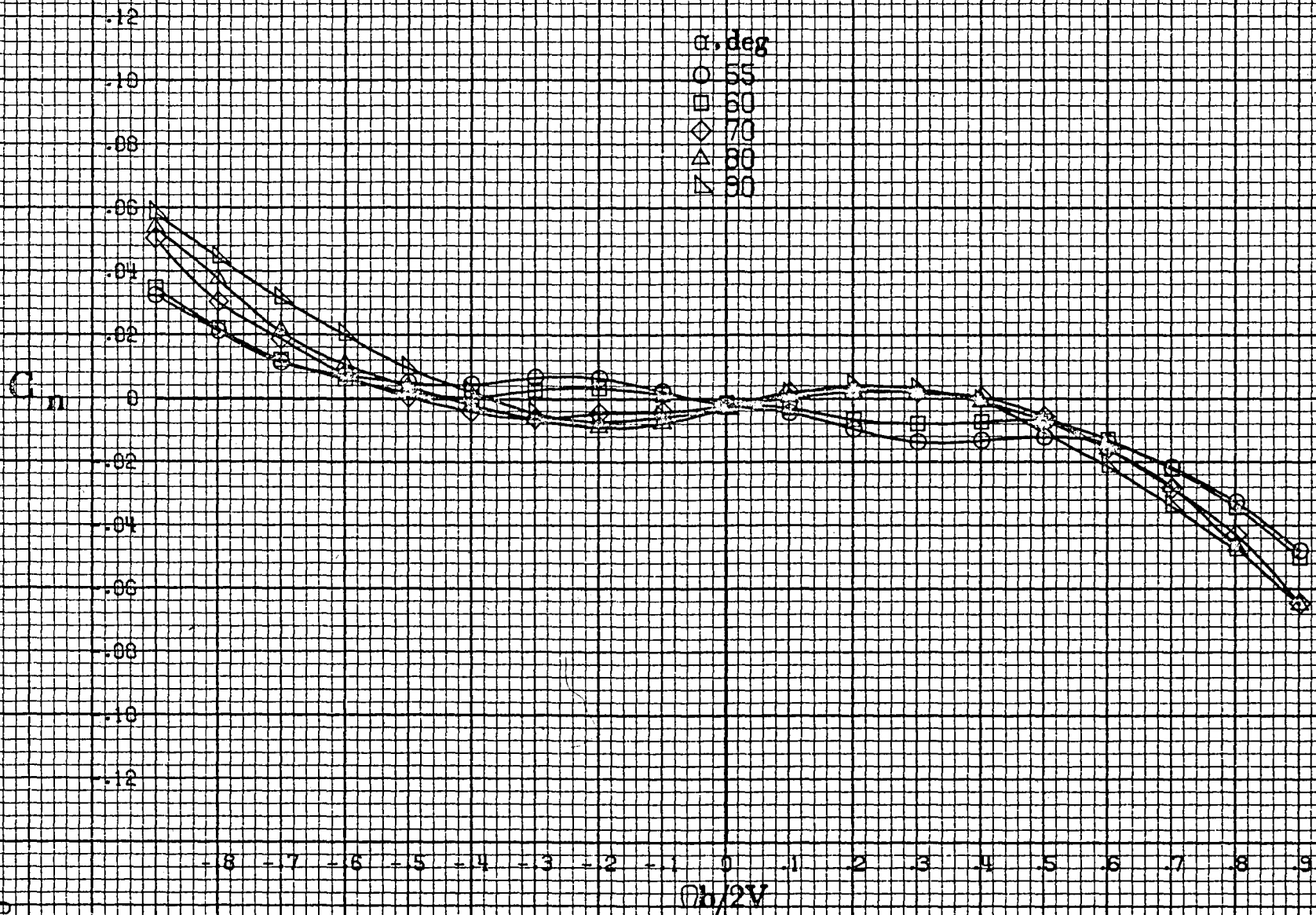
.12
.10
.08
.06
.04
.02
0
-.02
-.04
-.06
-.08
-.10
-.12

-8 -7 -6 -5 -4 -3 -2 -1 0 .1 .2 .3 .4 .5 .6 .7 .8 .9

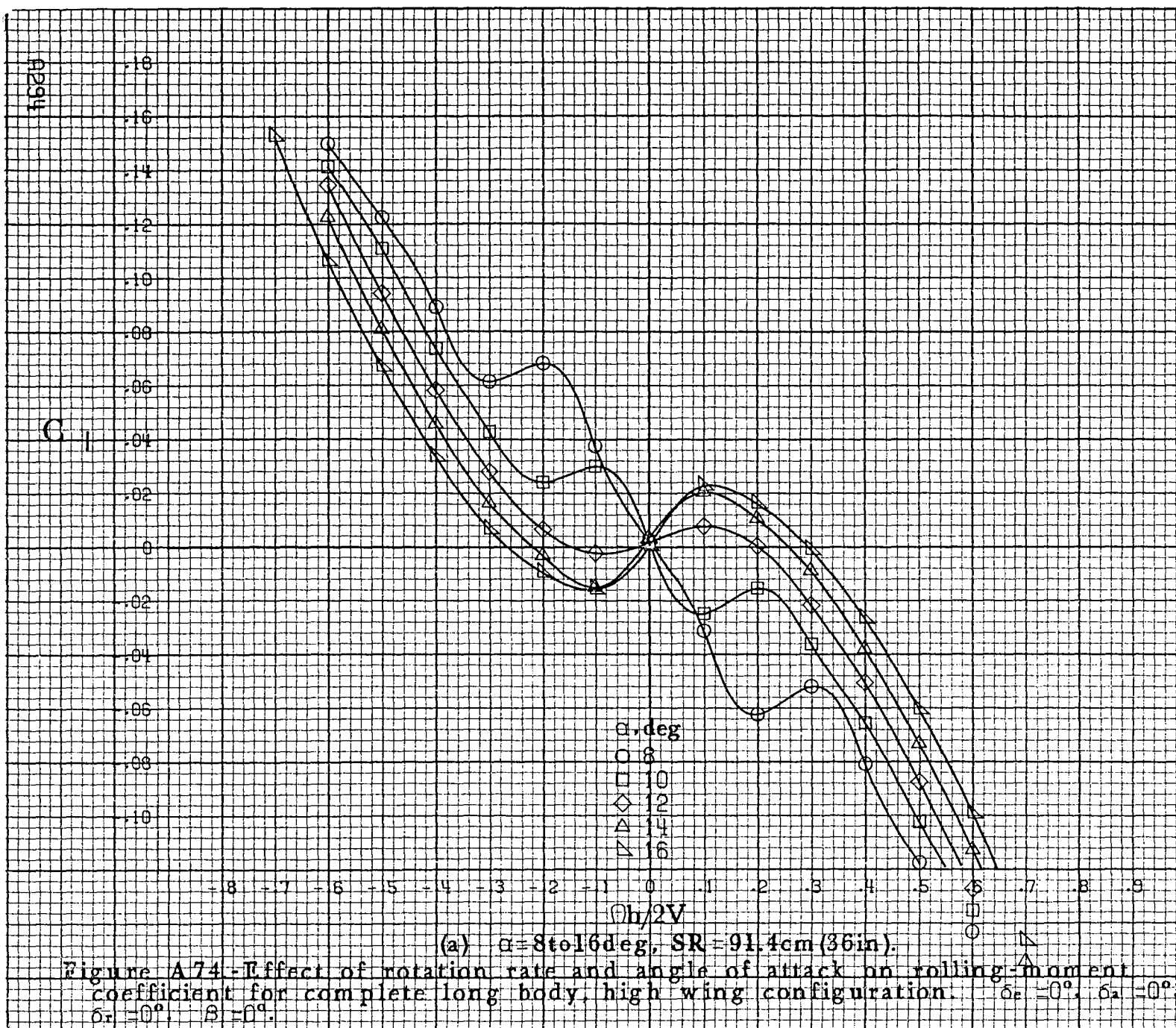
$b/2V$

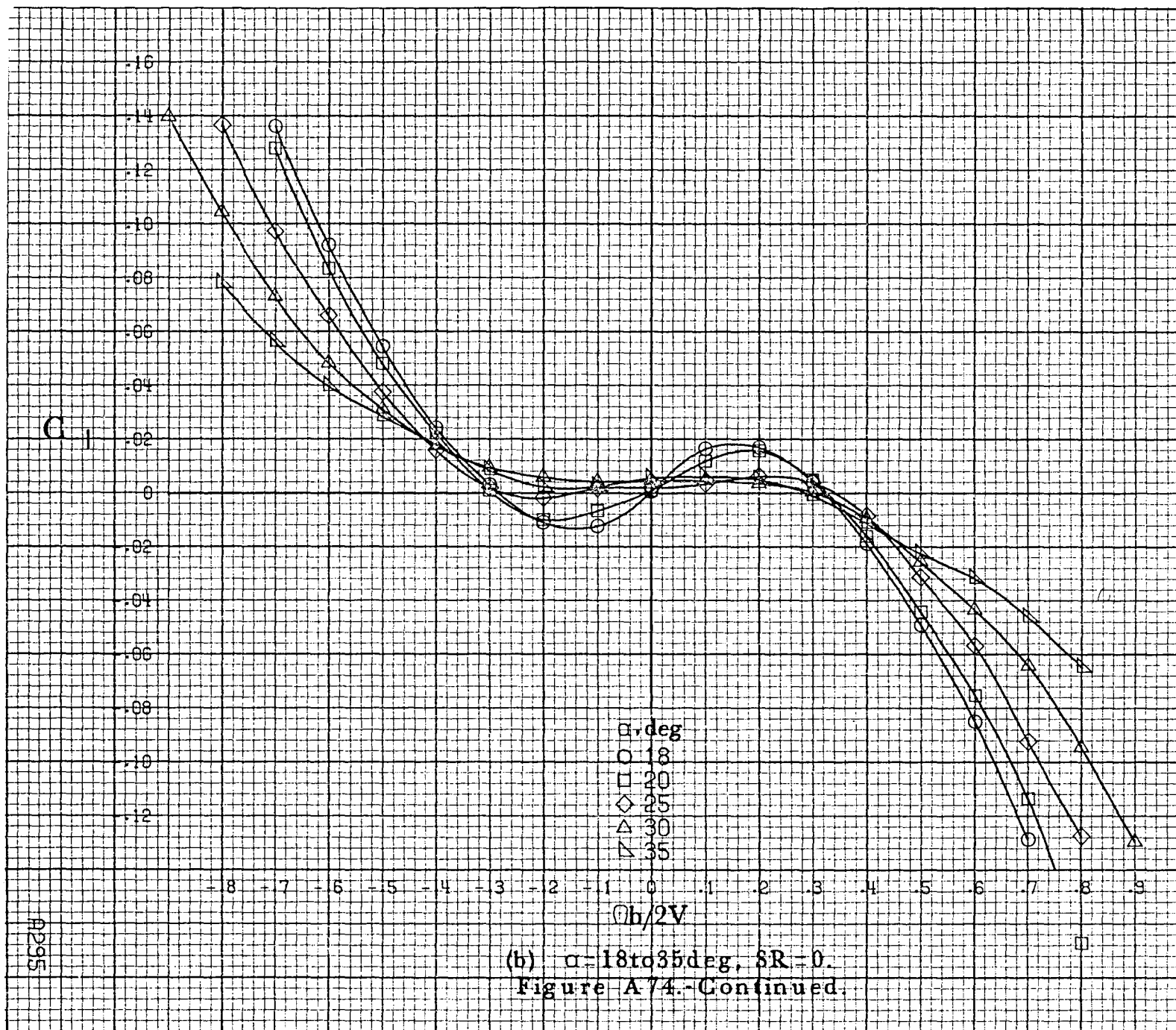
(c) $\alpha=30$ to 50 deg, $SR=0$.
Figure A73.-Continued.





(d) $\alpha = 55$ to 90° , $SR = 0$.
Figure A73.-Concluded.





A296

C

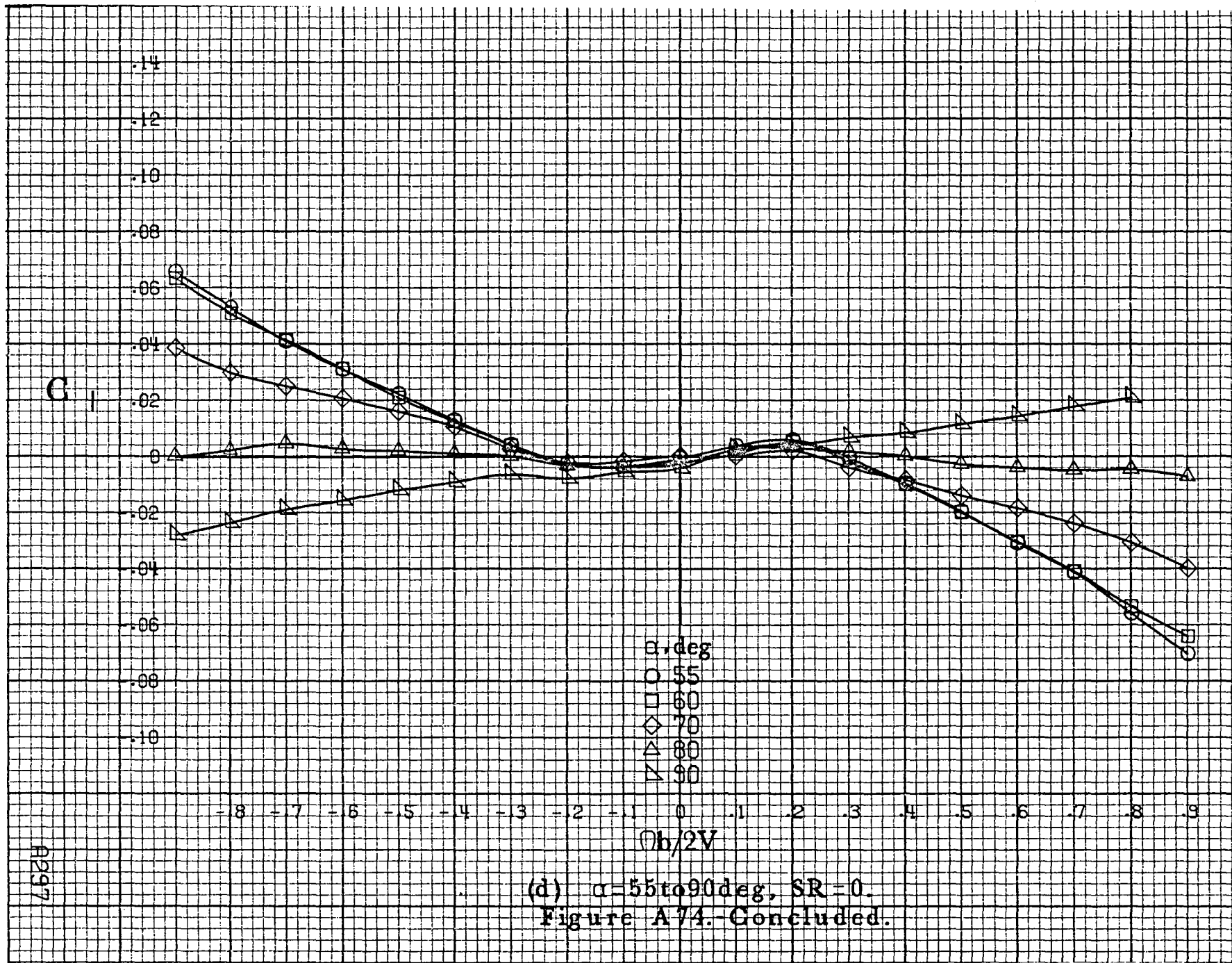
-18
-16
-14
-12
-10
-8
-6
-4
-2
0
-2
-4
-6
-8
-10

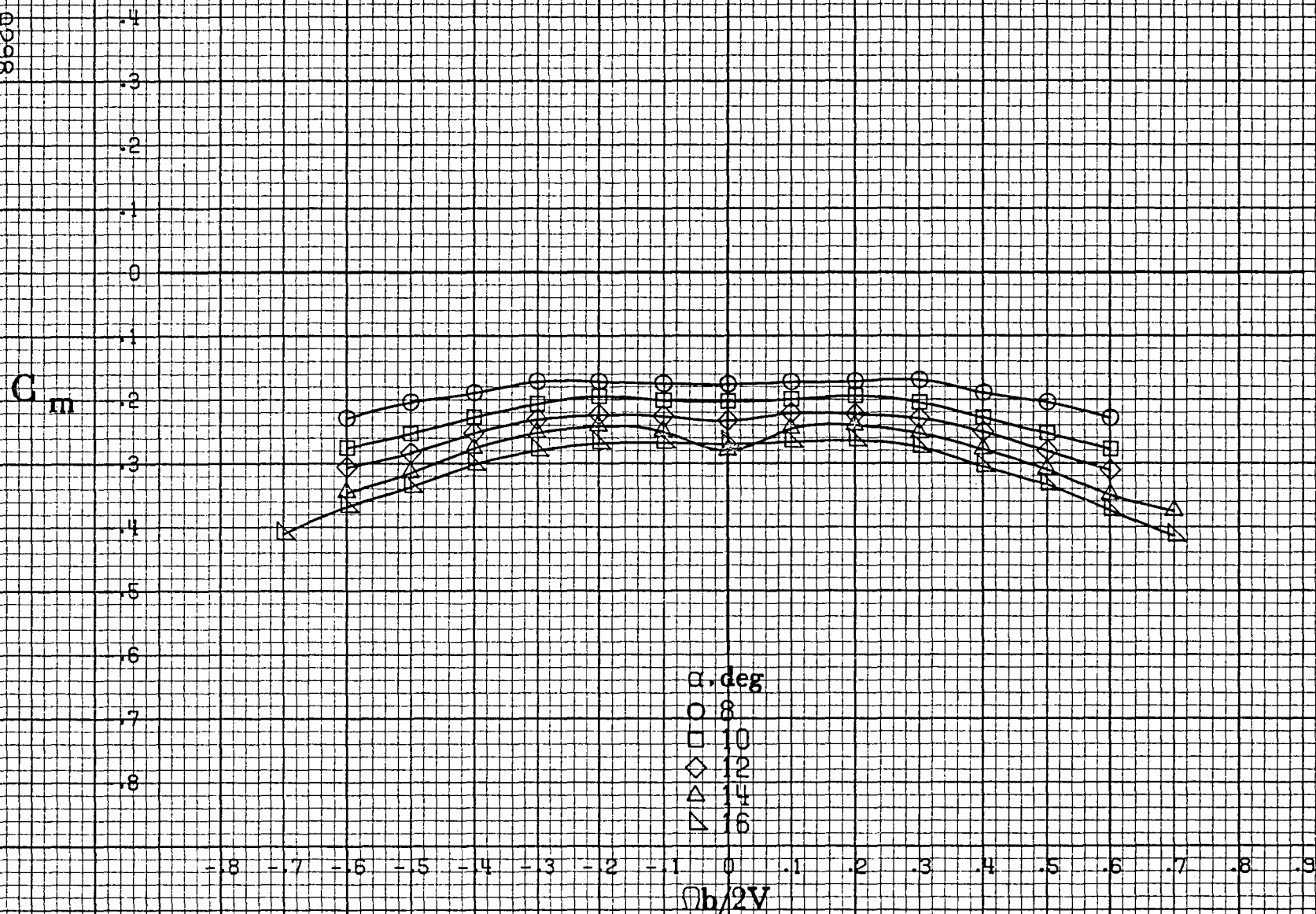
α, deg
○ 30
□ 35
◇ 40
△ 45
▽ 50

-8 -7 -6 -5 -4 -3 -2 -1 0 .1 .2 .3 .4 .5 .6 .7 .8 .9
 $\phi h/2V$

(a) $\alpha=30 \text{ to } 50 \text{ deg, } SR=0.$
Figure A74.-Continued.

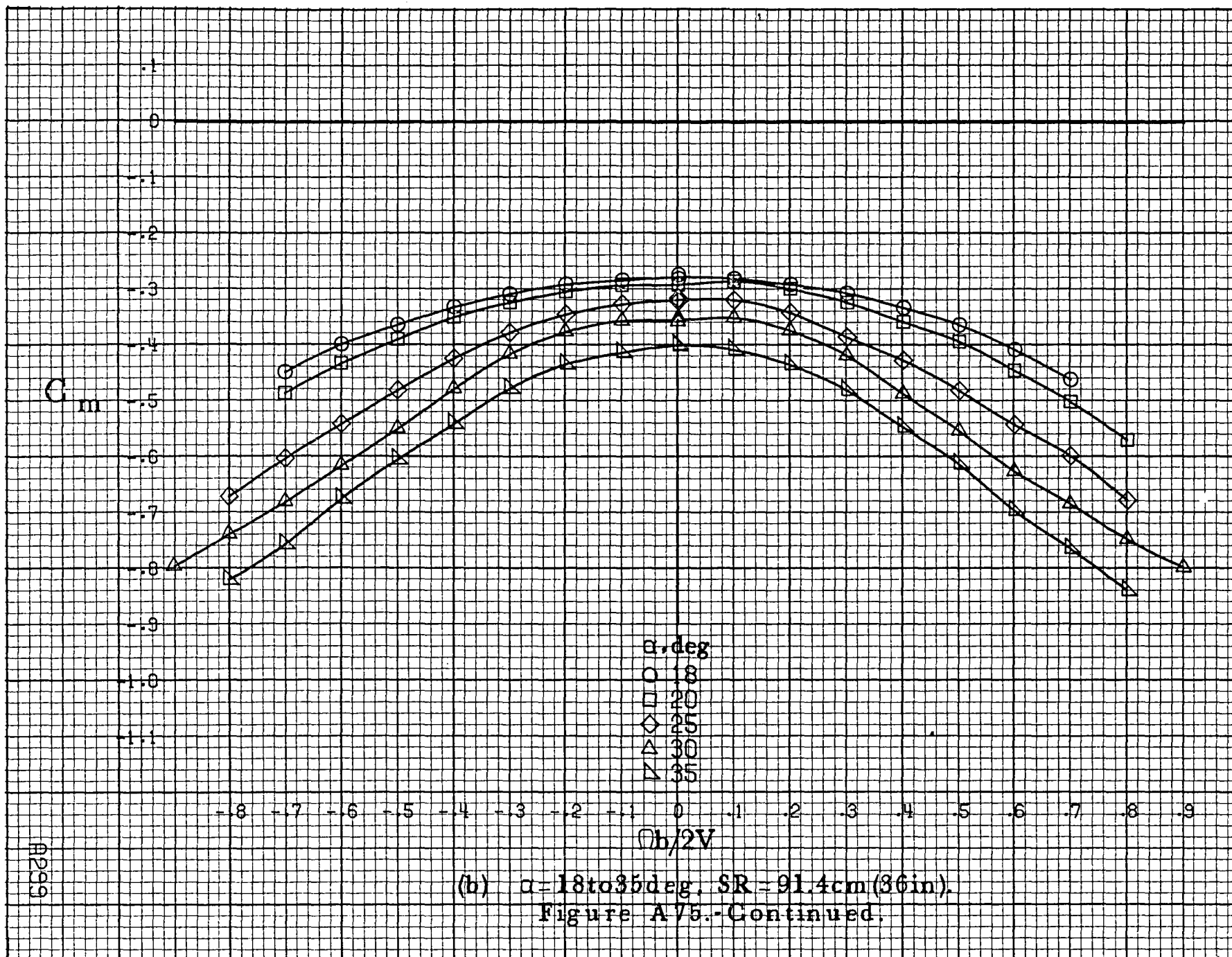
○

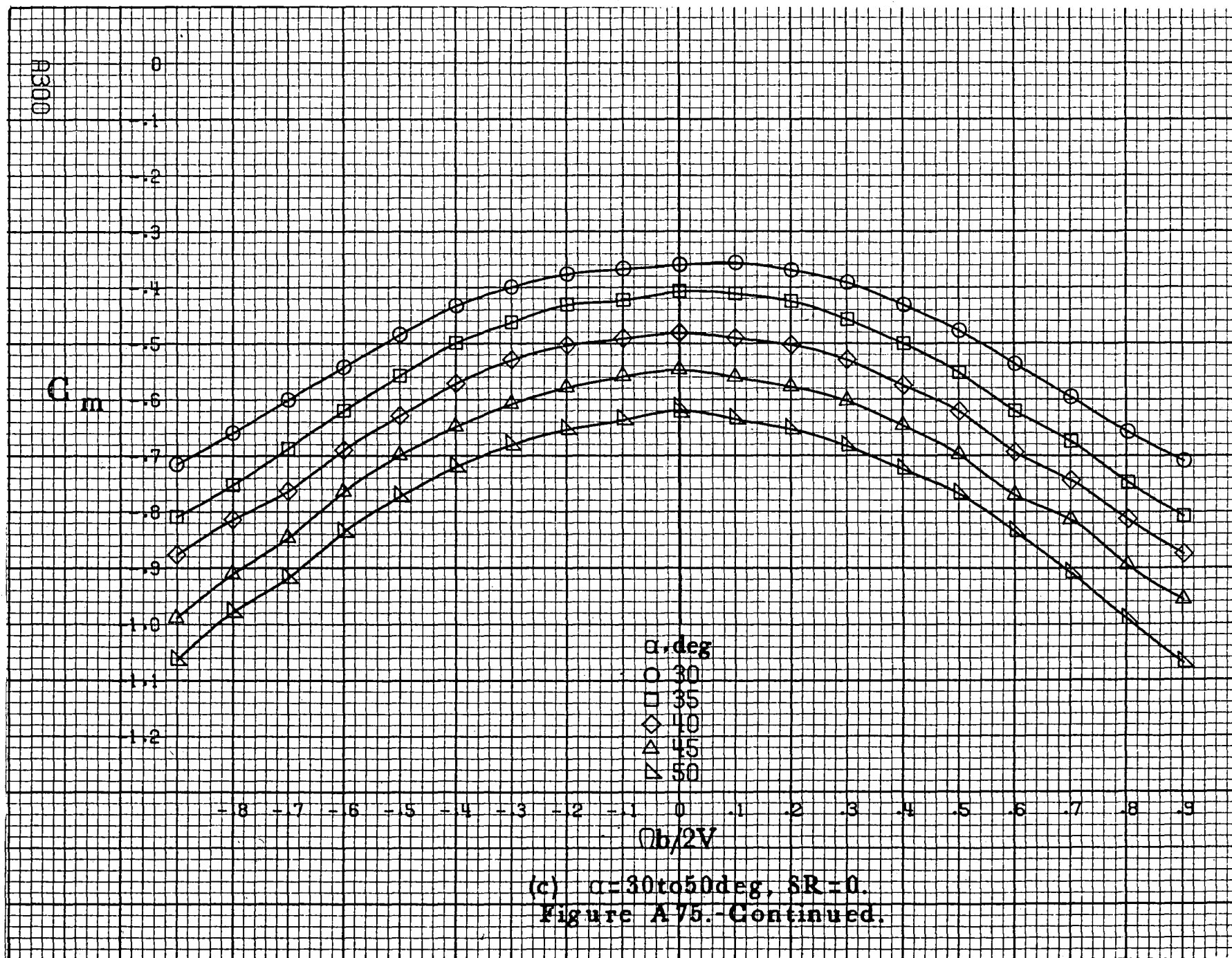


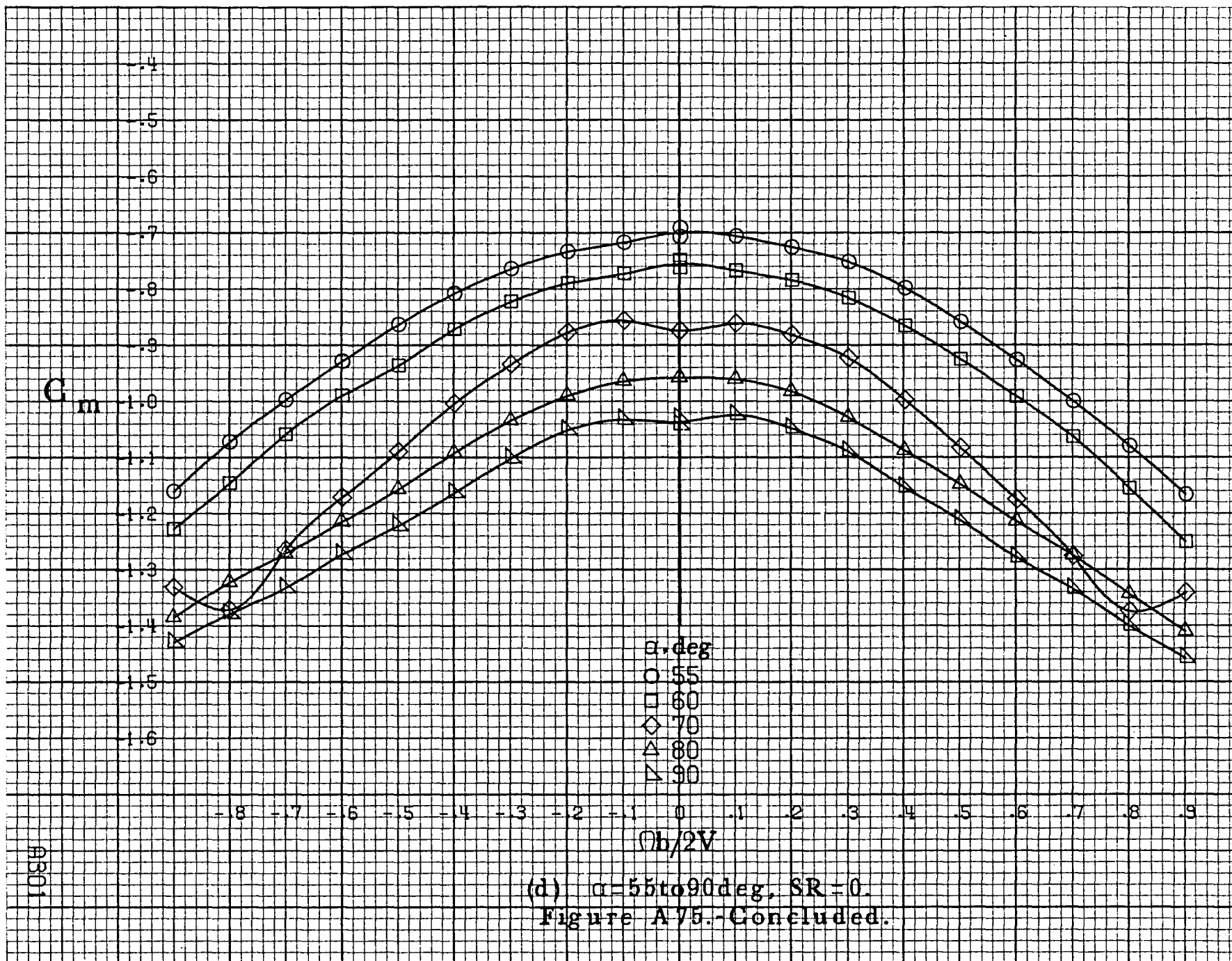


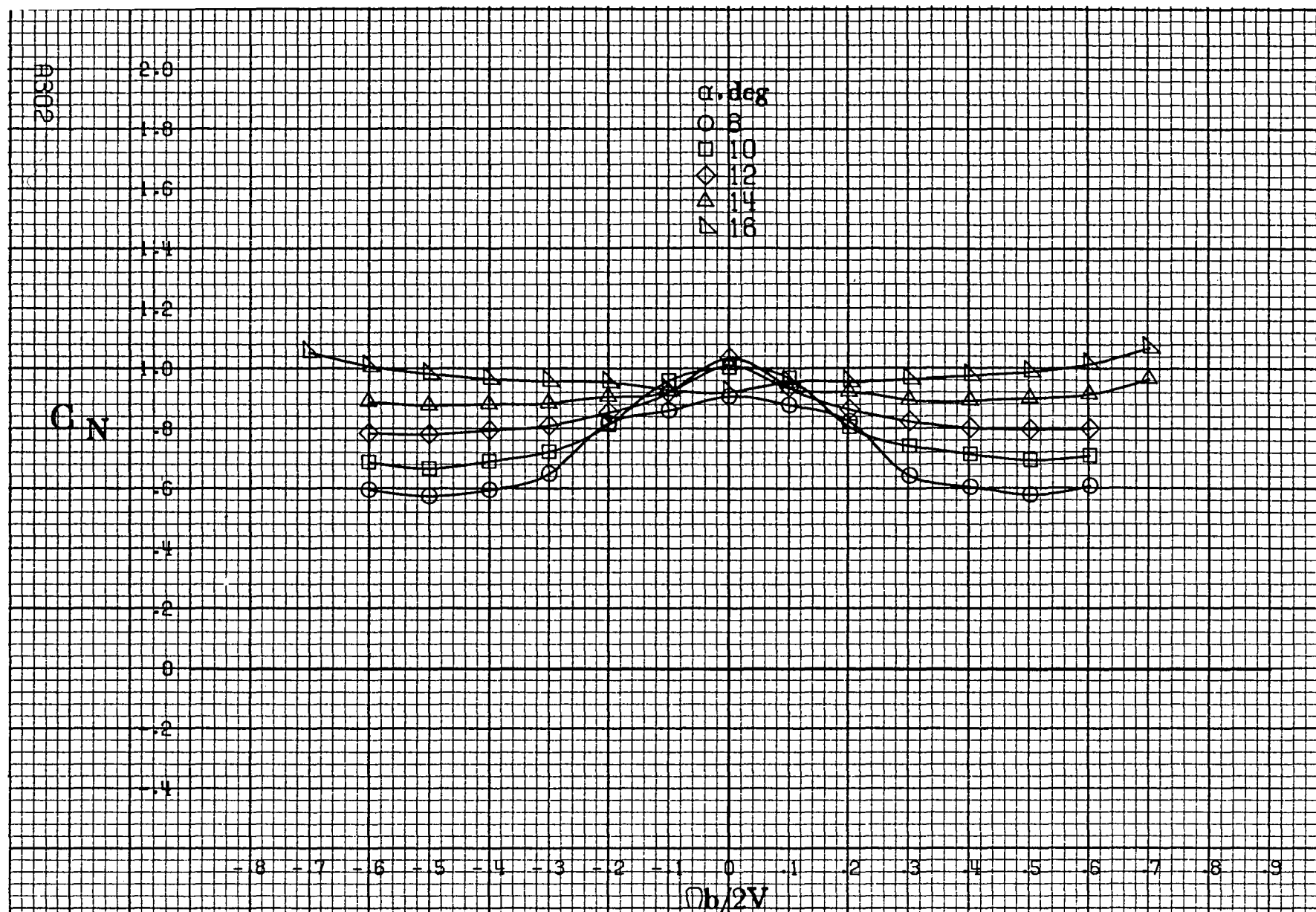
(a) $\alpha = 8$ to 16° , $SR = 91.4\text{cm (36in)}$.

Figure A75.-Effect of rotation rate and angle of attack on pitching-moment coefficient for complete long body, high wing configuration. $\delta_e = 0^\circ$, $\delta_a = 0^\circ$, $\delta_r = 0^\circ$, $\beta = 0^\circ$.



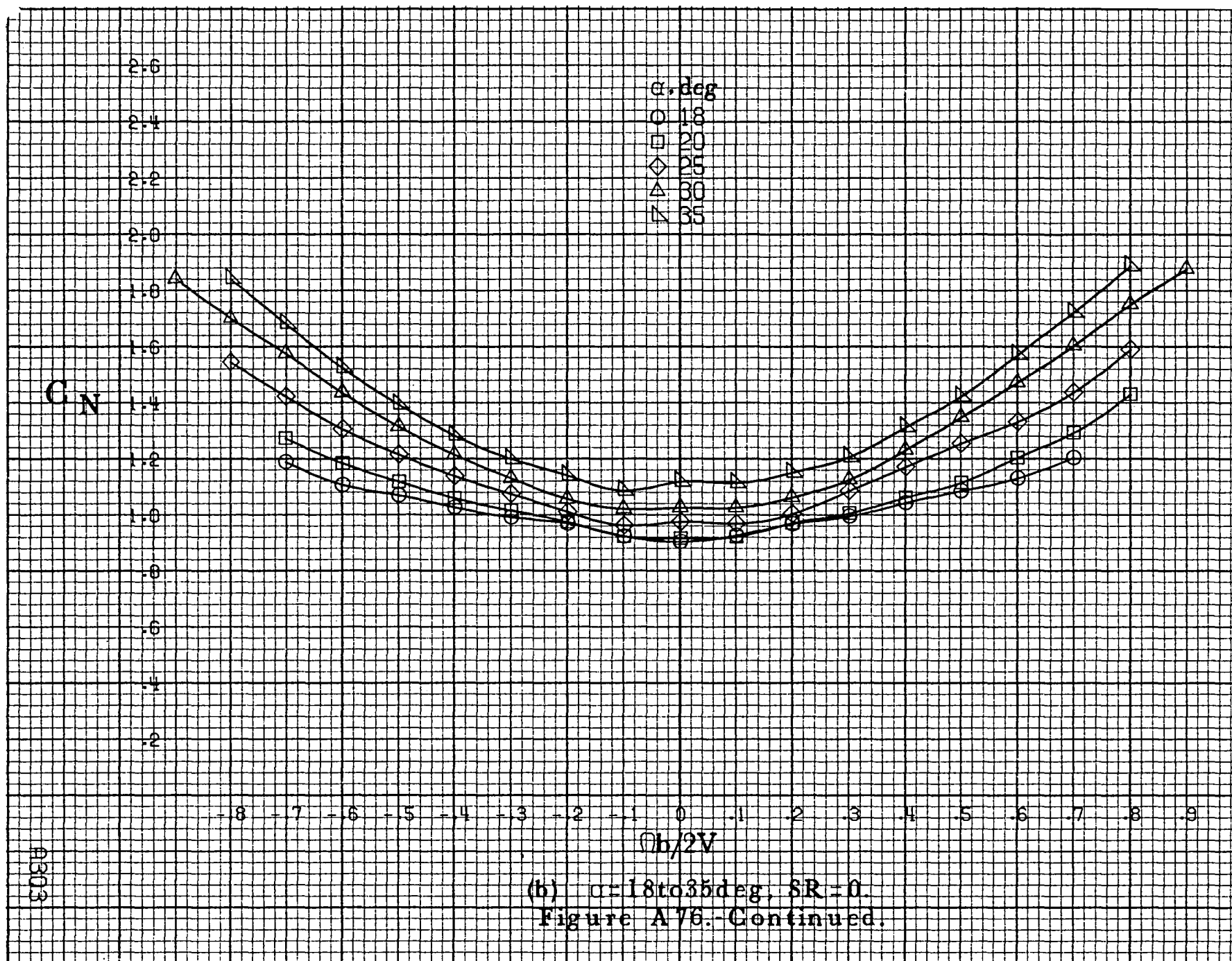




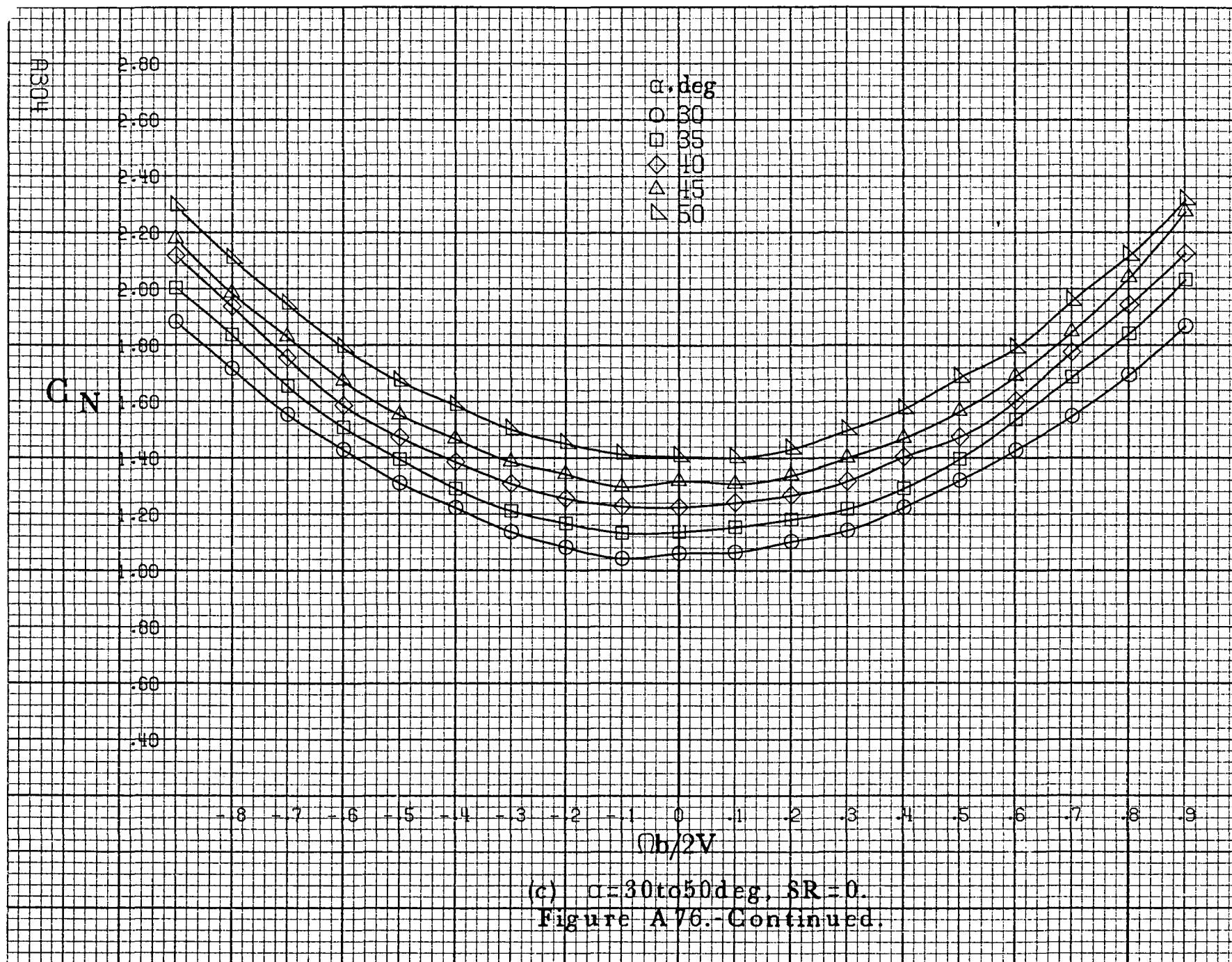


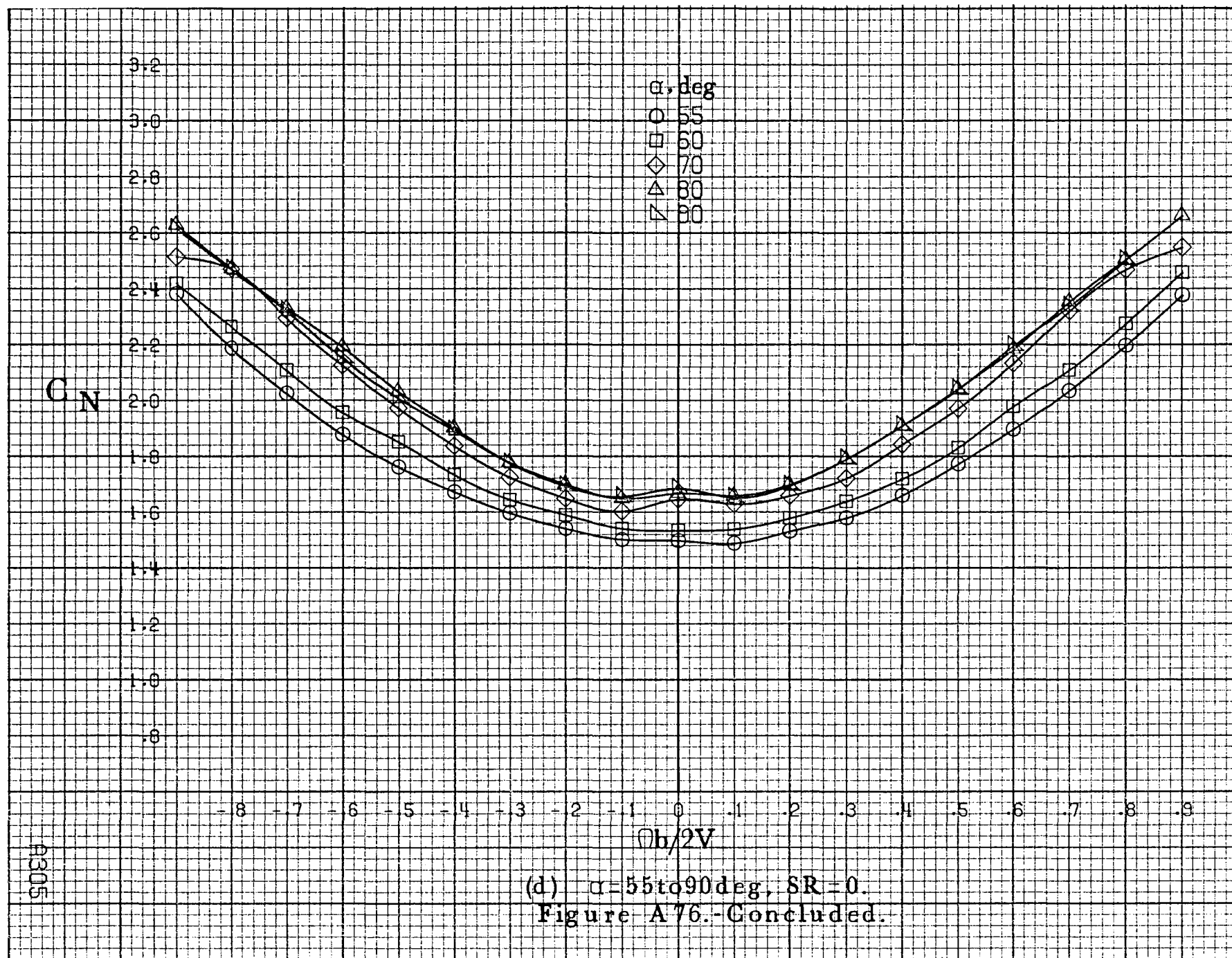
(a) $\alpha = 8$ to 16° , $SR = 91.4 \text{ cm (36 in.)}$.

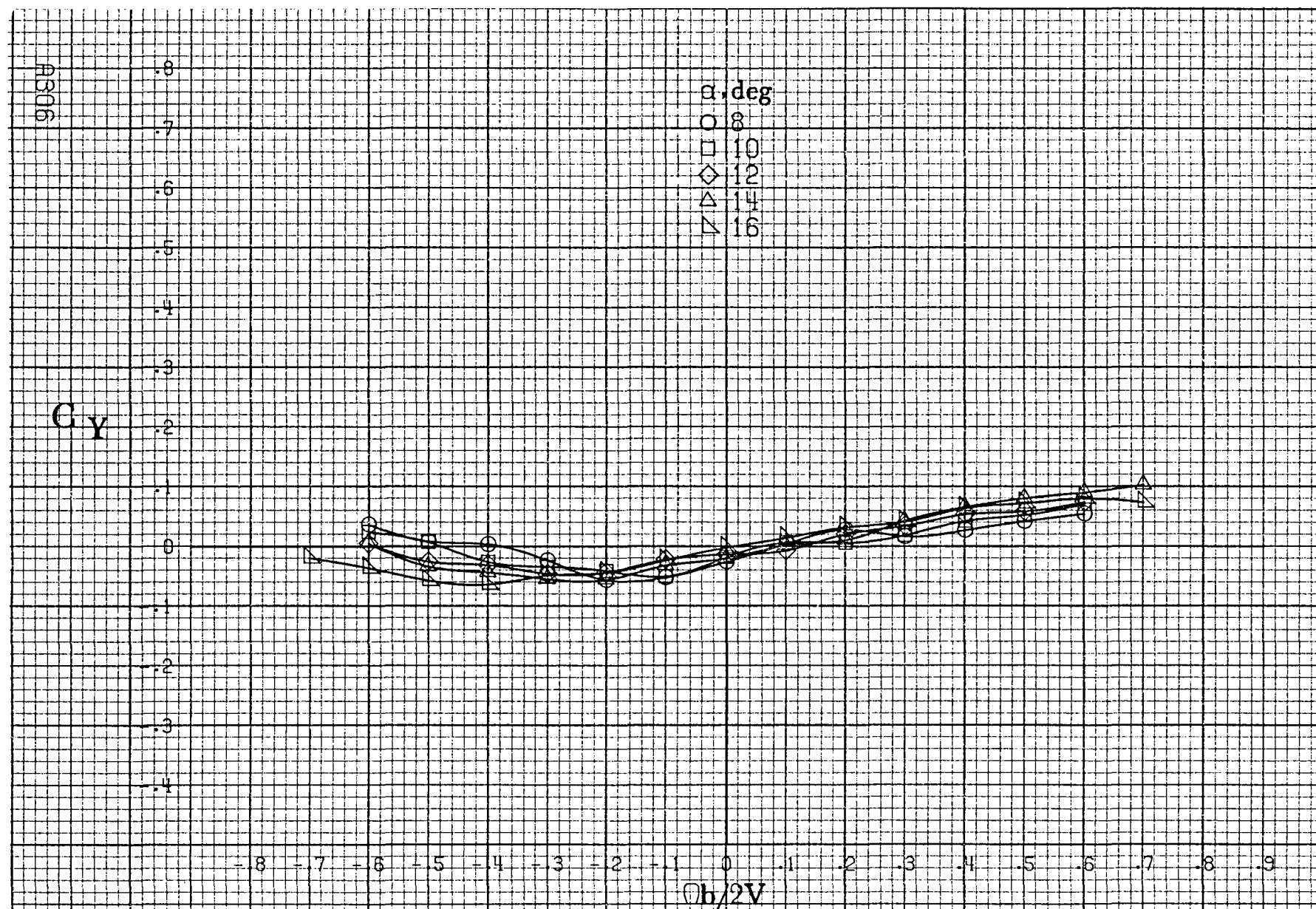
Figure A76 - Effect of rotation rate and angle of attack on normal-force coefficient for complete long body, high wing configuration. $\delta_e = 0^\circ$, $\delta_a = 0^\circ$, $\delta_r = 0^\circ$, $\beta = 0^\circ$.



(b) $\alpha=18$ to 35° , $SR=0$.
Figure A76.-Continued.

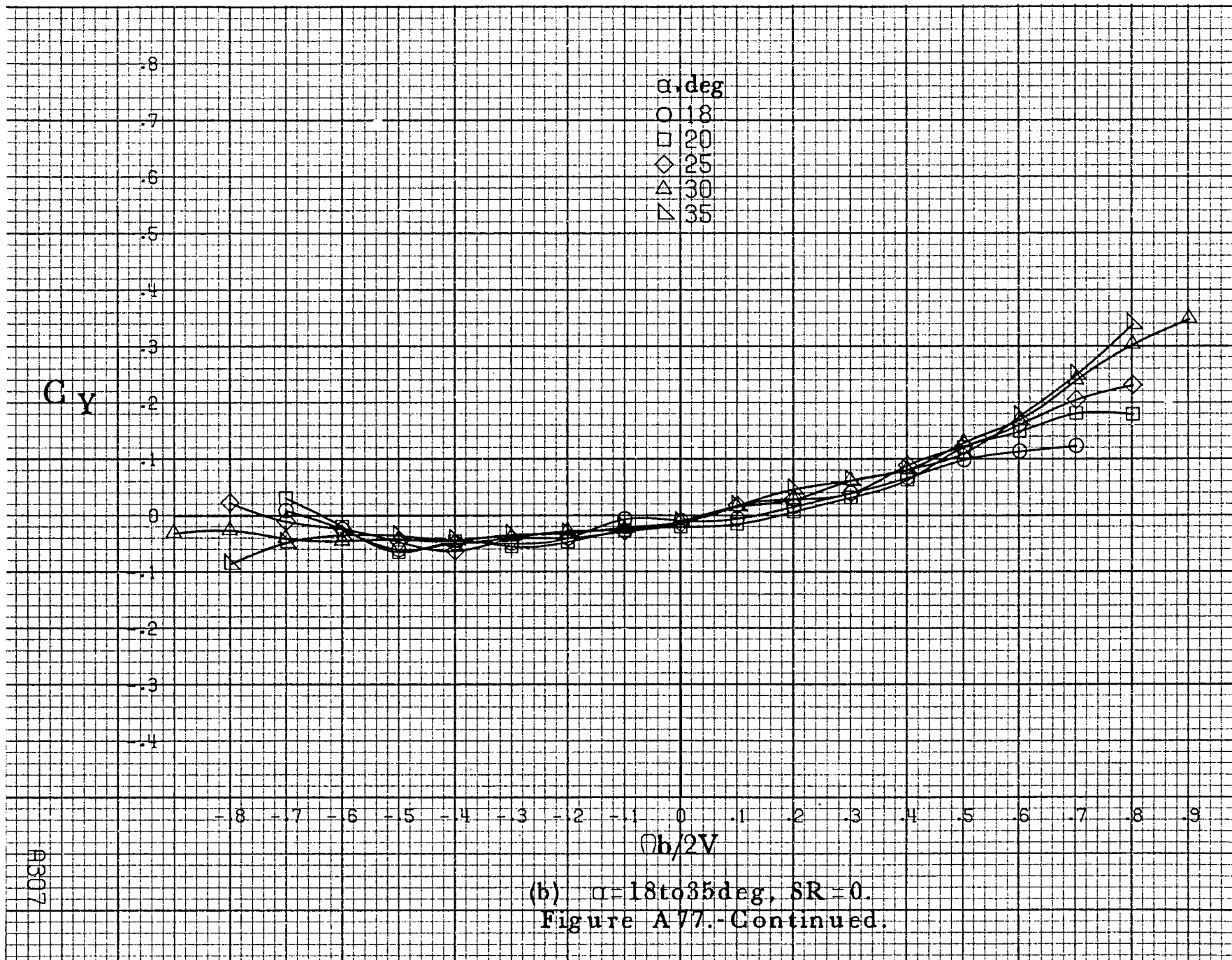


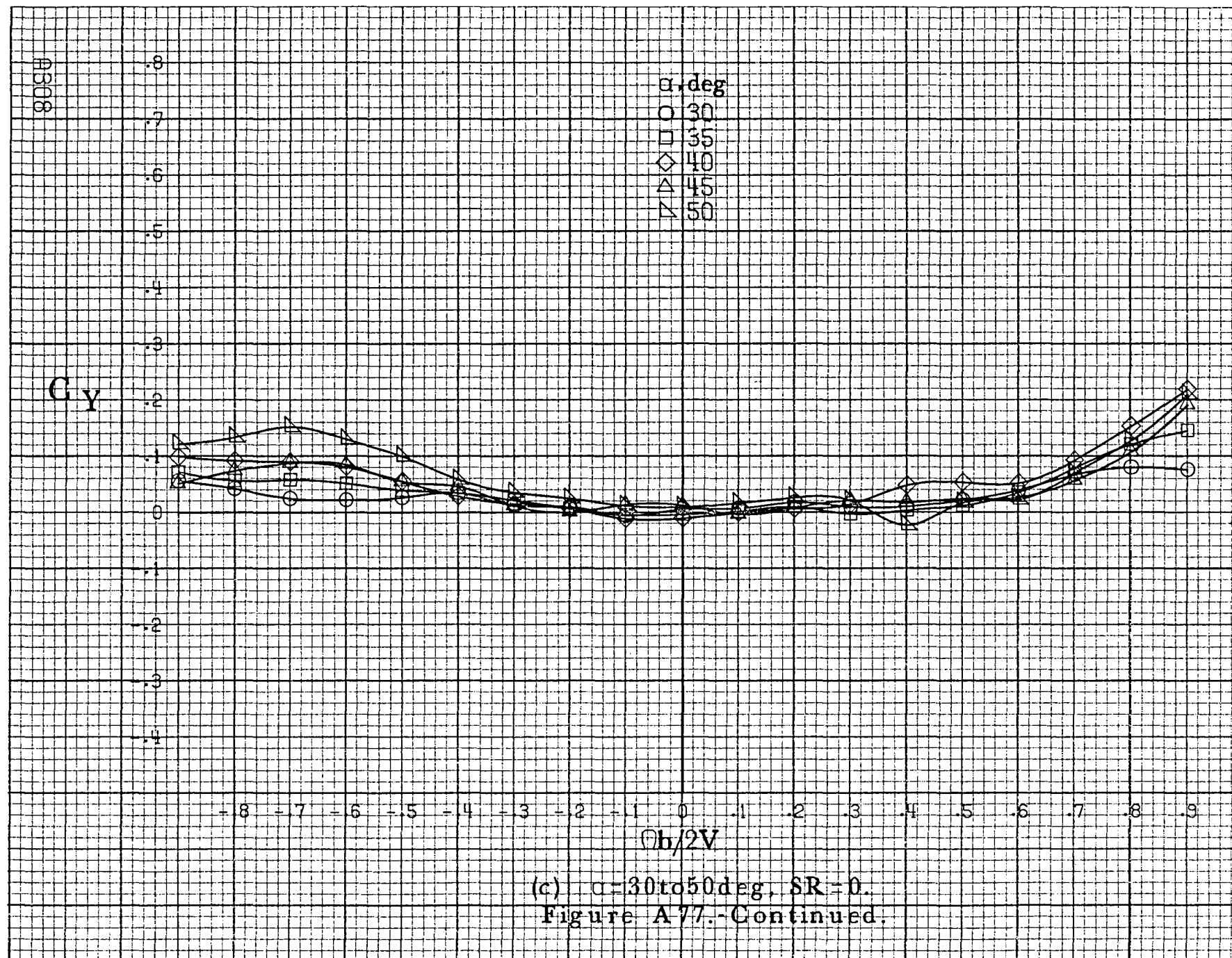


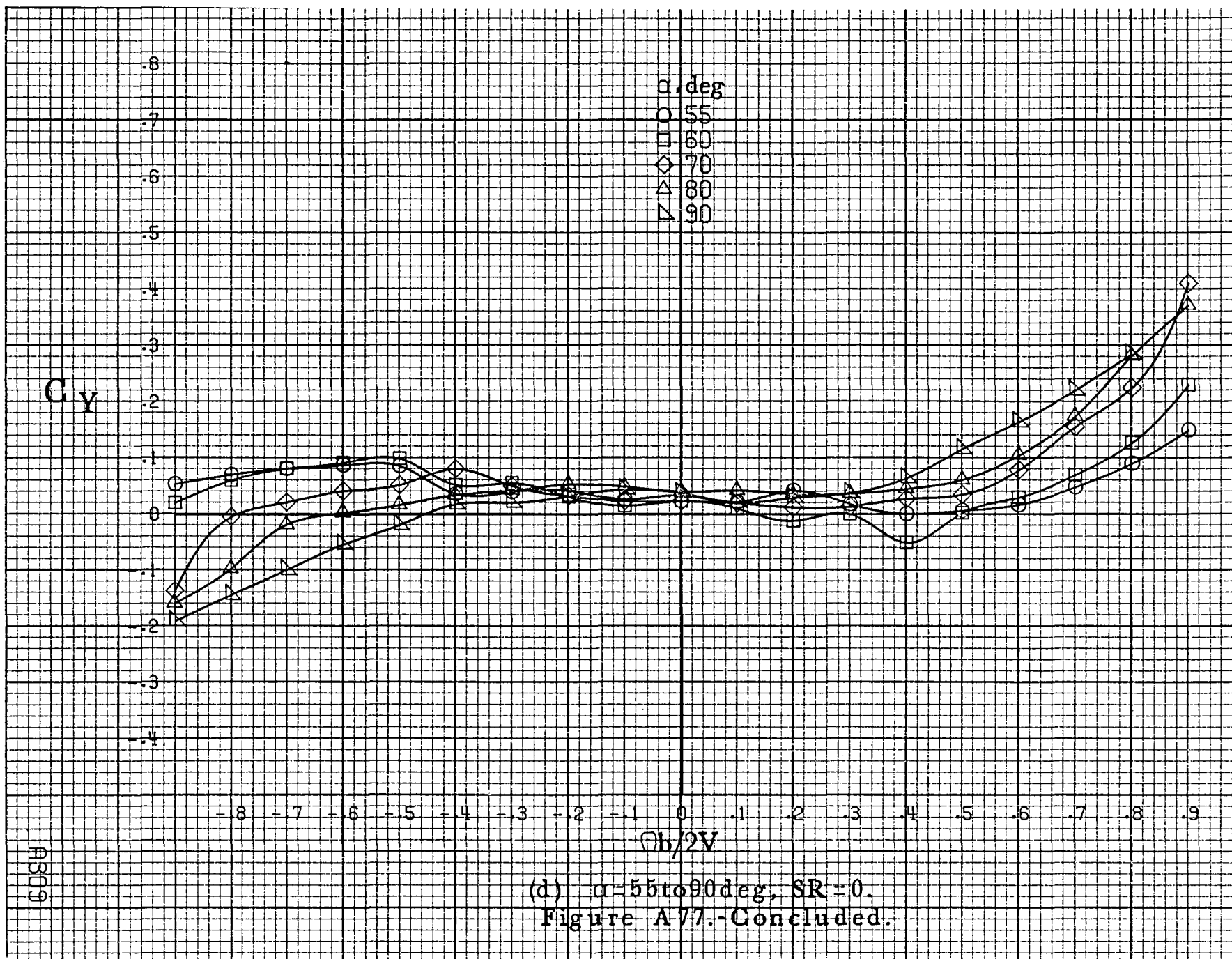


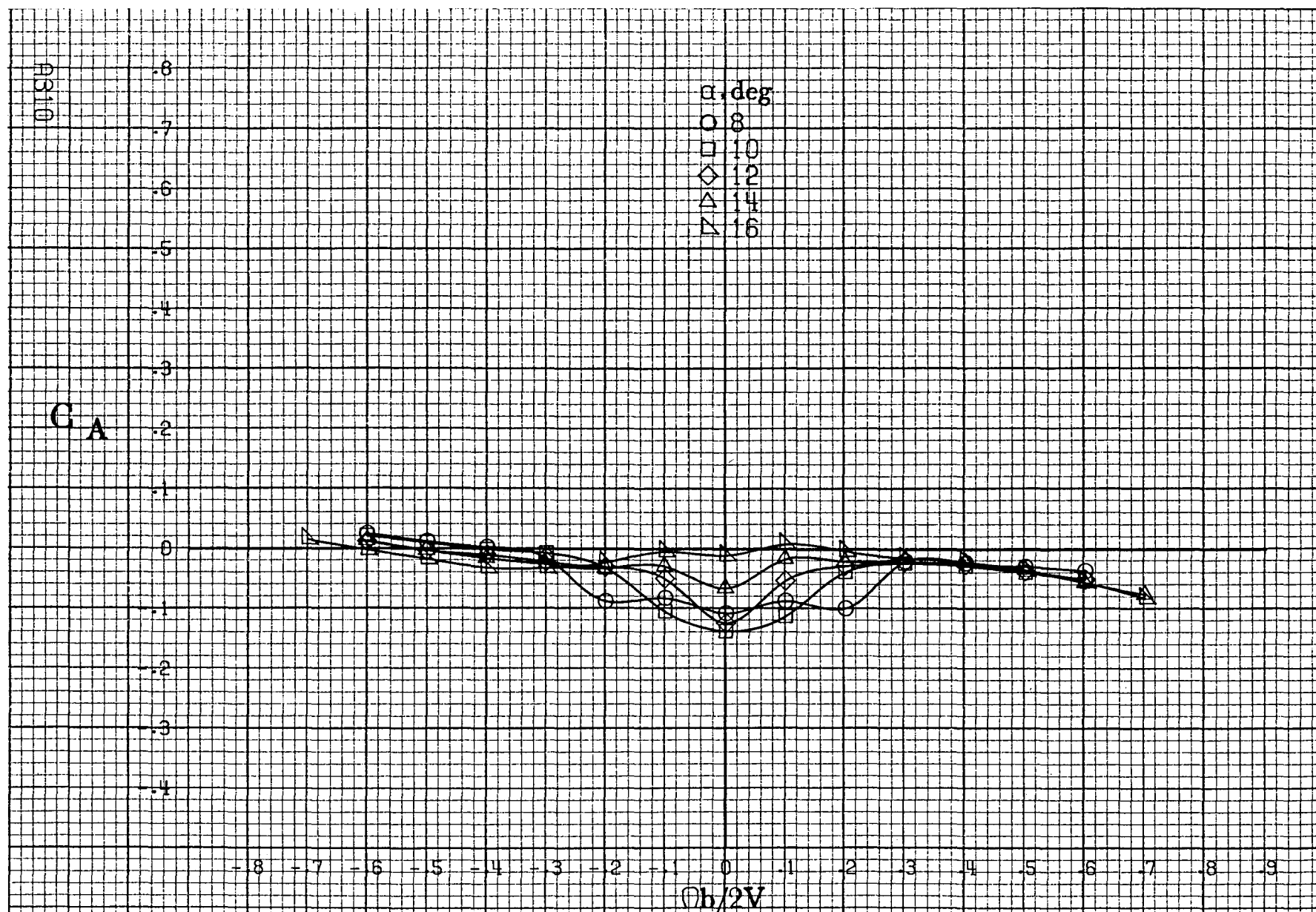
(a) $\alpha = 8 \text{ to } 16 \text{ deg}$, $SR = 91.4 \text{ cm (36 in)}$.

Figure A77 - Effect of rotation rate and angle of attack on side-force coefficient for complete long body, high wing configuration. $\delta_e = 0^\circ$, $\delta_a = 0^\circ$, $\delta_r = 0^\circ$, $\beta = 0^\circ$.



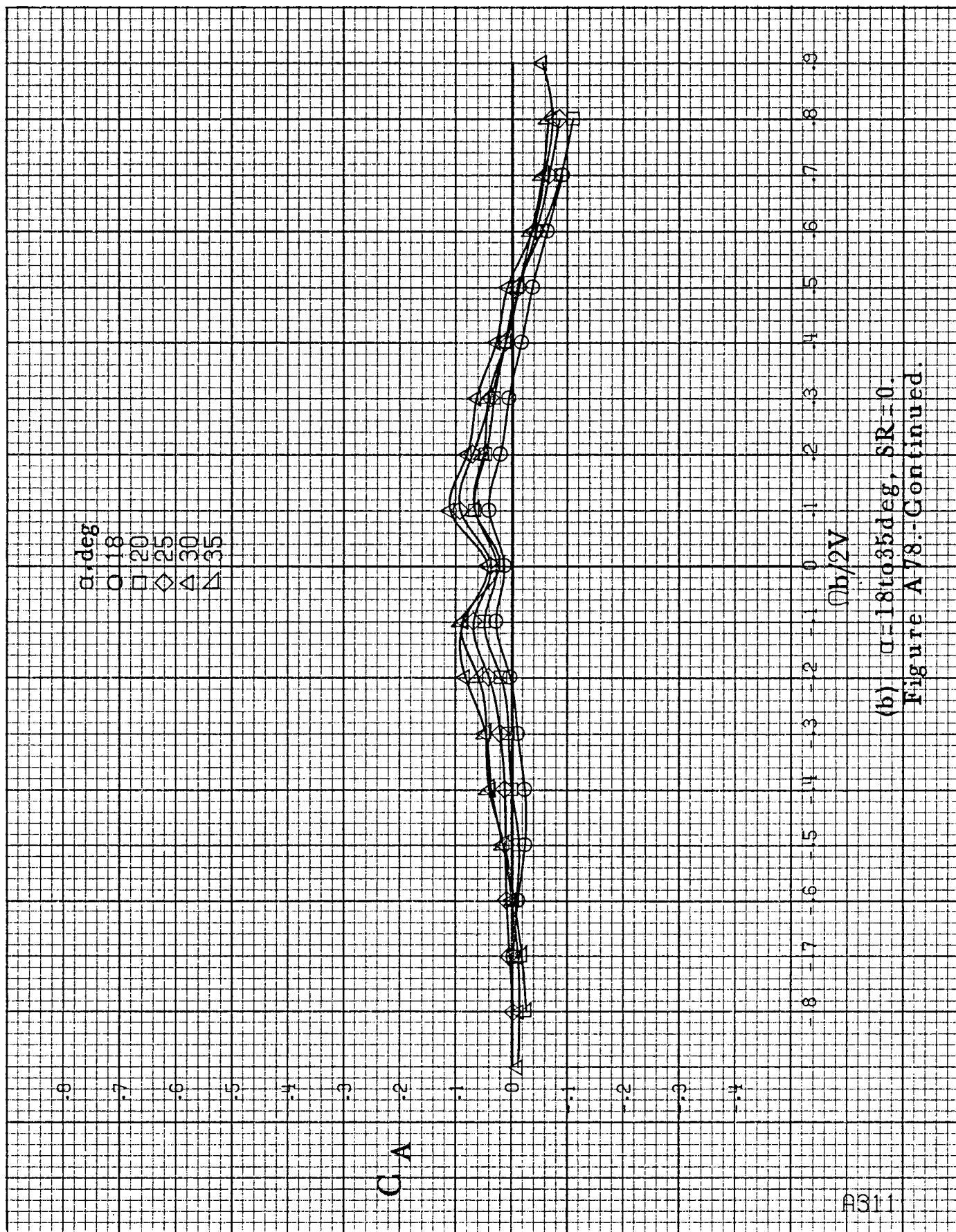




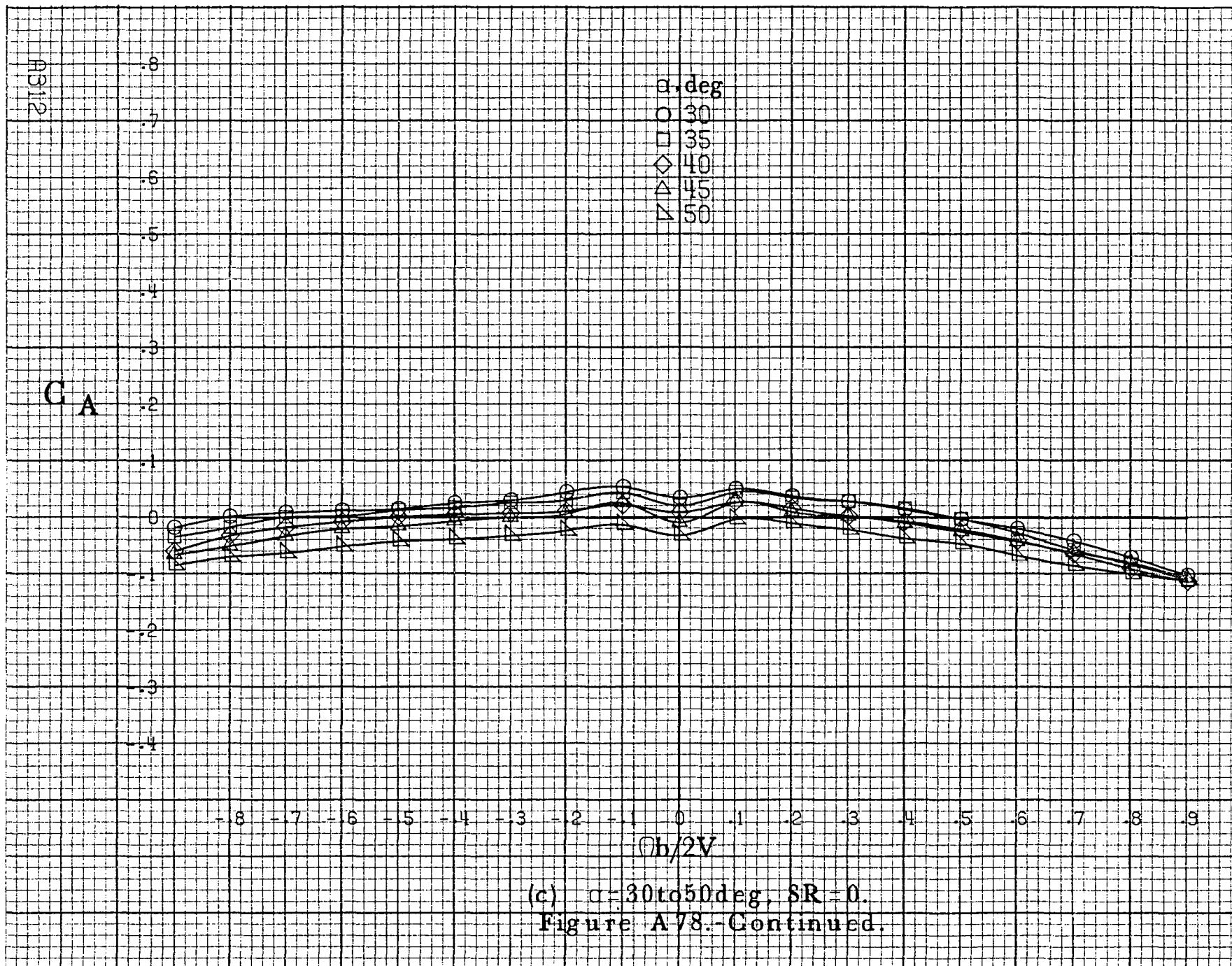


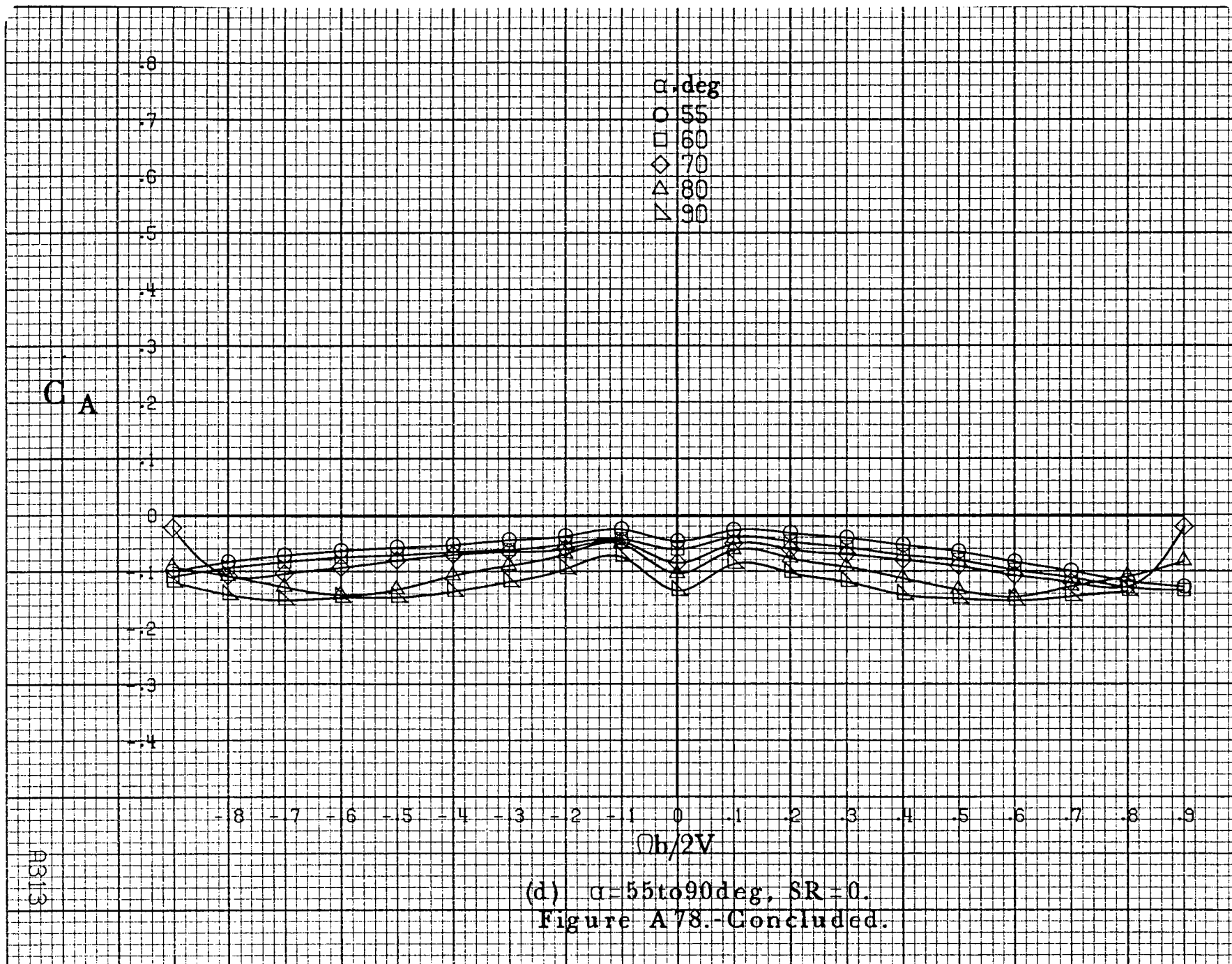
(a) $\alpha = 8$ to 16 deg, $SR = 91.4 \text{ cm (36 in)}$.

Figure A78.-Effect of rotation rate and angle of attack on axial-force coefficient for complete long body, high wing configuration. $\delta_e = 0^\circ$, $\delta_a = 0^\circ$, $\delta_r = 0^\circ$, $\beta = 0^\circ$.



(b) $\alpha = 18$ to 35° , $SR = 0$.
Figure A78.-Continued.





1. Report No. NASA CR-3246		2. Government Accession No.		3. Recipient's Catalog No.	
4. Title and Subtitle ROTARY BALANCE DATA FOR A TYPICAL SINGLE-ENGINE GENERAL AVIATION DESIGN FOR AN ANGLE-OF-ATTACK RANGE OF 8° TO 90°. I - INFLUENCE OF AIRPLANE COMPONENTS FOR MODEL D.				5. Report Date March 1983	
				6. Performing Organization Code	
7. Author(s) John Ralston				8. Performing Organization Report No.	
9. Performing Organization Name and Address Bihle Applied Research, Inc. 400 Jericho Turnpike Jericho, New York 11753				10. Work Unit No.	
				11. Contract or Grant No. NAS1-16205	
12. Sponsoring Agency Name and Address National Aeronautics and Space Administration Washington, D.C. 20546				13. Type of Report and Period Covered Contractor Report	
				14. Sponsoring Agency Code 505-43-13-01	
15. Supplementary Notes Langley Technical Monitor: James S. Bowman, Jr. Topical Report					
16. Abstract The influence of airplane components, as well as wing location and tail length, on the rotational flow aerodynamics is discussed for a 1/6-scale general aviation airplane model. The airplane was tested in a built-up fashion (i.e., body, body-wing, body-wing-vertical, etc.) in the presence of two wing locations and two body lengths. Data were measured, using a rotary balance, over an angle-of-attack range of 8° to 90°, and for clockwise and counter-clockwise rotations covering an $\Omega b/2V$ range of 0 to 0.9.					
17. Key Words (Suggested by Author(s)) General aviation Spinning Rotary balance High angle-of-attack wind tunnel data				18. Distribution Statement Unclassified - Unlimited Subject Category 02	
19. Security Classif. (of this report) Unclassified		20. Security Classif. (of this page) Unclassified		21. No. of Pages 390	
				22. Price* A17	

National Aeronautics and
Space Administration

Washington, D.C.
20546

Official Business
Penalty for Private Use, \$300

SPECIAL FOURTH CLASS MAIL
BOOK

Postage and Fees Paid
National Aeronautics and
Space Administration
NASA-451



NASA

POSTMASTER: If Undeliverable (Section 158
Postal Manual) Do Not Return
